T2R2 東京科学大学 リサーチリポジトリ
Science Tokyo Research Repository

論文 / 著書情報
Article / Book Information

題目(和文)	
Title(English)	Real-Time and Real-Space Tracking of the Self-Assembly of Block Copolymer Thin Films
著者(和文)	アルヴィン チャンドラ
Author(English)	Alvin Chandra
出典(和文)	学位:博士(工学), 学位授与機関:東京工業大学, 報告番号:甲第11608号, 授与年月日:2020年9月25日, 学位の種別:課程博士, 審査員:早川 晃鏡,扇澤 敏明,芹澤 武,松本 英俊,戸木田 雅利
Citation(English)	Degree:Doctor (Engineering), Conferring organization: Tokyo Institute of Technology, Report number:甲第11608号, Conferred date:2020/9/25, Degree Type:Course doctor, Examiner:,,,,
学位種別(和文)	博士論文
Type(English)	Doctoral Thesis

Powered by T2R2 (Science Tokyo Research Repository)

Fall 2020 Doctoral Thesis

Real-Time and Real-Space Tracking of the Self-Assembly of Block Copolymer Thin Films

Tokyo Institute of Technology
School of Materials and Chemical Technology
Department of Materials Science and Engineering
Hayakawa Group
Alvin Chandra

This page was intentionally left blank.

Preface

To the juniors of the Hayakawa Group or anyone who may be reading my thesis, thank you for taking the time to go through my thesis. I would like to first say that I was only able to complete this thesis with the support of those around me. There were definitely times when things were difficult and not going as planned, but I was never alone in my endeavors. Contrary to what many may think, it is definitely okay to make mistakes. Nobody gets things right the first time and we can just slowly and gradually learn from our mistakes and move on. If somewhere along the way, you realize that graduate school is not for you, that is okay too. There are many other options out there. With a little courage, we can explore what we want to do anywhere. The world is beautiful and precious. No matter what path you choose, do remember that we are never alone and that there will always be someone there for you. Even if we have never met in person, if you have any questions, be it about research, career decisions, or otherwise difficult topics to bring up with the professors, please feel free to reach out to me at alvin.chandra.chan@gmail.com at any time. I will be willing to listen to any questions or just to talk. Once again, thank you to everyone who has supported me in my 25+ years. It has been mostly good so far and I hope to share the good times with you as well. Again, it is okay to fail. It is okay to want to quit. It is okay to say No. Let's work things out together. Thank you for reading.

早川研の後輩やこの博士論文を読んでいただいている方々へ、私はこの数年間、周囲に支えられ、この博士論文を完成することができました。途中で、つらい時とやめたい時は多々ありましたが、最初から最後まで、私は決して独りぼっちではありませんでした。仲間として支え合うことで、どんなつらいことがあっても乗り越えられると思います。私たちはいつだっても孤独ではありません。これは絶対に忘れてはいけないことです。また、研究や就職活動、英語でのコミュニケーションなど、人生で新しいことに挑戦するときはもちろ

ん躓いたり、間違えたりすることはたくさんあります。あまり言われたことがないかもしれませんが、間違いをしてもいいです。人間はどうしてもいつか、どこかでミスをします。ちょっとしたミスをしたからって、終わりではありません。新しいことを学んで、先に進めばいいと思います。周りには話を聞いてくれる人、助けてくれる人は絶対にいます。研究には向いていない、大学院をやめたい、周りからのプレッシャーが半端ないなどと思ってしまう時もあるかもしれません。そう思うことは悪いことではありませんし、大学院をやめるのも選択肢の一つです。人生は一度しかないので、好きのように生きればいいと思います。研究以外で、楽しくできることはたくさんあるでしょう。もし何か相談したいことがあれば、研究やキャリアのことでも、先生方に言いにくいことでも、なんでもいいですので、遠慮なく alvin.chandra.chan@gmail.com で私に連絡してください。今まで周囲の皆に支えていただいたように、私は皆を手伝いたいです。これからの良いことも、できれば皆にも分けてあげたいと思います。最後に改めて皆にお伝えしたいです。ありがとうございました、これからもよろしくお願いします。

Alvin Chandra

Table of Contents

Preface 3

Chapter 1 General Introduction 9

1-1 The Information Age 9

1-2 193 nm Photolithography: The Current Generation 11

1-3 Next-Generation Lithography (NGL) 15

1-4 Block Copolymer Lithography (BCPL) 18

1-5 Directing the Self-Assembly Process 21

1-6 Directed Self-Assembly (DSA): The Current State 25

1-7 Polystyrene-*block*-Poly(methyl methacrylate) (PS-*b*-PMMA) 30

1-8 BCP Self-Assembly 31

1-9 How to Increase χ_{eff} 35

1-10 Etch Selectivity 39

1-11 Controlling the Interfaces 44

1-12 Synthesis of the BCP 52

1-13 Metrologies for the Analysis of BCP Nano-assemblies 56

1-14 Real-Time and Real-Space Tracking of BCP Self-Assembly 63

1-15 Scope of this Study 70

1-16 References 74

Chapter 2 Evolution of Ordered Structures in PS-*b*-PMMA Thin Films on Unpatterned and COOL Process DSA Substrates 95

2-1 Introduction 95

2-2 Experimental Section 97

2-2-1 Materials 97

2-2-2 Instruments 97

2-3 Results and Discussion 98

2-3-1 Development of a Fingerprint Pattern 98

2-3-2 Structural Evolution in COOL Process DSA Substrates 104

2-4 Conclusion 118

2-5 References 119

Chapter 3 Real-Time and Real-Space Evolution and Alignment of Lamellae on Chemically Pre-Patterned SMART™ Process DSA Substrates 121

3-1 Introduction 121

3-2 Experimental Section 122

3-2-1 Instruments 122

3-2-2 Sample Preparation 123

3-3 Results and Discussion 123

3-3-1 Incremental Annealing Profile 123

3-3-2 Isothermal Annealing after Incremental Annealing 140

3-4 Bibliography 146

3-5 References 147

Chapter 4 Defect Dynamics and Annihilation Pathways of Lamellar Patterns under the Influence of SMART™ Process Chemoepitaxial DSA 151
4-1 Introduction 151
4-2 Experimental Section 154
4-2-1 Instruments 154
4-2-2 Sample Preparation 154
4-3 Results and Discussion 154
4-3-1 Notes on Limitations of the AFM System 156
4-3-2 Snapshots of Isothermal Experiments 160
4-3-3 Defect Evolution and Annihilation Pathways 236
4-3-4 Orientational Defects 237
4-3-5 Disclination Defects 253
4-3-6 Dislocation Defects 267
4-3-7 Other Defect Types 268
4-3-8 Complicated Defect Areas 270
4-3-9 Ultra-High-Speed Defect Tracking 277
4-4 Conclusion 284
4-5 References 284

Chapter 5 Evolution and Hexagonal Arrangement of Dot Patterns in Perpendicular Cylinders on Chemically Pre-Patterned DSA Substrates 289
5-1 Introduction 289
5-2 Experimental Section 290
5-2-1 Instruments 290
5-2-2 Sample Preparation 291
5-3 Results and Discussion 291
5-4 Conclusion 303
5-5 References 304

Chapter 6 Synthesis of Poly(3(2,2',2'',4,4',4'',6-heptaethyl polyhedral oligomeric silsesquioxane)propyl methacrylate)-*block*-poly(2,2,2-trifluoroethyl methacrylate) (PMAPOSS-*b*-PTFEMA) 305
6-1 Introduction 305
6-2 Experimental Section 306
6-2-1 Materials 306
6-2-2 Instruments 307
6-2-3 Synthesis of PMAPOSS 307
6-2-4 Synthesis of PTFEMA 308
6-2-5 Synthesis of PMAPOSS-*b*-PTFEMA in Toluene/HFIP 308
6-2-6 Synthesis of PMAPOSS-*b*-PTFEMA in 1,4-Dioxane 309
6-2-7 Synthesis of PTFEMA-*b*-PMAPOSS 309
6-2-8 Film Preparation 310
6-3 Results and Discussion 310
6-3-1 Synthesis and Characterization of PMAPOSS and PTFEMA 310
6-3-2 Planning for the Synthesis of the BCPs 313
6-3-3 Solubilities of MAPOSS, PMAPOSS, and PTFEMA 314
6-3-4 Synthesis and Characterization of PMAPOSS-*b*-PTFEMA 315

6-3-5 Synthesis and Characterization of PTFEMA-*b*-PMAPOSS 317
6-3-6 Bulk Morphologies of the Synthesized BCPs 318
6-4 Conclusion 324
6-5 References 324

Chapter 7 Disorder-Order Evolution of Sub-10 nm Perpendicular Lamellar Structures of PMAPOSS-*b*-PTFEMA Thin Films on Bare Silicon Substrates 327
7-1 Introduction 327
7-2 Experimental Section 328
7-2-1 Materials 328
7-2-2 Instruments 328
7-2-3 Sample Preparation 329
7-3 Results and Discussion 330
7-3-1 Sample Preparation 330
7-3-2 Identifying the Microdomains in AFM Phase Images 335
7-3-3 Thermal Annealing for Combinatorial Studies 336
7-3-4 Growth of Perpendicular Lamellae from “Disorder” 337
7-4 Conclusion 344
7-5 References 345

Chapter 8 Conclusion and Future Prospects 349
8-1 Closing Remarks 349

Appendix: Supporting Information 353
A-1 Matlab Codes for Orientational Order Parameter 353
A-2 Matlab Codes for Correlation Length 365
A-3 List of In Situ AFM Videos 375

List of Publications and Presentations 376

Acknowledgements 381

This page was intentionally left blank.

Chapter 1: General Introduction

1-1 The Information Age

As I write this thesis in the midst of the SARS-CoV-2 (severe acute respiratory syndrome coronavirus 2, COVID-19) outbreak on my laptop while staying at home and communicating with others online through web meetings and calls, it is apparent that we have become extremely reliant on our computers and the ability to transmit large amounts of information and data over long distances. Reflecting on the many epochs of history, each era has revolved around the latest ideas and technologies engineered from a novel material. With the invention of plastics, the transistor, and the internet in the 20th century, the Information Age was ushered in at the turn of the millennium. The Information Age is characterized by the transfer of huge quantities of information around the globe and is also known as the Silicon Age. This stems from the fact that a large proportion of the materials used as the foundation of our technologies, and particularly in the minute transistors that acts as the main working component for our integrated circuits and computers, is comprised of the Main Group IV element, silicon (Si).

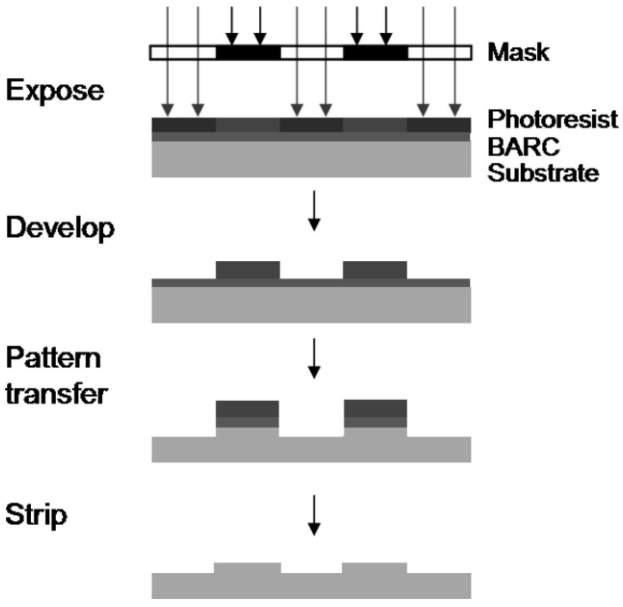


Figure 1-1. Schematic of a photolithographic process using a photoresist and mask. Reprinted with permission from Sanders, D. P., *Chem. Rev.* **2010**, *110* (1), 321-360. Copyright 2010 American Chemical Society.

In the pursuit of stronger and faster computers, the number of transistors found in an integrated circuit has doubled every two years. This observation, made in the mid-1960s, has come to be known as Moore's Law.[1] In order to increase the number of transistors in a given area (areal density), the ability to process silicon and develop circuitry patterns at smaller and smaller length scales is essential. Conventionally, a technique known as optical or photolithography is used to imprint the patterns needed to form the circuitry of an integrated circuit onto silicon wafers (Fig. 1-1).[2] A specific wavelength of light is shone through a patterned mask onto a resist laid atop a silicon wafer. Depending on the type of resist used, either the area exposed to or covered from the light can be selectively removed. This leaves behind a topographic pattern which is then transferred down onto the silicon wafer, yielding a circuitry pattern consisting of combinations of basic geometries such as lines and spaces (L/S), or an array of holes or pillars. The first photolithography process produced patterns with line features of ~10 μm using a light source with a 436 nm wavelength (g-line). Although integrated circuits with thinner circuitry need to be developed to increase the areal density of the transistors, the minimum domain spacing obtainable using photolithographic techniques is inherently reliant on the wavelength of light used. This is described by the Rayleigh Equation,

$$R = k_1 \frac{\lambda_0}{n \cdot \sin\theta} \qquad (1\text{-}1)$$

where k_1 is the Rayleigh coefficient of resolution, λ_0 is the wavelength of light in vacuum, n is the refractive index of the incident medium, θ is the angular aperture of the lens, and $n \cdot \sin\theta$ is also referred to as the numerical aperture (NA) of the imaging system.[2] Traditionally, to reduce the minimum domain spacing achievable, the light source was changed progressively to reduce the wavelength of light released. With each change, novel resists and processing techniques needed to be developed, adding to the costs of research, development, and production.[3] The λ_0 of the light source went from 436 nm in the 1970s down to 405 nm (h-line), 365 nm (i-line), 248 nm (KrF laser), 193 nm (ArF laser), and finally,[2] pilot production lines of a next-generation lithography (NGL) technology using 13.5 nm

(extreme ultraviolet, EUV) light sources have started to be implemented industrially around 2018 – 2019.[4] This decrease in the wavelength of light used has enabled us to develop precise and minute patterns with domain spacings ranging from 10 μm down to 30 – 40 nm,[5,6] thereby driving forward the development of faster and stronger computers.

1-2 193 nm Lithography: The Current Generation

Prior to the implementation of the first NGL technique involving EUV lithography (EUVL), the decrease in λ_0 used by the photolithographic family of technologies stalled at the 193 nm technology node which uses an ArF laser as a light source. At the time, significant efforts had been made to develop new resists and processing techniques for the implementation of what was then thought of to be *the next-generation* 157 nm technology node. However, due to numerous technical issues and significantly rising costs, the development of 157 nm lithography was abandoned by the mid-2000s.[7] Instead, efforts were diverted to extending the capabilities of existing 193 nm lithography while other NGL technologies were being developed.

The Rayleigh Equation (Eq. 1-1), which describes the minimum resolution limit R for photolithographic technologies, indicates that aside from decreasing λ_0, the NA of the imaging system can be increased. Specifically, the refractive index of the incident medium n, and the angular aperture of the lens used θ can be adjusted to decrease R. Given that k_1 is a constant at ~0.25, λ_0 = 193 nm, and that the maximum limit for NA = 0.93 in vacuum, we can determine the patterning limit for 193 nm ArF lithography in vacuum to be ~52 nm. However, if the incident medium is changed from a vacuum to a higher refractive index fluid, such as by immersing the refractive lens in water (n = 1.44), the NA can be increased to 1.35, enabling a minimum theoretical full-pitch resolution of 36 nm.[8] However, as the quality of the patterns drops significantly when developing patterns near the resolution limit, 80 nm is agreed to be the minimum practical full-pitch resolution for 193 nm immersion lithography.[9] To further achieve smaller pattern dimensions with high fidelity, further innovations were necessary.

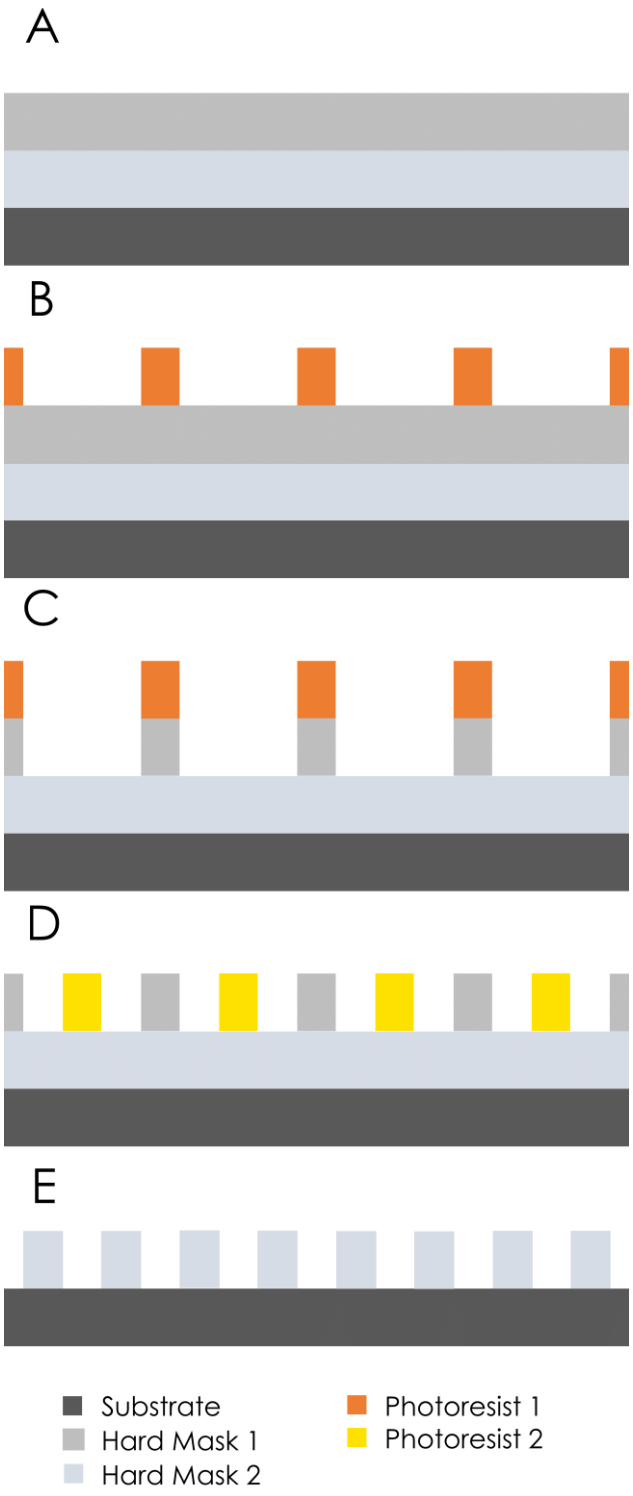


Figure 1-2. Illustration of the litho-etch-litho-etch (LELE) multiple patterning process. (A) Onto a layered substrate with two hard masks on top, (B) a photoresist is first patterned at a given periodicity and (C) the pattern is transferred onto the first hard mask. (D) Upon removal of the first photoresist, a second photoresist is patterned at the same periodicity as

the first, but shifted exactly half the periodicity to one side. (E) The final pattern is transferred down onto the hard mask to yield a final pattern density that is twice that of the initial photoresist pattern density.

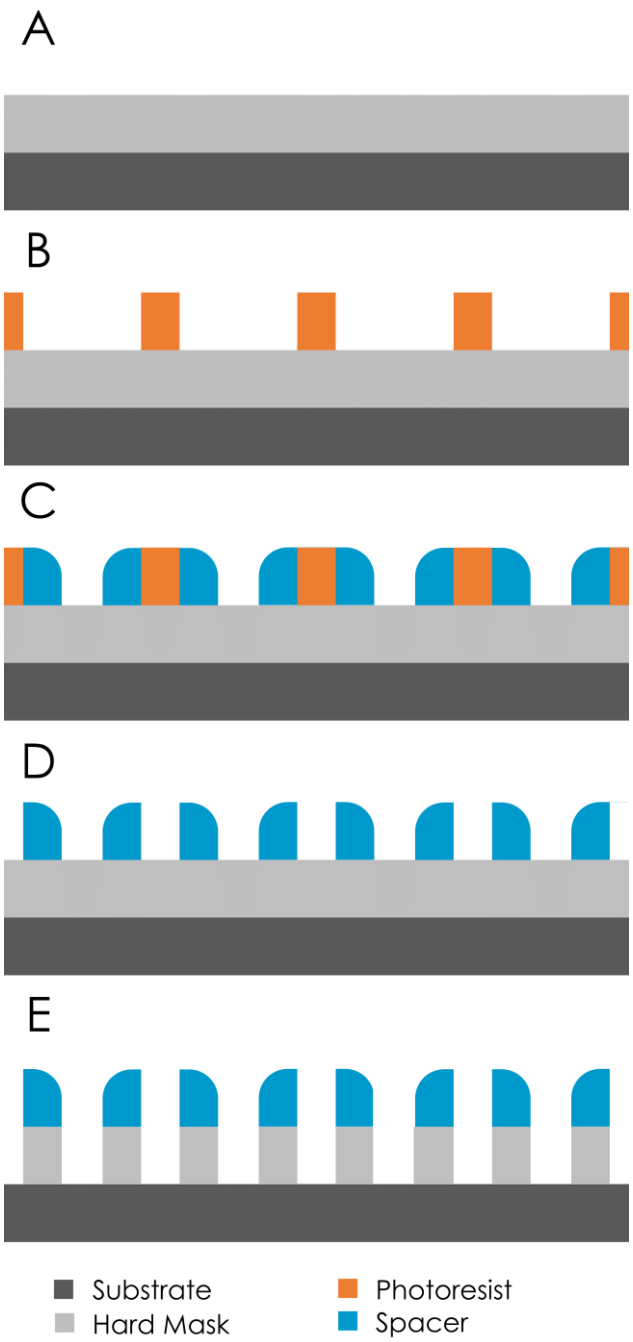


Figure 1-3. Illustration of the self-aligned double patterning (SADP) process. (A) Onto a multi-layered substrate with a hard mask at the top, (B) a photoresist is first patterned at a given periodicity. (C) Spacers are deposited directly onto the sides of the photoresist without needing precise alignment procedures, and (D) the photoresist is stripped. (E) The pattern is

etched into the hard mask to yield a pattern density double that of the initial photoresist pattern.

In addition to 193 nm immersion lithography, a number of multiple patterning techniques were developed to further extend the capabilities of 193 nm lithography.[10,11] Particularly, double patterning techniques such as litho-etch-litho-etch (LELE, Fig. 1-2) and self-aligned double patterning (SADP, Fig. 1-3) gained significant traction industrially. A relatively simple addition to single exposure 193 nm immersion lithography, LELE involves a two-step patterning process. Firstly, a pattern is developed at a given length scale. Then, the mask or substrate is moved slightly, and a second exposure results in a final pattern that exhibits twice the density of the first. However, LELE requires extremely precise angstrom-scale alignment for the development of a final pattern with even spacing between the trenches, thus complicating the production process. In contrast, SADP avoids the need for alignment by depositing a spacer directly onto the side walls of a topographic pattern developed from a single exposure. The initial pattern is then removed, and the remaining spacers are automatically at the desired high-density etch spacing. Technically, further miniaturization of the pattern sizes could be achieved by simply repeating the process once (self-aligned quadruple patterning, SAQP), or even twice (self-aligned octuple patterning, SAOP) to achieve a final pattern one-fourth or one-eighth that of the initial pattern domain spacing. Assuming an initial pattern of 80 nm was achieved with a single exposure of 193 nm immersion lithography, SADP, SAQP, and SAOP can theoretically yield patterns with domain spacings of 40, 20, and 10 nm. Although a domain spacing of 20 or 10 nm can make 193 nm immersion lithography with SAQP or SAOP competitive as an NGL candidate, each additional processing step increases the cost of production exponentially, halves throughput, and allows for opportunities for mistakes in production. Therefore, a lithographic technology that is capable of forming reliable, defect-free patterns at low cost and high-throughput is highly desirable.

1-3 Next Generation Lithography (NGL)

As the microelectronics industry continues to demand for the capability to pattern at smaller dimensions while avoiding undesirable multiple processing methods, novel NGL technologies need to be developed. For many years, the NGL candidates that have gained the most attention from academia and industry include electron beam lithography (e-beam lithography, EBL),[12–14] scanning probe lithography (SPL),[15,16] nanoimprint lithography (NIL),[17,18] EUVL,[19–21] and block copolymer lithography (BCPL).[22,23]

Both EBL and SPL fall under a category known as 'maskless lithography', in that a pre-patterned mask is not required to change the pattern produced. Based on similar principles, the roots of EBL can be traced back to traditional scanning electron microscopy (SEM) technologies.[24] By focusing an electron beam onto an e-beam resist, a detailed pattern can be drawn directly onto the surface. Additionally, as EBL does not rely on lenses to diffract light, EBL does not face a theoretical resolution limit and can be used to prepare minute and precise patterns with half-pitch features in the sub-10 nm length scale.[25] Similarly, SPL finds its origins in surface probe microscopy (SPM) technologies.[15] SPL encompasses a range of techniques, all of which center around the use of a probe to print a pattern onto a surface.[16] The most basic method involves using the probe to directly, mechanically, and physically scratch a pattern onto the surface, likely damaging both the probe and the surface. In recent years however, more sophisticated SPL patterning options have become available.[16] Patterns could be developed by either adding to or removing material from a substrate through mechanical, chemical, thermal, or electrical probe-surface interactions. For example, by using a thermally heated probe, heat could be used to efficiently remove material from a substrate without having to mechanically remove material. Alternatively, the thermally heated probe could be used to induce thermally activated reactions to alter the functionalities of the surface or deposit thermally active materials onto the surface. By utilizing a probe to directly imprint a pattern onto a surface, SPL is also capable of constructing minute sub-10 nm half-pitch patterns. However, the crux of 'maskless' lithographic technologies such as EBL and SPL is that the throughput is

significantly lower as these techniques require the direct printing of patterns one line at a time. Therefore, although EBL and SPL can be useful for developing precise sub-10 nm half-pitch patterns at small scales, it is not possible to efficiently implement EBL and SPL in high volume manufacturing.

In direct contrast to the 'maskless' lithographic techniques that require the line-by-line writing of patterns, NIL focuses on the opposite approach. As the name implies, *nanoimprint* lithography *imprints* nanometer-scale patterns onto a resist using a preformed template,[26] similar to the ancient art of block printing. As the pattern is impressed onto a resist, the resist flows to take on the topographic pattern of the template and is typically cured by heating or ultraviolet (UV) irradiation. Once the template is removed, the resist stays in the shape of the topographic pattern which can then be transferred onto the substrate. Given that this process could be conducted on a rolling production line, NIL has the potential for extremely high throughput for mass manufacturing. However, the main issue with NIL is that a reliable, defect-free template must first be manufactured through other means. Additionally, if the surface is not perfectly flat or if the template has been relatively worn out, bubbles and defects could form in the imprinted pattern, raising concerns over the reliability of NIL.

Subsequently, as the successor to the photolithographic family of technologies, EUVL has gained one of the most traction in industrial research and development, with various companies already implementing pilot production lines using EUVL.[5,6] Compared to traditional 193 nm immersion lithography, EUVL utilizes a light source with a wavelength of 13.5 nm,[19,20,27] thereby potentially allowing for patterning at significantly smaller domain spacings. However, the NA for EUVL is currently limited to ~0.33,[6] giving a theoretical minimum full-pitch resolution limit of 26 nm. However, as seen in 193 nm immersion lithography, the development of patterns near the theoretical resolution limit results in high levels of defectivity. Therefore, instead of relying on multiple patterning processes with 193 nm immersion lithography coupled with LELE or SADP, the mass production of patterns with domain spacings on the 30 – 40 nm scale using single exposure EUVL has been realized.[5,6] Among issues such as needing a much stronger light source with significantly higher power

output and energy consumption due to the low quantum efficiency of available resists, controlling the stochastics during the pattern development process in the resist to reduce defectivity, and difficulties in increasing the NA, directly patterning sub-10 nm half-pitch (or sub-20 nm full-pitch) patterns using single exposure EUVL is highly challenging. Regardless, the demand for patterning capabilities at decreasingly smaller dimensions remains. Therefore, to produce sub-20 nm full-pitch patterns using photolithography, multiple patterning processes using either the traditionally reliable 193 nm immersion lithography and SAQP, or double exposure EUVL with LELE or SADP is required. In any case, multiple patterning complicates the production process, lowers throughput, and increases the cost of manufacturing and is undesirable.

Conversely, BCPL can be used to mitigate the issues of cost, throughput, and resolution limits. Block copolymer (BCP) lithography is based on the bottom-up self-assembly of BCPs,[23,28–34] a category of materials in which multiple polymers are connected together at a number of junction points. Compared to the alternative NGL technologies, BCPL offers a number of advantages. Firstly, BCPs are relatively cheap materials to produce, and special equipment is not required to fully integrate BCPL into existing semiconductor manufacturing lines, thereby reducing the cost of production, and maintaining high throughput. Additionally, the self-assembled nanostructures of BCPs can form ordered patterns with half-pitch domain spacings down to ~2 nm,[35] a distance that approaches the limits for the quantum tunneling of electrons in Si materials. Therefore, BCPL holds great potential as a NGL candidate. While the potential for smooth integration into existing production lines and the bottom-up nature of BCP self-assembly allows for BCPL to overcome issues of cost, throughput, and resolution limits, numerous challenges remain before BCPL can be implemented industrially for high volume manufacturing.

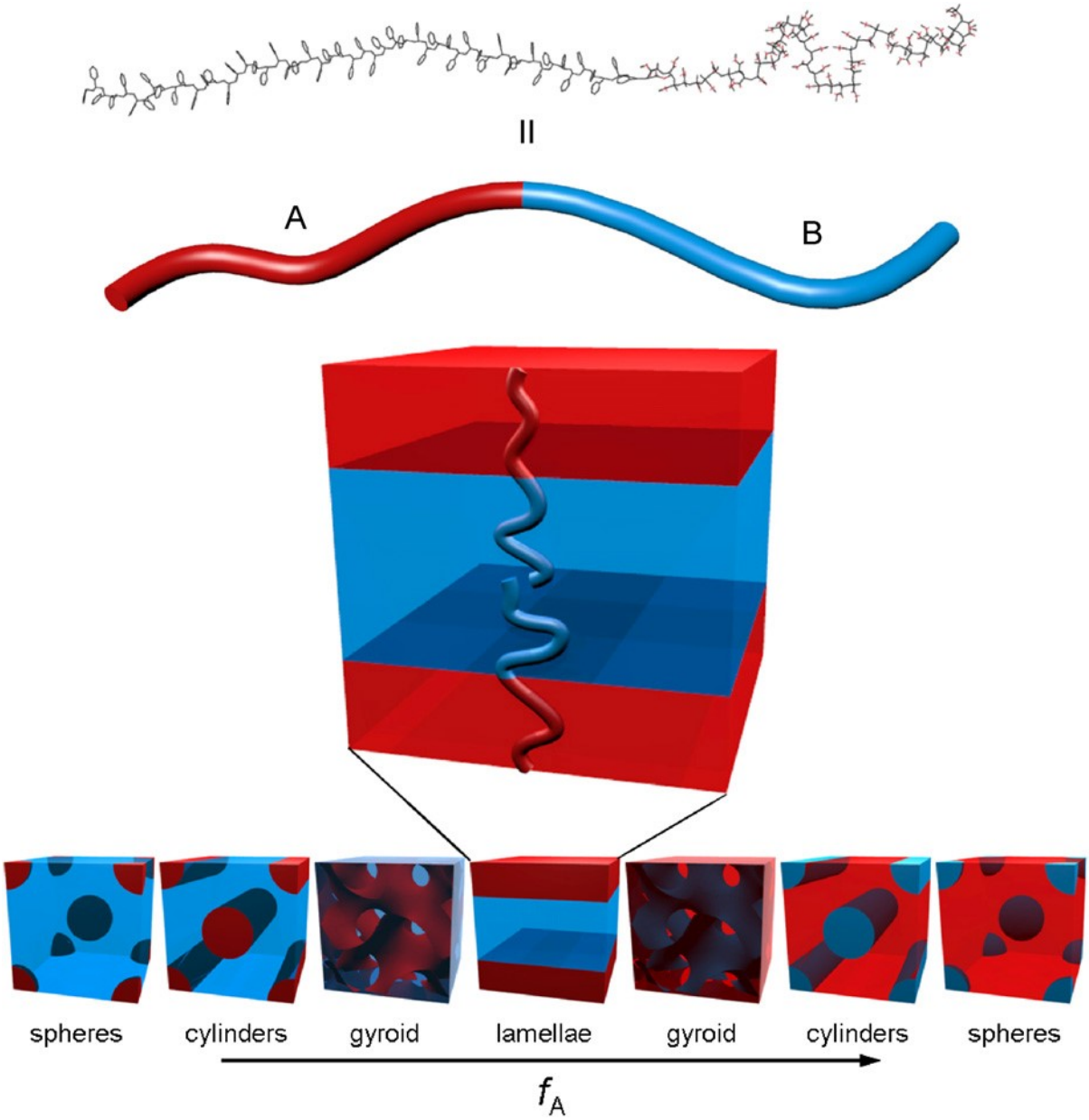


Figure 1-4. Illustration of the self-assembly of an AB-type diblock copolymer into ordered nanostructures including spheres, cylinders, gyroid, and lamellae, depending on the volume fraction (*f*) of the A block. Reprinted with permission from Darling, S. B., *Prog. Polym. Sci.* **2007**, *32* (10), 1152-1204. Copyright 2007 Elsevier B. V.

1-4 Block Copolymer Lithography (BCPL)

The self-assembly of BCPs (Fig. 1-4) have been studied since the 1960s, however, the earliest studies typically focused on the self-assembly behavior in the bulk or melt.[36] While the self-assembly behavior of BCPs without the interference of external interfaces can be academically interesting, the BCPs need to self-assemble into ordered structures while

supported on a substrate in order to be used as a resist in lithographic applications. As the substrate introduced a level of constraint, characterizing the nano-assemblies on BCP thin films was comparatively difficult and studies of BCP thin films began to be reported around 1980.[37–39] However, it was only in 1997 when Park and co-workers demonstrated the applicability of BCP self-assembly to lithography (Fig. 1-5).[22] Thin films containing a monolayer of a polystyrene-*block*-polybutadiene (PS-*b*-PB) BCP that forms PB spheres in a PS matrix were prepared as a template. By selectively removing the PB domain through ozonolysis, a hexagonally-packed array of holes, which could then be utilized to prepare contact holes in semiconductor devices or other applications such as ultrafiltration and matter transport, could be obtained. Alternatively, the authors also demonstrated that by first staining the PB domain with osmium tetroxide (OsO_4) to increase the etch resistance of the PB domain against reactive ion etching (RIE), the PS domain could then be selectively removed using a mixed carbon tetrafluoride (CF_4) and oxygen (O_2) RIE process, leaving behind a hexagonal array of dots that can be transferred onto the substrate to prepare bit patterned media or high-density magnetic storage devices. Furthermore, the authors also showed that by preparing thin films of a cylinder-forming PS-*b*-PB BCP on a silicon nitride (SiN) substrate, a fingerprint-like striped pattern formed. When one domain was removed from the fingerprint pattern, line and space (L/S) structures could be obtained for lithographic applications. More recently, it was also shown that perpendicularly-oriented lamellae could be used to form fingerprint-like striped patterns, similar to that formed by parallel cylinders.[40,41] These fingerprint lamellae could then also be used to form the L/S structures for lithographic applications once one domain is selectively removed. With these demonstrations of the possibility for applying BCP self-assembly to lithography, both academia and industry began investing significant effort to the research and development of BCPL.

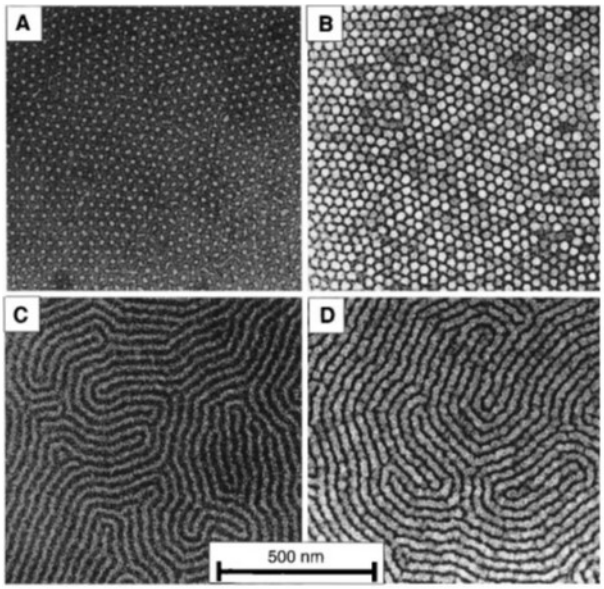


Figure 1-5. Scanning electron microscopy (SEM) micrographs of (A) a hexagonally-arranged spherical monolayer that was used to form a (B) hexagonally-arranged dot pattern, and (C) parallel cylinders forming a fingerprint-like structure that was used to develop (D) line and space structures on a thin film. Reprinted with permission from Park, M. et al *Science* **1997**, *276*, 1401-1404. Copyright 1997 American Association for the Advancement of Science.

For BCPL to become a viable technology in the mass manufacturing of semiconductor devices, a number of requirements as listed below, have to be met.

1. Defectivity: the defectivity of the self-assembled structure must be lower than 0.01 defect counts per cm^2.
2. Resolution: the BCP must self-assemble into ordered structures with sub-10 nm half-pitch domains.
3. Architecture: the BCP structure must be able to develop the required pattern.
4. Chemistry: the synthesized BCP must be free of metal residues that can remain on the substrate and interfere with electrical functionalities of the semiconductor device and possess sufficiently high etch contrast.
5. Orientation: the self-assembled structures of the BCP need to align in the appropriate direction for each application.

6. Annealing: the self-assembly process of the BCP must be completed in a timely, safe, reliable, and repeatable manner.

The different challenges listed above are issues found in the various steps of the BCPL process. However, as these processes are all connected, solutions for one challenge may pose as a challenge for another. Therefore, although solutions have been proposed for each challenge have been reported in the two dozen years since the first report proposing the use of BCPs in lithographic applications, industrial implementation of BCPL has not been realized as all of the challenges need to be resolved simultaneously.

1-5 Directing the Self-Assembly Process

In a survey of the participants of the 4th International Symposium on DSA 2018, a conference with a varied mix of academic and industrial participants from integrated chip manufacturers, material suppliers, equipment suppliers, etc., an overwhelming majority reported that the defectivity of the self-assembled structures on thin films is the most critical issue faced by BCPL.

As shown by early studies in BCPL,[22,40,41] the self-assembled structures of BCPs on unpatterned thin films are highly random and riddled with defects. For lithographic applications, the ability to reliable form straight lines is imperative. Therefore, various processes were developed to guide the self-assembly process and reduce the defectivity of the BCP structures.[42–51]

One of the earliest attempts at inducing long-range alignment in BCP structures involved using a directional shear force to align the domains in the direction of the force applied.[42,43] Shear alignment has traditionally been used in industrial manufacturing, particularly in the roll-casting and molding of plastic materials. Although a relatively simple mechanical process, shear alignment is largely restrictive to inducing long-range ordering in the bulk or melt and is difficult to apply to thin films for lithographic applications.

Alternatively, in place of mechanical alignment, an electric or magnetic field could also be used to align the BCP domains.[44–48] By applying a strong electric or magnetic field to a BCP film, rapid alignment of the domains on a large scale becomes possible. However, the

efficiency of alignment is reduced on thin films with thicknesses less than one μm due to surface interactions. Furthermore, to align the BCP domains using electromagnetic fields, not only is a lot of power required, special polymers with high dielectric contrasts (e.g. amphiphilic polymers) or magnetic susceptibility (e.g. liquid crystallinity) are required, thus limiting the applicability of electromagnetic field alignment to fairly special cases.

Another alignment method that is applicable to thin film systems and has wider applicability is the use of zone or gradient annealing.[49–52] A freshly spin-coated thin film is in a nearly disordered, highly random, and mixed state. Typically, to induce self-assembly, the thin film is annealed thermally on a hot plate or in an oven, or by introducing solvent vapor to reduce the glass transition temperature of the BCPs and act as an accelerant for self-assembly. However, such typical annealing methods are anisotropic and will produce structures with high degrees of random orientation and defectivity. Therefore, by introducing a thermal or photothermal gradient, self-assembly can begin at a starting point and the domains can align along the same direction as the moving front of the thermal gradient. However, although zone or gradient annealing can be effective in inducing long-range ordering of BCP thin film samples, this method requires annealing of the BCP domains to be conducted essentially “line-by-line”, reducing the potential throughput of the process and decreases the effectiveness for high volume manufacturing.

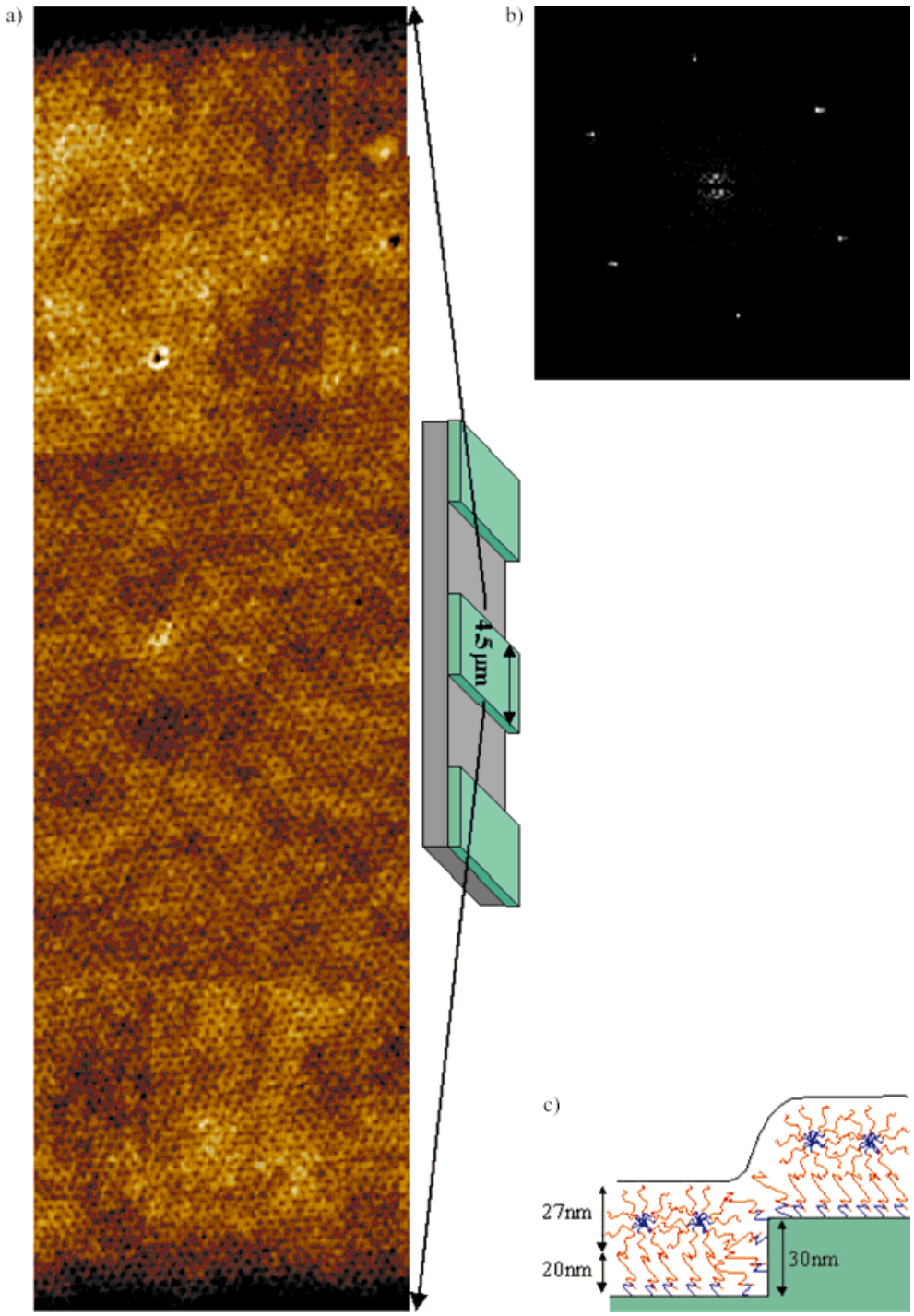


Figure 1-6. (a) Scanning force microscopy (SFM) image of hexagonally-arranged spheres on a graphoepitaxial DSA substrate. (b) Fast-fourier transformation (FFT) profile of (a) indicating the single crystalline, hexagonal-packing of the structure. (c) Illustration of the effect of the topographic guides. Reprinted with permission from Segalman, R. et al, *Adv. Mater.* **2001**, *13* (15), 1152-1155. Copyright 2001 John Wiley & Sons, Inc.

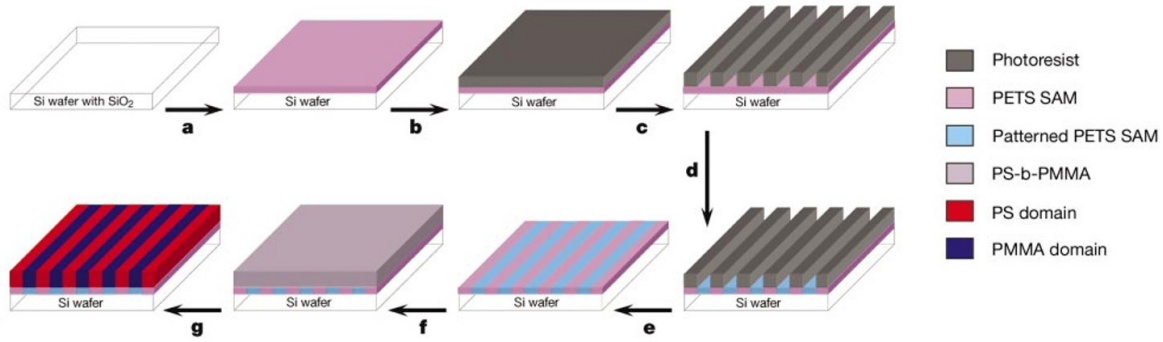


Figure 1-7. Schematic for the preparation of the first chemoepitaxial guides for the DSA of PS-*b*-PMMA. Reprinted with permission from Kim, S. O. et al, *Nature* **2003**, *424*, 411-414. Copyright 2003 Springer Nature Limited.

Compared to the aforementioned competitors, the Directed Self-Assembly (DSA) process has likely gained the most traction among researchers.[53,54] To induce long-range alignment and ultimately reduce the defectivity of the BCP thin film structures, BCPs are spun onto pre-patterned substrates with physical or chemical guides to direct the self-assembly process. Segalman and co-workers first demonstrated the long-range ordering of a monolayer of spherical domains with a domain spacing (L_0) of 27 nm on a topographically pre-patterned substrate with guiding mesas 30 nm in height and 4.5 μm widths (Fig. 1-6).[53] They reported that the steps of the mesas act to nucleate epitaxial growth, facilitating the formation of a single crystalline array of hexagonally-packed spheres over a large area. Subsequently, Kim and co-workers at the University of Wisconsin–Madison developed a strategy to produce flat substrates containing chemical guides interspersed between chemically modifying neutral layers to induce long-range alignment in symmetric and lamellar polystyrene-*block*-poly(methyl methacrylate) (PS-*b*-PMMA) (Fig. 1-7).[54] Alternating linear stripes with line widths equivalent to the BCP half-pitch feature size and containing chemical guides that possessed increased affinities towards either the PS or PMMA block in PS-*b*-PMMA were deposited onto the film. This caused the PS and PMMA domains to wet along each chemical guide, allowing for the perpendicular orientation of the microdomains and the long-range alignment of the microdomains. However, as chemical guides had to be

pre-patterned at the same pattern density as the BCP, chemical guides that could be spaced further apart while still enabling the perpendicular orientation and long-range alignment of the microdomains, thereby increasing the *multiplication factor* of the original pre-pattern density, needed to be developed.

Since the earliest reports, the DSA process using topographical guides has come to be known as graphoepitaxial alignment, while the use of chemical guides is termed chemoepitaxial alignment. However, in recent studies, chemical guides with a topographical pattern have begun to appear as well. Although graphoepitaxial DSA experiments are easier to conduct due to the simplicity of preparing a topographical substrate, it is likely that hybridizing grapho- and chemoepitaxial DSA can serve to further reduce the defectivity of BCP thin films, increasing the industrial viability of BCPL.

1-6 Directed Self-Assembly (DSA): The Current State

Given the high potential for BCPL, numerous international consortiums have been set up over the years to facilitate cooperation between academia and industries. The goals were to scale up BCPL and DSA research to 300 mm wafer scales, increase integration with conventional top-down lithographic production lines, and develop DSA as a viable lithographic technology for the mass production of 30 nm full-pitch L/S patterns. To date, at least four DSA processes compatible with conventional lithographic technologies have been developed.

In an early demonstration of DSA integration in 2011, Cheng and co-workers at IBM utilized photoresists conventionally used in 193 nm immersion lithography to prepare multi-layered chemical guides through a ‘lift-off’ process to apply DSA to both lamellar and cylindrical PS-*b*-PMMA for the preparation of well-aligned L/S patterns and contact hole shrinking.[55] The use of exclusively commercially available materials highlighted the increasing possibility of fully integrated DSA with existing lithographic production lines.

Subsequently in 2012, the most widely used DSA process now, termed ‘LiNe’ flow (Liu-Nealey), was invented at the University of Wisconsin–Madison by Chi-Chun Liu and Paul F. Nealey, through a collaboration between the Nealey and Gopalan groups.[56] The

LiNe flow process for preparing chemically pre-patterned DSA substrates is illustrated in Fig. 1-8. Characteristically, a cross-linkable PS (X-PS) layer is first prepared on a substrate. A photolithographic resist is then used to develop a linear pattern at the desired guide pitch (L_s). Using an oxygen-containing plasma, the line pattern was then etched into the underlying X-PS layer and trimmed to the line width of the BCP to be used. The removal of the photoresist yields chemical guides with a trapezoidal shape in the cross-section. The top surface of the X-PS guide remains preferential towards PS microdomains. However, the side-walls of the guide stripes were exposed to oxygen plasma during the trimming process. This oxidizes the side walls of the guide stripes and renders them preferential towards the relatively hydrophilic PMMA instead. Therefore, upon backfilling of a neutral layer into the interspaces between the guides and the spin-coating of PS-*b*-PMMA, the PS microdomains are able to align above the X-PS guides while PMMA can align on the adjacent side walls. With guides that are attractive towards both domains, the facile long-range alignment of the microdomains becomes possible. Since the first report of LiNe flow DSA, the Nealey group has partnered with other academic and international industrial collaborators,[57–61] including imec, CEA-LETI, Merck, and Tokyo Electron (TEL) to push towards integration of DSA with conventional lithographic production lines at the 300 mm wafer scale.

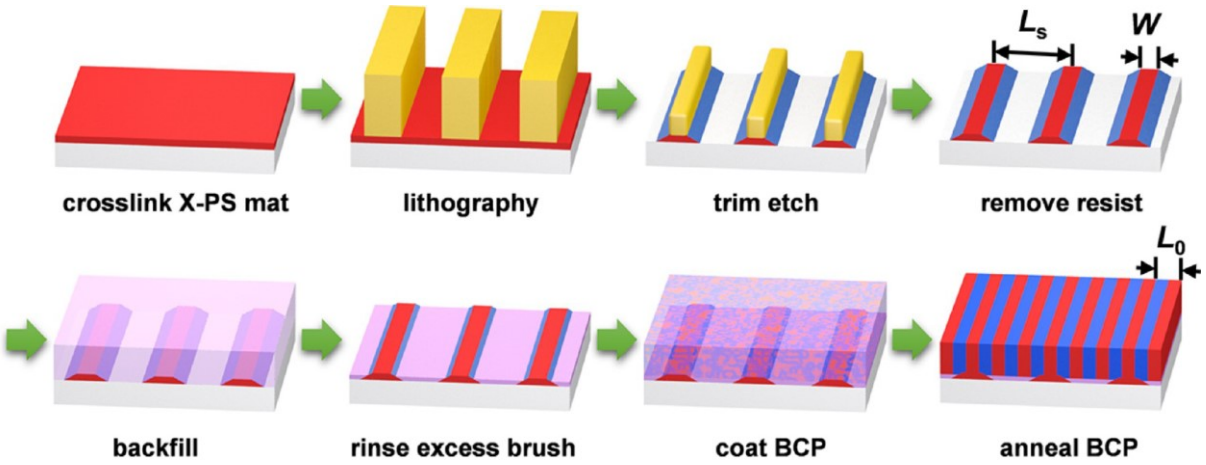


Figure 1-8. Schematic for the formation of chemical pre-patterns and the LiNe flow DSA process. Reprinted with permission from Ren, J. et al, *ACS Appl. Mater. Interfaces* **2018**, *10* (27), 23414-23423. Copyright 2018 American Chemical Society.

Domestically in Japan, the Evolving Nano-process Infrastructure Development Center (EIDEC, formerly EUVL Infrastructure Development Center) consortium was set up as a collaborative project under the New Energy and Industrial Technology Development Organization (NEDO). EIDEC served to develop novel NGL technologies including DSA and included collaborations between Toshiba (corporation name changed to Toshiba Memory, and now known as Kioxia), Tokyo Ohka Kogyo (TOK), Kyoto University, the Tokyo Institute of Technology, and more. Under the EIDEC project, the development of DSA substrates using the coordinated line epitaxy (COOL) process was investigated for potential pilot production lines.[62–64] The COOL process aims to reduce the number of processes required for preparing the pre-patterned chemical guides required for the chemoepitaxial alignment of BCPs. By using a photoresist that can become PMMA-preferential upon plasma treatment, the preparation of PMMA-preferential guide stripes could potentially be prepared without needing additional pinning materials. A schematic for the preparation of chemoepitaxial guide stripes based on the COOL process is illustrated in Fig. 1-9. In anticipation of lithographic applications, a multi-layered substrate with a spin-on glass (SOG) hard resist on the top layer is used. A photoresist was installed and a line pattern at the desired guide pitch was developed. Using a combination of oxygen and carbon tetrafluoride (CF_4) plasma, the photoresist was trimmed to the line width of the BCP to be used and the SOG layer was partially etched as well. This reactive ion etching (RIE) treatment oxidizes the surfaces of the guide stripes and causes the guides to become preferential towards PMMA. A neutral layer was then backfilled into the interspaces between the guide stripes and upon spin-coating and annealing of a PS-*b*-PMMA BCP, the PMMA domains could be expected to align onto the guide stripes and direct the self-assembly of the BCP microdomains.

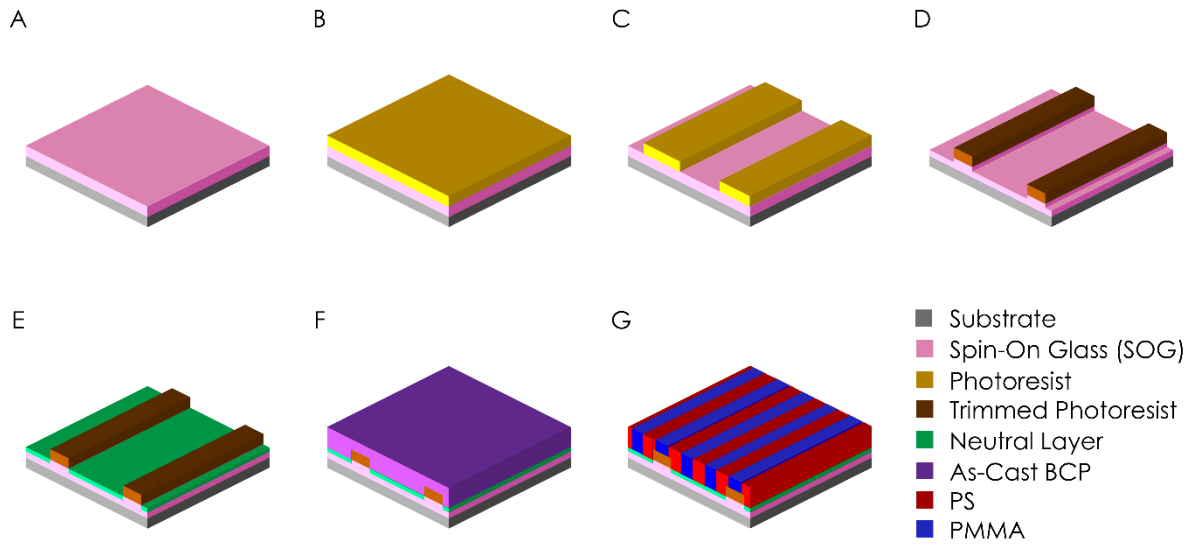


Figure 1-9. Schematic for the preparation of chemical pre-patterns and the COOL DSA process. (A) A multi-layered silicon (Si)-based substrate with a spin-on glass (SOG) hard resist layer on the surface is used. (B, C) A pre-pattern is installed on the photoresist and (D) trimmed to guides at the appropriate length scales. (E) A neutral layer is added in the interspaces between the guides and (F) the BCP, PS-*b*-PMMA, is spin-coated onto the thin film. (G) After an annealing process, well-aligned striped patterns can be obtained.

Remarkably, in an indication of industrial eagerness to insert DSA into high volume manufacturing, AZ Electronic Materials reported on the development of the Surface Modification for Advanced Resolution Technology™ (SMART™) flow DSA process independent of academic collaborators in 2013.[65] Subsequently, AZ Electronic Materials was acquired by Merck KGaA in 2014 and other industrial collaborators such as Tokyo Electron (TEL) have continued to work on the optimization of the SMART™ DSA process.[66–68] Characteristically, the SMART™ process uses both grapho- and chemo-epitaxial influences to induce the long-range alignment of the microdomains. A schematic for the preparation of DSA guides using the SMART™ process is outlined in Fig. 1-10. Firstly, a neutral layer is prepared on a substrate. A photoresist is used to develop a line pattern at 3X multiplication (i.e. 90 nm pitch, when using a 30 nm L_0 PS-*b*-PMMA). This line pattern is then etched into the neutral layer and the photoresist is removed. A weakly PS-preferential pinning material is

then coated and baked onto the substrate. Upon removal of the excess PS pinning material, a thin layer of the PS pinning material covers the interspaces between the neutral layers. Additionally, a topographic terrace-like pattern is achieved between the mesas of the neutral layers and the trenches with the PS pinning material. After spin-coating and annealing, the topographically-defined neutral layer and chemical guides can strongly nudge the BCP microdomains toward long-range, defect-free alignment. Most interestingly, Muramatsu and co-workers at TEL have reported achieving a defect density of 0.18 counts per cm^2 using SMART™ process DSA substrates.[68] Although pattern transfer onto the underlying substrate increased the final defect density, decades of research on BCPL and DSA have brought us significantly closer to achieving the target of less than 0.01 defect counts per cm^2. To finally achieve that last reduction in the defect density of the BCP structures, detailed studies on the real-time self-assembly behavior and defect annihilation mechanisms are imperative.

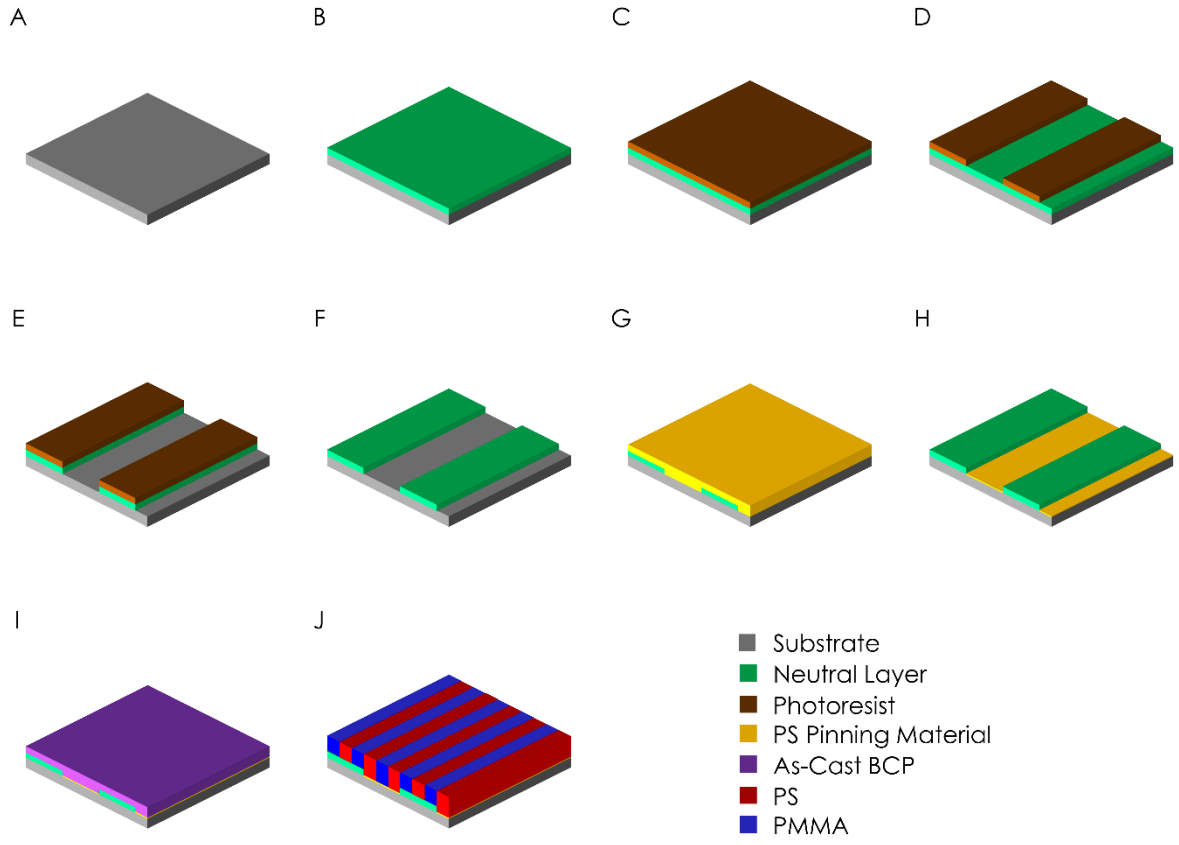
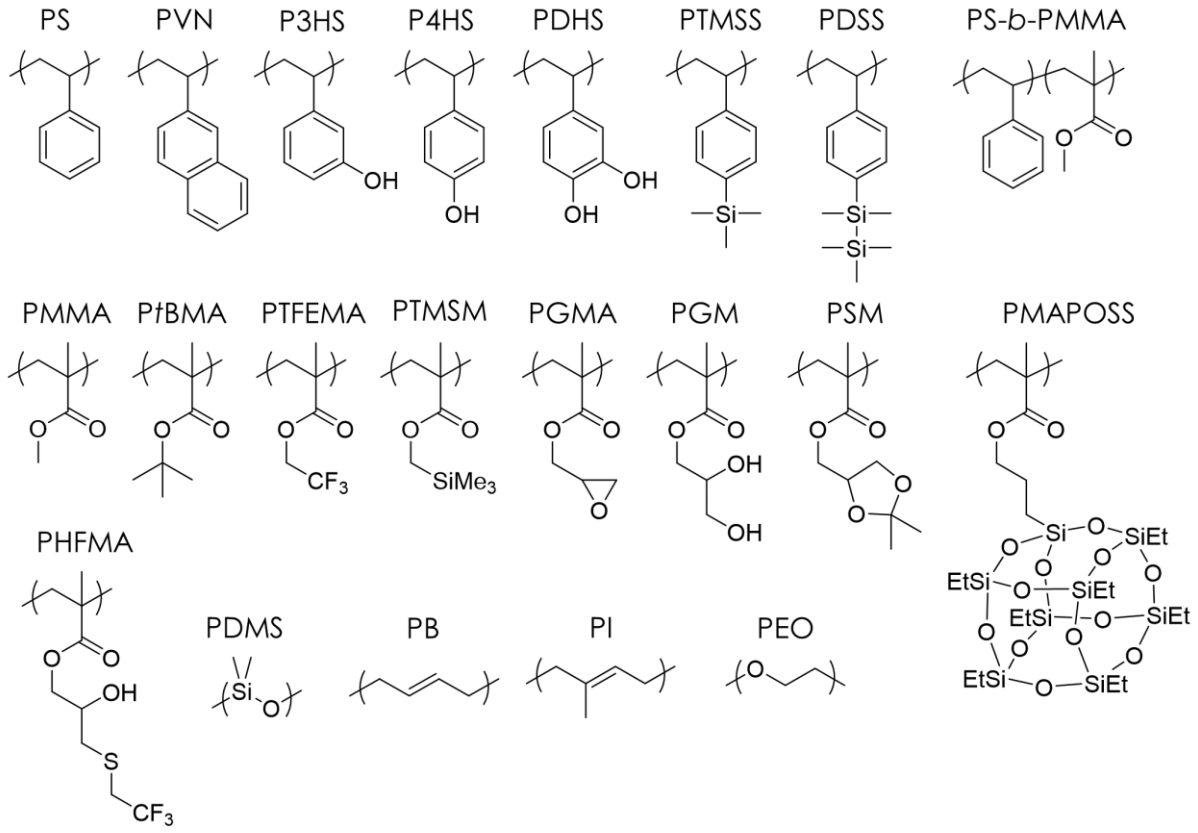


Figure 1-10. Schematic for the preparation of chemical pre-patterns and the SMART™ DSA process. (A, B) A neutral layer is first installed onto a substrate and (C, D) a pre-pattern is

first developed using a photoresist. (E) The pre-pattern is transferred down onto the neutral layer and (F) and the photoresist is stripped from the thin film. (G) A weakly PS-preferential pinning material is coated and baked onto the thin film and (H) the excess is removed. (I) A PS-*b*-PMMA BCP is spun onto the thin film and (J) well-aligned striped patterns can be obtained after annealing.

1-7 Polystyrene-*block*-Poly(methyl methacrylate) (PS-*b*-PMMA)

One commonality of all the aforementioned pilot DSA programs is that PS-*b*-PMMA was used as the BCP. This is a direct result of the fact that PS-*b*-PMMA is not only composed of the cheap, commodity basic materials of polystyrene (PS) and poly(methyl methacrylate) (PMMA), but also because PS-*b*-PMMA fulfills a large number of the industrial requirements listed above in 1-4 Block Copolymer Lithography (BCPL).



Schematic 1-1. Chemical structures of various polymers that have been studied for BCPL.

Although now known as the workhorse of the BCPL field, PS-*b*-PMMA was only first studied on thin films by Russell and co-workers at IBM and the University of Massachusetts,

Amherst around the 1990s.[69–71] These studies revealed that PS-*b*-PMMA can form lamellae mixed orientations on thin films, with perpendicular orientation near the substrate and parallel orientation near the free surface. They hypothesized that by inducing complete perpendicular orientation of the lamellar structures, L/S patterns could potentially be obtained. Subsequently, in near-simultaneous breakthroughs by the Gopalan and Nealey groups at the University of Wisconsin–Madison,[40] and through a collaboration between the Ryu group at Yonsei University (South Korea), the Hawker group at the University of California, Santa Barbara, and the Russell group at the University of Massachusetts, Amherst,[41] fully perpendicularly-oriented PS-*b*-PMMA lamellae were obtained on thin films with chemically-modifying neutral layers. Additionally, PS-*b*-PMMA can be easily synthesized by anionic polymerization using low cost commodity materials without leaving any metallic residues that could potentially interfere with the electrical properties of devices and possesses moderate etch contrast between the blocks.

However, despite the pros of using PS-*b*-PMMA, defectivity is still a work in progress and pristine PS-*b*-PMMA is incapable of forming sub-10 nm half-pitch structures. Nevertheless, the goal of the DSA consortiums was to reduce the defectivity found in DSA to sufficient levels for insertion into 30 nm full-pitch production nodes. Therefore, PS-*b*-PMMA was appropriately chosen as the main workhorse of the field. To truly increase the industrial viability of BCPL and DSA, further research is required to develop a system capable of improving on PS-*b*-PMMA and fulfilling all the industrial requirements listed earlier.

1-8 BCP Self-Assembly

To develop novel BCP systems that can replace PS-*b*-PMMA and insert DSA into industrial applications, the fundamental self-assembly behavior of BCPs must first be discussed.

The basic building blocks of BCPs are the monomers, the repeating units that constitute polymers. Monomers can range from relatively small molecules such as ethylene (C_2H_4) to large macromonomers consisting of a pre-made polymer functionalized with a vinylic end-group. Generally, when monomers are polymerized to yield a polymer, the

physicochemical properties are significantly changed. For example, although styrene is liquid, the polymer obtained through the polymerization of styrene, polystyrene (PS), is solid. This is due to the fact that as the molecular weight of the molecule increases, the temperature at which the sample transitions from a solid to liquid increases. Furthermore, although monomers such as styrene or methyl methacrylate (MMA) are miscible, the polymers derived from these monomers do not mix, and if blended together, will separate into distinct, independent, macroscopic phases, behavior that is akin to that of oil and water when mixed.[28,29,31,72,73] This difference in the mixing of the monomers and unmixing of the polymers can be attributed to the system trying to balance the enthalpies and entropies of mixing. In general, similar units attract whereas dissimilar units repel each other. Therefore, the mixing of dissimilar monomers or polymers contribute an enthalpic penalty to the free energy of mixing of the system. However, dissimilar monomers can mix despite this enthalpic penalty as the entropic penalty to large numbers of small molecules physically separating into distinct phases is significantly larger. With a smaller entropic penalty due to the repeating units being chemically bound together in a polymer, the enthalpic penalty of mixing becomes dominant, leading to phase separation in blended polymers.

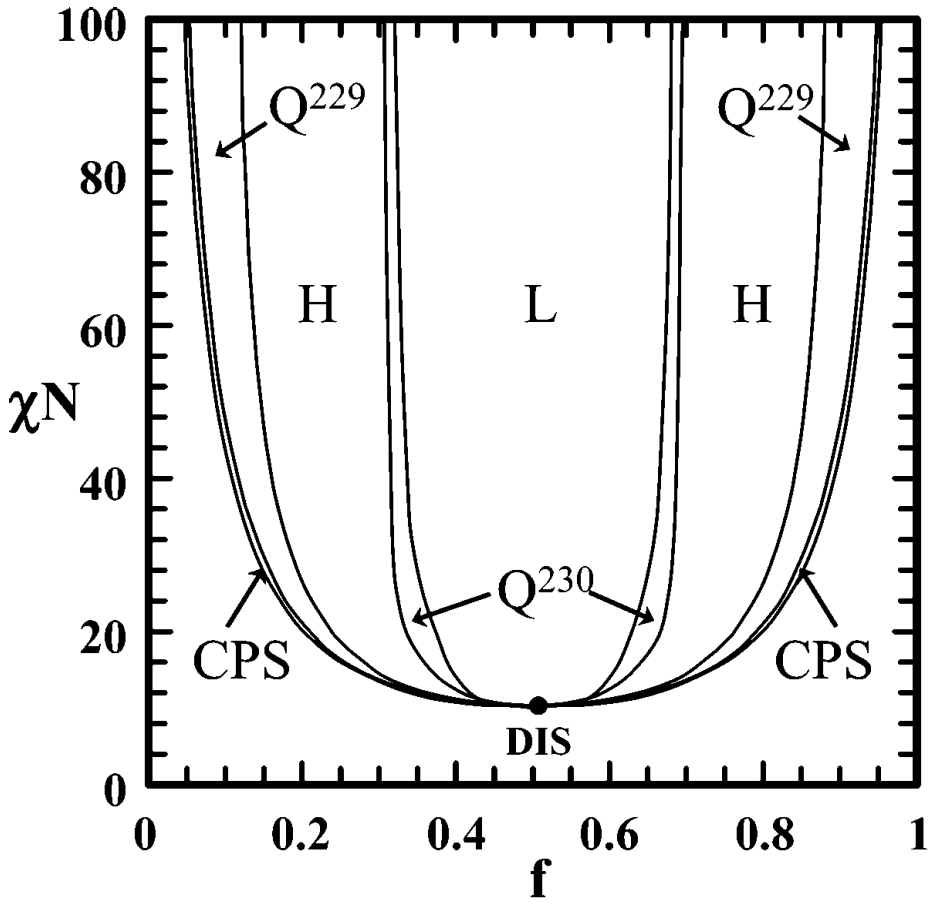


Figure 1-11. Phase diagram of a diblock copolymer showing the different morphologies accessible by changing the volume fraction (*f*) of one block, and the product of the strength of segregation and total degree of polymerization (χN). Reprinted with permission from Cochran, E. W. et al, *Macromolecules* **2006**, *39* (7), 2449-2451. Copyright 2006 American Chemical Society.

The phase behavior of polymers become more interesting when two or more chemically distinct polymers are bound together at a number of junction points.[31,32,34,74–77] Such macromolecules are known as BCPs and the simplest case of a diblock copolymer involves two polymers covalently bound at a single junction point on the ends of either polymer. The two distinct "blocks" of the BCP would work towards phase separation due to the chemical dissimilarities between the blocks. However, the covalent bond linking the two blocks prevents macrophase separation. Instead, the BCP "microphase separates" and self-assembles into distinct phases with length scales on the order of the polymer chains of each block. By controlling the volume fraction of each block (*f*), the strength of segregation

between the blocks, represented with the Flory-Huggins interaction parameter (χ_{eff}), and the total degree of polymerization (N), the morphology of the BCPs can be controlled. In the simplest case of the diblock copolymer, phase separation and self-assembly occurs when the product of the Flory-Huggins interaction parameter and the total degree of polymerization ($\chi_{eff}N$) is larger than 10.495,[30] and depending on the aforementioned factors, spheres, hexagonally-packed cylinders, double gyroid, and lamellar phases can be obtained (Fig. 1-11).[78] Furthermore, as the domain spacing (d or L_0) of the microphase-separated structures is inherently dependent on the lengths of the polymer chains and the degree of stretching in the polymer chains, d for lamellae in the strong segregation regime can be predicted as,

$$d \approx bN^{a}\chi_{eff}^{1/6} \quad (2)$$

where a = $^1/_2$ or $^2/_3$ in the weak or strong segregation limit, and b is the statistical segment length.[31] Note that the terminologies, pitch, full-pitch, period, periodicity, domain spacing, d, and L_0 are used interchangeably in the literature, with a preference for L_0 when applied to thin films and BCPL. Additionally, line-width, half-pitch, and feature size, all of which represent the length of one domain of a striped pattern, are also used interchangeable in the literature.

These self-assembled structures of BCPs open up numerous pathways for advanced engineering applications that require novel patterns and ordered nanostructures. Particularly, for lithographic applications, L/S structures could be obtained from the striped patterns of perpendicularly-oriented lamellae or parallel cylinders on thin films. For such applications however, parallel cylinders are less favorable as they stack in a hexagonal manner, limiting the height of the resist to a single monolayer of cylinders, reducing the aspect ratio of any potentially developable L/S pattern. In contrast, although simple mechanical and other restraints do apply, perpendicular lamellae do not have a theoretical height limit on thin films, making larger aspect ratios accessible.

Aside from L/S structures, perpendicularly-oriented cylinders can also be used to prepare holes and pillars for the fabrication of contact holes and bit-patterned media devices.

However, due to the relatively simplicity of the structures accessible by diblock copolymers, namely spheres, hexagonally-packed cylinders, gyroid, and lamellae, additional creativity may be required to obtain other "less conventional" structures that could potentially be useful in lithographic applications as well.[79–81] Nevertheless, the focus of this thesis lies in developing and applying diblock copolymers to lithographic applications, and thus the term BCP and diblock copolymer may be used interchangeably unless otherwise stated.

1-9 How to Increase χ_{eff}

Upon deciding the target structure, the BCP must now be designed and synthesized as well. When designing a BCP for lithographic applications, the requirements listed in 1-4 Block Copolymer Lithography (BCPL) must be fulfilled as much as possible. Firstly, as BCPs self-assemble only when $\chi_{eff}N$ is greater than 10.5, and as shown in Eq. 2, d scales with N^a and $\chi_{eff}^{1/6}$, to drive self-assembly toward sub-10 nm half-pitch structures, BCPs with large χ_{eff} and small N are desirable.[75] In the case of PS-*b*-PMMA, χ_{eff} is known to be 0.039 at 150 °C, giving a lower limit of $d \approx 18 – 22$ nm.[71,82] The relatively low value of χ_{eff} for PS-*b*-PMMA can be attributed to the fact that PS-*b*-PMMA contains relatively similar moieties with carbon (C), hydrogen (H), and oxygen (O) constituents, while not possessing any significant hydrophilicity or hydrophobicity in either block. Therefore, to obtain a BCP with higher χ_{eff}, the repeating units need to be replaced and designed from scratch or functionalized to yield new repeating units.

Although N can be controlled easily be simply lowering the molecular weight of the BCP, altering χ_{eff} is more complicated. The χ_{eff} of any two pairs of monomers are constant as χ_{eff} represents the interaction parameter between the two monomers. Based on the basic concept of similar units attract while dissimilar units repel, to design a BCP with a high χ_{eff}, moieties with large chemical differences need to be installed onto each block of the BCP. Strategies for increasing the chemical dissimilarities in a BCP typically involve the addition of heteroatoms or amphiphilicity.

Particularly, the addition of silicon (Si) or fluorene (F) to a block can significantly enhance χ_{eff}. When PS is paired with poly(dimethyl siloxane) (PDMS), PS-*b*-PDMS exhibits a χ_{eff} of 0.11 at 150 °C,[83] an almost three-fold increase compared to PS-*b*-PMMA. This facilitated the formation of sub-10 nm striped patterns of parallel cylinders with d = 17 nm and 8 nm half-pitch features.[84] Therefore, a family of Si-containing BCPs have been developed to increase χ_{eff} and reduce the minimum d accessible. With pendant Si-containing functionalities,[85–90] poly(trimethylsilylstyrene) (PTMSS), poly(pentamethyldisilylstyrene) (PDSS), and poly(methyltrimethylsilyl methacrylate) (PTMSM), χ_{eff} can be enhanced to 0.024 or 0.11 for PS-*b*-PTMSS and PS-*b*-PDSS, respectively. Additionally, the addition of polyhedral oligomeric silsesquioxane (POSS), a unique functionality with a well-defined cage structure, and enhanced thermal stabilities and etch resistance to oxygen reactive ion etching (O_2-RIE), to the side chain of a methacrylyl monomer yields the polymer known as poly(3(2,2',2",4,4',4",6-heptaethyl polyhedral oligomeric silsesquioxane)propyl methacrylate) (PMAPOSS). When paired with PMMA, PMMA-*b*-PMAPOSS thin films could exhibit well-defined hexagonal dot patterns with sub-10 nm features and a dot density of 5.9 Tb/inch^2.[91] Additionally, χ_{eff} for such PMAPOSS-containing BCPs were found to be significantly higher than PS-*b*-PMMA as well, with χ_{eff} for PS-*b*-PMAPOSS and PMMA-*b*-PMAPOSS reported to be 0.140 and 0.146 at 150 °C, respectively.[92]

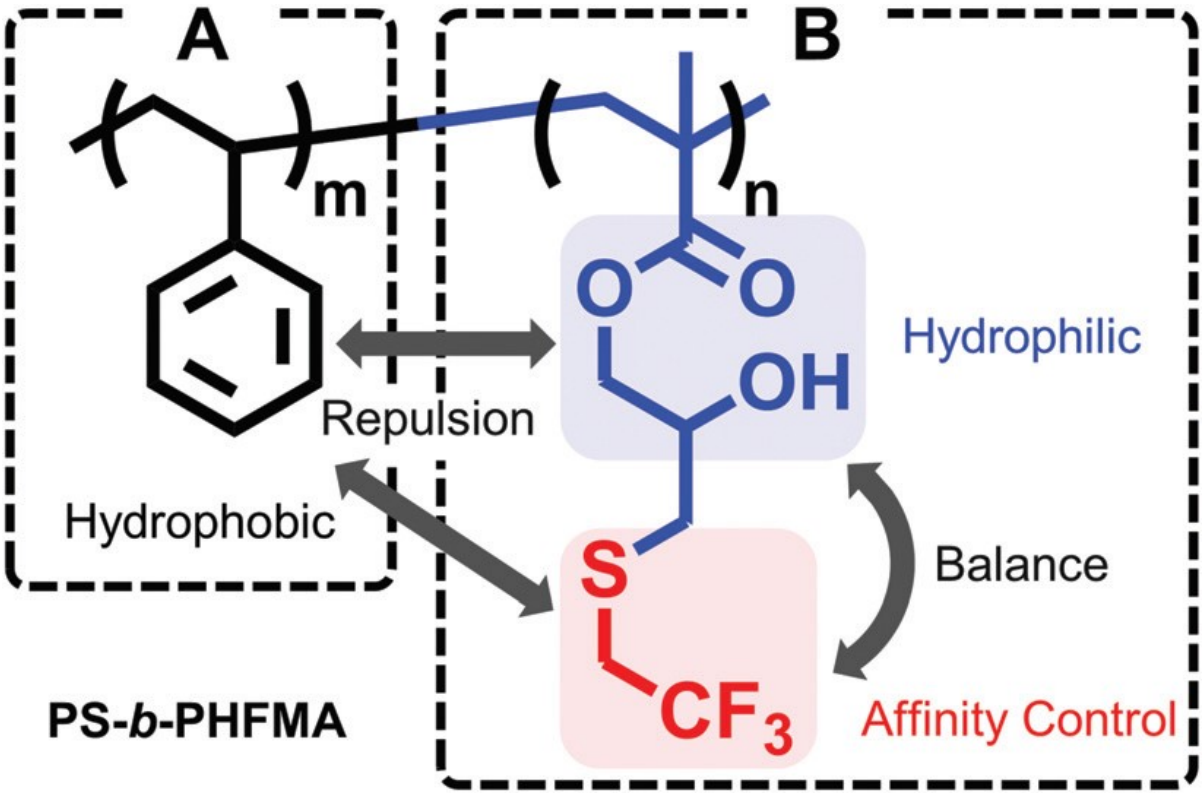


Figure 1-12. Illustrative concept to design a fully organic-organic, strongly-segregating BCP while maintaining balanced surface affinities. Reprinted with permission from Yoshimura, Y. et al, *Soft Matter* **2019**, *15*, 3497-3506. Copyright 2019 Royal Society of Chemistry.

In addition to Si, the addition of fluorinated moieties to BCPs has also been shown to increase χ_{eff}. Yoshimura and co-workers demonstrated that by using a parent precursor polymer of polystyrene-*block*-poly(glycidyl methacrylate) (PS-*b*-PGMA), fluorinated functionalities could be introduced to the glycidyl moiety on the PGMA block.[93] The introduction of a trifluoroethyl functionality onto PGMA enhanced χ_{eff} from 0.14 in PS-*b*-PGMA at 150 °C to 0.17 in the fluorinated derivative, polystyrene-*block*-poly[2-hydroxy-3-(2,2,2-trifluoroethylsulfanyl)propyl methacrylate] (PS-*b*-PHFMA), at 150 °C (Fig. 1-12). This χ_{eff} value of PS-*b*-PHFMA is 4.8 times compared to that of PS-*b*-PMMA (0.038 at 150 °C), thereby facilitating the formation of sub-5 nm lamellae with d = 9.6 nm. Therefore, fluorination was shown to be a useful method for increasing the strength of segregation between the blocks of a BCP.

Another common method for increasing the chemical incompatibilities of a BCP is to introduce amphiphilicity. For example, in the case of PS-*b*-PHFMA and PS-*b*-PGMA stated above, the authors reported that in addition to the effect of fluorination, the presence of hydrophilic and hydrophobic contributed to increasing χ_{eff} of the BCPs.[93] The glycidyl moiety in PGMA is inherently hydrophilic while PS is slightly hydrophobic. Since, hydrophobic and hydrophilic functionalities naturally do not mix well, the estimated χ_{eff} for PS-*b*-PGMA was already approximately three times that of PS-*b*-PMMA. The addition of the hydrophilic trifluoroethyl functionality to PGMA also caused the ring opening of the glycidyl moiety and the formation of a relatively hydrophilic hydroxy group on the same side chain. Therefore, it was postulated that these hydrophobic and hydrophilic functionalities also helped enhance χ_{eff} of PS-*b*-PHFMA. This idea of combining hydrophobic and hydrophilic functionalities to produce increase χ_{eff} has existed for a long time. In a study by Park and co-workers in 2008, they reported the formation of 7 nm half-pitch lamellae using a 5,000 g mol^{-1} polystyrene-*block*-poly(ethylene oxide) (PS-*b*-PEO) blended with low molecular weight organosilicate oligomers.[94] Furthermore, the BCPs that have reported the lowest accessible domain spacings have utilized multiple hydrophilic functionalities in a single repeating unit to increase χ_{eff} and reduce the N required to reach the threshold of $\chi_{eff}N$ = 10.5 for self-assembly. In a series of studies, Russell and co-workers realized d = 5.4 nm lamellae in bulk samples of poly(glycerol monomethacrylate)-*block*-polystyrene (PGM-*b*-PS) through the acid hydrolysis of poly(solketal methacrylate)-*block*-polystyrene (PSM-*b*-PS).[35,95,96] The presence of two hydroxy functionalities on the methacrylyl block significantly increased the hydrophilicity of the block, and when paired with relatively hydrophobic PS, sub-3 nm features could be obtained. However, due to interfacial and confinement effects, when PSM-*b*-PS was applied to thin films, the lowest accessible lamellar domain spacing was limited to d = 9.4 nm.

Additionally, in the pursuit of the smallest domain spacing, a family of polyhydroxystyrene (PHS)-based BCPs have been prepared by a number of research groups around the world.[97–100] In a series of reports by Gopalan and co-workers, they first

reported the synthesis of poly(4-hydroxystyrene)-*block*-polystyrene (P4HS-*b*-PS) which exhibited a χ_{eff} of 0.12 at 150 °C and could form lamellae down to d = 11.6 nm.[99] In a follow-up report, it was revealed that by using an isomer of PHS, namely poly-3-hydroxystyrene (P3HS), the lowest accessible lamellar periodicity when paired with poly(*t*-butylstyrene) (P*t*BS) was 8.8 nm.[98] Furthermore, by combining the hydrophilic P3HS with a hydrophobic PDMS block, P3HS-*b*-PDMS lamellae with d = 7.4 nm could be obtained. Scattering data also revealed a high χ_{eff} of 0.39 at 150 °C, a ten-fold increase compared to PS-*b*-PMMA and over three times that of P4HS-*b*-PS.[97] Based on a similar concept, Kwak and co-workers synthesized a PHS-based BCP with two hydroxy functionalities on the PHS block. The BCP, polydihydroxystyrene-*block*-polystyrene (PDHS-*b*-PS) was shown to be capable of self-assembly even at an extremely low molecular weight of 2,100 g mol^{-1}.[100] The obtained lamellae showed d = 5.9 nm and small angle X-ray scattering (SAXS) experiments revealed a large χ_{eff} of 0.72. These experiments show that by combining polymers multiple hydrophilic functionalities and hydrophobic character, χ_{eff} can be significantly enhanced, increasing the accessibility of ordered structures with decreasingly smaller d.

1-10 Etch Selectivity

To produce the topographic L/S pattern, dots, or pillars for use as a resist in lithographic applications, one of the blocks in the BCP must be amenable to a selective etching process or possess increased resistance to an etching process, relative to the other block. Therefore, when designing a novel BCP for lithographic applications, functionalities that enhance etch contrast between the blocks are often included.

The methods used to etch or remove polymeric domains can be categorized as either dry or wet etch techniques. While dry etch techniques include a wide variety of options such as the use of ultraviolet (UV) or X-ray irradiation, ozonolysis, and oxygen plasma or reactive ion etching (RIE), wet etch techniques typically involve hydrolysis using an acid or base.[101–107] Although wet etching through hydrolysis can provide superior etch selectivity compared to dry etch techniques as they target specific functionalities in the polymer, the developed patterns can collapse easily due to capillary action upon removal of the solvent

after etching.[108] This becomes a larger issue as *d* decreases and the aspect ratios of the L/S structures increase. Therefore, high-χ_{eff} BCPs are usually designed with dry etch techniques in mind.

Though now almost ubiquitous in the field of BCPL, the selective removal of one block of PS-*b*-PMMA was first demonstrated by Thurn-Albrecht and co-workers in 2000.[103] With well-known photodegradation properties, PMMA is susceptible to X-ray and UV irradiation and is traditionally in photolithography as a negative tone resist. On the other hand, the behavior of PS is less well-defined as a simultaneous mix of cross-linking, chain-scission, and oxidation can occur under UV irradiation. Thurn-Albrecht and co-workers showed that upon exposure to 25 J cm^{-2} of UV irradiation,[103] PS thin films become insoluble. In contrast, PMMA could be degraded even at a lower dose of UV irradiation of 3.4 J cm^{-2}. Based on this difference in behavior upon exposure to UV irradiation, the authors demonstrated the development of a topographic pattern of holes by selectively removing the minor PMMA domain in an array of perpendicularly-oriented PS-*b*-PMMA cylinders.

Ozonolysis has also been shown to be an effective method for selective etching as ozonolysis mechanistically selectively targets non-aromatic double bonds only.[109] As a reaction, ozonolysis has a long history and is the cause of unwanted degradation in many rubber-based products such as gloves and tires. For the preparation of topographically well-defined nanostructures based on the self-assembly of BCPs however, ozonolysis is a useful tool. Lee and co-workers demonstrated the preparation of mesoporous membranes after the selective removal of the polyisoprene (PI) block in films of a BCP synthesized through the polymerization of (4-vinylphenyl)-2-propoxysilane and isoprene.[107] Hashimoto and co-workers also produced bicontinuous nanochannels based on a double gyroid morphology formed by polystyrene-*block*-polyisoprene (PS-*b*-PI).[106] The selective removal of the PI block rich in 1,4-content enhanced the susceptibility of the block to ozonolysis and facilitated the production of bicontinuous gyroid nanochannels. However, as ozonolysis necessarily requires the presence of non-aromatic C=C double bonds, the polymers which ozonolysis can be applied to are limited to ‘rubbers’ such as PI, or polybutadiene (PB).

On the other hand, plasma or reactive ion etching (RIE) is widely used in the microfabrication of integrated circuits to remove a variety of substrate materials.[102,110,111] Typically, a gas such as oxygen (O_2), carbon tetrafluoride (CF_4), or argon (Ar) is injected into a low-pressure chamber where an electromagnetic field converts the gas into a plasma. By placing the sample between two electrodes of opposite charge, ions from the plasma bombard the surface to remove material. Furthermore, the gas injected can be changed, depending on the material and outcome desired. When O_2 plasma is applied to an organic material, the ions can react with the carbon (C), nitrogen (N), oxygen (O), and hydrogen (H) in the system and the kinetic energy from the ions can also effectively sputter and physically remove the material as well. On the other hand, heavier elements such as Si are less affected by oxygen plasma. To etch away Si material, CF_4 gas is typically used instead. For conventional photolithography, after a pattern has been developed on a resist, the pattern is transferred onto the substrate with CF_4 plasma as it can react with both organic and inorganic material. Therefore, by using BCPs where one block is resistant and the other susceptible to O_2-RIE, pattern development via BCPL that can be seamlessly integrated into conventional lithographic production lines can be achieved. Asakawa and co-workers measured the etch rate of various polymers including PS, PB, PHS, P*t*BMA, PMMA, and polyvinylnaphthalene (PVN) upon O_2-RIE treatment, and determined that the etch rate was related to the number and ratio of carbon atoms to oxygen atoms per segment.[112] As a demonstration, thin films of PS-*b*-PMMA which forms PMMA spheres in a PS matrix were prepared. The PMMA spheres were removed with O_2-RIE and backfilled with spin-on glass which then acted as a hard mask for the preparation of patterned magnetic media. Ting and co-workers later investigated the etch rate ratio between PS and PMMA with different mixtures of etch gases and determined that while pure Ar and O plasma can provide superior etch contrast, significant damage and deformation to the remaining PS walls could be observed. Instead, an Ar/O_2 mixture provided superior etching capabilities, providing adequate etch contrast white maintaining relatively smooth PS walls in the developed L/S pattern. Even so, both PS and PMMA are fully organic polymers containing only C, N, H, and

O. Farrell and co-workers also worked towards optimizing both the conditions for the selective etching of PMMA via RIE, and the pattern transfer process down onto Si substrates as well (Fig. 1-13).[111] Although PS and PMMA etch away at different rates, the PS domain can get damaged upon exposure to RIE treatment. Therefore, the development of BCPs with higher etch contrast against RIE treatment is desirable.

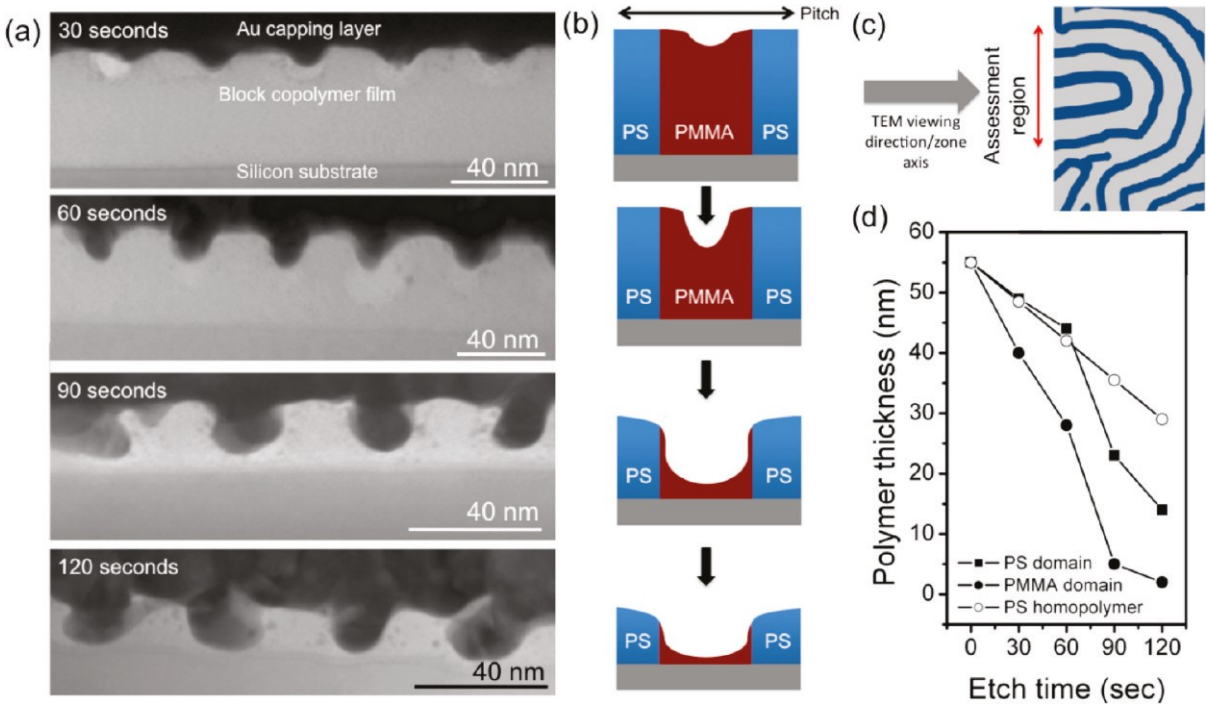


Figure 1-13. (a) TEM images and (b) the corresponding illustrative representation of a PS-*b*-PMMA perpendicular lamellar thin film upon PMMA removal via RIE treatment. (c) Schematic of the direction of viewing relative to the BCP thin film. (d) Plot of remaining film thickness against etch time. Reprinted with permission from Farrell, R. A. et al, *Macromolecules* **2010**, *43* (20), 8561-8655. Copyright 2010 American Chemical Society.

To that end, as polymers have been used as resists in the microfabrication industry for many years, methods to increase or decrease the etch resistance of polymers have been studied. Similar to methods for increasing χ_{eff}, heteroatoms are typically introduced to the polymer. When heavier elements such as Si or aluminum (Al) are added onto a polymer, the etch resistance toward RIE treatment increases.[2] Alternatively, adding fluorinated moieties to the polymer can have the opposite effect and increase the susceptibility of the polymer toward RIE treatment.[92,113] Such heteroatom functionalities could be included in the original

repeating units of the polymers, or could be added on in a post-polymerization functionalization, and examples have already been discussed above. For example, PS-*b*-PDMS is the most basic Si-containing BCP. While the organic PS is on one block, the PDMS block consists of repeating units of -SiO- atoms in the main chain of the other block. The Si content in PDMS enhances the etch resistance toward O_2-RIE and although the PS block remains while PMMA gets removed by O_2-RIE in PS-*b*-PMMA, PS is removed while the PDMS block remains unetched by O_2-RIE. Aside from adding Si to increase the etch contrast of a BCP, F could also be added to increase the susceptibility of a polymer towards dry etching treatment. Maeda and co-workers reported the development of a novel BCP, polystyrene-*block*-poly(2,2,2-trifluoroethyl methacrylate) (PS-*b*-PTFEMA).[113] With F-containing functionalities on every repeating unit of the poly(2,2,2-trifluoroethyl methacrylate) (PTFEMA) block, PTFEMA exhibited a significantly increased susceptibility toward electron beam and UV irradiation.

Furthermore, it is also possible to improve the etch contrast of organic polymers such as PS-*b*-PMMA or PS-*b*-PGMA through a post-polymerization functionalization reaction. As discussed earlier, if the original polymer had a moiety in which novel functionalities could be introduced, as in PS-*b*-PGMA, the physicochemical properties could also be easily altered. While in the case of PS-*b*-PGMA, trifluoroethyl functionalities could be introduced onto PGMA easily,[93] the etch contrast of PS-*b*-PMMA can be altered using sequential infiltration synthesis (SIS).[114] Typically, trimethyl aluminum selectively reacts with the carbonyl group in the PMMA domain to establish a foundation in which a number of precursor materials such as silicon dioxide (SiO_2), titanium dioxide (TiO_2), zinc oxide (ZnO), or tungsten (W) can grow. Once the precursor material has been established in the PMMA domain, the etch resistance of the PMMA domain toward dry etching techniques can be significantly increased, allowing for the PS domain to be removed by O_2-RIE treatment. Based on these methods, novel BCPs with high etch contrast can be designed for effective lithographic applications.

1-11 Controlling the Interfaces

One crucial aspect that must be controlled in BCPL is the effect of the interfaces. Unlike “bulk films” where the morphology of the film is more important and the interfaces can be effectively ignored, the effect of the substrate and free interface cannot be ignored in thin films. Additionally, it should be noted that even within the larger materials or polymers field, depending on the application, the terminology, “thin film”, is loosely defined. For example, in the rubber industry, a glove with a thickness of 100 μm may be considered thin. In BCPL however, the term “thin film” is generally applied to polymeric films prepared by a spin-coating process and can have thicknesses ranging from several nanometers to several micrometers. Nevertheless, for effective application as a lithographic tool, the film thickness of a BCP thin film is generally between 30 to 150 nm.

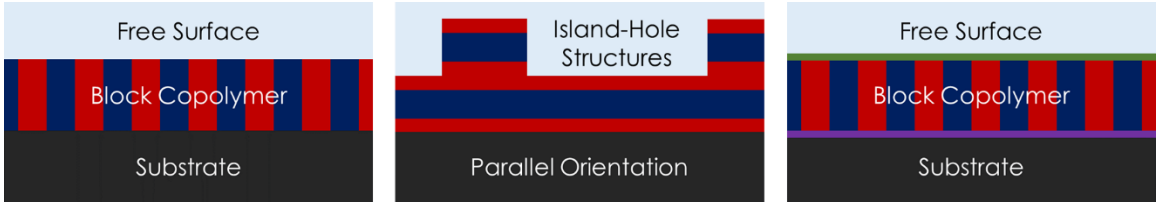


Figure 1-14. Illustration of a BCP thin film under the influence of the free surface and the substrate. Typically, BCPs orient flat and parallel relative to the substrate, forming terraced island-hole structures due to preferential interactions at the interfaces. With a neutral layer (purple) and/or top-coat (green), preferential interactions can be eliminated, facilitating perpendicular orientation of the BCP structures.

The substrate and free interfaces exert strong influence on the self-assembly behavior of BCPs on thin films (Fig. 1-14). Generally, interactions between two materials can be attractive or repulsive. A polymeric thin film can either be unstable, metastable, or stable, depending on the interactions between the polymer, substrate, and free interface. When a polymer possesses strong affinity and can interact strongly with a substrate, the polymer can cover the substrate and “wet” the substrate, forming a metastable or stable thin film. However, if the polymer-substrate interactions are unfavorable, the polymer film becomes unstable, and works towards reducing polymer-substrate contact by “dewetting” from the

surface and aggregating into droplets with maximum polymer-polymer and minimum polymer-substrate contact.

When a thin film is prepared using a BCP, the behavior of the thin film can become more complicated as the number of interactions increases with the number of chemically distinct components in the system. For BCP thin films, the polymer$_i$-polymer$_{i+1}$, polymer$_i$-substrate, and polymer$_i$-free interface interactions, where i represents the i^{th} block in the BCP, can affect the self-assembly behavior. As in the case of a simple homopolymer, a BCP thin film can be stable, metastable, or unstable, depending on the interactions of the BCP with the substrate.[115–118] Additionally, while the polymer$_i$-polymer$_{i+1}$ interactions generally dictate the morphology of the BCP in the bulk, the polymer$_i$-interfacial interactions can also affect the morphology and phase behavior in thin films through confinement and affinity effects. For example, although the relatively complex double gyroid phase is found easily in bulk films, there have been very few reports of preparing double gyroid thin films, despite potential applications in optoelectronic devices. Of the few reports, the double gyroid thin films are generally thicker than 100 nm, as the double gyroid system becomes unstable at film thicknesses less than three times the periodicity or 3 L_0.[119,120]

More importantly for BCPL, the orientation of the BCP microdomains are heavily dictated by the interfacial interactions. If the polymer$_i$-substrate interactions are more favorable relative to the polymer$_{i+1}$-substrate interactions, polymer$_i$ can selectively wet the substrate to maximize polymer$_i$-substrate and minimize polymer$_{i+1}$-substrate contact. Similarly, if the polymer$_i$-free interface interactions are more favorable, polymer$_i$ can segregate towards the free interface to form a wetting layer covering the free surface of the thin film. Therefore, in the cases whereby one polymer strongly interacts with an interface, selective wetting leads to the formation of layers of microdomains with parallel orientation on thin films. In the case of parallel lamellae where polymer$_i$ strongly interacts with the substrate, polymer$_i$ selectively wets the substrate and flat layers of lamellae accumulate above. At the top layer exposed to the free interface, a flat surface layer can form should there be physically enough polymer to cover the entire surface. However, if there is

insufficient polymer in the thin film to form a flat layer to cover the entire surface, a terraced "island-hole structure" with islands or holes at 1 L_0 heights or depths can form.[86,121–123] Furthermore, depending on the polymer$_f$-free interface interaction, the block that appears on the free surface and the nature of the island-hole structure can be affected. Regardless of which block wets the substrate, excepting physical restrictions such as in the case of mono- or bilayers, the block with the stronger free interface interaction can segregate to form a surface layer. If polymer A in a diblock copolymer system strongly interacts with both the substrate and the free interface, the thin film tends to exhibit symmetric wetting with film thicknesses at $n \times L_0$ intervals, where n is an integer. Conversely, if polymer A in a diblock copolymer system strongly interacts with the substrate, but polymer B interacts strongly interacts with the free interface, the thin film deviates toward asymmetric wetting with film thicknesses at $(n + 0.5)\ L_0$ intervals. The same conditions apply to parallel cylinders. However, although parallel lamellae form flat layers, parallel cylindrical structures exhibit striped patterns on the free surface which could potentially be used for forming L/S structures. Due to the strong interfacial effects that causes the selective wetting of one block onto the substrate, early demonstrations of BCPL have generally utilized thin films containing monolayers of parallel cylinders or spheres. As such monolayers can severely restrict the film thicknesses accessible for lithography, the ability to induce perpendicular orientation in BCPs is desirable.

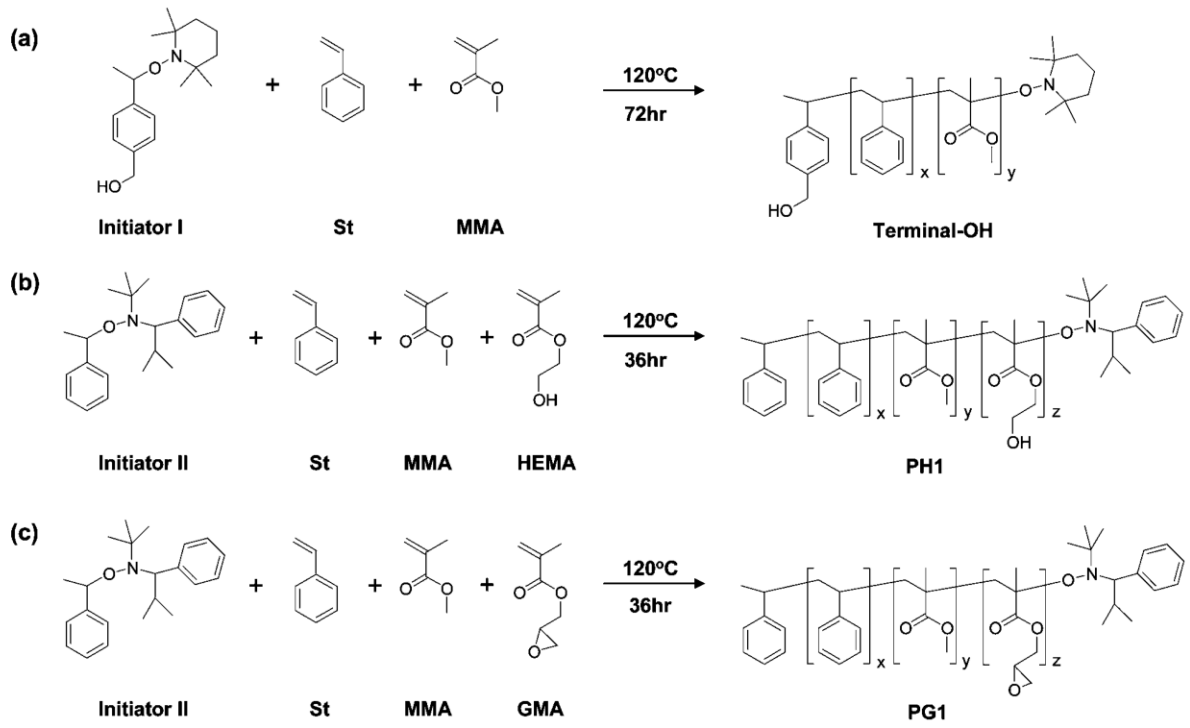


Figure 1-15. Schematic for the synthesis of PS and PMMA-containing random copolymers for use as neutral layers. Reprinted with permission from Han, E. et al, *Macromolecules* **2008**, *41* (23), 9090-9097. Copyright 2008 American Chemical Society.

To induce perpendicular orientation, the preferential interactions at the substrate and free interface need to be removed. When the substrate and free interface do not exhibit preferential interactions towards either block in a diblock copolymer, both blocks can wet the substrate and appear on the free interface equally, facilitating the perpendicular orientation of the BCP microdomains. In such cases, the substrate or free interface are defined as being *neutral* towards either block. However, as the substrate and free interface can have independent interactions with the blocks in a BCP, thin films with mixed orientations, in which the microdomains are perpendicular at one interface and parallel at another, can develop. In the case of PS-*b*-PMMA, the carbonyl groups in PMMA strongly interact with the exposed hydroxyl groups (-OH) on the surfaces of Si wafers. Therefore, the PMMA domain selectively wets bare Si wafers, leading to the formation of parallel structures. However, in a series of studies, Russell and co-workers prepared PS-*b*-PMMA thin films on Si wafers with a random copolymer (RCP) brush layer of the two blocks, polystyrene-*random*-poly(methyl

methacrylate) (PS-*r*-PMMA).[69,70,124,125] Although the exposed hydroxyl groups on bare Si exhibit preferential affinities with PMMA, the RCP brush layer of both PS and PMMA acted as a chemically-modifying *neutral layer*, eliminating the preferential interactions toward either block as both PS and PMMA moieties now appeared on the surface of the substrate. With the use of a PS-*r*-PMMA neutral layer, Russell and co-workers reported the formation of PS-*b*-PMMA lamellae with mostly perpendicular and mixed orientations where the lamellae were perpendicular near the substrate but parallel near the surface. Additionally, Kim and co-workers developed nanopatterned substrates that contained underlying stripes with alternating affinities towards the component blocks of PS-*b*-PMMA.[54] The PS and PMMA microdomains of PS-*b*-PMMA were able to wet the PS-preferential and PMMA-preferential guide stripes that were patterned onto the substrate, allowing for not only perpendicular orientation, but also chemoepitaxial long-range alignment in the same direction as the chemical guide stripes. However, while such a method is a good demonstration of the long-range alignment of perpendicular stripes in BCP thin films, the use of EUVL to make the pre-pattern at the same length scale as the BCP means that other methods need to be developed to make BCPL a viable, independent strategy. In later iterations of studies that focused on the perpendicular orientation of BCP nanostructures, the conditions required for optimizing the neutral layer needed by PS-*b*-PMMA were reported in near simultaneous breakthroughs by the Gopalan and Nealey (Fig. 1-15 and 1-16), and Ryu, Hawker, and Russell groups, as described earlier in section 1-7.[40,41]

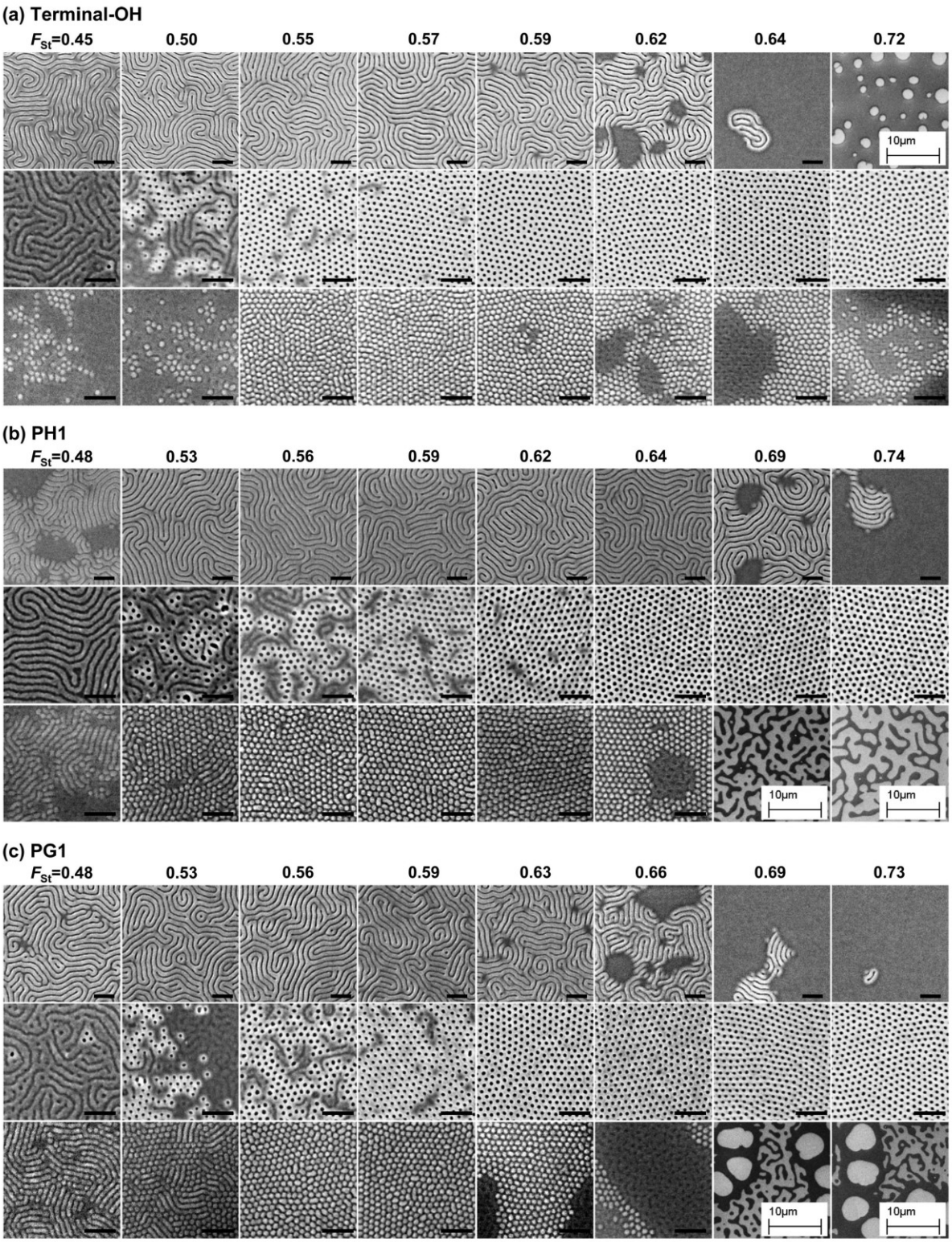


Figure 1-16. SEM images showing the extent of perpendicular orientation of lamella and cylinder-forming PS-*b*-PMMAs on random copolymers with varying PS and PMMA content. Reprinted with permission from Han, E. et al, *Macromolecules* **2008**, *41* (23), 9090-9097. Copyright 2008 American Chemical Society.

Since then, a number of methods for controlling the microdomain orientation of BCP thin films have been developed. In addition to the use of a neutral layer on the substrate, entropic and confinement effects,[126,127] chemically-modifying top-coats,[88] solvent vapor annealing,[101] and designer BCPs with tailored chemical affinities have been used to induce perpendicular orientation in BCP thin films.[92,128–130]

Generally, there are two major methods that are used to propagate the self-assembly of a BCP thin film, thermal or solvent vapor annealing (SVA). Thermal annealing can be performed by simply heating the thin film on a hot plate or an oven that has been pre-set to a certain temperature. However, when BCPs with largely disparate surface affinities are thermally annealed, this results in the selective wetting of one microdomain onto the substrate or free interface, leading to the formation of undesired parallel orientation. On the other hand, the surface affinities of the microdomains are less influential when the BCP thin film is annealed under SVA. Particularly, although PS-*b*-PDMS typically forms parallel structures when thermally annealed, the SVA of PS-*b*-PDMS thin films leads to the perpendicular orientation of the microdomains.[101] Therefore, while SVA can facilitate the formation of perpendicular structures, SVA is less amenable to industrial applications. This is less due to technical issues, but more of due to the risk of using organic solvent vapor on large industrial scales. Thus, industrial research has tended to focus on developing techniques that allow for the perpendicular orientation of the microdomains using safer thermal annealing processes.

In addition to controlling the affinities of the substrate with a chemically-modifying neutral layer, the affinities at the free interface can also be controlled with the use of a chemically-modifying top-coat.[87,88,131] In contrast to PS-*b*-PMMA, which exhibits relatively similar surface free energies (SFEs), and perpendicular orientation can be achieved simply by adding a neutral layer to the substrate, hybrid organic-inorganic BCPs, typically with Si-containing moieties on one block, exhibit significantly disparate surface free energies. Therefore, the low SFE block tends to segregate selectively towards the free interface. This was remedied by Bates and co-workers through the use of a top-coat that adds a neutral

layer to the free interface.[88] As the free interface meets the neutrality condition, the high-χ, sub-10 nm perpendicular structure of PS-*b*-PTMSS-*b*-PS could be realized. By using a top-coat in conjunction with a pre-patterned DSA substrate, the development and pattern transfer of 5 nm half-pitch L/S patterns was realized by Lane and co-workers,[132] representing a huge step towards the development of defect-free sub-10 nm patterns for industrial use.

Aside from controlling the chemical properties of the interfaces, physical and entropic effects could also be used to induce the perpendicular orientation of BCP microdomains.[133] Such entropic effects could range from controlling the architecture of the BCPs to changing the physical properties of the thin film itself. Lu and co-workers succeeded in obtaining perpendicular structures in thermally-annealed PS-*b*-PDMS thin films by using a star-block PS-*b*-PDMS and an air plasma treatment.[133] Through entropic effects, the miktoarm architecture of the BCP encourages the parallel orientation of the BCP chains, and thus the perpendicular orientation of the microdomains. Additionally, the plasma treatment created a thin oxidative layer on the free interface that helped to reduce the selective segregation of one domain onto the free interface, enabling the formation of perpendicular cylinders and lamellae. Alternatively, the film thickness can also be adjusted to discourage the formation of parallel structures. When lamellar thin films are less than 1 L_0 in thickness, parallel orientation is avoided as there is insufficient polymer on the surface to form the bilayer characteristic of parallel lamellae. To form such parallel structures at <1 L_0 thickness, the BCP chains would need to exhibit increased stretching, thereby placing an entropic penalty on the formation of parallel structures and encouraging the perpendicular orientation of the BCP microdomains.

Another useful alternative to controlling the external interfaces and properties is to directly manipulate the chemical properties of the BCP itself. The ease of forming perpendicular PS-*b*-PMMA structures on thin films easily can be directly attributed to the similar surface affinities of the two constituent blocks. Therefore, based on this idea, by designing BCPs with similar surface affinities, easy perpendicular orientation through simple thermal annealing processes could potentially achieved. Seshimo and co-workers reported

development of Si-containing PS-*b*-PDMS-derived BCPs that are capable of forming sub-10 nm perpendicular lamellae without the use of a top-coat.[134] Notoriously, polysiloxane-based BCPs tend to form parallel structures on thin films due to the disparate surface affinities of the blocks. Generally, polysiloxanes exhibit hydrophobicity and have a low SFE. However, by functionalizing poly(methylvinyl siloxane) (PMVS), a polysiloxane that is analogous to PDMS with a vinyl side group, with a hydroxyl group-containing functionality, the surface affinity of the functionalized-PMVS block can be adjusted to roughly that of PS. Using a BCP of PS and the hydroxy-functionalized PMVS, PS-*b*-PMHxOHS, Seshimo and co-workers proved this concept by reporting the formation of thermally-annealed 9 nm perpendicular lamellae. Subsequently, in a series of studies, Hayakawa and co-workers also reported on the perpendicular orientation of thermally annealed thin films of a Si- and F-containing BCP, PMAPOSS-*b*-PTFEMA.[92,128–130,135] It was reported that the Si-containing PMAPOSS and the F-containing PTFEMA blocks were both hydrophobic and exhibited similar SFEs, facilitating the perpendicular orientation of lamellae on bare Si wafers, using simple thermal annealing under ambient conditions.

Therefore, to achieve perpendicular orientation on thin films, a large number of possible solutions have been developed, ranging from controlling the chemical affinities of the interfaces and the BCPs to optimizing the processing conditions for perpendicular orientation. However, when scaling up processes to industrial scale, it is generally desirable to keep the number of processing steps required to a minimum. Thus, a strongly-segregating BCP that is capable of forming sub-10 nm perpendicular structures using simple thermal annealing processes would be close to ideal.

1-12 Synthesis of the BCP

Based on the criteria discussed earlier, novel candidate BCPs can be designed and synthesized. Generally, polymers are synthesized through either a chain polymerization, polyadditon, or polycondensation reaction. The former involves the chain initiation of the polymerization process, followed by a propagation process in which the chains grow in length, and a chain transfer or termination process that can end the polymerization. On the

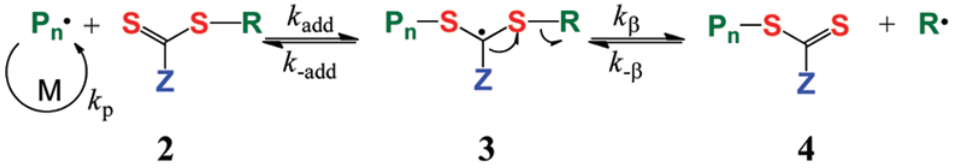
other hand, the two latter reactions are also known as step-growth polymerization, and generally involve the growth of the polymer chain through sequential addition or condensation reactions between the monomers. The synthesis of polymers using these fairly traditional techniques usually results in less well-defined primary structures. This is because the polymerization of the monomers occurs in a random and uncontrolled manner, resulting in a polymer with a wide range of chain lengths, and a large dispersity. However, to ensure reliable self-assembly on thin films, the BCPs should exhibit well-defined primary structures, controllable molecular weights, and low dispersities. Additionally, for resist applications in the microelectronics industry, metal residues should be avoided. This is due to the fact that residual metals could cause undesirable short circuits after pattern transfer. Meanwhile, a number of “living” or “controlled” polymerization techniques that allow for the synthesis of BCPs with well-defined primary structures, controllable molecular weights, and low dispersities have been developed.[136] The living polymerization of a monomer was first demonstrated by Szwarc in 1956.[137,138] By using a carbanionic initiator, the near-instant initiation and slower growth of the polymer could be achieved. In this manner, the random initiation and propagation of the polymer chains could be prevented. Additionally, without the addition of an external influence, the propagating anions of the polymeric chains remain active or “alive”. Hence, the reaction has come to be known as living anionic polymerization. On the other hand, the fact that chain propagation hinges on the presence of an active carbanion, which can get terminated in the presence of an active proton, the types of monomers that can be polymerized via anionic polymerization is limited.

Meanwhile, a family of polymerization techniques known as reversible deactivation radical polymerization (RDRP) presents a great alternative to living anionic polymerization. Also known as “living” or “controlled” radical polymerization (LRP/CRP), RDRP is a class of radical polymerization which are generally characterized by reversible interchange between a majority dormant species that does not polymerize and a small quantity of active species that allows for the growth of the polymer chains. Generally, the end of the propagating chain is functionalized with a capping-agents such as a halogen, nitrogen (N)-containing

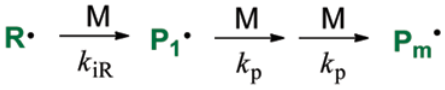
functionality or thiocarbonyl moiety. When the ends of the polymer chains are capped by the respective functionalities, the polymer chains are dormant and cannot propagate. However, the end-caps can reversibly cleave away from the polymer chain, revealing an active radical that is capable of propagation. By keeping the equilibrium largely on the side of the dormant species and maintaining a high rate of reversible activation and deactivation, the propagation of all the polymer chains can be kept relatively similar, thereby achieving the synthesis of a polymer with well-defined primary structures, controllable molecular weights, and low dispersities. However, unlike living anionic polymerization, a small percentage of "dead" chains will be included in the final polymer as the radicals that were initially used to initiate the reaction get terminated. Therefore, the term "living" or "controlled" radical polymerization has been discouraged. Nevertheless, the well-controlled synthesis of polymers can be achieved with such methods and the term RDRP has been recommended by the International Union of Pure and Applied Chemistry (IUPAC). While united by a single terminology, the RDRP family encompasses a wide range of polymerization techniques. In the 1980s, Moad and co-workers experimented with the synthesis of polymers in the presence of a nitrogen (N)-containing chain trapping agent.[139] This eventually led to the development of nitrogen-mediated polymerization (NMP) in 1993 whereby nitroxides are used to control the polymerization reaction.[140] Such nitroxides could form stable radicals that reversibly attach and detach from the ends of a propagating polymer chain, allowing for the metal-free, controlled polymerization of styrenic monomers. Subsequently, controversially in 1995, two halogen-mediated RDRP techniques were reported nearly simultaneously. Kato and co-workers reportedly used a chlorine (Cl) end-cap and a ruthenium (Ru) catalyst to control the polymerization of methyl methacrylate.[141] Showing "living"-like behavior, the molecular weight of the synthesized PMMA was shown to increase proportionally with monomer conversion. Additionally, narrow dispersities with $Đ < 1.4$ had been obtained, suggesting that the controlled synthesis of a well-defined PMMA had been achieved. Meanwhile, Wang and co-worker used a bromine (Br) end-cap and a copper (Cu) catalyst for the controlled synthesis of PS,[142] in a reaction termed atom transfer radical polymerization

(ATRP). Unlike living anionic polymerization, these halogen-mediated RDRP techniques were shown to be able to polymerize a large variety of monomers. However, the use of metal catalysts renders the BCPs synthesized by these options as less desirable for applications in the microelectronics industry. Subsequently, the youngest major member of the RDRP family is known as the reversible activation-deactivation chain transfer (RAFT) process. First reported by Moad and co-workers, the same researchers who performed the initial experiments that led to the development of NMP, the RAFT process involves a sulfur (S)-containing thiocarbonyl functionality that is known as an *iniferter* (from initiator/ transfer agent/terminator), a chain transfer agent (CTA), or simply RAFT agent. In this report, the term CTA will be used for standardization.[143,144] While the thiocarbonyl functionality forms the main core functionality of the CTA, different functional groups can be added to optimize the CTA for the polymerization of different monomers. Generally, an “R”-group is capable of reversibly attaching and detaching from the thiocarbonyl functionality, revealing an active radical site that allows for the initiation and propagation of a polymer chain. Additionally, a “Z”-group is found alpha to the thiocarbonyl functionality. By changing the functionalities on the R- and Z-groups, the controlled polymerization of a large variety of monomers, including methacrylates, styrenics, and vinyl acetates can be achieved. Additionally, as a metal catalyst is not required in the RAFT process, polymers synthesized via RAFT can be freely applied to the microelectronics industry.

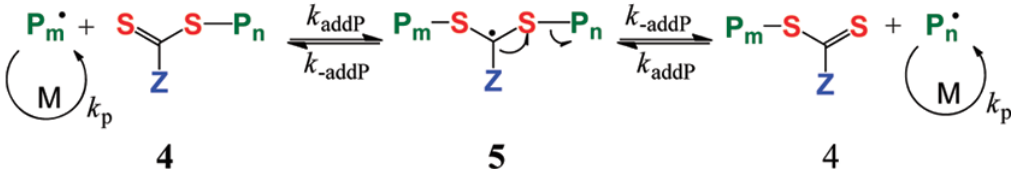
Initialization:



Reinitiation:



Main equilibrium:



Schematic 1-2. Illustration of the chemical equilibria during the synthesis of a polymer via the RAFT process. Reprinted with permission from Keddie, D. J. et al, *Macromolecules* **2012**, *45* (13), 5321-5342. Copyright 2012 American Chemical Society.

1-13 Metrologies for the Analysis of BCP Nano-assemblies

The self-assembled, ordered structures of BCPs can range in feature sizes from 5 to 300 nm. Simple observation techniques such as optical microscopy is generally limited to approximately 200 nm. Therefore, alternative metrologies are needed to evaluate the ordered nanostructures formed by BCPs. The techniques used to characterize these self-assembled structures can generally be categorized into two categories, depending on whether the techniques evaluate an averaged, global result, or a detailed, localized result. Additionally, while a range of metrologies have been developed to study the nanometer-scale self-assembled morphologies of BCPs, different methods need to be employed for the study of bulk and thin film samples. Traditionally, the nano-assemblies formed by BCP bulk samples and thin films have been studied using small-angle X-ray scattering (SAXS) (Fig. 1-17), small-angle neutron scattering (SANS), grazing-incidence SAXS (GI-SAXS), transmission electron microscopy (TEM), scanning transmission electron microscopy (STEM), scanning electron microscopy (SEM), or atomic force microscopy (AFM). Each

technique provides a different perspective towards the self-assembled structures and must contend with different constraints. Therefore, depending on which aspect of BCP self-assembly is to be studied, different techniques need to be utilized.

The characterization of BCP structures using SAXS or SANS involves irradiating the sample with either an X-ray or a neutron beam.[145–148] Based on the elastic scattering of the X-ray or neutrons as they pass through the sample, a scattering profile which can reveal the nature of the BCP morphologies can be obtained. Therefore, SAXS and SANS are frequently employed to determine the phase behavior of BCPs. However, such scattering techniques target the reciprocal space of the ordered structures, yielding an averaged, global result. While certain “local” information such as the correlation length can be extracted from the widths of the primary peaks, direct changes in the structure of specific defects cannot be observed using scattering techniques. Additionally, as the X-ray irradiation or neutrons need to pass through the sample for analyses, SAXS and SANS cannot be applied to thin films supported on a hard substrate. Instead, the near-surface region of a thin film can be examined by using an almost parallel incident angle. When X-rays are irradiated at such an angle, this technique has come to be known as GI-SAXS and scattering profiles that can yield reciprocal-space information about the structure and ordering of the thin film surface can be obtained.[69,70,149]

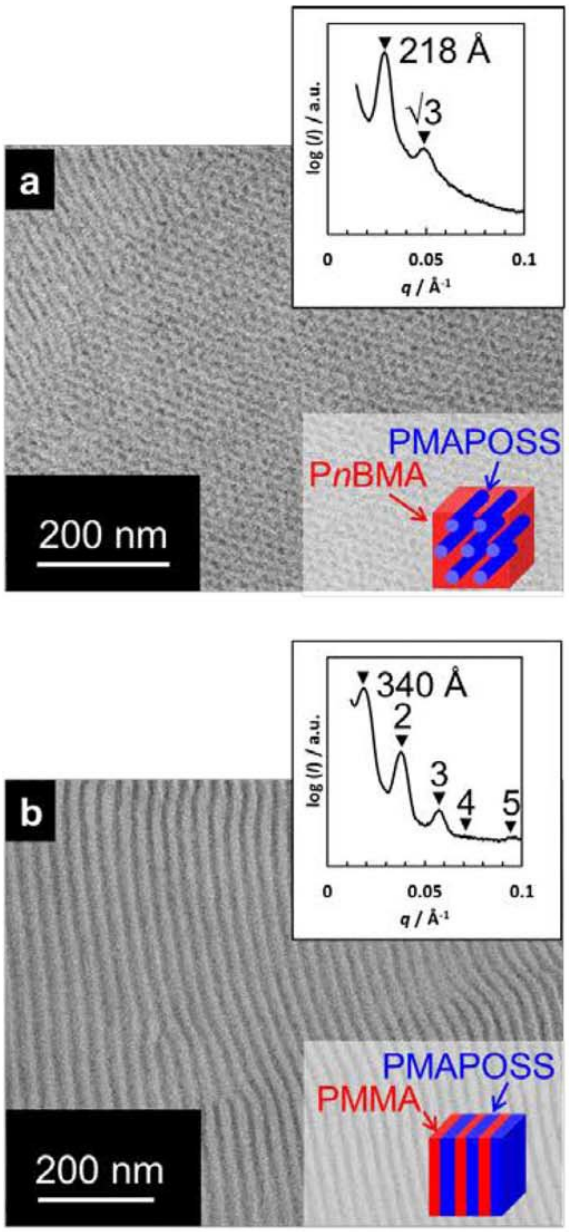


Figure 1-17. A combination of TEM and SAXS analyses for the identification of hexagonally-packed cylindrical and lamellar structures in BCPs. Adapted with permission from Kato, F. et al, *Polym. Chem.* **2017**, *55* (13), 2234-2242. Copyright 2017 Wiley Periodicals, Inc.

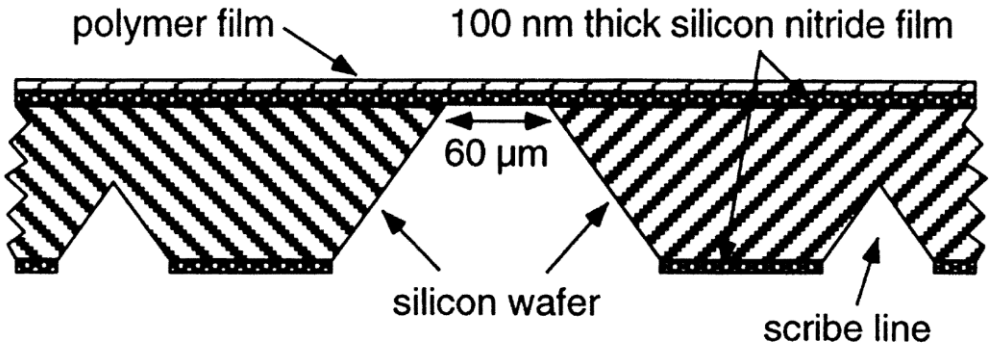


Figure 1-18. Illustration for the preparation of a window for the TEM analysis of a BCP thin film. Reprinted with permission from Morkved, T. L. et al, *Polym.* **1998**, *39* (16), 3871-3875. Copyright 1998 Elsevier Science Ltd.

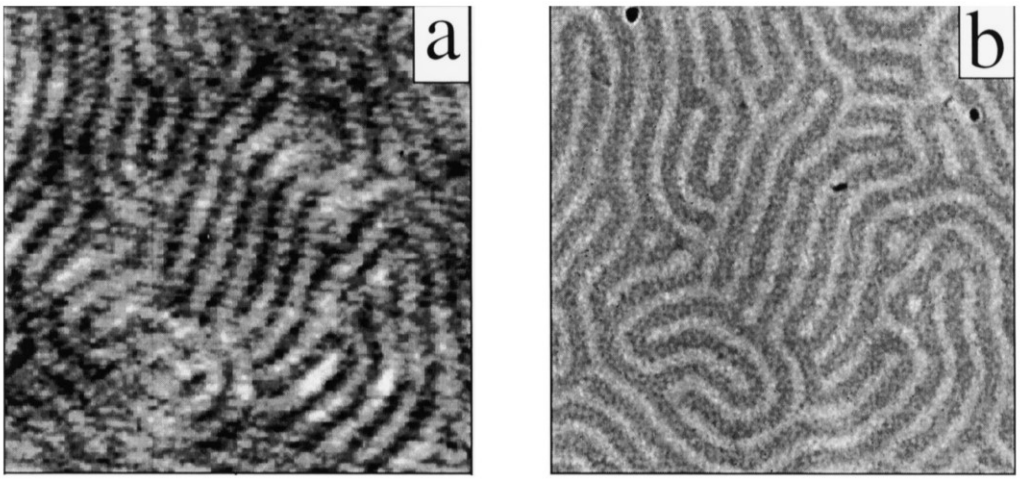


Figure 1-19. (a) AFM topography image and (b) TEM micrograph of a specific area found on a parallel cylinder-forming PS-*b*-PMMA thin film. Adapted with permission from Morkved, T. L. et al, *Polym.* **1998**, *39* (16), 3871-3875. Copyright 1998 Elsevier Science Ltd.

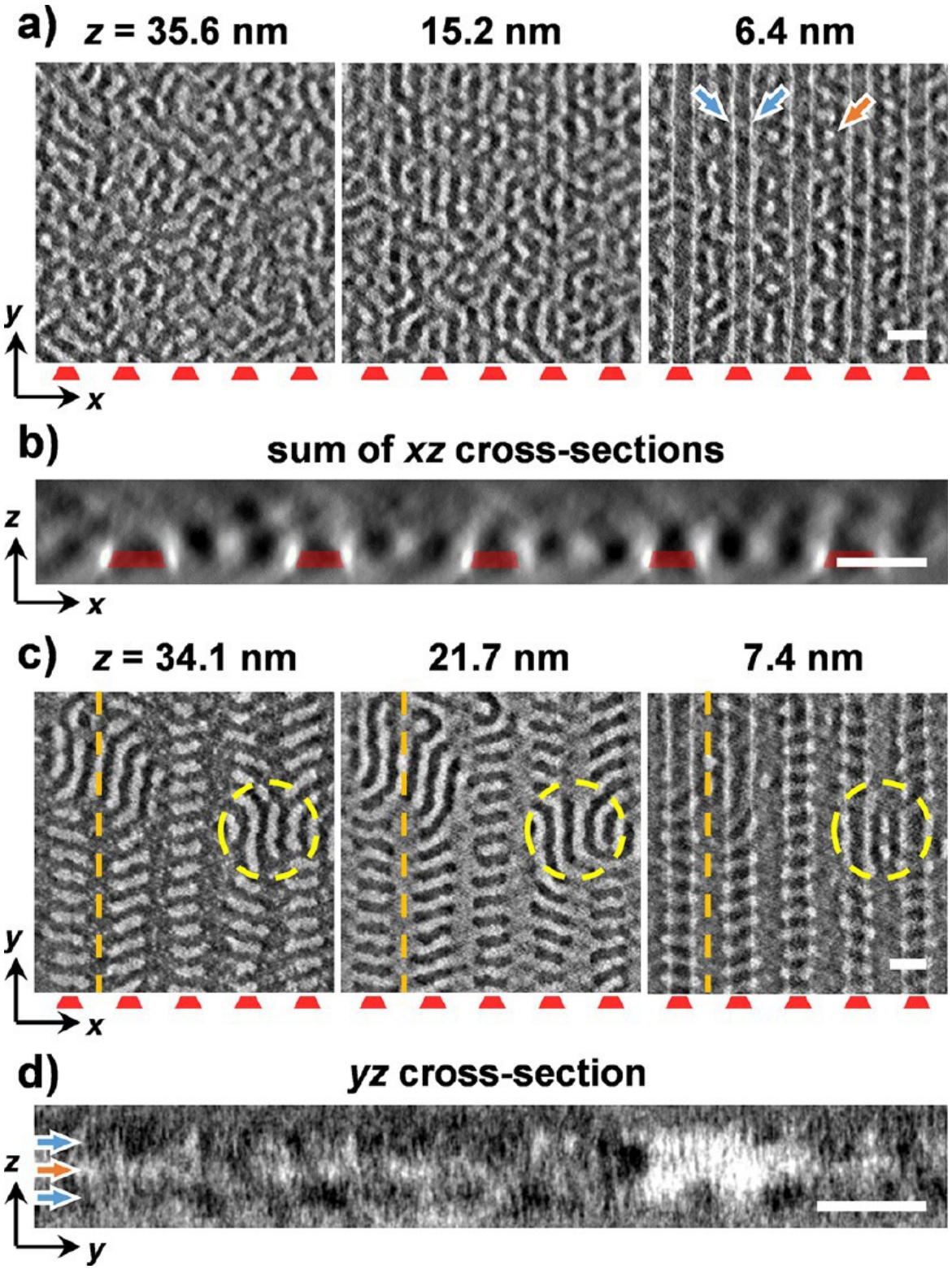


Figure 1-20. STEM tomography digitally-stitched images showing the 3D defect structure found in a PS-*b*-PMMA thin film prepared on LiNe flow DSA substrates. Reprinted with permission from Ren, J. et al, *ACS Appl. Mater. Interfaces* **2018**, *10* (27), 23414-23423. Copyright 2018 American Chemcial Society.

In contrast to the scattering techniques, TEM, STEM, SEM, and AFM can be used to directly image the BCP structures in real space. The bulk structures of a BCP can be characterized using TEM and STEM,[150–152] which detects electrons that have transmitted through a sufficiently thin sample. As the electrons pass through the sample, an image contrast can be obtained depending on a number of factors such as the positional thickness on the film or the atomic number of the elements at each location. Therefore, TEM and STEM can be used to study the BCP structures in real-space, yielding direct, visual results of the BCP structure and any defects that form. Given additional detectors, STEM analyses can also be used to obtain scattering results similar to those obtained from SAXS or SANS, or even map the areal concentration of different elements on the sample. Furthermore, as TEM and STEM detects the electrons that have passed through the sample, by changing the angle at which the samples are analyzed, a three-dimensional projection can be obtained from a series of tilted two-dimensional images.[58,60,152,153] Such tomographic techniques especially useful as the real structures formed by BCPs occupy three-dimensional space. Therefore, metrologies that can evaluate a BCP structure in three dimensions are highly desirable. However, there are also drawbacks to using TEM and STEM. For the electrons to be able to pass through the BCP samples, the samples typically need to be sectioned into ultrathin films that are less than 100 nm thick as thicker samples typically prevent electron transmission. Such ultrathin sections are typically sliced out from a bulk sample using an ultramicrotome. In the case of thin films however, although BCP thin films are typically less than 100 nm thick, the supporting substrate is usually a millimeter-thick Si-based wafer, thus preventing TEM or STEM analyses. Having said that, thin film substrates have been prepared to enable the TEM or STEM analysis of BCP thin films. Morkved and co-workers stripped the surface oxide layers from a Si wafer and deposited 100 nm thick silicon nitride films on both sides of the Si wafer (Fig. 1-18 and 1-19).[154] A photoresist was then used to develop a pattern on the backside of the Si wafer and using carbon tetrafluoride (CF_4) reactive ion etching (RIE), the bottom layer of silicon nitride and the silicon found between the photoresists were removed, leaving behind a small window whereby the substrate was a

100 nm thick silicon nitride film. The BCP was then deposited atop the thin film and upon annealing, TEM analysis could be carried out through the window. Using similar substrates with windows patterned into the backsides of the wafers, Segal-Peretz and co-workers published a series of reports which studied the defect structure in the depths of PS-*b*-PMMA thin films with LiNe flow DSA guides.[58,60] Additionally, using STEM tomography by stitching together multiple images obtained at incremental tilt angles, they were able to show the three-dimensional structure of a stitch morphological defect (Fig. 1-20), a defect unique to chemoepitaxial DSA processes such as LiNe flow DSA, thereby demonstrating the usefulness of such 3D analytical techniques.

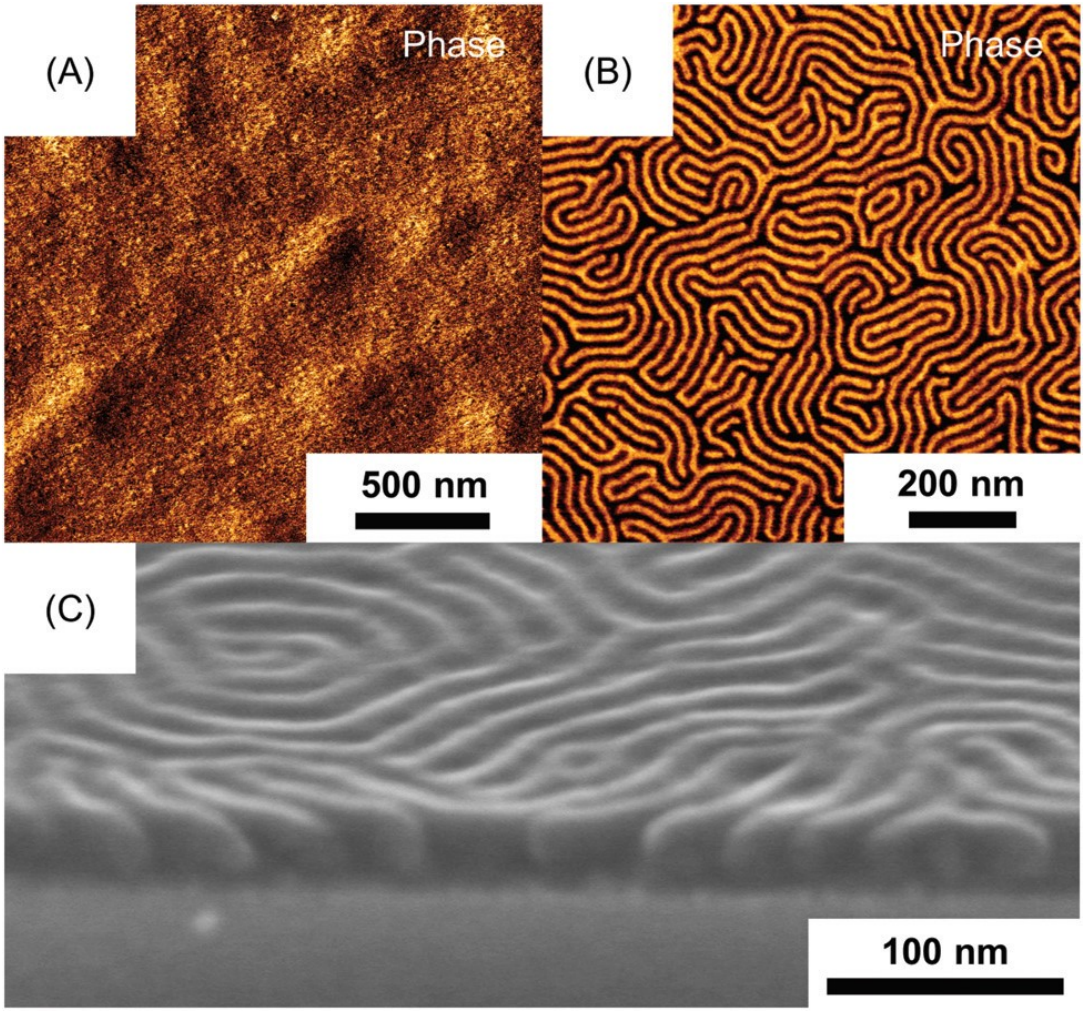


Figure 1-21. AFM phase contrast images of (A) parallel lamellae and (B) perpendicular lamellae. (C) Tilted SEM image showing the edge of a thin film with perpendicularly-oriented

lamellae. Reprinted with permission from Yoshimura, Y. et al, *Soft Matter* **2019**, *15* (17), 3497-3506. Copyright 2019 Royal Society of Chemistry.

For simpler analyses of BCP thin films, SEM and AFM are typically employed (Fig. 1-21).[93,129,135] Instead of detecting the electrons transmitted through a sample, a sample is imaged via SEM in real-space using a focused electron beam and detects the secondary electrons released from the sample upon excitement. When applied to the surfaces, edges, or cross-sections of a thin film, topographic 2D maps can be obtained. On the other hand, AFM utilizes a probe to scan a surface using a number of different imaging modes. The most basic contact mode AFM simply involves the dragging of a microcantilever across a surface, allowing for the topography of the image to be mapped in a line-by-line manner. However, contact mode AFM tends to be relatively noisy as softer, low stiffness cantilevers are required. To image the surface of a BCP thin film, intermittent contact mode AFM, also known as alternating current (AC) mode AFM, is typically utilized. In AC mode, the microcantilever is oscillated near its resonance frequency and repeatedly taps a surface for imaging. As the microcantilever scans the surface, the topographic profile of the area can be mapped in a similar manner to contact mode AFM. Additionally, depending on a number of factors such as the topographic contrast and the inherent mechanical properties of the material examined, a phase shift can be detected in the driving signal of the oscillating cantilever. This produces a phase contrast image that allows for the mapping of different materials on the surface and is particularly useful for analyzing the nanometer-scale structures of BCPs. In the case of the most well-studied BCP for lithographic applications, PS-*b*-PMMA, the PS domain is known to appear dark while the PMMA domain appears bright in the phase images.

1-14 Real-Time and Real-Space Tracking of BCP Self-Assembly

To work towards fulfilling the industrial requirements of 0.01 defects per cm^2, a complete understanding of the mechanisms behind the evolution of self-assembled structures and the annihilation of defects must be developed. There have been numerous reports that studied the defectivity of BCPs in the bulk, on unpatterned thin films, and also on

DSA substrates.[60,131,155–161] Particularly, recent studies have focused on optimizing the DSA substrates to reduce the defect density of the system. Generally, it was found that dislocation defects are most commonly observed in BCP thin films prepared on DSA substrates, so much so that the defect densities reported are specifically the number of dislocations per unit area.[131,159] However, other defects such as disclinations can be expected to appear in linear patterns with 2D symmetry. It remains unclear as to why dislocation defects are so common in DSA thin films. Therefore, in order to develop a better understanding of the self-assembly and defectivity of BCPs, detailed analyses of the growth and transformations of the self-assembled structures on BCP thin films need to be carried out.

For such studies of BCP self-assembly, a non-destructive and non-invasive analytical technique which yields 3D information about the local and global nature of the BCP bulk and/or thin film structure in real-time, real-space, and reciprocal-space simultaneously should be used. However, such metrologies do not exist. Each of the analytical techniques used to study BCP self-assembly, as discussed in 1-13 Metrology for the Analysis of BCP Nano-assemblies, have their respective benefits and drawbacks, and generally are used to study different aspects of BCP self-assembly. To determine the exact mechanisms for the evolution of BCP structures and track the changes in individual defect configurations as they proceed to annihilate, a metrology that offers real-time and real-space imaging is required. Although scattering techniques have been used to study the disorder-to-order and order-to-order transitions of BCP structures in real time, such scattering techniques offer only globalized, averaged reciprocal-space data, defectivity studies relying solely on scattering cannot be used to elucidate the local changes in defect configuration.

On the other hand, TEM, STEM, SEM, and AFM can be used to study the BCP structures in real-space. Early studies typically used one of these metrologies to track specific defect sites upon the repeated sequential annealing, quenching, and ex situ imaging of a given area on the thin film. Sibener and co-workers published a series of reports detailing the changes in the BCP surface structure,[57,154,155,160–164] initially using ex situ AFM

and parallel cylinder-forming BCPs, and later extending their analyses to real-time, real-space, and in-situ AFM analysis of a perpendicular lamella-forming PS-*b*-PMMA on LiNe flow DSA substrates. In their earlier studies, they observed the stochastic evolution of defects on a fingerprint pattern of parallel PS-*b*-PMMA cylinders. Using repeated annealing, quenching, and imaging of the same defect area, they were able to show how the BCP structures can change from one configuration to another (Fig. 1-22).[160,161] Additionally, although they were able to track the development and development of stich morphological defects, a defect type unique to chemoepitaxial DSA processes, in a recent report,[57] it took many years before a real-time and real-space metrology could be developed for the analysis of BCP thin film structures.

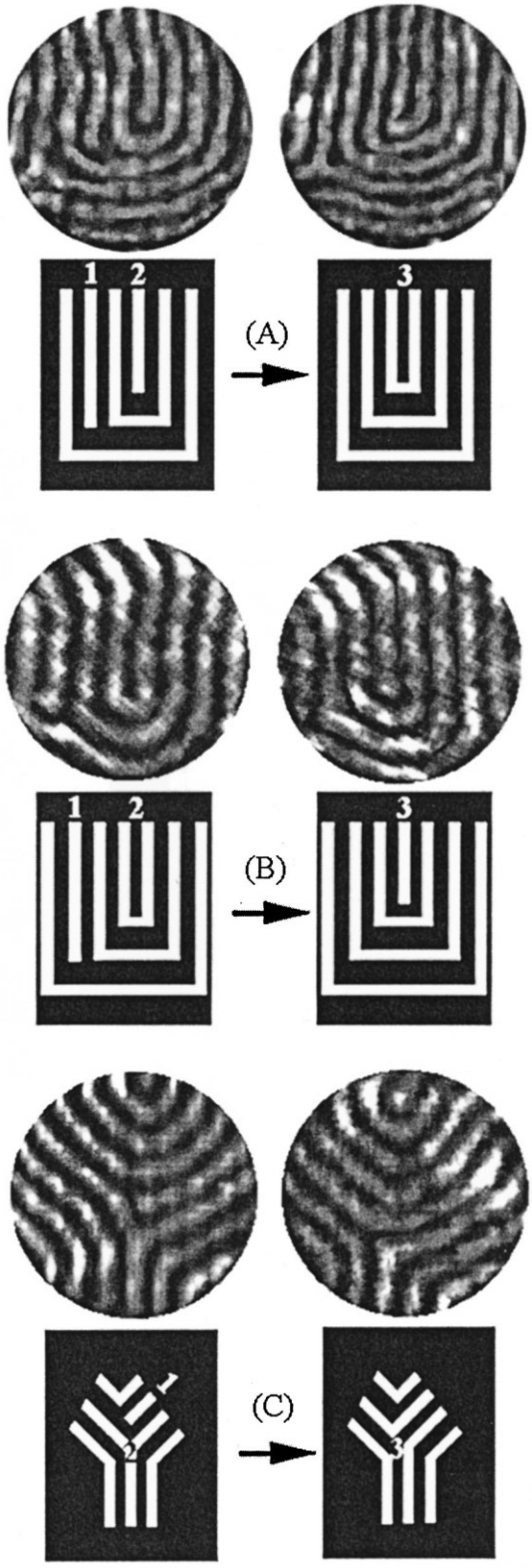


Figure 1-22. AFM images and the corresponding illustrations of different configurations of specific individual defects after repeated annealing, quenching, and imaging. Reprinted with permission from Hahm, J. and Sibener, S. J. *J. Chem. Phys.* **2001**, *114*, 4730-4740. Copyright 2001 American Institute of Physics.

The real-time and real-space analysis of BCP structure has been difficult due in part to the fact that the electron microscopy techniques such as SEM, TEM, and STEM, are not inducive for real-time imaging. Both TEM and STEM require the preparation of sufficiently thin sections of the BCP sample, a possible destructive process. Additionally, as TEM and STEM analyses rely on the contrast between elements with different atomic numbers, one domain of the BCP typically must first be selectively stained with a heavier element such as by exposing the BCP sample to iodine (I_2), osmium tetroxide (OsO_4), or ruthenium tetroxide (RuO_4).[119,153,165] Although acceptable for ex situ analysis, the heavy elements could potentially interfere with the self-assembly process of continued annealing was applied. Similarly, SEM is not applicable for the constant, long-term observation of the same location. As electrons are irradiated onto the sample surface, the secondary electrons released from the excited molecules are detected by the SEM for imaging. This typically leads to electron charge-up that damages and slowly etches away at the film surface. Additionally, SEM is mainly sensitive to topographic changes in the film. Therefore, one domain is typically selectively, and destructively etched away prior to SEM imaging, thus preventing the real-time observation of BCP structures.

Therefore, the only remaining metrology that can offer both real-time and real-space imaging of a BCP sample is AFM. By adding a heating element to the sample mounting stage of an AFM, the in situ thermal annealing of the BCP sample becomes possible. Intermittent contact or AC mode AFM can then be used to image the BCP surface and produce a phase contrast image to map the location of the BCP microdomains without damaging the film surface. However, as the microcantilever can physically expand or distort upon thermal heating, the microcantilever must first be allowed to stabilize prior to AFM imaging. Building upon past ex situ studies, Knoll and co-workers reported observed the real-time and real-space order-to-order transition in a BCP thin films using in situ AFM at an isothermal annealing temperature.[166] Using thin films of PS-*b*-PB-*b*-PS, they directly documented the nucleation and growth of a perforated lamellar domain from parallel cylinders, and the annihilation of a patch of parallel cylindrical defects. Subsequently, Yufa

and co-workers demonstrated the real-time and real-space in situ AFM analysis of parallel cylinders of PS-*b*-PMMA between 150 to 245 °C.[163] They found that the correlation length of the cylindrical grains grew gradually as the temperature increased. Finally, in a relatively recent report, Raybin and co-workers imaged the disappearance of defects unique to lamellar PS-*b*-PMMA thin films prepared on LiNe flow DSA substrates (Fig. 1-23).[57] These earlier studies prove that in situ AFM can be a useful tool for tracking the growth, evolution, and annihilation of self-assembled structures and defects on BCP thin films in real-time and real-space. However, there remains numerous mysteries behind the fundamental self-assembly mechanisms of BCPs. Therefore, to fully characterize the self-assembly behavior of BCP thin films, further detailed studies using in situ AFM are imperative.

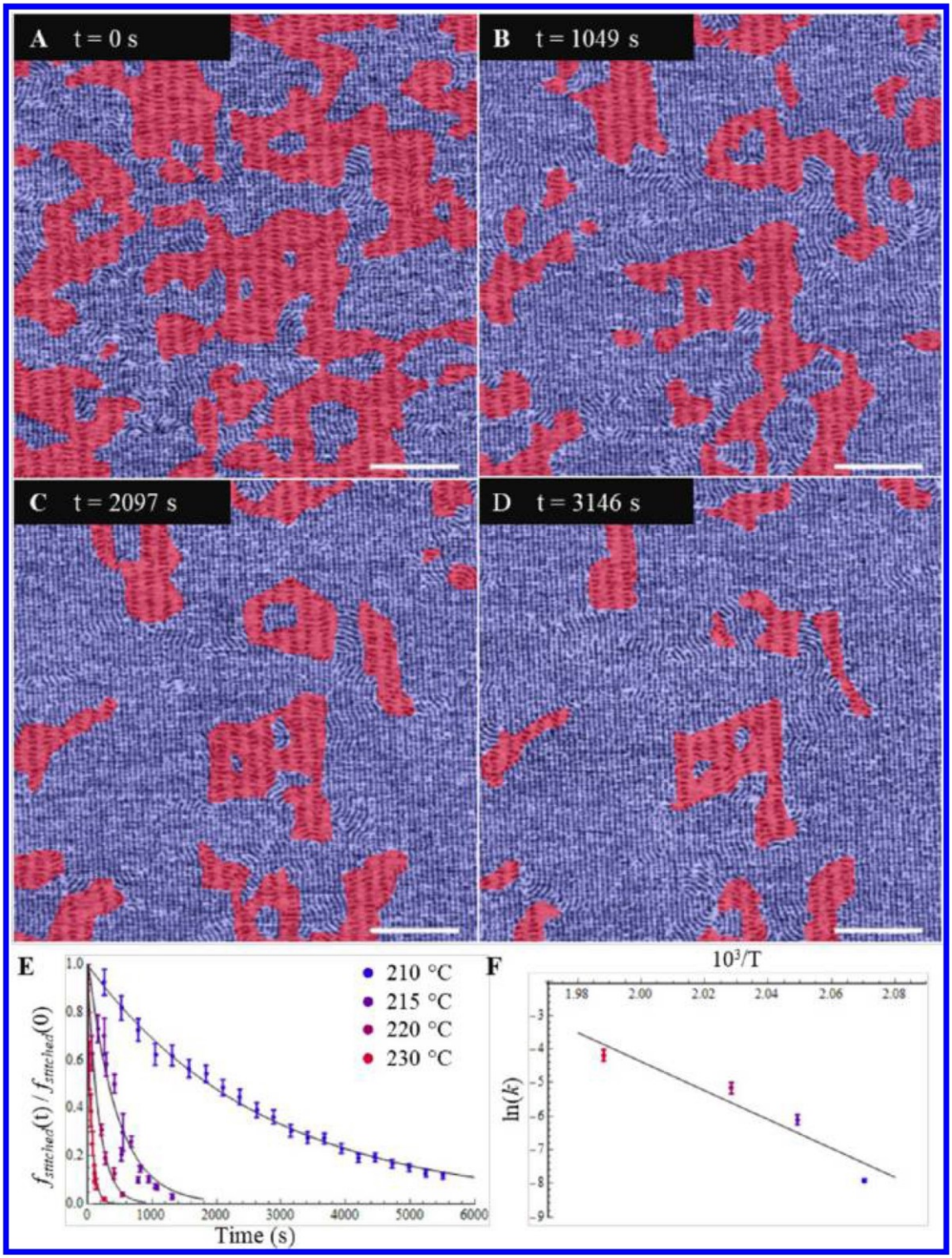


Figure 1-23. (A-D) In situ AFM images obtained at 210 °C, (E) the plots of the areal fraction of the stitch morphological defects count over time, and (F) an Arrhenius plot for the calculation of the apparent energy barrier towards defect annihilation. Reprinted with permission from Raybin, J. et al, *Nano Lett.* **2017**, *17* (12), 7717-7723. Copyright 2017 American Chemical Society.

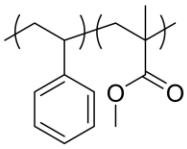
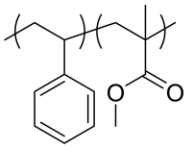
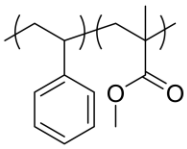
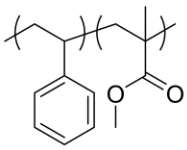
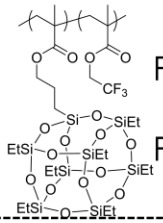
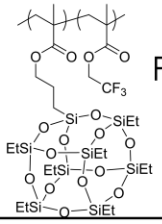
Chapter	BCP	Focus
Ch. 2 Unpatterned and COOL DSA	 PS-*b*-PMMA LAM L_0 = 30 nm	Evaluating a Novel DSA Process
Ch. 3 Incremental SMART™ DSA	 PS-*b*-PMMA LAM L_0 = 30 nm	Disorder-Order Evolution of Perpendicular LAM on DSA Substrate
Ch. 4 Isothermal SMART™ DSA	 PS-*b*-PMMA LAM L_0 = 30 nm	Mechanisms for Growth & Defect Annihilation
Ch. 5 Incremental HEX-CYL DSA	 PS-*b*-PMMA CYL L_0 = 36 nm	Disorder-Order Evolution of Perpendicular CYL on DSA Substrate
Ch. 6 Synthesis of PMAPOSS-*b*-PTFEMA	 PMAPOSS-*b*-PTFEMA or PTFEMA-*b*-PMAPOSS	Optimizing the RAFT Synthesis of PMAPOSS & PTFEMA
Ch. 7 Evolution of PMAPOSS-*b*-PTFEMA	 PMAPOSS-*b*-PTFEMA LAM L_0 = 16 nm	Disorder-Order Evolution via Combinatorial Studies

Figure 1-24. Illustrative outline for each main chapter in this thesis

1-15 Scope of this Study

In this thesis, fundamental research initiatives to work towards fulfilling the targets outlined in 1-4 Block Copolymer Lithography (BCPL) will be undertaken (Fig. 1-24). To

reiterate, the following research challenges need to be resolved before BCPL can become an industrially viable technology. Firstly, steps must be taken towards achieving a defect density of less than 0.01 defects per cm^2 (Defectivity). The BCPs must also be able be able to form the required perpendicular lamellar striped or perpendicular hexagonally-arranged cylindrical lithographic patterns (Architecture & Orientation) at sub-10 nm feature sizes (Resolution), while having been synthesized via metal-free synthetic routes and exhibiting sufficiently high etch contrasts for pattern transfer processing (Chemistry). Furthermore, to maintain compatibilities with industrial scale production lines, the development of the BCP structures needs to proceed via simple thermal annealing processes that avoid the use of dangerous organic vapors or energy-intensive electromagnetic fields (Annealing).

Although the number of challenges presented to the field of BCPL appears daunting, decades of research have built a strong foundation with which the challenges can be met head on. Particularly, with the exception of the issue of defectivity, the other issues have been well-studied one issue at a time, and numerous solutions have been proposed to resolve each of the issues. As BCP self-assembly is inherently a bottom-up process, a similar bottom-up approach should be used to resolving the challenges. To that end, by introducing functionalities to design a novel BCP with targeted properties, most of the issues can be resolved. For example, PS-*b*-PMMA is capable of resolving almost all the listed issues, excepting the defectivity and resolution. By changing the volume fraction of the blocks, PS-*b*-PMMA is capable of forming lamellae for linear striped patterns and cylinders for hexagonally-arranged dot patterns. Additionally, by introducing a chemically-modifying layer of a random copolymer of the constituent monomers onto a Si substrate, preferential interactions at the substrate interface can be removed. By performing thermal annealing between 200 to 290 °C, preferential interactions can also be removed from the free interface, thereby facilitating the perpendicular orientation of the patterns formed by PS-*b*-PMMA. Finally, PS-*b*-PMMA can be easily synthesized via anionic polymerization without leaving metal residues in the polymer and the PMMA domain can be etched away faster

than the PS domain, providing an etch contrast which can be used for pattern transfer onto the substrate.

The listed requirements are generally dependent on the primary structure of the BCP and are not independent from each other. By changing the primary structure of the BCP, such as by introducing Si moieties to one block, the strength of segregation can increase and the minimum resolution attainable by the BCP can be reduced. However, at the same time, the interfacial affinities of the BCP can change significantly, preventing the perpendicular orientation or thermal annealing of the thin films. Therefore, based on the various trade-offs between the BCP properties, PS-*b*-PMMA represents the best balance for fulfilling most of the requirements. As a result, most academic and industrial researchers have used PS-*b*-PMMA as the main BCP for potential lithographic applications and various DSA processes that can be integrated into regular microelectronics production lines have been developed.

Therefore, in this study, the issue of defectivity is first tackled using PS-*b*-PMMA thin films prepared on DSA substrates for eventual integration into industrial production lines. However, as foreign particles such as dust can present nucleation sites for defects to appear, DSA substrates must be prepared and processed in extremely well-controlled clean room environments. Therefore, without access to a clean room, the actual realization of 0.01 defects per cm^2 is out of the scope of this study. Instead, fundamental studies focusing on the self-assembly behavior of the BCP thin films are undertaken. Particularly, issues such as the processes that occur and drive self-assembly at the earliest stages of the transformation from a disorder-like state to a well-ordered state have remained a mystery. Additionally, while it is well known that by annealing a BCP thin film, ordered structures can be obtained and defects can form and disappear over time, the mechanisms by which these defects form, grow, and annihilate have not been investigated in detail, in part due to a lack of metrologies for conducting such investigations. Without an exact understanding of the origins, evolution, and annihilation of defects, the complete removal of defects would likely remain impossible. Therefore, using high-speed in situ AFM coupled with a thermal heating

stage, the real-time and real-space ordering of BCP structures and the origins and annihilation pathways of defects is first investigated.

Moving on from the limitations of PS-*b*-PMMA, the synthesis and self-assembly behavior of a well-designed, strongly-segregating, hybrid BCP that is capable of forming perpendicular structures using simple ambient thermal annealing processes is also investigated. Earlier studies have shown that with Si- and F-containing blocks that exhibit similar surface affinities,[92] PMAPOSS-*b*-PTFEMA is capable of forming sub-10 nm lamellae that are oriented perpendicularly on thin films using simple ambient thermal annealing processes. Additionally, by utilizing the RAFT process, PMAPOSS-*b*-PTFEMA can be synthesized without leaving behind residual metals that could potentially interfere with future potential device applications. Furthermore, while the Si-containing PMAPOSS block is resistant to RIE treatment, the F-containing PTFEMA block exhibits increased susceptibilities to etching techniques, increasing the etch contrast between the blocks. Therefore, PMAPOSS-*b*-PTFEMA not only fulfills all the requirements that PS-*b*-PMMA fulfills, but also improves on the resolution and chemistry of the BCP. As PMAPOSS-*b*-PTFEMA is a relatively newly designed BCP, the synthesis via RAFT is first optimized in this study. Following that, the growth and evolution of the sub-10 nm perpendicular lamellar structures are investigated using a combination of in situ AFM, GI-SAXS, and cross-sectional SEM, allowing for a detailed analysis of the changes in the BCP surface and cross-sectional structures. Building upon the real-time and real-space studies of the evolution of BCP structures and defects in this study, the realization of sub-10 nm BCP patterns with <0.01 defects per cm^2 could hopefully be realized in the near future.

1-16 References

(1) Moore, G. E. Cramming More Components onto Integrated Circuits. *Electronics* **1965**, *38* (8), 114-119. DOI: 10.1109/n-ssc.2006.4785860.

(2) Sanders, D. P. Advances in Patterning Materials for 193 Nm Immersion Lithography. *Chem. Rev.* **2010**, *110* (1), 321–360 DOI: 10.1021/cr900244n.

(3) Dammel, R. R. Cost-Effective Sub-20 Nm Lithography: Smart Chemicals to the Rescue. *J. Photopolym. Sci. Technol.* **2011**, *24* (1), 33–42 DOI: 10.2494/photopolymer.24.33.

(4) EUV Lithography Finally Ready for Chip Manufacturing - IEEE Spectrum https://spectrum.ieee.org/semiconductors/nanotechnology/euv-lithography-finally-ready-for-chip-manufacturing.

(5) De Silva, A.; Meli, L.; Goldfarb, D. L.; Felix, N. M. Fundamentals of Resist Stochastics Effect for Single-Expose EUV Patterning. *Proc. SPIE* **2019**, *109570*, 109570F. DOI: 10.1117/12.2515926.

(6) van Setten, E.; Bottiglieri, G.; McNamara, J.; van Schoot, J.; Troost, K.; Zekry, J.; Fliervoet, T.; Hsu, S.; Zimmermann, J.; Roesch, M.; Bilski, B.; Graeupner, P. High NA EUV Lithography: Next Step in EUV Imaging. *Proc. SPIE* **2019**, *109570*, 1095709. DOI: 10.1117/12.2514952.

(7) Trybula, W. J. Status of 157-Nm Optical Lithography. *J. Microlithogr. Microfabr. Microsystems* **2005**, *4* (1), 1–5 DOI: 10.1117/1.1860401.

(8) Totzeck, M.; Ulrich, W.; Göhnermeier, A.; Kaiser, W. Pushing Deep Ultraviolet Lithography to Its Limits. *Nat. Photonics* **2007**, *1* (11), 629–631 DOI: 10.1038/nphoton.2007.218.

(9) Raley, A.; Mack, C. A.; Liu, E.; Thibaut, S.; Ko, A. Benchmarking of EUV Lithography Line/Space Patterning versus Immersion Lithography Multipatterning Schemes at Equivalent Pitch. *Proc. SPIE* **2018**, *10809*, 1080915. DOI: 10.1117/12.2501680.

(10) Ronse, K.; Jansen, P.; Gronheid, R.; Hendrickx, E.; Maenhoudt, M.; Goethals, M.; Vandenberghe, G. Lithography Options for the 32nm Half Pitch Node and Beyond. In

Proceedings of the Custom Integrated Circuits Conference; 2008; Vol. 6924, pp 371–378.

(11) Finders, J.; Dusa, M.; Vleeming, B.; Megens, H.; Hepp, B.; Maenhoudt, M.; Cheng, S.; Vandeweyer, T. Double Patterning for 32nm and below: An Update. *Proc. SPIE* **2008**, *69240*, 692408 DOI: 10.1117/12.772780.

(12) Chang, T. H. P.; Nixon, W. C. Electron Beam Formation of 800 Å Wide Aluminium Lines. *J. Sci. Instrum.* **1967**, *44* (3), 231–234 DOI: 10.1088/0950-7671/44/3/420.

(13) Mann, H. T.; Jan, F. ELECTRON BEAM MASKING FOR ETCHING ELECTRICAL CIRCUITs, January 31, 1963.

(14) Altissimo, M. E-Beam Lithography for Micro-/Nanofabrication. *Biomicrofluidics* **2010**, *4* (2), 026503 DOI: 10.1063/1.3437589.

(15) Ringger, M.; Hidber, H. R.; Schlögl, R.; Oelhafen, P.; Güntherodt, H. J. Nanometer Lithography with the Scanning Tunneling Microscope. *Appl. Phys. Lett.* **1985**, *46* (9), 832–834 DOI: 10.1063/1.95900.

(16) Garcia, R.; Knoll, A. W.; Riedo, E. Advanced Scanning Probe Lithography. *Nature Nanotechnology*. Nature Publishing Group 2014, pp 577–587.

(17) Chou, S. Y.; Krauss, P. R.; Renstrom, P. J. Imprint of Sub-25 Nm Vias and Trenches in Polymers. *Appl. Phys. Lett.* **1995**, *67* (21), 3114 DOI: 10.1063/1.114851.

(18) Kooy, N.; Mohamed, K.; Pin, L. T.; Guan, O. S. A Review of Roll-to-Roll Nanoimprint Lithography. *Nanoscale Res. Lett.* **2014**, *9* (1), 1–13 DOI: 10.1186/1556-276X-9-320.

(19) Hawryluk, A. M.; Seppala, L. G. Soft X-Ray Projection Lithography Using an x-Ray Reduction Camera. **1988**, *6* (6), 2162 DOI: 10.1116/1.584107.

(20) Kinoshita, H.; Kurihara, K.; Ishii, Y.; Torii, Y. Soft X-Ray Reduction Lithography Using Multilayer Mirrors. **1989**, *7* (6), 1648 DOI: 10.1116/1.584507.

(21) Gwyn, C. W.; Stulen, R.; Sweeney, D.; Attwood, D. Extreme Ultraviolet Lithography. *J. Vac. Sci. Technol. B Microelectron. Nanom. Struct.* **1998**, *16* (6), 3142–3149 DOI: 10.1116/1.590453.

(22) Park, M.; Harrison, C.; Chaikin, P. M.; Register, R. A.; Adamson, D. H. Block

Copolymer Lithography: Periodic Arrays of ~1011 Holes in 1 Square Centimeter. *Science (80-.).* **1997**, *276* (5317), 1401–1404 DOI: 10.1126/science.276.5317.1401.

(23) Bates, C. M.; Maher, M. J.; Janes, D. W.; Ellison, C. J.; Willson, C. G. Block Copolymer Lithography. *Macromolecules* **2014**, *47* (1), 2–12 DOI: 10.1021/ma401762n.

(24) Möllenstedt, G.; Speidel, R. Elektronenoptischer Mikroschreiber Unter Elektronenmikroskopischer Arbeitskontrolle. *Phys. J.* **1960**, *16* (4), 192–198 DOI: 10.1002/phbl.19600160412.

(25) Chen, W.; Ahmed, H. Fabrication of 5-7 Nm Wide Etched Lines in Silicon Using 100 KeV Electron-Beam Lithography and Polymethylmethacrylate Resist. *Appl. Phys. Lett.* **1993**, *62* (13), 1499–1501 DOI: 10.1063/1.109609.

(26) Chou, S. Y.; Krauss, P. R.; Renstrom, P. J. Imprint Lithography with 25-Nanometer Resolution. *Science* **1996**, *272* (5258), 85–87 DOI: 10.1126/science.272.5258.85.

(27) Bjorkholm, J. E.; Bokor, J.; Eichner, L.; Freeman, R. R.; Gregus, J.; Jewell, T. E.; Mansfield, W. M.; Mac Dowell, A. A.; Raab, E. L.; Silfvast, W. T.; Szeto, L. H.; Tennant, D. M.; Waskiewicz, W. K.; White, D. L.; Windt, D. L.; Wood II, O. R. Reduction Imaging at 14 Nm Using Multilayer-Coated Optics: Printing of Features Smaller than 0.1 Mm. *J. Vac. Sci. Technol. B* **1990**, *8* (6), 1509 DOI: 10.1116/1.585106.

(28) Matsen, M. W.; Bates, F. S. Origins of Complex Self-Assembly in Block Copolymers. *Macromolecules* **1996**, *29* (23), 7641–7644 DOI: 10.1021/ma960744q.

(29) Matsen, M. W. The Standard Gaussian Model for Block Copolymer Melts. *J. Phys. Condens. Matter* **2001**, *14* (2), R21–R47 DOI: 10.1088/0953-8984/14/2/201.

(30) Fredrickson, G. H.; Helfand, E. Fluctuation Effects in the Theory of Microphase Separation in Block Copolymers On the Role of Hydrodynamic Interactions in Block Copolymer Microphase Separation Fluctuation Effects in the Theory of Microphase Separation in Block Copolymers. *J. Chem. Phys. Block Copolym. Soft Mater. Phys. Today J. Chem. Phys. J. Chem. Phys. J. Chem. Phys. J. Chem. Phys. II J. Chem.*

Phys. **1987**, *87* (10) DOI: 10.1063/1.453566.

(31) Matsen, M. W.; Bates, F. S. Unifying Weak-and Strong-Segregation Block Copolymer Theories. *Macromolecules* **1996**, *29* (4).

(32) Bates, F. S.; Fredrickson, G. H. Block Copolymers—Designer Soft Materials. *Phys. Today* **1999**, *52* (2), 32 DOI: 10.1063/1.882522.

(33) Darling, S. B. Directing the Self-Assembly of Block Copolymers. *Prog. Polym. Sci.* **2007**, *32* (10), 1152–1204 DOI: 10.1016/j.progpolymsci.2007.05.004.

(34) Bates, F. S.; Fredrickson, G. H. Block Copolymer Thermodynamics: Theory and Experiment. *Annu. Rev. Phys. Chem.* **1990**, *41* (1), 525–557 DOI: 10.1146/annurev.pc.41.100190.002521.

(35) Jeong, G.; Yu, D. M.; Mapas, J. K. D.; Sun, Z.; Rzayev, J.; Russell, T. P. Realizing 5.4 Nm Full Pitch Lamellar Microdomains by a Solid-State Transformation. *Macromolecules* **2017**, *50* (18), 7148–7154 DOI: 10.1021/acs.macromol.7b01443.

(36) Meier, D. J. Theory of Block Copolymers. I. Domain Formation in A-B Block Copolymers. *J. Polym. Sci. Part C Polym. Symp.* **1969**, *26* (1), 81–98 DOI: 10.1002/polc.5070260106.

(37) Hasegawa, H.; Hashimoto, T. Morphology of Block Polymers near a Free Surface. *Macromolecules* **1985**, *18* (3), 589–590 DOI: 10.1021/ma00145a051.

(38) Yamashita, Y. Surface Properties of Styrene-Tetrahydrofuran Block Copolymers. *J. Macromol. Sci. Part A - Chem.* **1979**, *13* (3), 401–413 DOI: 10.1080/00222337908068109.

(39) Thomas, H. R.; O'Malley, J. J. Surface Studies on Multicomponent Polymer Systems by X-Ray Photoelectron Spectroscopy. Polystyrene/Poly (Ethylene Oxide) Diblock Copolymers. *Macromolecules* **1979**, *12* (2), 323–329 DOI: 10.1021/ma60068a033.

(40) Han, E.; Stuen, K. O.; La, Y. H.; Nealey, P. F.; Gopalan, P. Effect of Composition of Substrate-Modifying Random Copolymers on the Orientation of Symmetric and Asymmetric Diblock Copolymer Domains. *Macromolecules* **2008**, *41* (23), 9090–9097 DOI: 10.1021/ma8018393.

(41) Ham, S.; Shin, C.; Kim, E.; Ryu, D. Y.; Jeong, U.; Russell, T. P.; Hawker, C. J. Microdomain Orientation of PS-b-PMMA by Controlled Interfacial Interactions. *Macromolecules* **2008**, *41* (17), 6431–6437 DOI: 10.1021/ma8007338.

(42) Albalak, R. J.; Thomas, E. L. Roll-Casting of Block Copolymers and of Block Copolymer-Homopolymer Blends. *J. Polym. Sci. Part B Polym. Phys.* **1994**, *32* (2), 341–350 DOI: 10.1002/polb.1994.090320216.

(43) Angelescu, D. E.; Waller, J. H.; Adamson, D. H.; Deshpande, P.; Chou, S. Y.; Register, R. A.; Chaikin, P. M. Macroscopic Orientation of Block Copolymer Cylinders in Single-Layer Films by Shearing. *Adv. Mater.* **2004**, *16* (19), 1736–1740 DOI: 10.1002/adma.200400643.

(44) Amundson, K.; Helfand, E.; Quan, X.; Hudson, S. D.; Smith, S. D. Alignment of Lamellar Block Copolymer Microstructure in an Electric Field. 2. Mechanisms of Alignment. *Macromolecules* **1994**, *27* (22), 6559–6570 DOI: 10.1021/ma00100a047.

(45) Crossland, E. J. W.; Ludwigs, S.; Hillmyer, M. A.; Steiner, U. Control of Gyroid Forming Block Copolymer Templates: Effects of an Electric Field and Surface Topography. *Soft Matter* **2010**, *6* (3), 670–676 DOI: 10.1039/b914421h.

(46) Crossland, E. J. W.; Ludwigs, S.; Hillmyer, M. A.; Steiner, U. Freestanding Nanowire Arrays from Soft-Etch Block Copolymer Templates. *Soft Matter* **2007**, *3* (1), 94–98 DOI: 10.1039/b609780d.

(47) Ferri, D.; Wolff, D.; Springer, J.; Francescangeli, O.; Laus, M.; Angeloni, A. S.; Galli, G.; Chiellini, E. Phase and Orientational Behaviors in Liquid Crystalline Main-Chain/Side-Group Block Copolymers. *J. Polym. Sci. Part B Polym. Phys.* **1998**, *36* (1), 21–29 DOI: 10.1002/(SICI)1099-0488(19980115)36:1<21::AID-POLB3>3.0.CO;2-X.

(48) Amundson, K.; Helfand, E.; Quan, X.; Smith, S. D. Alignment of Lamellar Block Copolymer Microstructure in an Electric Field. 1. Alignment Kinetics. *Macromolecules* **1993**, *26* (11), 2698–2703 DOI: 10.1021/ma00063a010.

(49) Majewski, P. W.; Yager, K. G. Millisecond Ordering of Block Copolymer Films via Photothermal Gradients. *ACS Nano* **2015**, *9* (4), 3896–3906 DOI:

10.1021/nn5071827.

(50) Berry, B. C.; Bosse, A. W.; Douglas, J. F.; Jones, R. L.; Karim, A. Orientational Order in Block Copolymer Films Zone Annealed below the Order-Disorder Transition Temperature. *Nano Lett.* **2007**, *7* (9), 2789–2794 DOI: 10.1021/nl071354s.

(51) Hashimoto, T.; Bodycomb, J.; Funaki, Y.; Kimishima, K. The Effect of Temperature Gradient on the Microdomain Orientation of Diblock Copolymers Undergoing an Order-Disorder Transition. *Macromolecules* **1999**, *32* (3), 952–954 DOI: 10.1021/ma981249s.

(52) Hu, H.; Gopinadhan, M.; Osuji, C. O. Directed Self-Assembly of Block Copolymers: A Tutorial Review of Strategies for Enabling Nanotechnology with Soft Matter. *Soft Matter*. 2014, pp 3867–3889.

(53) Segalman, R. A.; Yokoyama, H.; Kramer, E. J. Graphoepitaxy of Spherical Domain Block Copolymer Films. *Adv. Mater.* **2001**, *13* (15), 1152–1155 DOI: 10.1002/1521-4095(200108)13:15<1152::AID-ADMA1152>3.0.CO;2-5.

(54) Kim, S. O.; Solak, H. H.; Stoykovich, M. P.; Ferrier, N. J.; De Pablo, J. J.; Nealey, P. F. Epitaxial Self-Assembly of Block Copolymers on Lithographically Defined Nanopatterned Substrates. *Nature* **2003**, *424* (6947), 411–414 DOI: 10.1038/nature01775.

(55) Cheng, J. Y.; Sanders, D. P.; Truong, H. D.; Harrer, S.; Friz, A.; Holmes, S.; Colburn, M.; Hinsberg, W. D. Simple and Versatile Methods to Integrate Directed Self-Assembly with Optical Lithography Using a Polarity-Switched Photoresist. *ACS Nano* **2010**, *4* (8), 4815–4823 DOI: 10.1021/nn100686v.

(56) Liu, C. C.; Han, E.; Onses, M. S.; Thode, C. J.; Ji, S.; Gopalan, P.; Nealey, P. F. Fabrication of Lithographically Defined Chemically Patterned Polymer Brushes and Mats. *Macromolecules* **2011**, *44* (7), 1876–1885 DOI: 10.1021/ma102856t.

(57) Raybin, J.; Ren, J.; Chen, X.; Gronheid, R.; Nealey, P. F.; Sibener, S. J. Real-Time Atomic Force Microscopy Imaging of Block Copolymer Directed Self Assembly. *Nano Lett.* **2017**, *17* (12), 7717–7723 DOI: 10.1021/acs.nanolett.7b03881.

(58) Segal-Peretz, T.; Ren, J.; Xiong, S.; Khaira, G.; Bowen, A.; Ocola, L. E.; Divan, R.; Doxastakis, M.; Ferrier, N. J.; De Pablo, J.; Nealey, P. F. Quantitative Three-Dimensional Characterization of Block Copolymer Directed Self-Assembly on Combined Chemical and Topographical Prepatterned Templates. *ACS Nano* **2017**, *11* (2), 1307–1319 DOI: 10.1021/acsnano.6b05657.

(59) Rincon Delgadillo, P.; Harukawa, R.; Suri, M.; Durant, S.; Cross, A.; Nagaswami, V. R.; Van Den Heuvel, D.; Gronheid, R.; Nealey, P. Defect Source Analysis of Directed Self-Assembly Process (DSA of DSA). In *Alternative Lithographic Technologies V*; 2013; Vol. 8680, p 86800L.

(60) Ren, J.; Zhou, C.; Chen, X.; Dolejsi, M.; Craig, G. S. W.; Rincon Delgadillo, P. A.; Segal-Peretz, T.; Nealey, P. F. Engineering the Kinetics of Directed Self-Assembly of Block Copolymers toward Fast and Defect-Free Assembly. *ACS Appl. Mater. Interfaces* **2018**, *10* (27), 23414–23423 DOI: 10.1021/acsami.8b05247.

(61) Hur, S. M.; Thapar, V.; Ramírez-Hernández, A.; Khaira, G.; Segal-Peretz, T.; Rincon-Delgadillo, P. A.; Li, W.; Müller, M.; Nealey, P. F.; De Pablo, J. J. Molecular Pathways for Defect Annihilation in Directed Self-Assembly. *Proc. Natl. Acad. Sci. U. S. A.* **2015**, *112* (46), 14144–14149 DOI: 10.1073/pnas.1508225112.

(62) Kasahara, Y.; Seino, Y.; Kobayashi, K.; Kanai, H.; Sato, H.; Kubota, H.; Tobana, T.; Minegishi, S.; Miyagi, K.; Kihara, N.; Kodera, K.; Shiraishi, M.; Kawamonzen, Y.; Nomura, S.; Azuma, T. RIE Challenges for Sub-15 Nm Line-and-Space Patterning Using Directed Self-Assembly Lithography with Coordinated Line Epitaxy (COOL) Process. *Proc. SPIE* **2015**, *9428*, 94280S DOI: 10.1117/12.2085704.

(63) Seino, Y.; Kasahara, Y.; Sato, H.; Kobayashi, K.; Kubota, H.; Minegishi, S.; Miyagi, K.; Kanai, H.; Kodera, K.; Kihara, N.; Kawamonzen, Y.; Tobana, T.; Shiraishi, M.; Nomura, S.; Azuma, T. Directed Self-Assembly Lithography Using Coordinated Line Epitaxy (COOL) Process. *Proc. SPIE* **2015**, *9423*, 942316 DOI: 10.1117/12.2085697.

(64) Kato, T.; Konishi, J.; Ikota, M.; Yamaguchi, S.; Seino, Y.; Sato, H.; Kasahara, Y.; Azuma, T. Advanced CD-SEM Metrology for Qualification of DSA Patterns Using

Coordinated Line Epitaxy (COOL) Process. *Proc. SPIE* **2016**, *9778*, 977816 DOI: 10.1117/12.2218605.

(65) Kim, J.; Wan, J.; Miyazaki, S.; Yin, J.; Cao, Y.; Her, Y. J.; Wu, H.; Shan, J.; Kurosawa, K.; Lin, G. The SMART™ Process for Directed Block Co-Polymer Self-Assembly. *J. Photopolym. Sci. Technol.* **2013**, *26* (5), 573–579 DOI: 10.2494/photopolymer.26.573.

(66) Muramatsu, M.; Nishi, T.; You, G.; Ido, Y.; Kitano, T. Pattern Defect Reduction for Chemo-Epitaxy DSA Process. *Proc. SPIE* **2019**, *10960*, 109600W DOI: 10.1117/12.2514671.

(67) Muramatsu, M.; Nishi, T.; Ido, Y.; Kitano, T. Defect Mitigation of Chemo-Epitaxy DSA Patterns. *Proc. SPIE* **2020**, *11326*, 113260Y DOI: 10.1117/12.2551996.

(68) Muramatsu, M.; Nishi, T.; You, G.; Ido, Y.; Kitano, T. Defect and Roughness Reduction of Chemo-Epitaxy DSA Pattern. *Proc. SPIE* **2018**, *10584*, 105840M DOI: 10.1117/12.2297185.

(69) Mayes, A. M.; Russell, T. P.; Bassereau, P.; Baker, S. M.; Smith, G. S. Evolution of Order in Thin Block Copolymer Films. *Macromolecules* **1994**, *27* (3) DOI: 10.1021/ma00081a020.

(70) Mansky, P.; Russell, T. P.; Hawker, C. J.; Pitsikalis, M.; Mays, J. Ordered Diblock Copolymer Films on Random Copolymer Brushes. *Macromolecules* **1997**, *30* (22), 6810–6813 DOI: 10.1021/ma970675v.

(71) Russell, T. P.; Hjelm, Jr., R. P.; Seeger, P. A. Temperature Dependence of the Interaction Parameter of Polystyrene and Poly (Methyl Methacrylate). *Macromolecules* **1990**, *23*, 890–893 DOI: 10.1021/ma00205a033.

(72) Matsen M.W., S. M.; Mai, Y.; Eisenberg, A.; Matsen M.W., S. M. Self-Assembly of Block Copolymers. *Curr. Opin. Colloid Interface Sci.* **1996**, *1* (2011), 329–336 DOI: 10.1039/c2cs35115c.

(73) Grason, G. M. The Packing of Soft Materials: Molecular Asymmetry, Geometric Frustration and Optimal Lattices in Block Copolymer Melts. *Phys. Rep.* **2006**, *433* (1), 1–64 DOI: 10.1016/j.physrep.2006.08.001.

(74) Bates, F. S.; Fredrickson, G. H. Block Copolymers—Designer Soft Materials Fluctuation Effects in the Theory of Microphase Separation in Block Copolymers. *Phys. Today J. Chem. Phys. J. Chem. Phys. J. Chem. Phys. J. Chem. Phys. II J. Chem. Phys.* **1999**, *52* (3592) DOI: 10.1063/1.1677735.

(75) Sinturel, C.; Bates, F. S.; Hillmyer, M. A. High χ-Low N Block Polymers: How Far Can We Go? *ACS Macro Lett.* **2015**, *4* (9), 1044–1050 DOI: 10.1021/acsmacrolett.5b00472.

(76) Chanpuriya, S.; Kim, K.; Zhang, J.; Lee, S.; Arora, A.; Dorfman, K. D.; Delaney, K. T.; Fredrickson, G. H.; Bates, F. S. Cornucopia of Nanoscale Ordered Phases in Sphere-Forming Tetrablock Terpolymers. *ACS Nano* **2016**, *10* (5), 4961–4972 DOI: 10.1021/acsnano.6b00495.

(77) Epps, T. H.; Cochran, E. W.; Hardy, C. M.; Bailey, T. S.; Waletzko, R. S.; Bates, F. S. Network Phases in ABC Triblock Copolymers. *Macromolecules* **2004**, *37* (19), 7085–7088 DOI: 10.1021/ma0493426.

(78) Cochran, E. W.; Garcia-Cervera, C. J.; Fredrickson, G. H. Stability of the Gyroid Phase in Diblock Copolymers at Strong Segregation. *Macromolecules* **2006**, *39* (7), 2449–2451 DOI: 10.1021/ma0527707.

(79) Doerk, G. S.; Yager, K. G. Beyond Native Block Copolymer Morphologies. *Molecular Systems Design and Engineering*. Royal Society of Chemistry December 1, 2017, pp 518–538.

(80) Matsushita, Y.; Takano, A.; Vayer, M.; Sinturel, C. Nonclassical Block Copolymer Self-Assembly Resulting from a Constrained Location of Chains and Junctions. *Adv. Mater. Interfaces* **2020**, *7* (5), 1902007 DOI: 10.1002/admi.201902007.

(81) Guliyeva, A.; Vayer, M.; Warmont, F.; Faugère, A. M.; Andreazza, P.; Takano, A.; Matsushita, Y.; Sinturel, C. Thin Films with Perpendicular Tetragonally Packed Rectangular Rods Obtained from Blends of Linear ABC Block Terpolymers. *ACS Macro Lett.* **2018**, *7* (7), 789–794 DOI: 10.1021/acsmacrolett.8b00272.

(82) Wan, L.; Ruiz, R.; Gao, H.; Patel, K. C.; Albrecht, T. R.; Yin, J.; Kim, J.; Cao, Y.; Lin,

G. The Limits of Lamellae-Forming PS- b -PMMA Block Copolymers for Lithography. *ACS Nano* **2015**, *9* (7), 7506–7514 DOI: 10.1021/acsnano.5b02613.

(83) Kennemur, J. G.; Yao, L.; Bates, F. S.; Hillmyer, M. A. Sub-5 Nm Domains in Ordered Poly(Cyclohexylethylene)- Block -Poly(Methyl Methacrylate) Block Polymers for Lithography. *Macromolecules* **2014**, *47* (4), 1411–1418 DOI: 10.1021/ma4020164.

(84) Jung, Y. S.; Chang, J. B.; Verploegen, E.; Berggren, K. K.; Ross, C. A. A Path to Ultranarrow Patterns Using Self-Assembled Lithography. *Nano Lett.* **2010**, *10* (3), 1000–1005 DOI: 10.1021/nl904141r.

(85) Durand, W. J.; Blachut, G.; Maher, M. J.; Sirard, S.; Tein, S.; Carlson, M. C.; Asano, Y.; Zhou, S. X.; Lane, A. P.; Bates, C. M.; Ellison, C. J.; Willson, C. G. Design of High-χ Block Copolymers for Lithography. *J. Polym. Sci. Part A Polym. Chem.* **2015**, *53* (2), 344–352 DOI: 10.1002/pola.27370.

(86) Maher, M. J.; Bates, C. M.; Blachut, G.; Sirard, S.; Self, J. L.; Carlson, M. C.; Dean, L. M.; Cushen, J. D.; Durand, W. J.; Hayes, C. O.; Ellison, C. J.; Willson, C. G. Interfacial Design for Block Copolymer Thin Films. *Chem. Mater.* **2014**, *26* (3), 1471–1479 DOI: 10.1021/cm403813q.

(87) Maher, M. J.; Rettner, C. T.; Bates, C. M.; Blachut, G.; Carlson, M. C.; Durand, W. J.; Ellison, C. J.; Sanders, D. P.; Cheng, J. Y.; Willson, C. G. Directed Self-Assembly of Silicon-Containing Block Copolymer Thin Films. *ACS Appl. Mater. Interfaces* **2015**, *7* (5), 3323–3328 DOI: 10.1021/am508197k.

(88) Bates, C. M.; Seshimo, T.; Maher, M. J.; Durand, W. J.; Cushen, J. D.; Dean, L. M.; Blachut, G.; Ellison, C. J.; Willson, C. G. Polarity-Switching Top Coats Enable Orientation of Sub-10-Nm Block Copolymer Domains. *Science (80-.).* **2012**, *338* (6108), 775–779 DOI: 10.1126/science.1226046.

(89) Cushen, J. D.; Bates, C. M.; Rausch, E. L.; Dean, L. M.; Zhou, S. X.; Willson, C. G.; Ellison, C. J. Thin Film Self-Assembly of Poly(Trimethylsilylstyrene-b-d, l-Lactide) with Sub-10 Nm Domains. *Macromolecules* **2012**, *45* (21), 8722–8728 DOI: 10.1021/ma301238j.

(90) Cushen, J.; Wan, L.; Blachut, G.; Maher, M. J.; Albrecht, T. R.; Ellison, C. J.; Willson, C. G.; Ruiz, R. Double-Patterned Sidewall Directed Self-Assembly and Pattern Transfer of Sub-10 Nm PTMSS-b-PMOST. *ACS Appl. Mater. Interfaces* **2015**, *7* (24), 13476–13483 DOI: 10.1021/acsami.5b02481.

(91) Tada, Y.; Yoshida, H.; Ishida, Y.; Hirai, T.; Bosworth, J. K.; Dobisz, E.; Ruiz, R.; Takenaka, M.; Hayakawa, T.; Hasegawa, H. Directed Self-Assembly of POSS Containing Block Copolymer on Lithographically Defined Chemical Template with Morphology Control by Solvent Vapor. *Macromolecules* **2012**, *45* (1), 292–304 DOI: 10.1021/ma201822a.

(92) Nakatani, R.; Takano, H.; Chandra, A.; Yoshimura, Y.; Wang, L.; Suzuki, Y.; Tanaka, Y.; Maeda, R.; Kihara, N.; Minegishi, S.; Miyagi, K.; Kasahara, Y.; Sato, H.; Seino, Y.; Azuma, T.; Yokoyama, H.; Ober, C. K.; Hayakawa, T. Perpendicular Orientation Control without Interfacial Treatment of RAFT-Synthesized High-χ Block Copolymer Thin Films with Sub-10 Nm Features Prepared via Thermal Annealing. *ACS Appl. Mater. Interfaces* **2017**, *9* (37), 31266–31278 DOI: 10.1021/acsami.6b16129.

(93) Yoshimura, Y.; Chandra, A.; Nabae, Y.; Hayakawa, T. Chemically Tailored High-: χ Block Copolymers for Perpendicular Lamellae via Thermal Annealing. *Soft Matter* **2019**, *15* (17), 3497–3506 DOI: 10.1039/c9sm00128j.

(94) Park, S. M.; Park, O. H.; Cheng, J. Y.; Rettner, C. T.; Kim, H. C. Patterning Sub-10 Nm Line Patterns from a Block Copolymer Hybrid. *Nanotechnology* **2008**, *19* (45) DOI: 10.1088/0957-4484/19/45/455304.

(95) Yu, D. M.; Smith, D. M.; Kim, H.; Mapas, J. K. D.; Rzayev, J.; Russell, T. P. Morphological Evolution of Poly(Solketal Methacrylate)- *Block* -Polystyrene Copolymers in Thin Films. *Macromolecules* **2019**, *52* (10), 3592–3600 DOI: 10.1021/acs.macromol.9b00488.

(96) Yu, D. M.; Mapas, J. K. D.; Kim, H.; Choi, J.; Ribbe, A. E.; Rzayev, J.; Russell, T. P. Evaluation of the Interaction Parameter for Poly(Solketal Methacrylate)-Block-Polystyrene Copolymers. *Macromolecules* **2018**, *51* (3), 1031–1040 DOI:

10.1021/acs.macromol.7b02221.

(97) Azuma, K.; Sun, J.; Choo, Y.; Rokhlenko, Y.; Dwyer, J. H.; Schweitzer, B.; Hayakawa, T.; Osuji, C. O.; Gopalan, P. Self-Assembly of an Ultrahigh-χ Block Copolymer with Versatile Etch Selectivity. *Macromolecules* **2018**, *51* (16), 6460–6467 DOI: 10.1021/acs.macromol.8b01409.

(98) Kanimozhi, C.; Kim, M.; Larson, S. R.; Choi, J. W.; Choo, Y.; Sweat, D. P.; Osuji, C. O.; Gopalan, P. Isomeric Effect Enabled Thermally Driven Self-Assembly of Hydroxystyrene-Based Block Copolymers. *ACS Macro Lett.* **2016**, *5* (7), 833–838 DOI: 10.1021/acsmacrolett.6b00376.

(99) Sweat, D. P.; Kim, M.; Schmitt, A. K.; Perroni, D. V.; Fry, C. G.; Mahanthappa, M. K.; Gopalan, P. Phase Behavior of Poly(4-Hydroxystyrene-Block-Styrene) Synthesized by Living Anionic Polymerization of an Acetal Protected Monomer. *Macromolecules* **2014**, *47* (18), 6302–6310 DOI: 10.1021/ma501126t.

(100) Kwak, J.; Mishra, A. K.; Lee, J.; Lee, K. S.; Choi, C.; Maiti, S.; Kim, M.; Kim, J. K. Fabrication of Sub-3 Nm Feature Size Based on Block Copolymer Self-Assembly for Next-Generation Nanolithography. *Macromolecules* **2017**, *50* (17), 6813–6818 DOI: 10.1021/acs.macromol.7b00945.

(101) Jung, Y. S.; Ross, C. A. Orientation-Controlled Self-Assembled Nanolithography Using a Polystyrene - Polydimethylsiloxane Block Copolymer. *Nano Lett.* **2007**, *7* (7), 2046–2050 DOI: 10.1021/nl070924l.

(102) Ting, Y. H.; Park, S. M.; Liu, C. C.; Liu, X.; Himpsel, F. J.; Nealey, P. F.; Wendt, A. E. Plasma Etch Removal of Poly(Methyl Methacrylate) in Block Copolymer Lithography. *J. Vac. Sci. Technol. B Microelectron. Nanom. Struct.* **2008**, *26* (5), 1684–1689 DOI: 10.1116/1.2966433.

(103) Thurn-Albrecht, T.; Steiner, R.; DeRouchey, J.; Stafford, C. M.; Huang, E.; Bal, M.; Tuominen, M.; Hawker, C. J.; Russell, T. P. Nanoscopic Templates from Oriented Block Copolymer Films. *Adv. Mater.* **2000**, *12* (11), 787–791 DOI: 10.1002/(SICI)1521-4095(200006)12:11<787::AID-ADMA787>3.0.CO;2-1.

(104) Rzayev, J.; Hillmyer, M. A. Nanochannel Array Plastics with Tailored Surface Chemistry. *J. Am. Chem. Soc.* **2005**, *127* (38), 13373–13379 DOI: 10.1021/ja053731d.

(105) Mao, H.; Hillmyer, M. A. Macroscopic Samples of Polystyrene with Ordered Three-Dimensional Nanochannels. *Soft Matter* **2006**, *2* (1), 57–59 DOI: 10.1039/b513958a.

(106) Hashimoto, T.; Tsutsumi, K.; Funaki, Y. Nanoprocessing Based on Bicontinuous Microdomains of Block Copolymers: Nanochannels Coated with Metals. *Langmuir* **1997**, *13* (26), 6869–6872 DOI: 10.1021/la970967p.

(107) Lee, J. S.; Hirao, A.; Nakahama, S. Polymerization of Monomers Containing Functional Silyl Groups. 5. Synthesis of New Porous Membranes with Functional Groups. *Macrolecules* **1988**, *21* (1), 276–278 DOI: 10.1021/ma00179a057.

(108) Chini, S. F.; Amirfazli, A. Understanding Pattern Collapse in Photolithography Process Due to Capillary Forces. *Langmuir* **2010**, *26* (16), 13707–13714 DOI: 10.1021/la101521k.

(109) Hurd, C. D.; Christ, R. E. *The Ozonization of Triple Bonds*; UTC, 1936; Vol. 1.

(110) Harrison, C.; Park, M.; Chaikin, P. M.; Register, R. A.; Adamson, D. H. Lithography with a Mask of Block Copolymer Microstructures. *J. Vac. Sci. Technol. B Microelectron. Nanom. Struct.* **1998**, *16* (2), 544–552 DOI: 10.1116/1.589860.

(111) Farrell, R. A.; Petkov, N.; Shaw, M. T.; Djara, V.; Holmes, J. D.; Morris, M. A. Monitoring PMMA Elimination by Reactive Ion Etching from a Lamellar PS-b-PMMA Thin Film by Ex Situ TEM Methods. *Macromolecules* **2010**, *43* (20), 8651–8655 DOI: 10.1021/ma101827u.

(112) Asakawa, K.; Hiraoka, T. Nanopatterning with Microdomains of Block Copolymers Using Reactive-Ion Etching Selectivity. *Japanese J. Appl. Physics, Part 1 Regul. Pap. Short Notes Rev. Pap.* **2002**, *41* (10), 6112–6118 DOI: 10.1143/jjap.41.6112.

(113) Maeda, R.; Hayakawa, T.; Ober, C. K. Dual Mode Patterning of Fluorine-Containing Block Copolymers through Combined Top-down and Bottom-up Lithography. *Chem. Mater.* **2012**, *24* (8), 1454–1461 DOI: 10.1021/cm300093e.

(114) Tseng, Y. C.; Peng, Q.; Ocola, L. E.; Elam, J. W.; Darling, S. B. Enhanced Block Copolymer Lithography Using Sequential Infiltration Synthesis. *J. Phys. Chem. C* **2011**, *115* (36), 17725–17729 DOI: 10.1021/jp205532e.

(115) Maas, J. H.; Fleer, G. J.; Leermakers, F. A. M.; Cohen Stuart, M. A. Wetting of a Polymer Brush by a Chemically Identical Polymer Melt: Phase Diagram and Film Stability. *Langmuir* **2002**, *18* (23), 8871–8880 DOI: 10.1021/la020430y.

(116) Müller-Buschbaum, P.; Gutmann, J. S.; Lorenz-Haas, C.; Wunnicke, O.; Stamm, M.; Petry, W. Dewetting of Thin Diblock Copolymer Films: Spinodal Dewetting Kinetics. *Macromolecules* **2002**, *35* (6), 2017–2023 DOI: 10.1021/ma010192y.

(117) Seemann, R.; Herminghaus, S.; Neto, C.; Schlagowski, S.; Podzimek, D.; Konrad, R.; Mantz, H.; Jacobs, K. Dynamics and Structure Formation in Thin Polymer Melt Films. *J. Phys. Condens. Matter* **2005**, *17* (9), 267–290 DOI: 10.1088/0953-8984/17/9/001.

(118) Ashley, K. M.; Raghavan, D.; Douglas, J. F.; Karim, A. Wetting-De Wetting Transition Line in Thin Polymer Films. *Langmuir* **2005**, *21* (21), 9518–9523 DOI: 10.1021/la050482y.

(119) Park, H. W.; Im, K.; Chung, B.; Ree, M.; Chang, T.; Sawa, K.; Jinnai, H. Direct Observation of HPL and DG Structure in PS-b-PI Thin Film by Transmission Electron Microscopy. *Macromolecules* **2007**, *40* (7), 2603–2605 DOI: 10.1021/ma062826c.

(120) Ma, W.; Huang, W.; Ku, C.; Ho, R. Nanoporous Gyroid Metal Oxides with Controlled Thickness and Composition by Atomic Layer Deposition from Block Copolymer Templates. *J. Mater. Chem. C* **2016**, *4* (4), 840–849 DOI: 10.1039/C5TC02731D.

(121) Kim, S.; Bates, C. M.; Thio, A.; Cushen, J. D.; Ellison, C. J.; Willson, C. G.; Bates, F. S. Consequences of Surface Neutralization in Diblock Copolymer Thin Films. *ACS Nano* **2013**, *7* (11), 9905–9919 DOI: 10.1021/nn403616r.

(122) Maher, M. J.; Self, J. L.; Stasiak, P.; Blachut, G.; Ellison, C. J.; Matsen, M. W.; Bates, C. M.; Willson, C. G. Structure, Stability, and Reorganization of 0.5 L 0 Topography in Block Copolymer Thin Films. *ACS Nano* **2016**, *10* (11), 10152–10160 DOI: 10.1021/acsnano.6b05390.

(123) Suh, H. S.; Kang, H.; Nealey, P. F.; Char, K. Thickness Dependence of Neutral Parameter Windows for Perpendicularly Oriented Block Copolymer Thin Films. *Macromolecules* **2010**, *43*, 4744–4751 DOI: 10.1021/ma100150j.

(124) Mansky, P.; Liu, Y.; Huang, E.; Russell, T. P.; Hawker, C. Controlling Polymer-Surface Interactions with Random Copolymer Brushes. *Science (80-.).* **1997**, *275* (5305), 1458–1460 DOI: 10.1126/science.275.5305.1458.

(125) Xu, T.; Hawker, C. J.; Russell, T. P. Interfacial Interaction Dependence of Microdomain Orientation in Diblock Copolymer Thin Films. *Macromolecules* **2005**, *38* (7), 2802–2805 DOI: 10.1021/ma048005u.

(126) Ferrarese Lupi, F.; Aprile, G.; Giammaria, T. J.; Seguini, G.; Zuccheri, G.; De Leo, N.; Boarino, L.; Laus, M.; Perego, M. Thickness and Microdomain Orientation of Asymmetric PS-b-PMMA Block Copolymer Films Inside Periodic Gratings. *ACS Appl. Mater. Interfaces* **2015**, *7* (42), 23615–23622 DOI: 10.1021/acsami.5b07127.

(127) Russell, T. P.; Chai, Y. 50th Anniversary Perspective: Putting the Squeeze on Polymers: A Perspective on Polymer Thin Films and Interfaces. *Macromolecules*. 2017, pp 4597–4609.

(128) Nakatani, R.; Takano, H.; Wang, L.; Chandra, A.; Tanaka, Y.; Maeda, R.; Kihara, N.; Minegishi, S.; Miyagi, K.; Kasahara, Y.; Sato, H.; Seino, Y.; Azuma, T.; Ober, C. K.; Hayakawa, T. Precise Synthesis of Fluorine-Containing Block Copolymers via RAFT. *J. Photopolym. Sci. Technol.* **2016**, *29* (5), 705-708.

(129) Chandra, A.; Nakatani, R.; Uchiyama, T.; Seino, Y.; Sato, H.; Kasahara, Y.; Azuma, T.; Hayakawa, T. Direct In Situ Observation of the Early-Stage Disorder–Order Evolution of Perpendicular Lamellae in Thermally Annealed High-χ Block Copolymer Thin Films. *Adv. Mater. Interfaces* **2019**, *6*, 1801401 DOI: 10.1002/admi.201801401.

(130) Takano, H.; Wang, L.; Tanaka, Y.; Maeda, R.; Kihara, N.; Seino, Y.; Sato, H.; Kawamonzen, Y.; Miyagi, K.; Minegishi, S.; Azuma, T.; Ober, C. K.; Hayakawa, T. Vertical Oriented Lamellar Formation of Fluorine- and Silicon-Containing Block Copolymers without Neutral Layers. *J. Photopolym. Sci. Technol.* **2015**, *28* (5), 649–

652 DOI: 10.2494/photopolymer.28.649.

(131) Doise, J.; Koh, J. H.; Kim, J. Y.; Zhu, Q.; Kinoshita, N.; Suh, H. S.; Vandenberghe, G.; Willson, C. G.; Ellison, C. J. Strategies for Increasing the Rate of Defect Annihilation in the Directed Self-Assembly of High-χ Block Copolymers. *ACS Appl. Mater. Interfaces* **2019**, *11* (51), 48419–48427 DOI: 10.1021/acsami.9b17858.

(132) Lane, A. P.; Yang, X.; Maher, M. J.; Blachut, G.; Asano, Y.; Someya, Y.; Mallavarapu, A.; Sirard, S. M.; Ellison, C. J.; Willson, C. G. Directed Self-Assembly and Pattern Transfer of Five Nanometer Block Copolymer Lamellae. *ACS Nano* **2017**, *11* (8), 7656–7665 DOI: 10.1021/acsnano.7b02698.

(133) Lu, K. Y.; Lo, T. Y.; Georgopanos, P.; Avgeropoulos, A.; Shi, A. C.; Ho, R. M. Orienting Silicon-Containing Block Copolymer Films with Perpendicular Cylinders via Entropy and Surface Plasma Treatment. *Macromolecules* **2017**, *50* (23), 9403–9410 DOI: 10.1021/acs.macromol.7b02218.

(134) Seshimo, T.; Maeda, R.; Odashima, R.; Takenaka, Y.; Kawana, D.; Ohmori, K.; Hayakawa, T. Perpendicularly Oriented Sub-10-Nm Block Copolymer Lamellae by Atmospheric Thermal Annealing for One Minute. *Sci. Rep.* **2016**, *6* (1), 19481 DOI: 10.1038/srep19481.

(135) Nakatani, R.; Chandra, A.; Uchiyama, T.; Nabae, Y.; Hayakawa, T. Dynamic Ordering in High-χ Block Copolymer Lamellae Based on Cross-Sectional Orientational Alignment. *ACS Macro Lett.* **2019**, *8* (9), 1122–1127 DOI: 10.1021/acsmacrolett.9b00353.

(136) Grubbs, R. B.; Grubbs, R. H. 50th Anniversary Perspective: Living Polymerization - Emphasizing the Molecule in Macromolecules. *Macromolecules*. 2017, pp 6979–6997.

(137) Szwarc, M.; Levy, M.; Milkovich, R. Polymerization Initiated by Electron Transfer to Monomer. A New Method of Formation of Block Polymers. *Journal of the American Chemical Society*. American Chemical Society June 1, 1956, pp 2656–2657.

(138) Szwarc, M. “Living” Polymers. *Nature* **1956**, *178* (4543), 1168–1169 DOI:

10.1038/1781168a0.

(139) Moad, G.; Rizzardo, E.; Solomon, D. H. Selectivity of the Reaction of Free Radicals with Styrene. *Macromolecules* **1982**, *15* (3), 909–914 DOI: 10.1021/ma00231a042.

(140) Georges, M. K.; Veregin, R. P. N.; Kazmaier, P. M.; Hamer, G. K. Narrow Molecular Weight Resins by a Free-Radical Polymerization Process. *Macromolecules*. American Chemical Society 1993, pp 2987–2988.

(141) Kato, M.; Kamigaito, M.; Sawamoto, M.; Higashimura, T. Polymerization of Methyl Methacrylate with the Carbon Tetrachloride/Dichlorotris-(Triphenylphosphine)Ruthenium(II)/ Methylaluminum Bis(2,6-Di-Tert-Butylphenoxide) Initiating System: Possibility of Living Radical Polymerization. *Macromolecules*. American Chemical Society September 1, 1995, pp 1721–1723.

(142) Wang, J. S.; Matyjaszewski, K. Controlled/“Living” Radical Polymerization. Atom Transfer Radical Polymerization in the Presence of Transition-Metal Complexes. *J. Am. Chem. Soc.* **1995**, *117* (20), 5614–5615 DOI: 10.1021/ja00125a035.

(143) Keddie, D. J.; Moad, G.; Rizzardo, E.; Thang, S. H. RAFT Agent Design and Synthesis. *Macromolecules* **2012**, *45* (13), 5321–5342 DOI: 10.1021/ma300410v.

(144) Chiefari, J.; Chong, Y. K. (Bill); Ercole, F.; Krstina, J.; Jeffery, J.; Le, T. P. T.; Mayadunne, R. T. A.; Meijs, G. F.; Moad, C. L.; Moad, G.; Rizzardo, E.; Thang, S. H. Living Free-Radical Polymerization by Reversible Addition−Fragmentation Chain Transfer: The RAFT Process. *Macromolecules* **1998**, *31* (16), 5559–5562 DOI: 10.1021/ma9804951.

(145) Albert, J. N. L.; Epps, T. H. Self-Assembly of Block Copolymer Thin Films. *Mater. Today* **2010**, *13* (6), 24–33 DOI: 10.1016/S1369-7021(10)70106-1.

(146) Yue, Z.; Sivaniah, E.; Hashimoto, T. SAXS Analysis of the Order-Disorder Transition and the Interaction Parameter of Polystyrene-Block-Poly(Methyl Methacrylate). *Macromolecules* **2008**, *41* (24), 9948–9951 DOI: 10.1021/ma8013004.

(147) Kato, F.; Chandra, A.; Horiuchi, S.; Hayakawa, T. Morphological Dependence on the Addition of a Soft Middle Block Segment to Rigid POSS-Containing Triblock

Copolymers for Forming Cylindrical Nanostructures. *RSC Adv.* **2016**, *6* (67), 62172–62180 DOI: 10.1039/C6RA11113K.

(148) Kato, F.; Sugimoto, S.; Chandra, A.; Hayakawa, T. Morphology Control and Inducing a Curvature on the Domain Interface by Increasing the Steric Bulk of Polymethacrylate in POSS-Containing Diblock Copolymers. *J. Polym. Sci. Part A Polym. Chem.* **2017**, *55* (13), 2234–2242 DOI: 10.1002/pola.28610.

(149) Shelton, C. K.; Epps, T. H. Block Copolymer Thin Films: Characterizing Nanostructure Evolution with in Situ X-Ray and Neutron Scattering. *Polymer (Guildf).* **2016**, *105*, 545–561 DOI: 10.1016/J.POLYMER.2016.06.069.

(150) Müller, M.; Schick, M. Ordered Phases in Rod−Coil Diblock Copolymers. *Macromolecules* **1996**, *29* (27), 8900–8903 DOI: 10.1021/ma960782+.

(151) Li, Z.; Hur, K.; Sai, H.; Higuchi, T.; Takahara, A.; Jinnai, H.; Gruner, S. M.; Wiesner, U. Linking Experiment and Theory for Three-Dimensional Networked Binary Metal Nanoparticle-Triblock Terpolymer Superstructures. *Nat. Commun.* **2014**, *5*, 3247 DOI: 10.1038/ncomms4247.

(152) Jinnai, H.; Nishikawa, Y.; Spontak, R. J.; Smith, S. D.; Agard, D. a; Hashimoto, T. Direct Measurement of Interfacial Curvature Distributions in a Bicontinuous Block Copolymer Morphology. *Phys. Rev. Lett.* **2000**, *84* (3), 518–521 DOI: 10.1103/PhysRevLett.84.518.

(153) Jinnai, H.; Spontak, R. J.; Nishi, T. Transmission Electron Microtomography and Polymer Nanostructures. *Macromolecules* **2010**, *43* (4), 1675–1688 DOI: 10.1021/ma902035p.

(154) Morkved, T. L. L.; Lopes, W. a. A.; Hahm, J.; Sibener, S. J. J.; Jaeger, H. M. M. Silicon Nitride Membrane Substrates for the Investigation of Local Structure in Polymer Thin Films. *Polymer (Guildf).* **1998**, *39* (16), 3871–3875 DOI: 10.1016/S0032-3861(97)10218-X.

(155) Tong, Q.; Sibener, S. J. Visualization of Individual Defect Mobility and Annihilation within Cylinder-Forming Diblock Copolymer Thin Films on Nanopatterned Substrates.

Macromolecules **2013**, *46* (21), 8538–8544 DOI: 10.1021/ma401629s.

(156) Dai, H. J.; Balsara, N. P.; Garetz, B. A.; Newstein, M. C. Grain Growth and Defect Annihilation in Block Copolymers. *Phys. Rev. Lett.* **1996**, *77* (17), 3677–3680 DOI: 10.1103/PhysRevLett.77.3677.

(157) Tsori, Y.; Andelman, D.; Schick, M. Defects in Lamellar Diblock Copolymers: Chevron- and Ω-Shaped Tilt Boundaries. *Phys. Rev. E - Stat. Physics, Plasmas, Fluids, Relat. Interdiscip. Top.* **2000**, *61* (3), 2848–2858 DOI: 10.1103/PhysRevE.61.2848.

(158) Ryu, H. J.; Fortner, D. B.; Lee, S.; Ferebee, R.; De Graef, M.; Misichronis, K.; Avgeropoulos, A.; Bockstaller, M. R. Role of Grain Boundary Defects during Grain Coarsening of Lamellar Block Copolymers. *Macromolecules* **2013**, *46* (1), 204–215 DOI: 10.1021/ma3015382.

(159) Li, W.; Müller, M. Defects in the Self-Assembly of Block Copolymers and Their Relevance for Directed Self-Assembly. *Annu. Rev. Chem. Biomol. Eng.* **2015**, *6* (1), 187–216 DOI: 10.1146/annurev-chembioeng-061114-123209.

(160) Hahm, J.; Lopes, W. A.; Jaeger, H. M.; Sibener, S. J. Defect Evolution in Ultrathin Films of Polystyrene-Block-Polymethylmethacrylate Diblock Copolymers Observed by Atomic Force Microscopy. *J. Chem. Phys.* **1998**, *109* (23), 10111–10114 DOI: 10.1063/1.477702.

(161) Hahm, J.; Sibener, S. J. Time-Resolved Atomic Force Microscopy Imaging Studies of Asymmetric PS-b-PMMA Ultrathin Films: Dislocation and Disclination Transformations, Defect Mobility, and Evolution of Nanoscale Morphology. *J. Chem. Phys.* **2001**, *114* (10), 4730–4740 DOI: 10.1063/1.1342239.

(162) Tong, Q.; Zheng, Q.; Sibener, S. J. Alignment and Structural Evolution of Cylinder-Forming Diblock Copolymer Thin Films in Patterned Tapered-Width Nanochannels. *Macromolecules* **2014**, *47* (13), 4236–4242 DOI: 10.1021/ma500911y.

(163) Yufa, N. A.; Li, J.; Sibener, S. J. In-Situ High-Temperature Studies of Diblock Copolymer Structural Evolution. *Macromolecules* **2009**, *42* (7), 2667–2671 DOI:

10.1021/ma802751c.

(164) Ryu, H. J.; Tong, Q.; Sibener, S. J. Time-Resolved Analysis of Domain Growth and Alignment of Cylinder-Forming Block Copolymers Confined within Nanopatterned Substrates. *J. Phys. Chem. Lett.* **2013**, *4* (17), 2890–2895 DOI: 10.1021/jz4015794.

(165) Avgeropoulos, A.; Dair, B. J.; Hadjichristidis, N.; Thomas, E. L. Tricontinuous Double Gyroid Cubic Phase in Triblock Copolymers of the ABA Type. *Macromolecules* **1997**, *30* (19), 5634–5642 DOI: 10.1021/Ma970266z.

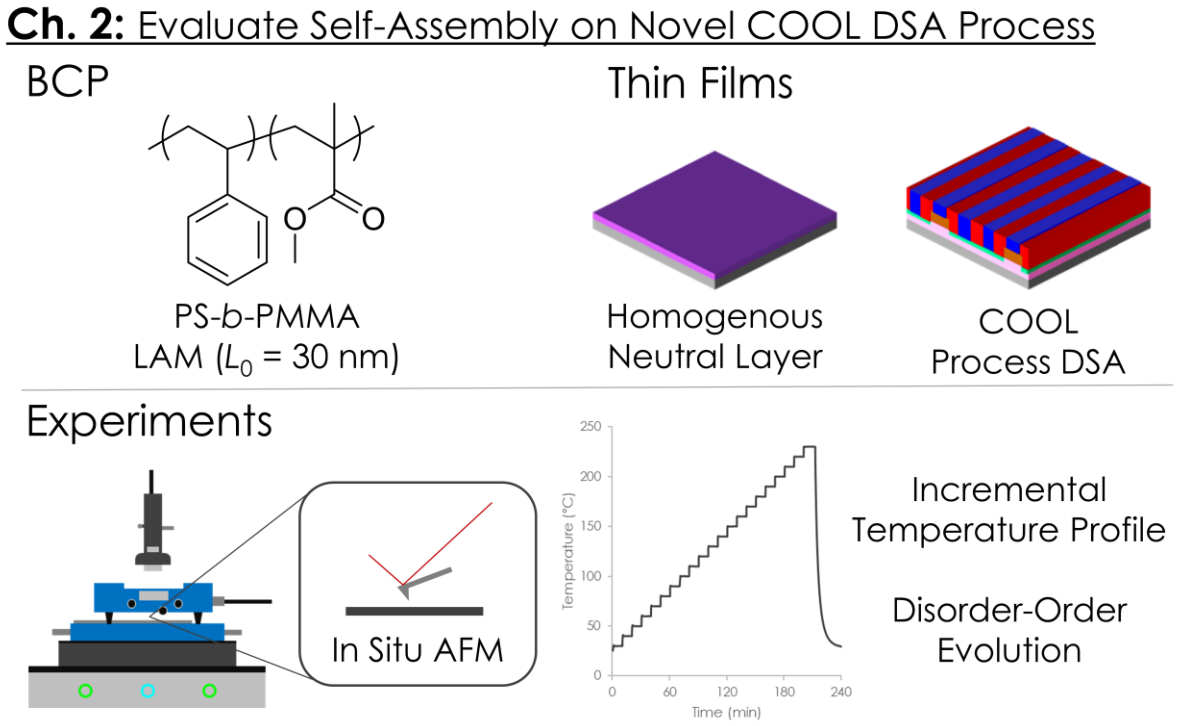
(166) Knoll, a; Lyakhova, K. S.; Horvat, a; Krausch, G.; Sevink, G. J. a; Zvelindovsky, a V; Magerle, R. Direct Imaging and Mesoscale Modelling of Phase Transitions in a Nanostructured Fluid. *Nat. Mater.* **2004**, *3* (12), 886–891 DOI: 10.1038/nmat1258.

This page was intentionally left blank.

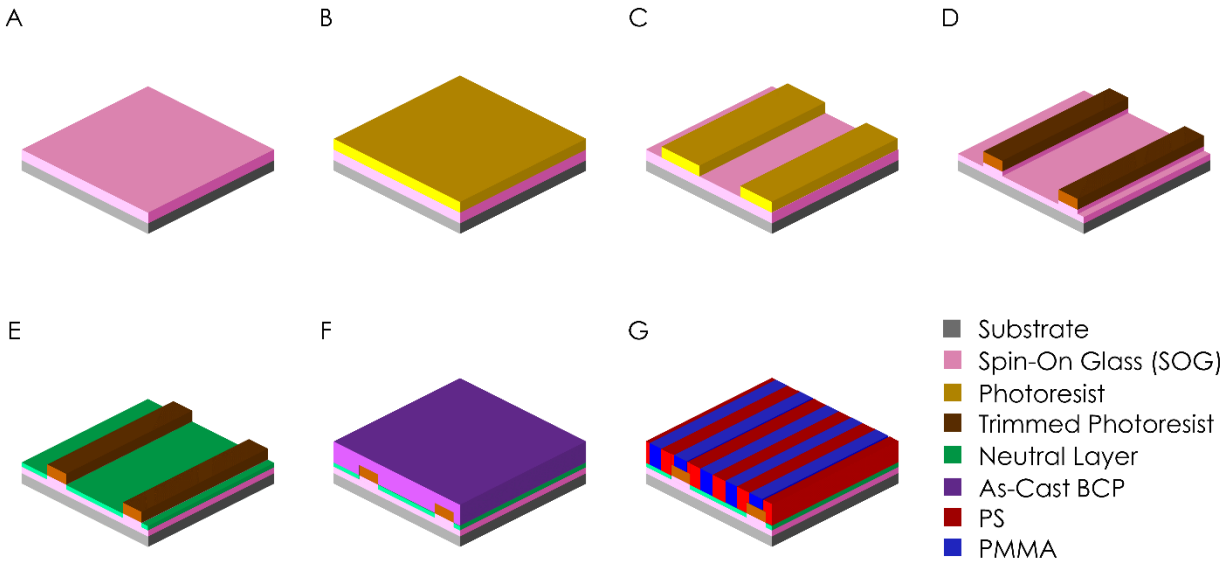
Chapter 2 Evolution of Ordered Structures in PS-*b*-PMMA Thin Films on Unpatterned and COOL Process DSA Substrates

2-1 Introduction

As discussed in the General Introduction in Chapter 1, PS-*b*-PMMA was chosen to be the main workhorse for the field of BCP lithography as it is capable of forming perpendicular lamellae with relative ease. However, the defectivity of the self-assembled structures formed on BCP thin films present a large challenge towards the industrial application of BCPs as lithographic resists. Therefore, to work towards reducing the defectivity of BCP thin films, it is imperative that the self-assembly behavior of BCP thin films get characterized in detail. To that end, a high-speed AFM equipped with a heating stage and a nitrogen (N_2) environment chamber can facilitate the real-time and real-space analysis of the growth of self-assembled structures of BCP thin films.[1–3] Previously, in situ AFM had been largely used to examine the growth of parallel structures. While Raybin and co-workers studied the defectivity of perpendicular lamellar structures of PS-*b*-PMMA on pre-patterned LiNe flow DSA substrates at high temperature isothermal annealing processes,[4] the growth of perpendicular lamellar structures from a disordered to an ordered state on unpatterned substrates had gone unreported. In this study (Schematic 2-1), the growth of perpendicular lamellae of PS-*b*-PMMA is studied via in situ AFM from a wide temperature range from 80 to 230 °C, allowing for the direct observation of the growth of ordered structures from a disordered, as-cast state, to a well-ordered state at annealing temperatures much higher than the roughly 100 °C glass transition temperatures (T_g) of PS and PMMA. Additionally, the DSA of PS-*b*-PMMA was also attempted on pre-patterned chemoepitaxial substrates prepared via the COOL process, illustrated in Scheme 2-2.[5–7] The growth of ordered structures was then examined in real-time and real-space using in situ AFM from 30 to 230 °C.



Schematic 2-1. Illustrative overview of the goals and content of Chapter 2.



Schematic 2-2. Illustration of the preparation of pre-patterned chemical guides for the DSA of PS-*b*-PMMA using the COOL process. (A-C) A photoresist is used to develop a line pattern on top of a multi-layered substrate with a spin-on glass (SOG) hard resist layer on top. (D) The photoresist is trimmed and the SOG guide partially etched using reactive ion

etching (RIE). (E) A neutral layer is backfilled into the interspaces between the guides and (F) the BCP is spin-coated and (G) annealed to attain long-range ordering.

2-2 Experimental Section

2-2-1 Materials

Thin films containing 30 nm-pitch lamella-forming PS-*b*-PMMA were obtained from EIDEC and used as received. The thin films were spin-coated from a dilute propylene glycol methyl ether acetate (PGMEA) solution onto a neutral layer consisting of a random copolymer of the constituent monomers to reduce selective interactions. The COOL process DSA thin films were also prepared as previously reported and illustrated in Schematic 2-2.[5–7] Concisely, a photoresist is prepared on a multi-layered silicon (Si) based substrate with a spin-on glass (SOG) hard resist on the top surface. A line pattern is developed at 90 nm periodicities, corresponding to a 3X multiplication factor for a 30 nm L_0 PS-*b*-PMMA. Using a combination of carbon tetrafluoride (CF_4) and oxygen (O_2) plasma reactive ion etching (RIE), the photoresist is trimmed to the line widths of the PS-*b*-PMMA. The plasma treatment oxidizes the photoresist and renders it PMMA-preferential. A neutral layer was backfilled into the interspaces between the guides and baked. After excess neutral layer was rinsed off, a 30 nm L_0 lamella-forming PS-*b*-PMMA was spin-coated onto the thin film to obtain film thicknesses of approximately 1 L_0 or 30 nm.

2-2-2 Instruments

A JPK Instruments NanoWizard ULTRA Speed A AFM (Bruker) equipped with a High Temperature Heating Stage (HTHS), a custom-made nitrogen (N_2) environment chamber, and Olympus microcantilevers (OCML-AC55TS) with resonance frequencies around 1.8 – 1.9 MHz at room temperature were used to record the atomic force microscopy (AFM) images in AC mode. The setpoint was pegged to 70% of the target amplitude, while the gain was set to 400 to minimize perturbations on the sample and no side effects were observed on the thin films upon in situ AFM imaging. To maintain an inert atmosphere, N_2 was flowed into the environment chamber at 0.5 ± 0.2 L min^{-1}. The background of the images was

subtracted using JPK Data Processing software and Fast-Fourier transformations were carried out using Matlab. The codes used on Matlab can be found in the Appendix.

2-3 Results and Discussion

2-3-1 Development of a Fingerprint Pattern

To characterize the self-assembly and formation of ordered structures from an as-cast, disorder-like state, a BCP thin film containing lamella-forming PS-*b*-PMMA were first prepared on unpatterned substrates. The self-assembly behavior of the as-cast thin film was then characterized using high-speed in situ AFM on a heating stage coupled with a custom-made N_2 environment chamber. With an imaging area of 1 × 1 μm^2, a resolution of 256 × 256 pixels, and a line rate of 4 Hz, one image can be obtained every 64 s. After examining the thin film at 20 °C for 10 min, the annealing temperature was raised to 80 °C. Subsequently, the annealing temperature was raised by 10 °C every 10 min, up to a maximum annealing temperature of 230 °C. Meanwhile, the formation of ordered structures on the thin film was recorded using in situ AFM and snapshot phase images can be found in Figure 2-1.

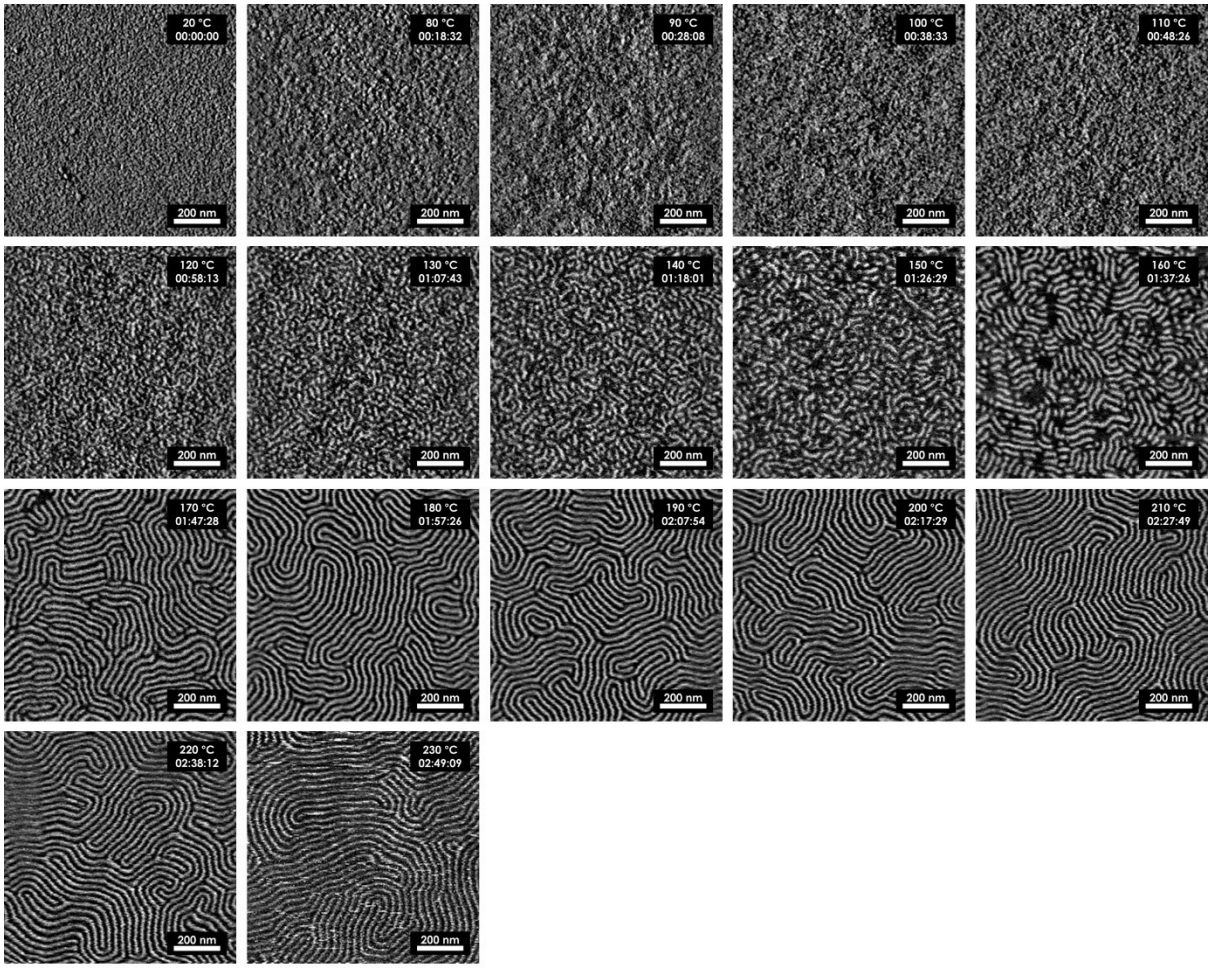


Figure 2-1. Snapshot phase images from the in situ AFM imaging of a lamella-forming PS-*b*-PMMA thin film prepared on unpatterned substrates. The temperature and time in hours:minutes:seconds can be found on the top right of each frame.

As the workhorse of the field of BCP lithography, PS-*b*-PMMA thin films have been well studied. It is well known that distinct microdomains exhibit a color contrast on AFM phase images obtained via AC mode. In the case of PS-*b*-PMMA, the dark domain (black) corresponds to PS whereas the bright domain (white) can be attributed to the PMMA domain.[8] In the first image obtained at 20 °C (Fig. 2-1), a featureless surface with a random mix of white, grey, and black pixels can be observed. Such as-cast BCP thin films are known to form a disorder-like state. Although the disorder-like state involves significant mixing and unfavorable interfacial contact between the microdomains, the BCP is kinetically frozen in place as the solvent evaporates during spin-coating and film preparation. Without the use of an annealing process, the chains of the BCP lack the mobility needed for translation and

long-range ordering typically cannot be achieved in an as-cast thin film. This featureless surface persists as the temperature is increased, even at temperatures up to 110 °C. As the glass transition temperatures (T_g) for PS-*b*-PMMA are expected to be slightly above 100 °C, it is unexpected that the thin film remains in a disorder-like kinetically frozen state in this lower temperature regime. By performing a Fast-Fourier transformation (FFT) on the phase images, corresponding two-dimensional (2D) scattering profiles can be obtained (Fig. 2-2). Azimuthally-integrating the 2D-FFT scattering profile then yields one-dimensional (1D) profiles. The domain spacing or L_0 can then be calculated from a primary scattering peak using the equation $d = 2\pi/q^*$, where q^* is the position of the primary peak. In the low temperature regime from 20 to 110 °C, distinct peaks that can be attributed to ordered scattering could not be detected in the corresponding FFT scattering profiles. This result is in line with the featureless surface as observed in the AFM phase images.

As the temperature was raised to 120 °C, short, irregular, and randomly-oriented lines can be observed on the AFM phase image. These irregular lines were then observed to grow in length as the temperature increased further to 130 °C. Additionally, micellar, bright dots could also be observed randomly in a dark matrix. While the appearance of linear structures is expected for lamella-forming BCPs, the presence of micellar dots suggests that the BCP may be adopting local cylindrical or spherical conformations. Using a rapid thermal annealing process (RTP) and ex situ characterization, Perego and co-workers showed that cylinders could be observed in the earliest stages of self-assembly in symmetric, lamella-forming BCP PS-*b*-PMMA thin films.[9] The local appearance of cylinders could be attributed to residual solvent effects that caused the local swelling of one domain, thereby resulting in the occasional

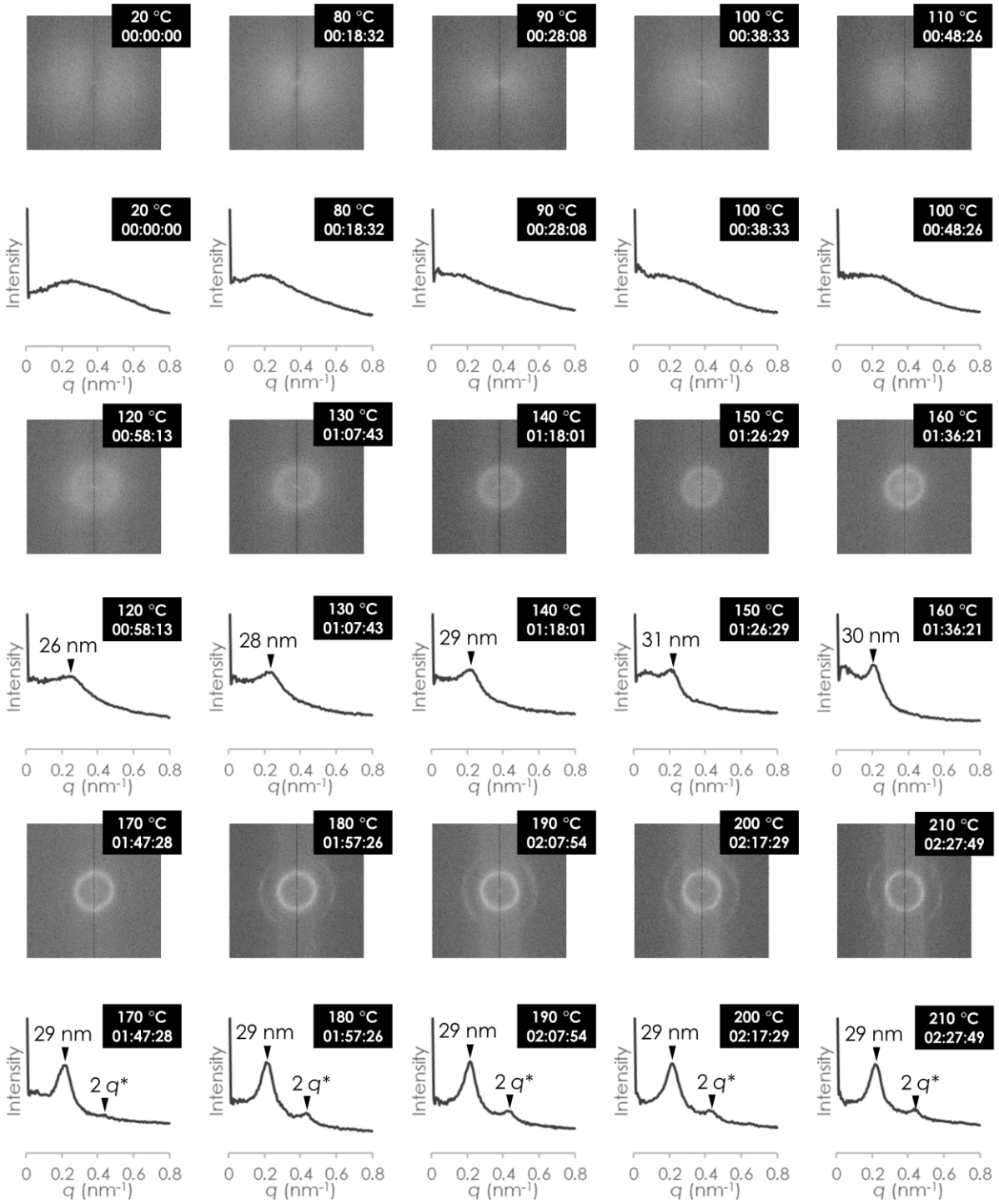


Figure 2-2. 2D and corresponding azimuthally-integrated 1D-FFT scattering profiles of the snapshot AFM phase images shown in Fig. 2-1, Part 1.

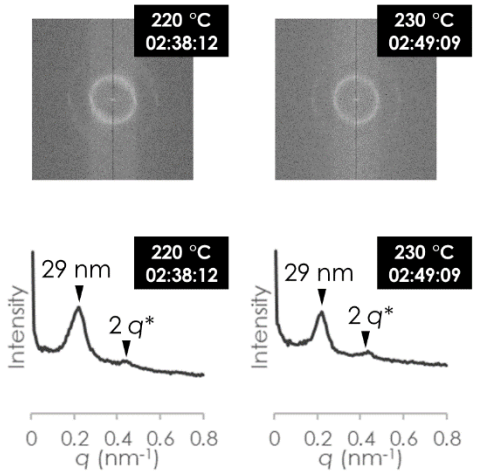


Figure 2-2. 2D and corresponding azimuthally-integrated 1D-FFT scattering profiles of the snapshot AFM phase images shown in Fig. 2-1, Part 2.

appearance of micellar dots on the thin film surface. Additionally, FFT analyses of the corresponding images revealed a weak, broadened, ring-shaped scattering peak. At 120 and 130 °C, the peak corresponded to L_0 = 26 nm and 28 nm, respectively. Compared to an expected pitch of approximately 30 nm, this L_0 is slightly lower, further suggesting that the chains of the BCP remain in an unrelaxed state at the very start of self-assembly.

Further increasing the temperature to 140, 150, and 160 °C resulted in the growth of the grains of lamellae and the gradual disappearance of micellar dots. However, the growth of small patches of the flat, dark domain could also be observed, particularly around the bright micellar dots. The flat, dark patches likely can be attributed to a selective segregation of PS onto the free interface. Previous studies have shown that the free interface shows a slight preference towards PS at temperatures below 200 °C.[10] This results in a tendency for relatively more PS to appear on the free interface. Furthermore, in ex situ studies of a lamella-forming PS-*b*-PMMA on preferential substrates, Peters and co-workers showed that at the early stages of self-assembly, lamellae of both perpendicular and parallel orientations could be observed on the thin film surfaces.[2] This could be explained by the domination of localized interactions between the nearest neighboring domains at the onset of self-assembly. As the BCPs were transitioning from a kinetically frozen, disorder-like state, long-range interactions remain limited as self-assembly begins. This causes the microdomains to

adopt configurations and orientations that are most favorable in the localized environments, resulting in the appearance of both perpendicular and parallel structures at the early stages of self-assembly. Furthermore, the corresponding FFT scattering profiles showed that the ring-shaped peak was gradually sharpening to form a distinct ring-shaped peak. Meanwhile, L_0 continued to rise to approximately 29 – 31 nm in this temperature range, closely reflecting the expected L_0 of the PS-*b*-PMMA used.

Above 170 °C, increasingly larger grains of lamellar stripes could be observed in the AFM phase images. The parallel orientation defects that appeared at lower temperatures disappeared and long-range ordering of lamellar stripes that formed a fingerprint-like pattern was observed at 230 °C. The scattering profiles obtained via FFT analyses also indicated the presence of higher order scattering peaks. A second concentric ring appeared on the 2D profiles and when azimuthally-integrated into 1D profiles, the second peak was found at a q:q^* ratio of 1:2, as expected of well-ordered lamellae. Additionally, L_0 was found to stabilize at 29 nm throughout this temperature range, in close agreement with the expected L_0 of the system.

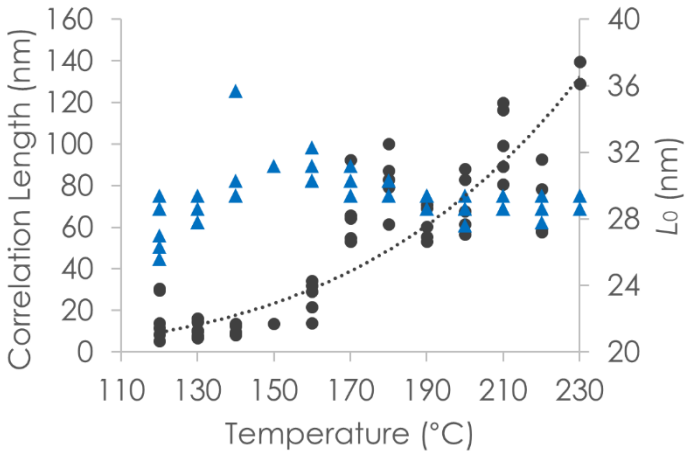


Figure 2-3. Plot of the measurable correlation length and L_0 against temperature for the in situ AFM experiment of lamella-forming PS-*b*-PMMA prepared on unpatterned substrates. The black circles correspond to the correlation length while the blue triangles correspond to the L_0.

By performing a quantitative analysis of the AFM phase images based on previously reported methods developed by Harrison and co-workers,[11,12] the degree of ordering can be quantified in terms of the correlation length of the lamellar grains. Firstly, the order parameter (Ψ) for 2D patterns can be defined as,

$$\Psi = \Psi_0 \exp(2i\theta) \quad \text{(x)}$$

where θ is the angle of local orientation of the microdomains. Upon calculating the orientation angles at each point, an autocorrelation function of two identical functions at the positional vector $\vec{r}$,

$$g(\vec{r}) = \frac{\int \psi(\vec{x})\psi^*(\vec{x}+\vec{r})\partial\vec{x}}{\int \psi(\vec{x})\psi^*(\vec{x})\,\partial\vec{x}} \quad \text{(x)}$$

can be used to obtain the correlation length which in turn, is defined as,

$$\text{real}(g(\vec{r})) = \langle\cos2(\theta-\theta(\vec{r}))\rangle \sim \exp(\frac{-r}{\xi}) \quad \text{(x)}$$

where $\theta(\vec{r})$ is θ offset by a distance r. The correlation lengths (ξ) calculated for each image were then plotted against the temperature and shown in Fig. 2-3, along with the plot of L_0 against temperature. However, as ordered structures could only be observed from 120 °C, only ξ and L_0 in the range of 120 to 230 °C was shown. Interestingly, as discussed in parts earlier, L_0 was observed to start at a slightly lower value of 26 nm at 120 °C, before climbing up to 31 nm at 150 °C and stabilizing at 29 nm at higher temperatures. Furthermore, the correlation length of the lamellar grains was initially extremely short, estimated to be approximately 17 ± 10 nm at 120 °C, before gradually growing with increasing temperature up to ca. 134 ± 5 nm at 230 °C, equivalent to approximately 4.6 times L_0.

2-3-2 Structural Evolution in COOL Process DSA Substrates

As shown above, while lamellar patterns with relatively long-range ordering can be obtained on PS-*b*-PMMA thin films prepared on unpatterned substrates, the lamellar stripes form a randomly-oriented, fingerprint-like pattern that is riddled with defects. To use the lamellar stripes for the fabrication of lines and spaces (L/S) in lithographic applications, a

defect-free, well-aligned pattern is required. Therefore, PS-*b*-PMMA thin films were subsequently prepared on pre-patterned substrates prepared via the COOL process. As described earlier, as the photoresist used to form a pre-pattern is trimmed via RIE, the photoresist becomes PMMA-preferential. With guide stripes spaced at 3X L_0 or 90 nm intervals and a neutral layer in the interspaces, the PS-*b*-PMMA microdomains could potentially be nudged towards long-range chemoepitaxial alignment. The evolution of structures formed through the self-assembly of PS-*b*-PMMA on COOL process DSA substrates was studied using in situ AFM. In situ AFM images were recorded with an image size of 2 × 2 μm^2, a resolution of 1024 × 1024 pixels, and a line rate of 8 Hz, yielding one image every 128 s. Images were first recorded at room temperature (r.t.) and at 10 °C intervals from 30 to 230 °C. The temperature was held constant for 10 min at each temperature to allow for in situ AFM imaging and the temperature profile of the experiment in shown in Fig. 2-4. Snapshots of the phase images obtained during in situ AFM experiment can be found in Fig. 2-5. An FFT transformation was performed on the obtained phase images and the 2D and 1D-FFT profiles are shown in Fig. 2-6. Additionally, height images from the in situ AFM experiment are also shown in Fig. 2-7.

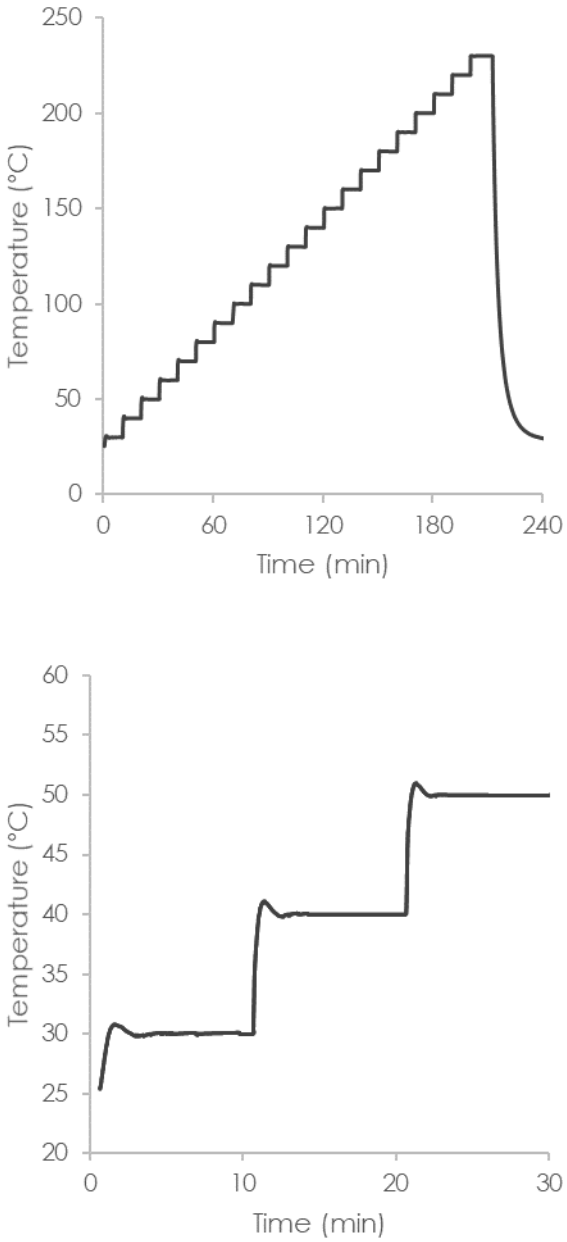


Figure 2-4. Temperature profile of the (left) entire and (right) partial in situ AFM experiment of the PS-*b*-PMMA thin film prepared on COOL process DSA substrates.

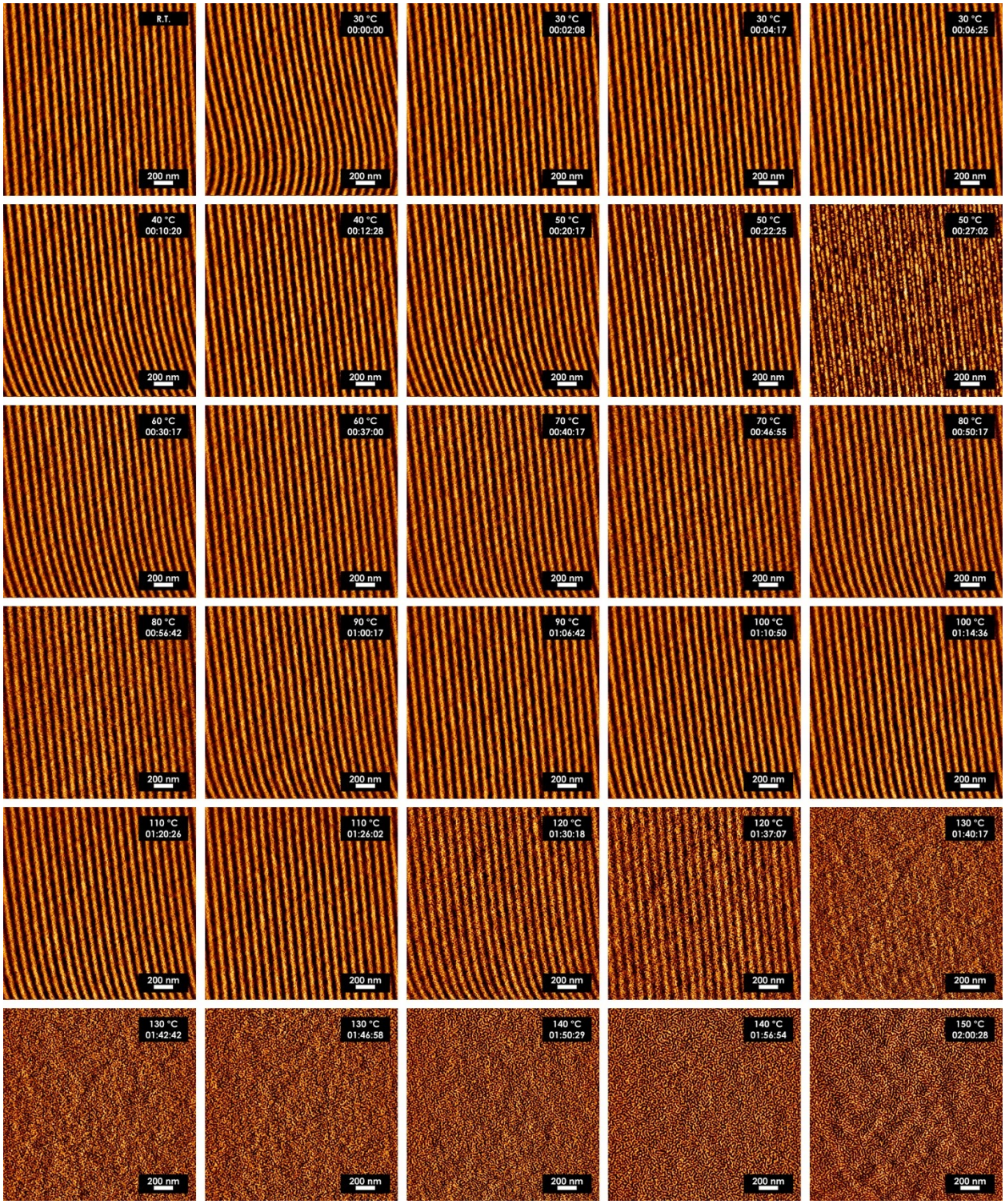


Figure 2-4. Snapshot AFM phase images from the in situ AFM experiment of PS-*b*-PMMA thin films prepared on COOL process DSA substrates from r.t. to 150 °C, Part 1.

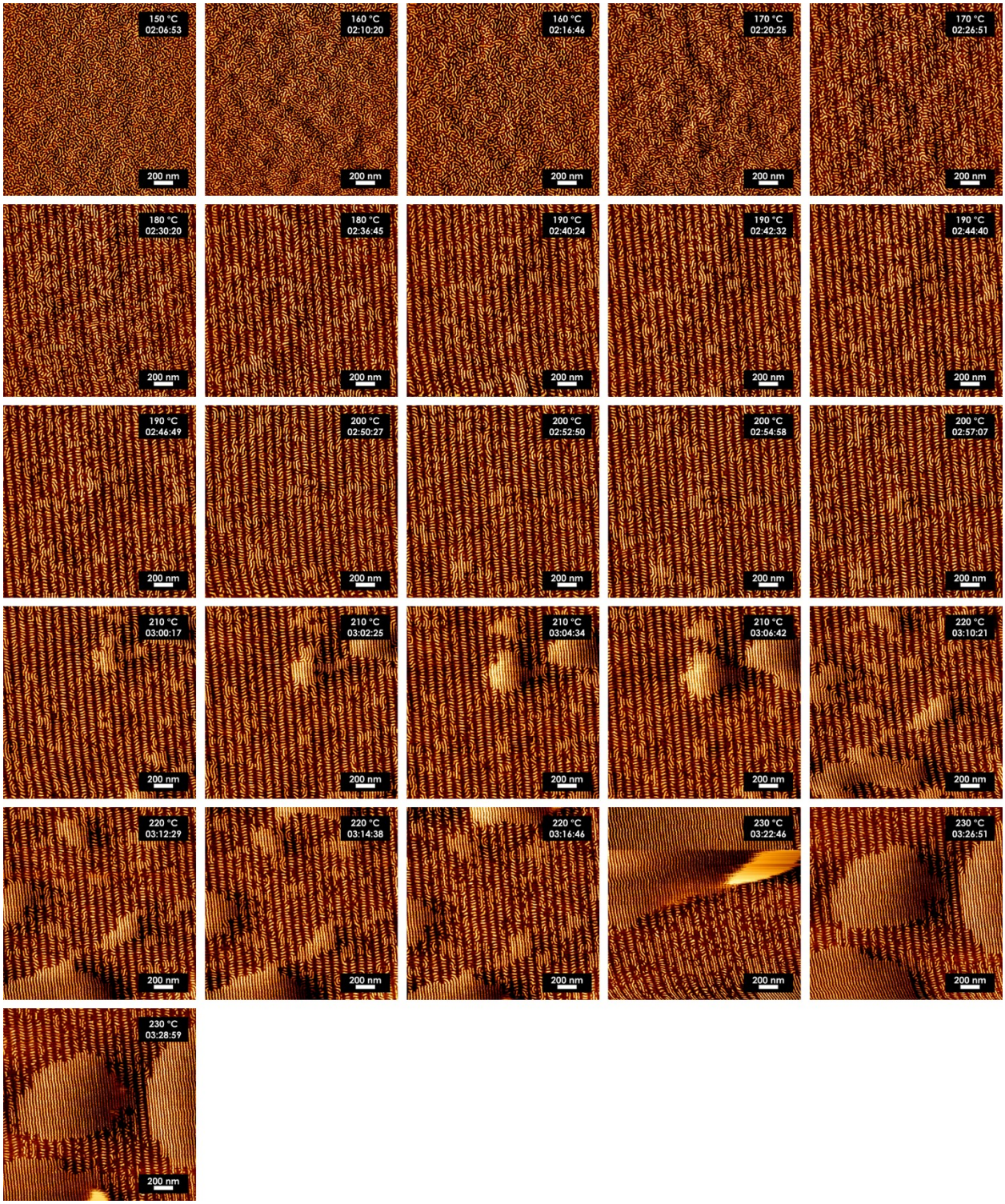


Figure 2-4. Snapshot AFM phase images from the in situ AFM experiment of PS-*b*-PMMA thin films prepared on COOL process DSA substrates from 150 to 230 °C, Part 2.

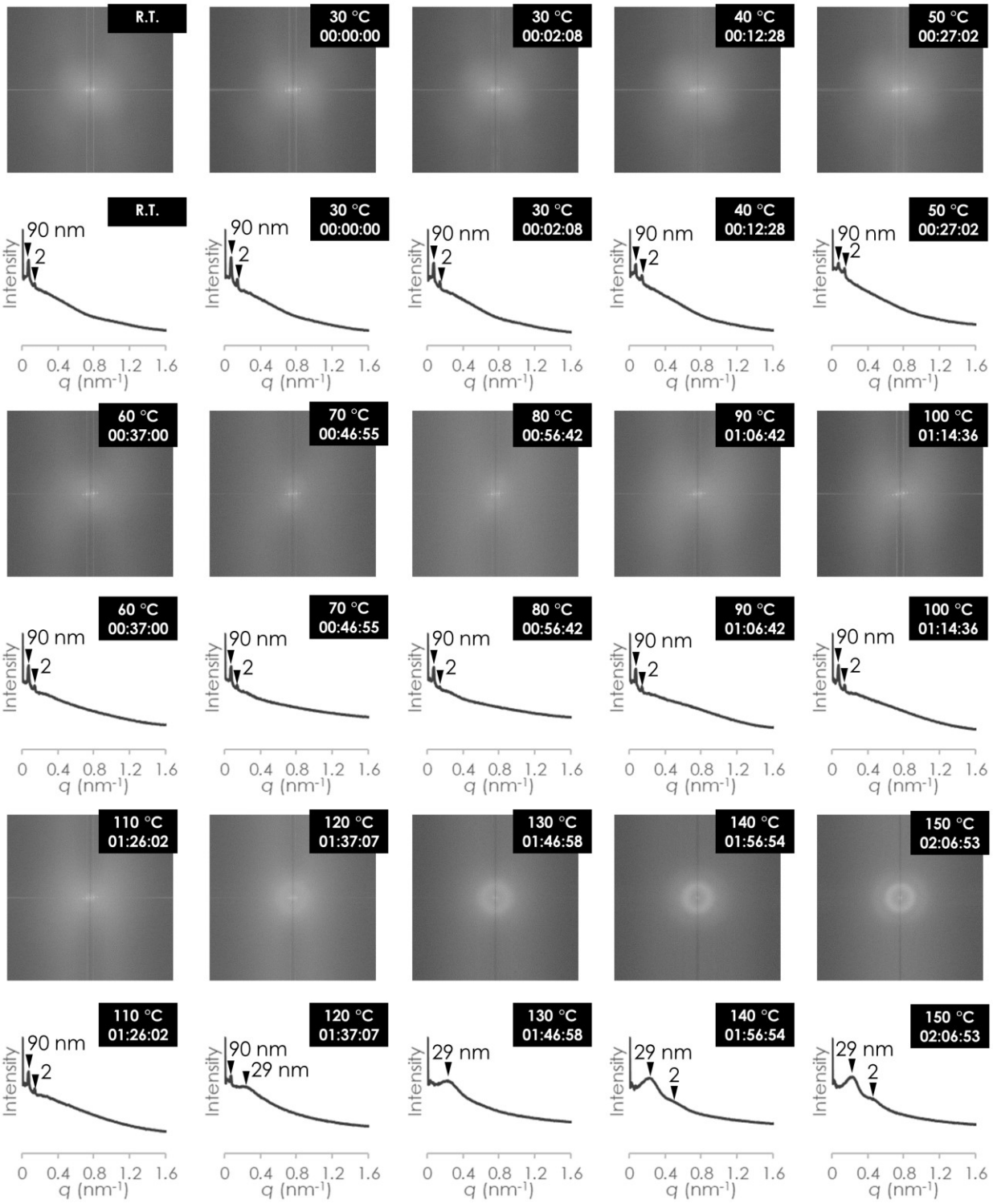


Figure 2-5. Two-dimensional (2D) and radially-integrated one-dimensional (1D) FFT scattering profiles of snapshot phase images from r.t. to 150 °C, Part 1.

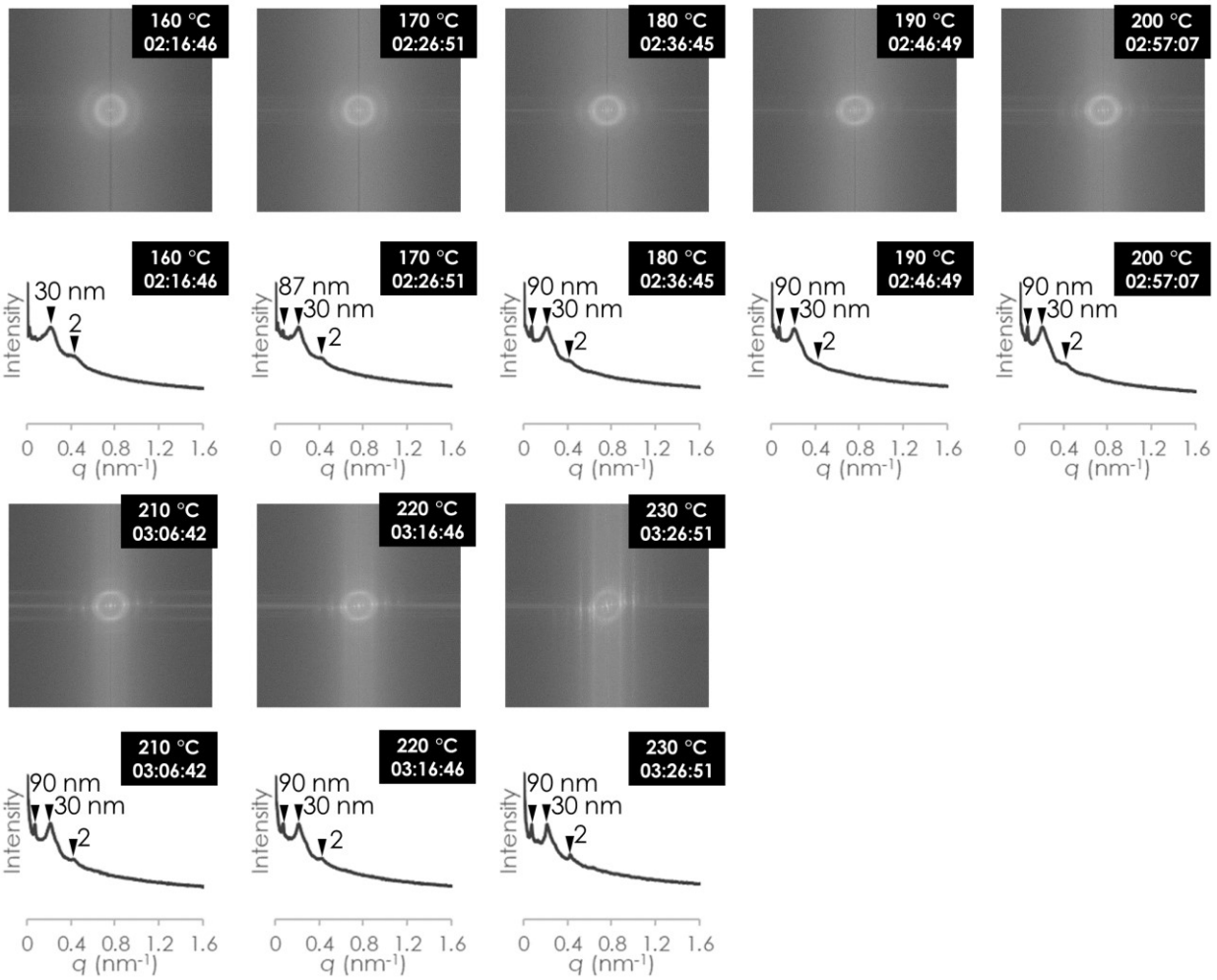


Figure 2-5. Two-dimensional (2D) and radially-integrated one-dimensional (1D) FFT scattering profiles of snapshot phase images from 150 to 230 °C, Part 2.

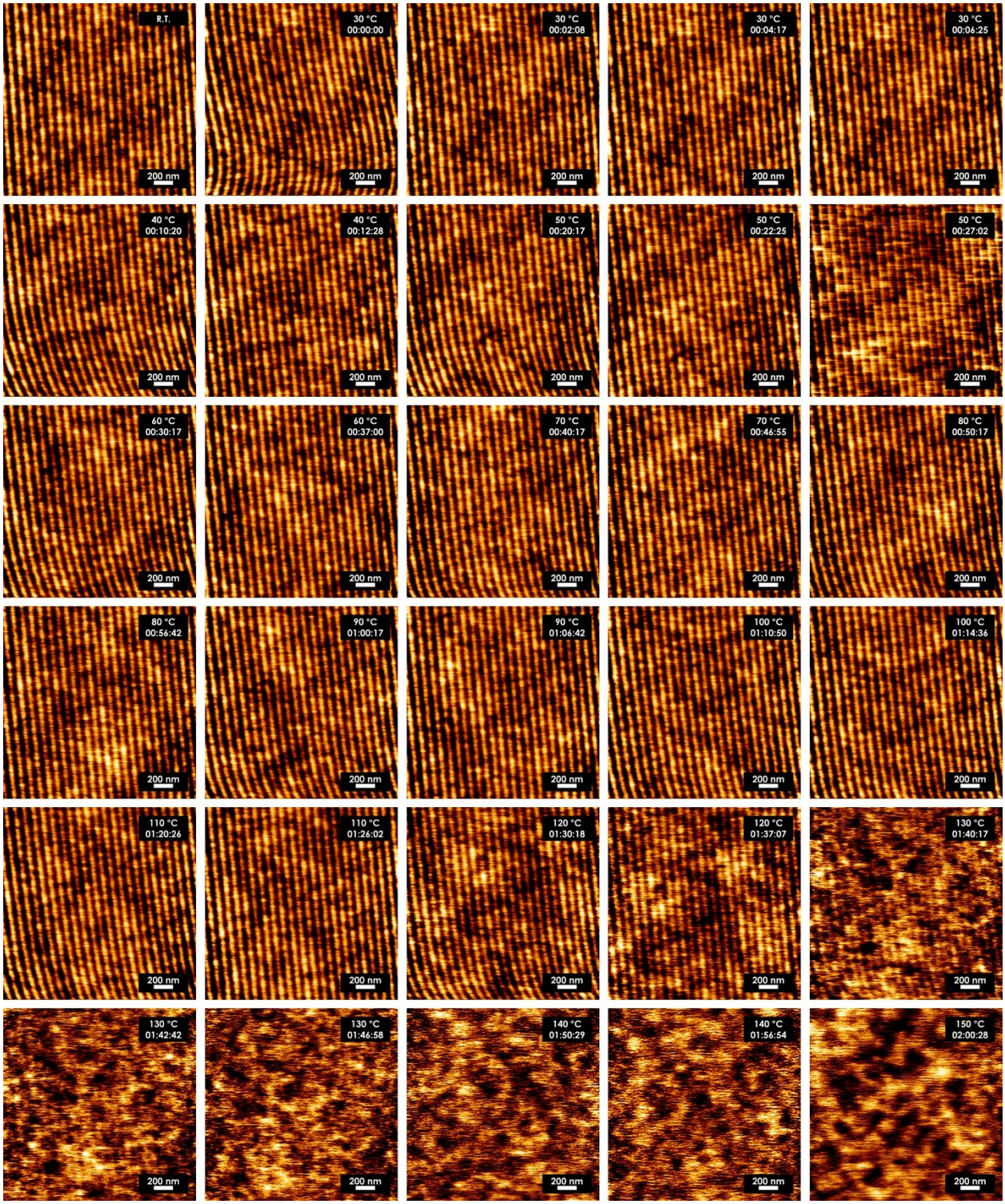


Figure 2-6. Snapshot AFM height images from the in situ AFM experiment of PS-*b*-PMMA thin films prepared on COOL process DSA substrates from r.t. to 150 °C, Part 1.

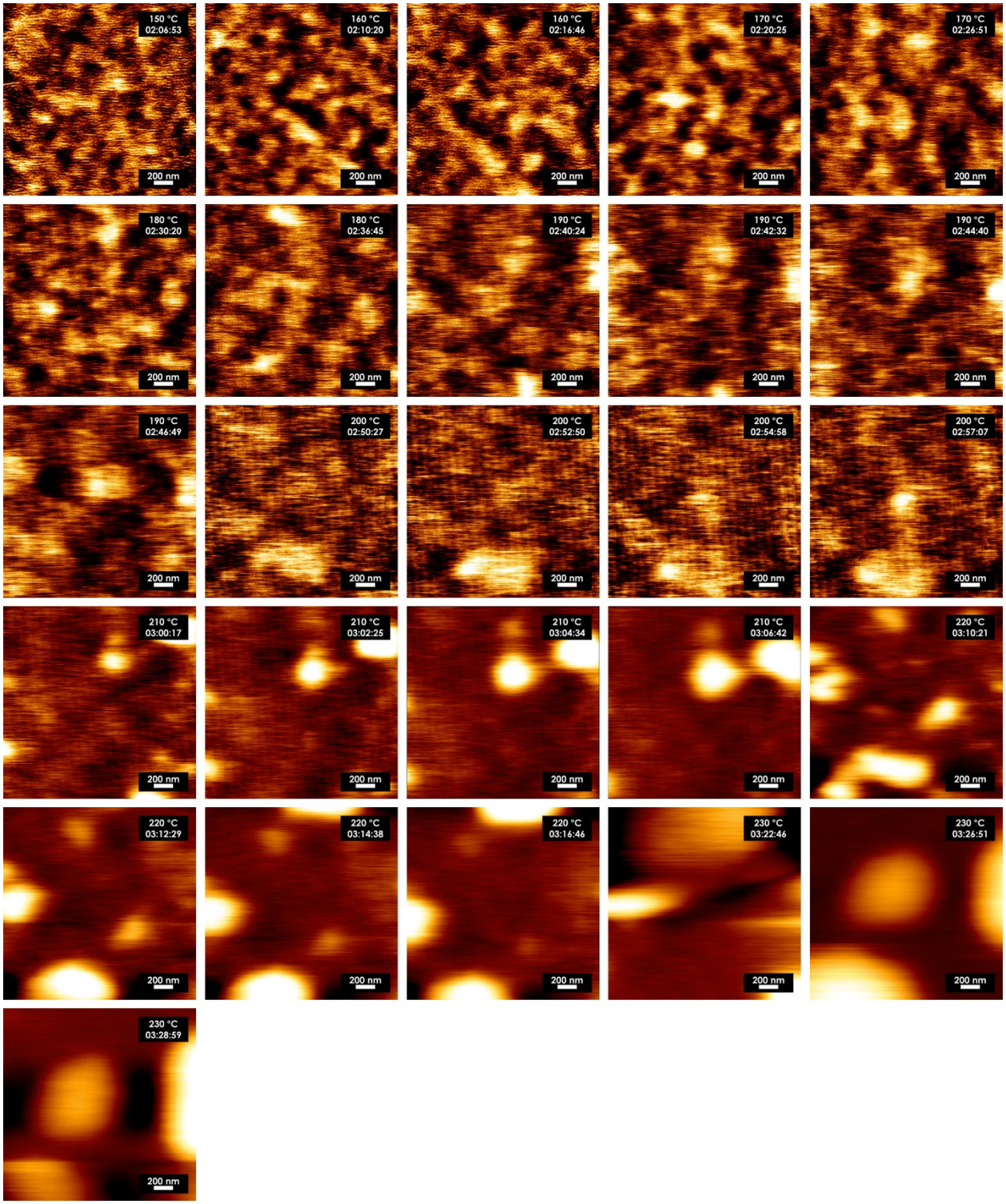


Figure 2-6. Snapshot AFM height images from the in situ AFM experiment of PS-*b*-PMMA thin films prepared on COOL process DSA substrates from 150 to 230 °C, Part 2.

The AFM phase and height images obtained at r.t. showed the presence of linear stripes that extend in the longitudinal direction with a slight diagonal tilt towards the left.

These stripes are spaced approximately 90 nm apart and have an amplitude of approximately 1 nm from peak to trough. The 90 nm spacing of the linear pattern corresponds well to that of the underlying chemical guides. While the AFM characterization of the as-cast PS-*b*-PMMA thin film prepared on unpatterned substrates appeared featureless and flat, the 90 nm spacing linear pattern observed in the as-cast thin film of PS-*b*-PMMA prepared on COOL process DSA substrates is likely indicative of the underlying guides. Aside from the presence of the 90 nm stripes, the presence of self-assembled structures could not be detected in the AFM images obtained at r.t. Additionally, two bright and sharp spots were observed in the 2D-FFT scattering profile of the phase image obtained at r.t. Upon radial integration, the 1D-FFT profile showed the presence of a primary and a secondary scattering peak at a 1:2 ratio relative to the position of the primary peak. Using the equation $d = 2\pi/q^*$, where q^* is the position of the primary peak, the spacing of the ordered structures can be estimated to be 90 nm. Since the scattering peaks can be attributed to the longitudinal linear stripes derived from the underlying chemical guides, the presence of a higher-ordered scattering peak and the 90 nm spacing is in good agreement with the observed images.

The temperature was then raised to 30 °C to begin the annealing process. The first AFM image obtained at 30 °C shows that the 90 nm linear pattern initially observed at r.t. became distorted and curved in the lower half of the image, before gradually straightening in the upper half of the image. This distortion was not observed in the second and later images obtained at 30 °C. Additionally, as shown in the temperature profile (Fig. 2-4), the temperature remains unstable in the first 3 min, overshooting the target temperature by 1 – 2 °C prior to stabilizing. Therefore, the initial distortion of the AFM image likely can be attributed to thermal fluctuations, and once the temperature has stabilized, the distortions disappear. Additionally, features that can be attributed to BCP microphase separation were not observed at 30 °C, and scattering peaks found at a ratio of 1:2 and with a periodicity of 90 nm could be observed in the FFT profiles. As the temperature increased further, the same trends were observed. While thermal noise reduced the quality of the final image

obtained at 50 °C, the first image obtained at each temperature generally showed a distorted pattern while straight linear stripes at 90 nm spacings could be observed in the later images obtained at each temperature. The scattering peaks also remained constant as there was little change in the images. This trend remained observable up to 110 °C. As the T_g of PS and PMMA are approximately 100 °C, the microdomains are simply kinetically frozen. These observations are in good agreement with the previous in situ AFM experiment on the unpatterned substrate, in which the microdomains remained kinetically frozen up to 110 °C as well.

When the temperature was raised to 120 °C however, small dark dots appeared randomly scattered throughout the film surface. Furthermore, in addition to the two sharp spots observed at lower temperatures, a weak, broad ring could be observed in the 2D-FFT profiles of the phase images obtained at 120 °C. The azimuthally-integrated 1D-FFT profile, however, shows that the second-order peak for 90 nm spacings disappeared. Additionally, a broad peak at a periodicity of 29 nm was observed. Therefore, the ring-shaped peak can likely be attributed to the microphase separation of the 30 nm-pitch PS-*b*-PMMA. This is also in good agreement with the previous experiment on the unpatterned substrate where a scattering peak corresponding to PS-*b*-PMMA microphase separation could only be observed from 120 °C. Unlike the experiment on the unpatterned substrate, linear patterns derived from the underlying guides could still be observed. However, interestingly as the temperature was raised to 130 °C, the linear pattern at 90 nm spacing began to disappear. In the first image obtained at 130 °C, a distorted linear pattern could be observed in the bottom half of both the phase and height images. However, as imaging continued, the lines disappeared from the top half of the images, and could no longer be observed in the second and later images obtained at 130 °C. This is reflected in the FFT scattering profiles where the spots and peak corresponding to 90 nm pitch spacing disappeared, leaving behind a single broad scattering peak at 29 nm periodicity. The pattern attributed to the underlying chemical guides likely disappeared as the annealing temperature was higher than the T_g's of PS and PMMA, expected to be at approximately 100 °C. This then allowed the

microdomains to flow and form a smooth and flat surface with dark dots scattered about randomly in a bright matrix.

As the annealing temperature was raised to 140 °C, the dots appear to elongate into short and irregular linear structures that were oriented randomly on the film surface. The corresponding FFT profiles also showed the appearance of a second scattering peak at a ratio of 1:2, relative to the primary peak, suggesting increased lamellar ordering on the film surface. As self-assembly processes are dictated by short-range interactions at the early stages of self-assembly, it is likely that the effects of the underlying chemical guides are minimal, thereby resulting in a random structure appearing at the onset of self-assembly.

The growth of the randomly-oriented linear structures continued until 160 °C, where a fingerprint like structure, commonly seen in perpendicular lamellae prepared on unpatterned substrates, can be observed. However, there also appears to be increased longitudinal alignment of the dark domains. This becomes more apparent as the temperature was raised further to 170 °C. The initially random, fingerprint-like structure appear divided by long, well-aligned, dark microdomains into approximately 90 nm spacing. In between the long, dark, linear microdomains, the microdomains of the BCP remain fairly randomly-oriented. The FFT profile of the corresponding images is in good agreement with the observations as a peak at 87 nm spacing can now be observed. As previous studies have shown that the PS and PMMA can be attributed to the dark and bright microdomains, respectively,[8] the longitudinally-aligned dark microdomains can be attributed to PS. However, although COOL process DSA substrates utilize chemical guides that are PMMA-preferential, the initial long-range alignment of the PS domain is unexpected. Nevertheless, it is likely that as the BCP achieves increased mobilities at the higher temperatures, the long-range ordering of the microdomains becomes possible at elevated temperatures. Additionally, while the alignment of the PS microdomain could be observed, the microdomains in the interspaces between the longitudinally-aligned PS microdomains remain randomly oriented at 170 °C.

With increased annealing temperature to 180 °C and above, the long-range alignment of the microdomains in the interspaces between the well-aligned PS

microdomains could be expected. However, instead of aligning in the longitudinal direction, in the same direction as the chemical guides, the microdomains appear to align laterally, normal to the direction of the chemical guides. This results in the formation of a ladder-like pattern appearing on the film surface, becoming most apparent at 200 °C. This ladder-like pattern was previously reported by Raybin and co-workers.[4] They studied the defectivity of PS-*b*-PMMA thin films prepared on chemically pre-patterned DSA substrates prepared via the LiNe flow which utilizes PS-preferential guides that also contain PMMA-preferential side walls and determined that this ladder-like pattern takes on a "stitch" morphology, where the PS and PMMA microdomains form a complex, interlaced 3D structure with increased PS segregation towards the interfaces. They proposed that the formation of this stitch defect can be attributed to the presence of PS-preferential guides on the substrate and the slight tendency for PS to segregate towards the free interface at temperatures below 210 °C. Therefore, such stitch defects are unique to chemoepitaxial DSA processes such as LiNe flow. In this study however, while the presence of such stitch defects could also be observed, the COOL process utilizes chemical guides that are preferential towards PMMA. Nevertheless, at such lower temperatures, the free interface is preferential towards PS. Therefore, it is likely that the formation of stitch defects is strongly dependent on the temperature and free interface, and can appear on PS-*b*-PMMA thin films under chemoepitaxial DSA, regardless of the preferential behaviors at the substrate.

Interestingly however, at 210 °C, while most of the image appear to form stitch defects and are initially laterally-aligned, the nucleation and growth of longitudinally-aligned lamellar stripes could be observed in the phase images. However, when compared to the analogous height images, it is apparent that the longitudinally-aligned stripes are beginning to bulge up and grow above the film surface. The line profiles of the height images (Fig. 2-7) obtained at 210 °C show that the area with longitudinally-aligned stripes gradually increase in height, from 3 nm in the first image to 7 nm in the final image obtained at 210 °C. As the temperature increased further, the growth of such islands of increased height remain observable on the thin film. While the majority of the microdomains appear low, flat, and

laterally-oriented into stitch defects, localized, large islands of longitudinally-aligned striped patterns could also be observed. Furthermore, at 230 °C, one such island is approximately 12 – 13 nm in height (Fig. 2-8), approaching a threshold height of 0.5 L_0, suggesting that the free interface is now neutral but the substrate is preferential towards one domain.

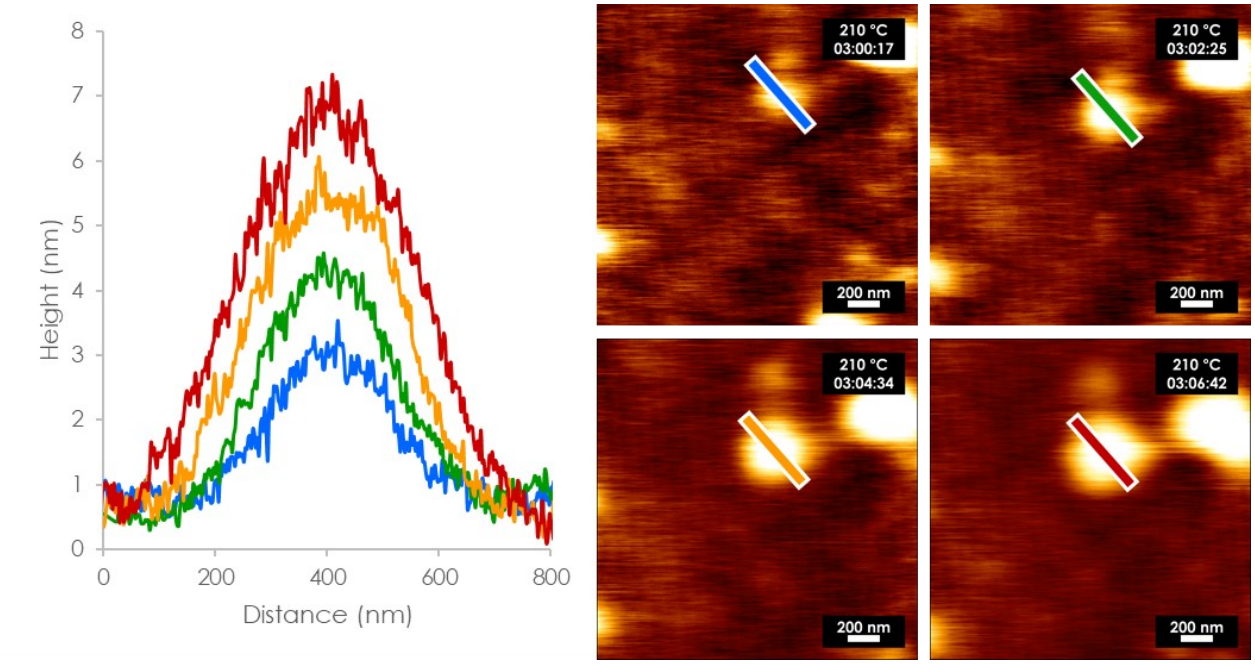


Figure 2-7. Height profiles of the lines shown in the phase images obtained during the in situ AFM experiment of the COOL process DSA thin film to the right.

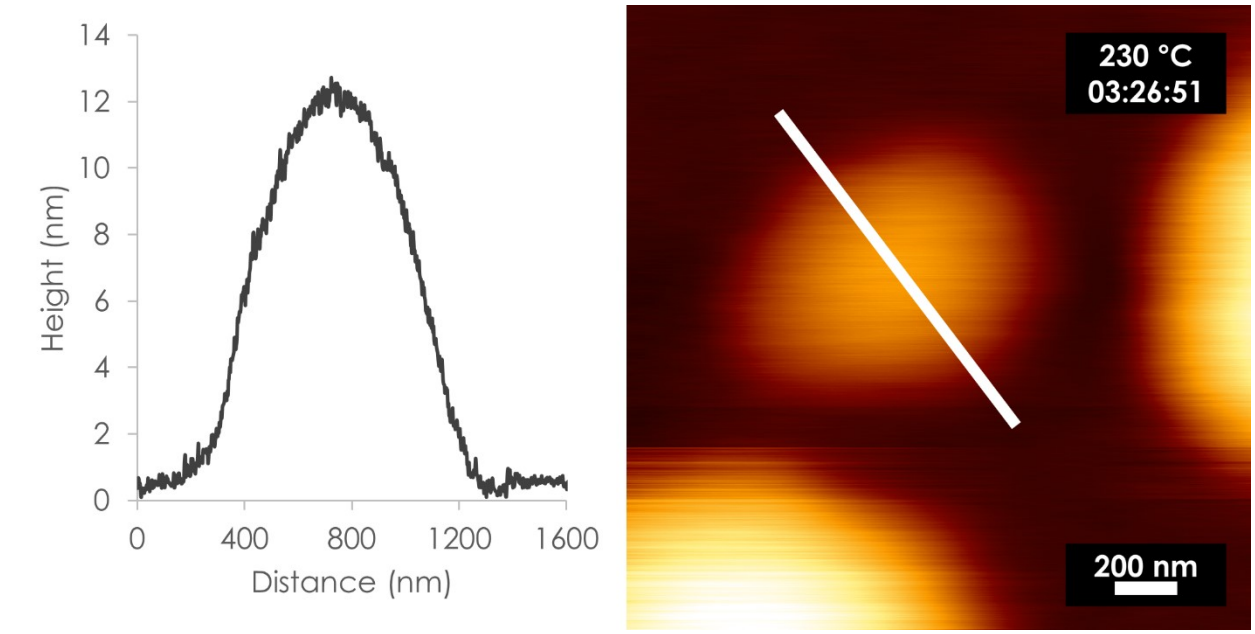


Figure 2-8. Height profile of the white line shown in the phase image obtained during the in situ AFM experiment of the COOL process DSA thin film to the right.

The formation of island-hole structures is highly indicative of disparate affinities at the substrate and the interface. However, island-hole structures are typically only seen in microdomains with parallel orientation. As parallel microdomains form layers stacked atop one another on a thin film, island-hole structures can form when there is insufficient polymer to fill up a full layer on the top surface. However, the layers of perpendicular structures are by definition normal to the substrate, therefore perpendicular structures can simple grow taller as more polymer is deposited. Nevertheless, the formation of islands of perpendicularly-oriented lamellae surrounded by stitch defects is observed in the in situ AFM experiments. As the stitch defects are unique to chemoepitaxial DSA, the formation of such island defects of perpendicular lamellar stripes is also likely unique to chemoepitaxial DSA processes. Additionally, as such island-hole structures are indicative of disparate affinities at the interfaces, the underlying chemically-modifying layer likely needs to be adjusted to prevent the formation of defects that originate from disparate affinities.

2-4 Conclusion

The in situ AFM experiments on lamella-forming PS-*b*-PMMA thin films on unpatterned and chemoepitaxial COOL process DSA substrates shows that the growth of ordered structures is highly temperature dependent. Additionally, as the initial structure formed is strongly dependent on short-range interactions between the closest neighboring microdomains, a random fingerprint-like structure is obtained at the early stages of self-assembly for both the thin films prepared on unpatterned and pre-patterned DSA substrates. As the temperature increased, the random fingerprint-like structure simply grows on the unpatterned substrate, while the long-range alignment of the PS microdomains could be observed on the thin film prepared on the DSA substrate. This completely divides the structure into columnar compartments at 90 nm intervals with randomly oriented linear structures found in the interspaces. However, due to disparate affinities at the interfaces, the growth of stitch defects, characterized by a ladder-like structure, and island structures of longitudinally-aligned lamellar stripes could be observed. To study the defectivity of such

DSA substrates, the affinities of the interfaces need to be optimized to prevent the formation of orientational defects and facilitate the complete formation of perpendicular lamellae.

2-5 References

(1) Mayes, A. M.; Russell, T. P.; Bassereau, P.; Baker, S. M.; Smith, G. S. Evolution of Order in Thin Block Copolymer Films. *Macromolecules* **1994**, *27* (3), 749–755 DOI: 10.1021/ma00081a020.

(2) Peters, R. D.; Stasiak, P.; Matsen, M. W.; Dalnoki-Veress, K. Morphology Induced Spinodal Decomposition at the Surface of Symmetric Diblock Copolymer Films. *ACS Macro Lett.* **2013**, *2* (5), 441–445 DOI: 10.1021/mz400159s.

(3) Collin, B.; Chatenay, D.; Coulon, G. et al. Ordering of Copolymer Thin Films As Revealed. *Macromolecules* **1992**, *25*, 1621–1622.

(4) Raybin, J.; Ren, J.; Chen, X.; Gronheid, R.; Nealey, P. F.; Sibener, S. J. Real-Time Atomic Force Microscopy Imaging of Block Copolymer Directed Self Assembly. *Nano Lett.* **2017**, *17* (12), 7717–7723 DOI: 10.1021/acs.nanolett.7b03881.

(5) Kato, T.; Konishi, J.; Ikota, M.; Yamaguchi, S.; Seino, Y.; Sato, H.; Kasahara, Y.; Azuma, T. Advanced CD-SEM Metrology for Qualification of DSA Patterns Using Coordinated Line Epitaxy (COOL) Process. *Proc. SPIE* **2016**, *9778*, 977816 DOI: 10.1117/12.2218605.

(6) Kasahara, Y.; Seino, Y.; Kobayashi, K.; Kanai, H.; Sato, H.; Kubota, H.; Tobana, T.; Minegishi, S.; Miyagi, K.; Kihara, N.; Kodera, K.; Shiraishi, M.; Kawamonzen, Y.; Nomura, S.; Azuma, T. RIE Challenges for Sub-15 Nm Line-and-Space Patterning Using Directed Self-Assembly Lithography with Coordinated Line Epitaxy (COOL) Process. *Proc. SPIE* **2015**, *9428*, 94280S DOI: 10.1117/12.2085704.

(7) Seino, Y.; Kasahara, Y.; Sato, H.; Kobayashi, K.; Kubota, H.; Minegishi, S.; Miyagi, K.; Kanai, H.; Kodera, K.; Kihara, N.; Kawamonzen, Y.; Tobana, T.; Shiraishi, M.; Nomura, S.; Azuma, T. Directed Self-Assembly Lithography Using Coordinated Line Epitaxy (COOL) Process. *Proc. SPIE* **2015**, *9423*, 942316 DOI: 10.1117/12.2085697.

(8) Hahm, J.; Sibener, S. J. Time-Resolved Atomic Force Microscopy Imaging Studies of

Asymmetric PS-b-PMMA Ultrathin Films: Dislocation and Disclination Transformations, Defect Mobility, and Evolution of Nanoscale Morphology. *J. Chem. Phys.* **2001**, *114* (10), 4730–4740 DOI: 10.1063/1.1342239.

(9) Perego, M.; Ferrarese Lupi, F.; Ceresoli, M.; Giammaria, T. J.; Seguini, G.; Enrico, E.; Boarino, L.; Antonioli, D.; Gianotti, V.; Sparnacci, K.; Laus, M. Ordering Dynamics in Symmetric PS-b-PMMA Diblock Copolymer Thin Films during Rapid Thermal Processing. *J. Mater. Chem. C* **2014**, *2* (32), 6655–6664 DOI: 10.1039/c4tc00756e.

(10) Mansky, P.; Russell, T. P.; Hawker, C. J.; Mays, J.; Cook, D. C.; Satija, S. K. Interfacial Segregation in Disordered Block Copolymers: Effect of Tunable Surface Potentials. *Phys. Rev. Lett.* **1997**, *79* (2), 237–240 DOI: 10.1103/PhysRevLett.79.237.

(11) Harrison, C.; Cheng, Z.; Sethuraman, S.; Huse, D. A.; Chaikin, P. M.; Vega, D. A.; Sebastian, J. M.; Register, R. A.; Adamson, D. H. Dynamics of Pattern Coarsening in a Two-Dimensional Smectic System. *Phys. Rev. E* **2002**, *66* (1), 011706 DOI: 10.1103/PhysRevE.66.011706.

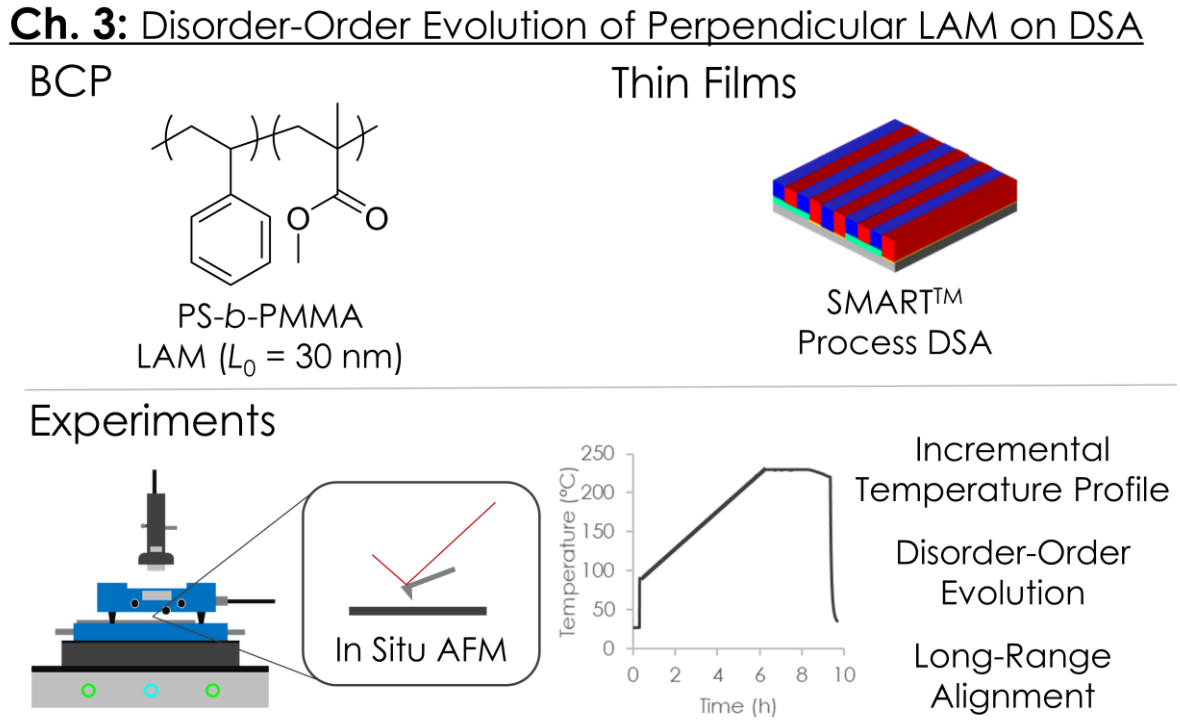
(12) Harrison, C.; Adamson, D. H.; Cheng, Z.; Sebastian, J. M.; Sethuraman, S.; Huse, D. A.; Register, R. A.; Chaikin, P. M. Mechanisms of Ordering in Striped Patterns. *Science (80-.).* **2000**, *290* (5496), 1558–1560 DOI: 10.1126/science.290.5496.1558.

Chapter 3 Structural Evolution of PS-*b*-PMMA Thin Films on Chemically Pre-Patterned DSA Substrates Prepared via the SMART™ Flow

3-1 Introduction

Defects formed by the self-assembled structures of BCPs can cause serious problems in the circuits produced from BCP resists. Therefore, for BCPs to become viable as a lithographic resist, the industry has set a target defect density of 0.01 defect counts per cm^2. To work towards this goal, numerous methods have been developed to *direct the self-assembly* of the BCPs. The use of pre-patterned directed self-assembly (DSA) substrates with guides that can nudge the microdomains towards long-range alignment is particularly useful as the production and use of such DSA guides can be fully compatible with existing microelectronics production lines. Therefore, pilot processes that are compatible with regular 300 mm wafer scales have been developed by various academic and industrial researchers around the world.[1–4] In Chapter 2, the self-assembly of PS-*b*-PMMA on pilot DSA guides produced using the COOL process, an original process developed by EIDEC, was explored. However, it was found that the interfacial incompatibilities led to the formation of a highly metastable stitch defect and the growth of localized islands of well-aligned lamellar patterns. While the COOL process requires fewer processing steps to produce the DSA guides, thereby possibly increasing the potential throughput of the process, the sensitivity of BCP microdomains towards interfacial affinities inherently requires more precise tuning of the interfacial properties of the DSA guides. To that end, DSA substrates produced via the Surface Modification for Advanced Resolution Technology™ (SMART™) process can provide improved guide performances.[3,5–7] As a neutral layer is first prepared and patterned, followed by the addition of guiding stripes, the neutral layer can be evenly distributed and coverage throughout the substrate can be ensured. Additionally, a topographic contrast between the neutral layer and the guiding stripes adds a graphoepitaxial effect that can serve to reduce the defectivity and increase long-range alignment of the microdomains. However, while Muramatsu and co-workers reported achieving a low defect density of 0.18

defect counts per cm^2,[5–7] to work towards 0.01 defect counts per cm^2, the defect density must still be reduced by an order of magnitude. Therefore, in this chapter (Schematic 3-1), to develop a better understanding of the mechanisms behind the growth and alignment self-assembled structures on SMART™ process DSA substrates, in situ AFM imaging was used to track the evolution of structures in an as-cast film from 90 to 230 °C. By analyzing the thin film with in situ annealing in real time and real space, the changes from disorder to order can be tracked in detail, potentially revealing the fundamental mechanisms behind the self-assembly of BCPs.



Schematic 3-1. Illustrative overview of the goals and content of Chapter 3.

3-2 Experimental Section

3-2-1 Instruments

A JPK Instruments NanoWizard ULTRA Speed A AFM (Bruker) equipped with a High Temperature Heating Stage (HTHS), a custom-made nitrogen (N_2) environment chamber, and an Olympus microcantilever (OCML-AC55TS) with a resonance frequency of 1.59 MHz and a drive amplitude of 9 V for a target amplitude of 1.0 V being required at room temperature were used to record the atomic force microscopy (AFM) images in AC mode.

The setpoint was pegged at 70% of the target amplitude, while the gain was set to 400 to minimize perturbations on the sample and no side effects were observed on the thin films upon in situ AFM imaging. Images 1 × 1 μm^2 in size with a resolution of 256 × 256 pixels were obtained at a line rate of 4 Hz, yielding one image every 64 s. To maintain an inert atmosphere, N_2 was flowed into the environment chamber at 0.5 ± 0.2 L min^{-1}. The AFM images were processed by subtracting the background using JPK Data Processing software. Fast-Fourier transformation (FFT) analyses of the phase images were conducted using ImageJ and Matlab.

3-2-2 Sample Preparation

As-cast thin films containing lamellae-forming PS-*b*-PMMA on pre-patterned substrates prepared using the SMART^{TM} process were received from Tokyo Electron Kyushu Limited, and were prepared as previously reported.[3,5–7] Briefly, a neutral layer is added onto a substrate. Using a photoresist, a linear pattern with a line-width of approximately 45 nm is developed at a 90 nm pitch. The photoresist is removed, and a weakly PS-preferential pinning material is spun onto the thin film. Upon coating and baking, excess PS-pinning material is removed, leaving behind a thin layer of PS-pinning guides in the interspaces between the patterned neutral layers. A 30 nm lamella-forming PS-*b*-PMMA was spin-coated on to yield thin films with a thickness of approximately 30 nm.

3-3 Results and Discussion

3-3-1 Incremental Annealing Profile

To examine the evolution of ordered structures under the influence of chemical guides, PS-*b*-PMMA thin films were prepared on chemically pre-patterned DSA substrates using the SMART^{TM} process. The symmetric PS-*b*-PMMA forms lamellae with a full-pitch domain spacing (L_0) of 30 nm, while chemical guides were spaced 90 nm apart, giving a multiplication factor of 3x. Using a high-speed AFM equipped with a heating stage and an N_2 environment chamber, the self-assembly behavior was documented in situ from the as-cast, nearly disordered state to the well-aligned, “defect-free” state. During the in situ AFM experiment, high quality images with an image size of 1 × 1 μm^2 and resolution of 256 × 256 pixels were

recorded every 64 s. After imaging the sample at 26 °C for 10 min, the temperature was raised to 90 °C and held for 10 min to allow for the temperature and cantilever to stabilize in the first 5 min. The temperature was subsequently raised every 5 min by 2 °C increments up to a maximum temperature of 230 °C (Fig. 3-1 and 3-2). The images obtained during the in situ AFM experiment were then compiled into a real-time and real-space video, and snapshots of the phase and height images, accompanied by Fast Fourier transform (FFT) analyses of the phase images, are found in Fig. 3-3 to 3-10. The rough-mean-squared (RMS) roughness was also calculated from the corresponding height images at each temperature and plotted in Fig. 3-11. Although the effects of thermal fluctuations and the relatively small scan area used increases the noisiness of the data, general trends could be observed alongside changes in the BCP structure as discussed below.

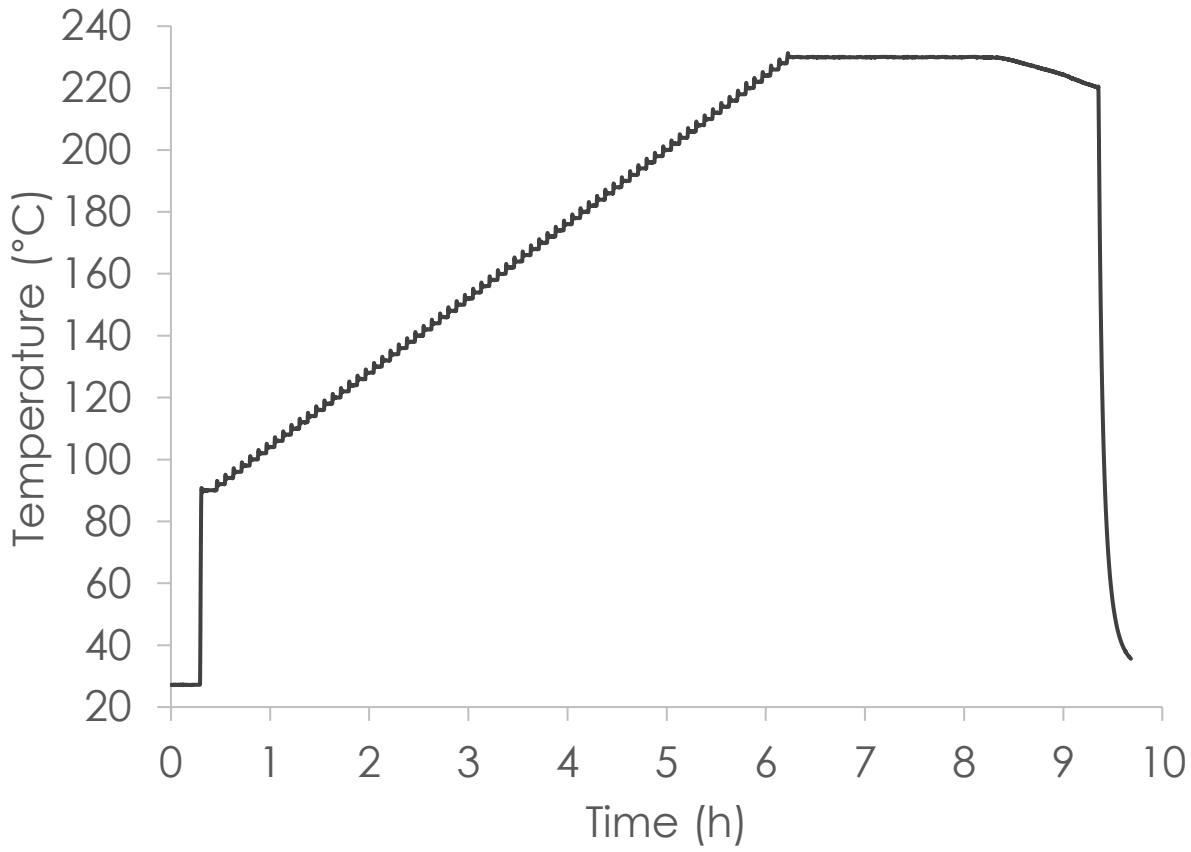


Figure 3-1. Temperature profile of the in situ AFM experiment with incrementally increasing annealing temperature.

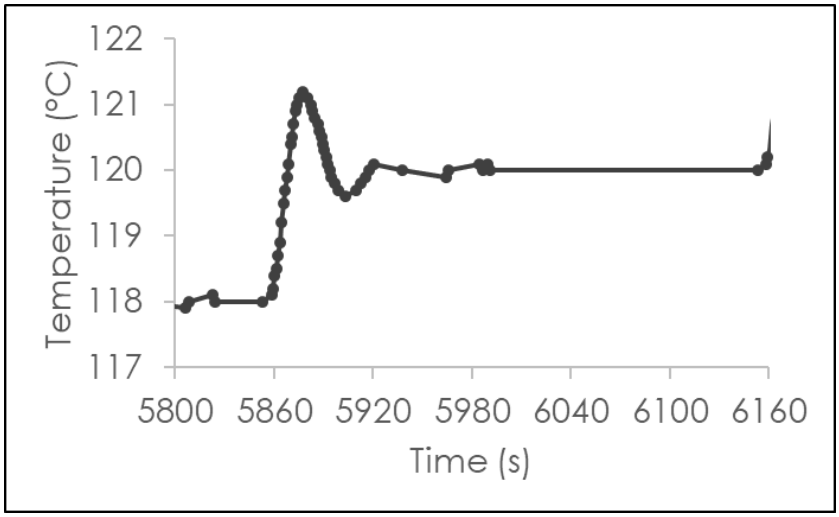


Figure 3-2. Plot of temperature against time that represents the fluctuation as the temperature is increased by 2 °C.

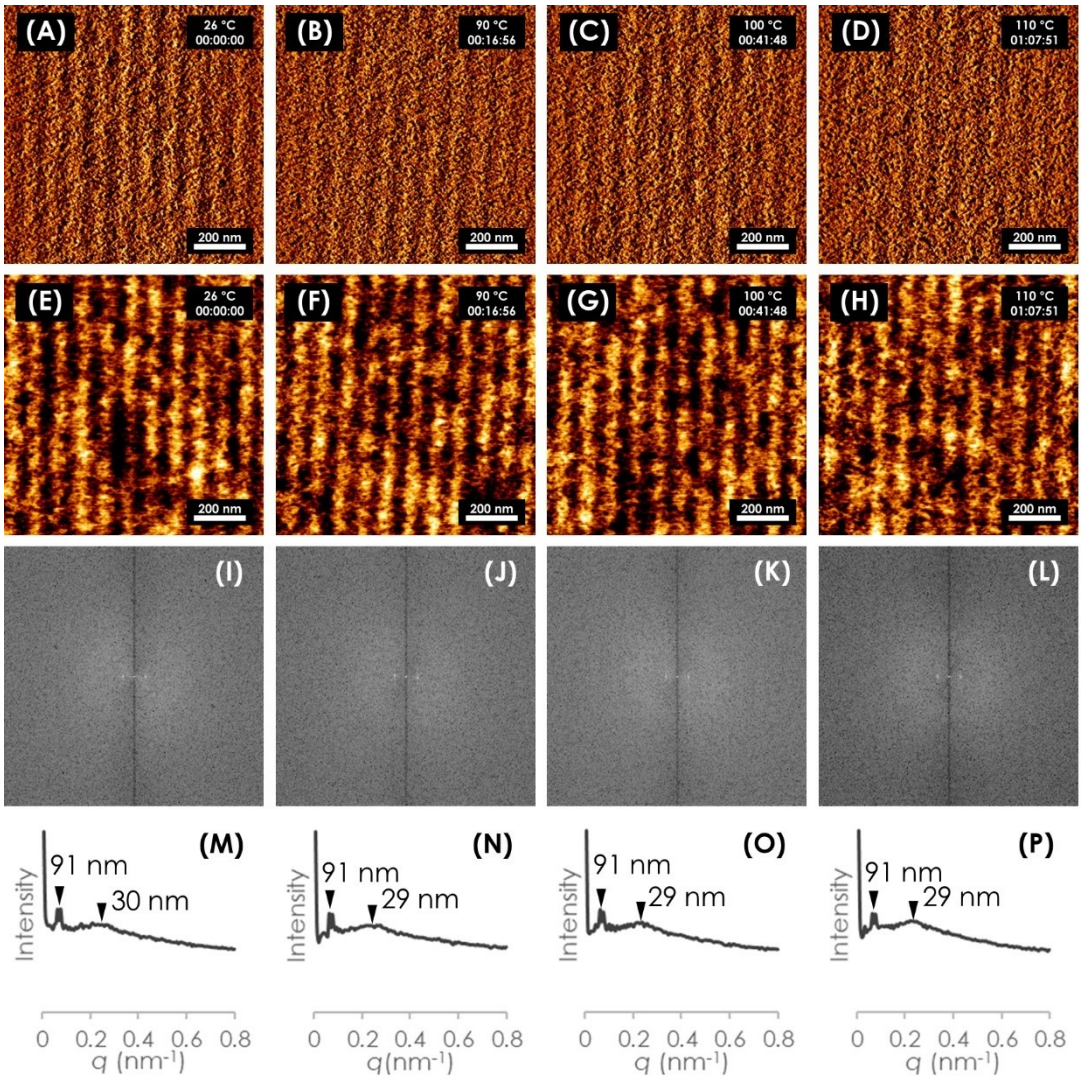


Figure 3-3. (A-D) Phase and (E-H) height images from the in situ AFM experiment from 26 to 110 °C. The temperature and time stamp in hours:minutes:seconds can be found in the top right of each image. (I-L) Two-dimensional (2D) Fast Fourier Transform (FFT) images of the phase images in A-D. (M-P) One-dimensional (1D) azimuthally-integrated profiles of the 2D-FFT images in I-L.

Spanning from room temperature at 26 °C to 230 °C, eight characteristic behaviors were found in the self-assembly of lamellae influenced by chemically pre-patterned DSA substrates. However, as AFM observations with in situ annealing are highly sensitive to thermal fluctuations, the imaging location could be observed to move about between changes in temperature. Nevertheless, when first imaged at 26 °C, random dark dots in a bright matrix and longitudinal stripes that are ~1 nm from peak to trough in height could be observed in the AFM images (Fig. 3-3A, 3-3B) at approximately 90 nm intervals. In the corresponding two-dimensional (2D) FFT image, two spots in the in-plane direction, near the center of the FFT image could be observed. Using the equation, $d = 2\pi/q^*$, where q^* is the position of the primary peak, the periodicities of the observed patterns can be estimated from the FFT images. Azimuthally integrating the 2D-FFT image yielded a 1D-FFT profile which revealed the presence of a small, sharp peak at ca. 91 nm and a broad, weak peak at ca. 30 nm. Since the longitudinal stripes at 90 nm intervals in the AFM images and the sharp peak at 91 nm in the FFT profiles correspond well with the pitch of the chemical guides (90 nm), the longitudinal 90 nm-pitch stripes are likely a result of the underlying guide pattern. Additionally, the random dark dots in a bright matrix observed in the phase image and the presence of a broad, low-intensity peak in the FFT profiles at 30 nm suggests that the as-cast PS-*b*-PMMA is weakly and locally microphase-separated. Considering that the bulk glass transition temperature (T_g) of PS-*b*-PMMA is ~100 °C, the thin film is likely simply kinetically frozen into a random, disorder-like state. Even as the annealing temperature increased from 26 to 90, 100, and 110 °C, the longitudinal stripes on the AFM images, the sharp peak at ca. 91 nm and the broad peak at ca. 30 nm in the FFT profiles could be detected. Furthermore, the rough-mean-squared (RMS) roughness (Fig. 3-11) calculated

from the height images obtained between 26 and 110 °C were relatively low and constant, averaging to 0.359 ± 0.007 nm, characteristic of smooth, spin-coated thin film surfaces.

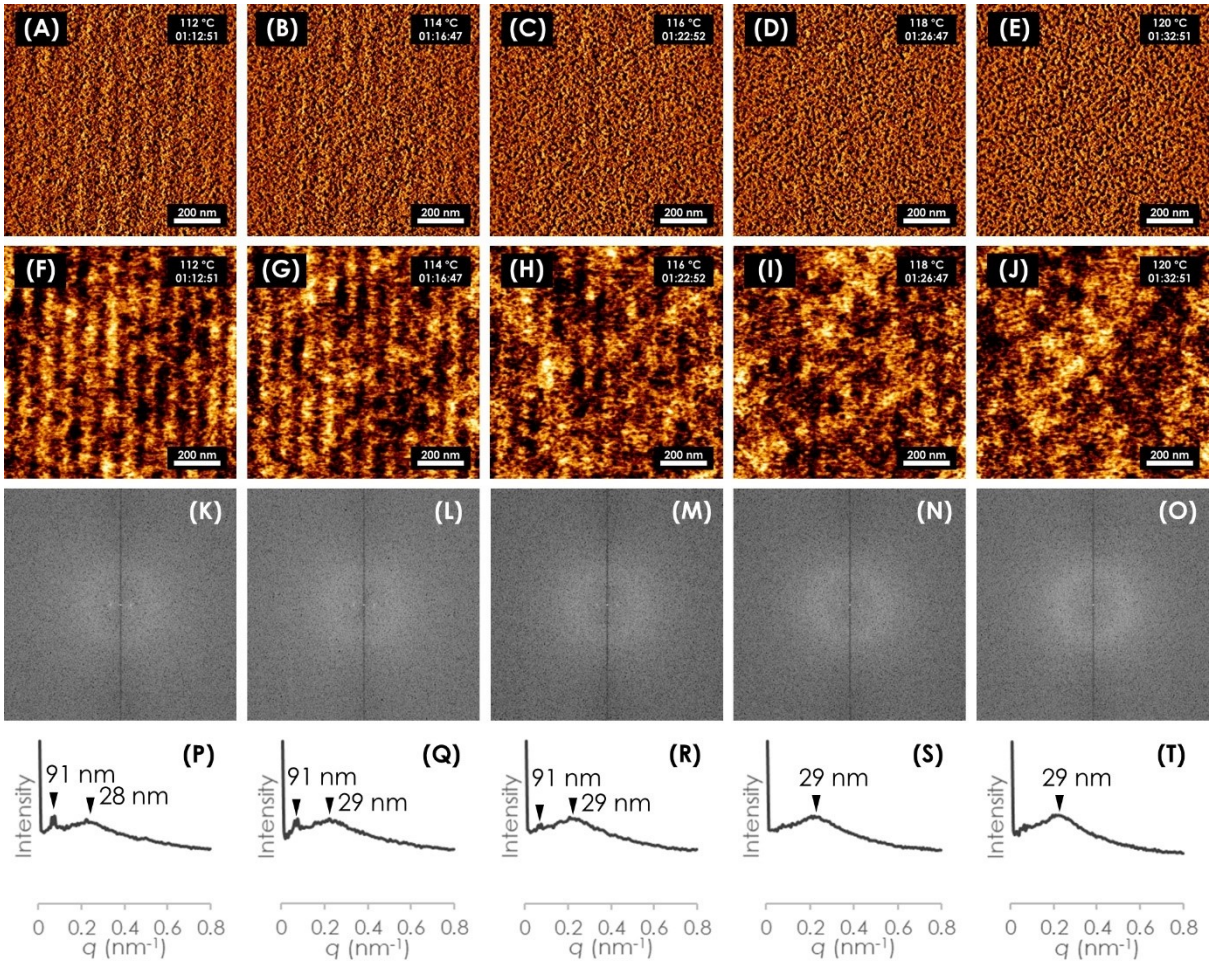


Figure 3-4. (A-E) Phase and (F-J) height images from the in situ AFM experiment from 112 to 120 °C. The temperature and time stamp in hours:minutes:seconds can be found in the top right of each image. (K-O) 2D-FFT images of the phase images in A-E. (P-T) 1D azimuthally-integrated profiles of the 2D-FFT images in K-O.

However, in the next temperature regime between 112 and 120 °C, the 90 nm-pitch longitudinal stripes disappeared gradually from the AFM images (Fig. 3-4). Similarly, the peak at 90 nm observed in the FFT profiles gradually weakened in intensity until it could no longer be observed at 118 °C. As the longitudinal stripes disappeared at 120 °C, only random dark dots in a bright matrix could be observed in the phase image. Additionally, a distinct, broad ring could be detected in the 2D FFT images as the temperature increased. The 1D FFT profiles revealed that the broad ring corresponded to d = ~29 nm and was

slowly increasing in intensity, suggesting a slow transition from a glassy to a rubbery state was occurring with increasing microphase separation of the PS-*b*-PMMA domains. Meanwhile, a slight decrease in the RMS roughness calculated from the height images could be observed, decreasing from 0.377 nm at 106 °C to 0.333 at 116 °C. Although the magnitude of the decrease is relatively small at –0.044 nm, this decrease is likely attributed to the disappearance of the longitudinal stripes which inherently only had a peak-to-trough height difference of >1 nm.

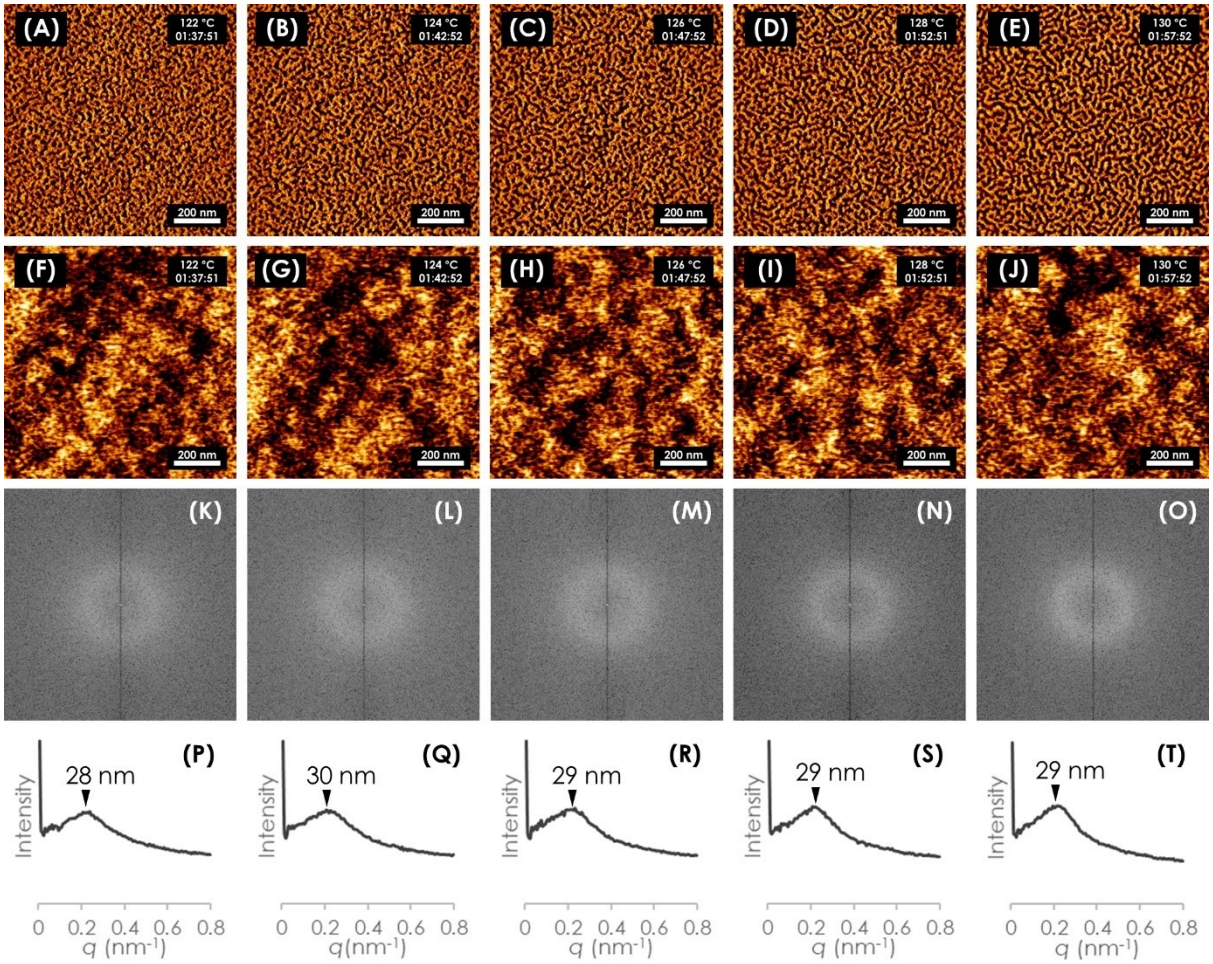


Figure 3-5. (A-E) Phase and (F-J) height images from the in situ AFM experiment from 122 to 130 °C. The temperature and time stamp in hours:minutes:seconds can be found in the top right of each image. (K-O) 2D-FFT images of the phase images in A-E. (P-T) 1D azimuthally-integrated profiles of the 2D-FFT images in K-O.

As the temperature was raised above 120 °C, the dark dots in the phase images could be observed to begin randomly connecting with the nearest neighbors, resulting in the

formation of short, irregular, and randomly-oriented lines. On the other hand, the 2D and 1D FFT profiles appear nearly unchanged, with a distinct, ring-shaped peak corresponding to *d* = ~30 nm.

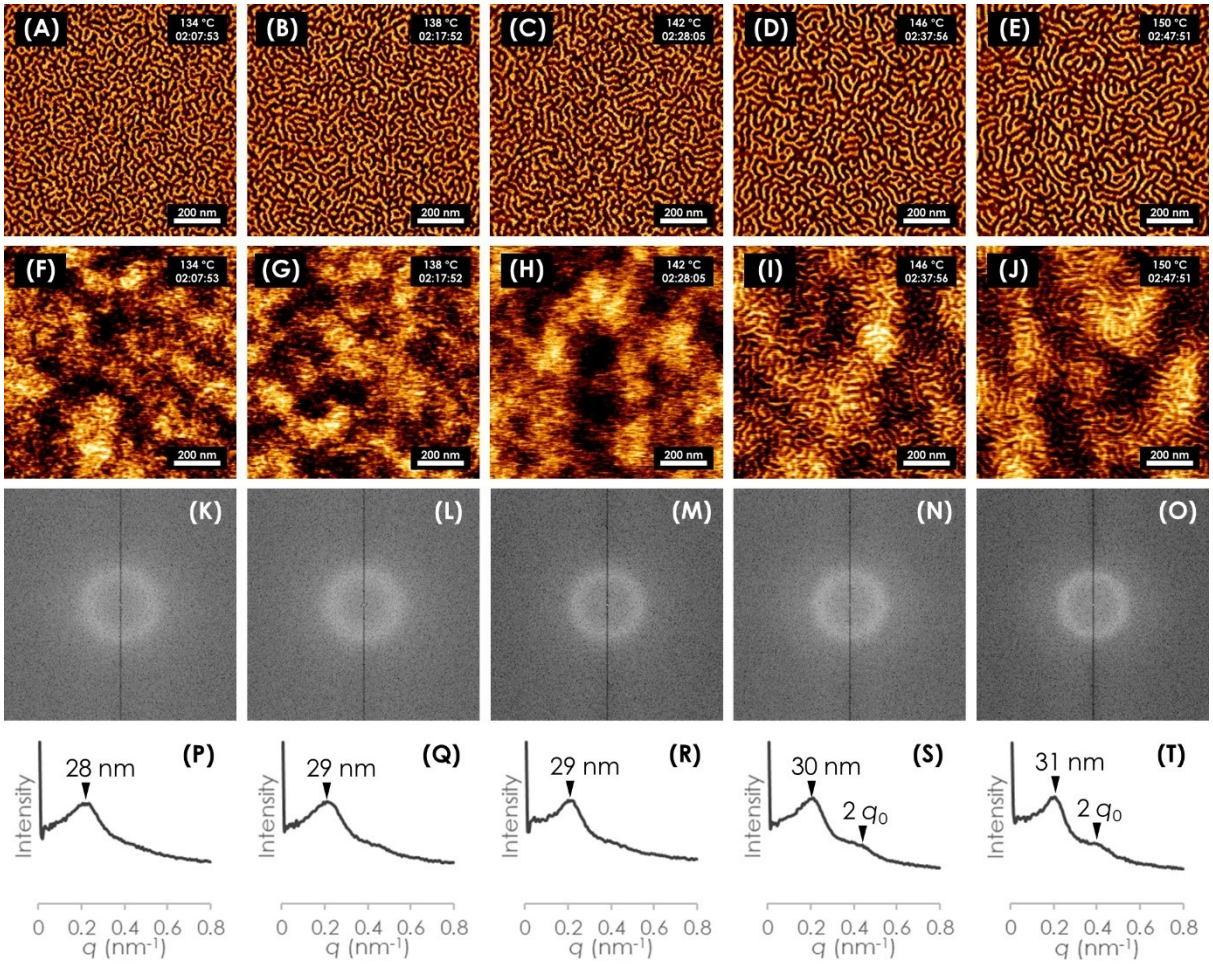


Figure 3-6. (A-E) Phase and (F-J) height images from the in situ AFM experiment from 134 to 150 °C. The temperature and time stamp in hours:minutes:seconds can be found in the top right of each image. (K-O) 2D-FFT images of the phase images in A-E. (P-T) 1D azimuthally-integrated profiles of the 2D-FFT images in K-O.

Between 130 and 150 °C, the short linear structures continued to link up with the nearest neighboring domains. At these relatively low temperatures, near the T_g's of PS-*b*-PMMA, the polymer chains likely do not possess sufficient energy for long distance translation and the influence of the underlying chemical guides have yet to be transmitted towards the film surface. A previous study also showed that at the earliest stages of self-assembly, the self-assembled domains at the surface are disconnected from those at the

substrate as the BCP structure is just as short and random internally in the thin film.[8,9] This results in the formation of a randomly-oriented, fingerprint-like structure characteristic of lamellar thin films prepared on unpatterned non-DSA substrates. In the FFT images, the ring-shaped peak corresponding to d = ~30 nm could be observed to sharpen and a secondary peak at q:q^* = 1:2, where q^* is the position of the primary peak, could be observed from 146 °C, suggesting increased ordering of the lamellae. During the growth of the fingerprint-like structure, the RMS roughness was observed to increase steadily from 0.33 nm at 116 °C to 0.49 nm at 150 °C. This increase in the RMS roughness of the surface is characteristic of a spinodal-like behavior as PS-*b*-PMMA starts to self-assemble from the disorder-like as-cast state to lamellae with increasing long-range ordering.

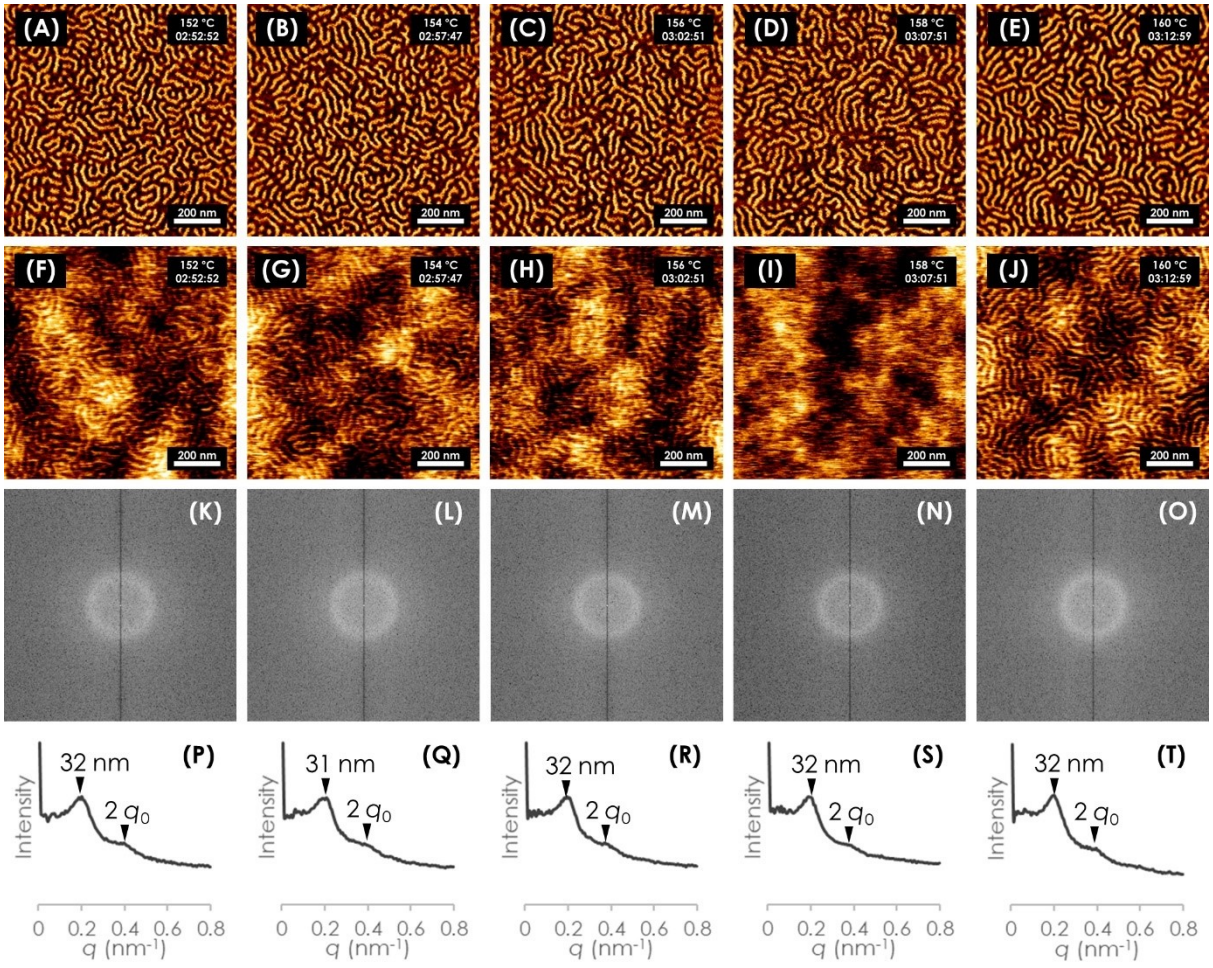


Figure 3-7. (A-E) Phase and (F-J) height images from the in situ AFM experiment from 152 to 160 °C. The temperature and time stamp in hours:minutes:seconds can be found in the

top right of each image. (K-O) 2D-FFT images of the phase images in A-E. (P-T) 1D azimuthally-integrated profiles of the 2D-FFT images in K-O.

As the temperature continues to increase to 160 °C, the fingerprint-like structure continues to grow. However, the growth of the domains appears less random, with dark domains, corresponding to PS in the phase images, appearing to form long lines in the longitudinal direction that cut across the fingerprint-like structure. Considering the chemical guides are PS-preferential, it is likely that the underlying chemical guides began affecting the self-assembly and alignment of the domains at the surface of the thin film. While the primary peak at ~30 nm and the secondary peak at q:q^* = 1:2 remain observable in the FFT profiles, the RMS roughness of the thin films decreased from 0.49 nm at 150 °C to 0.35~0.40 nm around 156 to 160 °C. This decrease in the RMS roughness of the thin film in the mid-stage of self-assembly could be attributed to self-assembly proceeding throughout the internal thin film as the BCP domains form connections from the substrate to the free surface.

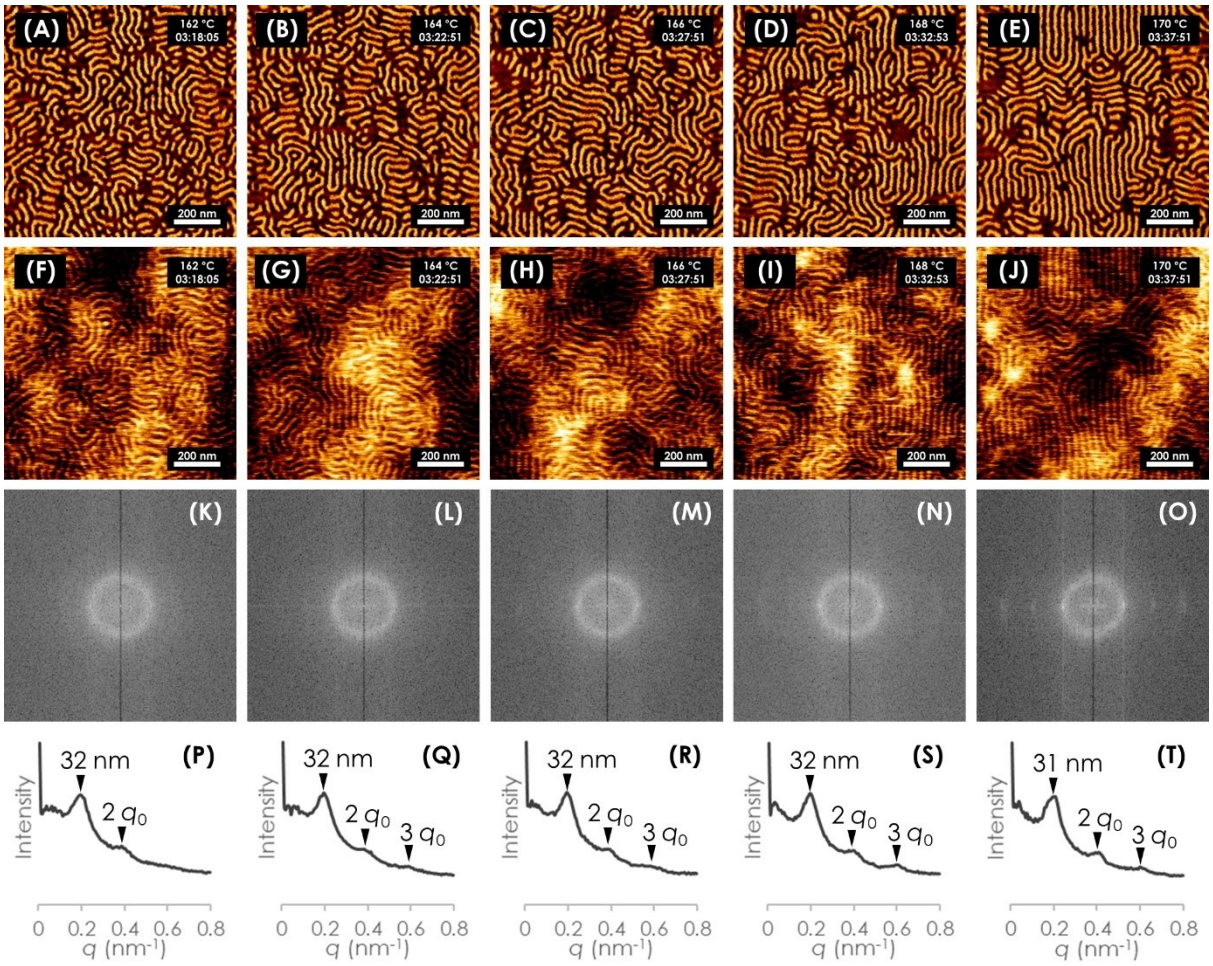


Figure 3-8. (A-E) Phase and (F-J) height images from the in situ AFM experiment from 162 to 170 °C. The temperature and time stamp in hours:minutes:seconds can be found in the top right of each image. (K-O) 2D-FFT images of the phase images in A-E. (P-T) 1D azimuthally-integrated profiles of the 2D-FFT images in K-O.

Above 160 °C, the BCP domains continue to grow in length. Additionally, between 162 and 168 °C, a majority of the lamellar grains appear to be aligned mostly either longitudinally in the same direction as the guides, or laterally in the normal direction relative to the guides, with randomly-oriented defects in between the grains. However, at 170 °C, the proportion of domains aligning longitudinally appear to increase significantly. In the 2D-FFT images, the ring-shaped peak appears to waver with increasing temperature while additional higher-order peaks at q:q^* = 1:2:3 could be observed in the 1D-FFT profile from 164 °C. Additionally, two spots corresponding to d = 30 nm could be observed in the in-plane direction of the 2-D FFT image at 166 °C and additional higher-ordered spots could also be observed at q:q^* = 1:2:3 above 168 °C.

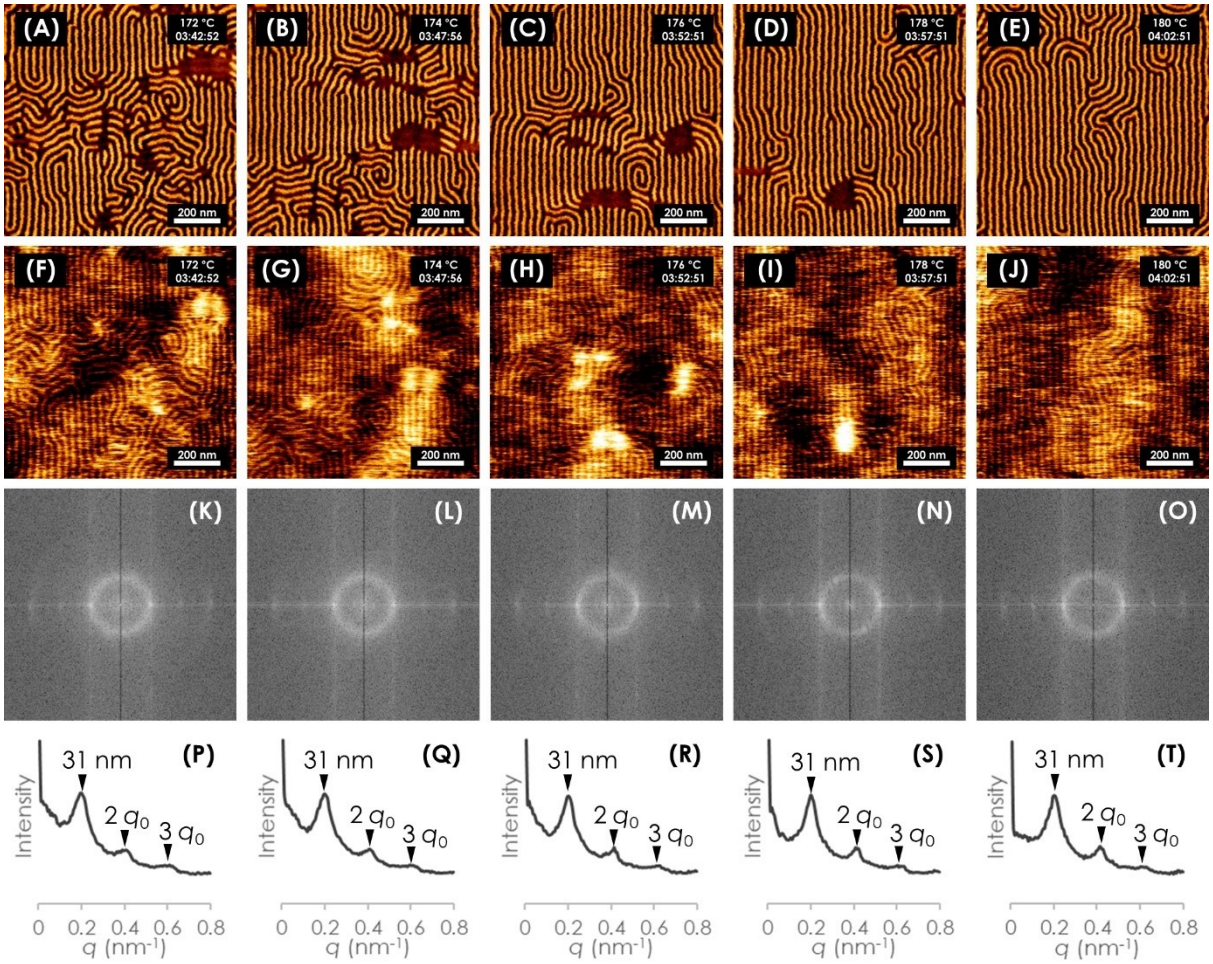


Figure 3-9. (A-E) Phase and (F-J) height images from the in situ AFM experiment from 172 to 180 °C. The temperature and time stamp in hours:minutes:seconds can be found in the top right of each image. (K-O) 2D-FFT images of the phase images in A-E. (P-T) 1D azimuthally-integrated profiles of the 2D-FFT images in K-O.

With increasing temperature, the rapid alignment of the BCP domains in the longitudinal direction could be observed in the AFM images (Fig. 3-9). However, between 172 – 178 °C, relatively large dark, flat areas could be observed in the phase image. These likely can be attributed to the surface segregation of PS and the formation of parallel lamellae. Mansky and co-workers previously showed that at lower temperatures below 210 – 230 °C, the free surface is slightly preferential to PS.[10] Additionally, since the chemical guides are PS-preferential, the formation of parallel lamellae with symmetric PS wetting could be encouraged, resulting in the growth of locally defective parallel lamellae as alignment began around 160 °C. This surface segregation of the PS domain was also

observed to have a height of ~1 nm, resulting in a relatively higher RMS roughness between 160 and 180 °C, peaking at 0.51 nm at 164 °C. Furthermore, the higher-ordered spots in the in-plane profile of the 2D-FFT image grew to arced curves as ordering increased while significant defects remain observable.

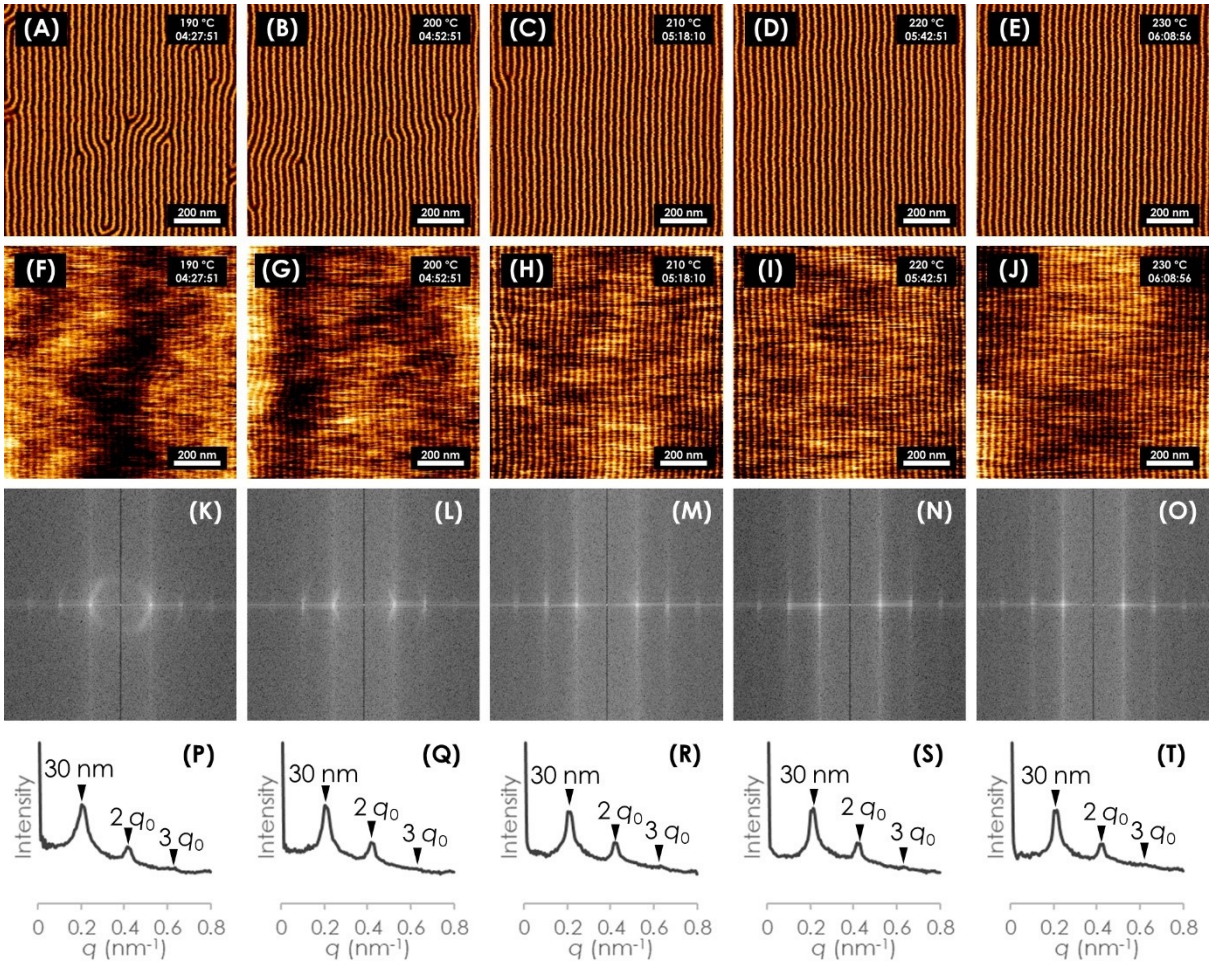


Figure 3-10. (A-E) Phase and (F-J) height images from the in situ AFM experiment from 190 to 230 °C. The temperature and time stamp in hours:minutes:seconds can be found in the top right of each image. (K-O) 2D-FFT images of the phase images in A-E. (P-T) 1D azimuthally-integrated profiles of the 2D-FFT images in K-O.

As the temperature increased further, parallel defects could no longer be observed and the rapid annihilation of disclination and dislocation defects was observed in the AFM images (Fig. 3-10). Specifically, above 220 °C, defects disappeared from the 1 × 1 μm^2 area of this in situ AFM experiment, with the lamellae all aligned longitudinally along the direction of the guides. At 190 °C, the ring of the primary peak in the 2D-FFT image appeared to

break up into arcs which grew smaller and concentrated into two spots in the in-plane direction with increased temperature. As defects disappeared from the AFM images, the ring completely disappeared from the 2D-FFT images. Instead, vertical lines and spots could be observed exclusively in the 2D-FFT images. Additionally, the primary peaks plotted on the 1D-FFT profiles corresponded to d = 30 nm, in good agreement with the L_0 of the PS-*b*-PMMA used. Interestingly, although there is significant thermal noise causing fluctuations from frame to frame, the RMS roughness of the thin film averages to 0.35 ± 0.03 nm, similar to the RMS roughness of 0.359 ± 0.007 nm seen at the start of the annealing process, from 26 to 110 °C.

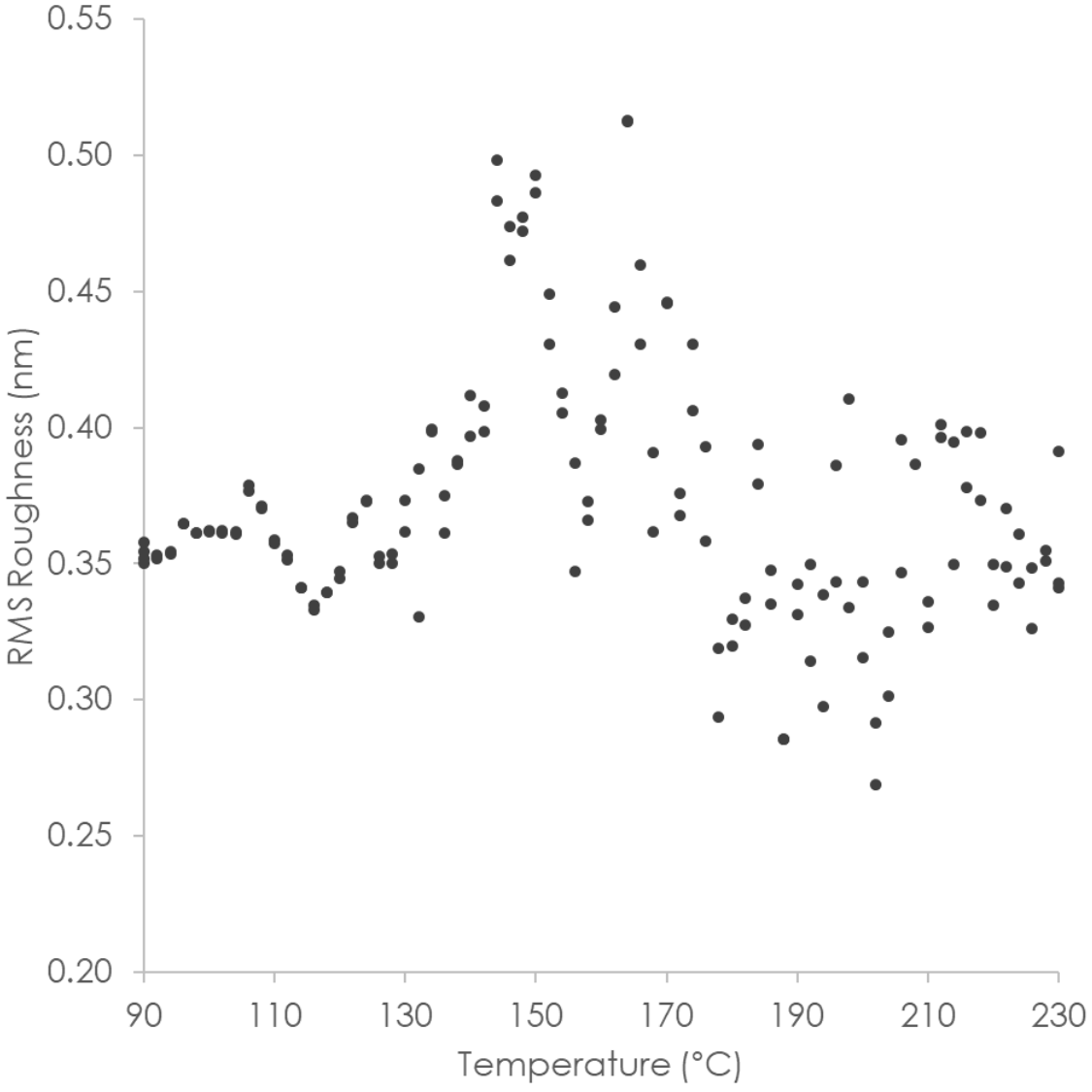


Figure 3-11. Plot of the rough-mean-squared (RMS) roughness of the thin film surface at each temperature and frame of the in situ AFM experiment.

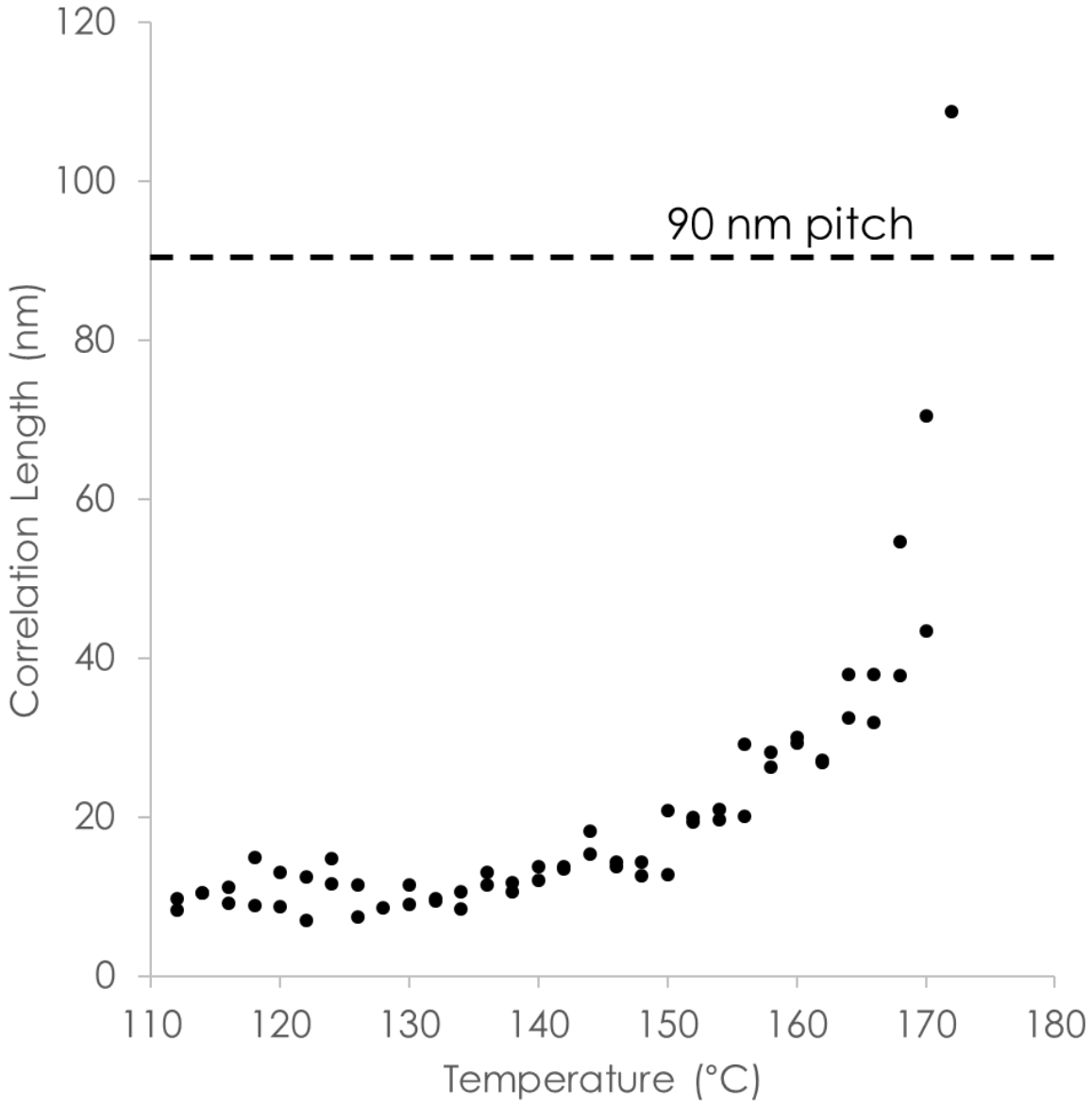


Figure 3-12. Plot of the correlation length of the lamellar grains measured between 110 to 180 °C.

The degree of ordering and extent of self-assembly for each image in the in situ AFM observation of the evolution of perpendicular lamellae under chemical guides can be quantified in terms of a correlation length (ξ) (Fig. 3-12) and an orientational order parameter (Ψ_2) (Fig. 3-13). Based on earlier studies on the time-evolved quantitative analysis of fingerprint-like striped patterns in parallel cylinders by Harrison and co-workers,[11–13] the

degree of ordering in the incremental annealing of the SMART™ process DSA thin film was quantified using Matlab software.[8]

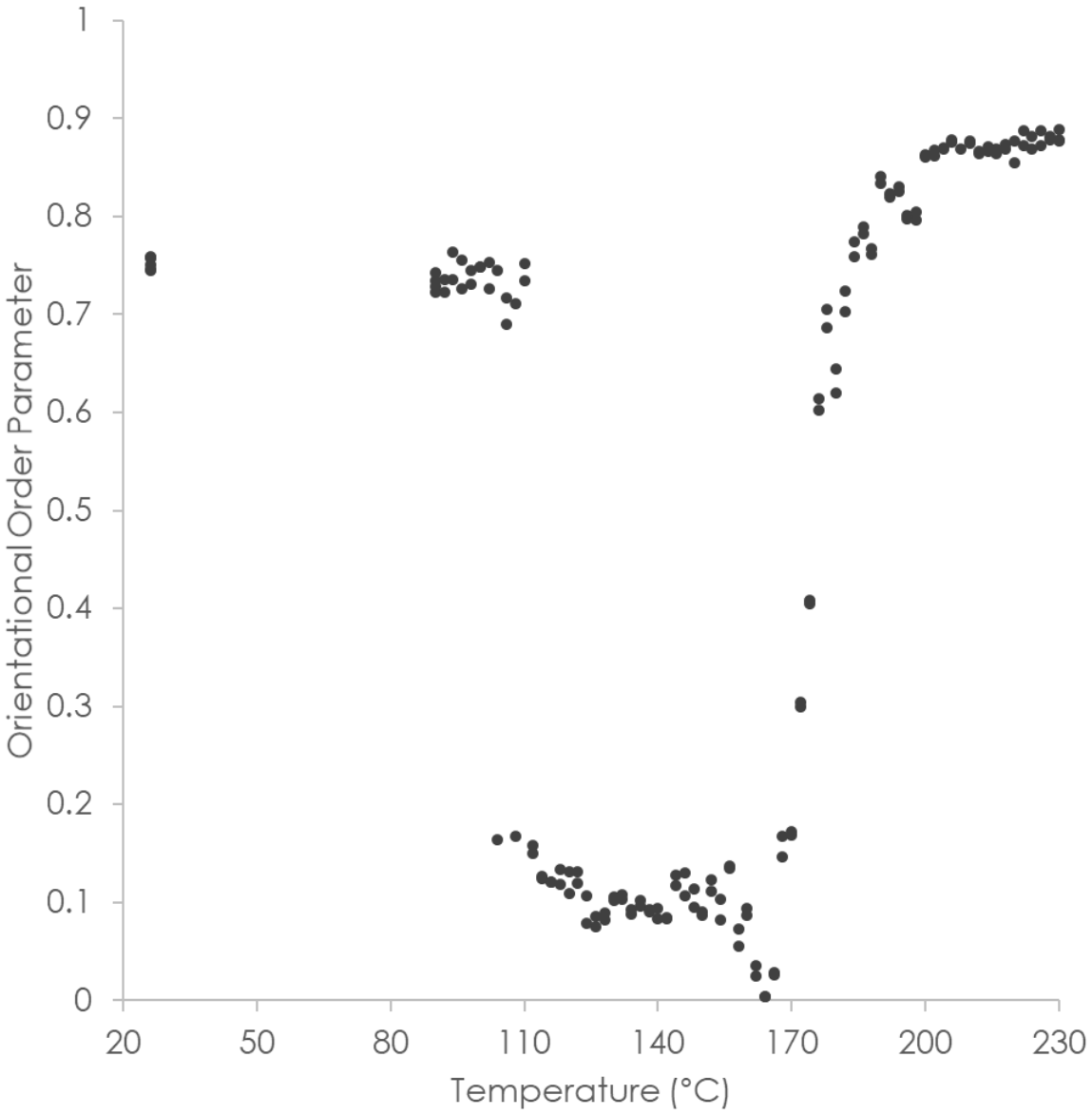


Figure 3-13. Plot of the degree of alignment quantified as an orientation order parameter (Ψ_2) for each frame of the in situ AFM experiment.

To quantify the degree of ordering, the order parameter (Ψ) for 2D patterns can be first defined as,[11,13,14]

$$\Psi = \Psi_0 \exp(2i\theta) \quad (3\text{-}1)$$

where θ is the local orientation of the microdomain. By calculating the angles at which the microdomains are oriented at each point, the AFM images can be converted into false color

images. Using an autocorrelation function $g(\vec{r})$, a cross-correlation of two identical functions at the positional vector $\vec{r}$, we obtain,

$$g(\vec{r}) = \frac{\int \psi(\vec{x})\psi^*(\vec{x}+\vec{r})\partial\vec{x}}{\int \psi(\vec{x})\psi^*(\vec{x})\,\partial\vec{x}} \quad (3\text{-}2)$$

In systems limited to local alignment, $g(\vec{r})$ decays exponentially as the distance between evaluated points increases. From this, the correlation length (ξ) of the system can be defined as,

$$\text{real}(g(\vec{r})) = \langle\cos 2(\theta - \theta(\vec{r}))\rangle \sim \exp\left(\frac{-r}{\xi}\right) \quad (3\text{-}3)$$

where $\theta(\vec{r})$ is the angle θ offset at a distance r away. However, the quantitative analysis in terms of the correlation length is limited for systems on the extreme low and high ends of ordering. For well-mixed, random systems near the disordered state, a correlation length cannot be estimated reliably. Conversely, for systems that are highly aligned, ξ goes to infinity and an alternative parameter is required to determine the degree of alignment in well-aligned DSA patterns. Nevertheless, ξ could be estimated for the images obtained between 112 and 172 °C, before the BCP microdomains exhibited significant long-range alignment. Between 112 and 150 °C, ξ was found to be low and nearly constant at 12 ± 3 nm. Above 150 °C however, ξ increased exponentially, reaching a value of 71 nm at 170 °C and a maximum of 109 nm at 172 °C before further calculations could no longer be carried out.

To overcome the limitations behind the calculation of ξ, the degree of alignment can instead be quantified as an orientational order parameter (Ψ_2) defined as,[15–18]

$$\psi_2 = \langle\cos[2(\theta_i - \theta_0)]\rangle \quad (x)$$

where θ_i is the local orientation angle of the microdomains, θ_0 is the angle of perfect longitudinal alignment (90°). When the pattern is perfectly aligned longitudinally, randomly, or laterally on the image, Ψ_2 = 1, 0, or –1, respectively. For analysis, the phase images were Fourier-filtered and smoothed to produce a 2D gradient. The local orientation angle θ_i was calculated in the same manner as the estimation of ξ and summated over all pixels to yield the degree of alignment as Ψ_2. Plotting Ψ_2 as a function of temperature, four distinct self-

assembly regimes can be found. Between 26 and 110 °C, an oddly high averaged value of $\Psi_2 = 0.74 \pm 0.01$ can be found. Although the system is nearly disordered, longitudinal stripes at 90 nm intervals attributed to the chemical guides can be detected on the AFM images. Therefore, the high value of $\Psi_2 = 0.74$ is likely a result of the influence of the pre-patterned substrate. However, as observed in the AFM images, the longitudinal 90 nm-pitch stripes began to disappear above 110 °C. This is reflected in Ψ_2 as it drops to 0.15 at 112 °C. As the temperature increases, Ψ_2 was observed to steadily decrease at a rate of –0.003 per 2 °C increment, down to a minimum of 0.004 at 164 °C. The corresponding AFM images indicated the slow but steady growth of the BCP microdomains in this temperature regime. As the microdomains extended through combinations with the nearest neighbors, a fingerprint-like pattern could be observed to develop between 130 and 150 °C. The stochastic and nearly isotropic growth of the fingerprint-like pattern likely caused Ψ_2 to decrease steadily as the system appeared random. However, as the temperature neared 160 °C, the influence of the underlying chemical guides could also be observed as PS domains began to align onto the guides and cut longitudinally across the grains of the fingerprint pattern. Particularly at 164 °C (Fig. 3-8), a mix of longitudinally and laterally aligned lamellae could be observed, thereby decreasing Ψ_2 to the minimum of 0.004 despite the fact that alignment of the PS domains began above 150 °C. Above 164 °C, Ψ_2 was observed to jump significantly at a rate of 0.07 per 2 °C increment, plateauing at 0.872 ± 0.008 above 200 °C. Referring back to the AFM images, the proportion of longitudinally aligned microdomains visibly grew above 170 °C and the rapid annihilation of defects could be observed between 170 and 200 °C as well. As the annealing temperature reached 200 °C, only a few dislocation defects could be observed, while most of the microdomains were in near perfect longitudinal alignment. Furthermore, although defects could no longer be observed above 220 °C, Ψ_2 peaked at a value of 0.889 in the final image obtained. Nevertheless, Ψ_2 is shown to be a useful tool for quantifying the degree of alignment in the system. In good agreement with the visual, qualitative aspect of the AFM images, four distinct regimes of self-assembly, namely a kinetically-frozen regime with the chemical

guides being detectable, a glass transition and stochastic growth of a random structure, alignment of the microdomains, and the annihilation of defects, are represented in the plot of Ψ_2 against temperature.

3-3-2 Isothermal Annealing after Incremental Annealing

After the temperature was increased incrementally up to 230 °C, the temperature was held constant and in situ imaging continued at larger image sizes for 2 h, at which point the HTHS heating stage was no longer capable of maintaining a constant temperature at 230 °C and the experiment had to be stopped. To gain a better understanding of the area surrounding the initial 1 × 1 μm^2 area, larger scan areas were used, and the images are shown in Fig. 3-14 to 3-18. These images were obtained at pixel resolutions of 1024 × 1024, 2048 × 2048, and 4096 × 4096. Therefore, typical “high-definition” television (HDTV) monitors with a display resolution of 1920 × 1080 pixels may not be able to display the images correctly without significant zooming in. Additionally, the phase images are shown as obtained, after a simple removal of the background using AFM data processing software without adding labels such as the time stamp and scale bar as image editing software can significantly reduce the quality of the saved images, resulting in the removal of pixels. Therefore, the timestamp and scan areas were included in the captions for each image.

The first image after the incremental experiment was obtained at a time (t) of 6:12:26 (Fig. 3-14) with a larger image size and resolution of 4 × 4 μm^2 and 1024 × 1024 pixels using a line rate of 2 Hz, thereby needing 8 min 32 s to image the entire area. The prior incremental experiment had been focused on the center 1 × 1 μm^2 of the 4 × 4 μm^2 image. Although the 1 × 1 μm^2 area had been free of defects, a single dislocation defect could be observed at the top of the 4 × 4 μm^2 image taken at 6:12:26. Performing the same orientational order parameter calculation here, we obtained Ψ_2 = 0.875. Subsequently, while the imaging location remained unchanged, the imaging area was enlarged to 10 × 10 μm^2 with a resolution of 2048 × 2048 pixels. The line rate remained at 2 Hz and imaging took 17 min 4 s to complete. This yielded an image with a single dislocation pair centered on the

upper-third of the image. Additionally, although thermal noise caused the distortion of the aligned lamellae into locally wavy patterns, Ψ_2 was observed to further increase to 0.926. The two final images were obtained at the maximum imaging size possible of 30 × 30 μm^2, at a resolution of 4096 × 4096 pixels and a line rate of 2 Hz. Requiring 34 min 8 s to finish imaging, the images revealed a total of six dislocation pair defects in the 30 × 30 μm^2 area and Ψ_2 was estimated to be ~0.91. When normalized at this rate, a defect density of 6.7 × 10^5 defects per cm^2 can be estimated. Considering the long annealing times at high temperatures, these defects are likely highly metastable and may be equilibrated. To achieve the near-perfect defect density of 0.01 defects per cm^2, a seven-magnitude decrease, further understanding of the bottom-up, stochastic behavior of BCP self-assembly and the detailed mechanisms as to how these defects form, evolve, and annihilate is required.

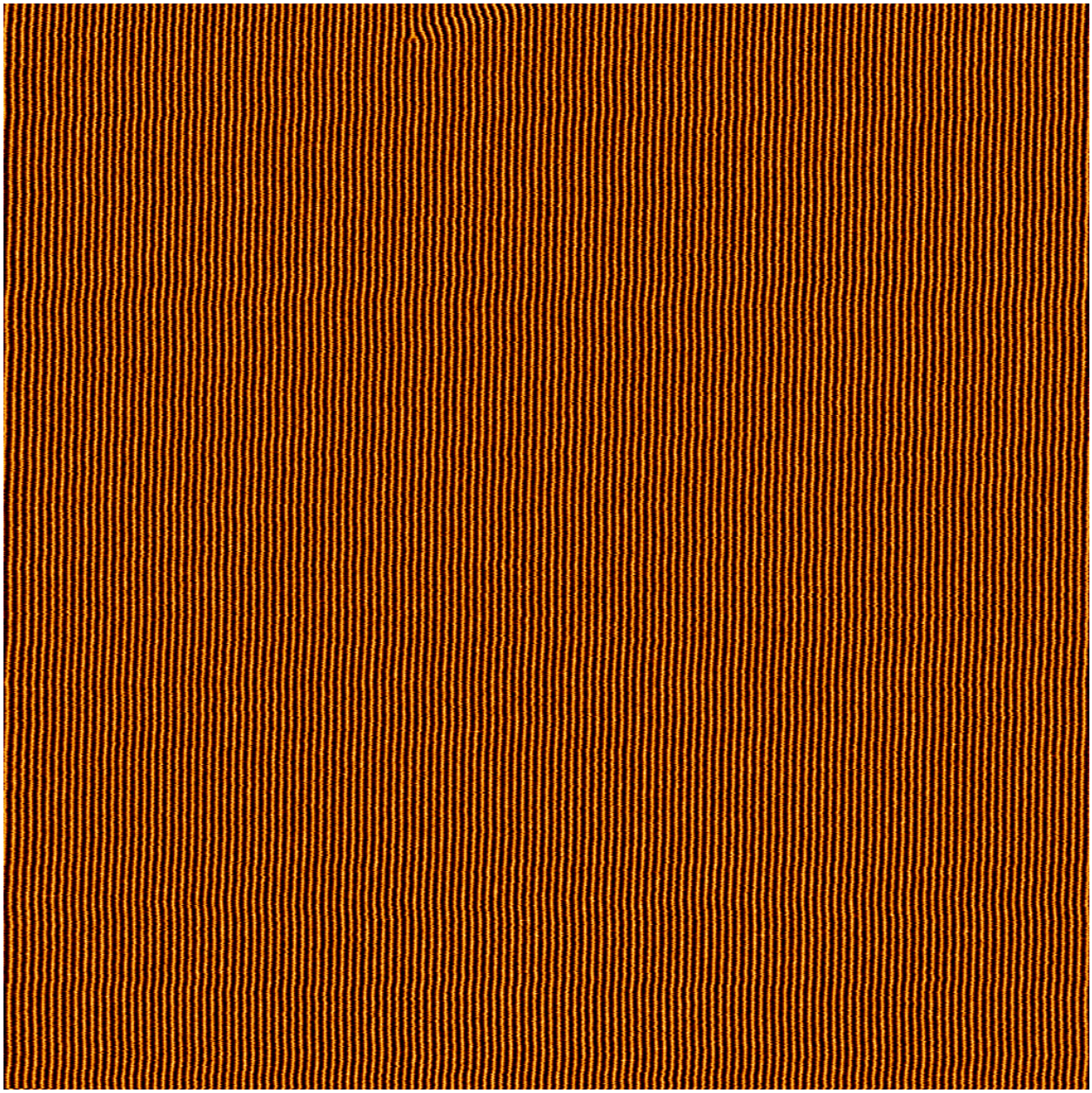


Figure 3-14. Phase image obtained over isothermal annealing conditions at 230 °C after incrementally increasing the annealing temperature from 90 to 230 °C. This image was obtained at t = 6:12:26, with a scan of 4 × 4 μm^2, a resolution of 1024 × 1024 pixels, and a line rate of 2 Hz, requiring 8 min 32 s to complete imaging.

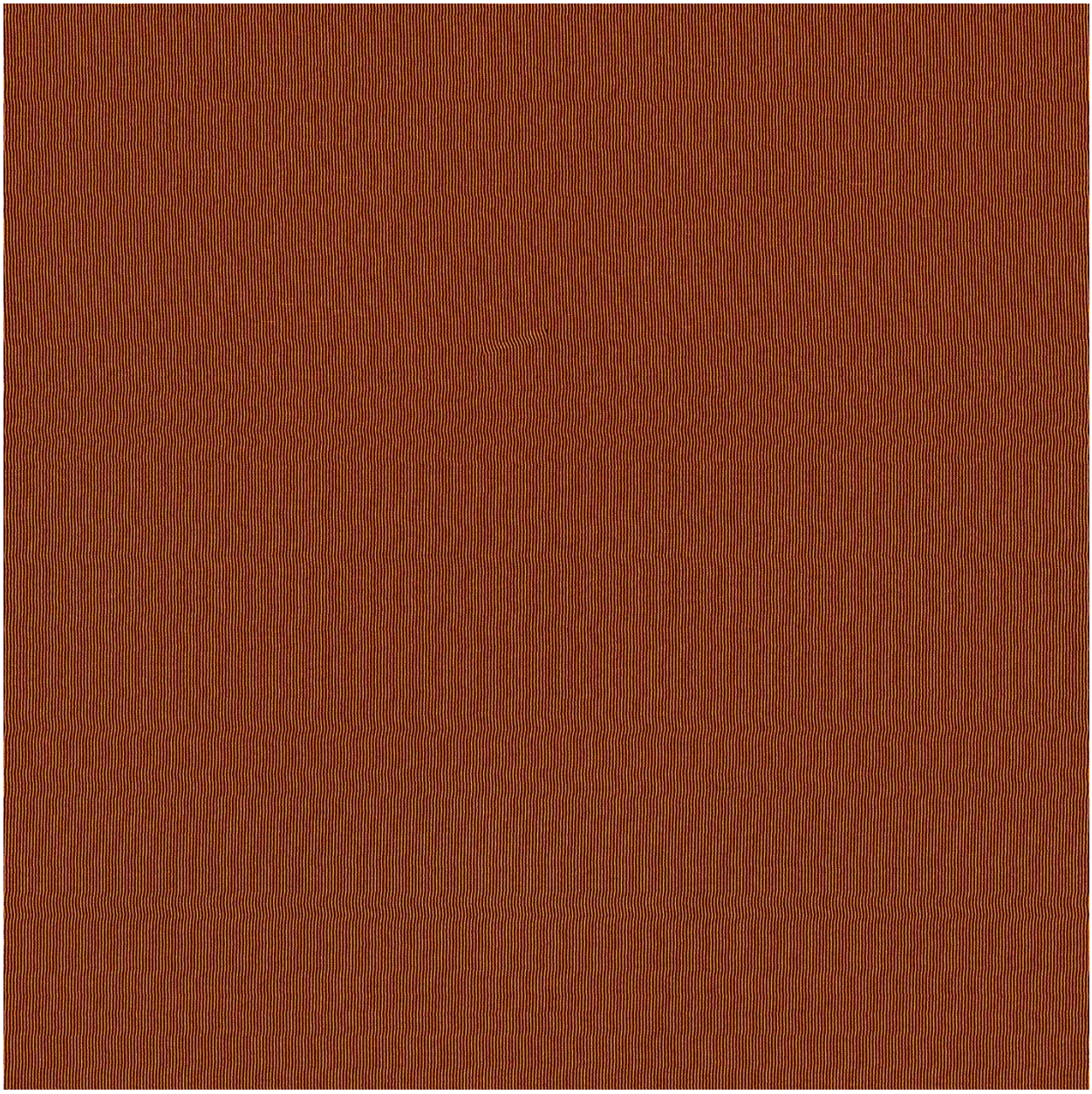


Figure 3-15. Phase image obtained over isothermal annealing conditions at 230 °C after incrementally increasing the annealing temperature from 90 to 230 °C. This image was obtained at t = 6:17:49, with a scan of 10 × 10 μm^2, a resolution of 2048 × 2048 pixels, and a line rate of 2 Hz, requiring 17 min 4 s to complete imaging.

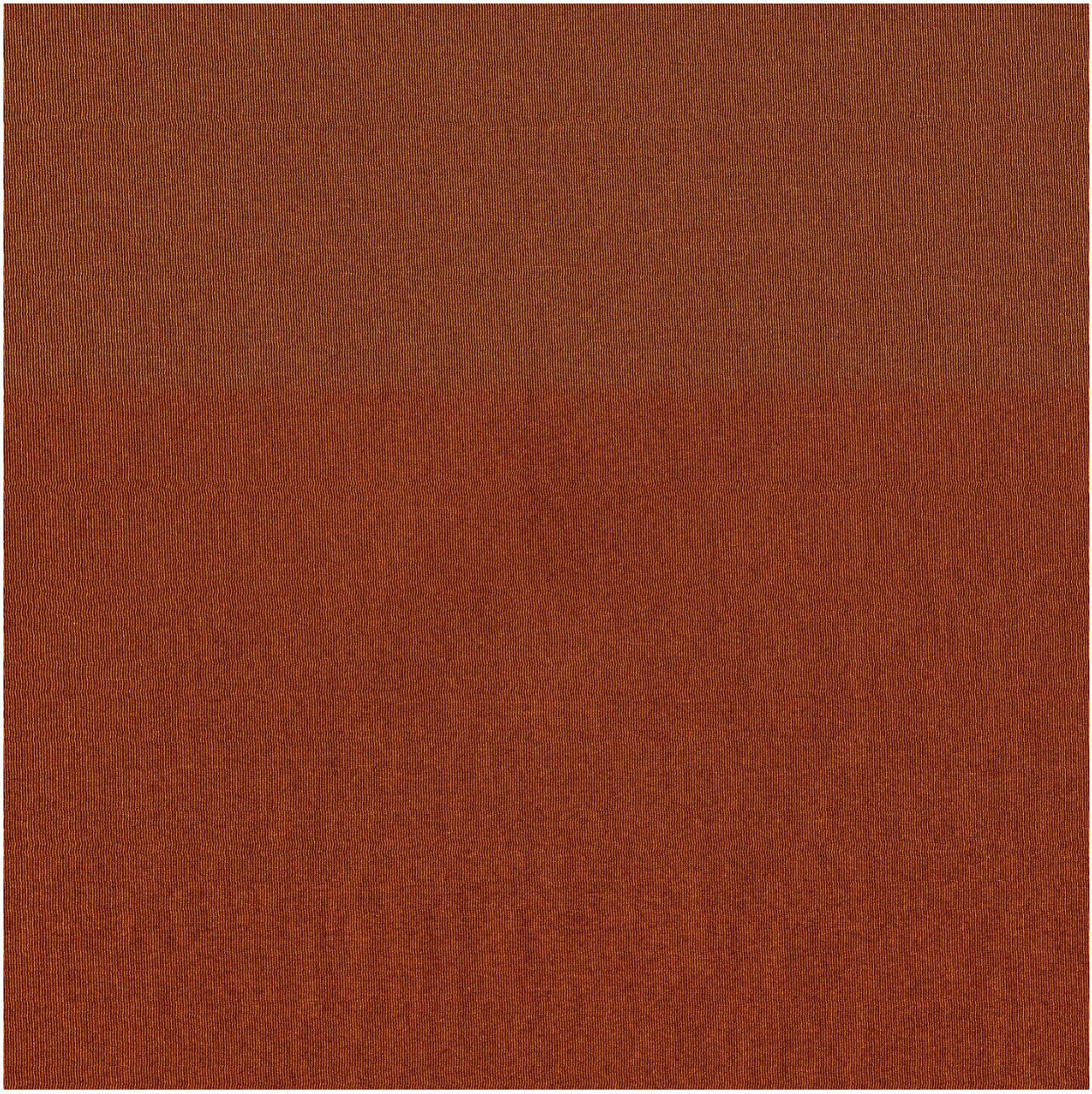


Figure 3-16. Phase image obtained over isothermal annealing conditions at 230 °C after incrementally increasing the annealing temperature from 90 to 230 °C. This image was obtained at t = 6:38:55, with a scan of 30 × 30 μm^2, a resolution of 4096 × 4096 pixels, and a line rate of 2 Hz, requiring 34 min 8 s to complete imaging.

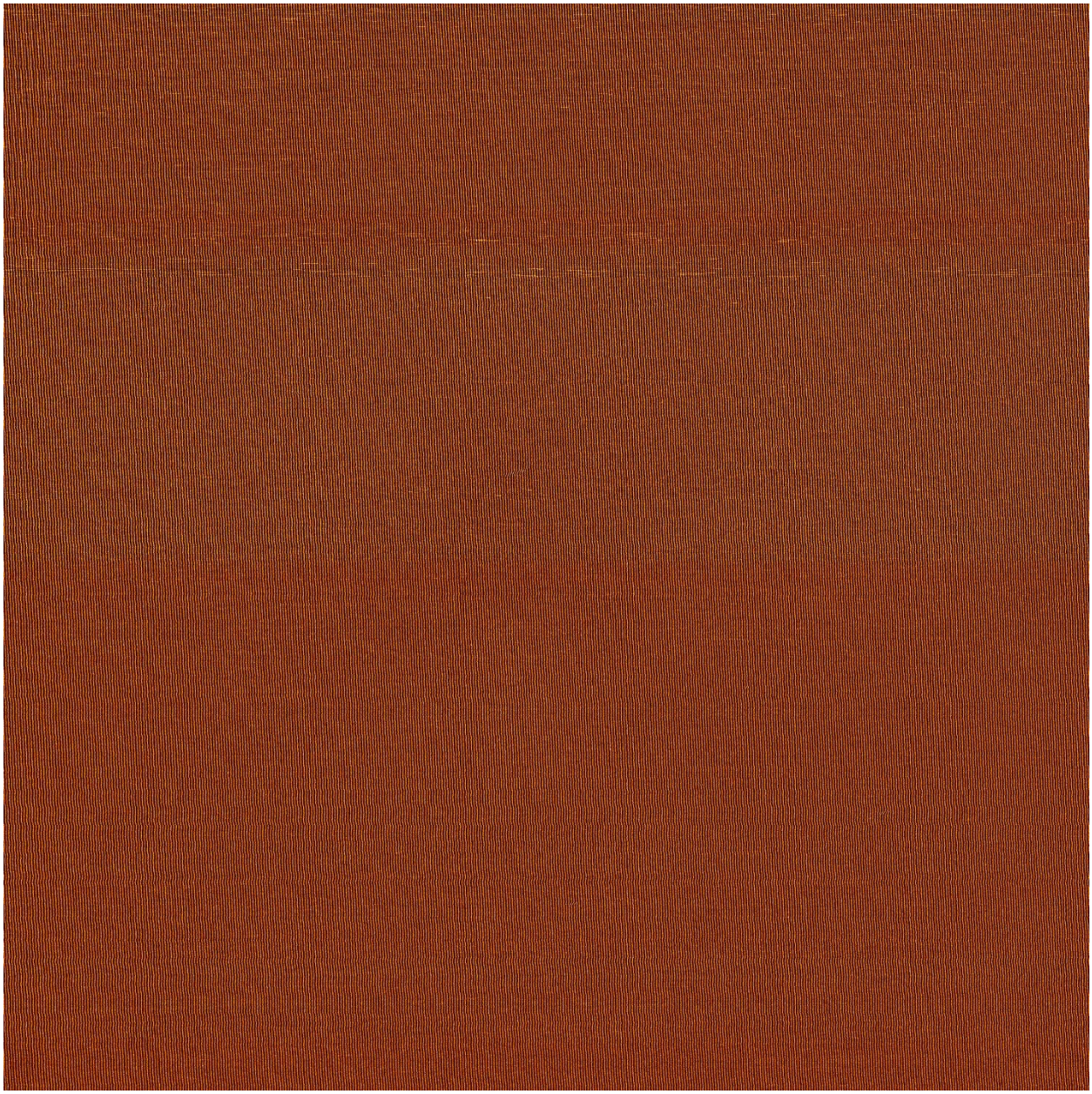


Figure 3-17. Phase image obtained over isothermal annealing conditions at 230 °C after incrementally increasing the annealing temperature from 90 to 230 °C. This image was obtained at t = 7:13:40, with a scan of 30 × 30 μm^2, a resolution of 4096 × 4096 pixels, and a line rate of 2 Hz, requiring 34 min 8 s to complete imaging.

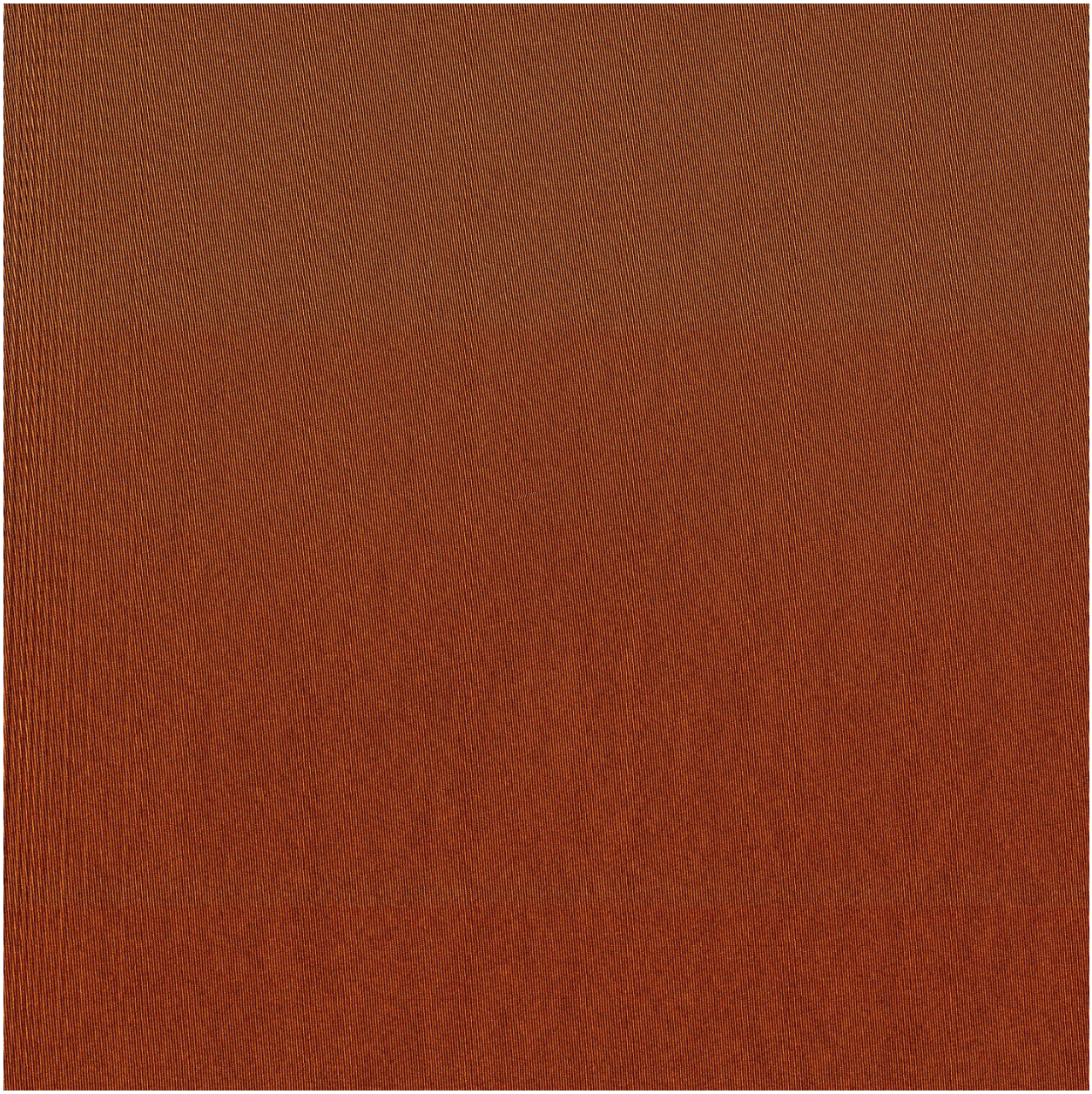


Figure 3-18. Phase image obtained over isothermal annealing conditions at 230 °C after incrementally increasing the annealing temperature from 90 to 230 °C. This image was obtained at t = 7:59:01, with a scan of 30 × 30 μm^2, a resolution of 4096 × 4096 pixels, and a line rate of 2 Hz, requiring 34 min 8 s to complete imaging.

3-4 Conclusion

Based on the in situ AFM experiment with incrementally increasing temperature, the evolution of well-aligned, “defect-free”, perpendicular lamellar microdomains from a nearly disordered state was documented in real time and real space. Several temperature regimes with characteristic behaviors could be observed. At temperatures significantly below the T_g’s

of the BCP, PS-*b*-PMMA, a kinetically frozen state whereby the underlying chemical guides could be observed at 90 nm intervals, resulting in an oddly high degree of alignment (Ψ_2 = 0.74). However, as the temperature increased and the BCP transitioned into the rubbery state, the BCP surface began to flow to form a flat surface and the underlying chemical guides could no longer be detected on the surface. In this early-stage of self-assembly, the BCP microdomains were observed to stochastically grow through linkages with the nearest neighbors, forming a random fingerprint-like structure with Ψ_2 approaching zero at 150 – 160 °C. Further increasing the temperature caused an explosive growth in the alignment of the microdomains and subsequent defect annihilation resulted in "defect-free" microdomains with Ψ_2 = 0.9 above 220 °C. With this study on the evolution and defect annihilation of lamellar PS-*b*-PMMA under the effect of chemoepitaxial DSA guides prepared using the SMART™ process, the nature of the bottom-up self-assembly process could be elucidated, bringing the field one step closer towards the realization of large-scale, "defect-free" self-assembled patterns.

3-5 References

(1) Liu, C. C.; Han, E.; Onses, M. S.; Thode, C. J.; Ji, S.; Gopalan, P.; Nealey, P. F. Fabrication of Lithographically Defined Chemically Patterned Polymer Brushes and Mats. *Macromolecules* **2011**, *44* (7), 1876–1885 DOI: 10.1021/ma102856t.

(2) Seino, Y.; Kasahara, Y.; Sato, H.; Kobayashi, K.; Kubota, H.; Minegishi, S.; Miyagi, K.; Kanai, H.; Kodera, K.; Kihara, N.; Kawamonzen, Y.; Tobana, T.; Shiraishi, M.; Nomura, S.; Azuma, T. Directed Self-Assembly Lithography Using Coordinated Line Epitaxy (COOL) Process. *Proc. SPIE* **2015**, *9423*, 942316 DOI: 10.1117/12.2085697.

(3) Kim, J.; Wan, J.; Miyazaki, S.; Yin, J.; Cao, Y.; Her, Y. J.; Wu, H.; Shan, J.; Kurosawa, K.; Lin, G. The SMART™ Process for Directed Block Co-Polymer Self-Assembly. *J. Photopolym. Sci. Technol.* **2013**, *26* (5), 573–579 DOI: 10.2494/photopolymer.26.573.

(4) Paquet, A.; Le Pennec, A.; Gharbi, A.; Giammaria, T. J.; Rademaker, G.; Pourteau, M.-L.; Mariolle, D.; Navarro, C.; Nicolet, C.; Chevalier, X.; Sakavuyi, K.; Pain, L.; Nealey, P.; Tiron, R. Spacer Patterning Lithography as a New Process to Induce

Block Copolymer Alignment by Chemo-Epitaxy. *Proc. SPIE* **2019**, *10958*, 109580M DOI: 10.1117/12.2514960.

(5) Muramatsu, M.; Nishi, T.; You, G.; Ido, Y.; Kitano, T. Defect and Roughness Reduction of Chemo-Epitaxy DSA Pattern. *Proc. SPIE* **2018**, *10584*, 105840M DOI: 10.1117/12.2297185.

(6) Muramatsu, M.; Nishi, T.; You, G.; Ido, Y.; Kitano, T. Pattern Defect Reduction for Chemo-Epitaxy DSA Process. *Proc. SPIE* **2019**, *10960*, 109600W DOI: 10.1117/12.2514671.

(7) Muramatsu, M.; Nishi, T.; Ido, Y.; Kitano, T. Defect Mitigation of Chemo-Epitaxy DSA Patterns. *Proc. SPIE* **2020**, *11326*, 113260Y DOI: 10.1117/12.2551996.

(8) Nakatani, R.; Chandra, A.; Uchiyama, T.; Nabae, Y.; Hayakawa, T. Dynamic Ordering in High-χ Block Copolymer Lamellae Based on Cross-Sectional Orientational Alignment. *ACS Macro Lett.* **2019**, *8* (9), 1122–1127 DOI: 10.1021/acsmacrolett.9b00353.

(9) Ren, J.; Zhou, C.; Chen, X.; Dolejsi, M.; Craig, G. S. W.; Rincon Delgadillo, P. A.; Segal-Peretz, T.; Nealey, P. F. Engineering the Kinetics of Directed Self-Assembly of Block Copolymers toward Fast and Defect-Free Assembly. *ACS Appl. Mater. Interfaces* **2018**, *10* (27), 23414–23423 DOI: 10.1021/acsami.8b05247.

(10) Mansky, P.; Russell, T. P.; Hawker, C. J.; Pitsikalis, M.; Mays, J. Ordered Diblock Copolymer Films on Random Copolymer Brushes. *Macromolecules* **1997**, *30* (22), 6810–6813 DOI: 10.1021/ma970675v.

(11) Harrison, C.; Adamson, D. H.; Cheng, Z.; Sebastian, J. M.; Sethuraman, S.; Huse, D. A.; Register, R. A.; Chaikin, P. M. Mechanisms of Ordering in Striped Patterns. *Science (80-.).* **2000**, *290* (5496), 1558–1560 DOI: 10.1126/science.290.5496.1558.

(12) Harrison, C.; Park, M.; Chaikin, P. M.; Register, R. A.; Adamson, D. H. Lithography with a Mask of Block Copolymer Microstructures. *J. Vac. Sci. Technol. B Microelectron. Nanom. Struct.* **1998**, *16* (2), 544–552 DOI: 10.1116/1.589860.

(13) Harrison, C.; Cheng, Z.; Sethuraman, S.; Huse, D. A.; Chaikin, P. M.; Vega, D. A.;

Sebastian, J. M.; Register, R. A.; Adamson, D. H. Dynamics of Pattern Coarsening in a Two-Dimensional Smectic System. *Phys. Rev. E* **2002**, *66* (1), 011706 DOI: 10.1103/PhysRevE.66.011706.

(14) Harrison, C.; Chaikin, P. M.; Huse, D. A.; Register, R. A.; Adamson, D. H.; Daniel, A.; Huang, E.; Mansky, P.; Russell, T. P.; Hawker, C. J.; Egolf, D. A.; Melnikov, I. V.; Bodenschatz, E. Reducing Substrate Pinning of Block Copolymer Microdomains with a Buffer Layer of Polymer Brushes. *Macromolecules* **2000**, *33* (3), 857–865 DOI: 10.1021/ma991551g.

(15) Davis, R. L.; Chaikin, P. M.; Register, R. A. Cylinder Orientation and Shear Alignment in Thin Films of Polystyrene-Poly(n-Hexyl Methacrylate) Diblock Copolymers. *Macromolecules* **2014**, *47* (15), 5277–5285 DOI: 10.1021/ma5012705.

(16) Marencic, A. P.; Adamson, D. H.; Chaikin, P. M.; Register, R. A. Shear Alignment and Realignment of Sphere-Forming and Cylinder-Forming Block-Copolymer Thin Films. *Phys. Rev. E - Stat. Nonlinear, Soft Matter Phys.* **2010**, *81* (1), 21507 DOI: 10.1103/PhysRevE.81.011503.

(17) Marencic, A. P.; Adamson, D. H.; Chaikin, P. M.; Register, R. A. Shear Alignment and Realignment of Sphere-Forming and Cylinder-Forming Block-Copolymer Thin Films. *Phys. Rev. E - Stat. Nonlinear, Soft Matter Phys.* **2010**, *81* (1), 011503 DOI: 10.1103/PhysRevE.81.011503.

(18) Vega, D. A.; Harrison, C. K.; Angelescu, D. E.; Trawick, M. L.; Huse, D. A.; Chaikin, P. M.; Register, R. A. Ordering Mechanisms in Two-Dimensional Sphere-Forming Block Copolymers. *Phys. Rev. E - Stat. Nonlinear, Soft Matter Phys.* **2005**, *71* (6) DOI: 10.1103/PhysRevE.71.061803.

This page was intentionally left blank.

Chapter 4 Defect Dynamics of PS-b-PMMA Thin Films on Chemically Pre-Patterned DSA Substrates Prepared via the SMART™ Flow

4-1 Introduction

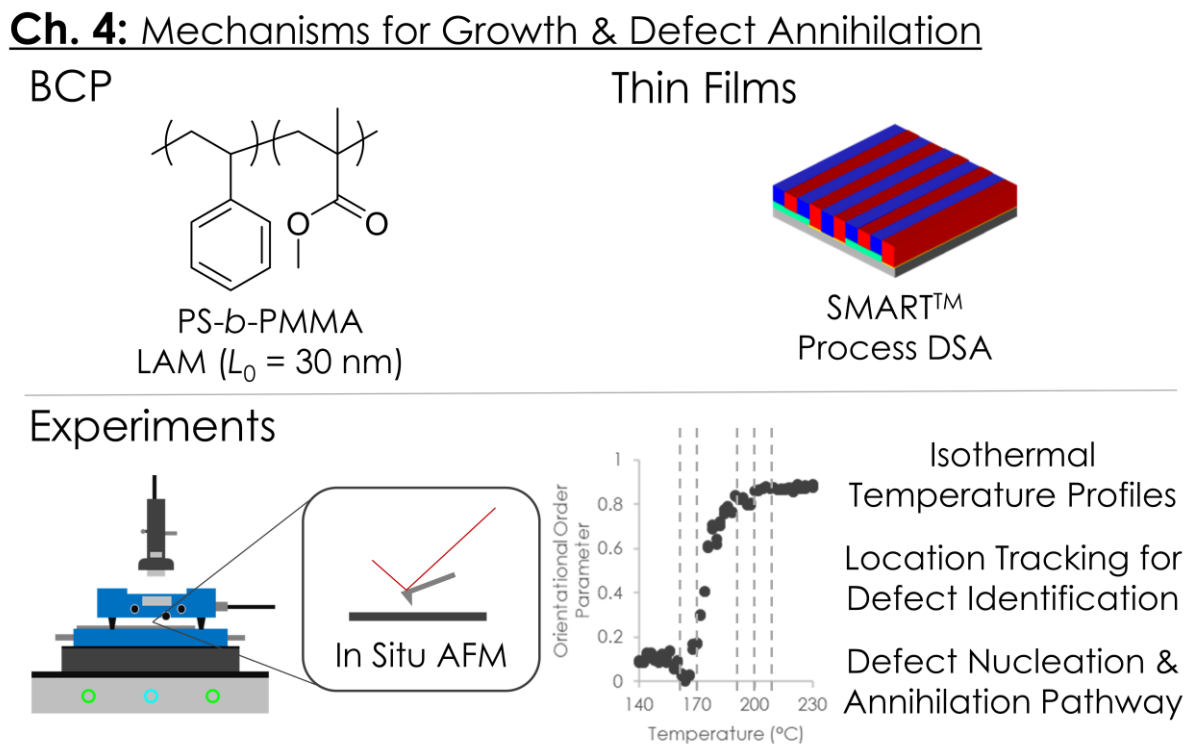
Defects can exist in almost any material that exhibits some degree of ordering. The bottom-up nature of BCP self-assembly results in the formation of randomly-oriented structures riddled with defects. While directed self-assembly (DSA) guides can be pre-patterned onto the substrates to nudge the structure into long-range alignment and defect annihilation, the development of defect-free structures remains challenging. This is likely in part due to the fact that the exact mechanisms and pathways behind the evolution and annihilation of defects have yet to be clarified. Defects in a two-dimensional linear pattern such as those formed by perpendicular lamellae or parallel cylinders typically take on the form of a dislocation defect where an additional plane is added to the structure, or a disclination defect that breaks the symmetry of the pattern. However, the interfacial affinities of the BCP and the substrate, and the use of DSA substrates that can guide the self-assembly behavior introduces additional constraints that can result in the formation of additional defects unique to BCP self-assembly.

For many years, Sibener and co-workers have studied the changes in BCP defect structure using atomic force microscopy (AFM).[1–8] Their earlier work generally utilized ex situ AFM with arrested annealing, repeated quenching, and imaging of the same area to observe the changes in defect configuration on a thin film.[6,7] While these studies were able to show how dislocation and disclination defects can change from one configuration to another, these studies were limited to parallel cylindrical structures on unpatterned substrates. While similar striped patterns can be obtained using both parallel cylinders and perpendicular lamellae, with fundamentally different morphologies, the mechanisms by which cylindrical and lamellar microdomains diffuse and change configurations is different. As cylinders are surrounded by a matrix domain, the microdomains are able to move about via both a climbing and a gliding mechanism. The climbing mechanism simply involves the parallel movement of the

microdomains. On the other hand, the gliding mechanism requires the perpendicular movement of the microdomains, relative to the interface. This necessitates the interdiffusion and penetration of one microdomain into another, thereby increasing the contact between the unlike domains and increasing the free energy barrier towards such movements. As the surrounding matrix is able to flow about the cylindrical minor domains, changes in the defect configuration can easily proceed via climbing mechanisms. However, lamellar morphologies are divided into alternating layers of each microdomain. Therefore, lamellar movements are restricted to the glide mechanism. As thin films of perpendicular lamellae hold greater potential as lithographic resists, further studies using perpendicular lamellar thin films are required. Therefore, in a more recent report, Sibener and co-workers studied the changes in a lamella-forming PS-*b*-PMMA thin film prepared on LiNe process DSA substrates.[8] In this report, they used in situ AFM to track the development and removal of a “stitch” morphological defect that was unique to LiNe flow chemoepitaxial DSA processes in real-time and real-space, thereby demonstrating the usefulness of in situ AFM as a tool for characterizing the defect behavior of a BCP thin film. By using in situ AFM to study the evolution of defects on lamella-forming BCP thin films, the fundamental mechanisms for the nucleation, growth, and annihilation of other defects could potentially be elucidated and clarified.

Furthermore, in addition to qualitative observations of the evolution of ordered structures on BCP thin films, the degree of ordering and extent of self-assembly can typically be quantified in terms of a number of different parameters. Typically the degree of ordering on a BCP thin film can be quantified in terms of the correlation length (ξ) of the grains, the defect density or the number of specific defects in a unit area, or an orientational order parameter (Ψ_2) that averages the local orientation angles of the microdomains across all pixels.[9] While the correlation length is useful for determining the average grain size, ξ goes to infinity for the well-aligned structures produced by DSA thin films. Therefore, numerous studies have chosen to simply count the number of defects that appear on the film surface and normalize the defect count against a unit area to yield the defect density in terms of the

number of defects per cm^2. Additionally, it was found that most defects found on DSA substrates are largely dislocation-type defects and thus, studies on defectivity have typically quantified the defect density specifically in terms of the dislocation defect density.[10,11] However, other types of defects such as disclinations are commonly observed in materials that exhibit a linear pattern and while earlier studies have shown how defects on BCP striped patterns can change from one configuration to another,[7] it remains unclear as to why dislocation defects are so commonplace in the DSA of BCPs Therefore, in this chapter (Schematic 4-1), the possible types of defects that can be found in the self-assembly of lamellae on SMART™ process DSA substrates are first identified and classified into specific categories, and the respective pathways towards defect annihilation are characterized in detail, using real-time and real-space tracking with in situ AFM under isothermal annealing conditions. Additionally, changes in the degree of ordering are quantified by an orientational order parameter that can explicitly determine the extent of self-assembly and alignment of the BCP microdomains without being restricted to specific defect types.



Schematic 4-1. Illustrative overview of the goals and content of Chapter 4.

4-2 Experimental Section

4-2-1 Instruments

A JPK Instruments NanoWizard ULTRA Speed A AFM (Bruker) equipped with a High Temperature Heating Stage (HTHS), a custom-made nitrogen (N_2) environment chamber, and Olympus microcantilever (OCML-AC55TS) with resonance frequencies of 1.6 – 1.9 MHz were used to record the atomic force microscopy (AFM) images in AC mode. The setpoint was pegged to 65 – 70% of the target amplitude, while the gain was set to 400 to minimize perturbations on the sample and no side effects were observed on the thin films upon in situ AFM imaging. Images 4 × 4 μm^2 in size with a resolution of 1024 × 1024 pixels were obtained at a line rate of 8 Hz, yielding one image every 128 s. To maintain an inert atmosphere, N_2 was flowed into the environment chamber at 0.5 ± 0.2 L min^{-1}. The AFM images were processed by subtracting the background using JPK Data Processing software. Fast-Fourier transformation (FFT) analyses of the phase images were conducted using ImageJ and Matlab.

4-2-2 Sample Preparation

As-cast thin films containing lamellae-forming PS-*b*-PMMA on pre-patterned substrates prepared using the SMART^{TM} process were received from Tokyo Electron Kyushu Limited, and prepared based on previously reported methods.[12–15] Briefly, a neutral layer is added onto a substrate. Using a photoresist, a linear pattern with a line-width of approximately 45 nm is developed at a 90 nm pitch. The photoresist is removed, and a weakly PS-preferential pinning material is spun onto the thin film. Upon coating and baking, excess PS-pinning material is removed, leaving behind a thin layer of PS-pinning guides in the interspaces between the patterned neutral layers. A 30 nm lamella-forming PS-*b*-PMMA was spin-coated on to yield thin films with a thickness of approximately 30 nm.

4-3 Results and Discussion

The in situ AFM experiment which documented the evolution of ordered structures in a wide range of temperatures in Chapter 3 revealed a number of temperature regimes with characteristic self-assembly behaviors. To further characterize the self-assembly behavior of

the microdomains at each of the characteristic temperature regimes, in situ AFM experiments whereby the temperature remained constant were conducted. To follow the evolution of the BCP structure and defectivity, a larger scan area is desirable.

When imaging a surface via AFM, there are often trade-offs between imaging size, speed, and resolution. For the incremental experiment in Chapter 3, a moderate imaging condition of 1 × 1 μm^2 at a resolution of 1024 × 1024 pixels and a line rate of 8 Hz was used, yielding on image every 64 s. However, as the imaging position can shift about due to thermal effects, a larger imaging area is required for detailed defectivity studies. Subsequently, to maintain the same quality of resolution, the number of pixels imaged must also be increased. Without changing the line rate, the rate at which horizontal stretches of pixels are imaged per second by the AFM, this simply increases the time required to obtain each image. However, at the same time, although the line rate can be increased to speed up imaging, the microcantilever oscillates at a relatively constant frequency. Therefore, the number of "taps" the microcantilever performs per second for imaging remains constant. By increasing the line rate, the number of times the microcantilever analyzes each pixel decreases, thereby reducing the overall quality of the image. Balancing the need for speed and large area imaging, while maintaining the quality of the images, in situ AFM imaging was conducted at an area of 4 × 4 μm^2 and a resolution of 1024 × 1024, using a line rate of 8 Hz, thereby allowing for one image to be obtained every 128 s, except where stated otherwise for the focused-area, super-high-speed experiment.

According to the incremental experiment in Chapter 3, the microdomains start to self-assemble into a random, fingerprint-like structure from approximately 110 to 160 °C. This stochastics-controlled structure exhibited a low degree of ordering, and when quantified as an orientational order parameter (Ψ_2), Ψ_2 was found to be less than 0.1 at 160 °C. However, above 170 °C, the microdomains were observed to swiftly align longitudinally onto the same direction as the chemical guides. Therefore, the first set of temperatures, 160 and 170 °C, was chosen to monitor the self-assembly behavior of the microdomains prior to and at the onset of long-range alignment. Additionally, as alignment was observed to proceed quickly at

higher temperatures, with Ψ_2 plateauing above 200 °C, isothermal in situ AFM experiments were also conducted at 190, 200, and 210 °C to study the defectivity and evolution of the BCP microdomains. Snapshots of the phase images obtained in the isothermal in situ AFM experiments can be found in Figures 4-1 to 4-5.

4-3-1 Notes on the Limitations of the AFM System

As a note for anyone wishing to perform similar in situ AFM experiments, appropriate hardware must first be chosen. In the Hayakawa group, the JPK Instruments NanoWizard ULTRA Speed A AFM is equipped with a Heating Cooling Module (HCM) and a High-Temperature Heating Stage (HTHS). The heating elements in both the HCM and HTHS are basically equivalent to hot-plates. Therefore, the maximum rate at which the temperature can be increased is approximately 60 °C per minute, and can slow down at higher temperatures. With a water-cooling system and nitrogen environment chamber built-in, the HCM is capable of relatively faster quenching from high temperatures, maintaining an inert atmosphere, and can even perform cryo-in situ AFM experiments at temperatures down to –30 °C. However, due to the additional equipment, the HCM is limited to a maximum temperature of 120 °C, too low for BCPs such as PS-*b*-PMMA. In contrast, the HTHS is simply a heating stage that is theoretically capable of reaching temperatures up to 300 °C (according to the manufacturer's specifications). However, in practice, the maximum temperature attainable is approximately 240 – 250 °C. Additionally, a nitrogen environment chamber is not pre-built into the HTHS. For the purpose of conducting in situ AFM experiments at temperatures around 200 °C, an inert atmosphere is desirable to prevent the oxidation and degradation of the BCPs. Therefore, an environmental chamber was custom-made with the Tokyo Institute of Technology Ookayama Design and Manufacturing Division (東京工業大学 技術部 大岡山設計工作部門). Additionally, without a cooling system, the HTHS is only able to cool samples through natural heat loss to the environment. Additionally, the JPK Instruments NanoWizard ULTRA Speed A AFM is equipped with three types of cantilever holders or glass blocks; a high-speed cantilever holder with an internal piezo, a

standard glass block with a screw system, and a standard glass block with a spring system. According to the manufacturers, the high-speed cantilever holder and the standard glass block with a screw system are not designed for experiments outside r.t. as both utilize a screw system to hold the microcantilevers in place. As thermal experiments can cause the expansion and contraction of the screw and screw hole, the threads and internal structure can get damaged over time. Additionally, the internal piezo and structure of the high-speed cantilever holder is extra-sensitive to high temperatures and thermal shock from large temperature fluctuations. Therefore, the standard glass block that keeps the microcantilever in place with a replaceable external spring system is recommended for in situ experiments at thermal extremes. However, without an internal piezo, the standard glass blocks are incapable of reaching frequencies larger than 400 kHz. With this limitation, high quality images cannot be obtained at high-speed. Therefore, although not ideal, to conduct high-speed in situ AFM and obtain high quality images, the high-speed cantilever holder must be used, and occasionally replaced if worn out and damaged. Additionally, the type of microcantilever used must be chosen. Ideally, to obtain high quality images with high speed imaging, microcantilevers with higher resonant frequencies are desirable. “Standard” microcantilevers with frequencies at approximately 300 kHz are incapable of high-quality and high-speed imaging. Nevertheless, higher quality cantilevers that are capable of high-quality and high-speed imaging are also commercially available, including the AC55 series by Olympus, and the Arrow and Ultra Short Cantilever (USC) series by NanoWorld. Although the USC cantilevers can provide the highest resonant frequencies, going up to 5 MHz, the tips of the USC microcantilevers are significantly smaller than the size of the laser beam emitted by the JPK Instruments NanoWizard ULTRA Speed A AFM, and therefore cannot be used. In turn, with resonant frequencies at approximately 1.6 – 2.4 MHz, both the Olympus AC55 series and NanoWorld Arrow series of microcantilevers likely offer similar performances. While our group has reported on the use of Olympus AC55 series microcantilevers for the in situ AFM imaging of BCP thin films,[16] others have reportedly used NanoWorld series microcantilevers for similar experiments.[8]

As is the case for most commercially available microcantilevers, the Olympus AC55 and NanoWorld Arrow series are available in multiple versions, one that is simply bare Si and one that has gold (Au) plating on the reverse side of the microcantilever. The Au plating is to increase the reflectivity of the microcantilever surface, allowing for more photons from the laser to get sent to the detector. Although the heating of an object with layers of different materials could cause possible warping, the effects of thermal fluctuation between the bare Si (AC55TN) and Au-coated (AC55TS) Olympus AC55 series microcantilevers appear similar. In contrast, the bare Si (AC55TN) microcantilevers are only capable of maintaining half the target amplitude of the Au-coated (AC55TS) microcantilevers, significantly reducing the sensitivity of the AC55TN microcantilevers. Therefore, Olympus AC55TS cantilevers were chosen for the in situ AFM experiments. However, it should also be noted that each individual AC55TS microcantilever can perform differently at higher temperatures. Such commercially available microcantilevers are typically designed and intended for use at r.t., rather than at elevated temperatures. Therefore, while the manufacturers guarantee that the microcantilevers are usable at r.t., the rate of failure for imaging at elevated temperatures is significantly higher. With the possibility of both manufacturing and end-user side issues such as defects in the Si during manufacturing, or dust building up on the microcantilever, the microcantilevers can fail at any temperature from 30 to 230 °C. This is because the microcantilevers require a certain drive amplitude, or driving power, to maintain a pre-determined target amplitude of oscillation at the resonant frequency of the microcantilevers. Upon thermal heating, the resonant frequency can shift up or down (but typically decreases), and the system is temporarily destabilized. Due to this destabilization, the drive amplitude required to maintain the same target amplitude of oscillation increases. If the system is capable of stabilizing at the elevated temperature, the required drive amplitude can eventually plateau or decrease back to its original levels, allowing for stable in situ AFM imaging. However, if the system is not able to stabilize at a certain temperature, the required drive amplitude can continue to rise. Once the required drive amplitude exceeds the limits of the AFM system, set to approximately 36 V by default, the AFM is no longer capable of

imaging with the microcantilever equipped. It is seemingly not possible to predict which microcantilevers are “ideal” and usable at elevated temperatures by simply testing the cantilever at room temperature. Furthermore, a microcantilever may be capable of imaging at 200 °C, fails at 210 °C as the drive amplitude requirements rise, but may also be capable of imaging at 220 °C as the system manages to stabilize at a different temperature. The fact that microcantilevers can fail to image at specific temperature windows, but remain capable of imaging at lower or higher temperatures suggests that the failure to image is not caused by thermal damage. Instead, there is likely a systematic mechanical reason that causes the failure at specific temperatures.

The destabilization and rise in drive amplitude requirement may also be relatively fast, exceeding the 36 V limit of the system within the first 5 min of reaching the temperature, or it may be relatively slow. If the drive amplitude requirement rises slowly over time, in situ AFM imaging becomes possible at first. However, as time passes at that temperature, the drive amplitude requirement can slowly creep up as the system does not stabilize and AFM imaging becomes impossible even though images could be obtained with little difficulty previously. Additionally, while the resonant frequency of the microcantilever can fluctuate with temperature, at certain temperatures, the resonant peak observed at r.t. can disappear completely, with another resonant peak appearing at a nearby frequency. Despite the appearance of a “new” resonant peak, imaging is not possible when the microcantilever is calibrated onto the new resonant peak. Therefore, each individual microcantilever must be tested at 10 °C increments in the entire range of temperatures to be used for the in situ experiment and the stability of the microcantilevers over time must be observed prior to conducting the actual situ AFM experiment. Generally, the microcantilevers are considered to have failed or inappropriate for high temperature in situ imaging if the resonant peak disappears, or if the drive amplitude required for imaging exceeds 30 V. Of 47 AC55TS microcantilevers tested from the set of Olympus AC55TS microcantilevers produced with the batch number 8C3313, seven were incapable of imaging at r.t., 13 exhibited significantly high drive amplitudes at r.t. and thus are unsuitable for elevated temperature imaging, four

failed between 50 – 80 °C, 14 failed between 130 – 200 °C, and one failed at 210 – 230 °C. In contrast, four cantilevers were observed to be stable at isotherms, while three were likely stable enough for imaging in the temperature range from 30 to 230 °C. Again, considering a large plurality of microcantilevers failed between 150 – 180 °C, there is likely a repeated, systematic, mechanical cause for the failure of the microcantilevers. Additionally, while only ~15% of the cantilevers are appropriate for use at elevated temperatures, the remaining cantilevers are nevertheless mostly usable at r.t..

Table 5-1. Number of microcantilevers that failed or are stable at various temperatures.

Fail at r.t.	Unsuitable for high temp.	Fail at 50 – 80 °C	Fail at 90 – 120 °C	Fail at 130 – 160 °C
7	13	2	2	7
Fail at 170 – 200 °C	Fail at 210 – 230 °C	Good at isotherms	Good at 30 – 230 °C	Total Number of Cantilevers
7	1	4	3	47

4-3-2 Snapshots of Isothermal Experiments

After recording AFM images at room temperature (r.t.), the annealing temperature was immediately raised to 160 (Fig. 4-1), 170 (Fig. 4-2), 190 (Fig. 4-3), 200 (Fig. 4-4), or 210 °C (Fig. 4-5) and in situ AFM images were recorded to track the evolution of the BCP structure in real-time and real-space. As seen in earlier experiments, the AFM images taken at room temperature revealed stripes at 90 nm intervals which can be attributed to the underlying chemical guides. After imaging at r.t. for 10 min, the temperatures were raised, and the system was allowed to stabilize for 5 – 10 min prior to imaging. Additionally, the annealing end times are moderately arbitrary. For example, while the in situ experiment was ended after 3 h at 210 °C as defects could no longer be observed in the 4×4 μm^2 area, the in situ experiment at 200 °C was prematurely ended after 1.5 h as the drive amplitude for imaging exceeded the limits of the AFM system. Additionally, the isothermal in situ experiments at 160 and 190 °C were arbitrarily stopped after 6 h, whereas the experiment at

170 °C was stopped after 12 h. From these experiments, patterns and self-assembly behaviors characteristic to each annealing temperature could be observed.

In this study of BCP defectivity under isothermal annealing conditions, the real-time and real-space growth of patterns are first described for each annealing temperature. Subsequently, the types of defects observed in the DSA of PS-*b*-PMMA on chemically pre-patterned substrates prepared via the SMART^{TM} process are identified and the mechanisms and pathways to annihilation are detailed.

In the first image obtained at 160 °C (Fig. 4-1) and at time, t = 00:19:15, a fingerprint-like structure with grains of randomly-oriented stripes sliced up by linear aggregations of the dark PS domain along the longitudinal direction could be observed. This is in good agreement with the AFM images obtained at 160 °C in the in situ AFM experiment with incrementally increasing annealing temperature. At the earliest stages of self-assembly between 130 and 150 °C in the incremental experiment, the BCP microdomains were observed stochastically interact and combine with the nearest neighbors, resulting in a random fingerprint-like pattern, similar to those seen on thin films prepared on unpatterned substrates. As the temperature was raised to 160 °C, the PS first domains begin to align onto the chemical guides, breaking up the grains of randomly-oriented stripes. As the structures formed by the BCPs is heavily influenced by the temperature, it is not surprising that similar “broken lamellar” structures are found when the annealing temperature was raised to 160 °C immediately. However, in contrast to the incremental experiment where the temperature was raised above 160 °C and well-aligned, defect-free lamellae could be obtained, continually annealing the PS-*b*-PMMA thin film at 160 °C resulted in the growth of dark, flat areas over time. In the final image obtained after 6 h of annealing, while well-aligned lamellae and other dislocation and disclination defects could be observed, a large proportion of the surface is also covered with the dark, flat areas. Additionally, as in the earlier incremental in situ AFM experiment, the degree of alignment can be quantified using an orientational order parameter (Ψ_2) (Fig. 4-6). The near-zero value of Ψ_2 = –0.05 obtained from the first image obtained at t = 00:19:15 is in good agreement with the apparent

randomness of the structure. As annealing continued, Ψ_2 was observed to grow roughly linearly at a rate of 0.0012 per min, reaching a value of 0.46 after 6 h of annealing. Previous studies have shown that the coarsening of BCP domains follows a power-law, scaling with t^a.[17] In the case of BCP thin films, *a* is typically found to be ~0.25,[18] whereas *a* can exceed upwards of 0.5 in the bulk.[9,19] This means that domain coarsening is typically relatively slow on thin films, attributed to the confinement of the BCP. However, in the case of SMART™ DSA thin films annealed at 160 °C, if the plot of Ψ_2 against time was formulated in terms of a power-law, Ψ_2 is found to scale at $t^{0.64}$. While the absolute values of the growth exponents should not be compared directly as earlier studies utilized parallel cylinder-forming BCPs on unpatterned substrates and quantified the changes in the degree of ordering in terms of a correlation length,[18] the self-assembly behavior of a BCP generally follows a power-law regardless of the metric used,[9,17] and general trends can be inferred. Therefore, although the relatively large value of *a* found when the thin film was annealed at 160 °C suggests that domain coarsening is significantly faster compared to typical BCP thin films on unpatterned substrates, changes in *a* at other temperatures must also be studied for comparisons within this study. However, even after 6 h of annealing at 160 °C, a large portion of the surface was covered by flat areas of parallel orientation defects that continue to grow in size. This resulted in near-zero orientation angles at the corresponding defect areas and limits the maximum Ψ_2 obtained after extended periods of annealing.

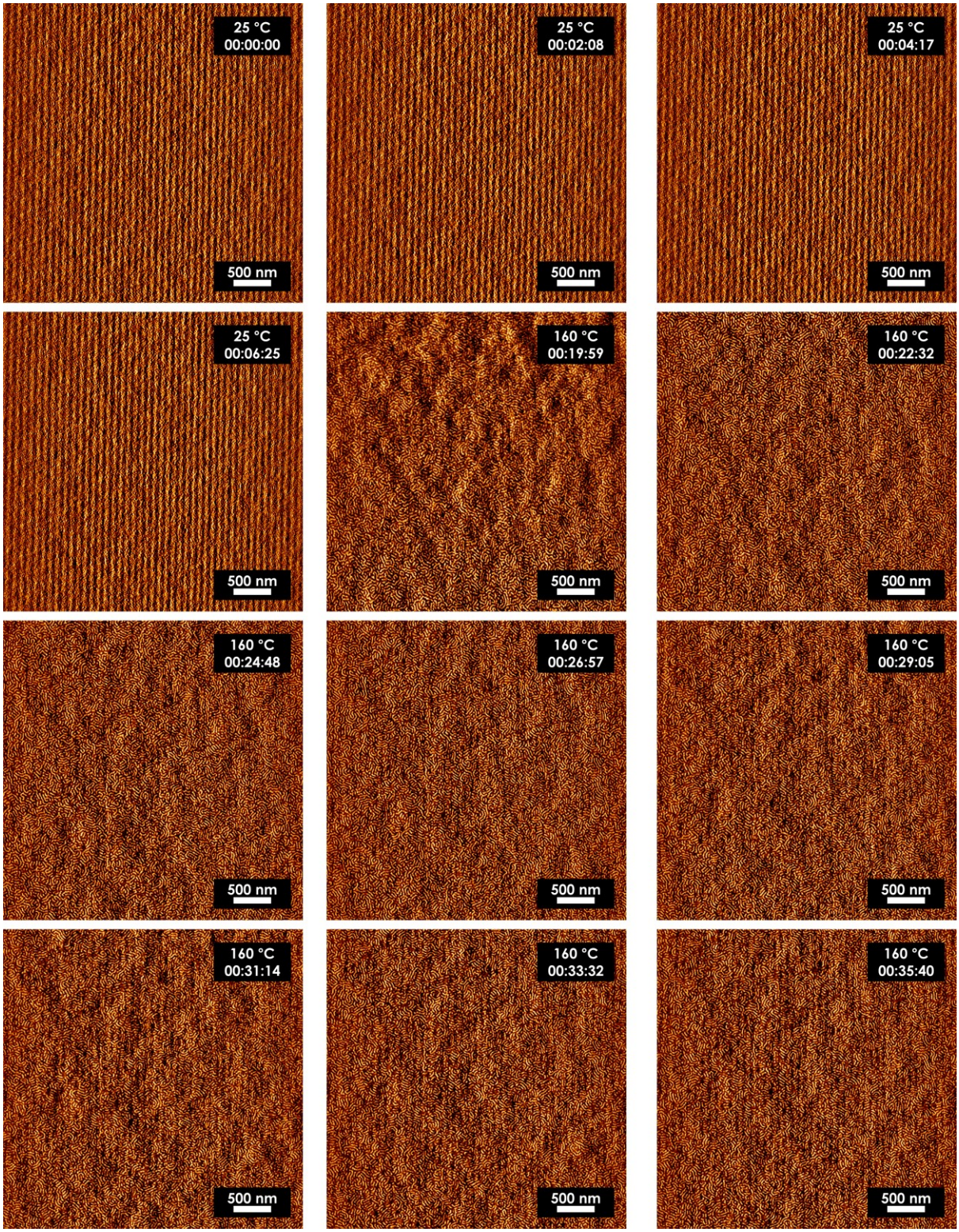


Figure 4-1. Snapshots of the phase images obtained from the isothermal in situ AFM experiment at 160 °C, Part 1.

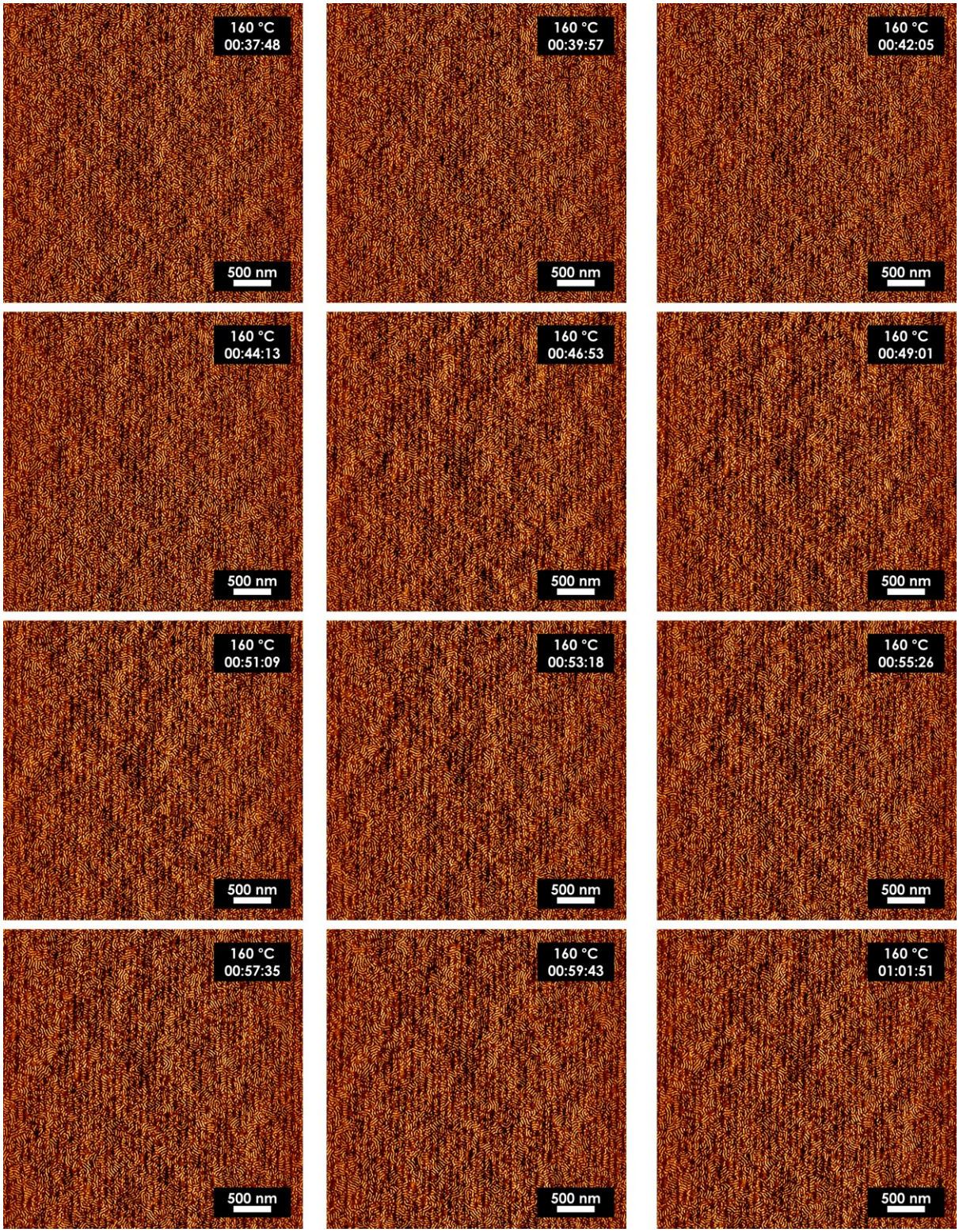


Figure 4-1. Snapshots of the phase images obtained from the isothermal in situ AFM experiment at 160 °C, Part 2.

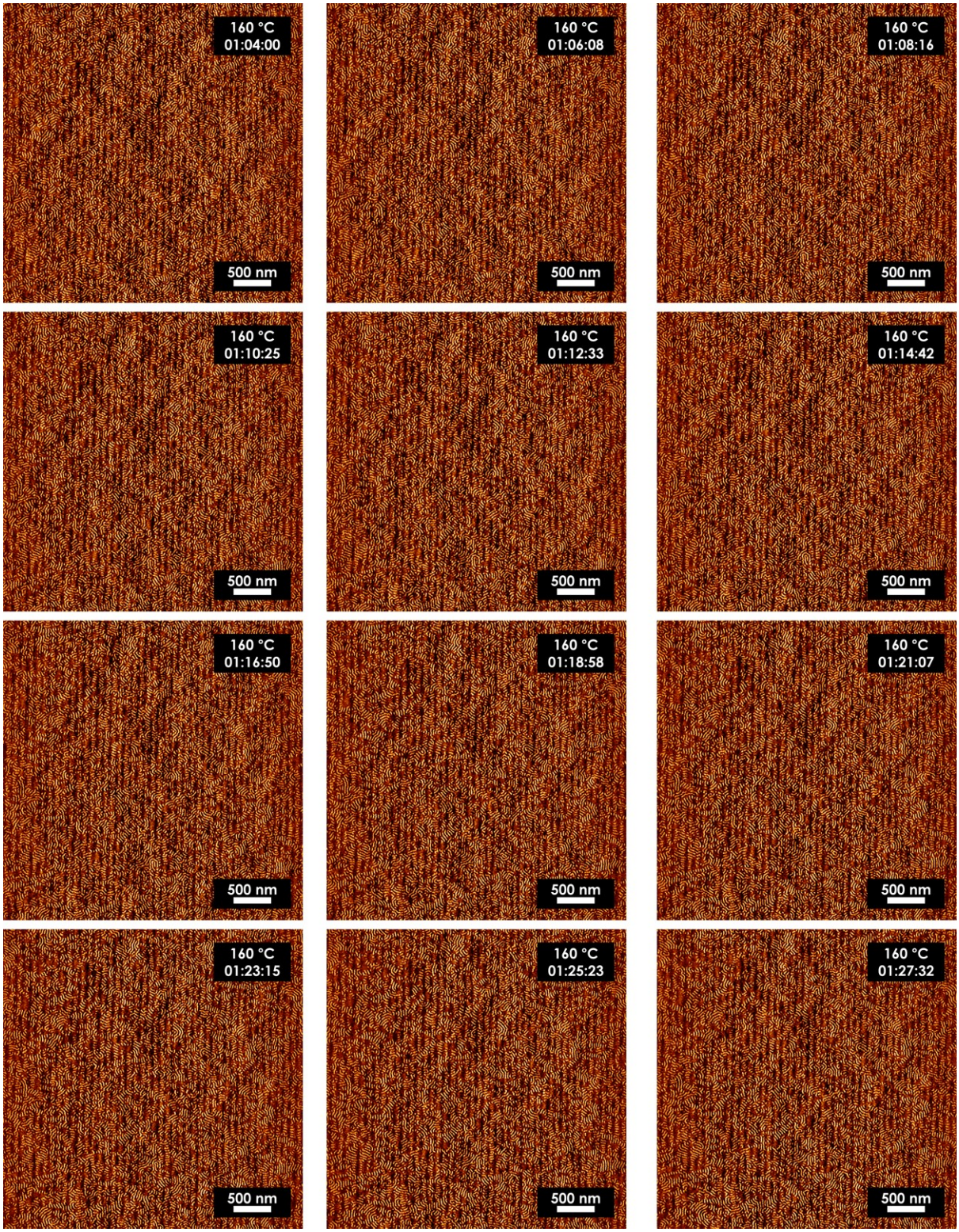


Figure 4-1. Snapshots of the phase images obtained from the isothermal in situ AFM experiment at 160 °C, Part 3.

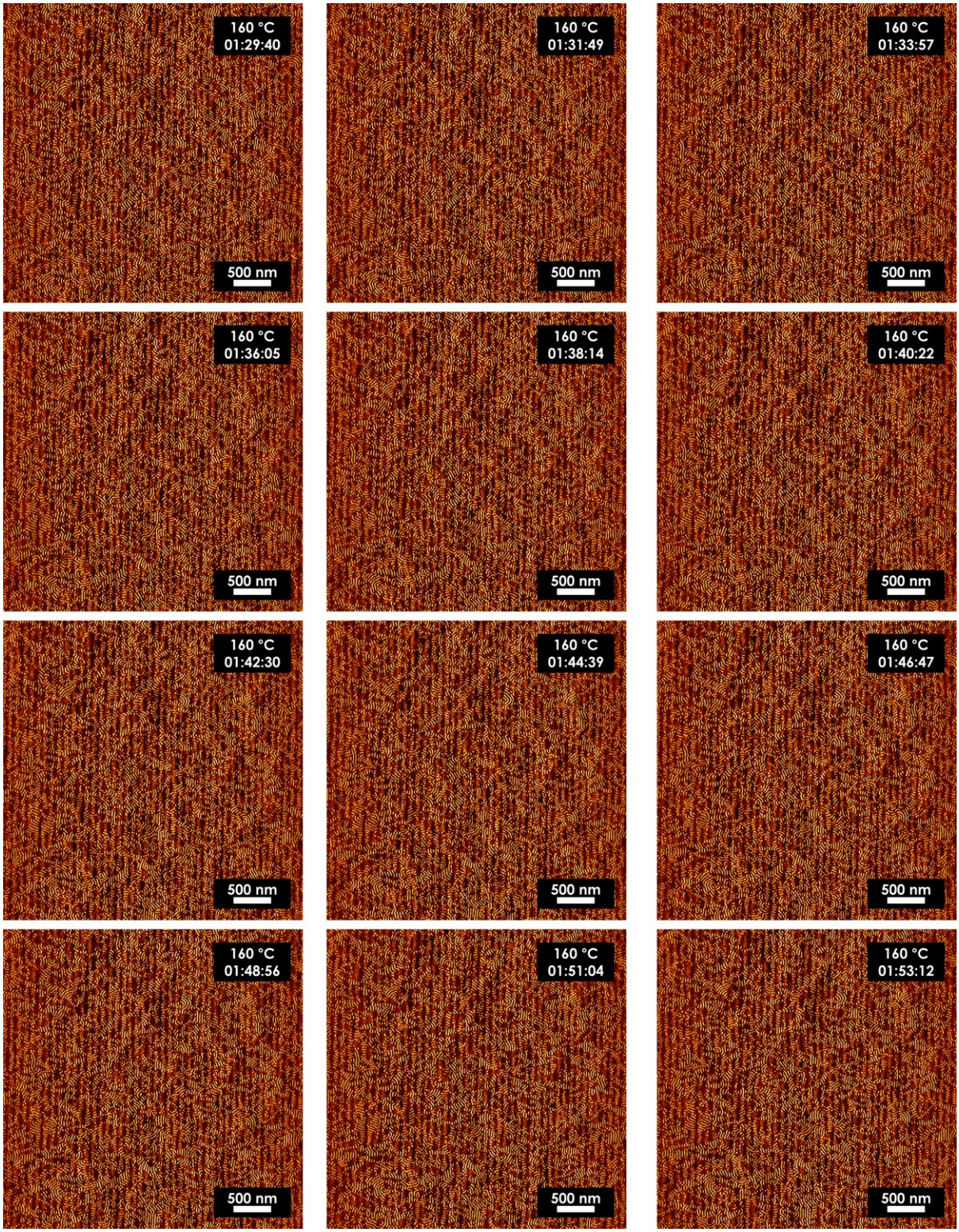


Figure 4-1. Snapshots of the phase images obtained from the isothermal in situ AFM experiment at 160 °C, Part 4.

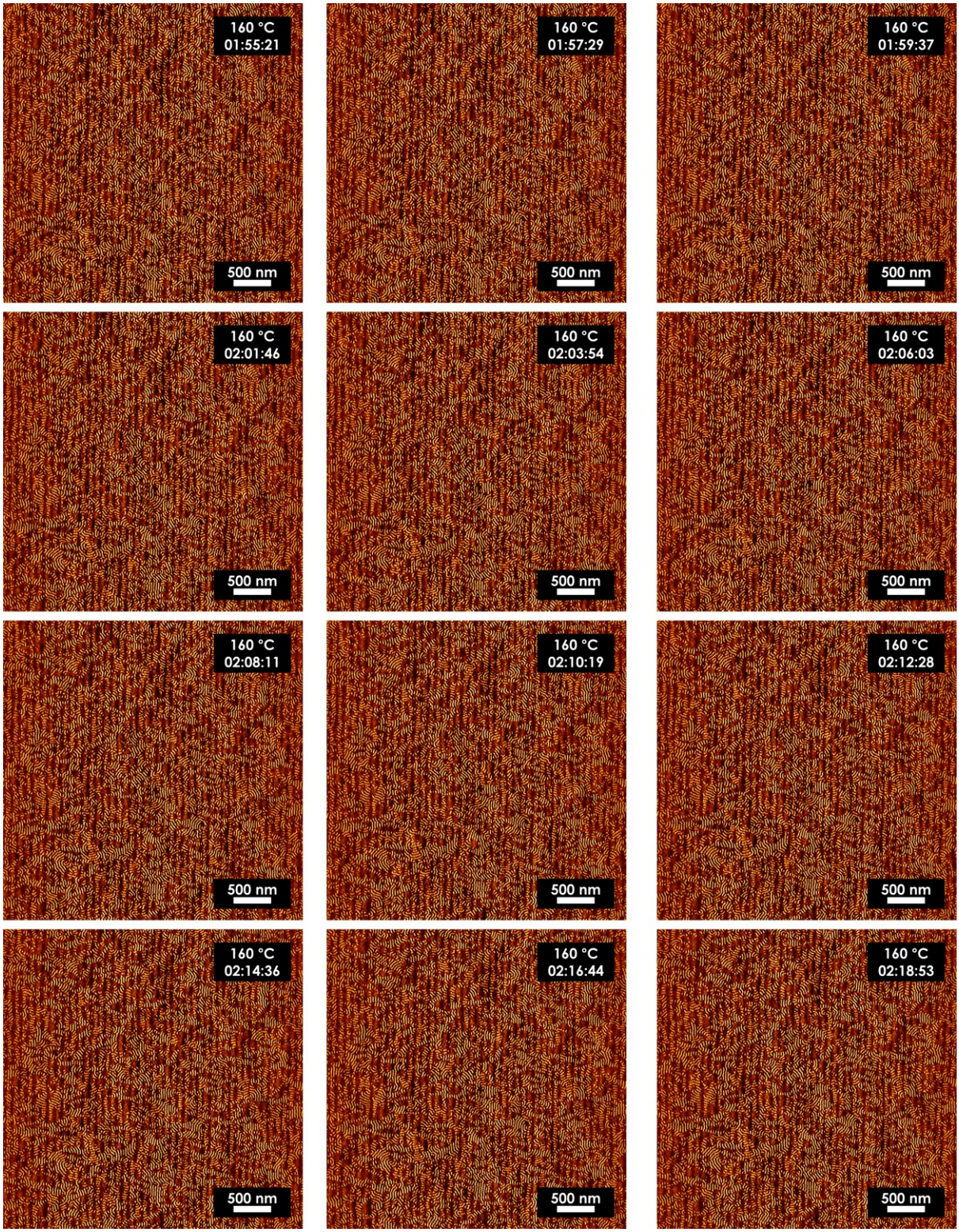


Figure 4-1. Snapshots of the phase images obtained from the isothermal in situ AFM experiment at 160 °C, Part 5.



Figure 4-1. Snapshots of the phase images obtained from the isothermal in situ AFM experiment at 160 °C, Part 6.

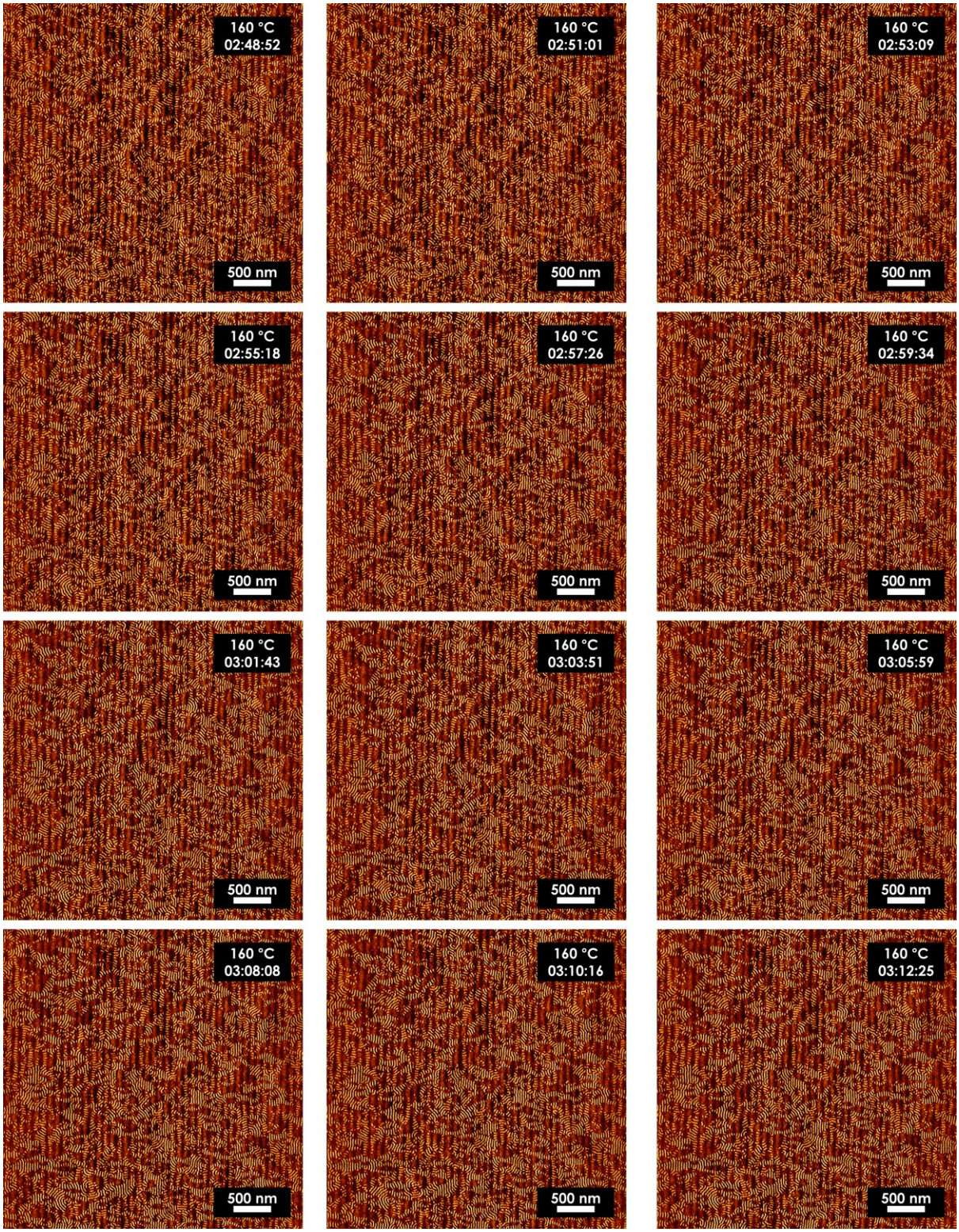


Figure 4-1. Snapshots of the phase images obtained from the isothermal in situ AFM experiment at 160 °C, Part 7.

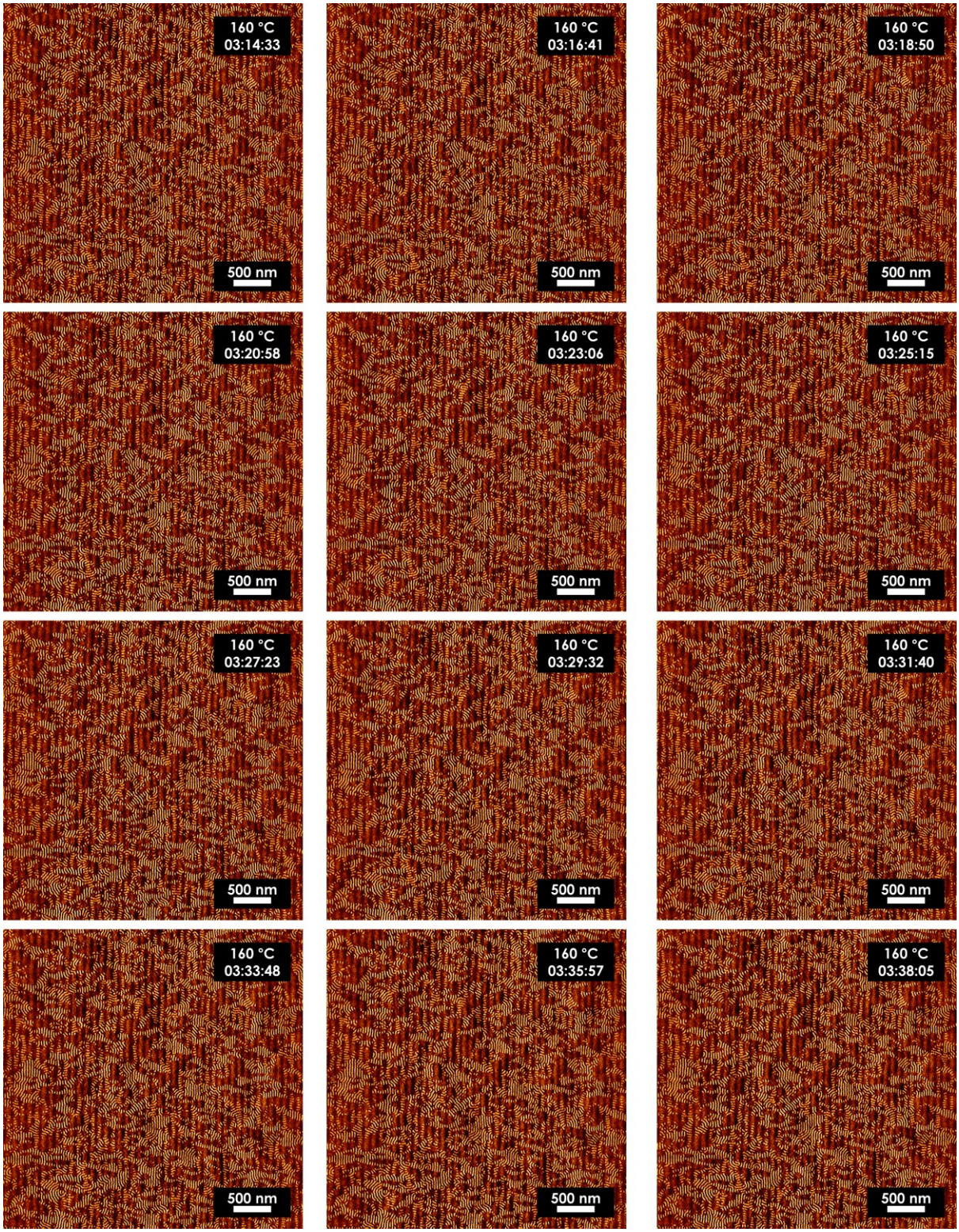


Figure 4-1. Snapshots of the phase images obtained from the isothermal in situ AFM experiment at 160 °C, Part 8.

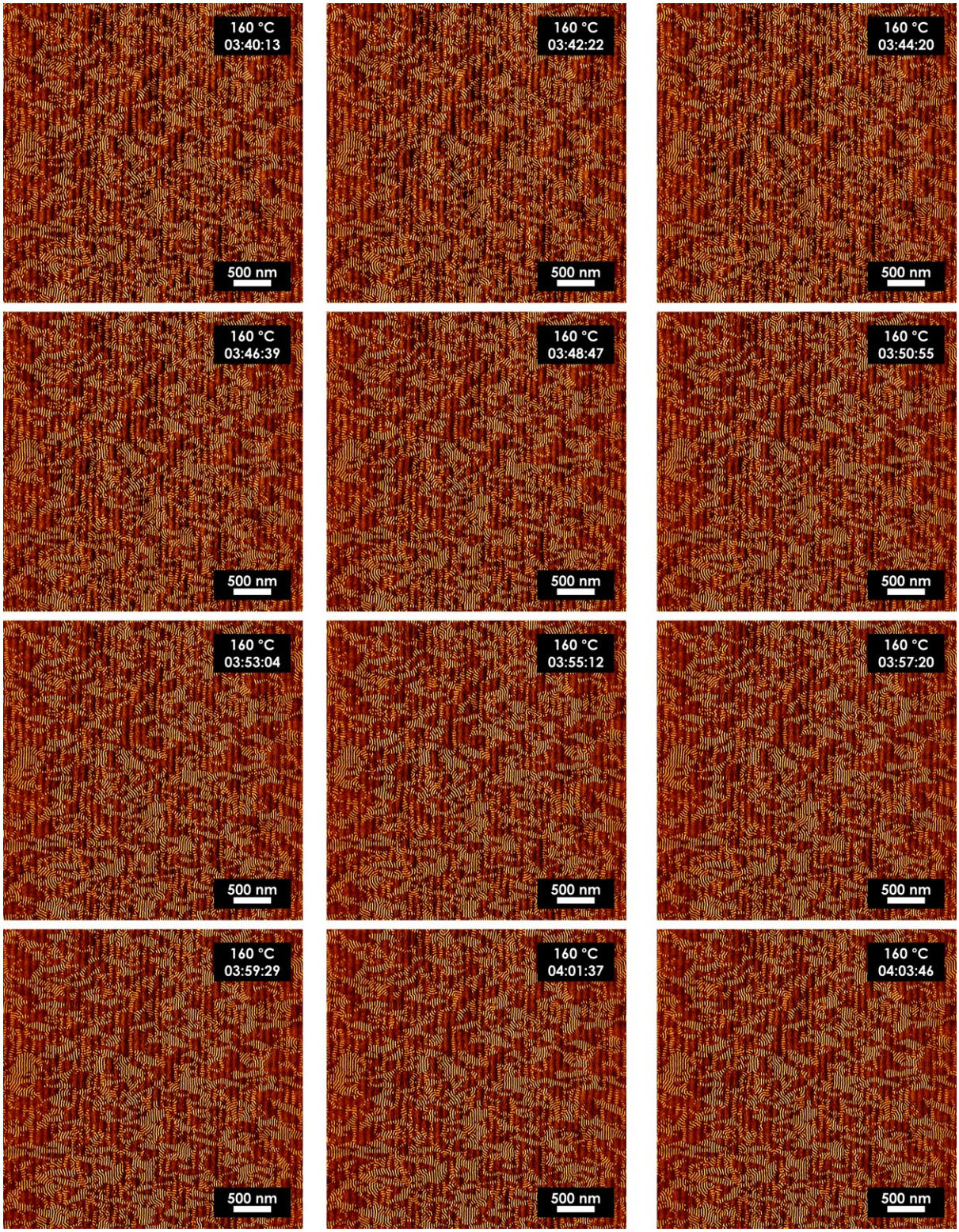


Figure 4-1. Snapshots of the phase images obtained from the isothermal in situ AFM experiment at 160 °C, Part 9.

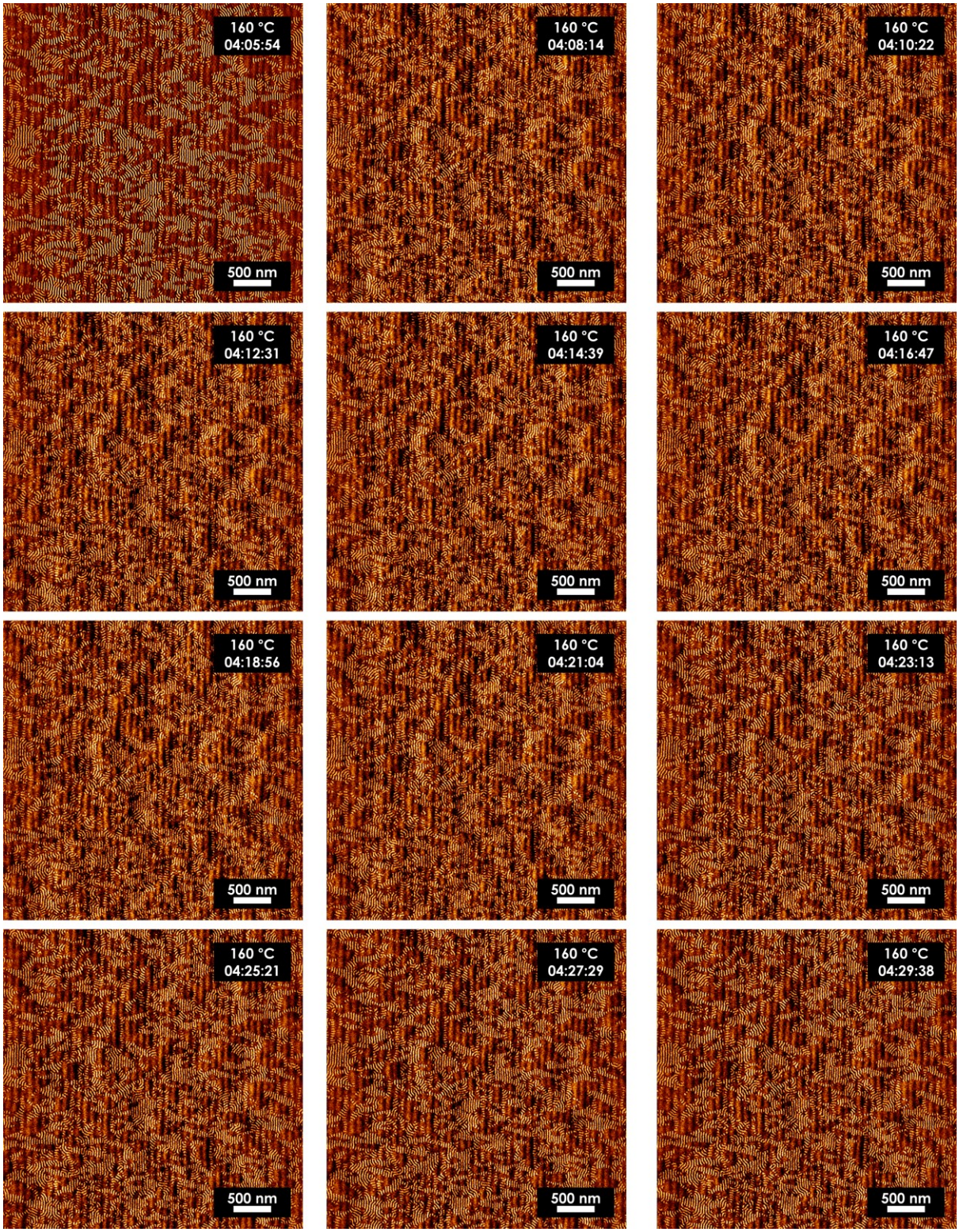


Figure 4-1. Snapshots of the phase images obtained from the isothermal in situ AFM experiment at 160 °C, Part 10.

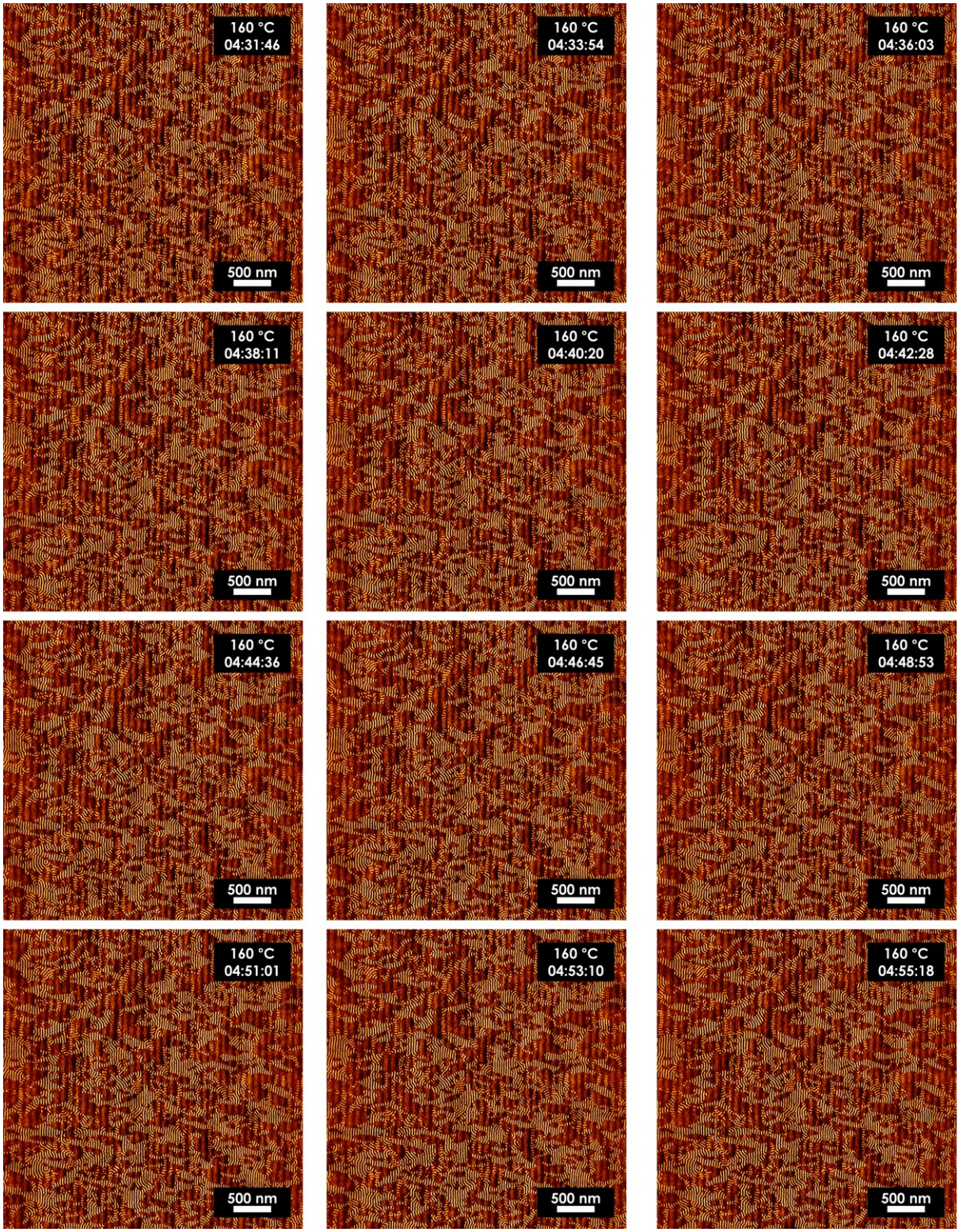


Figure 4-1. Snapshots of the phase images obtained from the isothermal in situ AFM experiment at 160 °C, Part 11.

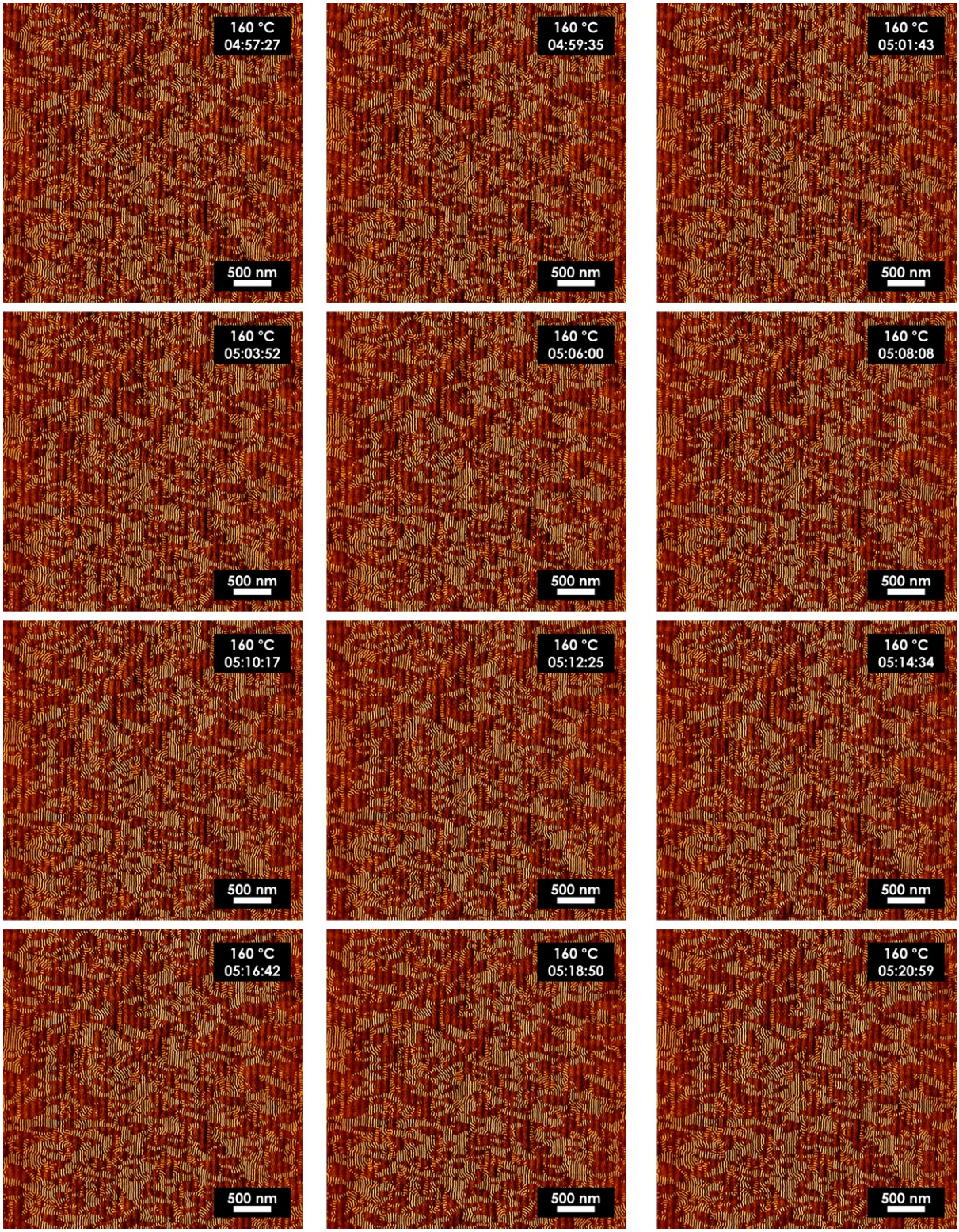


Figure 4-1. Snapshots of the phase images obtained from the isothermal in situ AFM experiment at 160 °C, Part 12.

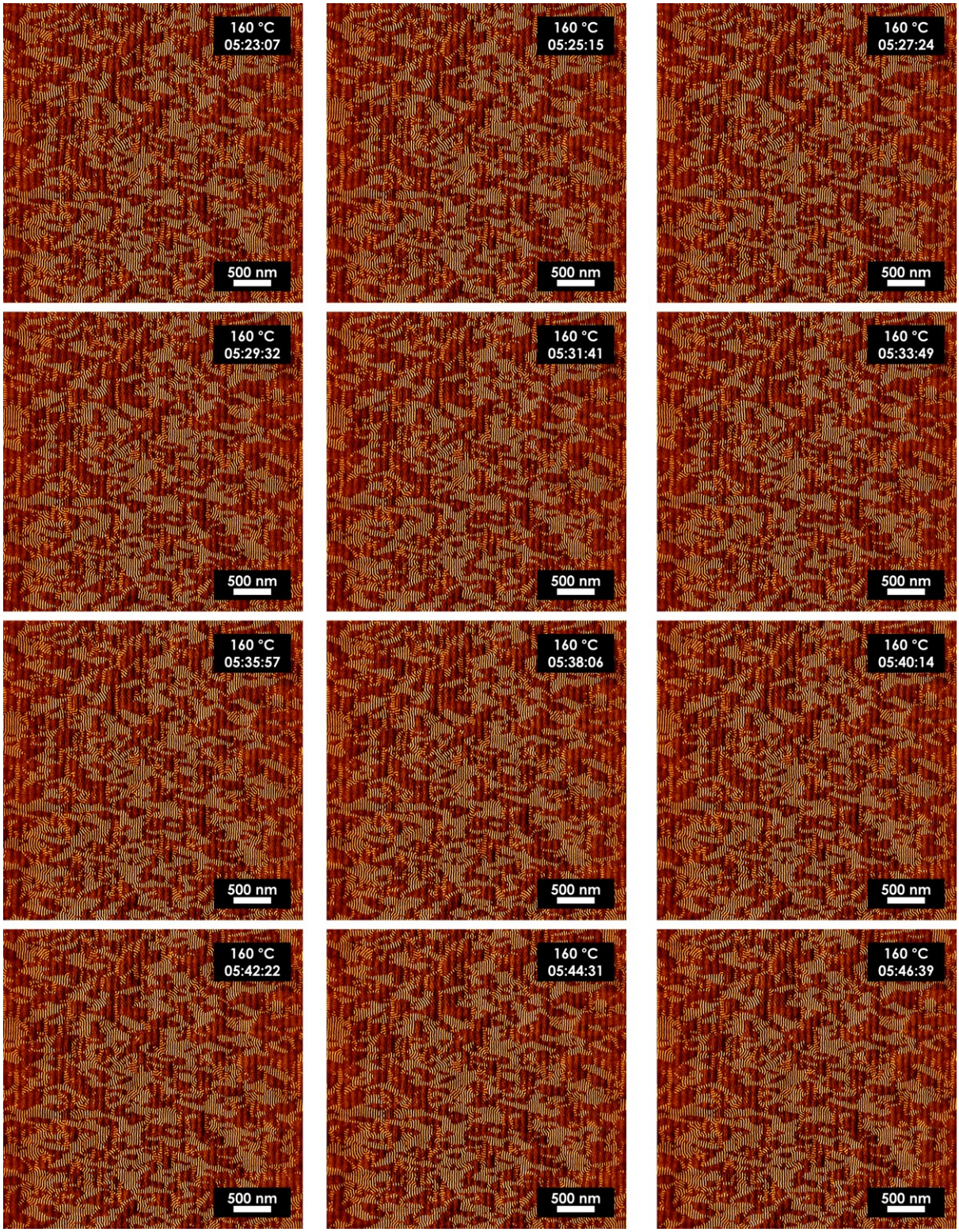


Figure 4-1. Snapshots of the phase images obtained from the isothermal in situ AFM experiment at 160 °C, Part 13.

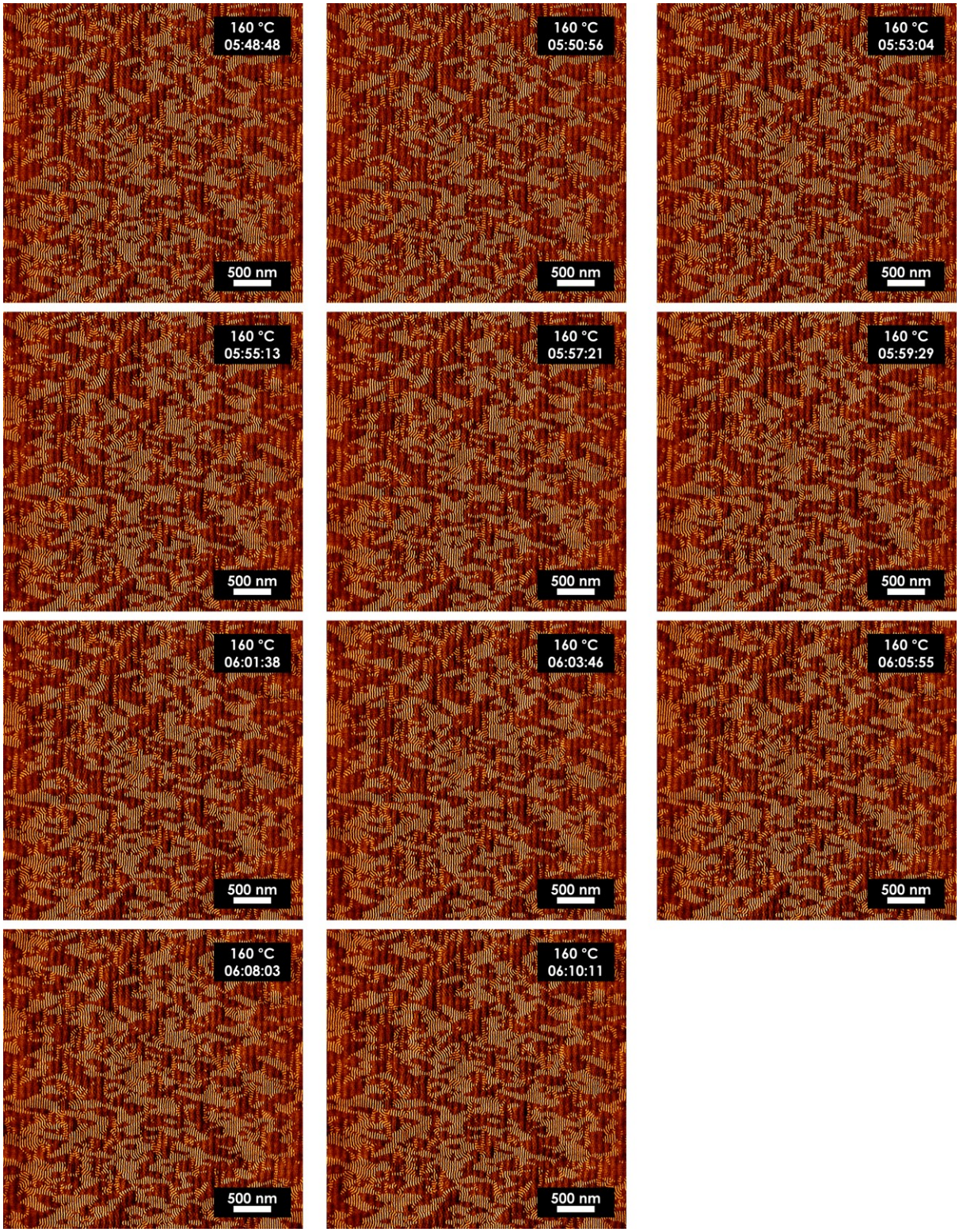


Figure 4-1. Snapshots of the phase images obtained from the isothermal in situ AFM experiment at 160 °C, Part 14.

According to the incremental in situ AFM experiment, the long-range alignment of the BCP microdomains began precipitously around 170 °C. Previously, as the PS domains start to align along the same direction as the chemical guides around 160 °C, the remaining PS-*b*-PMMA microdomains were also observed to begin rapid alignment in the interspatial regions between the guides near 170 °C. From a minimum of $\Psi_2 = 0.004$ at 164 °C, Ψ_2 was observed to grow rapidly at a rate of 0.07 per 2 °C increment as the temperature was raised to 170 °C and above. In this isothermal study, the initial image at t = 00:18:15 showed linear structures with partially random orientations. As in the incremental experiment, significant alignment of the PS domain into thick linear structures in the longitudinal direction at 90 nm spacings could be observed. This is reflected in the Fast-Fourier transform (FFT) of the image where a peak that corresponds to ~90 nm periodicities could be detected. Additionally, the longitudinal alignment of anisotropic, wide lamellar grains with relatively short correlation lengths in the interspatial region between the pre-aligned PS microdomains was detected. A quantitative analysis of the image also revealed that Ψ_2 can be estimated to be approximately 0.030. This near-zero value of Ψ_2 is in line with the fact that the initial pattern formed at the onset of self-assembly is highly random as interactions are limited to the closest neighboring microdomains. As annealing at 170 °C continued, it was revealed that two competing structures had begun to grow. While the longitudinal alignment of lamellar grains could be observed, flat, dark areas attributed to parallel lamellae with symmetric PS-wetting on the substrate and free surface grew simultaneously as the striped patterns. With extended annealing however, defects between the longitudinally-aligned lamellar grains could be observed to disappear. This is reflected in the growth of Ψ_2 over time. Starting at 0.030 in the initial image at t = 00:18:15, Ψ_2 grew at a rate of approximately 0.008 per minute in the first hour of annealing, before gradually slowing down by increasing at a rate of approximately 0.002 per minute between 1 and 4 h, and finally approaches a limit by increasing slowly at a rate of 0.0002 per minute after 4 h. If formulated to a power law however, it appears that there are also multiple stages in the coarsening and alignment of the microdomains. At $t < 1$ h, alignment scales with $t^{2.0}$, while at $1 < t < 4$ h, Ψ_2 scales with

$t^{0.42}$ and at t > 4 h, Ψ_2 scales with $t^{0.12}$. The initially large value of a = 2.0 suggests that the alignment of the microdomains proceeds extremely swiftly during the early stages of self-assembly. However, a is observed to first reduce to 0.42 between 1 < t < 4 h, this value is closer to the ~0.25 value expected for domain coarsening in BCP thin films, whereas, the value of a = 0.12 at annealing times longer than 4 h is much lower than the expected 0.25 value. While one may expect to observe a single growth exponent (a) during the coarsening of BCP microdomains, the presence of multiple growth stages with different growth exponents have been reported previously. Using rapid thermal processing (RTP) and the arrested annealing and quenching of lamella-forming PS-*b*-PMMA thin films, Perego and co-workers reported a multiple-stage growth,[20] with a fast ordering regime and a growth exponent of approximately 0.3 at earlier annealing times, and a slow ordering regime with a growth exponent around 0.1 or less at later annealing times. They attributed this multiple-stage growth to the presence of residual toluene solvent that preferentially expanded the PS domain, resulting in the formation of cylindrical-like structures within the thin film. As defects in cylindrical morphologies are able to annihilate via the less energetically expensive climbing motion due to the presence of a matrix that allows for defects to move about parallel to the BCP interface, rather than being restricted to gliding motions which require the perpendicular interpenetration of the microdomains against the BCP interface, cylindrical morphologies are able to coarsen relatively quickly on thin films, with Harrison and co-workers first reporting a coarsening growth exponent of 0.25 in parallel cylindrical striped patterns.[18] Additionally, Nakatani and co-workers found a two-stage growth in the degree of ordering in both the surface and also the cross-section of a lamellar thin film.[21] They found that during the early-stages of self-assembly, the microdomains at the surface and inner depths are initially disconnected and self-assemble independently of each other, with bicontinuous disorder-like structures initially found in the depths of the thin film and lamellar stripes on the film surface. The random structure in the depths of the thin film initially accelerated the growth of the correlation length and the cross-sectional orientational order parameter which quantified the degree of perpendicular alignment, exhibiting growth

exponents of 0.30 and 0.70 at 110 °C, respectively. However, as the random structure disappeared from the inner depths of the thin film as the lamellar structures proceeded to align perpendicularly and separate into lamellar layers, the growth exponents of the correlation length and orientational order parameter dropped to 0.05 and 0.16, respectively. This decrease in the growth exponent was attributed to the disappearance of the random disorder-like structure from the inner depths of the thin film. When the bicontinuous disorder-like random structure remained, defect annihilation could proceed via both climb and glide mechanisms. However, as the lamellae separated into distinct lamellar layers in the vertical direction, defects could only annihilate via glide mechanisms which pose large enthalpic penalties due to the required interpenetration of the microdomains.

In this study however, three stages were observed in the growth and long-range alignment of the BCP microdomains at 170 °C. While Perego and co-workers reportedly observed only two stages in the growth of the BCP microdomains, they used significantly higher temperatures of 250, 270 and 290 °C.[20] Therefore, the earliest stage of ordering may have been missed out. Additionally, Nakatani and co-workers utilized a BCP different from PS-*b*-PMMA, rendering direct comparisons of annealing temperatures impossible.[21] Nevertheless, the growth exponent of ~2.0, found in the first stage of annealing in this study, matches the growth exponent in bulk systems during the initial nucleation process, previously observed to go up to ~3.5.[19] While the microphase separation of the lamellar microdomains is expected to proceed via a spinodal decomposition process, the higher-ordered surface structures and defects formed by the microphase-separated BCP domains can proceed via another independent nucleation and growth, spinodal decomposition, or both simultaneously competing processes.[22] In the first hour of annealing, where a = 2.0, a mixture of perpendicular lamellar striped patterns and parallel defects can be observed. From the first highly random structure, both grains of lamellae and parallel defects appear to nucleate at numerous sites scattered about the thin film and gradually grow in size. This initial nucleation and growth of higher-ordered grains of lamellae could contribute to the relatively large growth exponent observed in the first hour of annealing. However, the latter

two stages of self-assembly, with growth exponents of 0.4 and 0.1, appear to match closely with the growth exponents observed by Perego and co-workers at ~0.3 and ~0.1 for ξ,[20] and also Nakatani and co-workers at 0.4 and 0.1 for ξ, and 0.7 and 0.2 for the cross-sectional Ψ.[21] While the first stage of self-assembly can proceed much faster as the lamellar grains can grow via nucleation from a randomly-oriented structure, later stage growth is limited to defect annihilation between the grains. As the surface structures separate into relatively large grains after 1 h of annealing, structural growth and alignment slows down. The further growth and alignment of the microdomains requires the relatively slower annihilation of defects between the grains and reorientation of the parallel structures. This results in a second stage of moderate growth, with a growth exponent of 0.4. Additionally, at this mid-stage, it is likely that the inner depths of the thin film have yet to fully develop into distinct lamellar layers, thereby still allowing slightly accelerated defect annihilation through both climb and glide motions. However, as the lamellar microdomains become separated into distinct lamellar layers, defect annihilation becomes restricted to glide motions, thereby slowing down the rate of growth and alignment to a growth exponent of ~0.1 in the late stage of self-assembly observed at 170 °C. Over long annealing times, the flat, dark areas of parallel lamellae could be observed to disappear and reorient into longitudinally-aligned perpendicular lamellae, starting with the parallel defect areas with smaller areas. After 12 h of annealing, a mostly longitudinally-aligned lamellar striped pattern with $\Psi_2 = 0.77$ could be observed. However, it is also apparent that small areas of flat, parallel lamellae remain scattered throughout the thin film. Therefore, Ψ_2 also remains limited to less than 0.8 when the thin film was annealed at 170 °C. To further increase Ψ_2, increased annealing temperatures would be required.

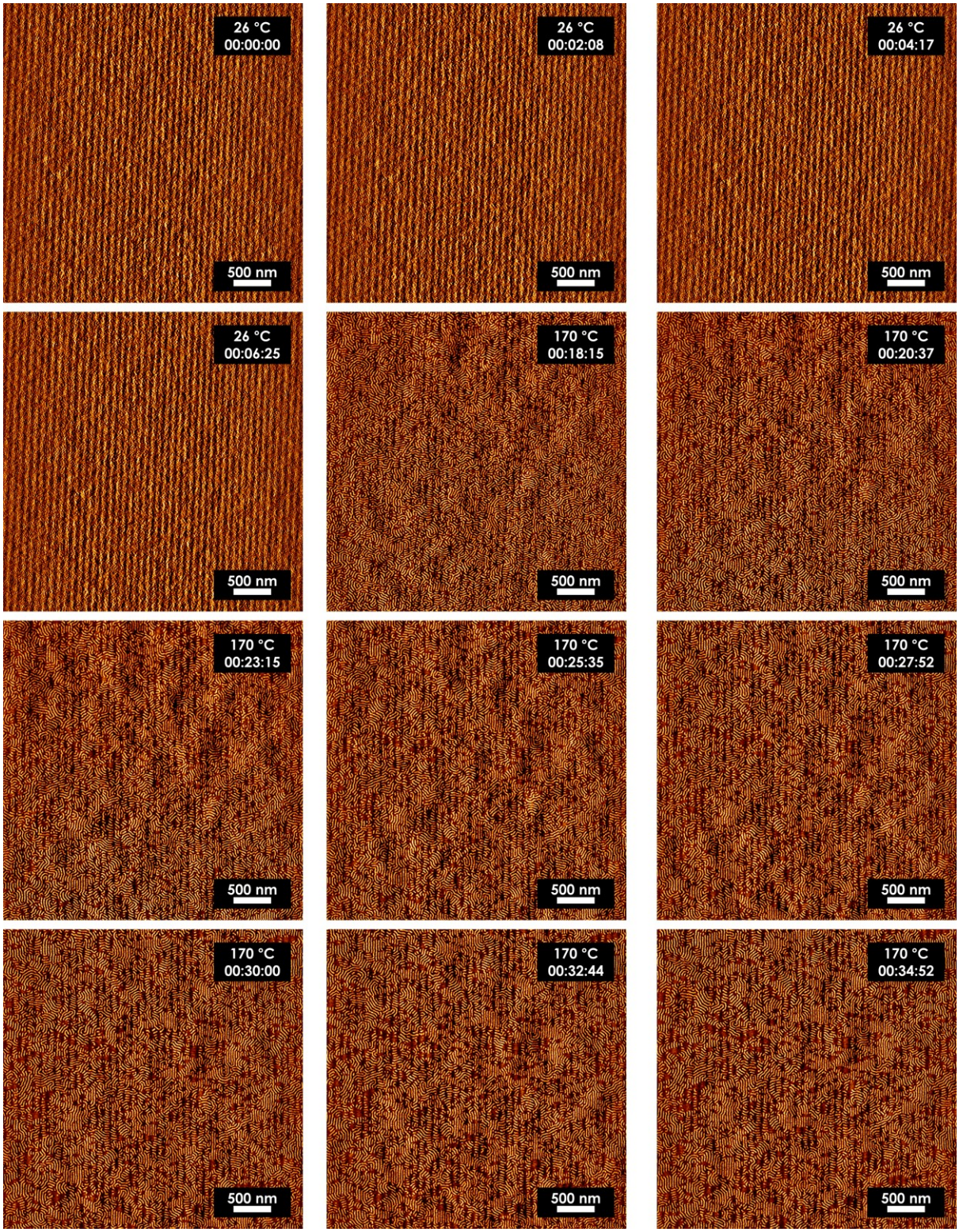


Figure 4-2. Snapshots of the phase images obtained from the isothermal in situ AFM experiment at 170 °C, Part 1.

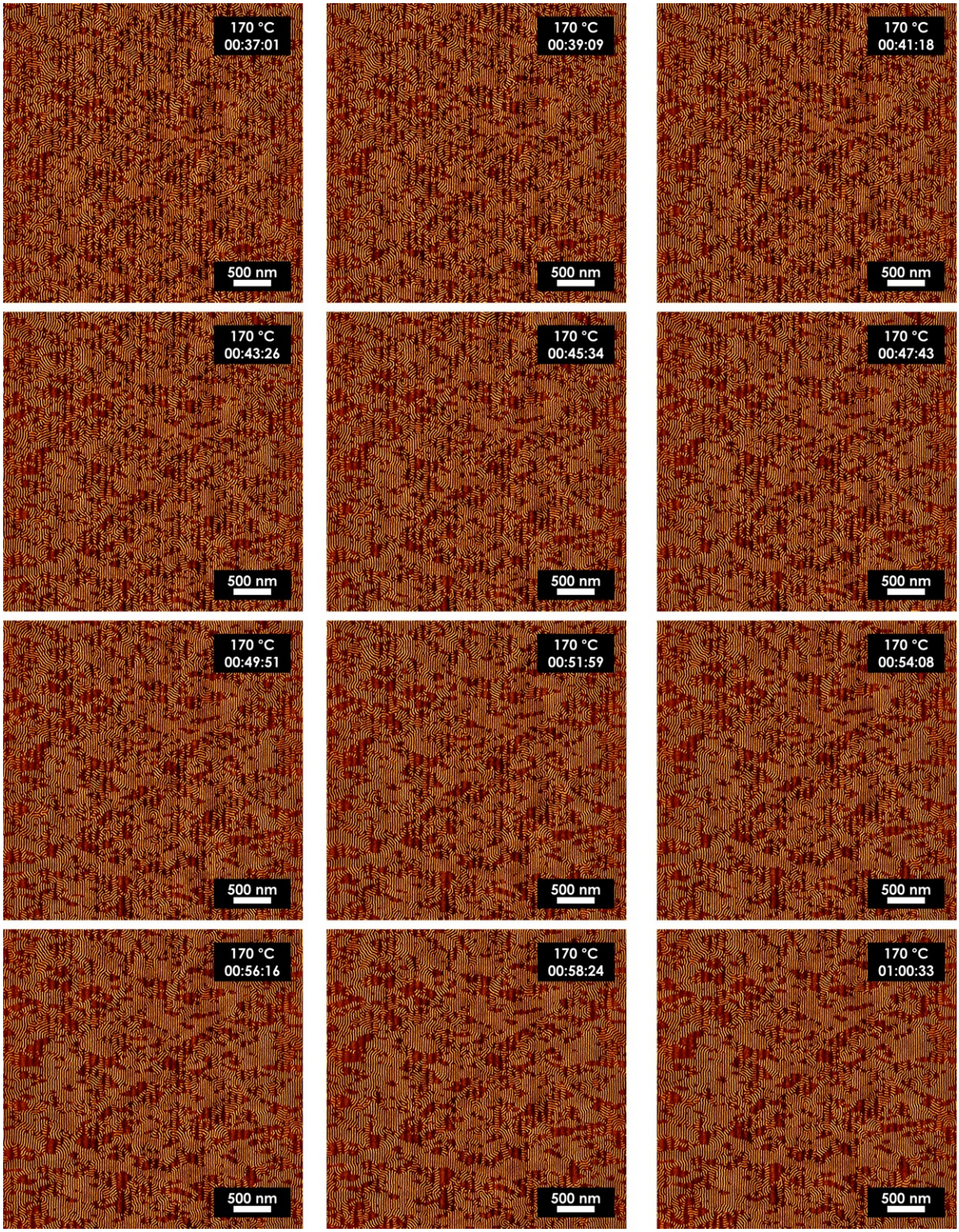


Figure 4-2. Snapshots of the phase images obtained from the isothermal in situ AFM experiment at 170 °C, Part 2.

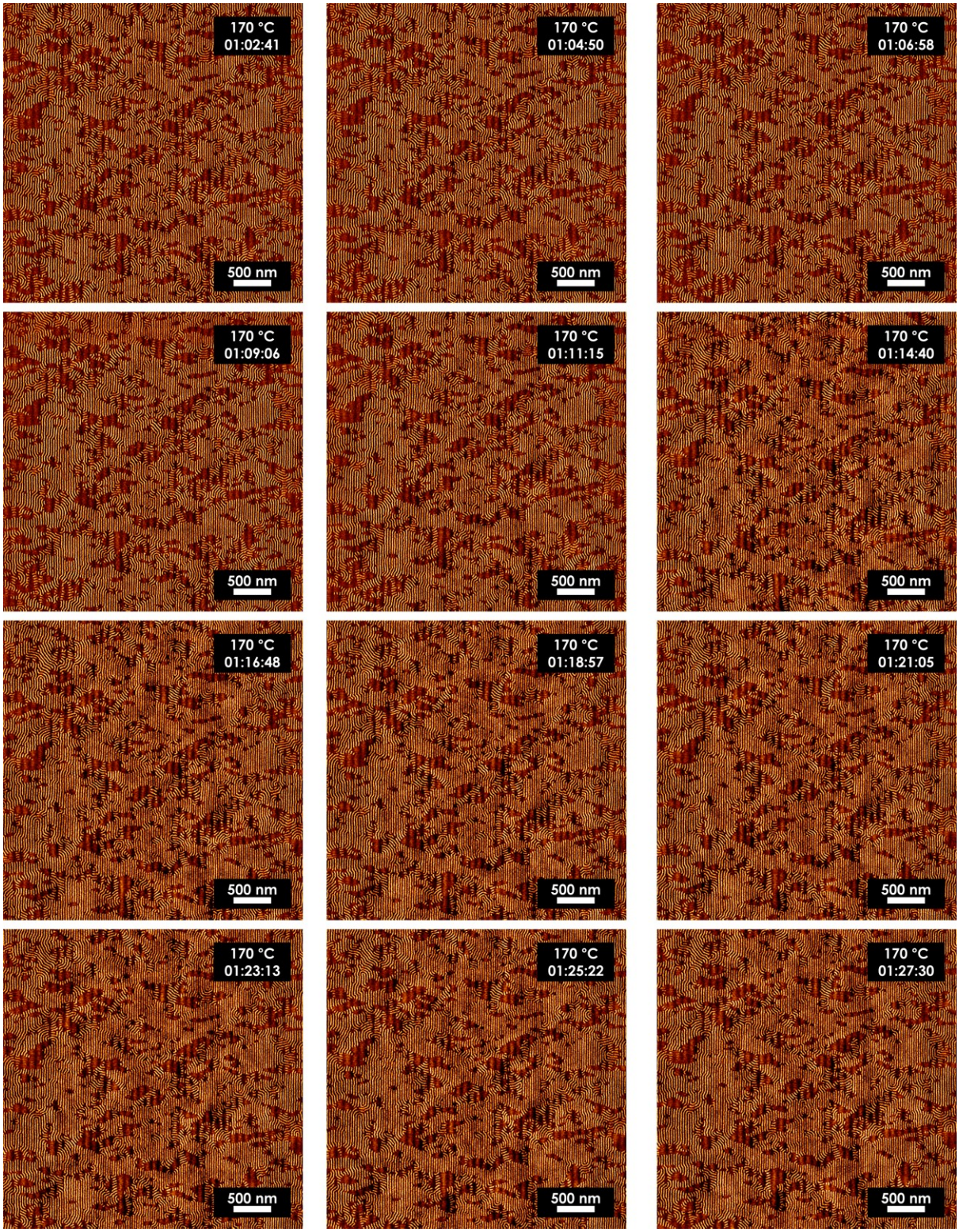


Figure 4-2. Snapshots of the phase images obtained from the isothermal in situ AFM experiment at 170 °C, Part 3.

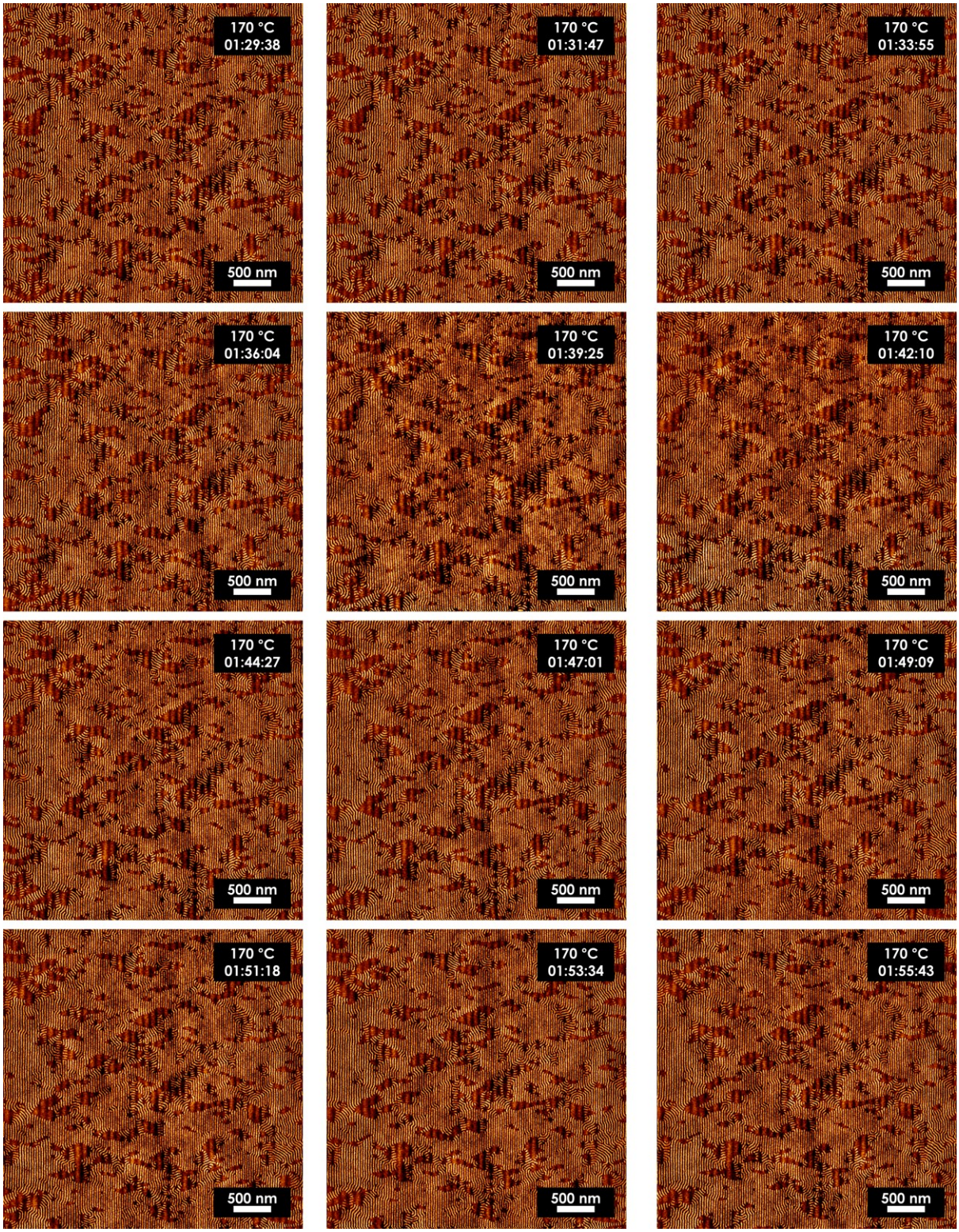


Figure 4-2. Snapshots of the phase images obtained from the isothermal in situ AFM experiment at 170 °C, Part 4.

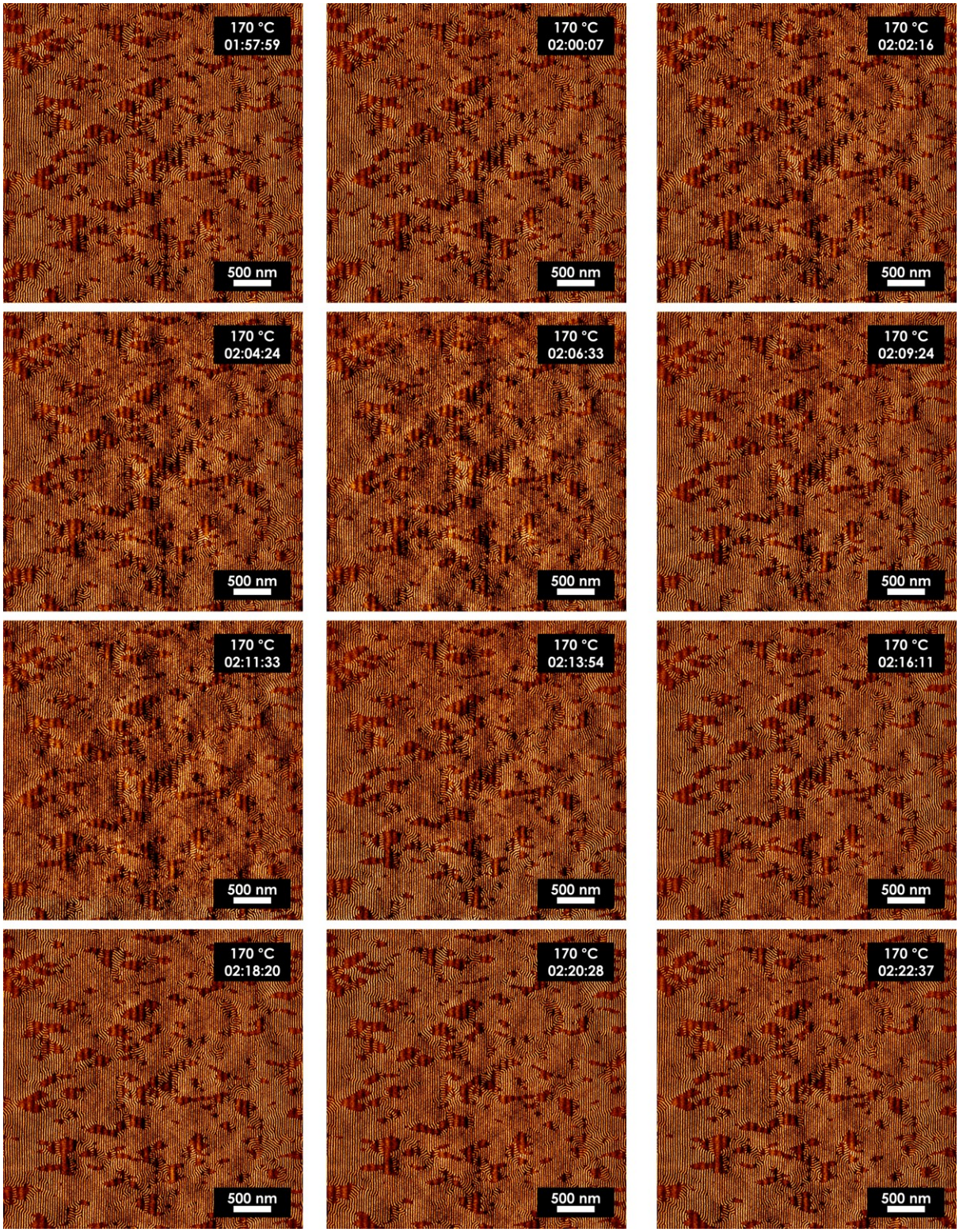


Figure 4-2. Snapshots of the phase images obtained from the isothermal in situ AFM experiment at 170 °C, Part 5.

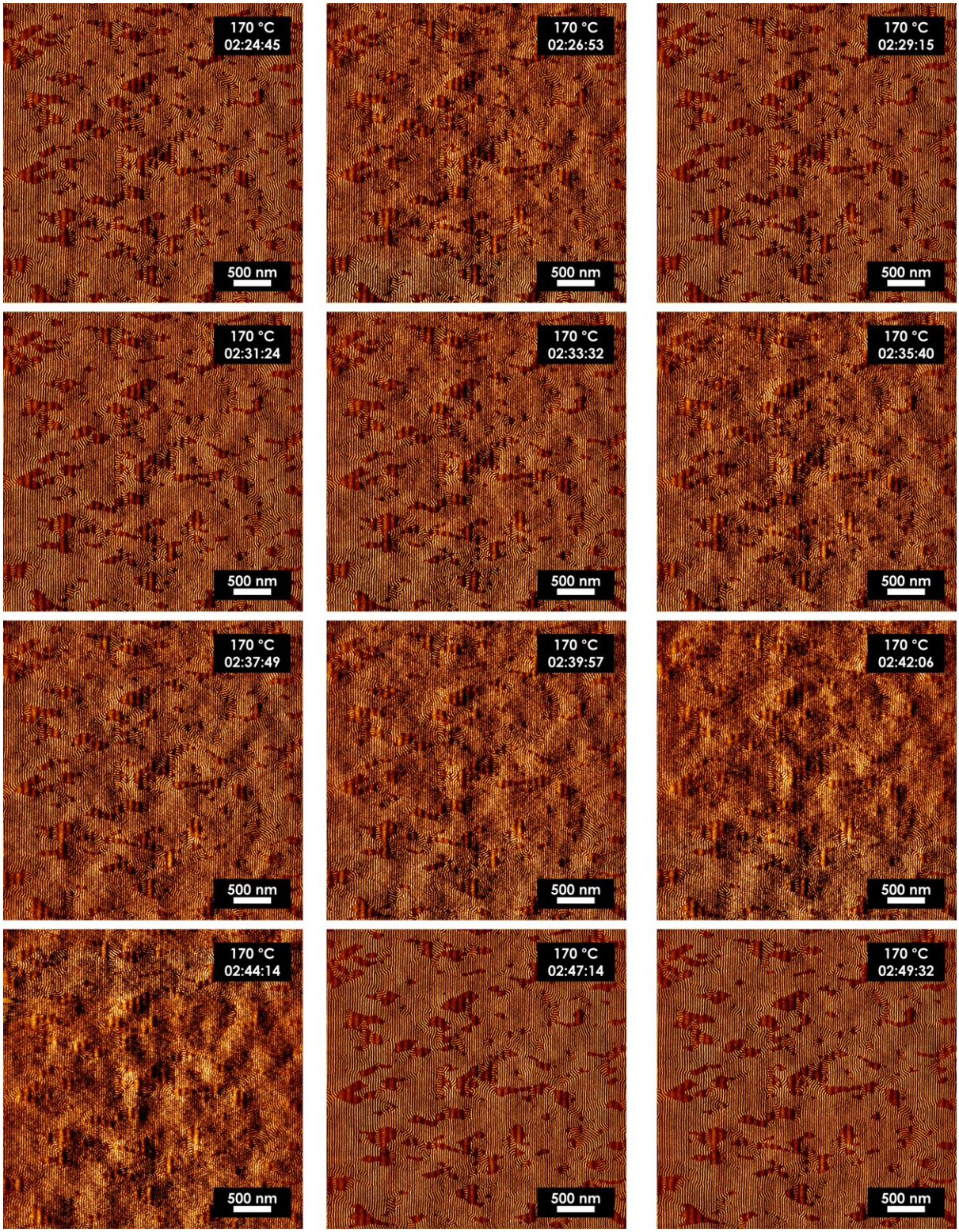


Figure 4-2. Snapshots of the phase images obtained from the isothermal in situ AFM experiment at 170 °C, Part 6.

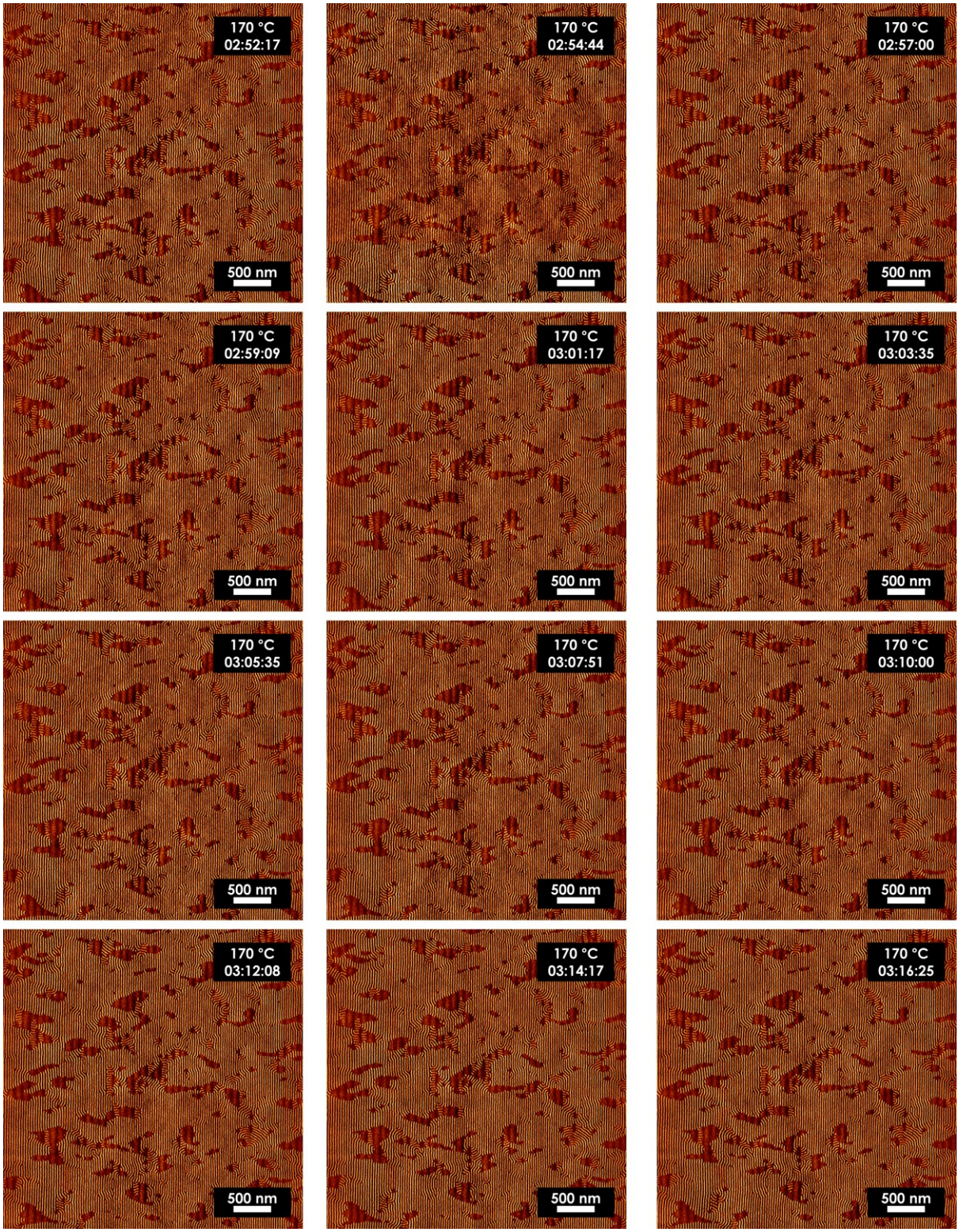


Figure 4-2. Snapshots of the phase images obtained from the isothermal in situ AFM experiment at 170 °C, Part 7.

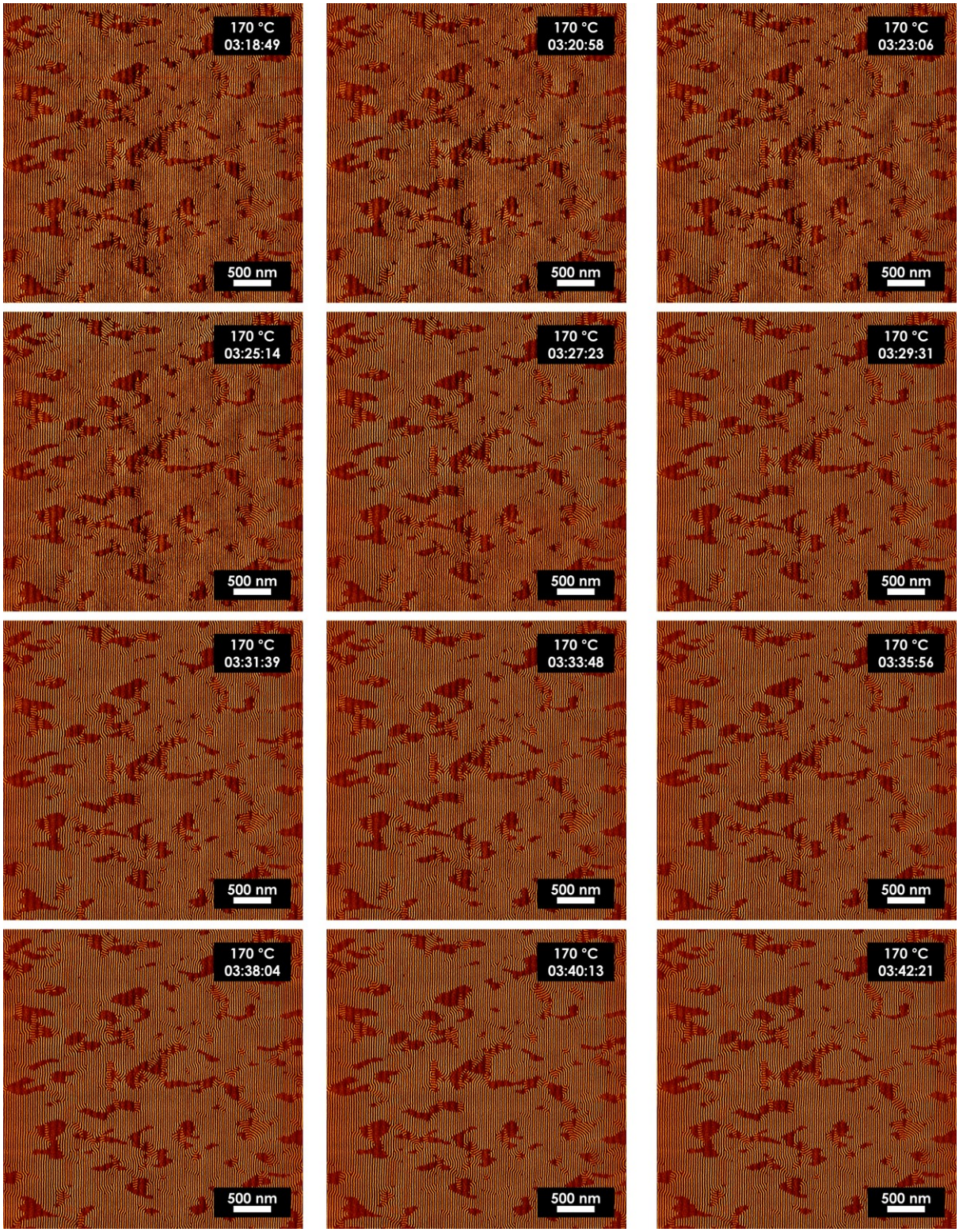


Figure 4-2. Snapshots of the phase images obtained from the isothermal in situ AFM experiment at 170 °C, Part 8.

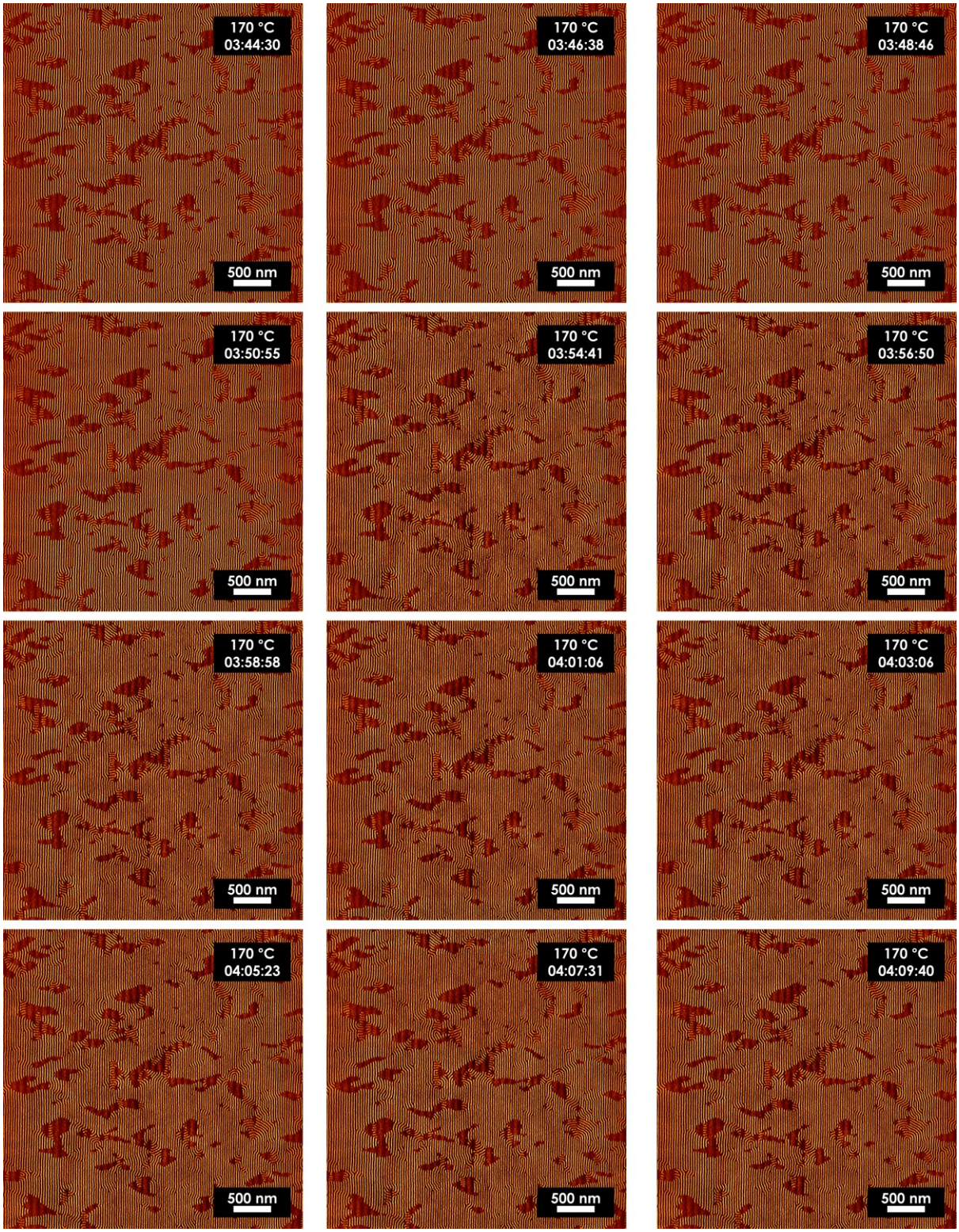


Figure 4-2. Snapshots of the phase images obtained from the isothermal in situ AFM experiment at 170 °C, Part 9.

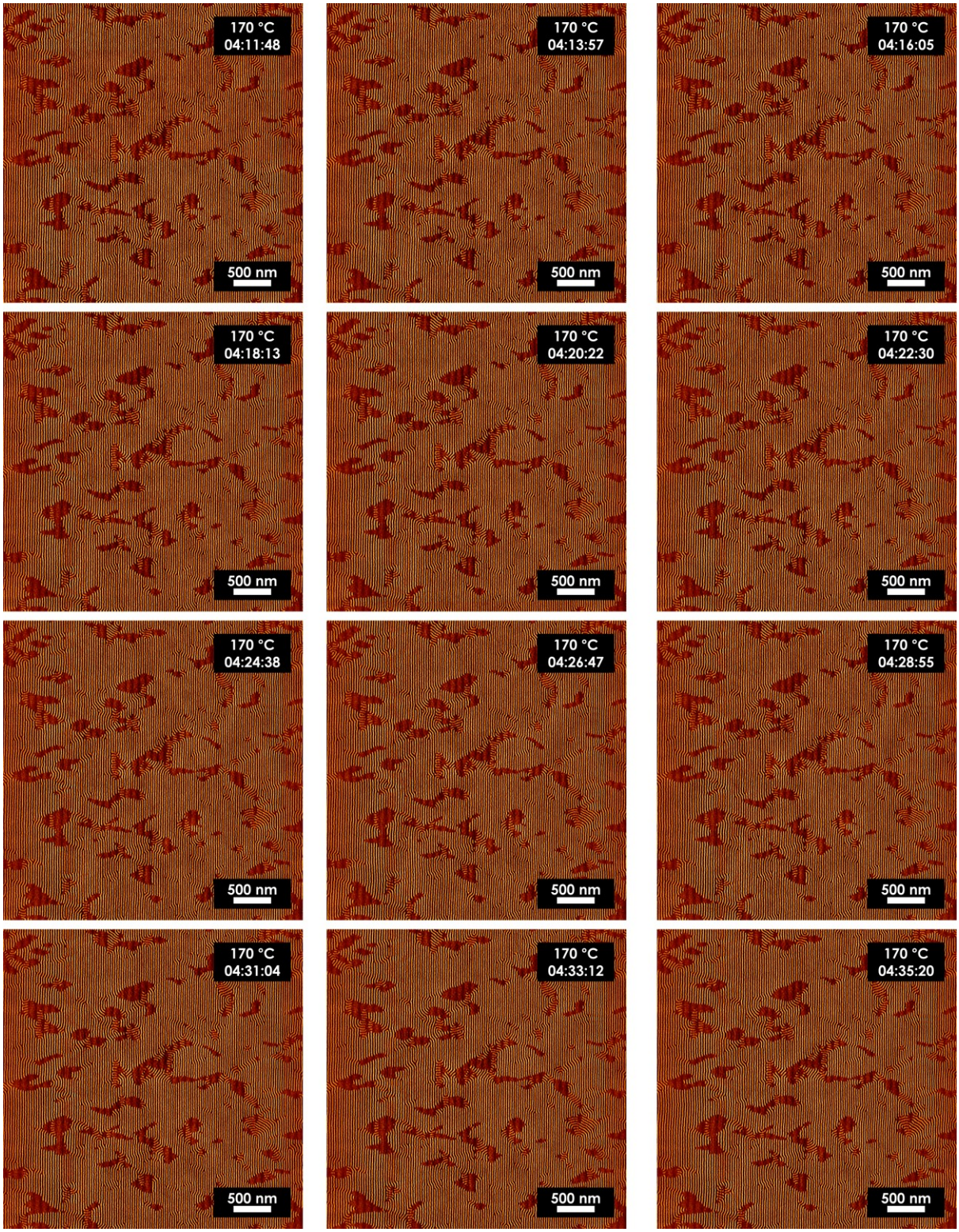


Figure 4-2. Snapshots of the phase images obtained from the isothermal in situ AFM experiment at 170 °C, Part 10.

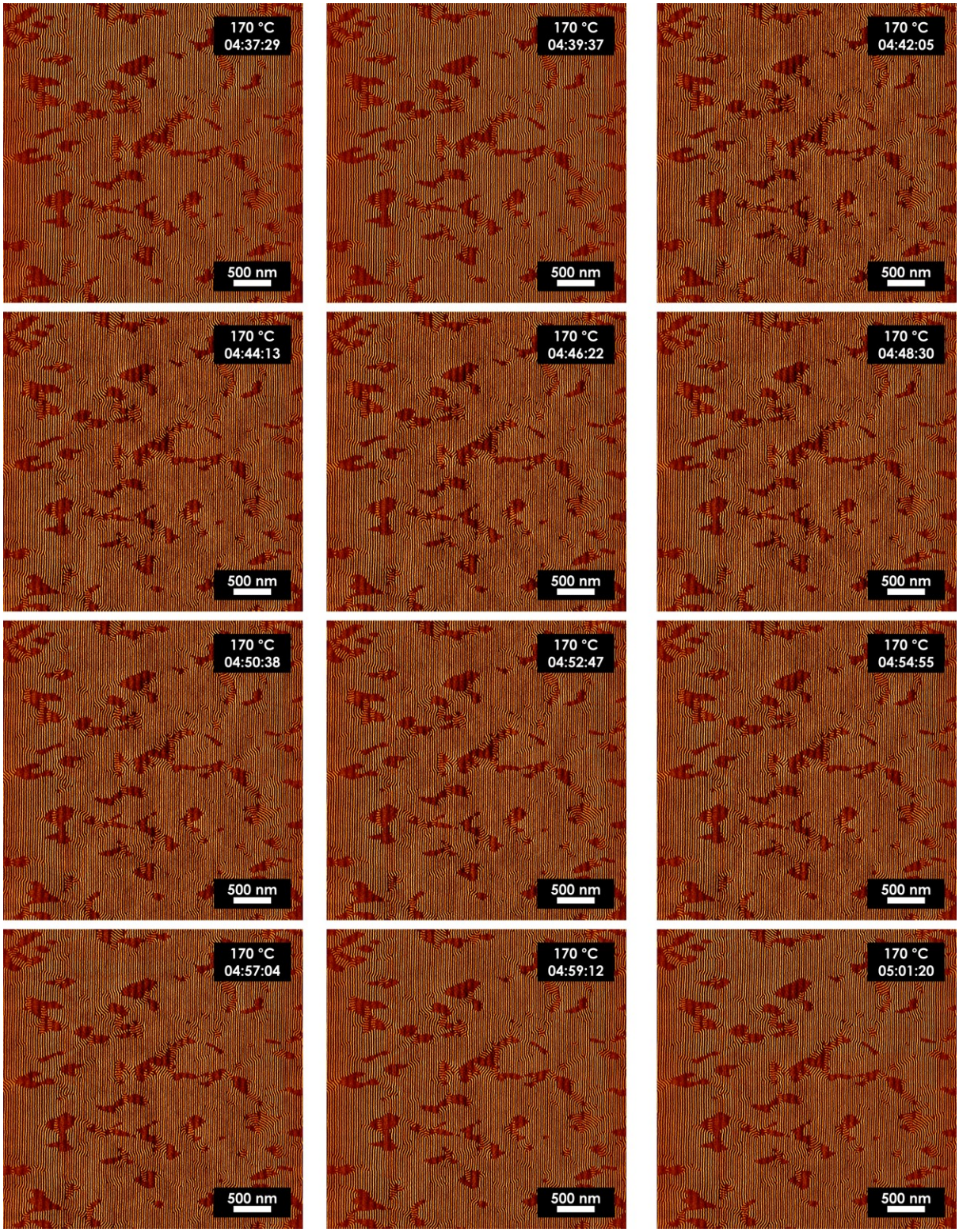


Figure 4-2. Snapshots of the phase images obtained from the isothermal in situ AFM experiment at 170 °C, Part 11.

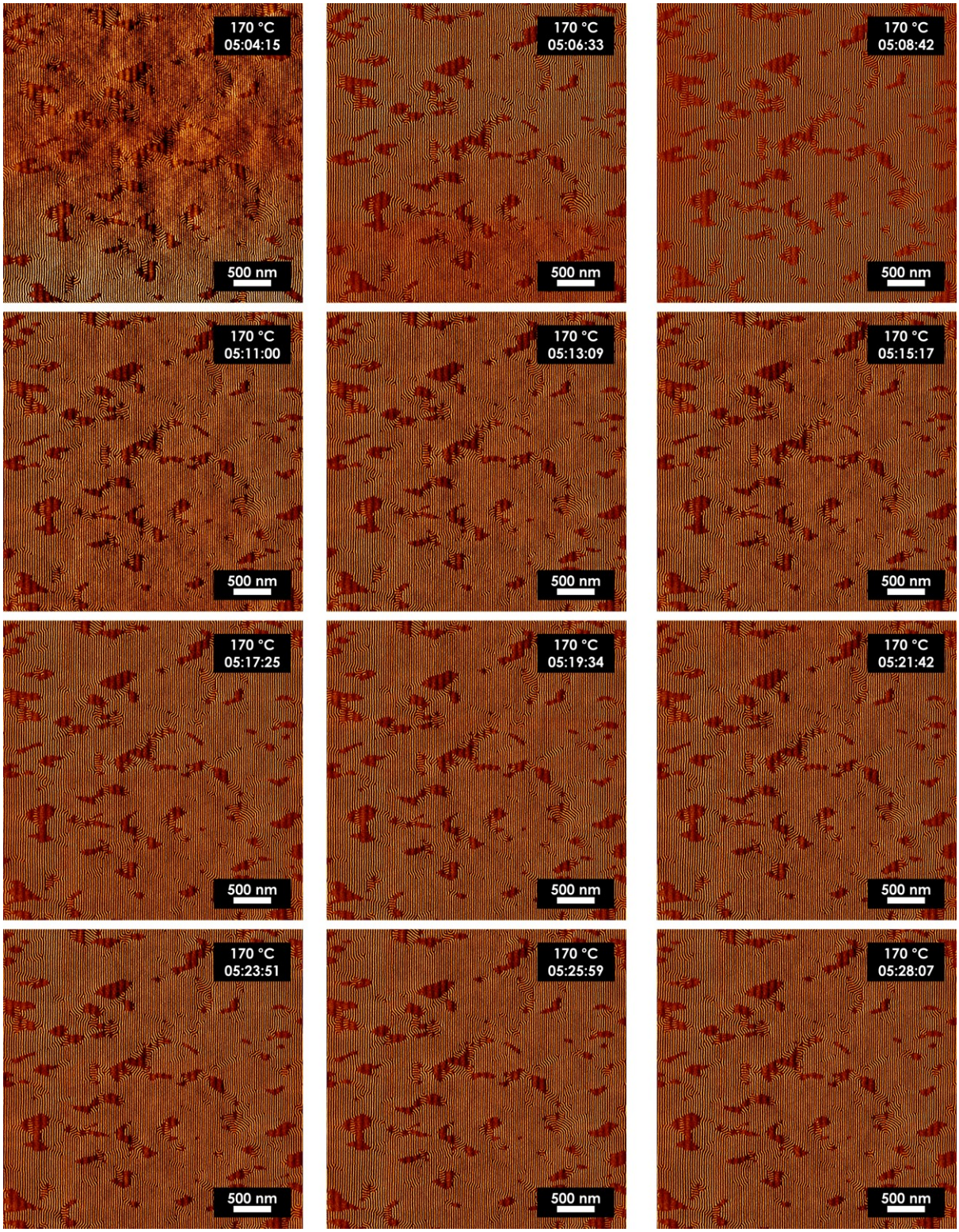


Figure 4-2. Snapshots of the phase images obtained from the isothermal in situ AFM experiment at 170 °C, Part 12.

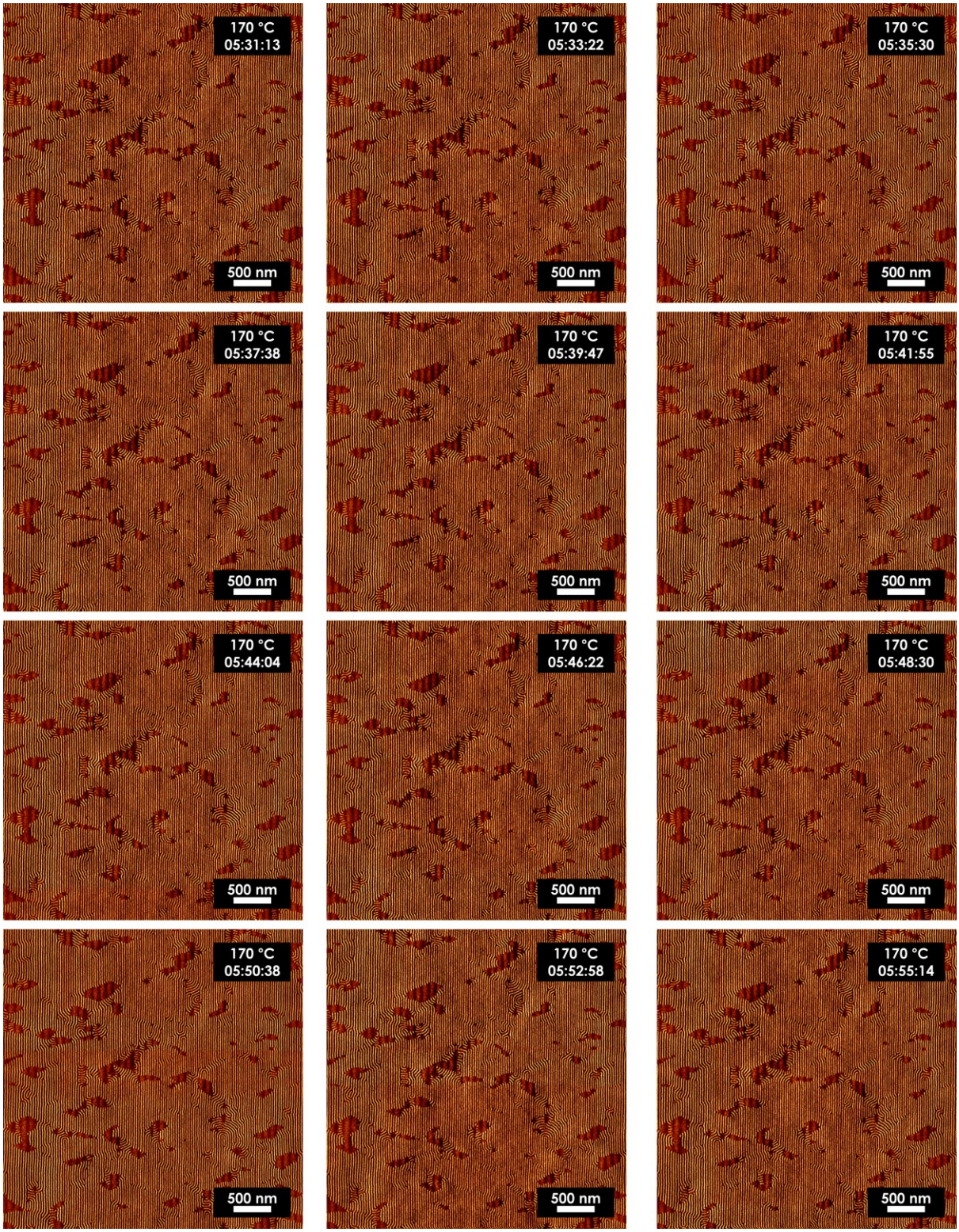


Figure 4-2. Snapshots of the phase images obtained from the isothermal in situ AFM experiment at 170 °C, Part 13.

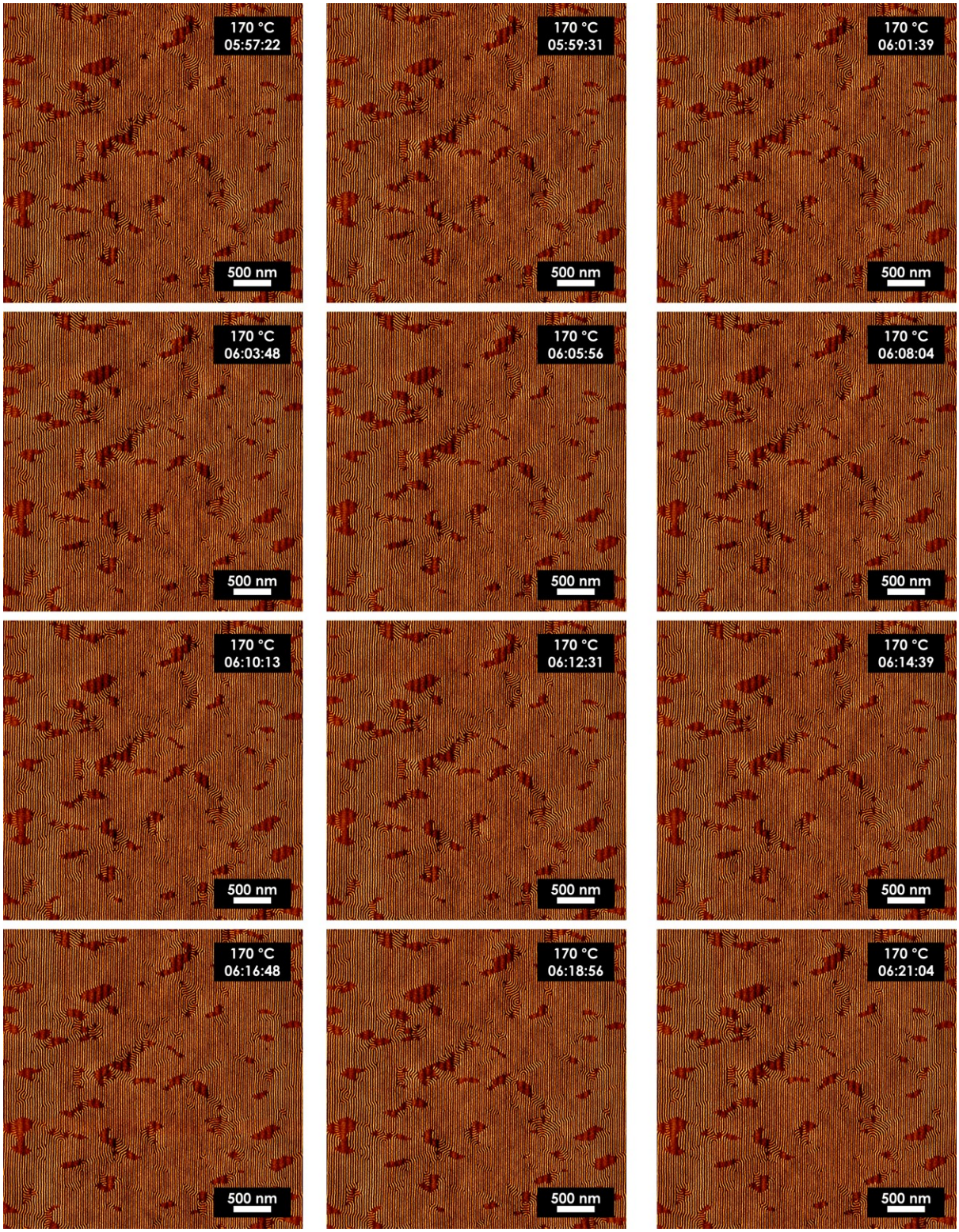


Figure 4-2. Snapshots of the phase images obtained from the isothermal in situ AFM experiment at 170 °C, Part 14.

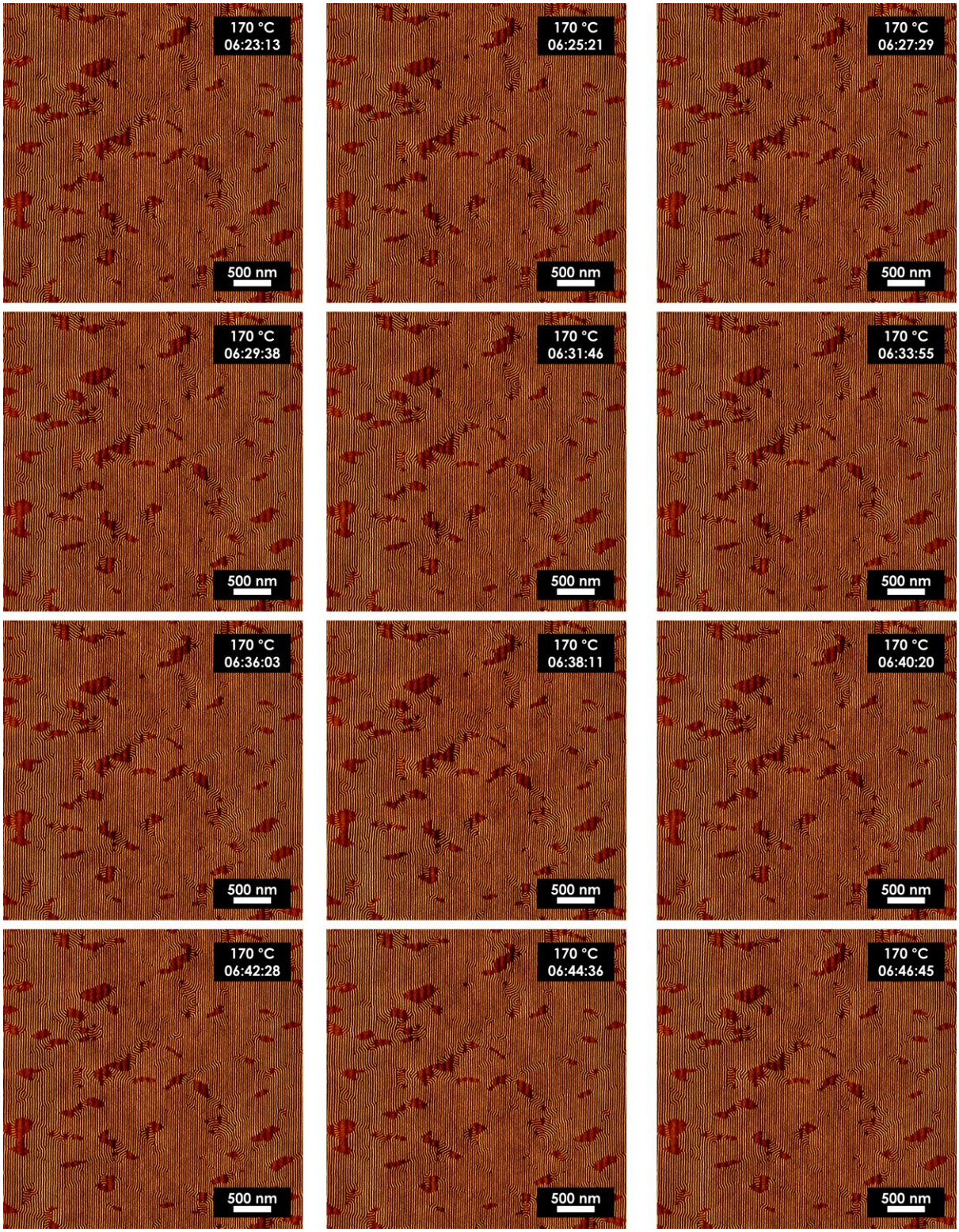


Figure 4-2. Snapshots of the phase images obtained from the isothermal in situ AFM experiment at 170 °C, Part 15.

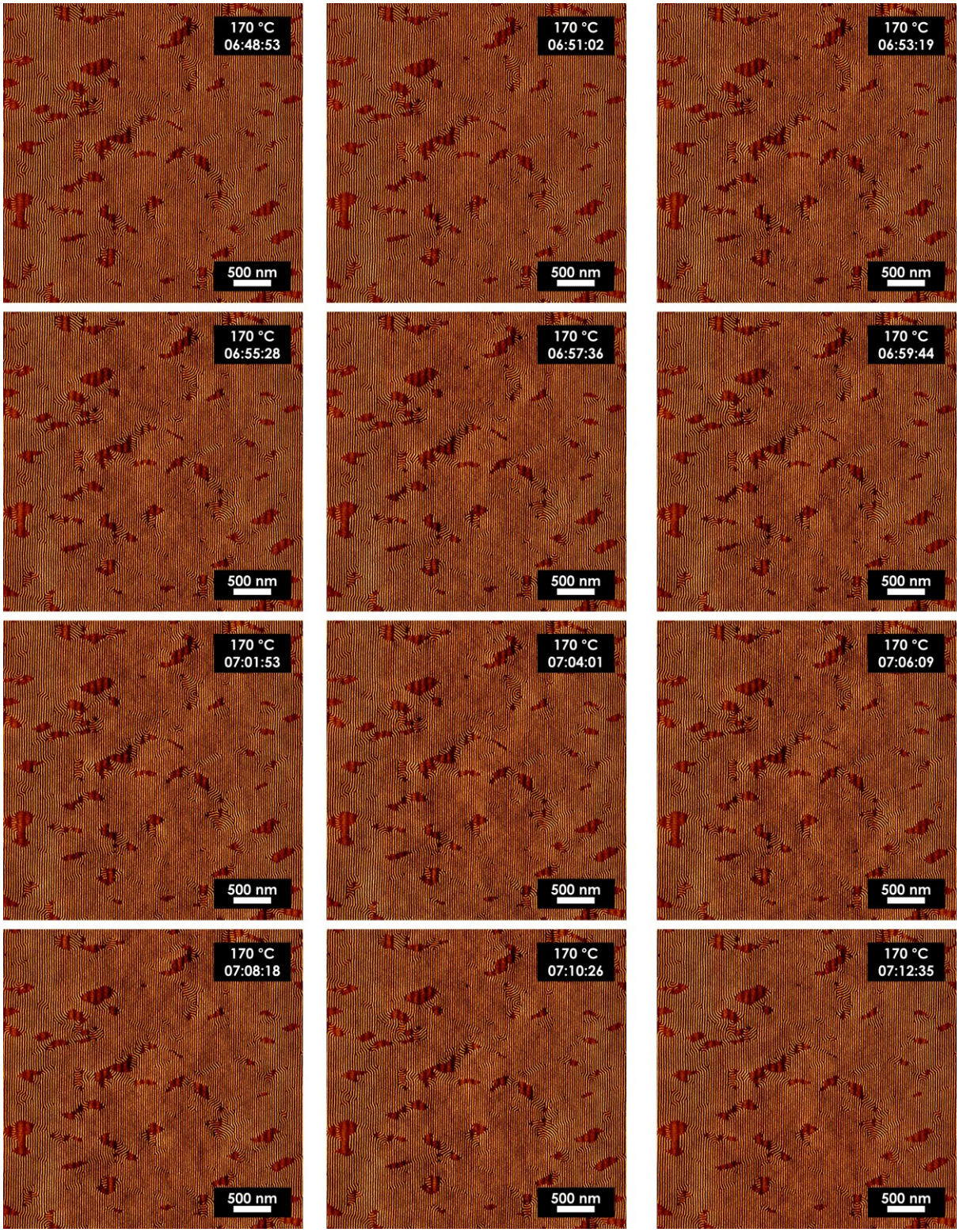


Figure 4-2. Snapshots of the phase images obtained from the isothermal in situ AFM experiment at 170 °C, Part 16.

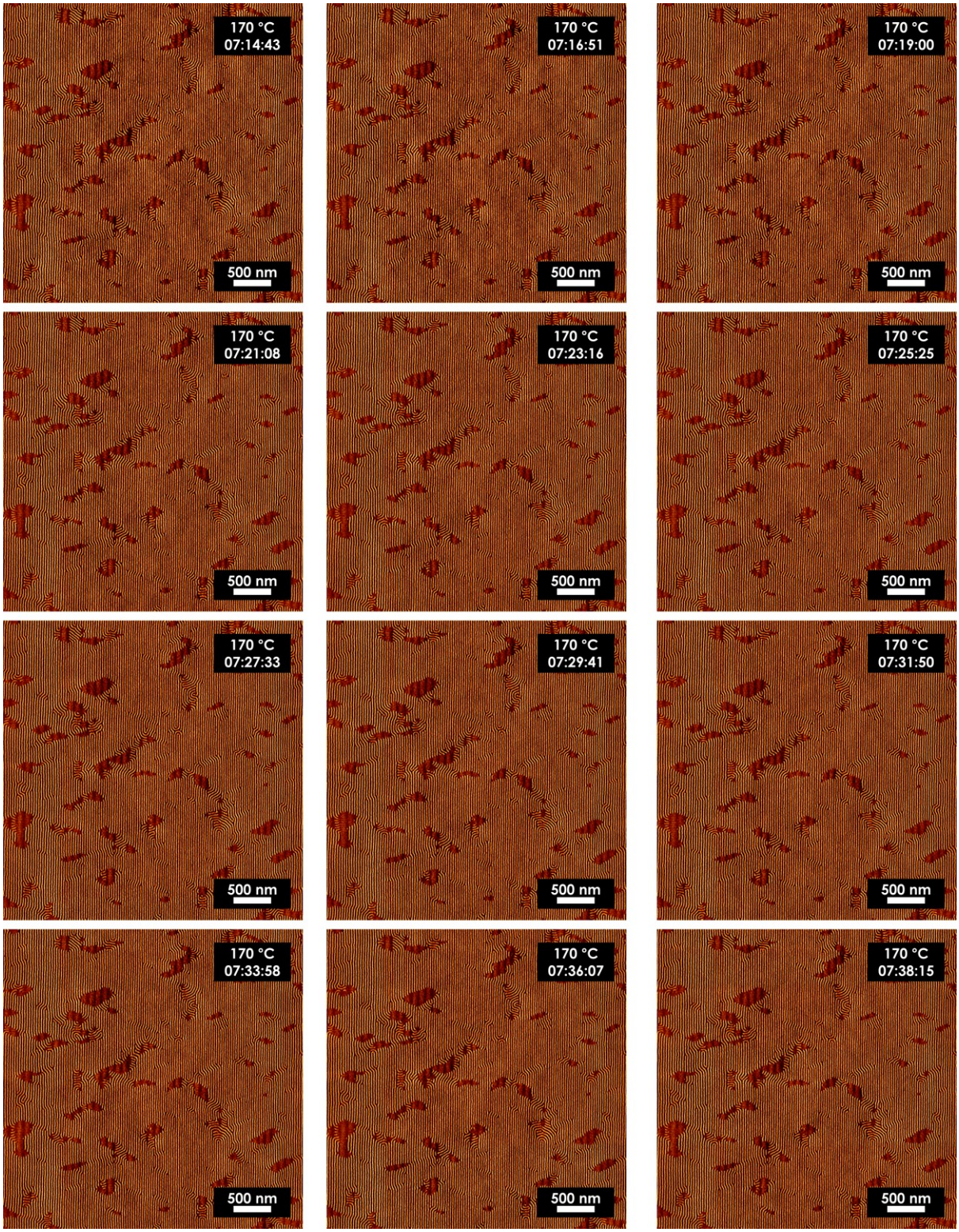


Figure 4-2. Snapshots of the phase images obtained from the isothermal in situ AFM experiment at 170 °C, Part 17.

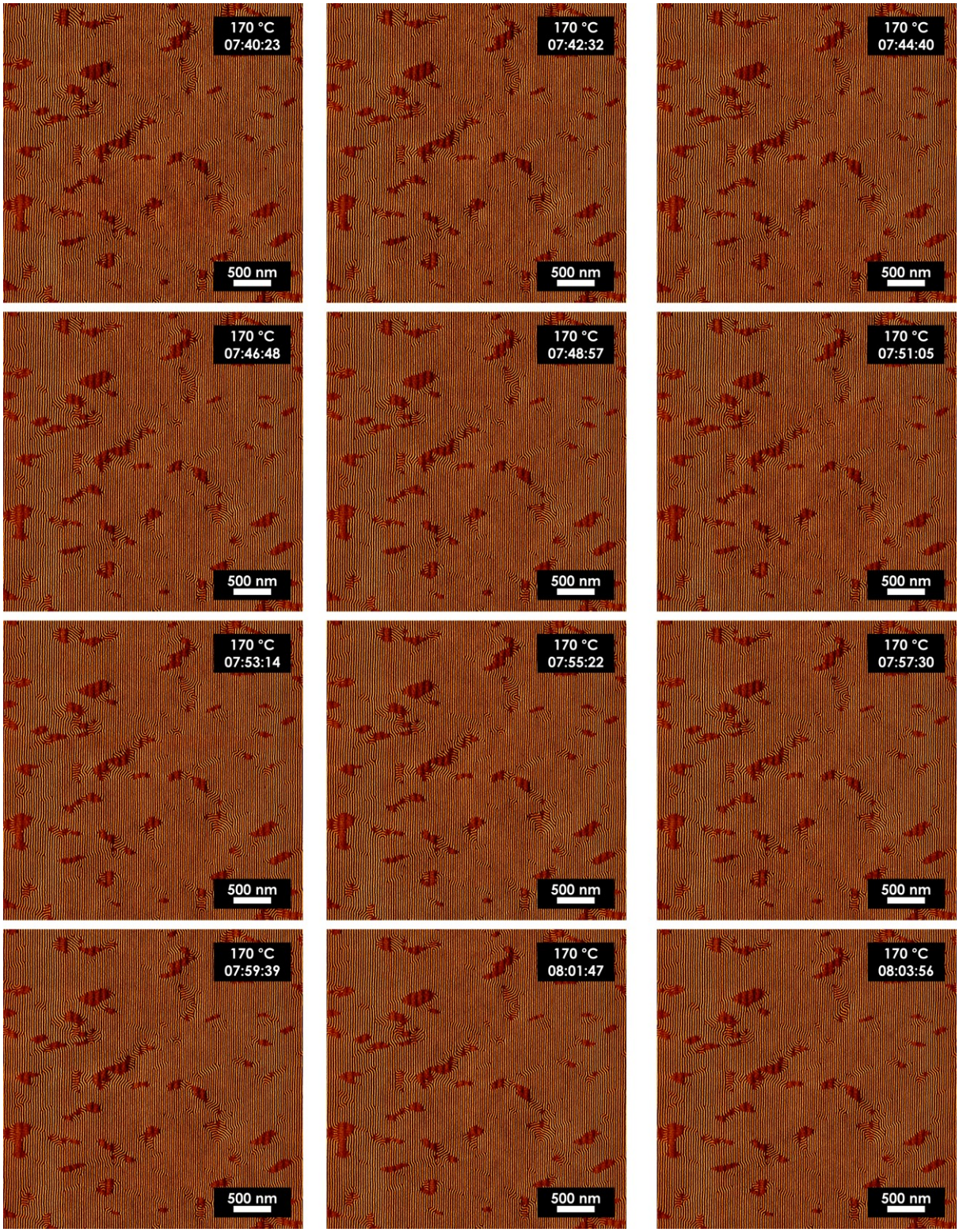


Figure 4-2. Snapshots of the phase images obtained from the isothermal in situ AFM experiment at 170 °C, Part 18.

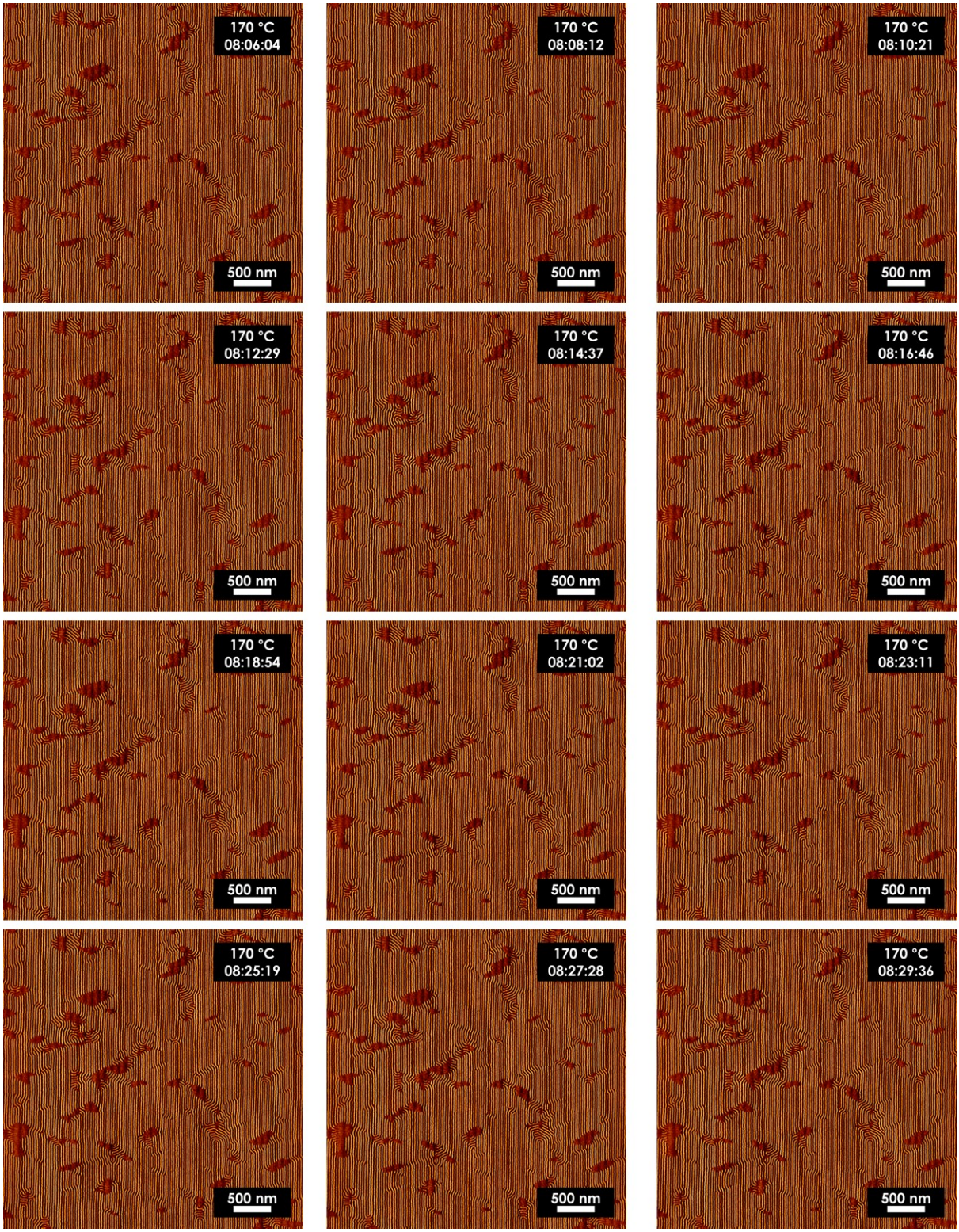


Figure 4-2. Snapshots of the phase images obtained from the isothermal in situ AFM experiment at 170 °C, Part 19.

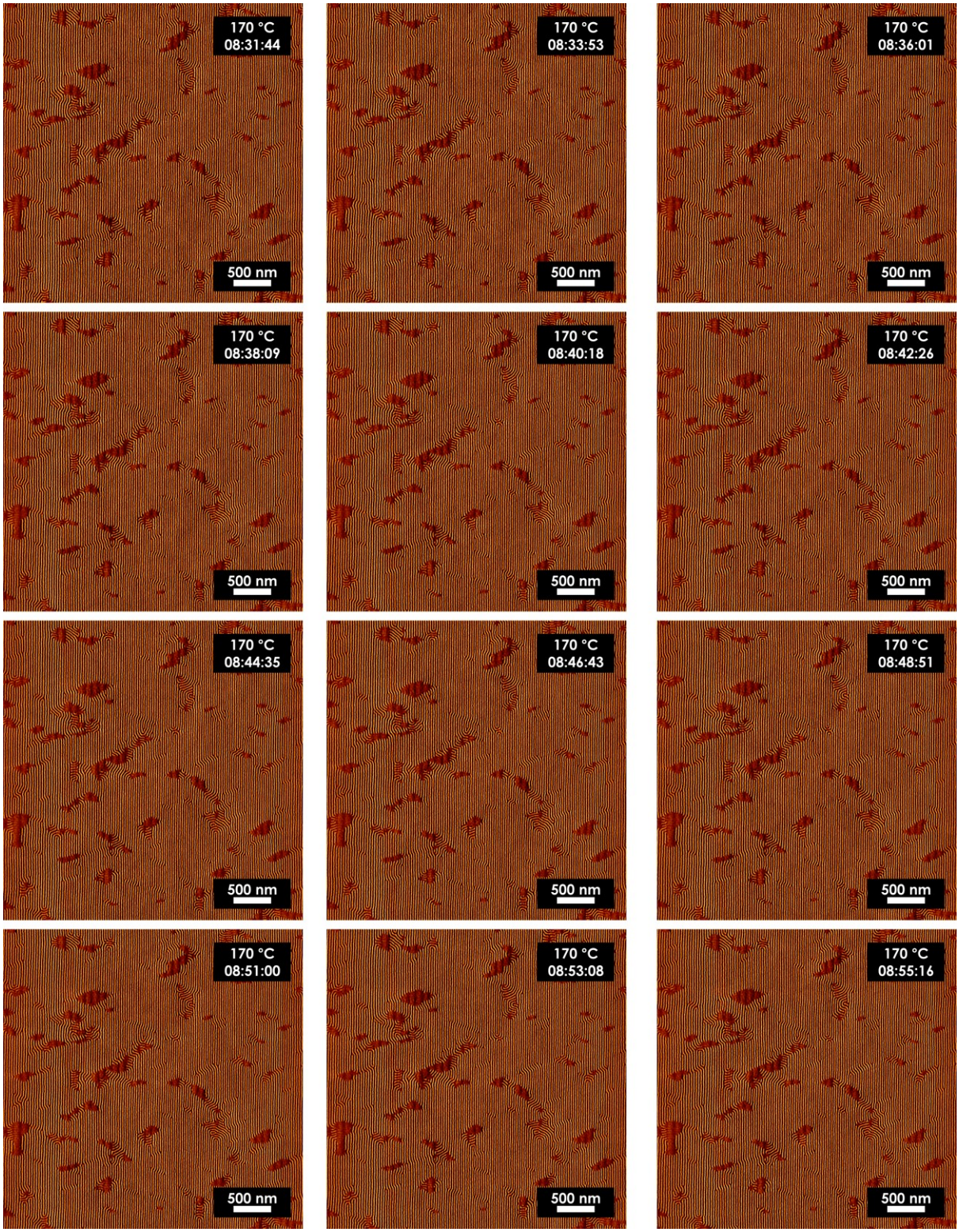


Figure 4-2. Snapshots of the phase images obtained from the isothermal in situ AFM experiment at 170 °C, Part 20.

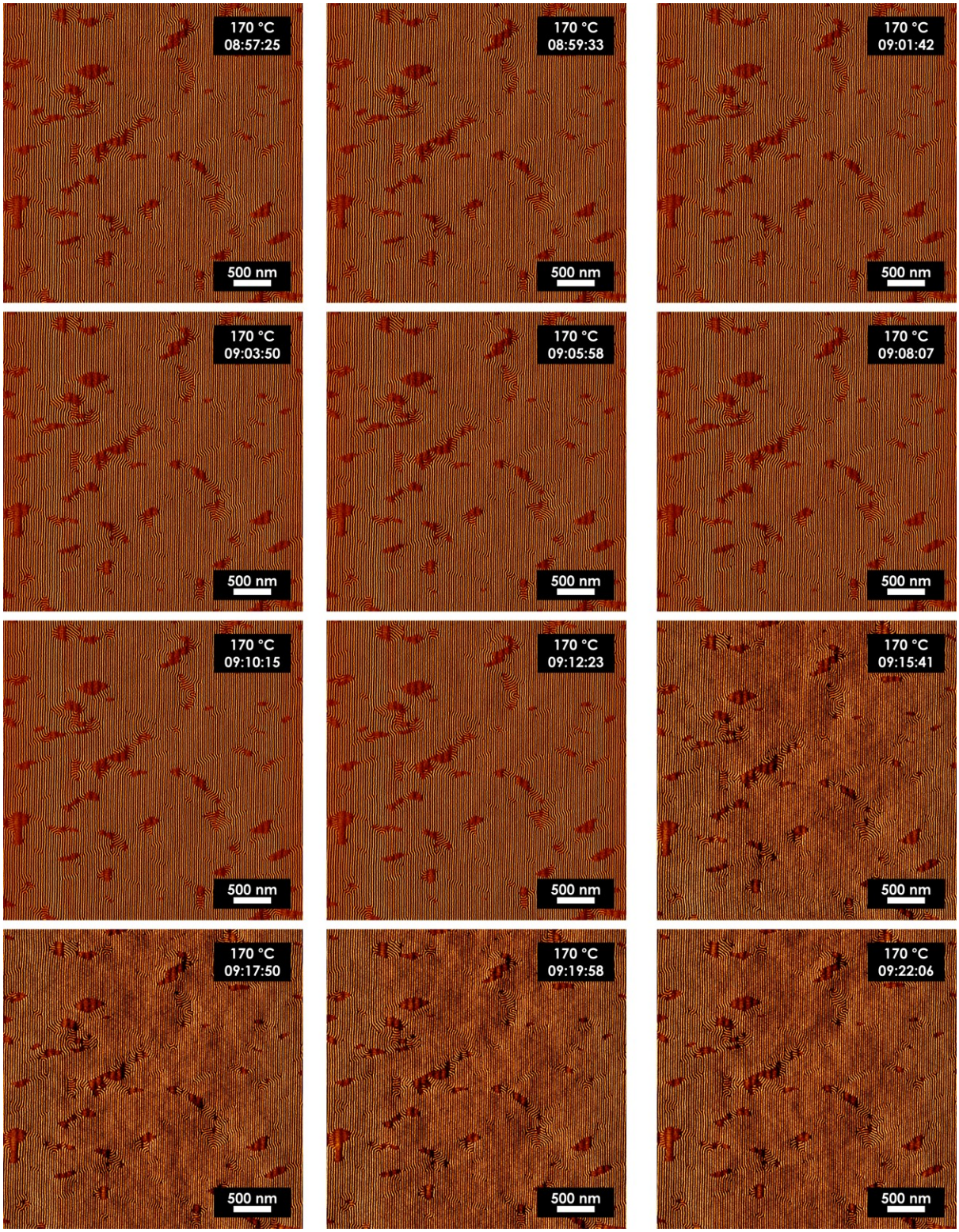


Figure 4-2. Snapshots of the phase images obtained from the isothermal in situ AFM experiment at 170 °C, Part 21.

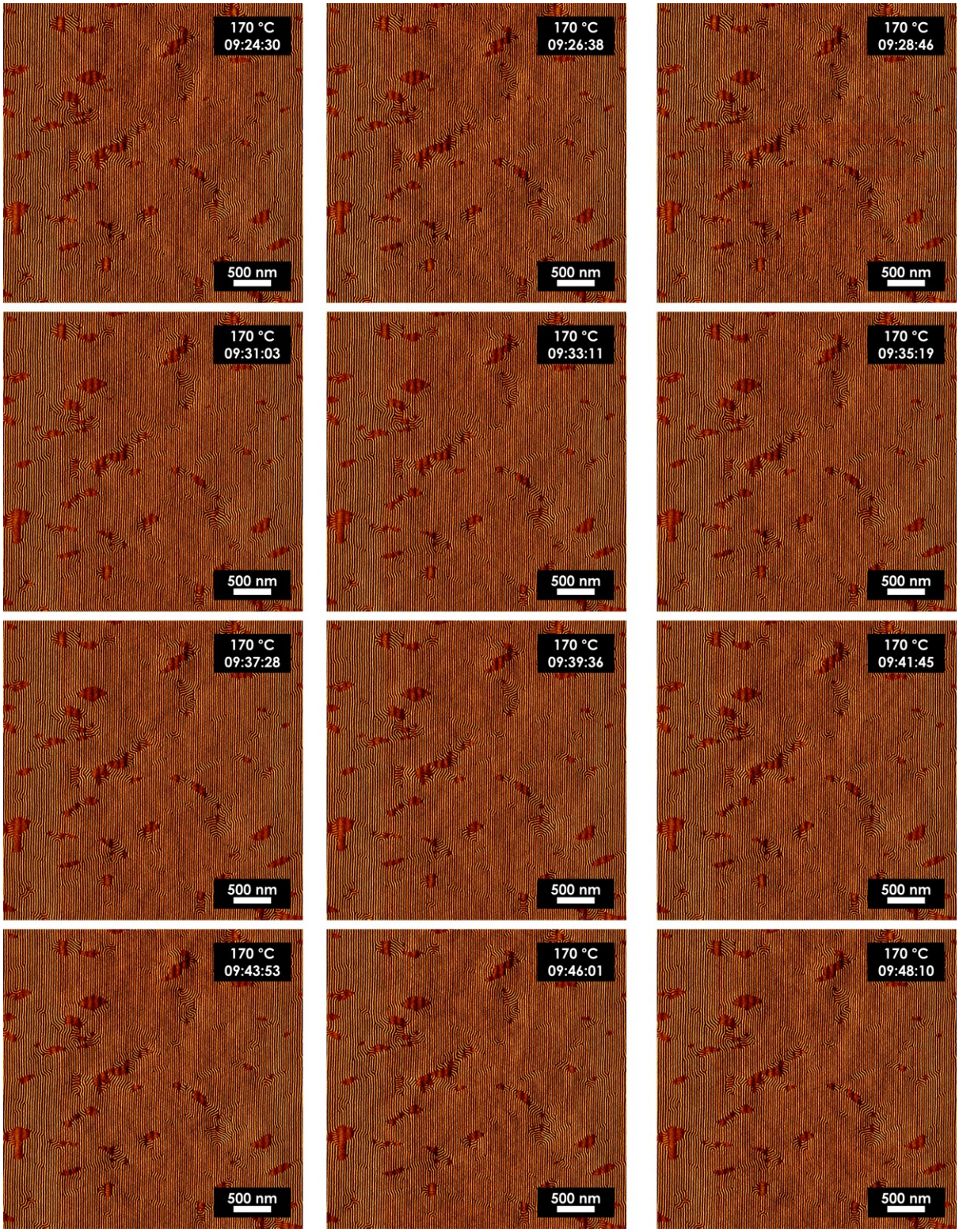


Figure 4-2. Snapshots of the phase images obtained from the isothermal in situ AFM experiment at 170 °C, Part 22.

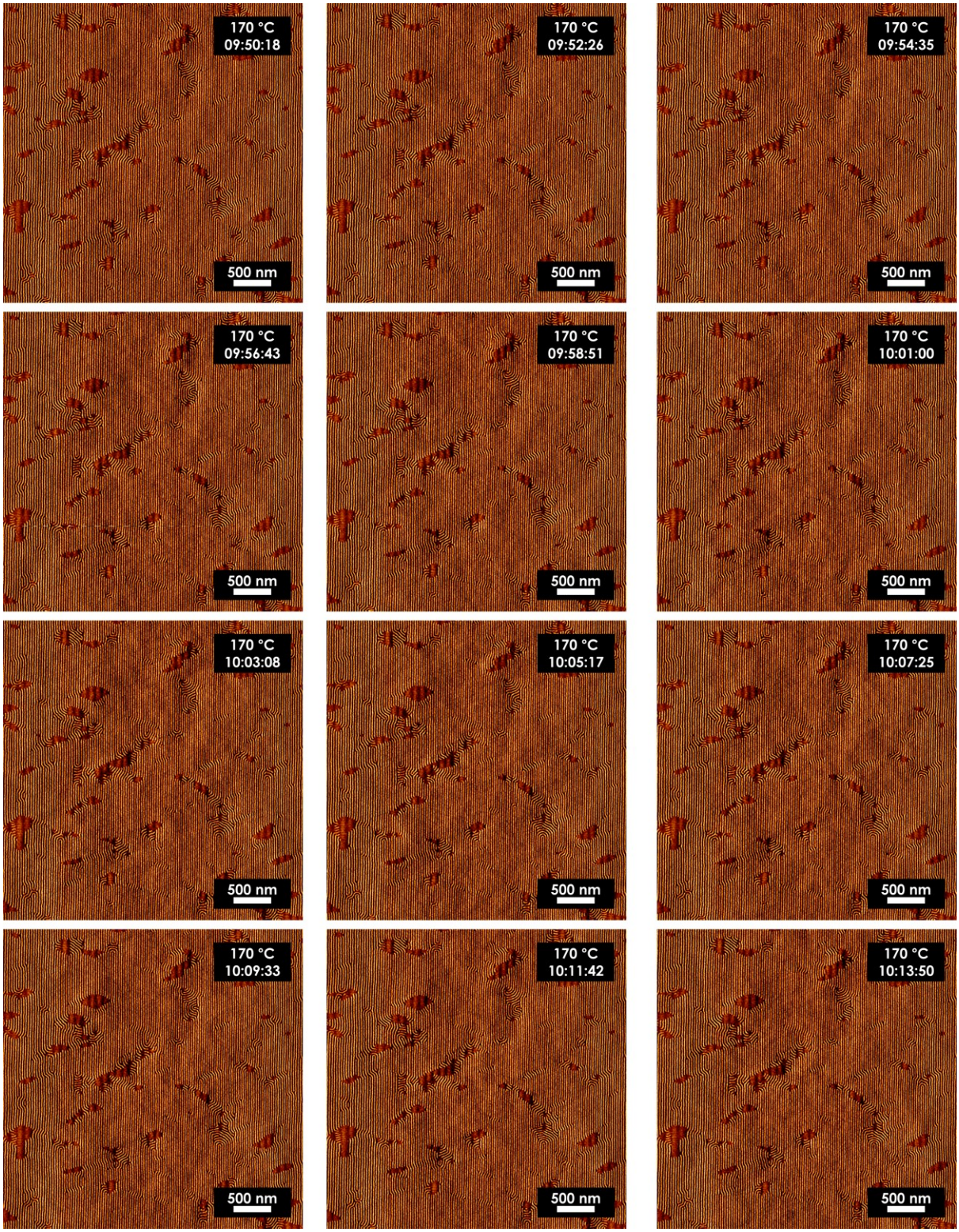


Figure 4-2. Snapshots of the phase images obtained from the isothermal in situ AFM experiment at 170 °C, Part 23.

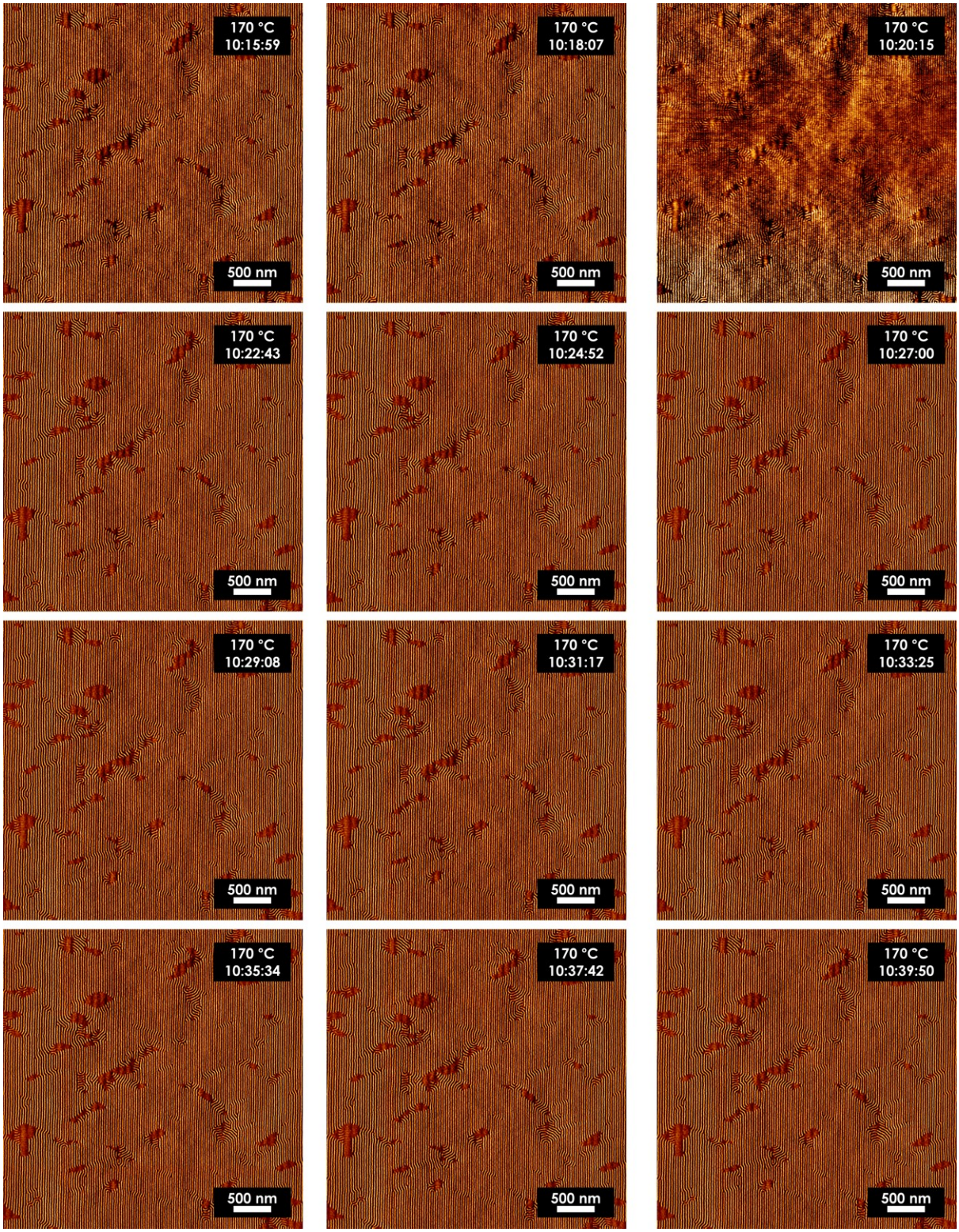


Figure 4-2. Snapshots of the phase images obtained from the isothermal in situ AFM experiment at 170 °C, Part 24.

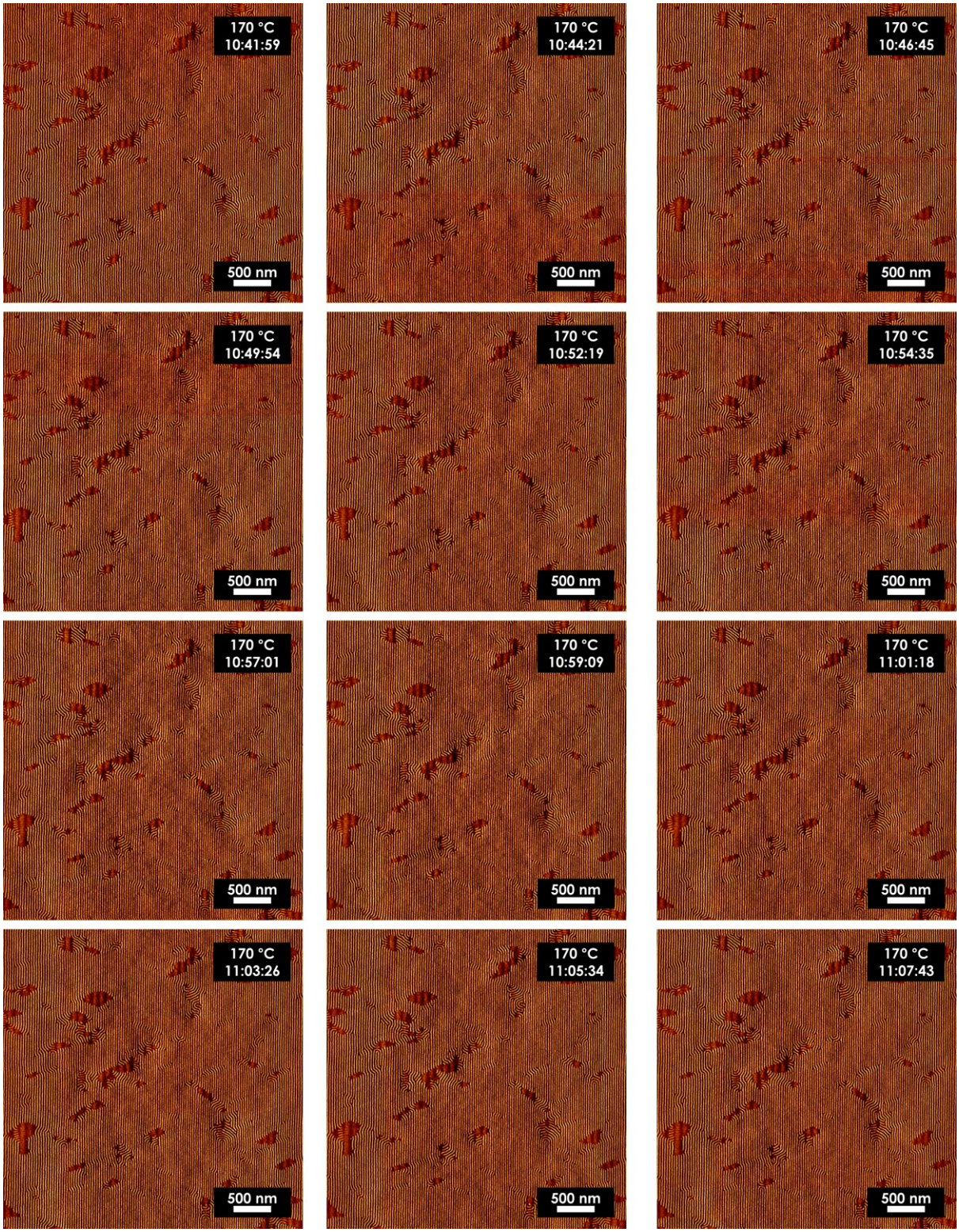


Figure 4-2. Snapshots of the phase images obtained from the isothermal in situ AFM experiment at 170 °C, Part 25.

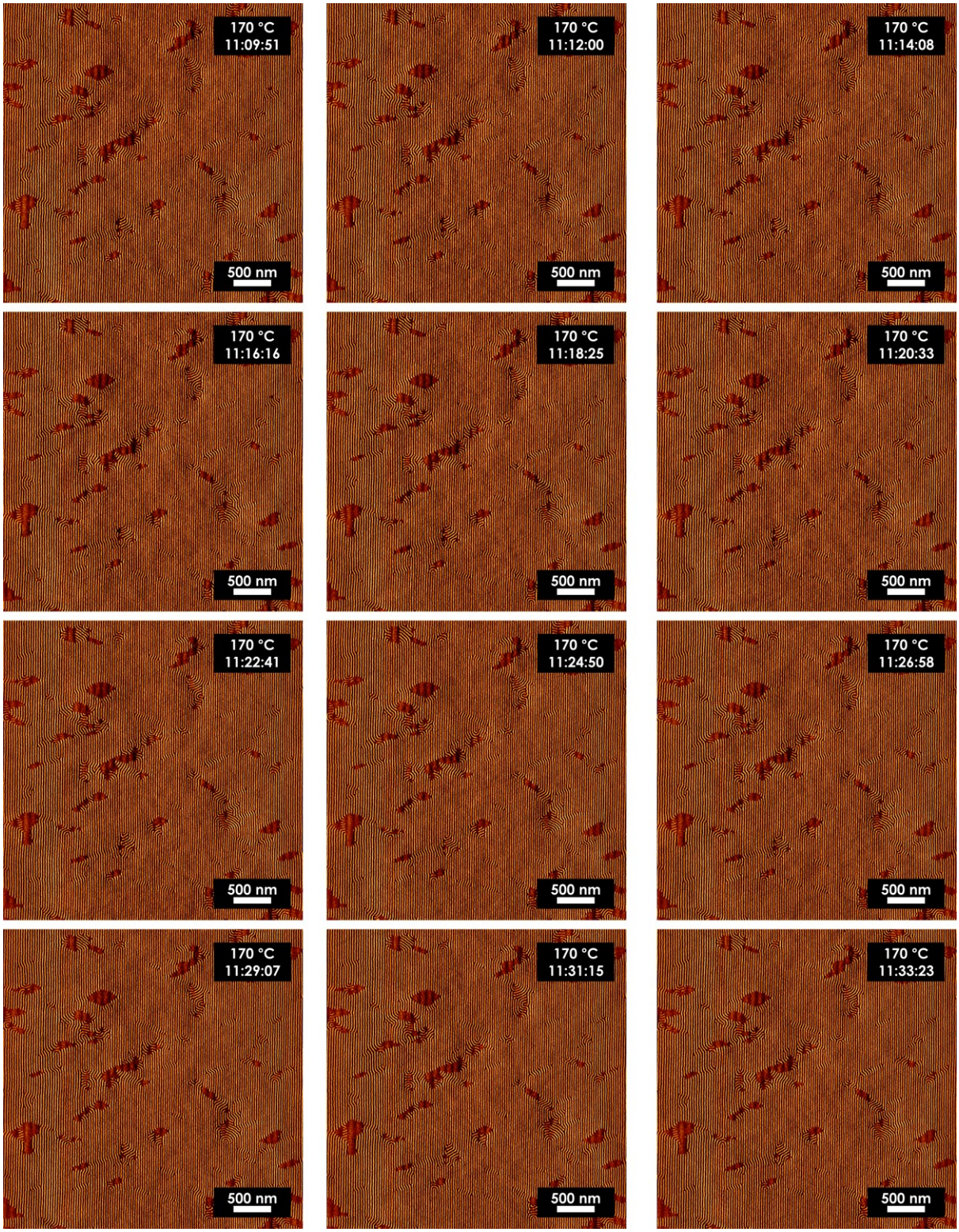


Figure 4-2. Snapshots of the phase images obtained from the isothermal in situ AFM experiment at 170 °C, Part 26.

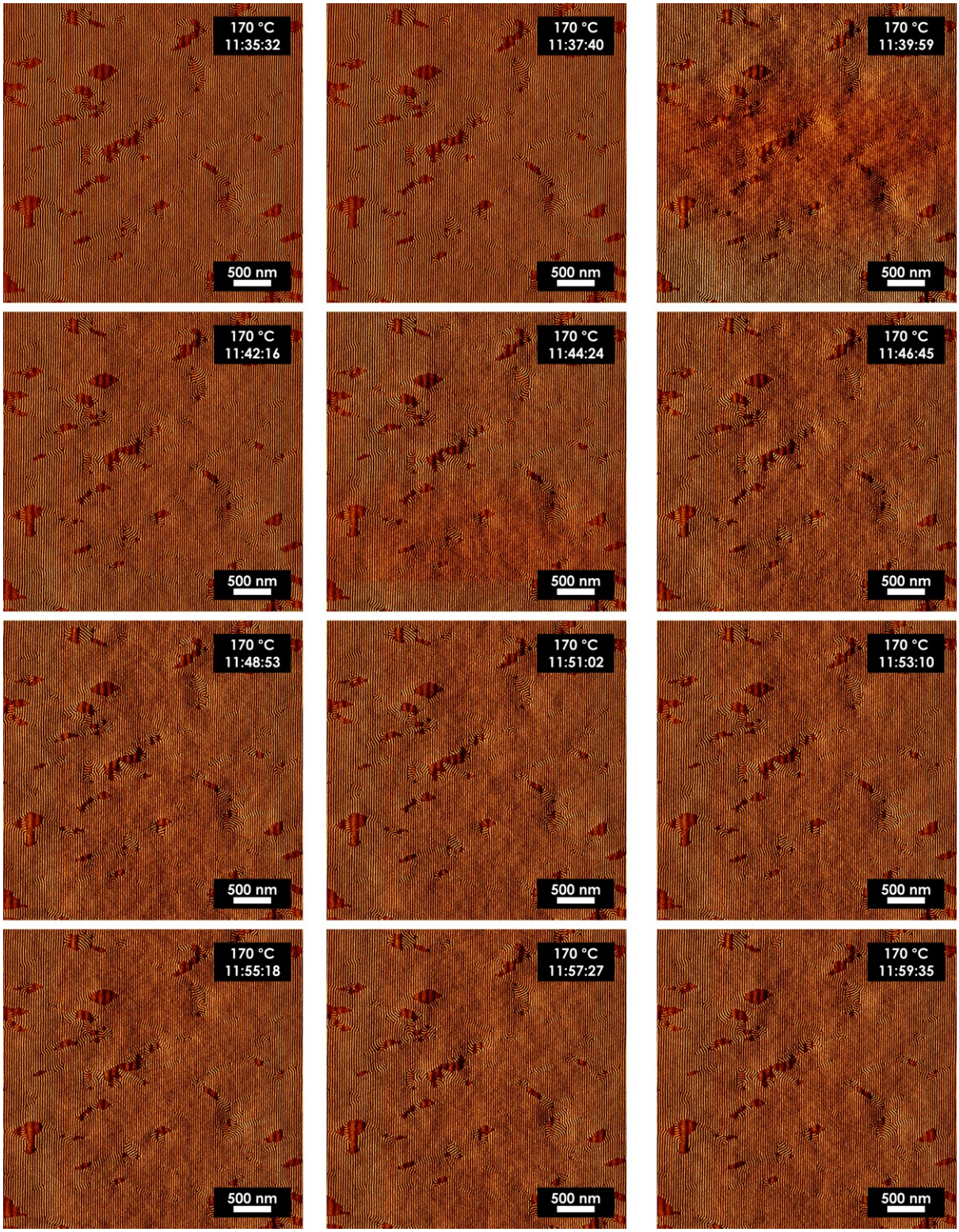


Figure 4-2. Snapshots of the phase images obtained from the isothermal in situ AFM experiment at 170 °C, Part 27.

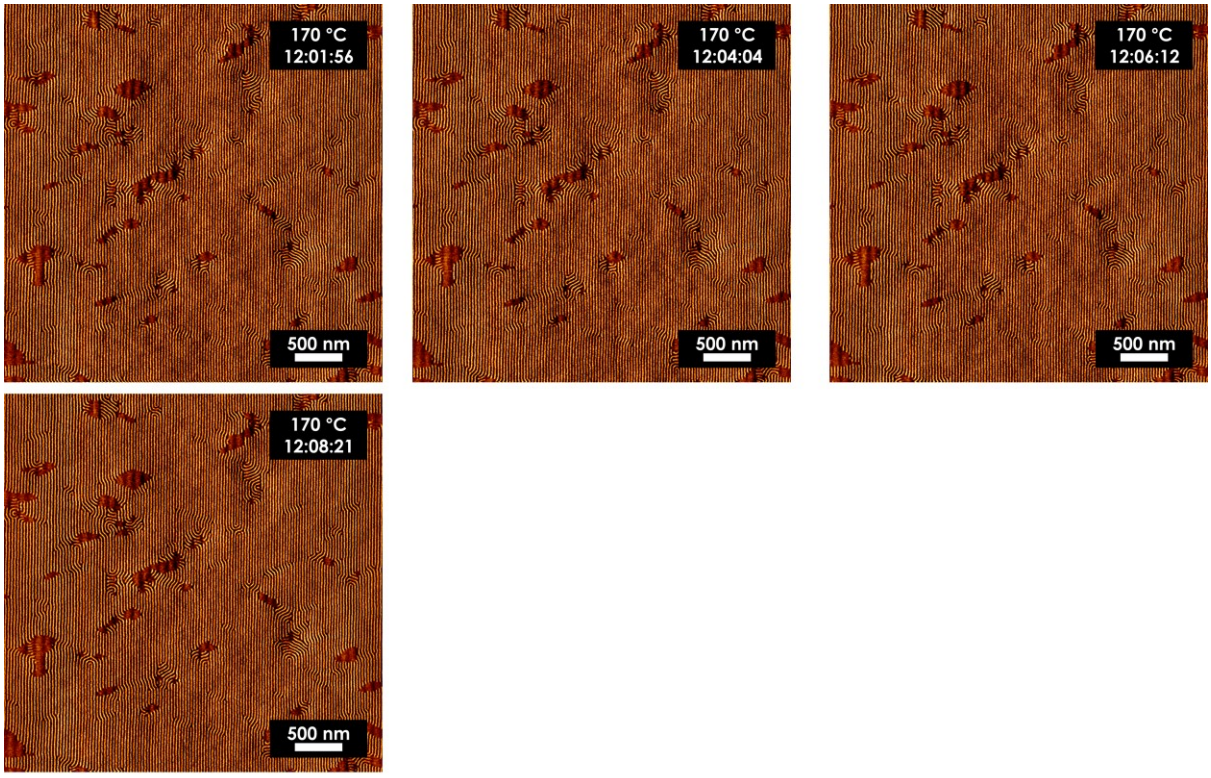


Figure 4-2. Snapshots of the phase images obtained from the isothermal in situ AFM experiment at 170 °C, Part 28.

The next set of isothermal annealing experiments were conducted at 190, 200, and 210 °C. In this temperature range in the earlier incremental in situ AFM experiment, longitudinally-aligned lamellar stripes covered large swaths of the imaged areas, with defects gradually disappearing as the temperature increased further, and Ψ_2 exceeded 0.8 as it continued to increase slowly at a rate of 0.001 per 2 °C increment. Conducting isothermal annealing experiments in this temperature range could facilitate the identification of sources resulting in the evolution of defects and their annihilation pathways to defect-free well-aligned states. As in the corresponding images in the incremental experiment, the first image obtained during the isothermal experiment at 190 °C (t = 00:20:24) showed a lamellar stripe pattern with a high degree of longitudinal alignment. However, numerous sizable defect areas with dislocations, disclinations, and occasionally parallel orientation defects could also be observed. Quantitative analysis of this image revealed a two-step increase in Ψ_2. The first image exhibited a relatively high Ψ_2 value of 0.73 and Ψ_2 was then observed to grow relatively quickly at a rate of 0.0087 per min in the first 15 min of annealing, before slowing

down to increasing at a rate of 0.00014, up to approximately $\Psi_2 = 0.85$ after 6 h. When fitted to a power-law, this yields a scaling factor of $t^{0.27}$ in the first 15 min, and $t^{0.03}$ for the rest of the experiment. This two-stage self-assembly behavior fits well with the previous studies, with a growth exponent close to 0.25 in the first stage, and a low growth exponent of $a < 0.1$ in the second stage.

The experiments at 200 and 210 °C also revealed trends similar to the thin film annealed at 190 °C. Although parallel defects could be observed in the first few images obtained at 190 °C, parallel defects could not be detected in any of the images obtained at 200 and 210 °C. Instead, relatively well-aligned lamellar stripes with scattered dislocation and disclination defects were observed from the earliest images obtained. Unfortunately, the experiment at 200 °C was stopped after 1.5 h of annealing as the drive amplitude required to continue using the microcantilever had exceeded the limits of the AFM system, preventing further analysis. However, for the experiment conducted at 210 °C, defects that appeared in the initial stages of annealing were observed to disappear over time and after 3 h of annealing, defects could no longer be observed in the 4 × 4 μm^2 imaged area. Performing quantitative analyses on the obtained images revealed Ψ_2 started at 0.80 and grew at a slow but steady pace of 0.0007 per min at 200 °C. When plotted against a power law, this yields a scaling factor of $t^{0.04}$, suggesting that the structure exhibits late-stage defect annihilation dynamics, as shown by the first images that showed a structure that is already mostly aligned. In contrast, despite the presence and lack of defects in the first and last images obtained at 210 °C respectively, Ψ_2 was observed to be relatively constant, fluctuating around 0.85 ± 0.01 from the first to the last images obtained at 210 °C. This can likely be attributed to thermal noise that can locally warp imaged areas into wavy sections, detracting the pattern from appearing perfectly longitudinally aligned. If plotted against a power law, this yields a scaling factor of $t^{0.001}$. As the structures were already mostly aligned from the start, with only 2-4 dislocations appearing here and there, the growth rate of the degree of alignment is expectedly low.

Comparing the plots of Ψ_2 against time for each temperature (Fig. 4-6), it is apparent that the degree of ordering in a BCP thin film under the influence of chemically pre-patterned SMART^{TM} process DSA guides exhibits a strong thermal and temporal dependence. The rate of increase in Ψ_2 can change depending on the annealing temperature and even at an isotherm, the rate of increase in Ψ_2 was observed to change over time. While Ψ_2 remained limited at 160 °C due to the low annealing temperature, multiple stages of self-assembly could be observed at 170 and 190 °C, with Ψ_2 increases swiftly earlier in the self-assembly process and slowing down as the system approaches a limit to a maximum Ψ_2. At 200 and 210 °C however, the system tends to fluctuate around a maximum Ψ_2, limited largely by thermal fluctuations that decreases the maximum Ψ_2 attainable.

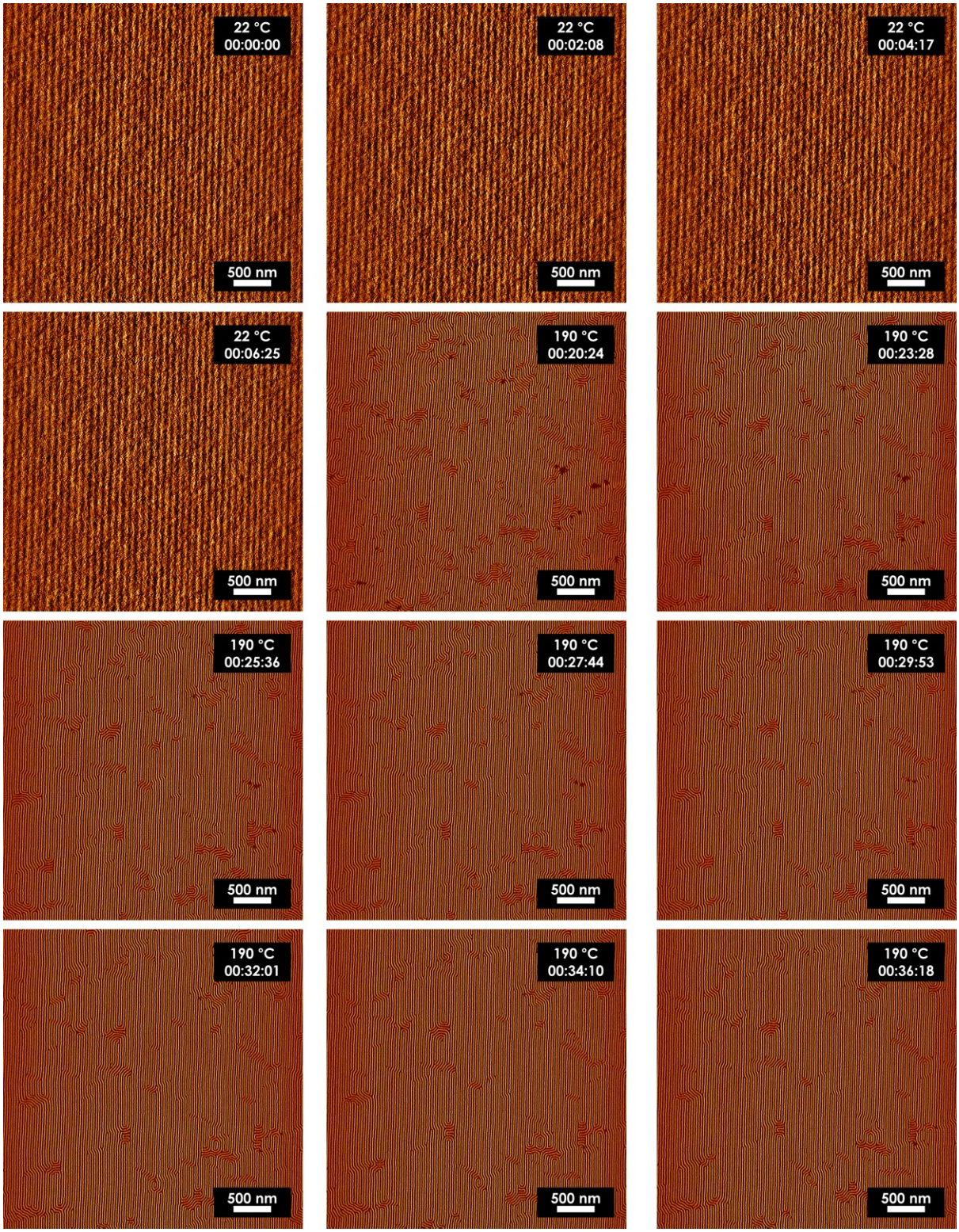


Figure 4-3. Snapshots of the phase images obtained from the isothermal in situ AFM experiment at 190 °C, Part 1.

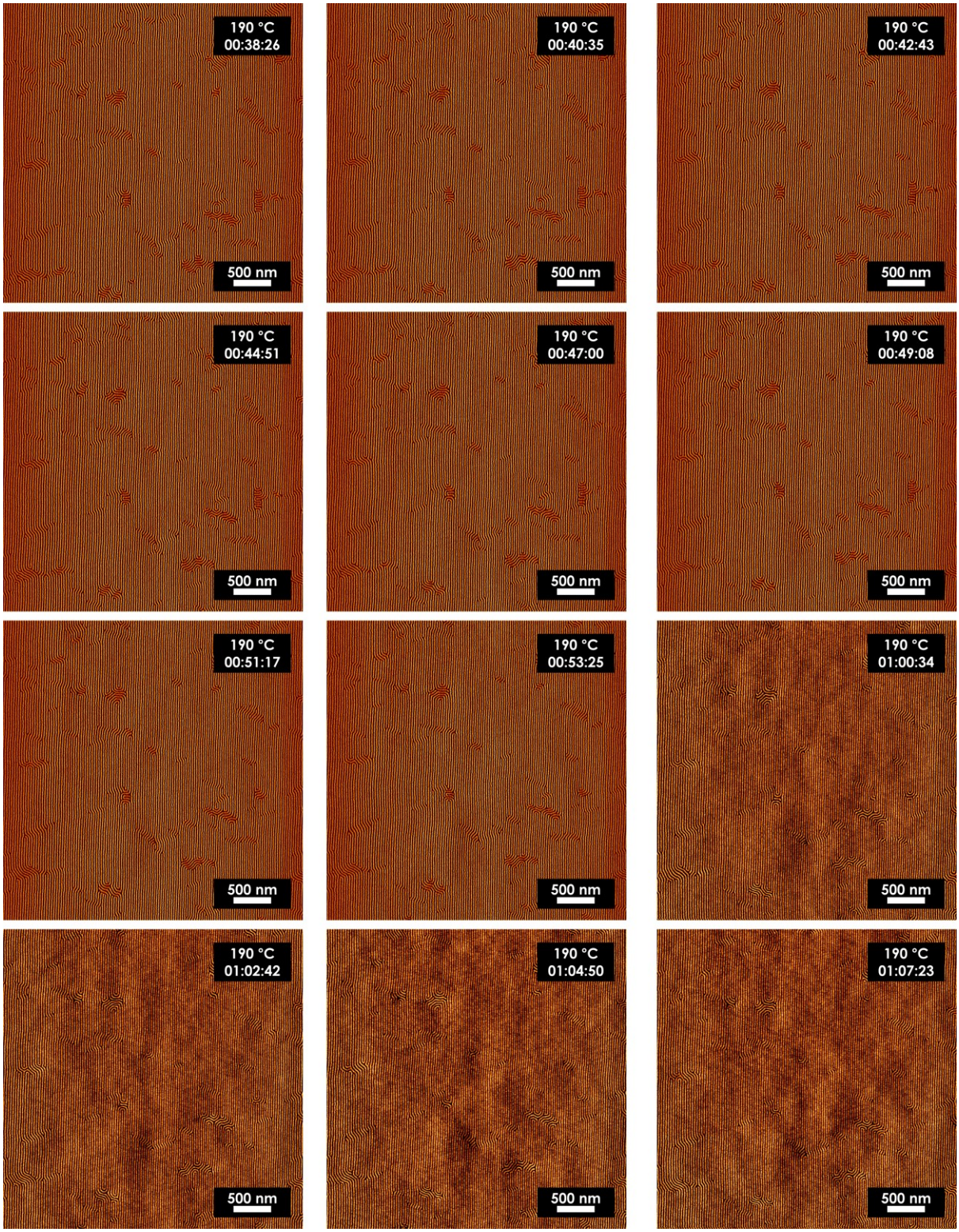


Figure 4-3. Snapshots of the phase images obtained from the isothermal in situ AFM experiment at 190 °C, Part 2.

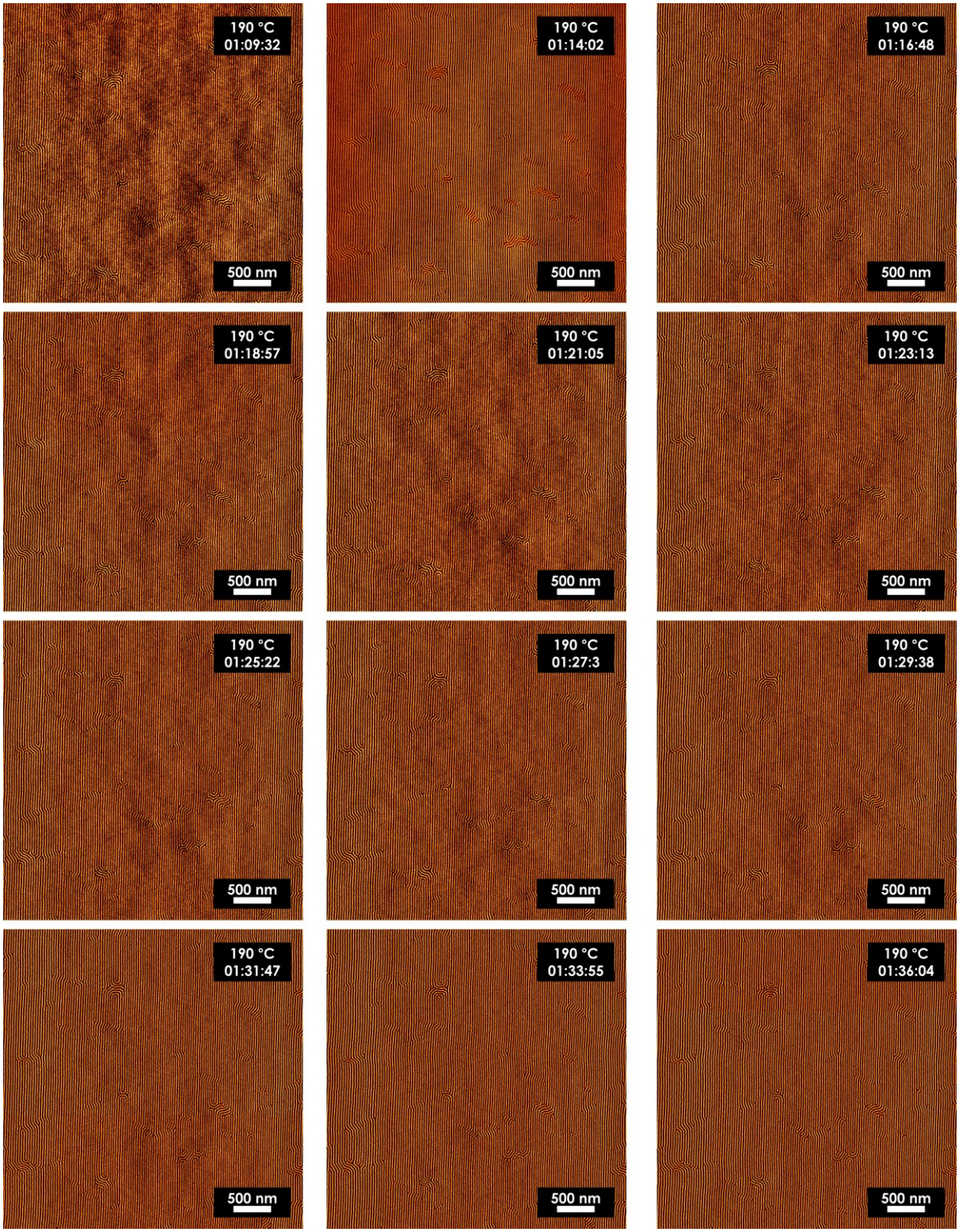


Figure 4-3. Snapshots of the phase images obtained from the isothermal in situ AFM experiment at 190 °C, Part 3.

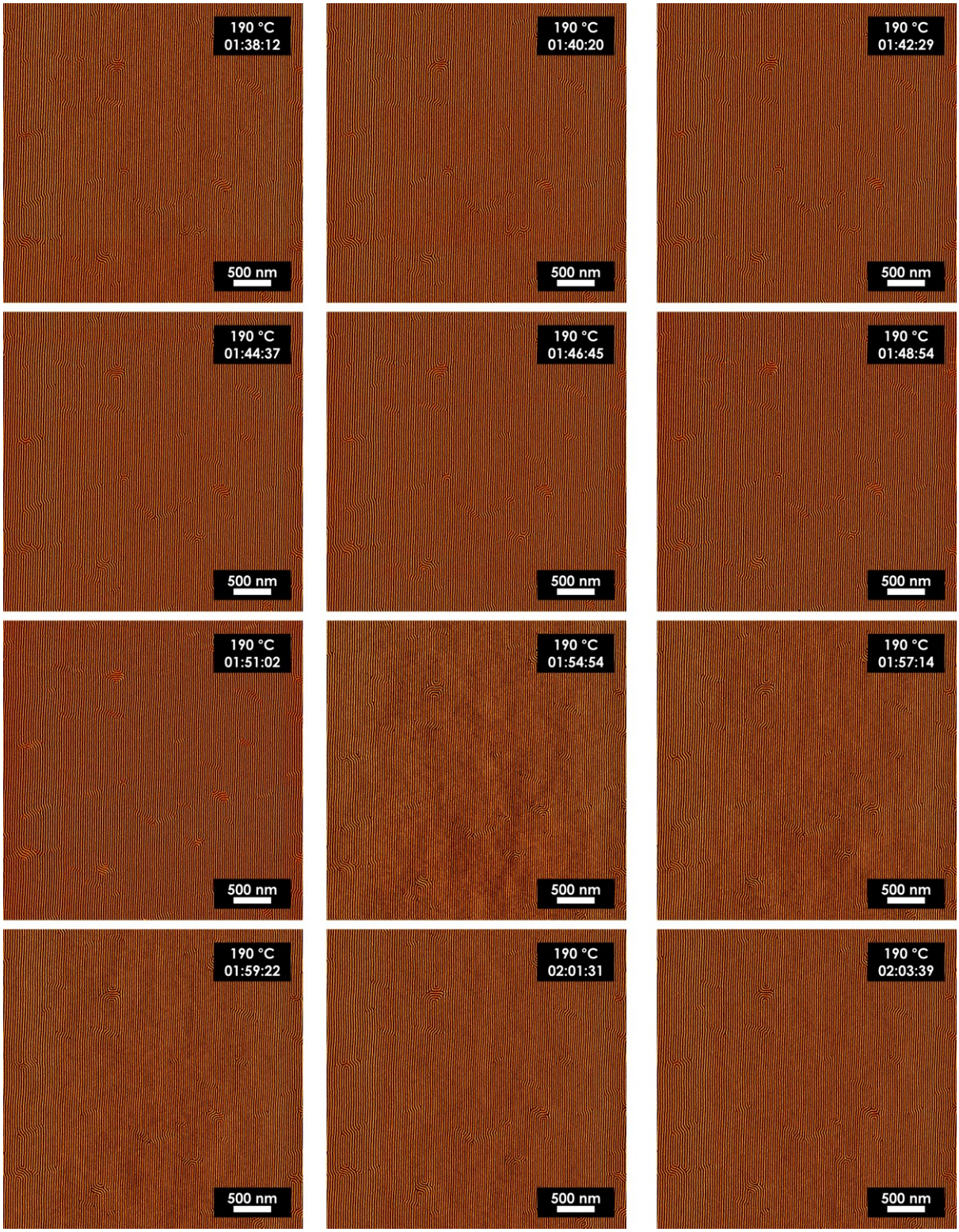


Figure 4-3. Snapshots of the phase images obtained from the isothermal in situ AFM experiment at 190 °C, Part 4.

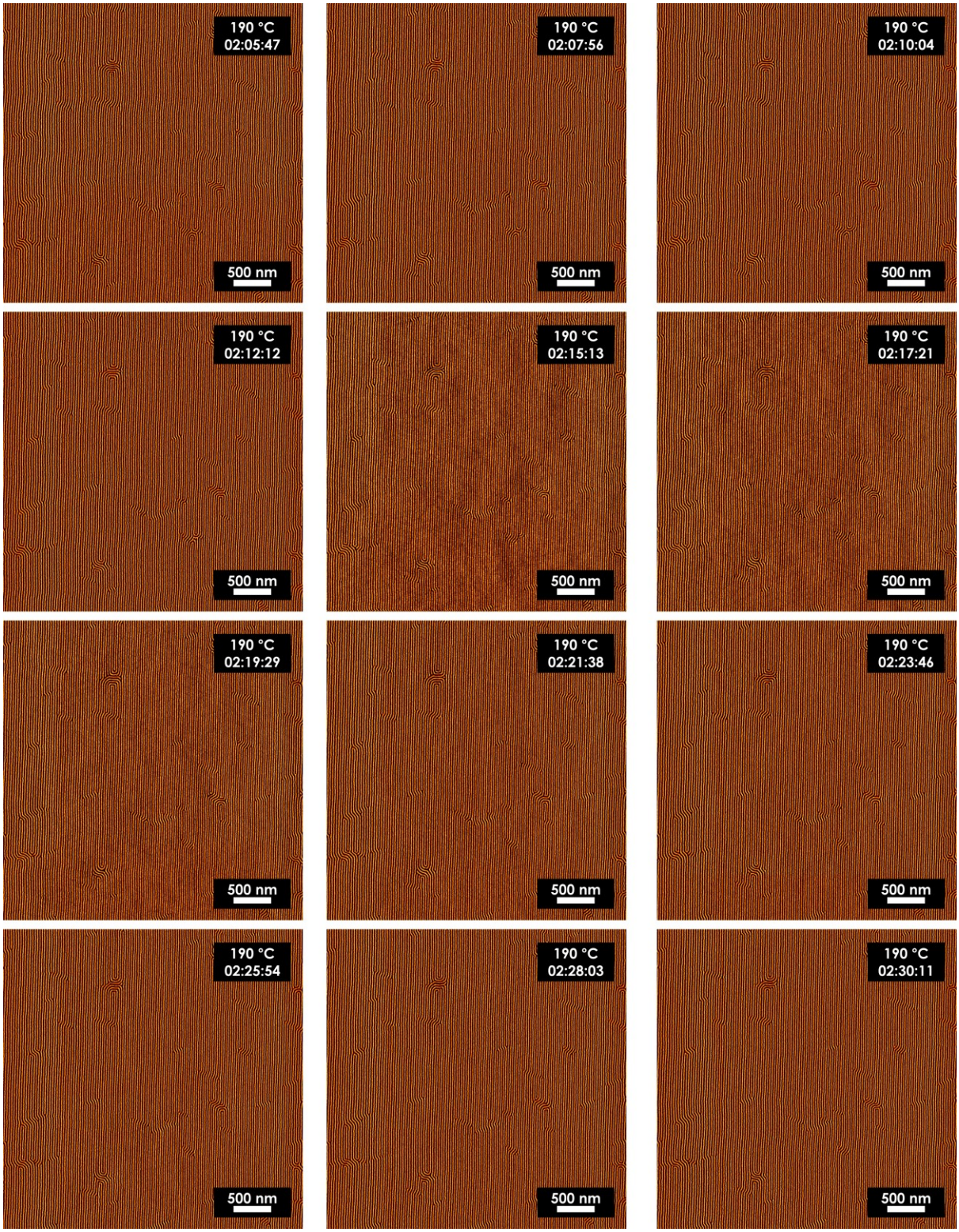


Figure 4-3. Snapshots of the phase images obtained from the isothermal in situ AFM experiment at 190 °C, Part 5.

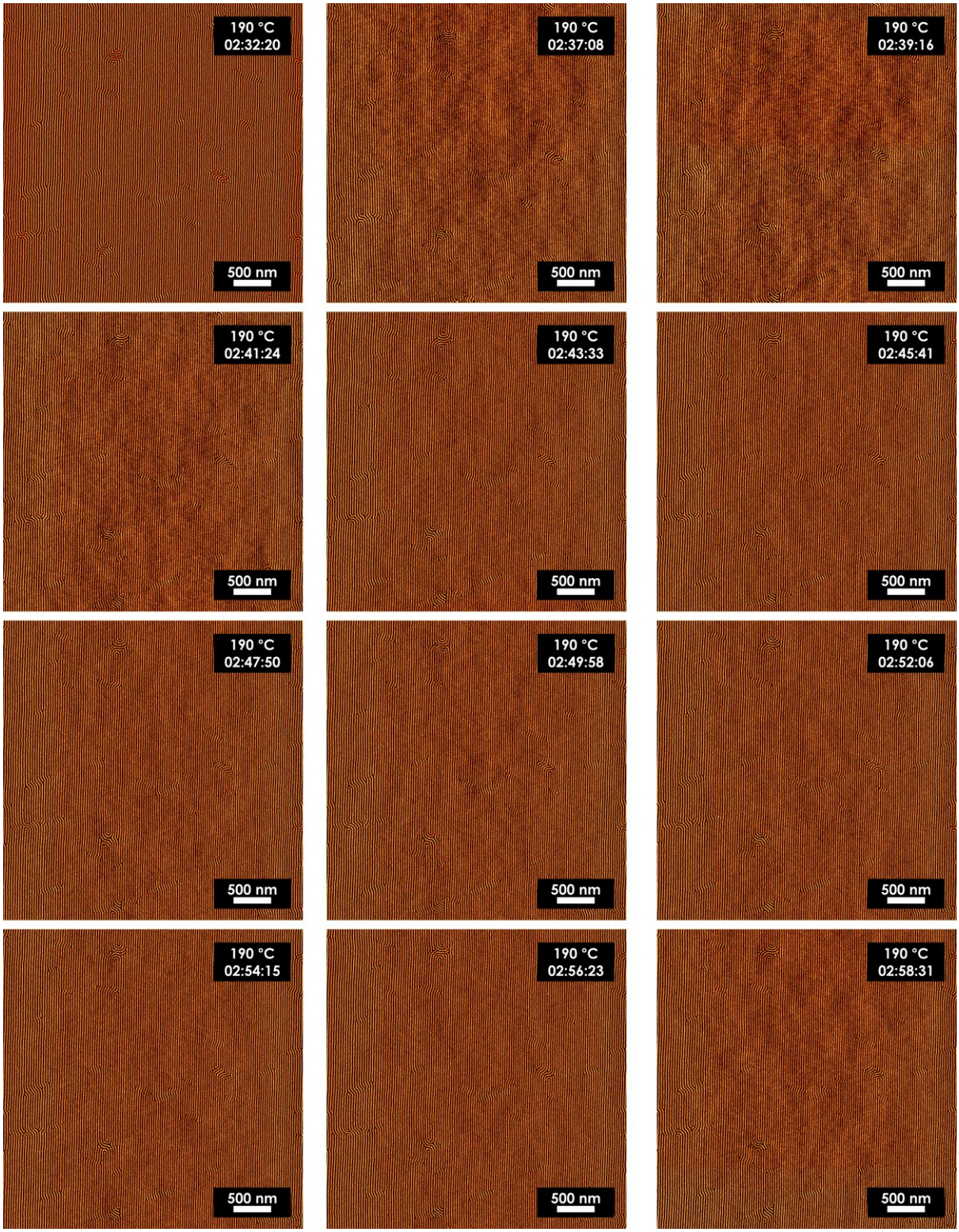


Figure 4-3. Snapshots of the phase images obtained from the isothermal in situ AFM experiment at 190 °C, Part 6.

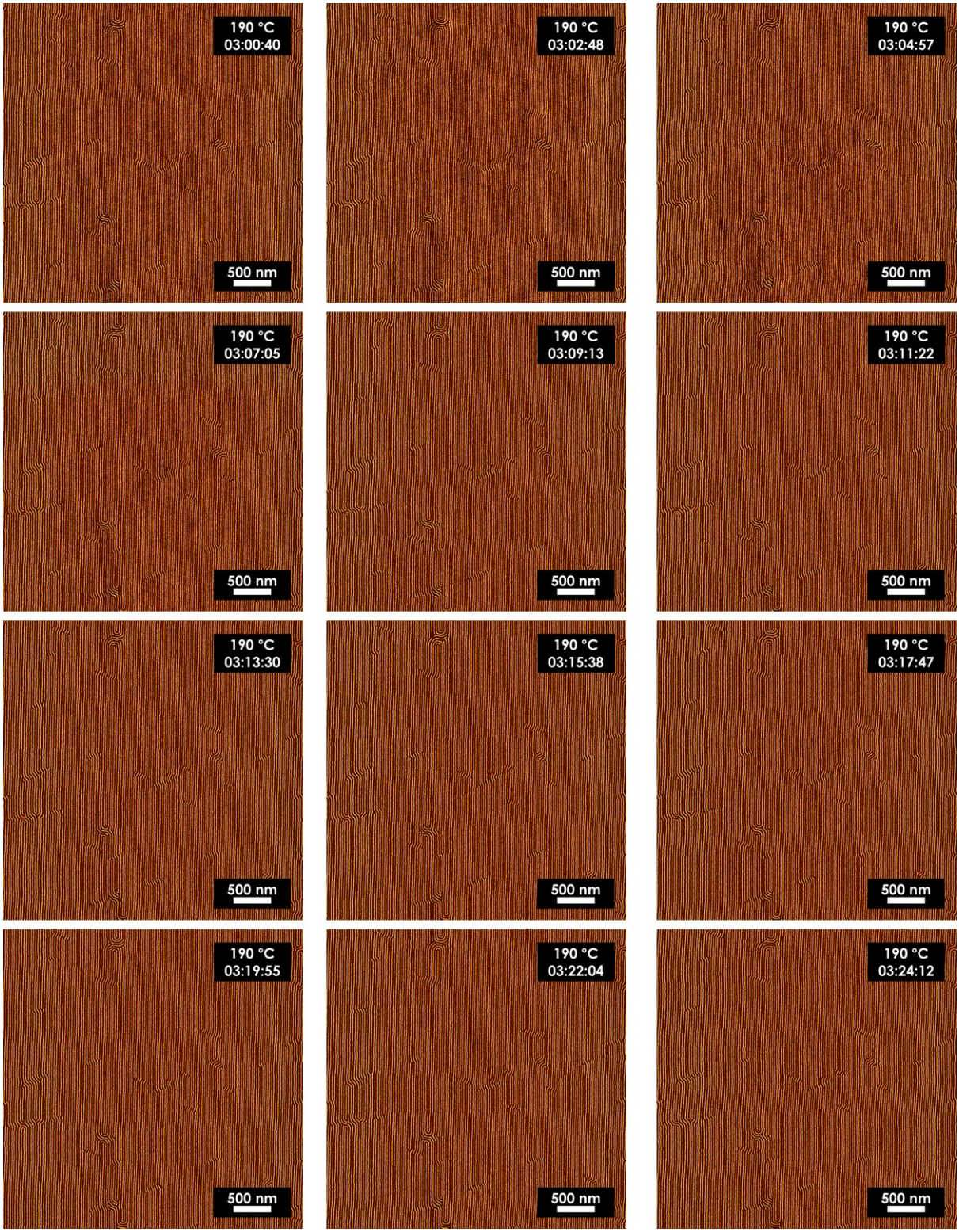


Figure 4-3. Snapshots of the phase images obtained from the isothermal in situ AFM experiment at 190 °C, Part 7.

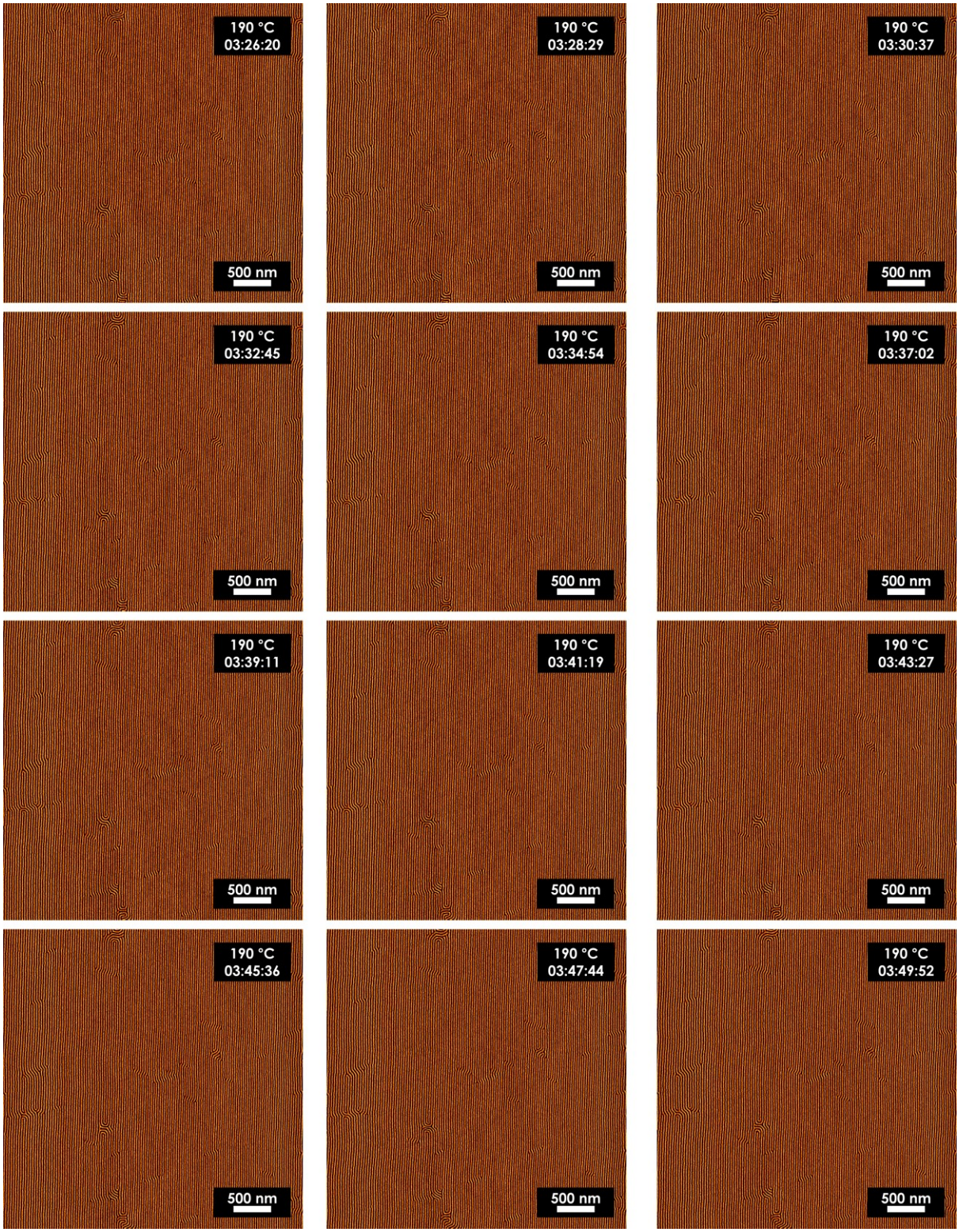


Figure 4-3. Snapshots of the phase images obtained from the isothermal in situ AFM experiment at 190 °C, Part 8.

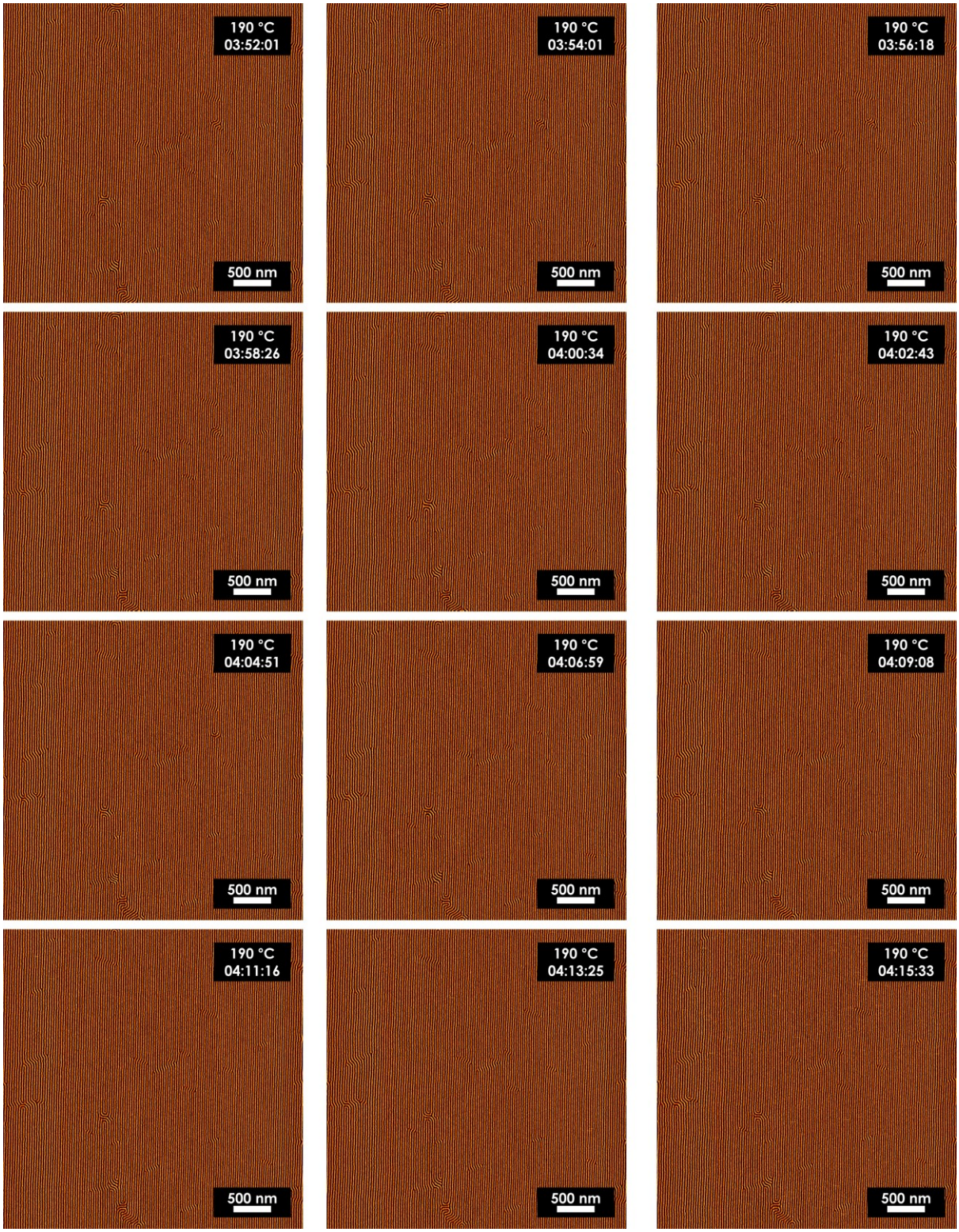


Figure 4-3. Snapshots of the phase images obtained from the isothermal in situ AFM experiment at 190 °C, Part 9.

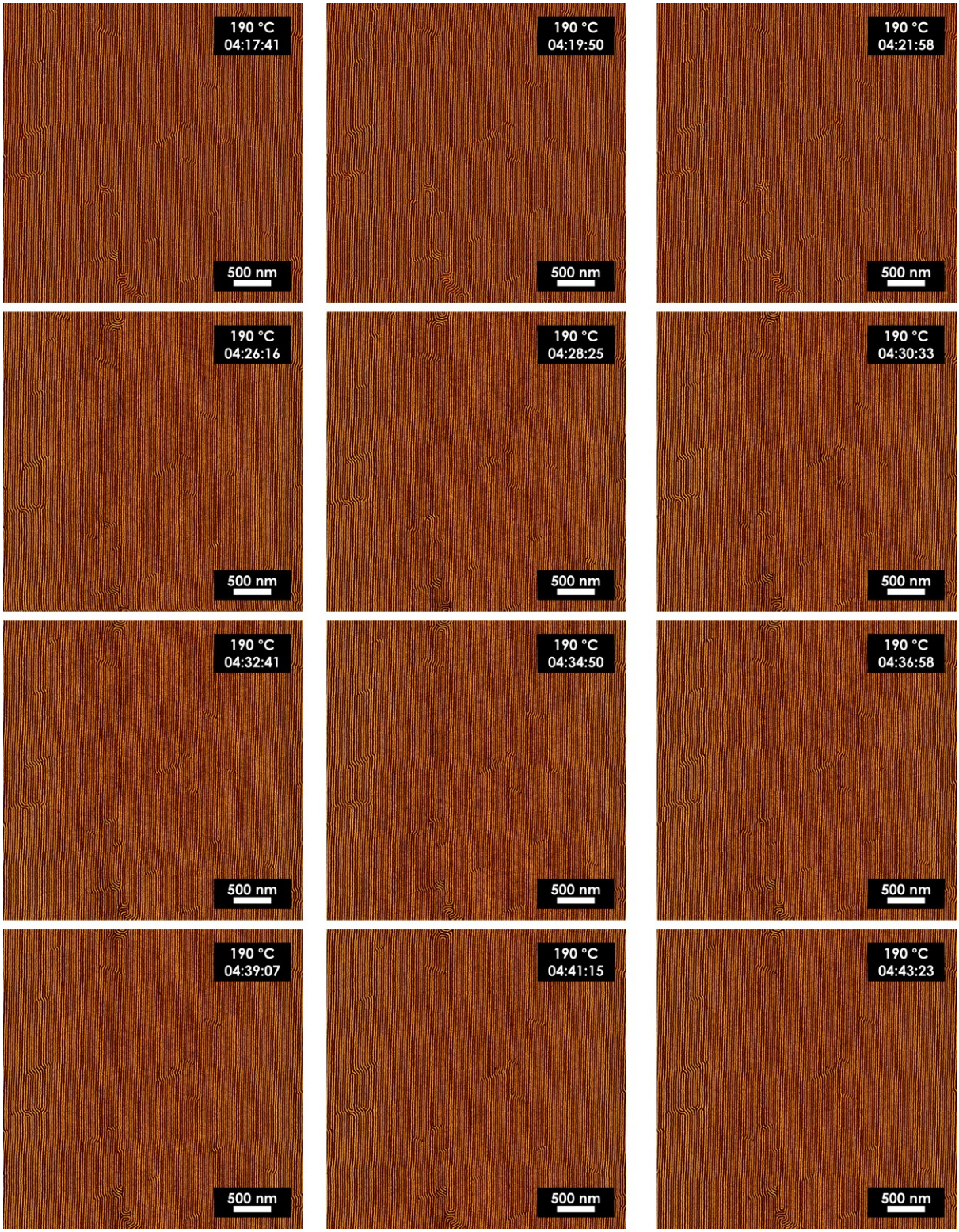


Figure 4-3. Snapshots of the phase images obtained from the isothermal in situ AFM experiment at 190 °C, Part 10.

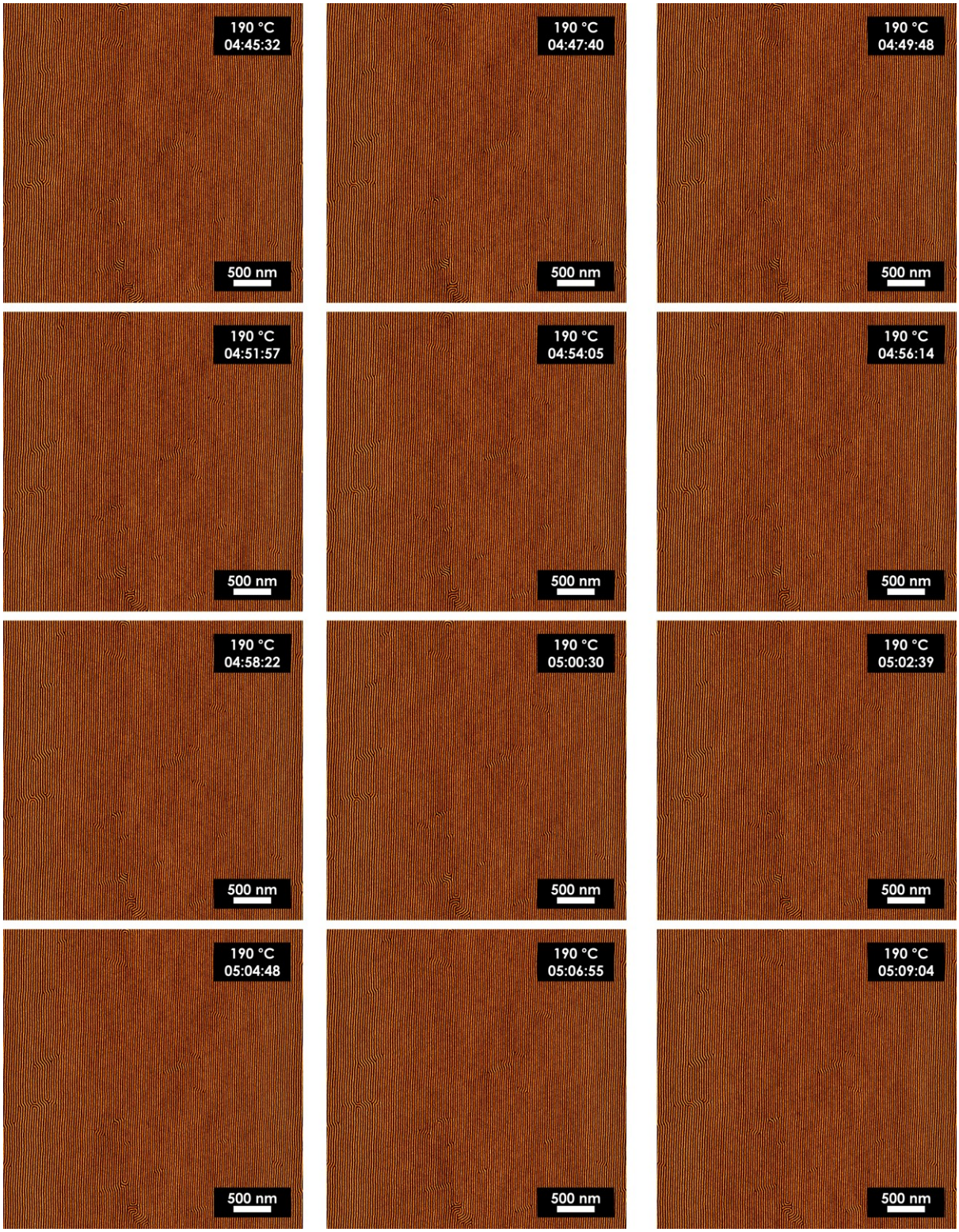


Figure 4-3. Snapshots of the phase images obtained from the isothermal in situ AFM experiment at 190 °C, Part 11.

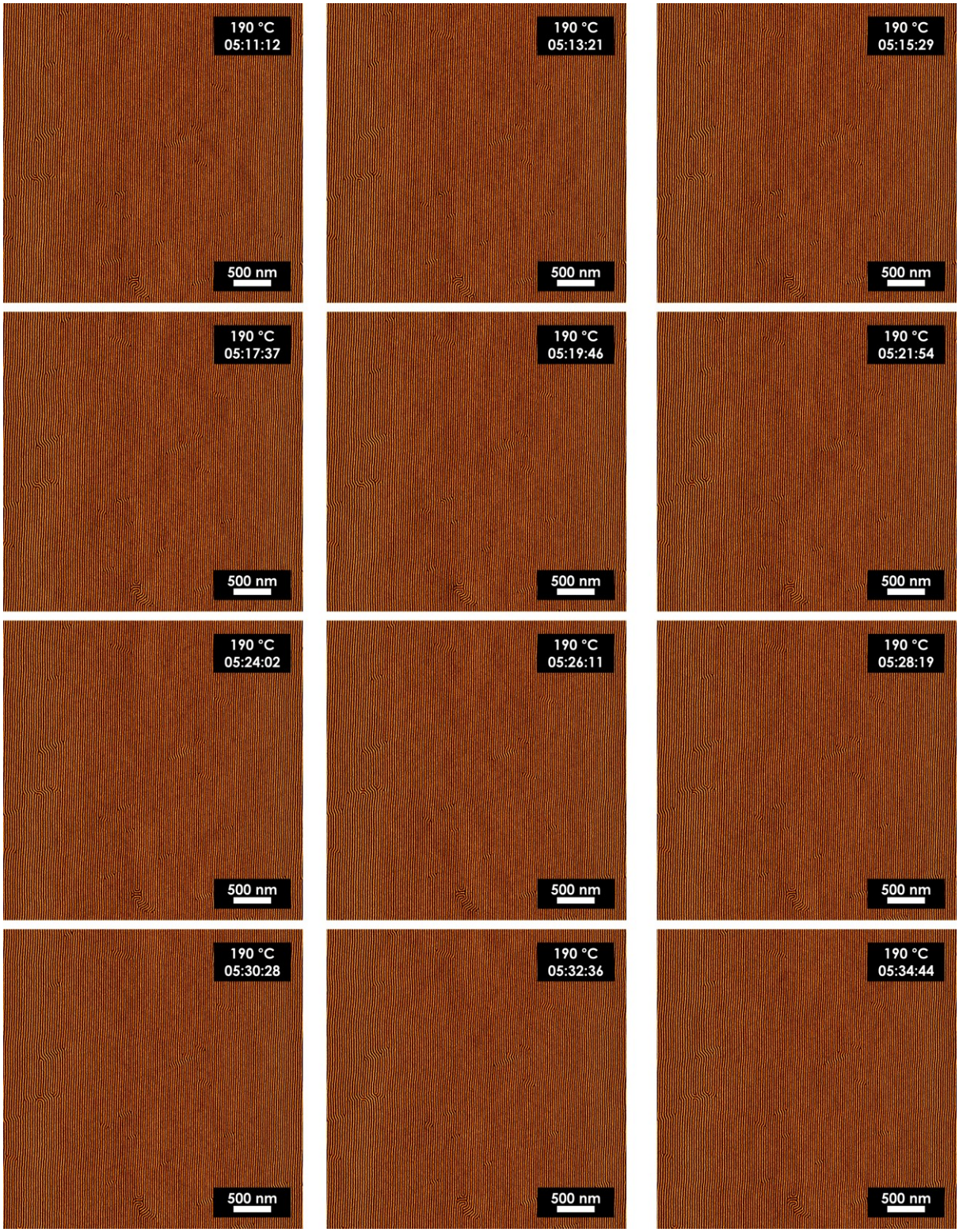


Figure 4-3. Snapshots of the phase images obtained from the isothermal in situ AFM experiment at 190 °C, Part 12.

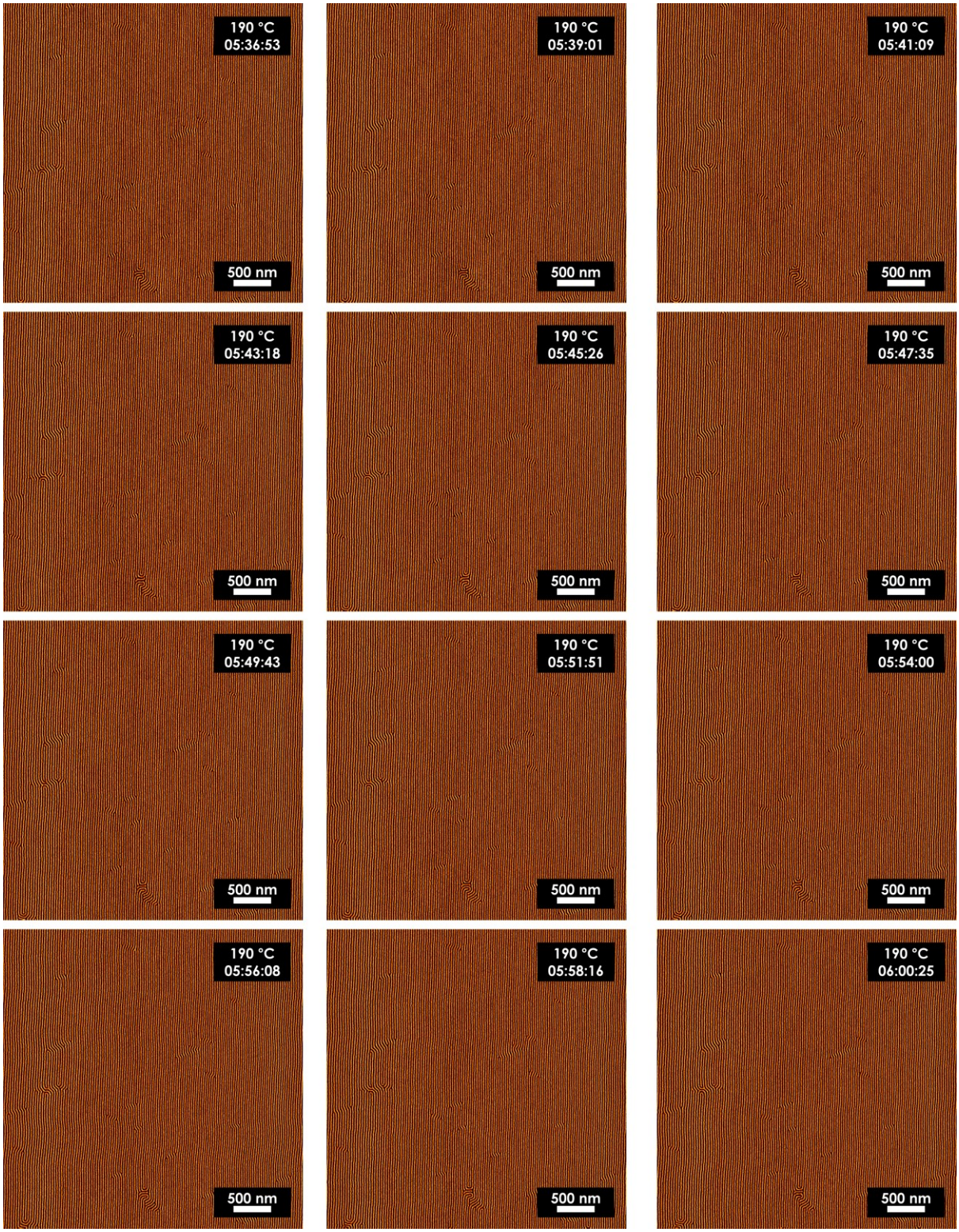


Figure 4-3. Snapshots of the phase images obtained from the isothermal in situ AFM experiment at 190 °C, Part 13.



Figure 4-3. Snapshots of the phase images obtained from the isothermal in situ AFM experiment at 190 °C, Part 14.

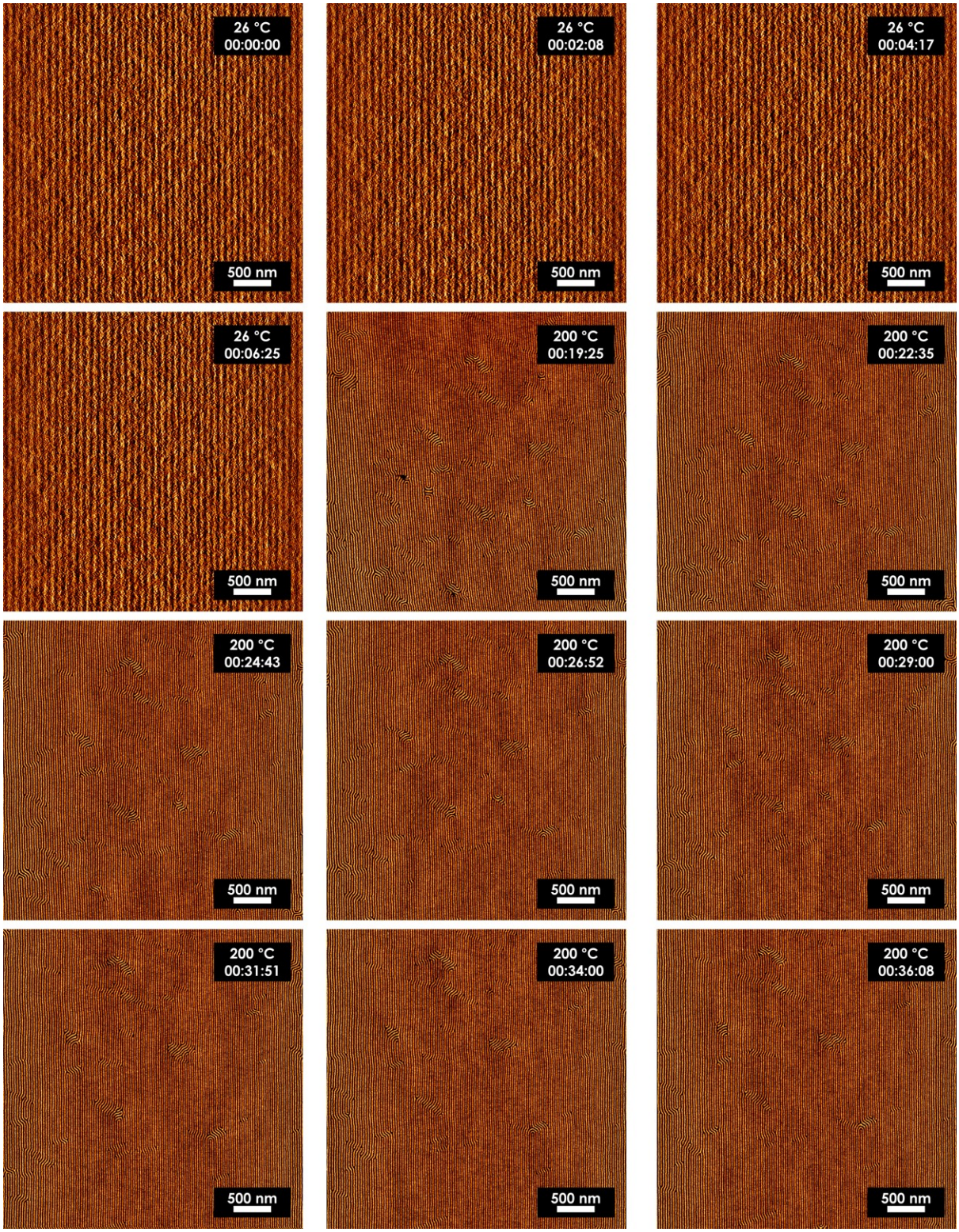


Figure 4-4. Snapshots of the phase images obtained from the isothermal in situ AFM experiment at 200 °C, Part 1.

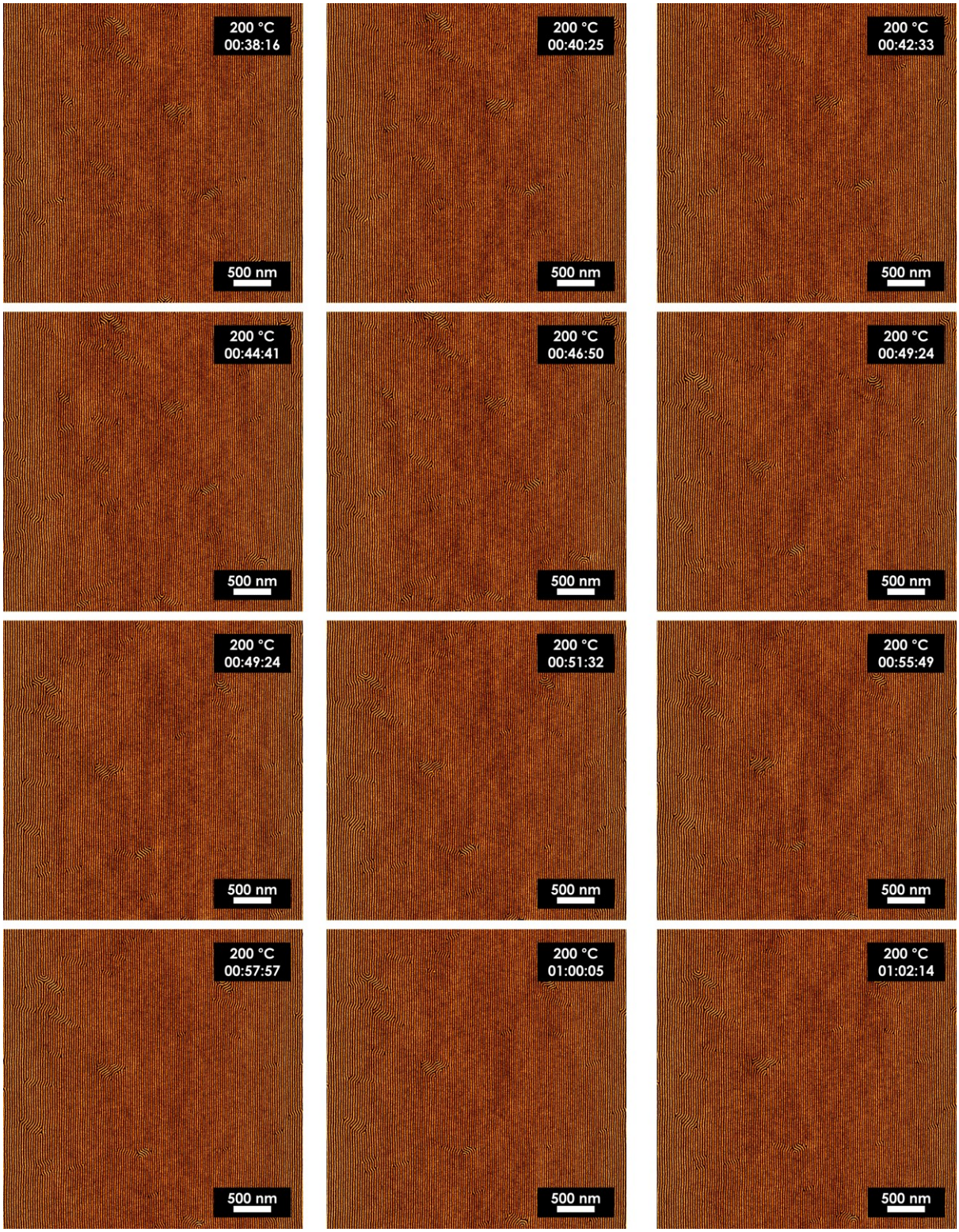


Figure 4-4. Snapshots of the phase images obtained from the isothermal in situ AFM experiment at 200 °C, Part 2.



Figure 4-4. Snapshots of the phase images obtained from the isothermal in situ AFM experiment at 200 °C, Part 3.

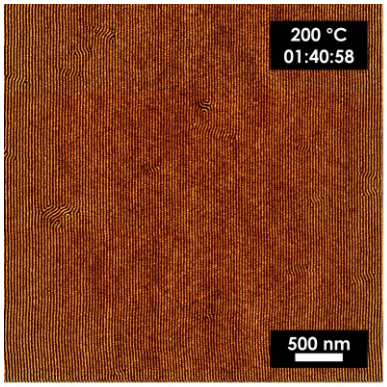


Figure 4-4. Snapshots of the phase images obtained from the isothermal in situ AFM experiment at 200 °C, Part 4.

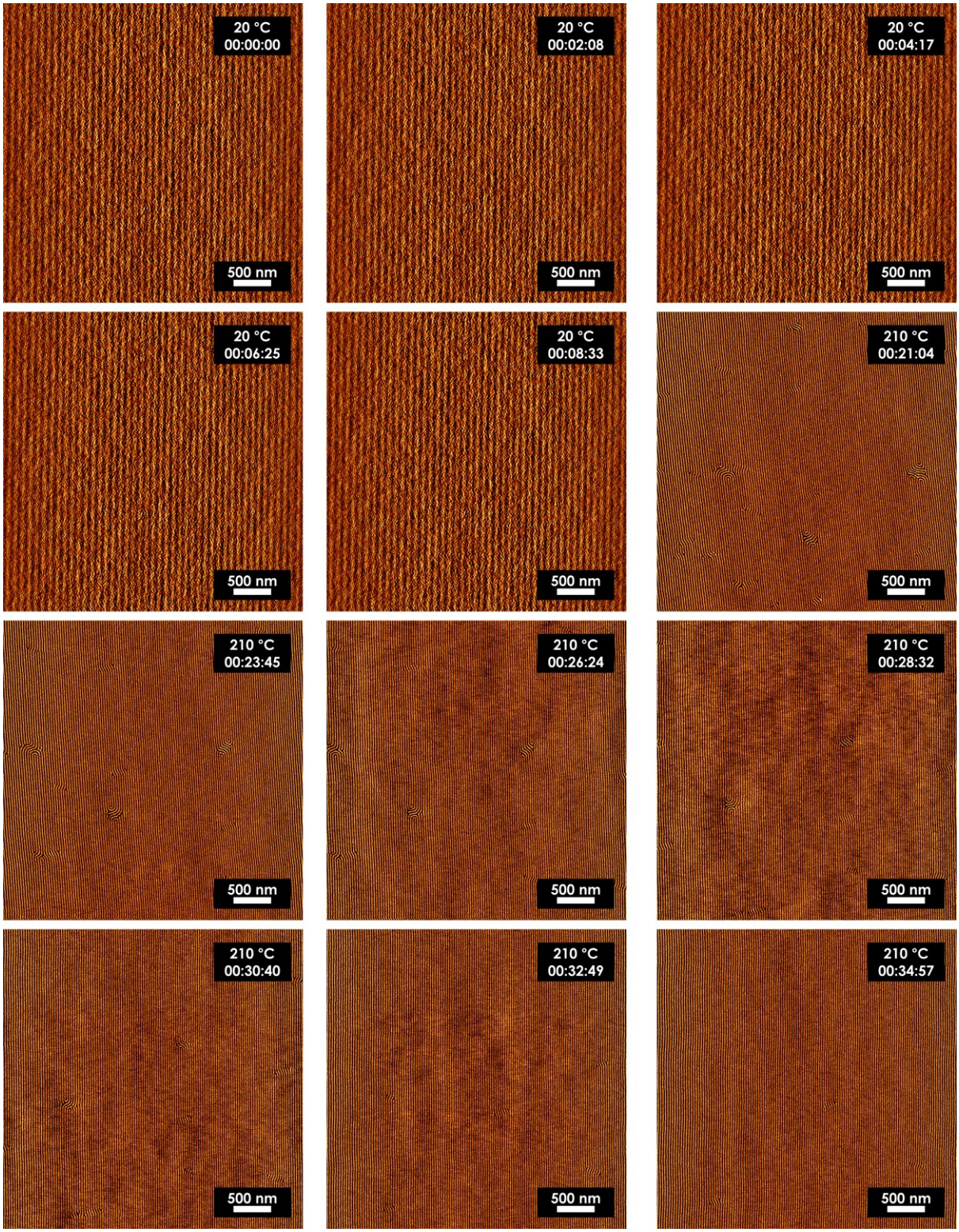


Figure 4-5. Snapshots of the phase images obtained from the isothermal in situ AFM experiment at 210 °C, Part 1.

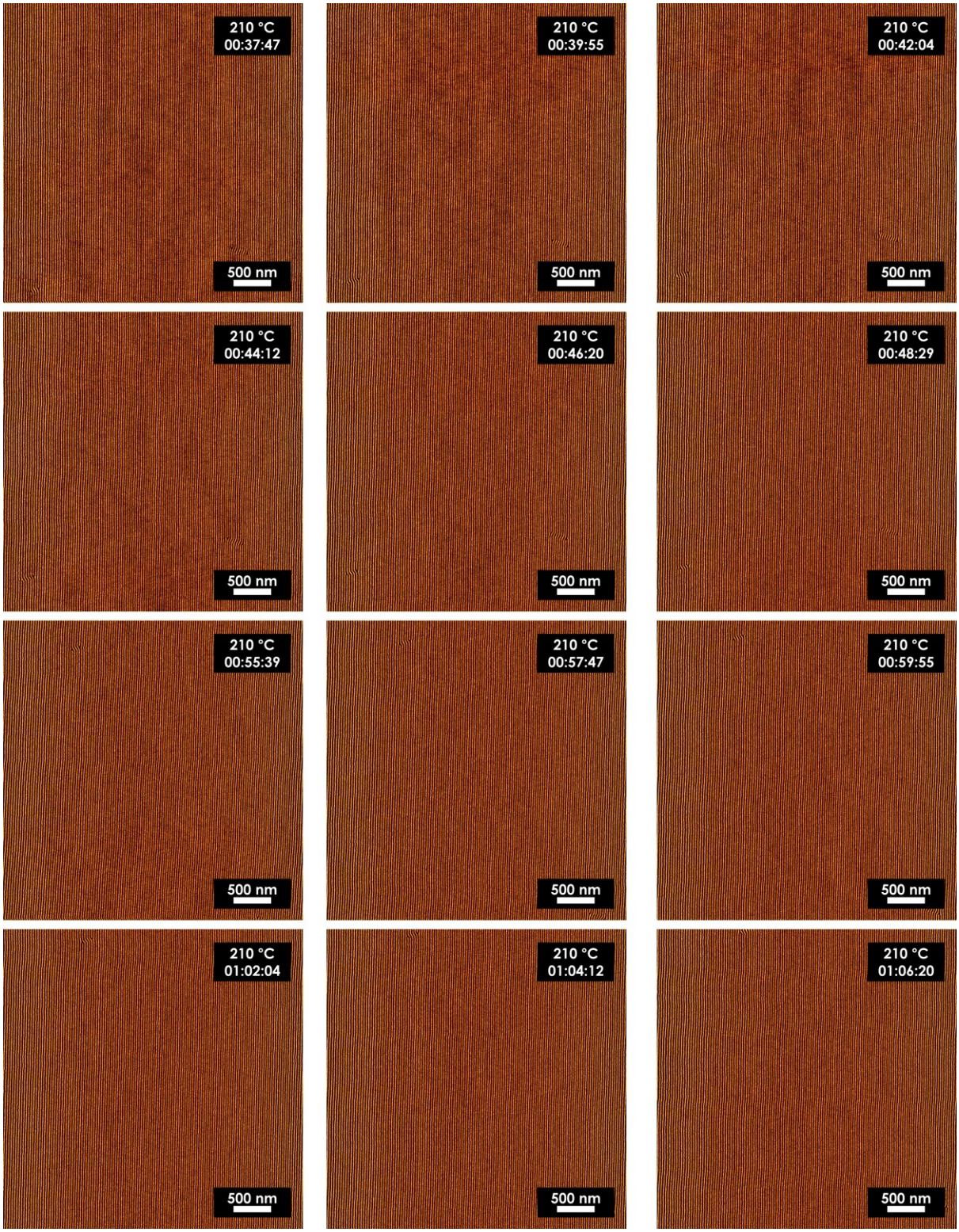


Figure 4-5. Snapshots of the phase images obtained from the isothermal in situ AFM experiment at 210 °C, Part 2.

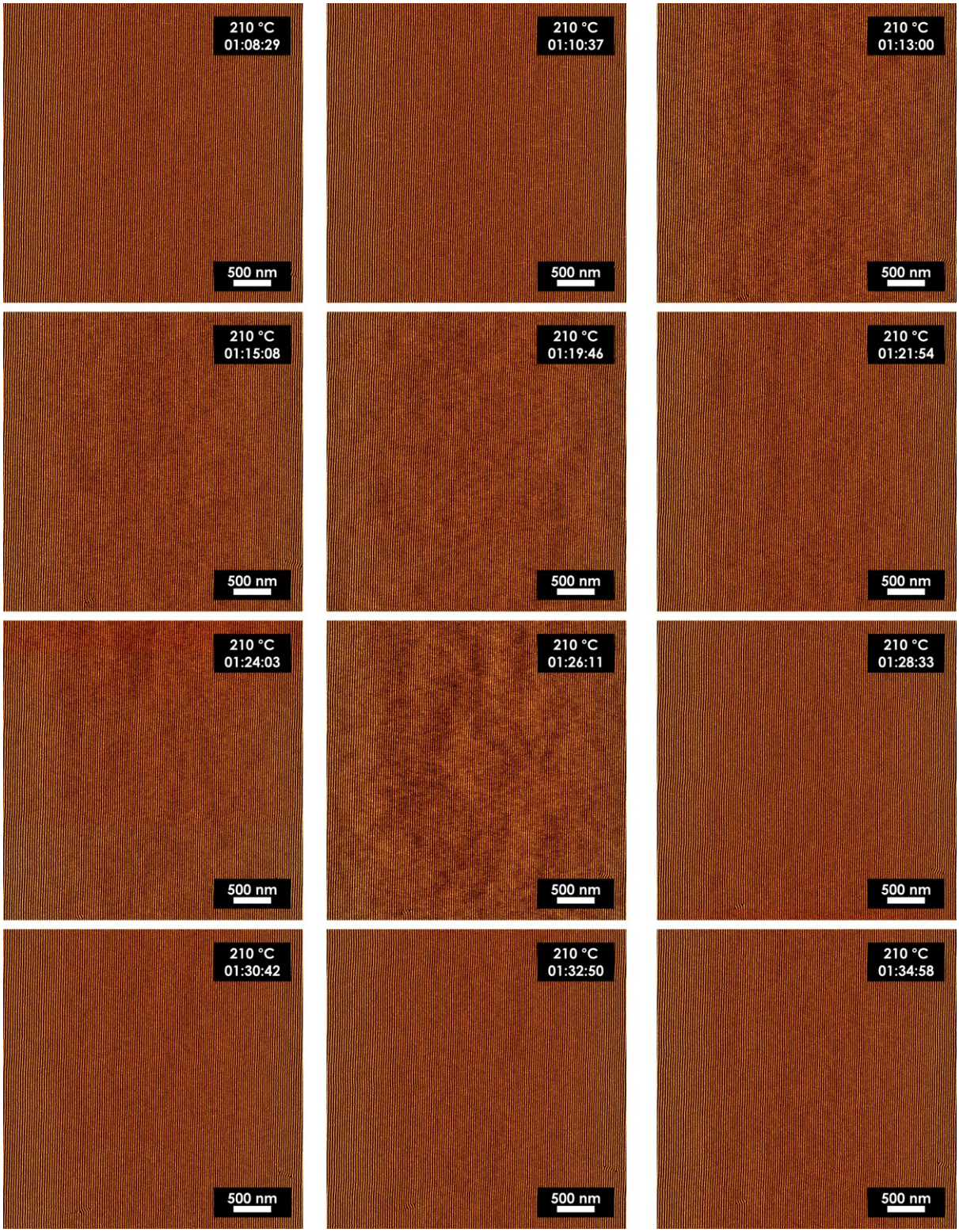


Figure 4-5. Snapshots of the phase images obtained from the isothermal in situ AFM experiment at 210 °C, Part 3.



Figure 4-5. Snapshots of the phase images obtained from the isothermal in situ AFM experiment at 210 °C, Part 4.



Figure 4-5. Snapshots of the phase images obtained from the isothermal in situ AFM experiment at 210 °C, Part 5.



Figure 4-5. Snapshots of the phase images obtained from the isothermal in situ AFM experiment at 210 °C, Part 6.

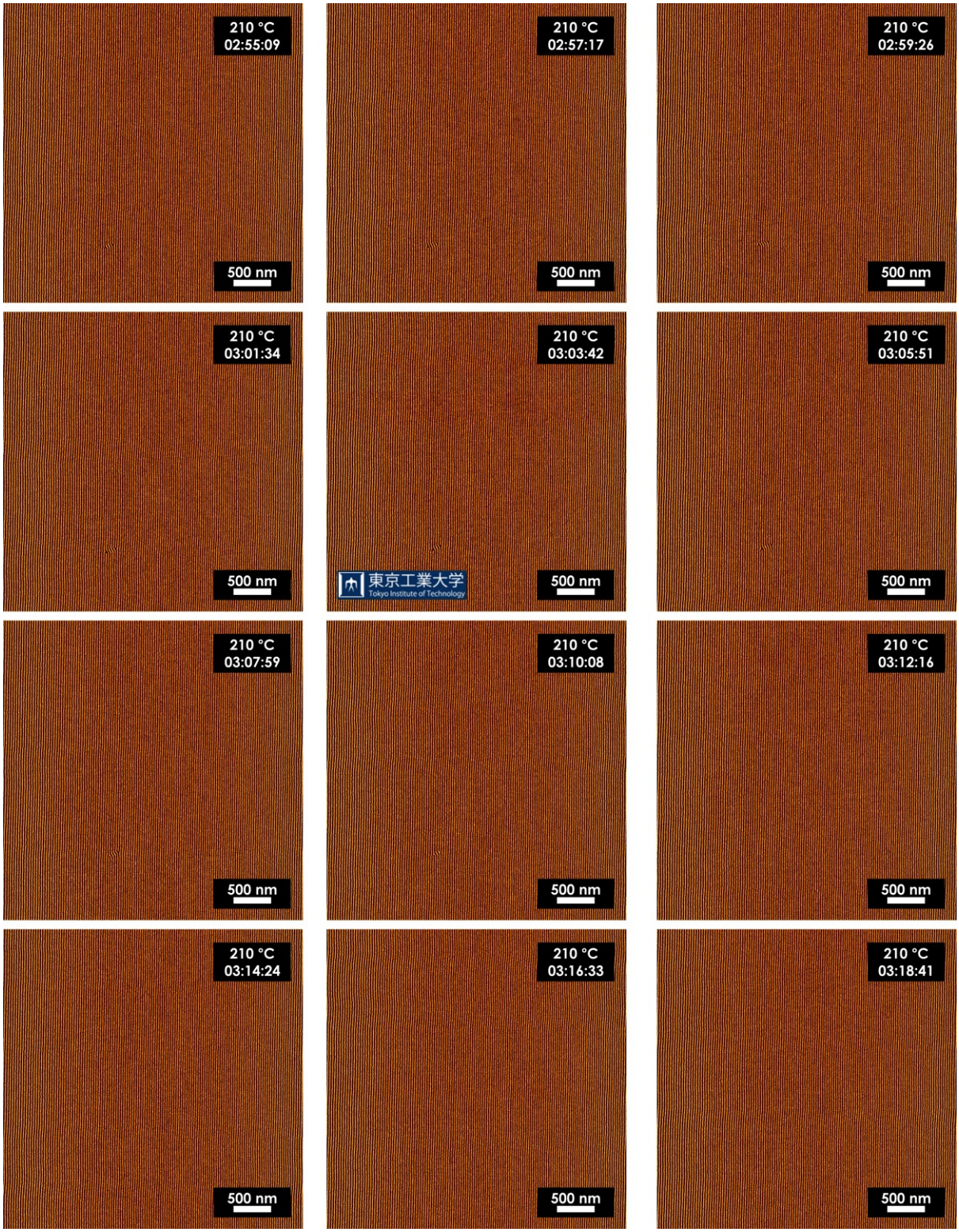


Figure 4-5. Snapshots of the phase images obtained from the isothermal in situ AFM experiment at 210 °C, Part 7.

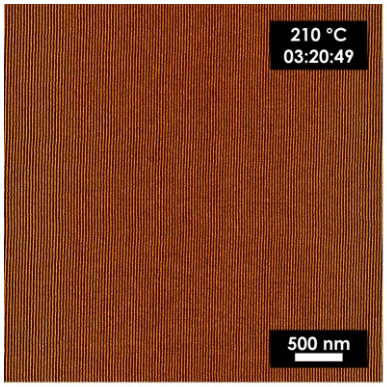


Figure 4-5. Snapshots of the phase images obtained from the isothermal in situ AFM experiment at 210 °C, Part 8.

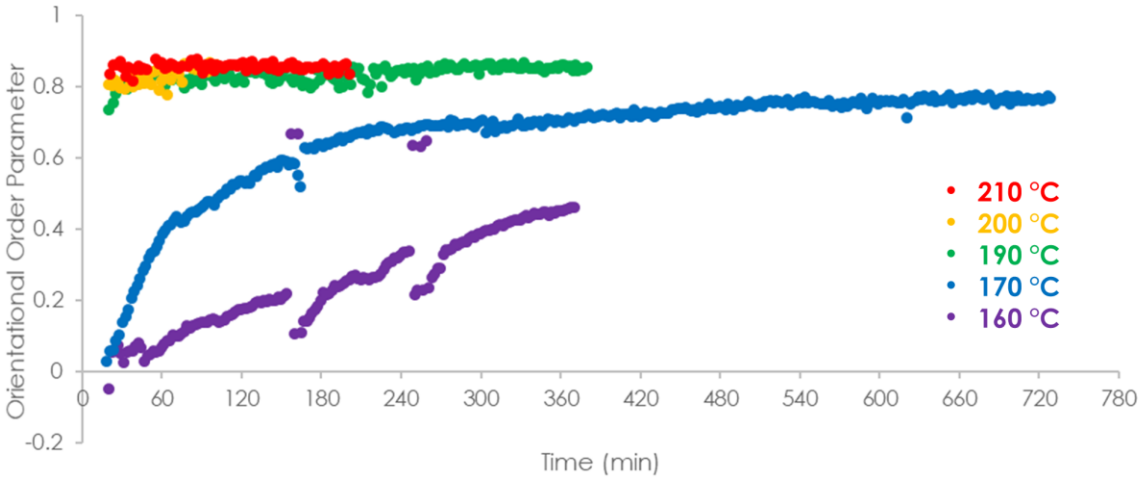


Figure 4-6. Plot of the orientational order parameter (Ψ_2) against time estimated for each frame obtained in the isothermal in situ AFM experiments.

4-3-3 Defect Evolution and Annihilation Pathways

Based on the isothermal in situ AFM experiments, four general categories of defects (Fig. 4-7) could be identified in the self-assembly process of perpendicular lamellae on chemically pre-patterned SMART^{TM} process DSA substrates. Firstly, one major defect category is the orientation of the microdomains relative to the substrate. Although lamellar microdomains oriented perpendicularly, or normal to the substrate, with both domains wetting the substrate simultaneously, the presence of defects in the form of parallel lamellae with selective wetting of the PS domain onto both the substrate and the free surface could be observed. Patches of ladder-shaped structures akin to “stitch” morphological defects

could also be occasionally observed. Additionally, as is common in any material with 2D symmetry, disclination and dislocation defects form the majority of the defects observed in the lamellar striped patterns. Finally, “transitional” defects that cannot be categorized as traditional disclination or dislocation defects could be observed as the microdomains link up and break apart stochastically.

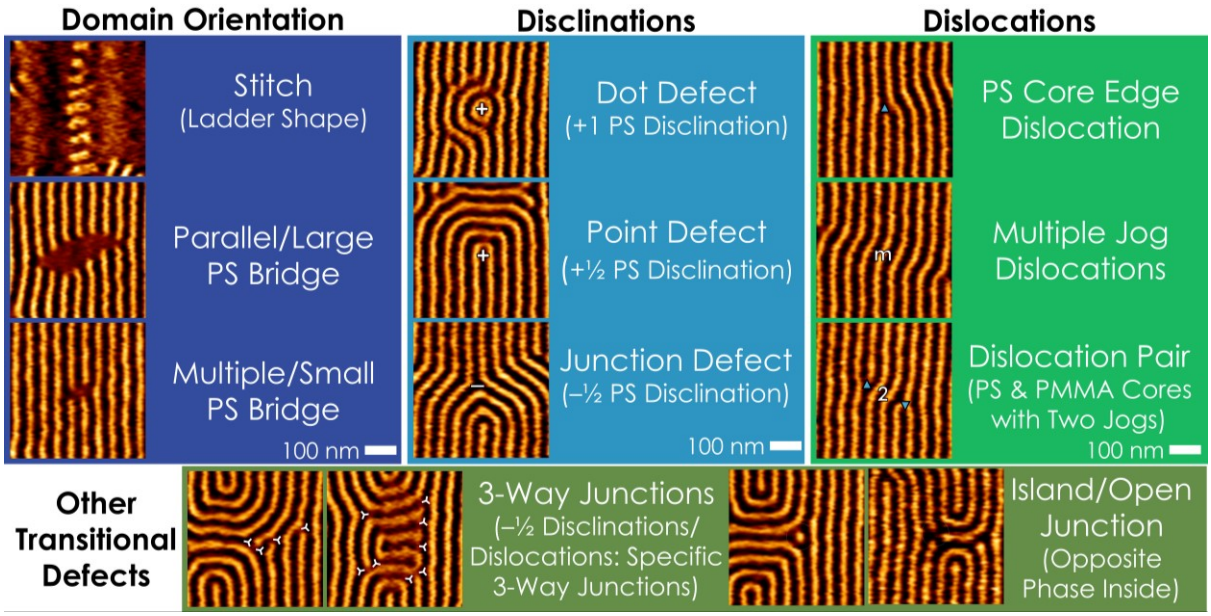


Figure 4-7. Collection of AFM phase images representing each category and type of defect found in the self-assembly of PS-*b*-PMMA on chemically pre-patterned SMART™ process DSA substrates.

4-3-4 Orientational Defects

Typically, orientational defects are simply layers of lamellae oriented parallel relative to the substrate. The orientation control of such parallel defects has been a longstanding challenge and the causes behind the formation of parallel defects have become relatively clear. When the substrate and/or free interface exhibits preferential affinities toward one block, the selective segregation of that block forms a wetting layer that induces the formation of parallel structures. In the case of PS-*b*-PMMA, a random copolymer of PS-*r*-PMMA is typically installed on the substrate to eliminate preferential interactions with the BCP. However, the surface free energies (SFEs) of the two blocks are slightly different, at 40.7 and 41.4 mJ m^{-2} for PS and PMMA, respectively at 20 °C.[23] Therefore, even if the substrate

fulfills the neutrality condition required for perpendicular orientation, the free interface can also exhibit preferential affinities towards one block. While the surface free energies of PS and PMMA cross over at approximately 170 °C when measured in the melt using the pendant drop method, Russell and co-workers revealed that on thin films, PS tends to segregate to the free interface at temperatures below 200 °C.[24] From this result, they suggested that the free interface in thin films is slightly preferential towards PS at lower temperatures but approaches neutrality at 200 °C, as both PS and PMMA become present in equal amounts at the surface.

In this study, parallel orientation defects could be observed on the surfaces of the thin films imaged at all times at 160 and 170 °C, and only in the first few images obtained at 190 °C. At 200 and 210 °C however, parallel orientation defects could not be detected in any image. This is in line with the early studies of the surface segregation of PS at lower temperatures. Since the free interface is slightly preferential towards PS at temperatures below 200 °C and local interactions dominate at the onset of self-assembly,[24,25] the appearance of patches of parallel orientation defects in the first images taken during the experiments annealed below 200 °C. However, the patches of parallel orientation defects eventually grew in size as annealing continued at 160 °C, suggesting that the PS preferential effects of the free interface dominate on the thin film, leading to a slow but gradual transformation from an initially mixed orientation state towards increased parallel orientation. On the other hand, while annealing at 170 °C led to an initial growth of grains with both perpendicular and parallel orientation, the parallel orientation defects were observed to annihilate slowly over time, starting with the patches of smaller size. The annihilation pathway of a representative parallel orientation defect is shown in Figure 4-8. The strange growth of patches parallel orientation defects at 160 °C has not been reported for other DSA processes, likely because “negative” results go unreported and also because in recent years, PS-*b*-PMMA is typically annealed at temperatures higher than 190 °C to accelerate the annealing process.

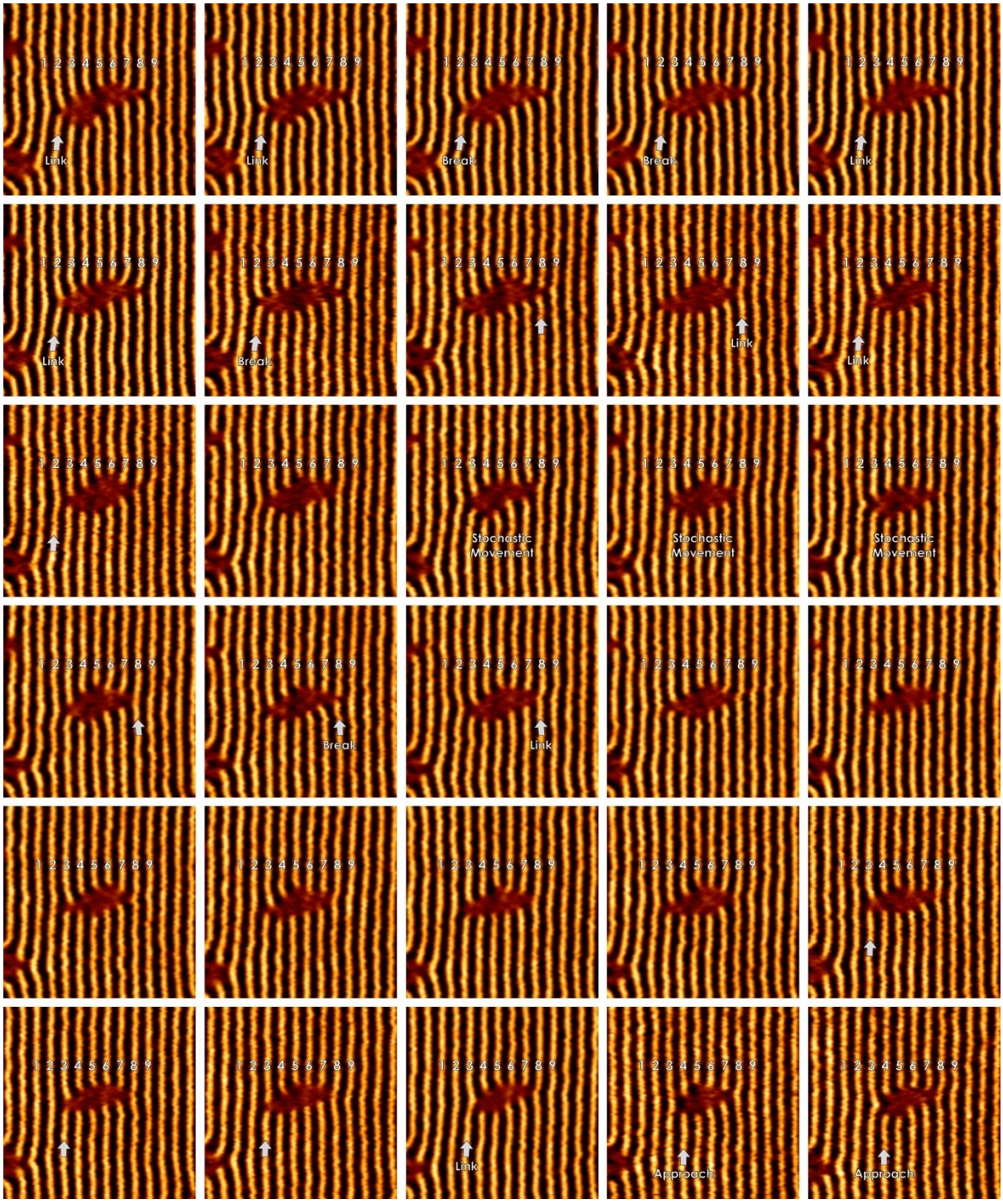


Figure 4-8. Phase images detailing the annihilation pathway of a representative parallel orientation defect obtained at 170 °C from *t* = 03:40:13 to 06:16:48, Part 1.

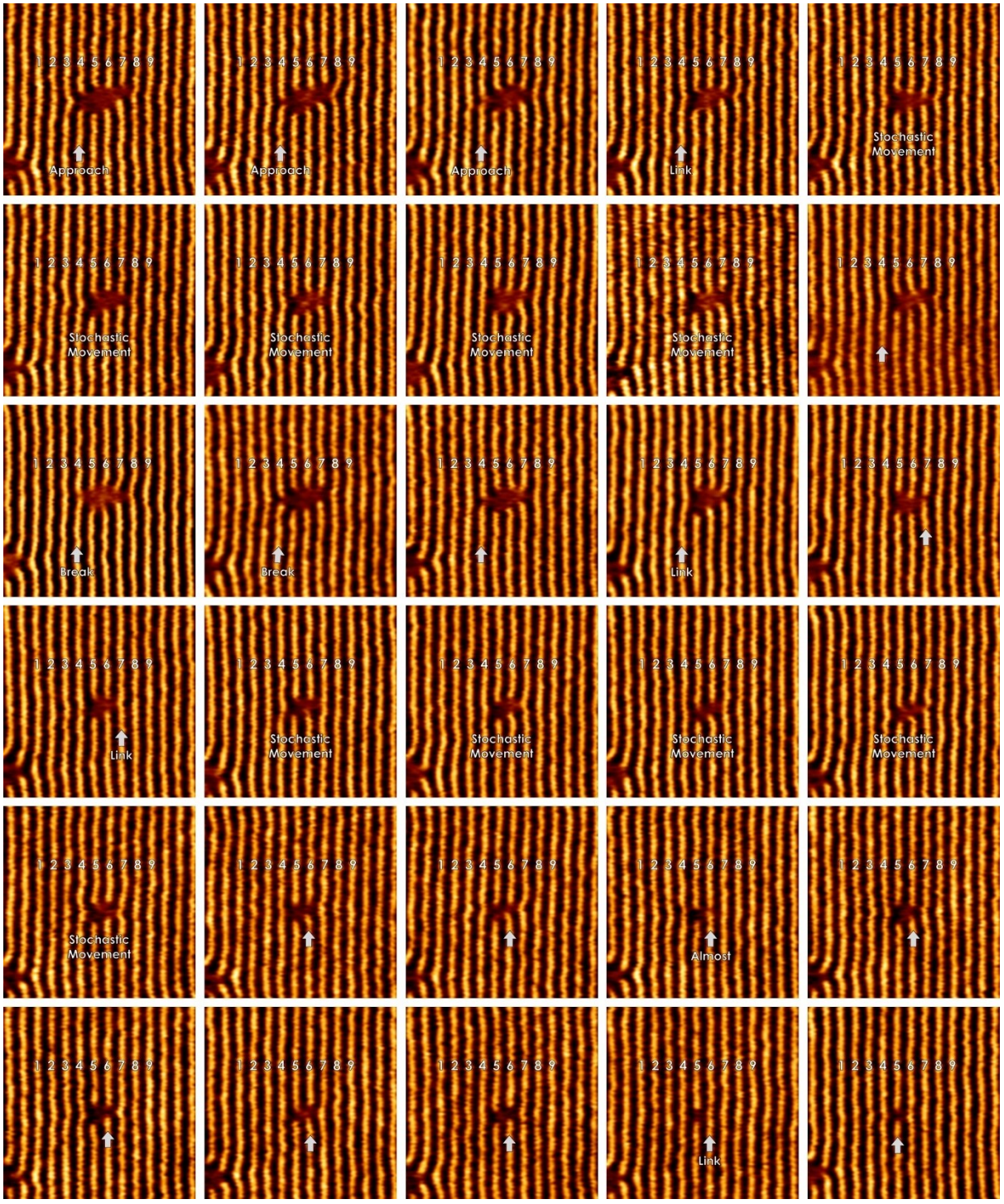


Figure 4-8. Phase images detailing the annihilation pathway of a representative parallel orientation defect obtained at 170 °C from *t* = 03:40:13 to 06:16:48, Part 2.

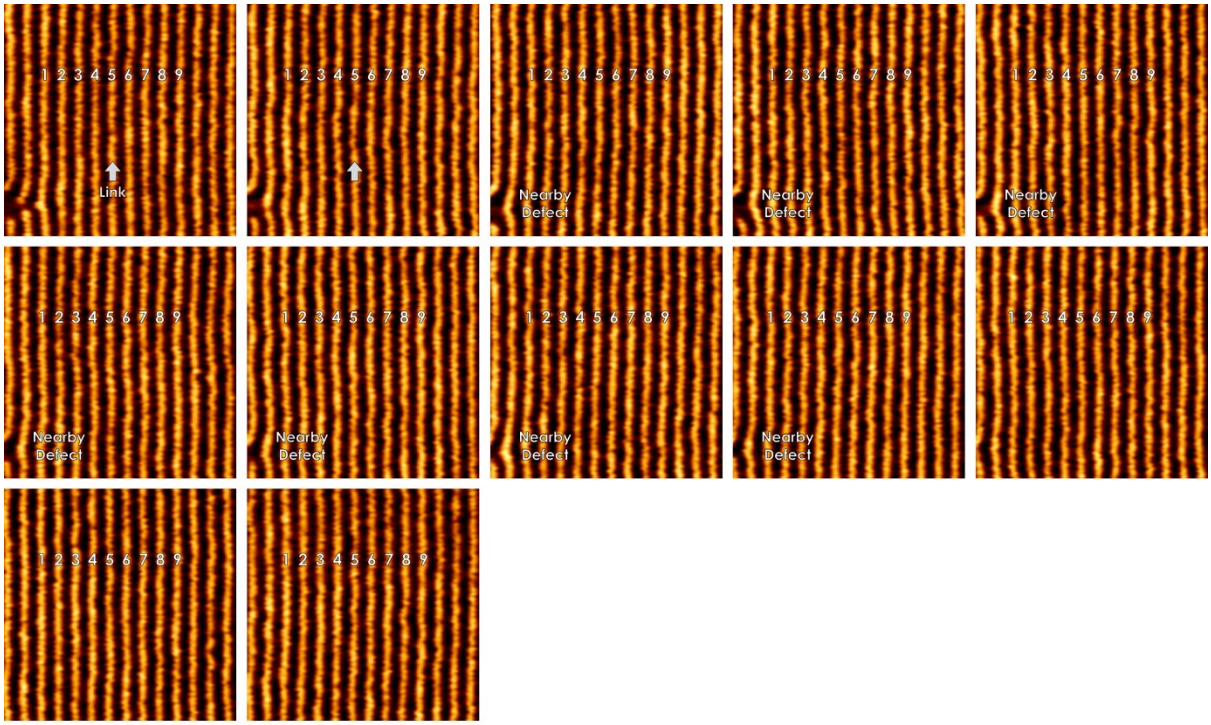


Figure 4-8. Phase images detailing the annihilation pathway of a representative parallel orientation defect obtained at 170 °C from *t* = 03:40:13 to 06:16:48, Part 3.

Although the original imaging areas were 4 × 4 μm^2, thermal effects caused the image to shift about in location, making visual tracking of defect sites difficult. In Fig. 4-8, a representative area with a parallel orientation defect was chosen from the isothermal in situ AFM experiment at 170 °C from *t* = 03:40:13 to 06:16:48. The representative defect was cropped out from each frame of the in situ AFM experiment and aligned manually on Microsoft PowerPoint based on the surrounding structures. By zooming in on to a specific defect area, the pathway towards defect annihilation can be studied in detail. In each frame found in Fig. 4-8, a parallel orientation defect that spans over seven stripes of the lamellar pattern is centered. With longitudinally well-aligned lamellar stripes surrounding the parallel orientation defect, this defect is also known as a multiple-bridge defect as the pattern transfer of such a defect can result in the formation of a bridge that connects multiple stripes together in the lateral direction. In the phase images, three distinct color contrasts can be visible. As PS-*b*-PMMA thin films have been well studied by non-contact AC mode AFM (commonly known as tapping mode AFM, a terminology that is trademarked by Bruker), the

dark, black domain in the phase image is commonly attributed to the PS domain, whereas the bright, yellow domain can be attributed to PMMA. On the other hand, a domain with a third color, dark orange-red, can also be seen on the defective areas. As the color contrast in the AFM phase image is set to dark and black on one extreme, bright and yellow on the other extreme, and orange-red in the center, the dark orange-red color of the defective area suggests that the PS and PMMA blocks are mixed to a certain extent in this area. Although the edges of the striped microdomains in contact with the defective area are not perfectly straight and longitudinally aligned, the stochastic linking and breaking of the stripes in the same "column" was observed. Additionally, this stochastic linking and breaking of the striped microdomains could only observed in the microdomains that were in direct contact with the defective area. For clear visualization and tracking, the stripes are labelled from 1 to 9 in Fig. 4-8, with the defective area located between stripes 2 to 8. Even though stripes 1 and 9 appear slightly distorted with a small bulge towards the defect area in the first image at t = 03:40:13, a dark PS domain separates the stripes from the defective area. Consequently, stochastic linking and breaking behaviors were not observed in stripes 1 and 9. This suggests that while the defective area can influence the shape of the surrounding "defect-free" areas, defects cannot cause the nucleation and growth of new defect sites on "defect-free" areas. Generally, the striped microdomains can be observed to either stochastically move towards or away from the opposite ends of the defect area. If the stripes at opposite ends of the defect move towards each other and are in relatively close proximity, the microdomains can link up to form a longitudinally-aligned, long, straight line. However, if the stripe remains in contact with the defect area, in the form of the orange-red domain, the stripe can also break up and reform into two stripes that oppose each other on the opposite ends of the defect area. However, if the opposite stripes manage to link up and separate from the defective domain by forming a dark PS microdomain that isolates the stripe from the defective area, the stripes can no longer be observed to break apart. This is particularly observed in stripes 2, 4, and 8. In Fig. 4-8, the opposite ends of these stripes could be observed to approach and link up in one frame, before breaking apart once again in the

next. However, stochastic movements eventually result in the stripes linking up and separating from the defect area, forming stable, well-aligned microdomains. Additionally, as the microdomains can only move stochastically and locally, the stripes were observed to link together starting from the stripes with opposite ends that are separated by the shortest distances. As the stripes with opposite ends separated by the shortest distances, stripes 2 and 8 were observed to connect first. Subsequently, the stochastic and local movement of the ends of the stripes either bring the opposite ends closer or away from each other. Over time, as chance brings the ends of the stripes together, the stripes link up one after another. As this parallel orientation defect originally took on the shape of a laterally-elongated diamond that is wider in the middle and tapers out at the edges, the stripes were observed to link up from the outer edges of the defect simultaneously. Eventually, the final bridge defect in stripes 5 and 6 disappeared as the ends of the separated stripes linked up, leaving behind a pristine, defect-free area of longitudinally well-aligned stripes. Over time, the nucleation of new defects from this area could not be observed, suggesting that a stable configuration had been achieved by the microdomains.

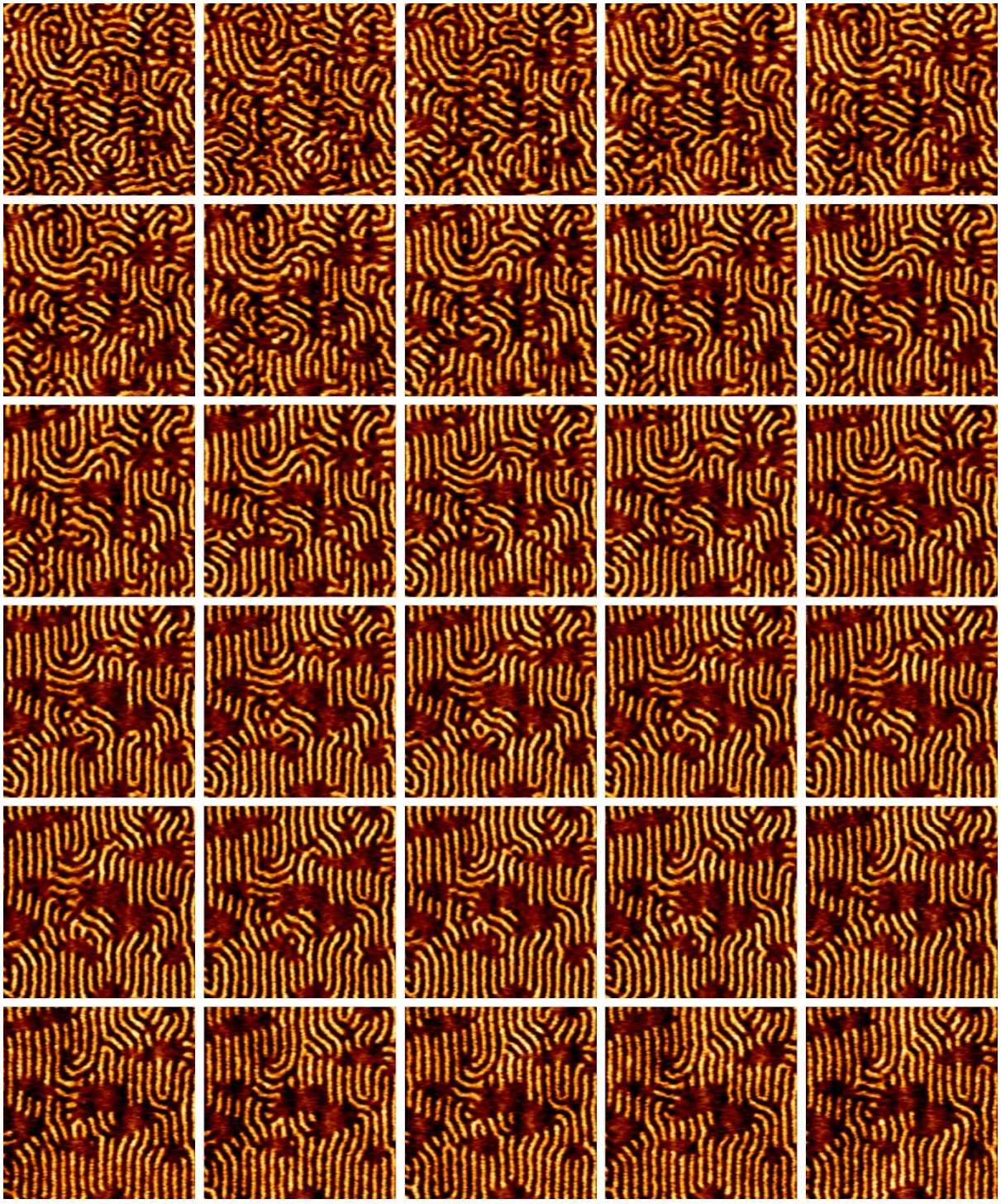


Figure 4-9. Phase images detailing the nucleation, growth, and annihilation of parallel orientation defects obtained at 170 °C from *t* = 00:18:15 to 07:21:08, Part 1.

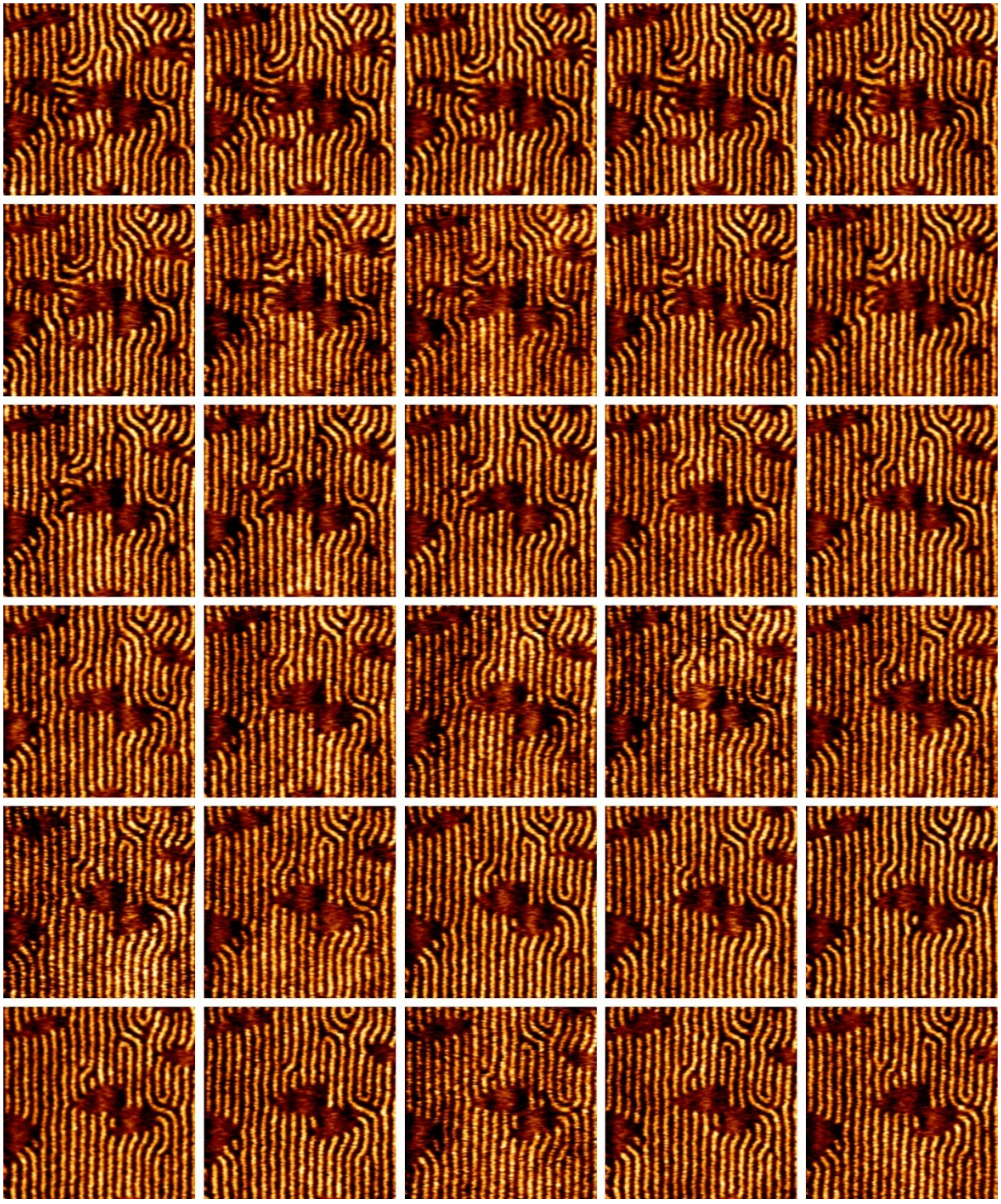


Figure 4-9. Phase images detailing the nucleation, growth, and annihilation of parallel orientation defects obtained at 170 °C from *t* = 00:18:15 to 07:21:08, Part 2.

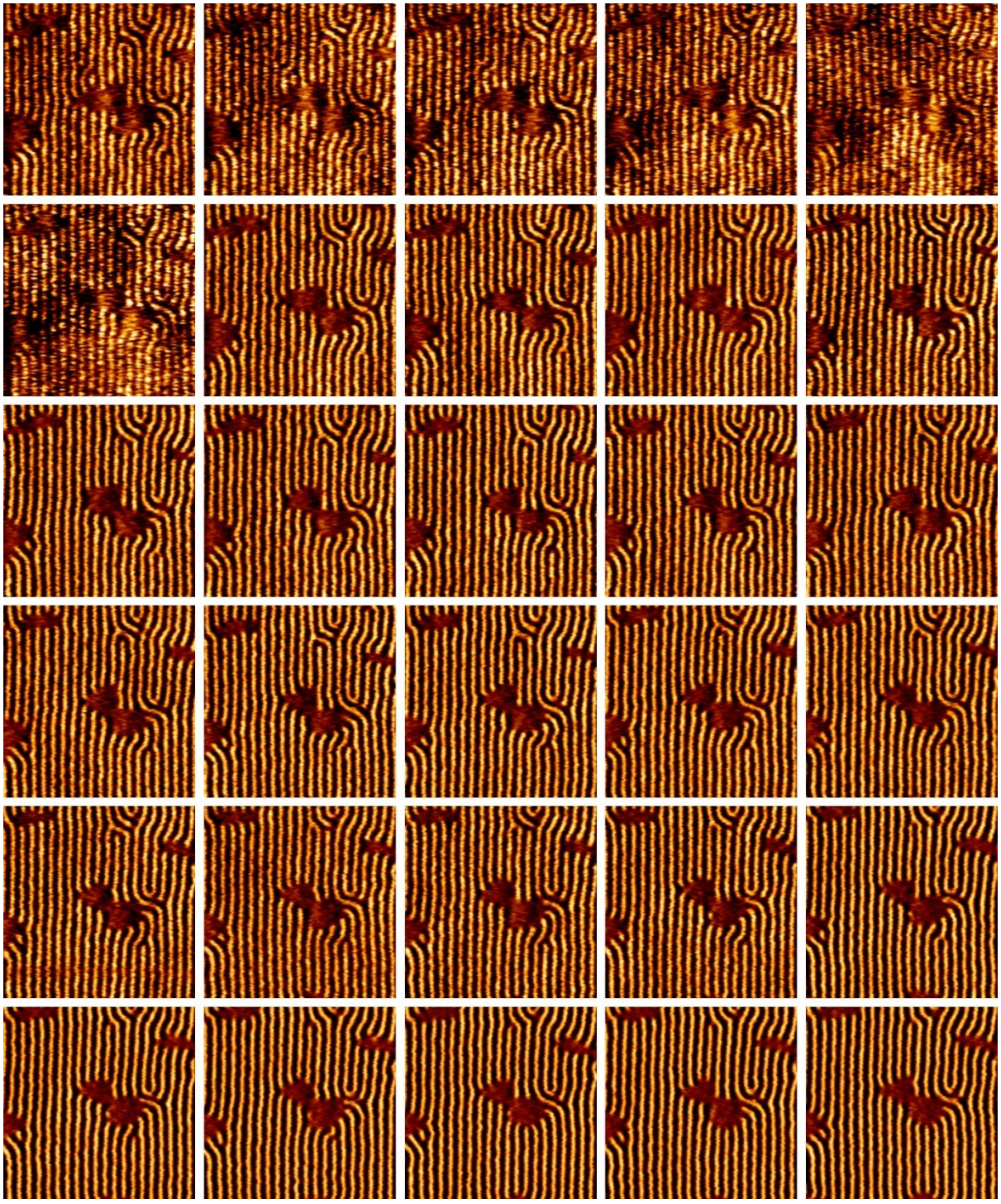


Figure 4-9. Phase images detailing the nucleation, growth, and annihilation of parallel orientation defects obtained at 170 °C from *t* = 00:18:15 to 07:21:08, Part 3.

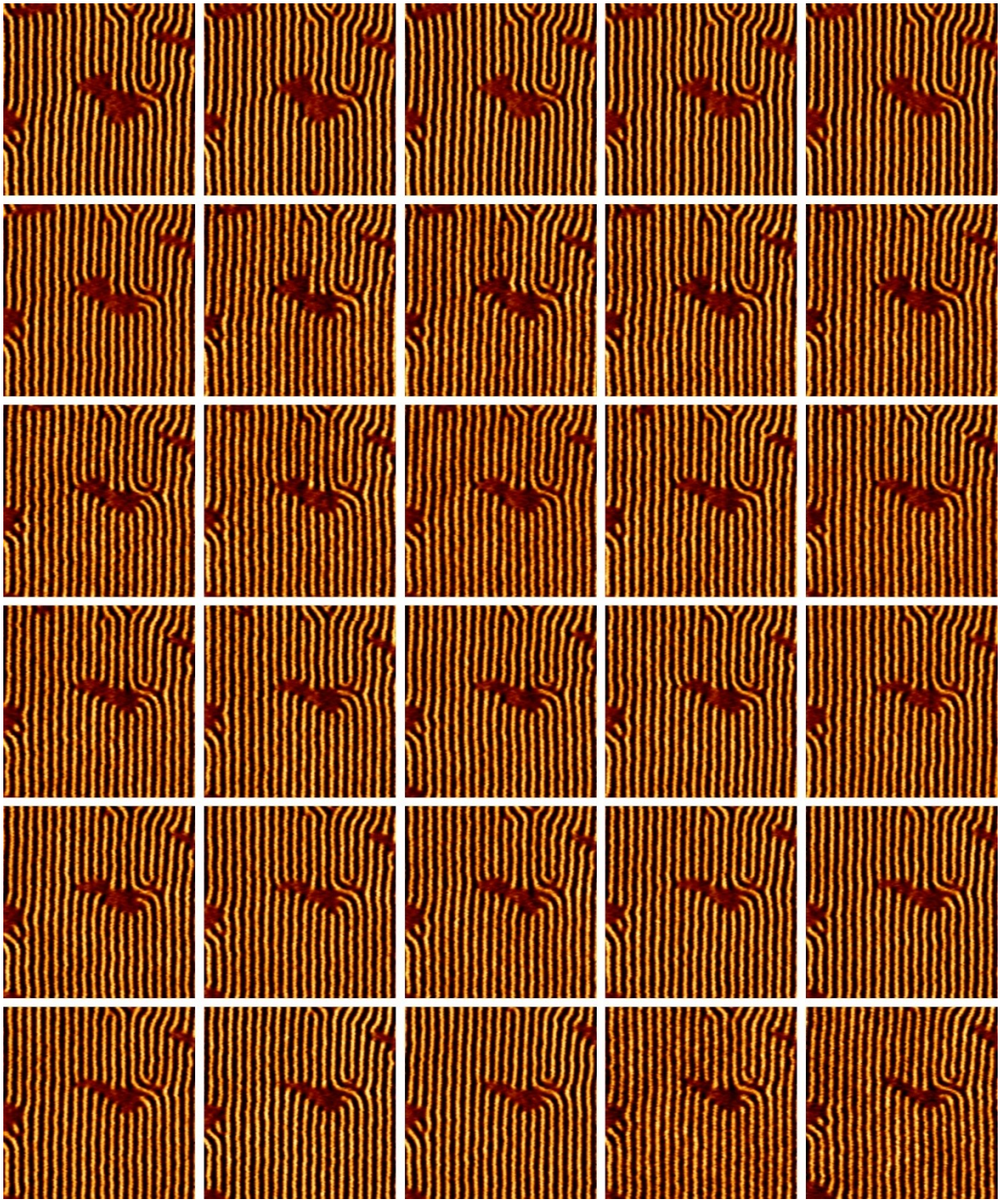


Figure 4-9. Phase images detailing the nucleation, growth, and annihilation of parallel orientation defects obtained at 170 °C from *t* = 00:18:15 to 07:21:08, Part 4.

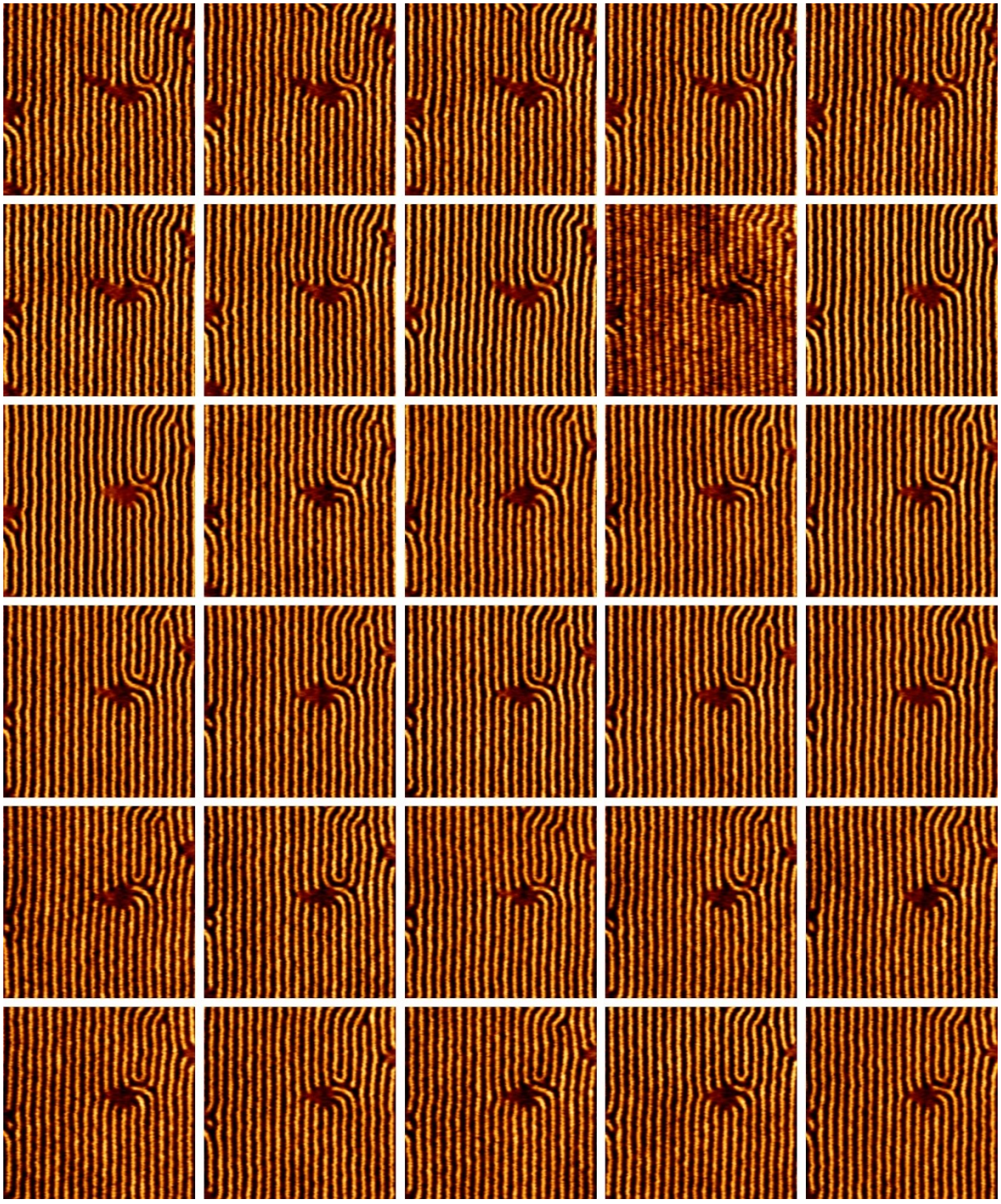


Figure 4-9. Phase images detailing the nucleation, growth, and annihilation of parallel orientation defects obtained at 170 °C from *t* = 00:18:15 to 07:21:08, Part 5.

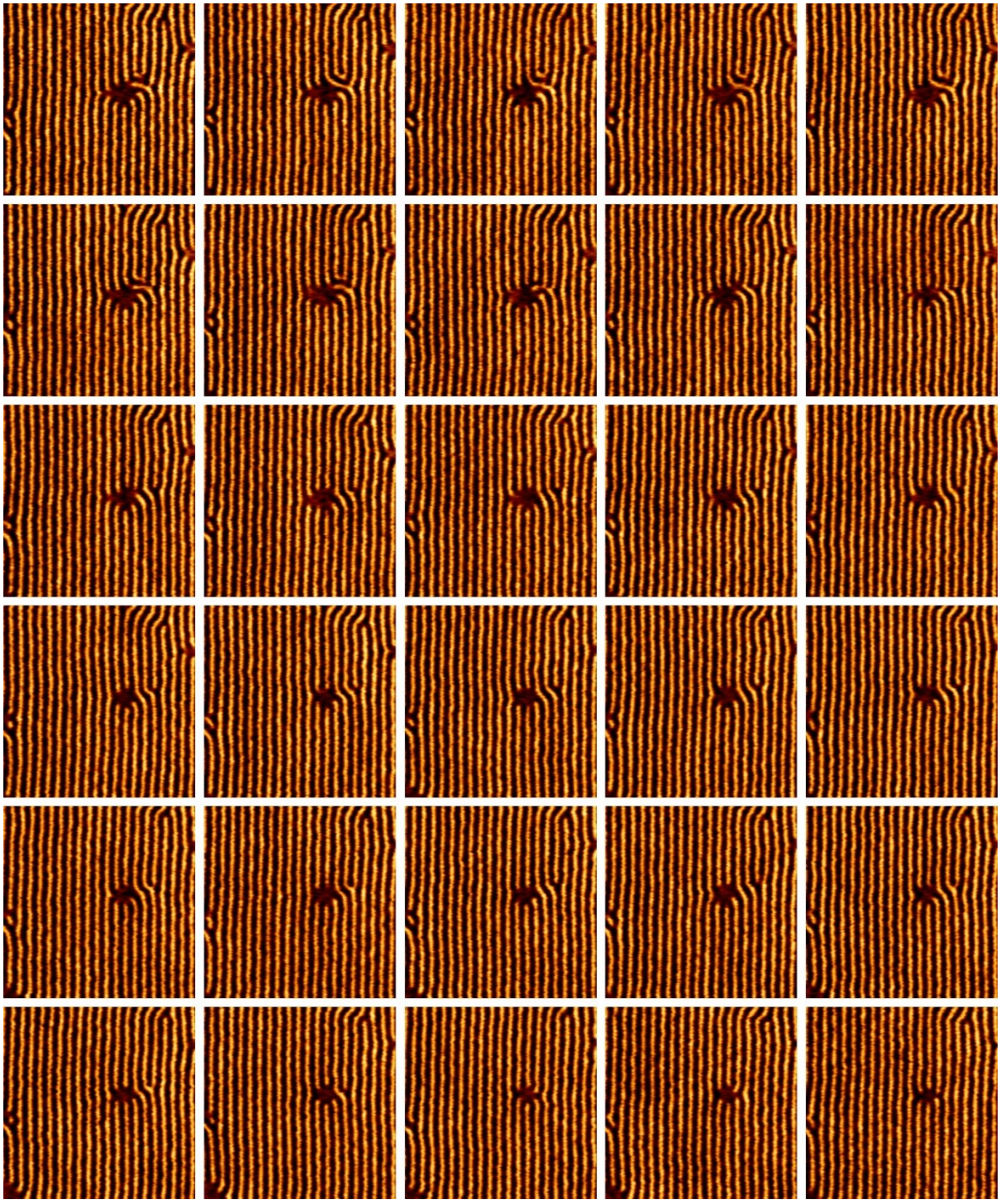


Figure 4-9. Phase images detailing the nucleation, growth, and annihilation of parallel orientation defects obtained at 170 °C from *t* = 00:18:15 to 07:21:08, Part 6.

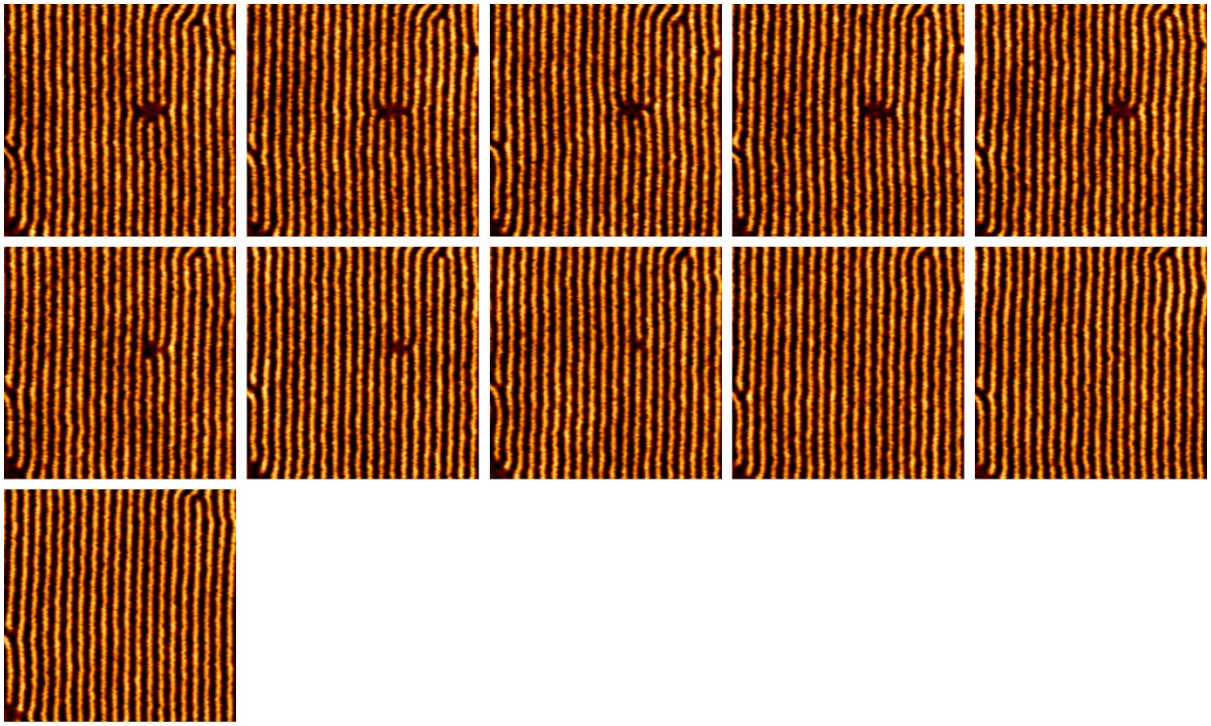


Figure 4-9. Phase images detailing the nucleation, growth, and annihilation of parallel orientation defects obtained at 170 °C from *t* = 00:18:15 to 07:21:08, Part 7.

In addition to the annihilation pathways, the origins and nucleation and growth mechanisms for the parallel orientation defects can be identified. As the initial structure at the onset of self-assembly is highly random, it may be difficult to follow the nucleation and growth mechanism of the parallel orientation defect. However, by compiling images that target the formation and annihilation of a specific defect region, the origins of such parallel orientation defects can be determined with ease. In Fig. 4-9, the nucleation, growth, and eventual annihilation of patches of parallel orientation defects during the isothermal in situ AFM experiment at 170 °C are shown. The first image obtained at *t* = 00:18:15 showed randomly-oriented grains of lamellar stripes that have been partially compartmentalized by the partial longitudinal alignment of PS in approximately 90 nm intervals. Interestingly, the PS microdomains that have begun longitudinal alignment appear thicker when compared to the surrounding striped pattern. Additionally, micellar, cylinder-like structures with dots of PMMA surrounded by a PS-rich area could be occasionally observed. Furthermore, it becomes apparent that as annealing continued, the thick PS-rich microdomains that initially

aligned in the longitudinal direction served as nucleation sites for the formation of flat, dark areas, indicative of parallel orientation defects. With further annealing, the growth of patches of parallel orientation defects and the long-range ordering and alignment of the lamellar striped pattern in the surrounding vicinity of the defects could be observed to occur simultaneously, leading to the formation of numerous small patches of parallel orientation defects. Over time however, the stochastic movement of the microdomains also led to the annihilation of the parallel orientation defects in the same manner as discussed earlier. Furthermore, the interactions between the parallel orientation defects and other defects can be interesting. One small parallel orientation defect found to the bottom right of the image can be observed to slowly re-orient into perpendicular striped lamellae. However, as the small parallel PS orientation defect disappears, the PS-rich area forms the core of a PS-core edge dislocation defect. This core of the edge dislocation defect can also be observed to transfer from one stripe to another, eventually becoming absorbed into a larger adjacent parallel orientation defect. In turn, this relatively large parallel orientation defect is connected to adjacent disclination defects. While the opposing ends of the striped pattern could be seen to approach and link together as expected on the left side of the defect area, which is surrounded simply by well-aligned longitudinal stripes, the stripes on the right appear to be unable to connect due to the presence of the disclination defect. This suggests that the connected disclination defect may be preventing the microdomains from reorienting, stalling the annihilation of the parallel orientation defect. However, stochastic linking and breaking could be observed at the disclination defect site. As the disclination moves from one stripe to another, it could be seen to evolve into a dislocation defect which eventually annihilated, leaving behind the original, multiple bridge parallel orientation defect. Once the surrounding defects had annihilated, the stripes in the multiple bridge defect were also observed to link up and heal in the same manner as observed before. The study of this relatively complex area suggests that while alignment of the PS microdomains on the chemical guides can serve to bring about long-range alignment of the striped pattern, it can also serve as a nucleation site for parallel orientation defects which remain visible on the thin film surface

even after 12 h of annealing. Additionally, multiple defects within a large complex defect area can influence the annihilation pathways of each other, with some defects potentially holding back others from annihilating as stochastic movements could become limited. Therefore, an environment which limits the nucleation of defects is highly desirable. As reported in numerous earlier works and also found in this study, the formation of parallel orientation defects depends strongly on the affinities at the free surface.[8,26] Therefore, a higher annealing temperature can simply be used to achieve neutrality on the free interface, eliminating the selective segregation of PS to the free surface and thereby preventing the nucleation of parallel orientation defects. With less potential defect nucleation sites, longitudinal alignment could be achieved much faster, as seen in the isothermal in situ experiments conducted at 200 and 210 °C.

In addition to simple parallel orientation defects, another sub-category of orientational defects is known as “stitch” morphological defects. Previously reported in a series of studies by Nealey and co-workers,[8,26,27] they described the defect as having a “stitching” morphology and is unique to chemoepitaxial DSA, with the formation of the defect partially attributed to the presence of PS-preferential guides on the substrate. The stitch morphological defect is characterized by the lateral orientation of lamellae orthogonal to lamellae which are oriented parallel relative to the substrate, aligned longitudinally in the same direction as the guides, and are found at the same pitch as the underlying chemical guides. This results in the formation of a collection of ladder-like stitched patterns on the surface. Based on similar isothermal in situ AFM imaging of 28 nm-pitch lamellar PS-*b*-PMMA thin films prepared on chemically pre-patterned LiNe flow DSA substrates, Nealey and co-workers discovered that large patches of stitch morphological defects formed when the annealing temperature was lower, particularly at 170 or 190 °C.[8,26,27] Such large areas of stitch morphological defects could not be observed in this study. Instead, as discussed earlier, patches of parallel orientation defects were observed at annealing temperatures below 200 °C. Furthermore, such parallel orientation defects were not found in the PS-*b*-PMMA thin films on chemically pre-patterned LiNe flow DSA guides used by Nealey and co-workers. This is likely attributed

to the fact that although the SMART™ process used to prepare the DSA pre-patterns in this experiment and the LiNe flow DSA used by Nealey and co-workers are at their basics, chemoepitaxial DSA processes with PS-preferential chemical guides, the preparation of the pre-patterns involve significantly different processes. The LiNe flow DSA process results in PS-preferential guide stripes that have the same line width as the PS domains used. However, the weakly PS-preferential guide stripes span a width of 1.5 L_0 in SMART™ process DSA substrates. As shown by simulative studies,[15] if the affinities towards PS are too strong, a PS wetting layer can form on the guide stripes. By using nearly-neutral, but still slightly PS-preferential substrates, the alignment of the PS microdomains while avoiding a PS wetting layer becomes possible. However, at the same time, should the free interface become preferential towards the PS domain, as in lower temperatures such as 160 and 170 °C, this could potentially facilitate the symmetrical substrate and surface wetting layer of PS, resulting in the formation of parallel lamellar defects. Therefore, with differences in the film thickness and other factors contributing to the complexity of self-assembly in BCPs under DSA, unique defects could appear for each DSA process and further detailed analyses of the annihilation mechanisms and pathways for defects that can be common to all or unique to each process are vital for the ultimate realization of “defect-free” structures.

4-3-5 Disclination Defects

Another major category of defects observed is disclination defects. Disclination defects can be found in a large variety of materials that exhibit periodic structures, including metals, ions, and liquid crystals. In the 2D striped pattern formed on the surface of thin films by the BCP microdomains, disclinations take on the form of a dot or point defect. A dot defect is also known as a +1 disclination defect. Traditionally, a +1 disclination defect is centered around a small circular area of one block, hence a dot defect, with concentric rings surrounding the dot. On the other hand, a point defect in the context of 2D striped patterns is found when the straight, aligned stripes abruptly end at a point, forming a +½ disclination defect. The stripes surrounding the end point then loop around the +½ disclination, breaking the symmetry of the pattern. However, the loops around the +½ disclination typically end

some distance away from the point defect, with “defect-free” stripes that can continue to maintain the symmetry of the striped pattern. In such a case, the +½ disclination point defect is typically paired with a three-way junction defect that can also be classified as a –½ disclination.

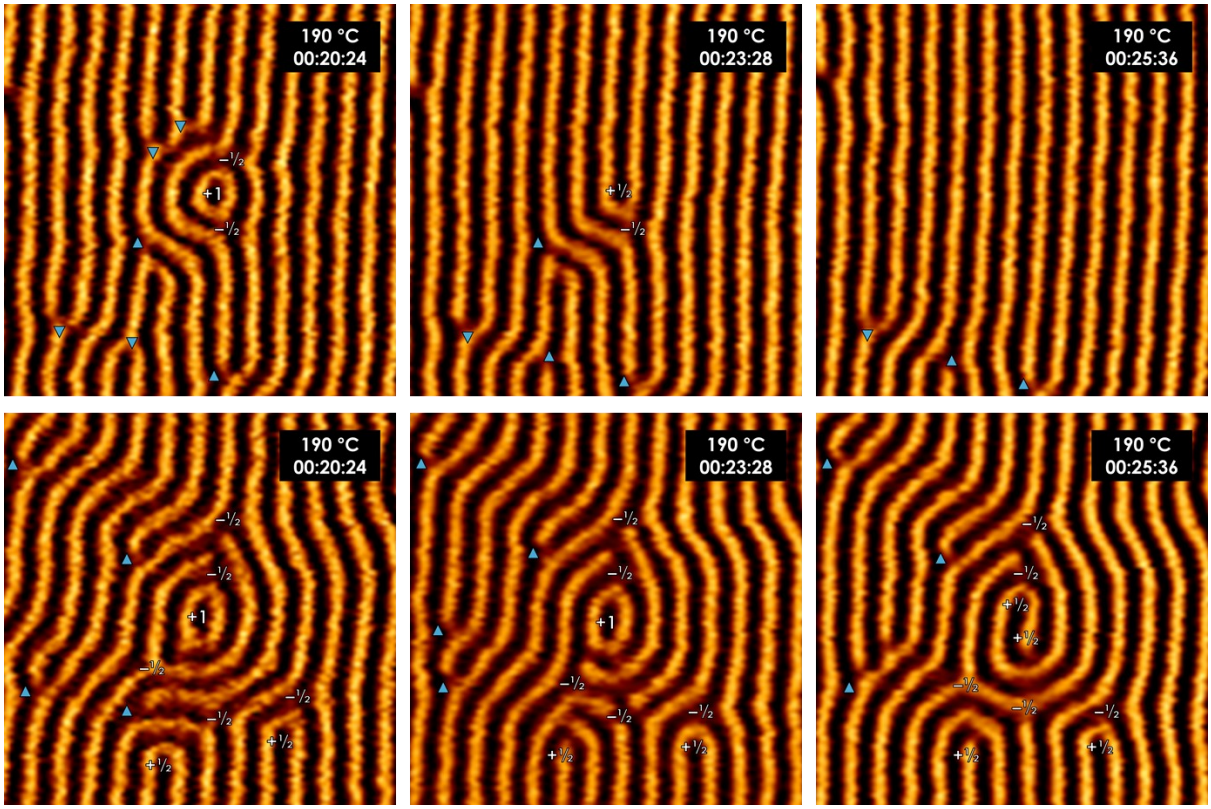


Figure 4-10. Phase images showing the transformation of +1 disclination dot defects into +½ disclination point defects. Disclination defects are labelled as +1, +½, and –½ when clearly identifiable and dislocations are indicated by upright (PS-core) and upside-down (PMMA-core) triangles.

In this study, while large areas of concentric rings cannot be observed, small dot defects were occasionally detected. However, these +1 disclination defects were found to quickly transform into +½ disclination defects (Fig. 4-10). Coupled with the relatively rarity of +1 disclinations, this suggests that +1 disclination defects are relatively less metastable and can quickly devolve into +½ disclinations for annihilation.

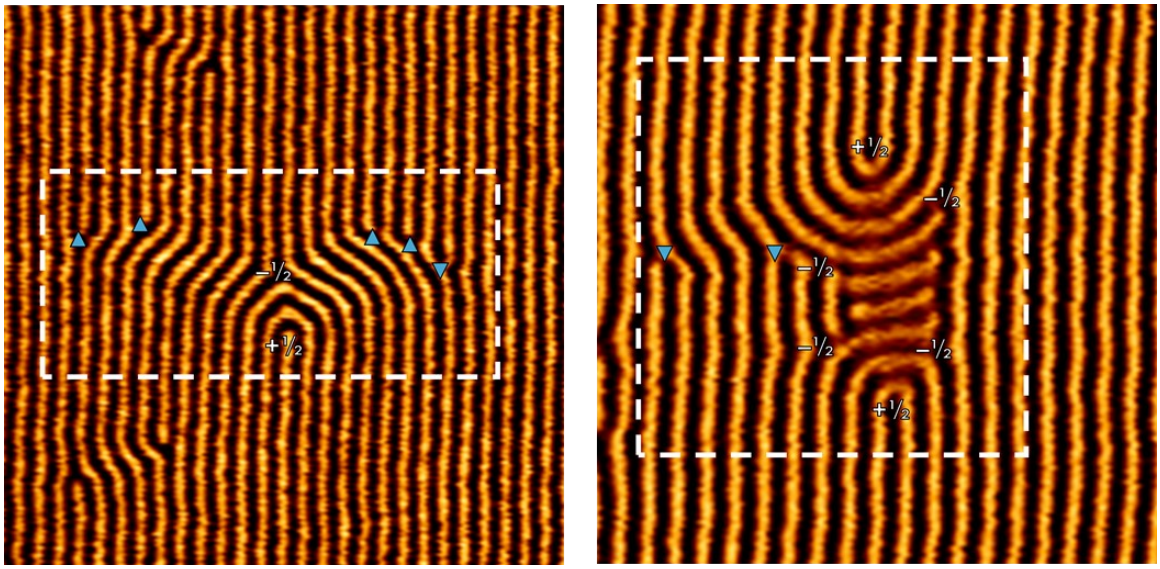


Figure 4-11. Phase images with representative configurations of disclination defects highlighted within the dashed area. (Left) Disclination pair consisting of +½ and –½ disclinations surrounded by dislocation jogs. (Right) Apposing disclination pair of two +½ point disclinations.

In contrast, +½ disclinations are commonly observed and can typically be found in two different configurations of larger complex defects (Fig. 4-11). In one configuration, a disclination pair of +½ and –½ disclinations can be found in the center of a chevron-shaped complex defect area. Stripes could be observed to loop around the +½ disclination point at the center of the defect area. When the looped stripes become adjacent to “defect-free”, longitudinally aligned areas, a –½ disclination junction defect splits the looping stripes into diagonal stripes that radiate away from the center, forming multiple jogs. At the extreme ends of the defect area, dislocation defects can be found between the multiple jog stripes and the surrounding “defect-free”, longitudinally-aligned stripes. Alternatively, +½ disclination point defects can be observed apposed to another +½ disclination defect. In this case, the two +½ disclinations are found in close proximity to each other and the point defects can be seen to face each other, with the stripes extended in the opposite directions. In the defect area between the two +½ disclination points, multiple loops or laterally-aligned stripes separate the two point defects. In turn, junction defects that could potentially be classified as either –½ disclination or dislocation defects appear at the interface between the defective

and well-aligned areas. For comparison, when such apposing disclinations are found in thermally-equilibrated bulk samples with long-range ordering, a disclination quadrupole is formed. As the stripes surrounding the two apposing +½ disclination points meet at the center of the defect area between the disclination points, two junction defects in the form of –½ disclinations divide the defect symmetrically. However, in the case of thin films prepared on pre-patterned DSA substrates, guides strongly nudge the microdomains towards alignment and the “ideal” configuration of apposing disclination quadrupoles cannot be observed. Instead, a less well-defined defect area with multiple junction defects can typically be observed in the area between the apposing +½ disclinations points. Nevertheless, although these complex defect configurations are based around +½ disclination point defects, they exhibit annihilation pathways unique to each configuration.

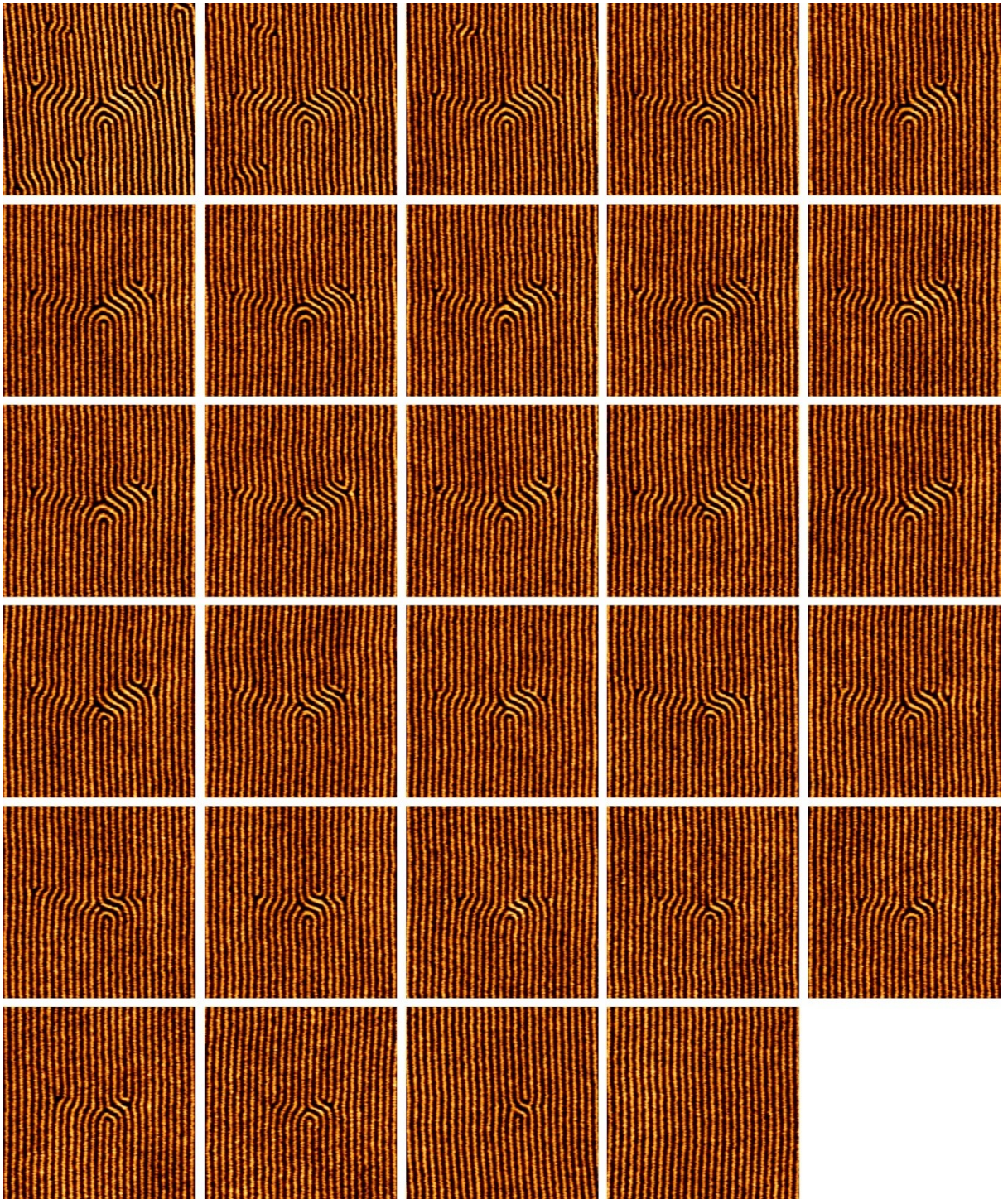


Figure 4-12. Phase images showing the annihilation pathway of a ±½ disclination pair defect obtained at 200 °C from *t* = 00:19:25 to 01:25:39.

The annihilation pathway of a representative ±½ disclination pair defect is shown in Fig. 4-12. The images were obtained during the isothermal in situ AFM experiment at 200 °C from *t* = 00:19:25 to 01:25:39. In the first image of the series, a chevron-shaped defect area with a ±½ disclination pair in the center and multiple jogs radiating outwards that end in

disclination defects. Interestingly, the +½ disclination pair at the core of the defect area is relatively metastable, and stochastic linking and breaking of the microdomains at the point defect could not be observed. Instead, the stochastic linking and breaking of the microdomains could be observed in the "junction-type" defect sites. The three-way junctions at the –½ disclination site and the dislocations at the outer edges of the defect area were shown to switch randomly from one linkage to another. Particularly, on the left half of the chevron, multiple dislocation sites could be observed in the first few images; one at the extreme left end and one directly above the jogs. While the dislocation at the end remained relatively unchanged, the dislocation directly above the jogs was transferred gradually transferred to stripes on the right, before annihilating as it came into contact with the –½ disclination at the center of the defect. From then, the left side of the chevron-shaped defect is analogous to a dislocation pair defect, consisting of the dislocation on the extreme left and the junction at which the –½ disclination is located. Through stochastic linking and breaking of the dislocation on the extreme left, the dislocation stripe traversed towards the ±½ disclination pair at the center of the defect area, before annihilating to leave behind the right half of the initially chevron-shaped defect. Meanwhile, a similar annihilation pathway could be observed on the right side of the chevron-shaped defect. At the same time as the stochastic evolution of the dislocation defects on the left, stochastic linking and breaking at the junctions of the multiple dislocation sites could be observed on the right half. Here, multiple dislocation sites were observed to travel towards the ±½ disclination pair at the center of the chevron-shaped defect. After the dislocations analogous to a dislocation pair on the left side of the chevron-shaped defect annihilated, the remnants of the ±½ disclination pair and the right half of the chevron-shaped defect form a dislocation pair defect as well. Finally, following the annihilation of the second dislocation pair, the area became free of defects.

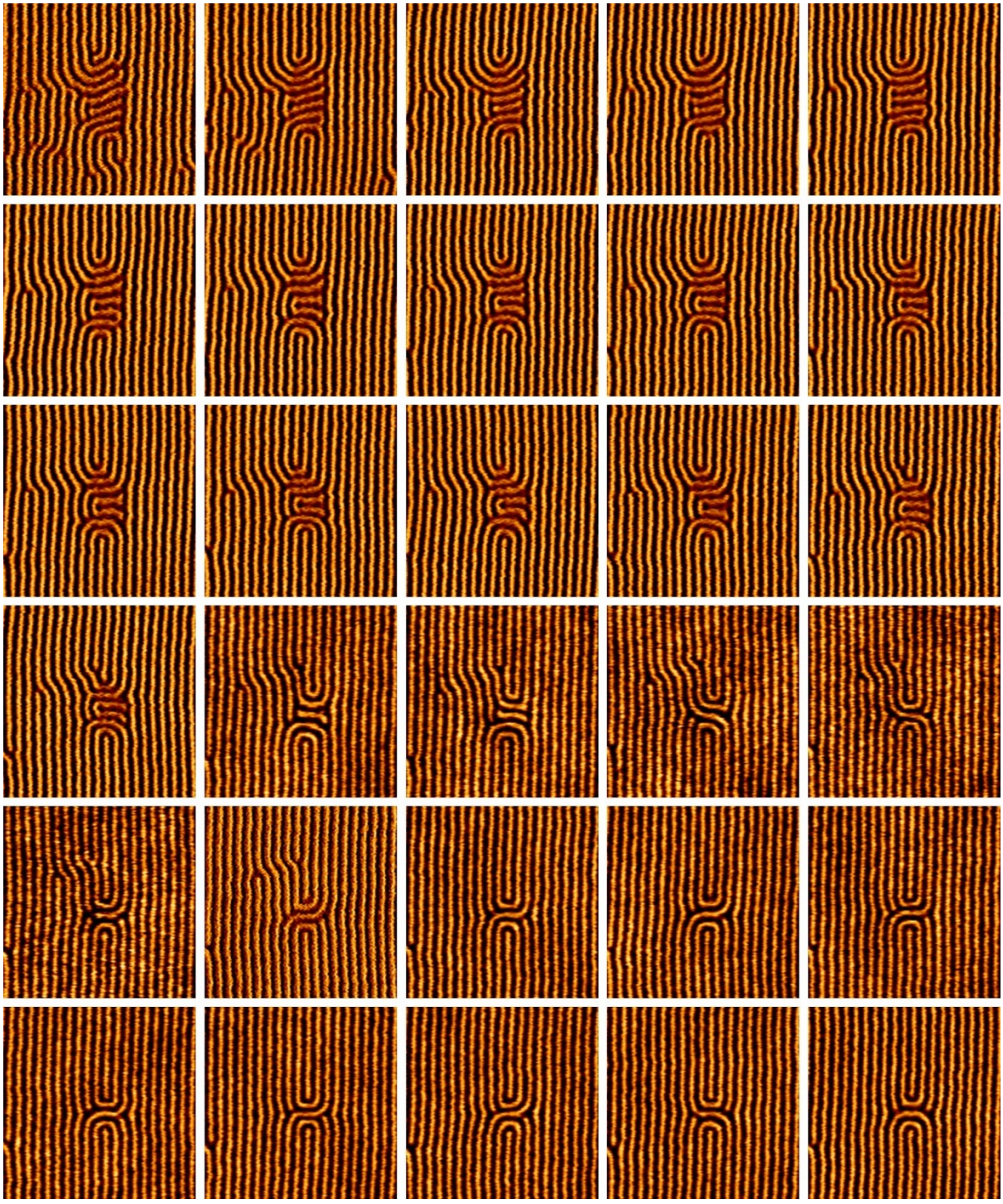


Figure 4-13. Phase images showing the annihilation pathway of apposing +½ disclinations captured at 190 °C from *t* = 00:20:24 to 01:57:14, Part 1.

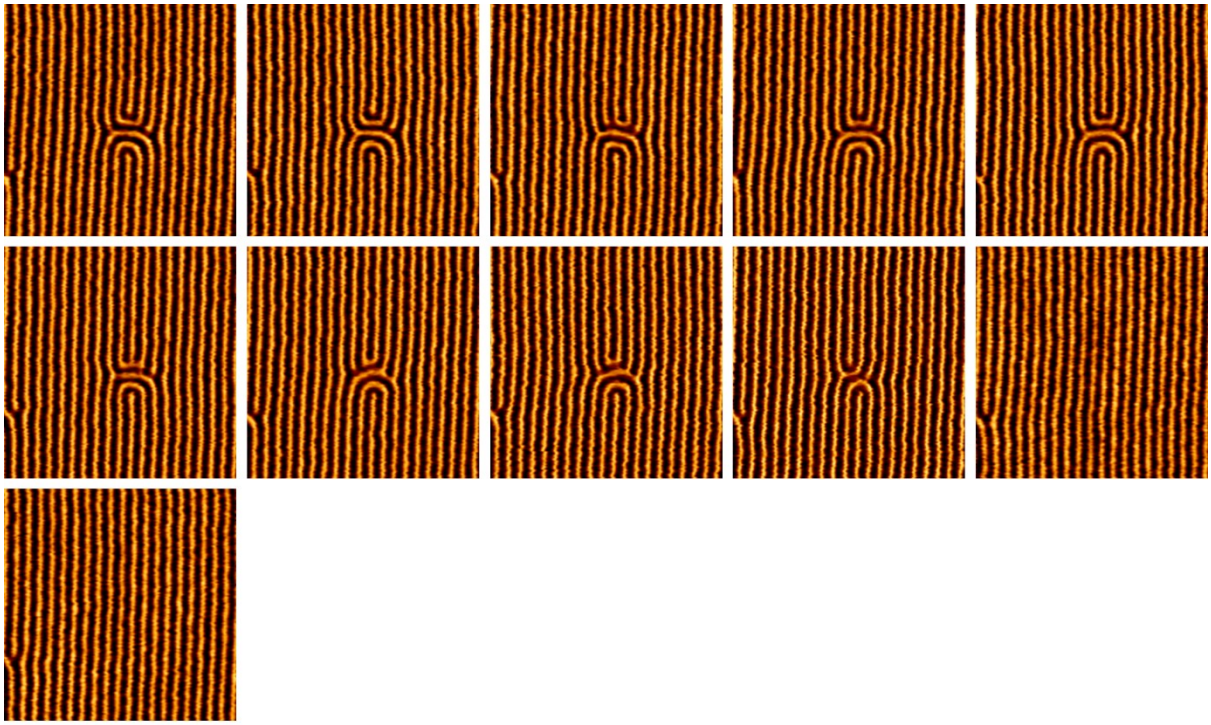


Figure 4-13. Phase images showing the annihilation pathway of apposing +½ disclinations captured at 190 °C from *t* = 00:20:24 to 01:57:14, Part 2.

When two apposing +½ disclination point defects are found pointing towards each other, these disclination defects exhibit annihilation mechanisms that are similar to but distinct from ±½ disclination pairs. Apposing +½ disclinations are typically found in relatively close proximity, only a few stripes apart in the lateral direction, but could be further apart longitudinally. In Fig. 4-13, the initial image is seemingly random and complicated, however, two PMMA-core +½ disclinations can be observed among other multiple defect sites. Additionally, the two PMMA-core +½ disclinations are separated by 9 laterally-oriented stripes. In the second image, the presence of two apposing PS-core +½ disclination point defects becomes clearer. This shows that unlike in the case of ±½ disclination pairs, where the +½ disclination is relatively stable and stochastic linking and breaking cannot be observed, the +½ disclination point defect site can undergo stochastic linking and breaking, transferring from one row or column of stripes to another. In this way, the +½ disclinations were observed to gradually approach one another, reducing the number of lateral stripes separating the two defect sites. Eventually, the two +½ disclination points line up on the

same column of stripes. Two three-way junction defects found to the sides of the +½ disclination points could be seen to open and close as the linkages transfer from one stripe to another. The apposing +½ disclinations appear to remain mostly unchanged in this disclination quadrupole-like configuration, excepting stochastic linking and breaking at the junctions, for approximately 30 min, suggesting that the disclination quadrupole-like configuration is relatively metastable. However, as one +½ disclination stochastically shifts to the next column, the +½ disclination sites are able to further approach and form a dislocation pair which swiftly annihilates. These experiments show that disclination defects are rarely, if ever, found and behave independently. The +½ disclination point defects always appear with junction defects that can be identified as less well-defined multiple-way junctions, –½ disclinations, or dislocations. Additionally, while multiple configurations of disclination defects can exist to form larger complicated defect areas, disclinations were always observed to undergo a transformation into dislocation defects prior to annihilation, suggesting that the defects can be highly correlated, and also possible explaining the prevalence of dislocation defects in DSA thin films.

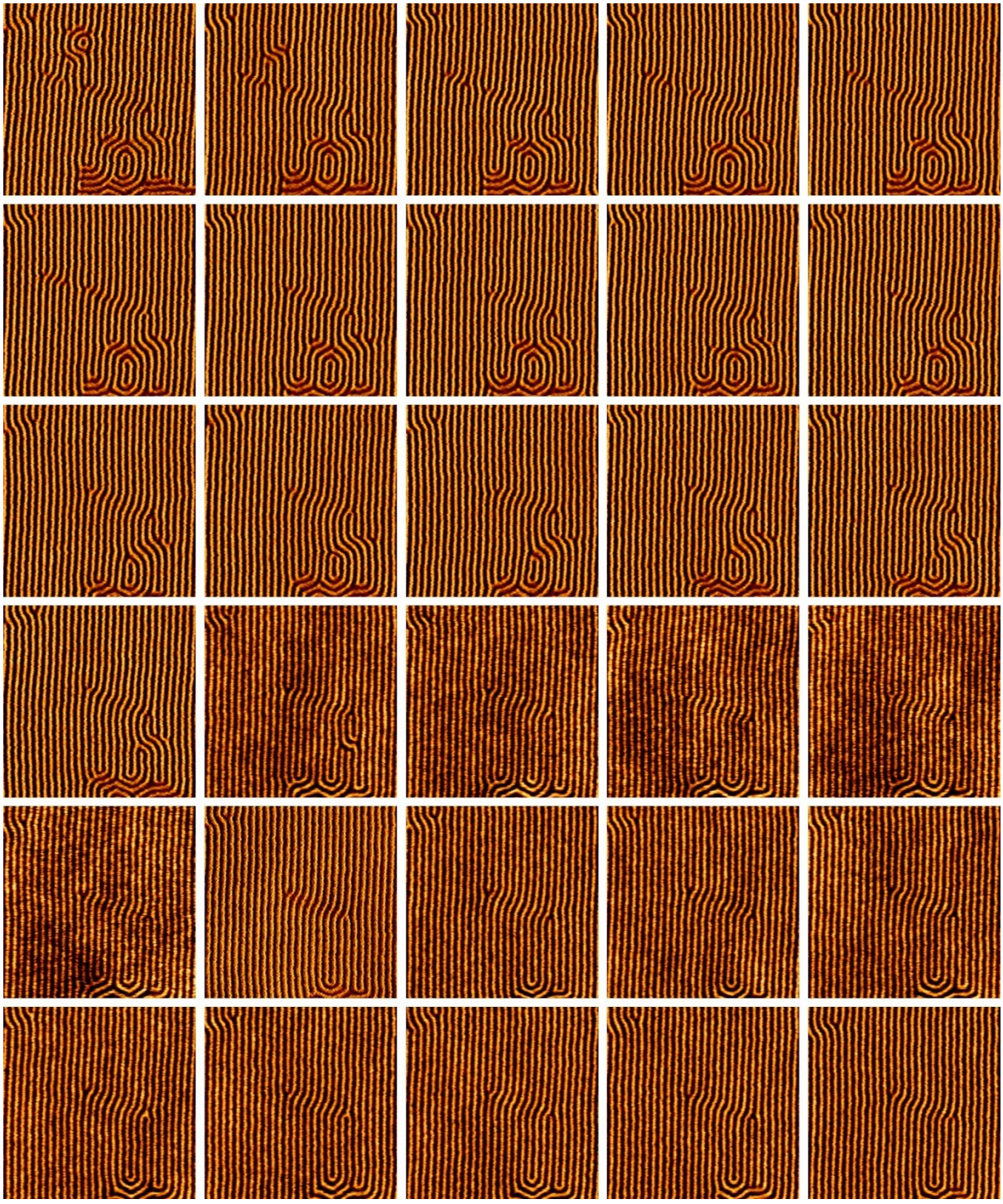


Figure 4-14. Phase images showing the annihilation pathway of dislocation pair defects during the isothermal in situ AFM experiment at 190 °C from *t* = 00:20:24 to 06:06:50, Part 1.

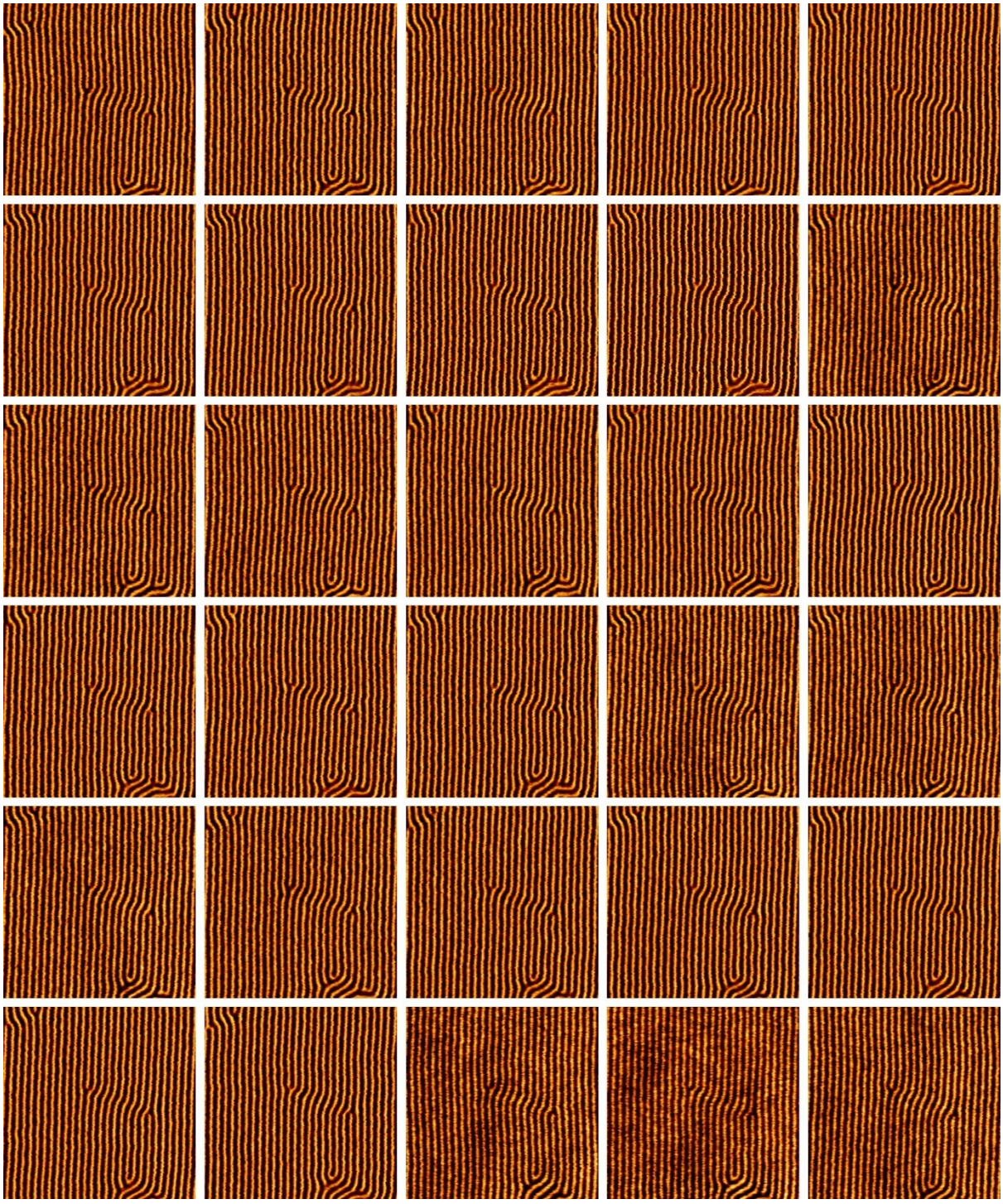


Figure 4-14. Phase images showing the annihilation pathway of dislocation pair defects during the isothermal in situ AFM experiment at 190 °C from *t* = 00:20:24 to 06:06:50, Part 2.

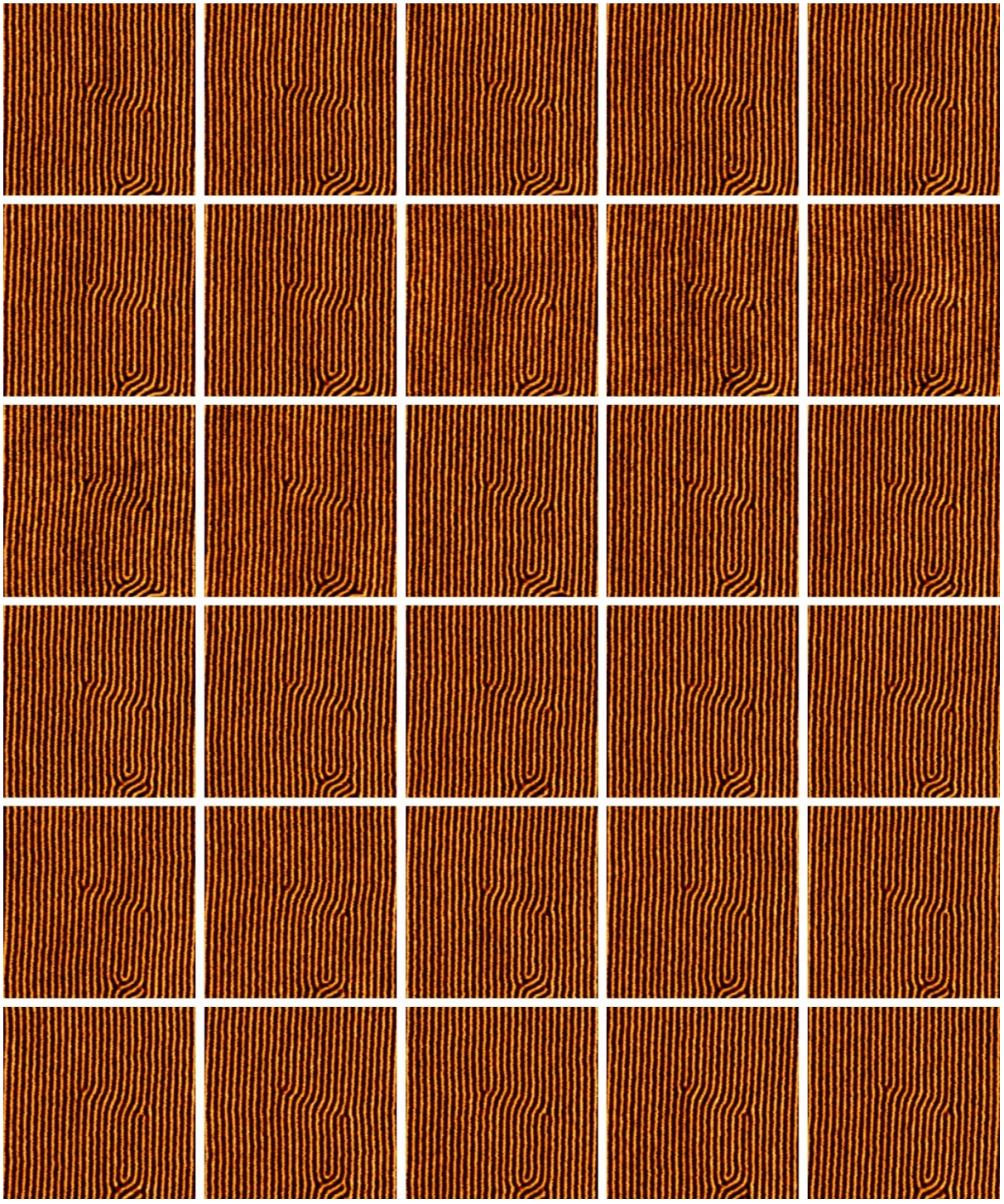


Figure 4-14. Phase images showing the annihilation pathway of dislocation pair defects during the isothermal in situ AFM experiment at 190 °C from *t* = 00:20:24 to 06:06:50, Part 3.

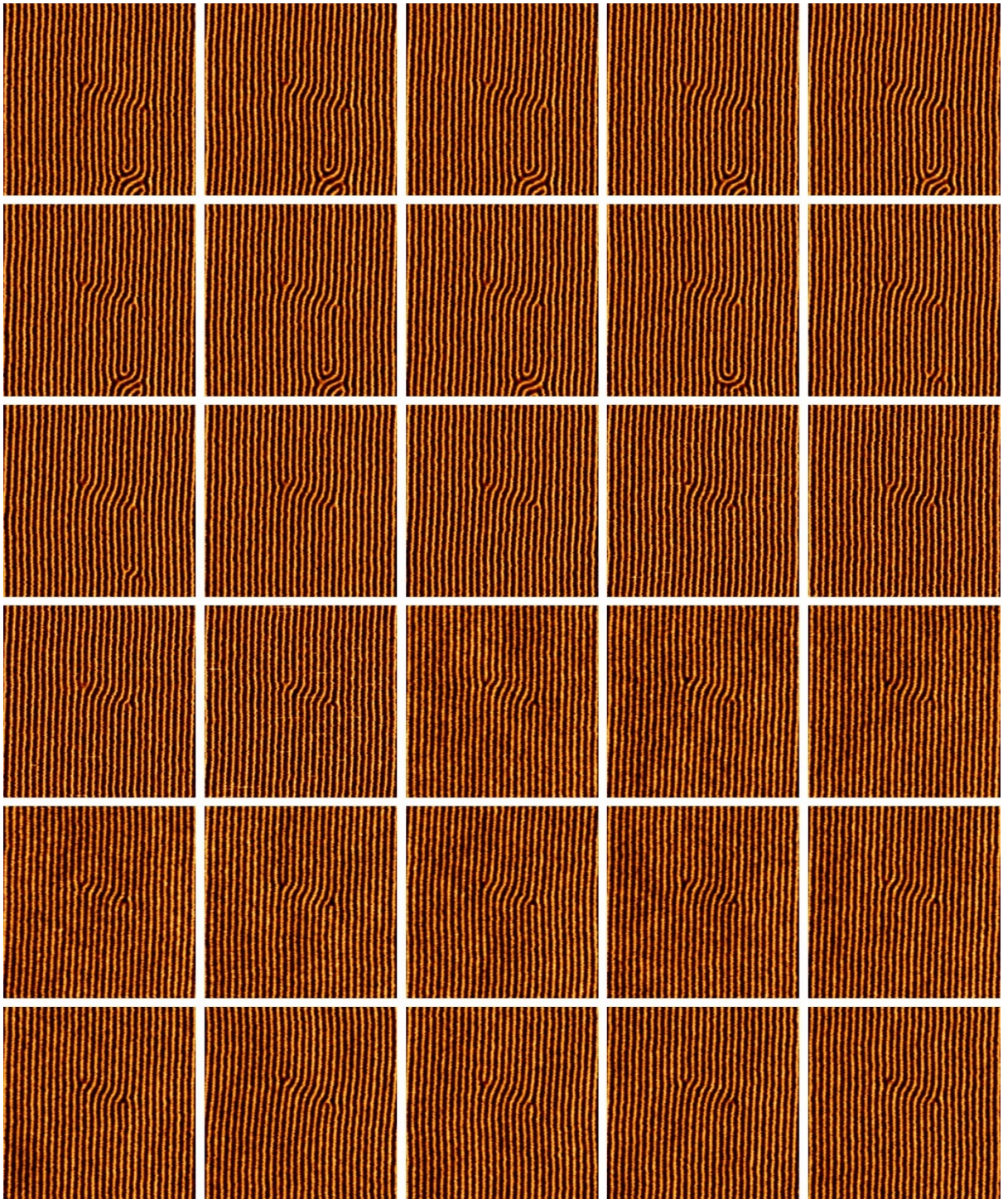


Figure 4-14. Phase images showing the annihilation pathway of dislocation pair defects during the isothermal in situ AFM experiment at 190 °C from *t* = 00:20:24 to 06:06:50, Part 4.

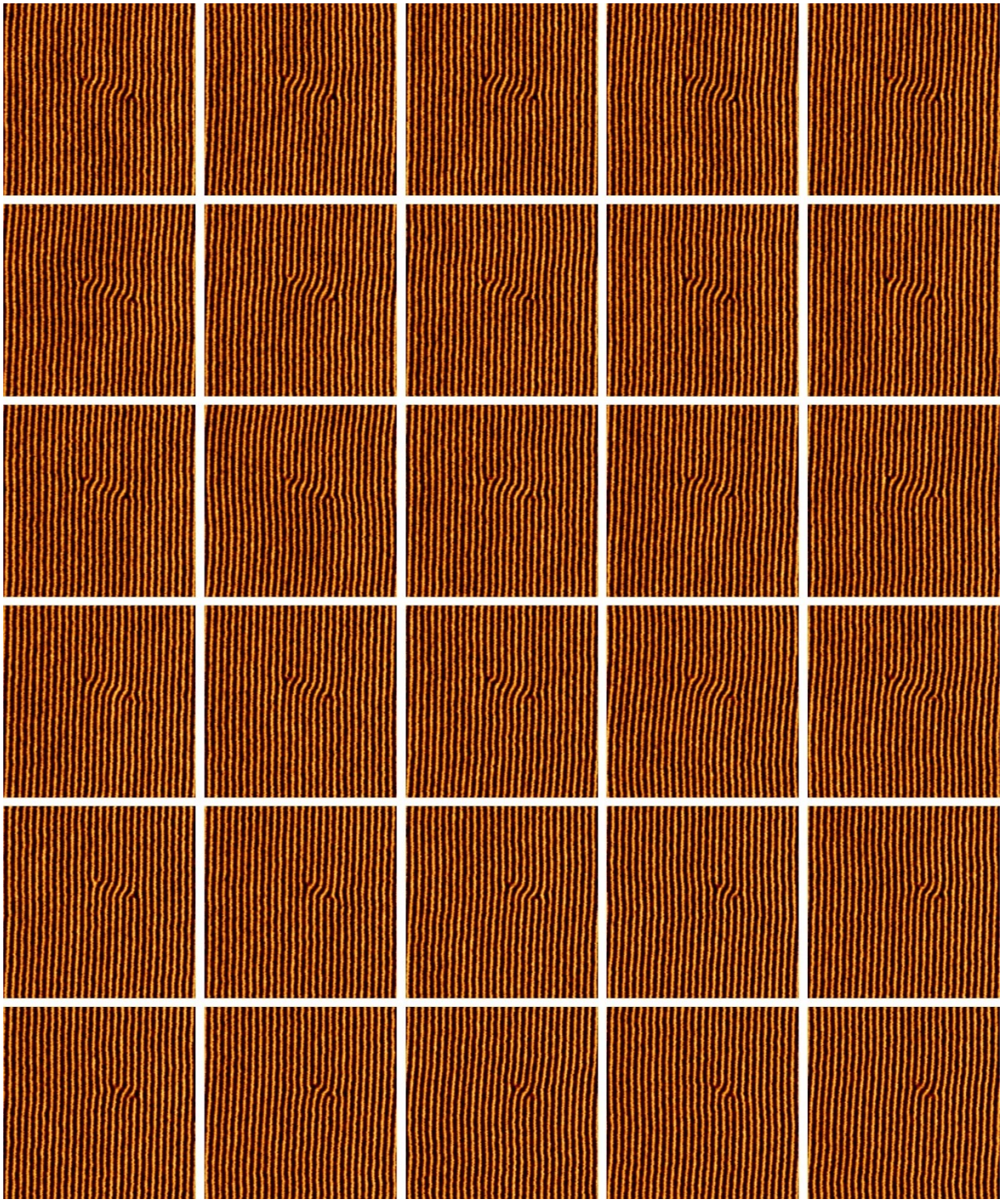


Figure 4-14. Phase images showing the annihilation pathway of dislocation pair defects during the isothermal in situ AFM experiment at 190 °C from *t* = 00:20:24 to 06:06:50, Part 5.

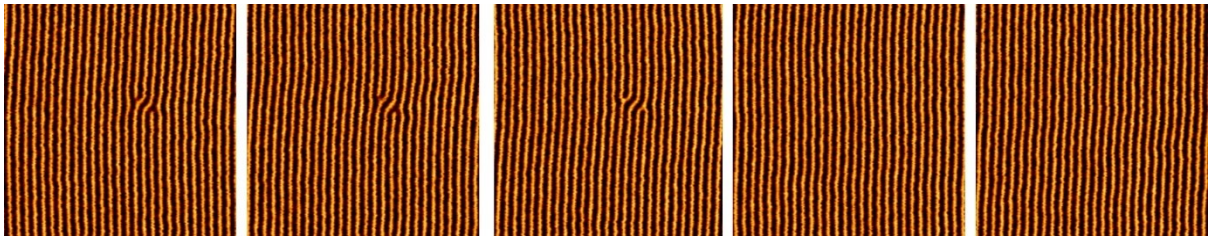


Figure 4-14. Phase images showing the annihilation pathway of dislocation pair defects during the isothermal in situ AFM experiment at 190 °C from *t* = 00:20:24 to 06:06:50, Part 6.

4-3-6 Dislocation Defects

Although the annihilation of dislocation defects appeared briefly earlier, the detailed annihilation mechanism of such dislocation defects will be discussed in detail here. In the DSA of lamellar BCPs, dislocations are typically found in pairs. Typically, two Y-shaped junction defects in opposite directions are separated by a number of diagonal stripes in between. As the Y-shaped junction defects are typically found next to well-aligned, straight stripes, they can also be classified as edge dislocation defects. Meanwhile, the diagonal stripes separating the edge dislocations are termed jogs. Additionally, depending on the domain that constitutes the Y-shaped edge dislocation defect, the dislocation can either be a PS- or PMMA-core edge dislocation defect. In Fig. 4-14, the annihilation pathway of dislocation pairs in the isothermal in situ AFM experiment at 190 °C from *t* = 00:20:24 to 06:06:50 is shown. While numerous complex defects can be seen in the initial image, two dislocation pair defects can be seen in the center. One dislocation pair is found centered on the image, with PS- and PMMA-core edge dislocations on either side, separated by 8 jogs in between. Another is found slightly upwards and to the left of the dislocation pair in the center of the image. This smaller dislocation pair consists of two PMMA-core dislocations separated by a single PS jog. Although the two dislocation pairs appear connected, being in the same general diagonal direction, the PMMA-core dislocations on the right of the smaller dislocation pair defect and the left of the larger dislocation pair defect are separated by two stripes of well-aligned, defect-free lamellae. Therefore, the two dislocation pairs do not act as one large dislocation pair defect. Instead, the smaller dislocation pair defect with fewer jogs separating the edge dislocations was observed to annihilate first, with the larger dislocation

pair defect being unaffected. Focusing on the large dislocation pair centered in the images, the stripes within the edge dislocations on either side can be observed to stochastically link up with the neighboring stripe. By linking up with the neighboring stripe, the location of the edge dislocation gets transferred by one column and the phase at the core of the edge dislocation switches. Over time, the edge dislocations approach each other and the number of jogs separating the dislocations reduce. Once the edge dislocations are directly adjacent to each other, the dislocation pair defect annihilates.

4-3-7 Other Defect Types

Although a perfectly-aligned, defect-free state minimizes the interfacial contact between the microdomains, kinetic barriers can prevent the annihilation of defects. This results in the formation of metastable defects that can take on a variety of conformations. While most of these metastable defects can be categorized as either orientation, disclination, or dislocation defects, the identification of these defects can heavily depend on the surrounding structure. In some cases, the defect area can be riddled with so many defects that the classification for each defect site becomes less well-defined. Such defects are particularly apparent in the areas surrounding a disclination defect. For example, in Fig. 4-11, a defect that can be classified as both a –½ disclination and a dislocation defect can be found in the phase image obtained at 190 °C at 00:23:28. In the image, this defect is labelled as a –½ disclination in the image and basically forms a three-way junction of the PS microdomain. Two “arms” of the three-way junction extend straight up and straight down in the longitudinal direction, forming a well-aligned line of PS. The remaining “arm” of the three-way junction extends diagonally away from the longitudinally-aligned line. Such a structure is characteristic of a PS-core dislocation. However, at the same time, this three-way junction defect is found directly next to a +½ disclination point defect, therefore, it also fits the classification for a disclination pair as a –½ disclination defect. While this defect is labelled as a –½ disclination defect, it is likely that the defect can be identified as a three-way junction defect, a –½ disclination defect, and a dislocation defect at the same time. Three-way junction defects are simply any defect sites whereby three lamellar stripes meet

together at a single point and depending on the surrounding structure, some three-way junction defects can be additionally defined as –½ disclination defects and/or dislocation defects.

Additionally, when multiple three-way junction defects are found adjacent to each other, the classification of such defects into disclination or dislocation defects becomes difficult. During the annihilation of apposing +½ point disclinations in Fig. 4-13, multiple laterally-oriented lines are found in the defect area between the two +½ disclinations. At the interface between these laterally-oriented lines and the well-aligned longitudinally-oriented lines, three-way junction defects can be found. Such three-way junctions can neither be easily identified as –½ disclinations nor as dislocations. While such three-way junctions eventually disappear as the apposing +½ disclination defect annihilates, these defects are less well-defined and can only be classified as the broad category of three-way junction defects.

Furthermore, the patterns formed by the microdomains evolve through stochastic linking and breaking processes with the nearest neighboring microdomains. As the microdomains link up or break away from each other, transitional defect types that cannot be categorized as orientation, disclination, or dislocation defects can form. These transitional defects are typically found in the vicinity of disclination defects and are based on three-way junction defects. In a three-way junction defect, the three “arms” of the defect meet at a single point and the entire defect consists of one of the microdomains. However, one of the “arms” or stripes can break away from the single point. This results in two arms remaining connected and one arm separated by the opposite microdomain. This is seen frequently during the annihilation of the annihilation of disclinations in Fig. 4-12 and 4-13, and can simply be considered as two adjacent three-way junctions of the opposite phase to the original three-way junction, or a “half-open junction”. However, as the movement of the microdomains are inherently stochastic and random, the separation of all three “arms” of the junction defect have also been observed. In such a case, the three “arms” of the defect appear to meet at a single point. However, the single point exhibits the opposite phase to the

three “arms”, resulting in the formation of a transitional “open junction” defect. This open junction defect typically disappears swiftly as two of the arms recombine to form a “half-open junction” defect.

4-3-8 Complicated Defect Sites

Now that the mechanisms behind the annihilation of each basic defect configuration have been clarified, the defect annihilation pathway of complicated defect areas with multiple numbers and types of defects connected to one another can be discussed in detail. The annihilation of a complex defect area with multiple defects is tracked in Fig. 4-15 and 4-16.

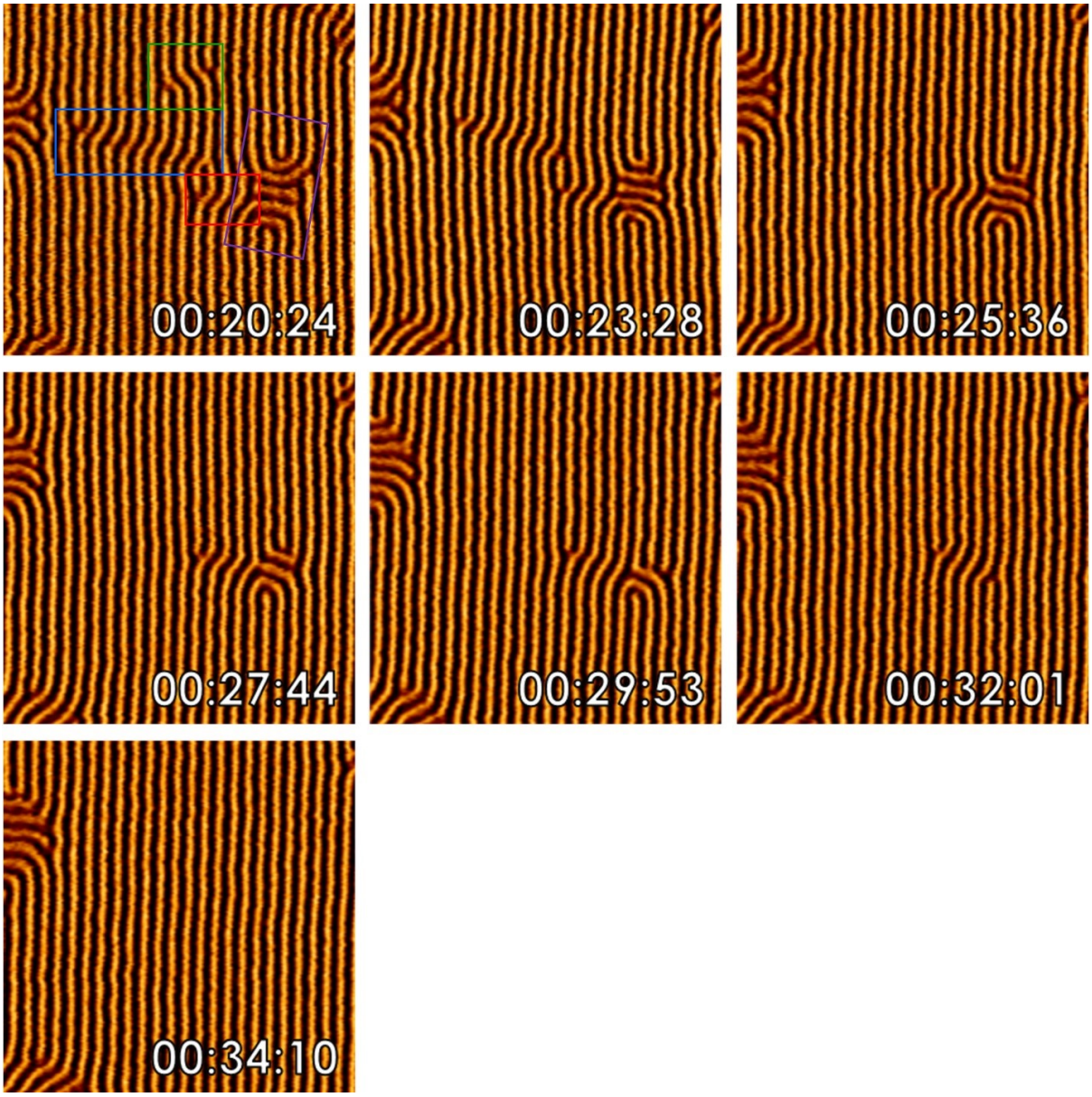


Figure 4-15. AFM phase images highlighting the annihilation mechanisms of a large complex defect area obtained at 190 °C from *t* = 00:20:24 to 00:34:10. Various defects are highlighted in the first image in green, blue, red, and purple boxes.

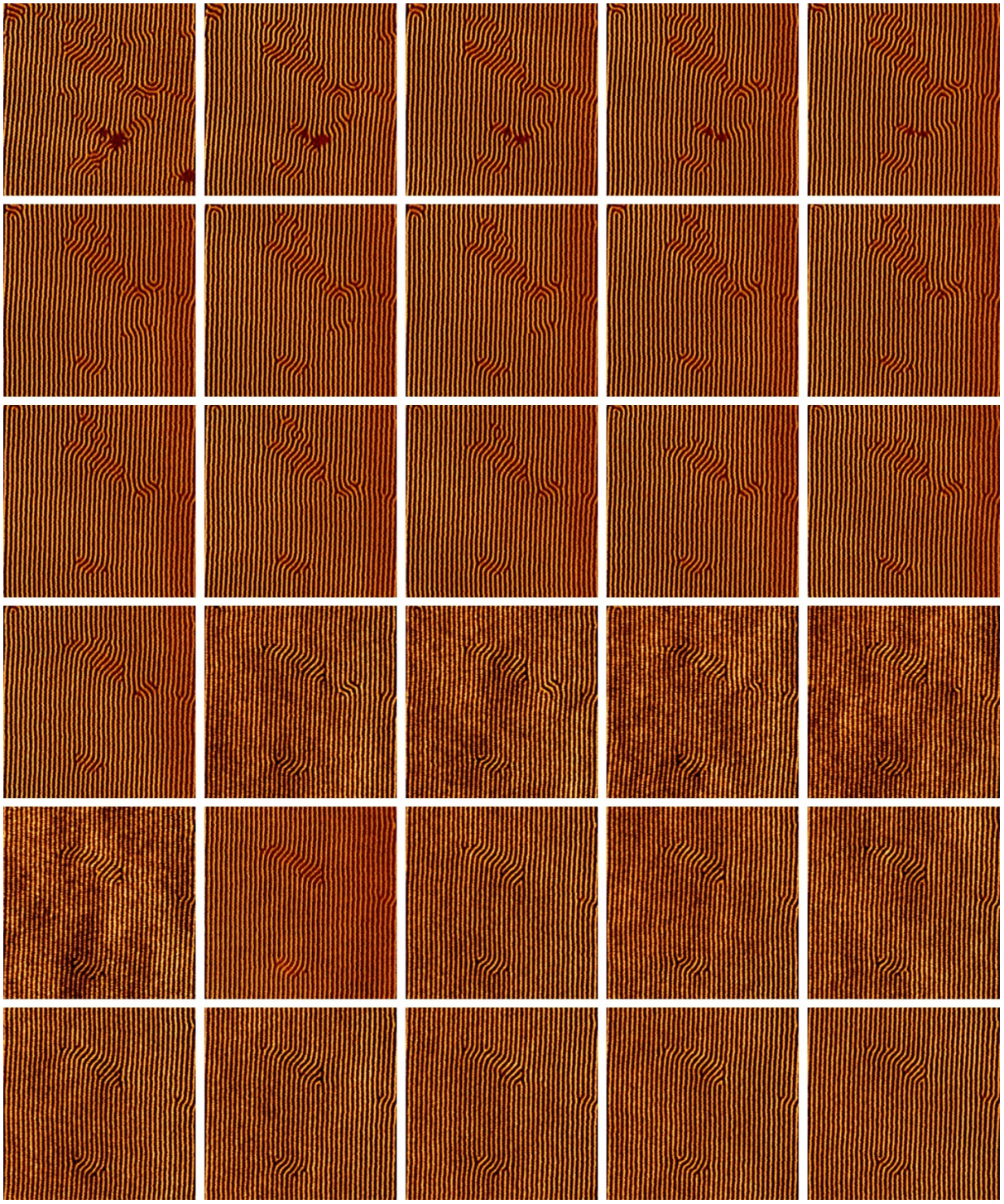


Figure 4-16. AFM phase images highlighting the annihilation mechanisms of a large complex defect area obtained at 190 °C from *t* = 00:20:24 to 04:39:07, Part 1.

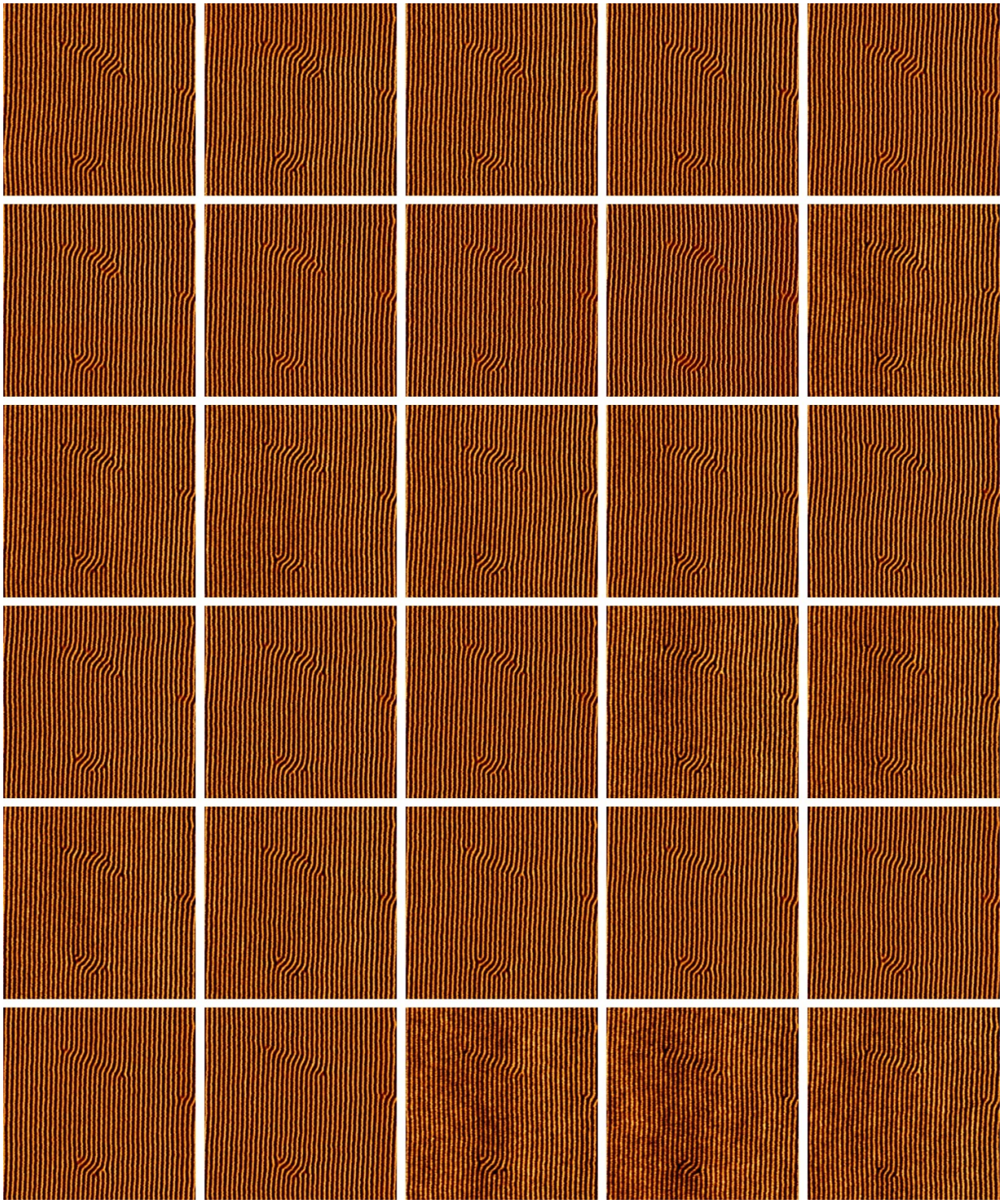


Figure 4-16. AFM phase images highlighting the annihilation mechanisms of a large complex defect area obtained at 190 °C from *t* = 00:20:24 to 04:39:07, Part 2.

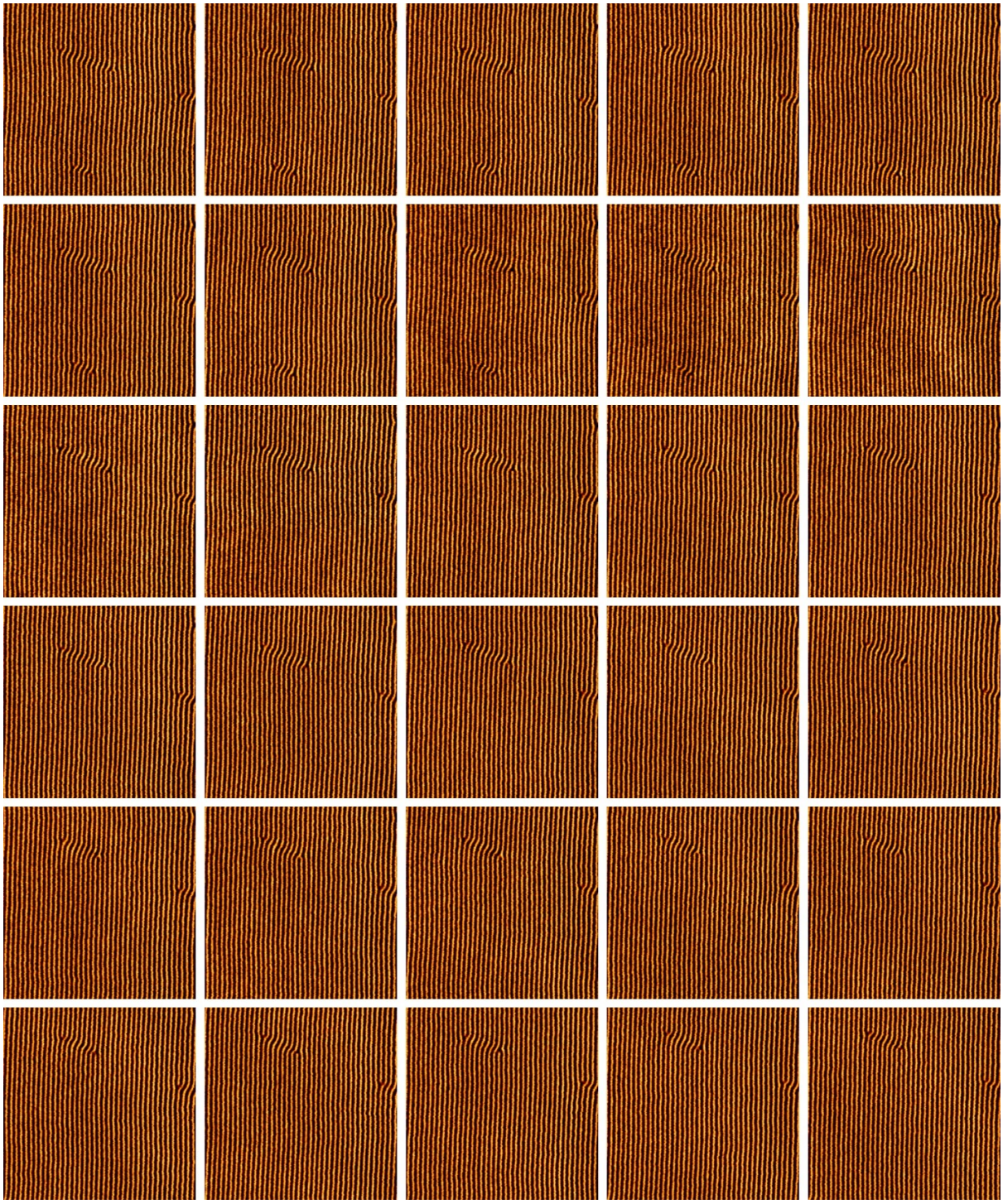


Figure 4-16. AFM phase images highlighting the annihilation mechanisms of a large complex defect area obtained at 190 °C from *t* = 00:20:24 to 04:39:07, Part 3.

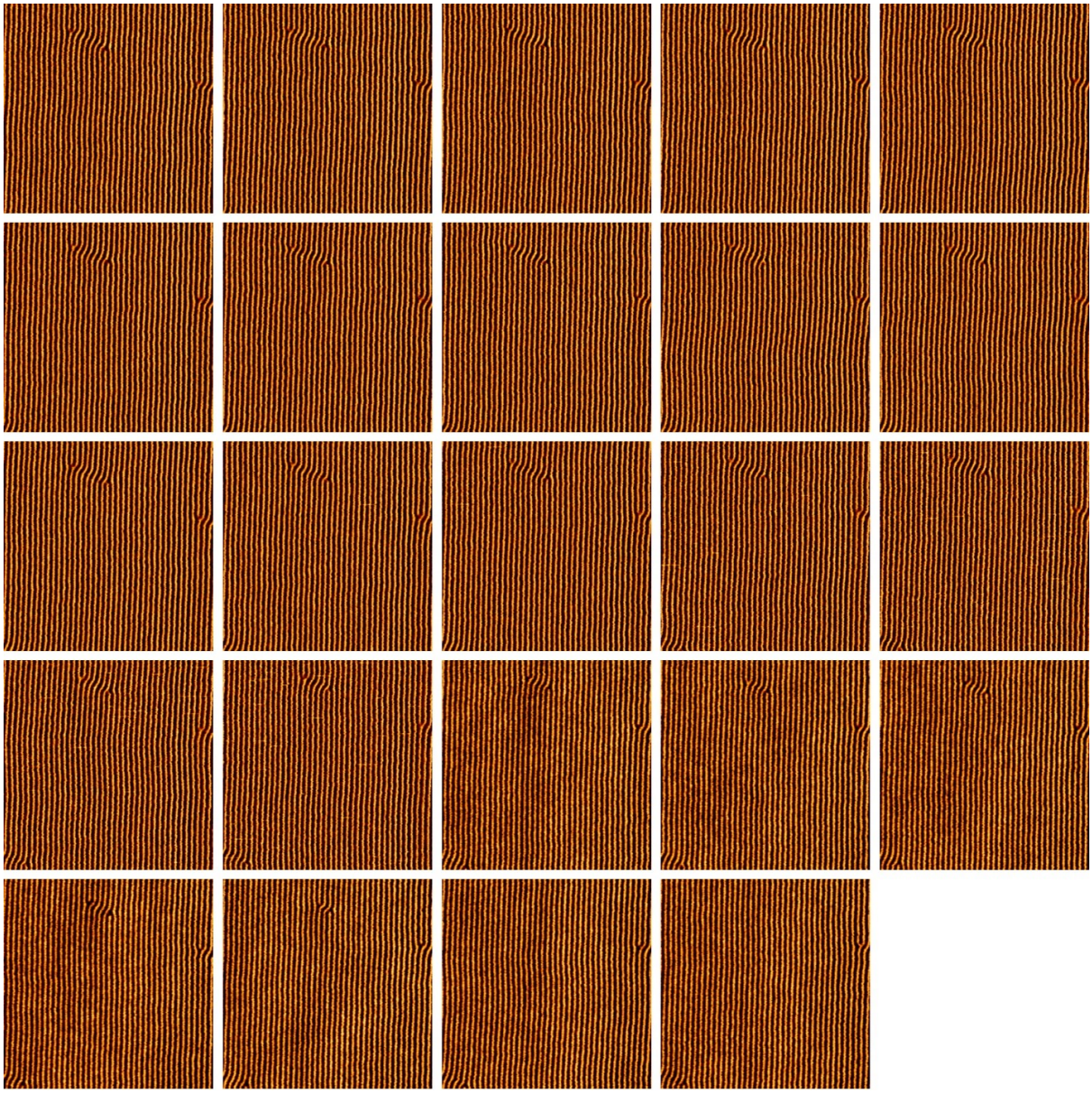


Figure 4-16. AFM phase images highlighting the annihilation mechanisms of a large complex defect area obtained at 190 °C from *t* = 00:20:24 to 04:39:07, Part 4.

Firstly, the annihilation of defects from a large area with multiple defects is shown in Fig. 4-15. These images were cropped out from the AFM phase images obtained at 190 °C from *t* = 00:20:24 to 00:34:10. In the center of the first image obtained at *t* = 00:20:24, a large area with multiple defects can be observed. This large defective area appears to be compounded from multiple smaller basic defects which are highlighted inside colored boxes. Three dislocation defects are highlighted in green, blue, and red, while an apposing disclination defect that contains multiple three-way junction defects and is directly connected

to one of the dislocations (in red) is observed. In the second image obtained at *t* = 00:23:28, the dislocation highlighted in green in the first image can no longer be observed, while the other defects remained. However, while the large dislocation highlighted in blue initially contained nine PS jogs in the first image, the number of PS jogs reduced to seven in the second image. Additionally, the apposing +½ point disclinations were initially both PMMA-core disclinations. However, in the second image, one of the +½ disclinations had shifted to a PS-core. Subsequently, in the third image obtained at *t* = 00:25:36, the initially large dislocation boxed in red had disappeared while the +½ disclination had switched back to a PMMA-core. Simultaneously, the number of lateral stripes separating the disclinations had decreased from five to four. At this point, a disclination pair with a chevron-like shape could be identified. The center of the chevron-shaped disclination pair defect (at the lower part of the initially purple box), remains unchanged from the first image, while the nearby apposed disclination approaches the core of the chevron-shaped defect. Therefore, an annihilation pathway observed earlier in chevron-shaped disclination pair defects can be observed. In the fourth image, the number of lateral stripes separating the two +½ disclination point defects gets reduced further to three and in the fifth image at *t* = 00:29:53, the +½ disclination in the top half of the initially purple box disappears, leaving behind a dislocation with multiple adjacent three-way junction defects. In the next image at *t* = 00:32:01, the right half of the chevron-shaped defect annihilates, leaving behind a simple dislocation pair defect separated by four PS jogs which disappears in the final image in this series at *t* = 00:34:10. Therefore, this focused snapshot suggests that while the initial defective area can consist of multiple numbers and types of defects, defect annihilation proceeds by the sequential annihilation of smaller, “easier to manage”, basic parts. This suggests that there are multiple metastable states and kinetic barriers to defect annihilation, and will not immediately annihilate instantly.

While Fig. 4-15 provides a small snapshot into a complicated defective area, the area observed is still relatively small and annihilation proceeds relatively quickly. In Fig. 4-16, a larger area with multiple complex defects that annihilate gradually over time is shown. These

images were obtained at 190 °C from *t* = 00:20:24 to 04:39:07. In the initial image, large defect areas with disclinations, dislocations, and orientational defects can all be observed. However, as seen earlier in Fig. 4-15, the defects annihilate sequentially and in parts. The parallel orientational defects could be observed to annihilate by slowly merging and reorienting into perpendicular lamellar stripes. The dislocations also initially consisted of multiple dislocations that were directly adjacent to one another. The smaller dislocations either annihilated independent of the bigger dislocations or the cores of the dislocations migrated and merged with the bigger dislocation, forming one large dislocation pair defect with multiple jogs in between. Meanwhile, the disclinations approached to annihilate, leaving behind dislocation pairs which also eventually approached and annihilated as expected. Therefore, as the linking and breaking of the microdomains are inherently stochastically-controlled and local translational movements, the annihilation of large complicated defects proceeds through a chain of small, local evolutions that eventually result in the long-range alignment of the striped microdomains.

4-3-9 Ultra-High-Speed Defect Tracking

While the isothermal in situ AFM experiments yield one image every 128 s, this is only fast enough for studying the mesoscopic overall behavior of the defects. To further study the stochastic linking and breaking of the defects, ultra-high-speed imaging is required. Therefore, to determine the speed at which the translation of the microdomains occurs, the rate at which in situ AFM images were obtained must be increased. After defects could no longer be observed in the 4 × 4 μm^2 area during the isothermal in situ AFM experiment at 210 °C, the imaging location was changed and centered onto a dislocation pair defect found elsewhere on the thin film surface. Additionally, as the cantilever may not be as stable in the first few images, the speed of imaging was gradually increased. Initially, image was recorded with an area of 500 × 500 nm^2, a resolution of 128 × 128 pixels, and a line rate of 12 Hz, yielding one image every 10 s. The line rate was slowly increased to 24 Hz, thereby allowing for one image to be obtained every 5 s. Subsequently, as the dislocation pair defect was sufficiently small, the imaging area was reduced to 250 × 250 nm^2, while the resolution

remained at 128 × 128 pixels, and the line rate was increased to 64 Hz. This allowed for one image to be recorded every 2 s, enabling the ultra-high-speed imaging of the evolution of the defect. Although it would be possible to record one image per second or possibly higher, to achieve such speeds, the line rate would need to be doubled or the pixels halved. This essentially reduces the quality of the images obtained by half, increases the influence of noise, and reduces the reliability With an image size of 250 × 250 nm^2, a resolution of 128 × 128 pixels, and a line rate of 64 Hz, one image was obtained every 2 s. The ultra-high-speed imaging of the dislocation pair defect was performed over approximately one hour. This yielded a total of over 1500 frames, making it difficult to show as a series of still images. Therefore, a 5 min long video is posted directly as a .avi file in Video 4-1 and certain snapshots of the linking and breaking of the microdomains are shown in Fig. 4-17 to 4-20. The first image (Fig. 4-17) shows a dislocation pair defect with PS- and PMMA-core dislocations separated by three PS jogs.

The ultra-high-speed imaging experiment yielded one image every 2 s, allowing for the precise tracking of the evolution of the microdomains. As previously seen in the annihilation mechanism for orientational defects, three distinct color contrasts could be observed in the phase images obtained. As usual, the dark phase can be attributed to the PS microdomain while the bright phase can be attributed to PMMA. However, a third orange-red phase can be frequently observed in the phase images. When more apparent, these orange-red areas are highlighted in a white circle in Fig. 4-18, 4-19, and 4-20. While various images remain solely dark and bright, indicating separate PS and PMMA domains, the orange-red phases can be seen to frequently extend from the tip of the stripe that ends at one of the dislocations to either the nearest jog or the adjacent longitudinally-aligned stripe. Additionally, these orange-red phases can be observed to extend in one image, before retracting and disappearing in the next. Alternatively, these orange-red phases were also observed prior to the linking of or after the breaking of the microdomains. These suggest that the orange-red phases are indicative of a transition state between different configurations of the defect. Typically, the microdomains in a defect move through either a “climbing” or a

“gliding” motion. The climbing motion typically accounts for movements in the same direction as the stripes, whereas the gliding motion refers to movements of microdomains perpendicular to the stripe direction. As climbing motion can be achieved by simple movements parallel to the interfaces, lamellar stripes are unable to annihilate via climbing motions as the microdomains are divided into distinct layers. For lamellar stripes to annihilate, one microdomain must diffuse normally into another in a gliding process. As this process requires the mixing of the domains, there can be a large free energy barrier to defect annihilation. The orange-red line seen in the AFM images is likely the proto-transition state between different configurations of the defect indicative of the microdomains diffusing across the interface to attempt to link up or break away from its neighboring microdomains. Indeed, such behaviors have been predicted previously. In a series of reports, Hur and co-workers simulated the pathway towards annihilation in dislocation dipole or pair defects.[28,29] Based on particle-based simulations of perpendicular lamellae under the influence of chemical guides, they found that prior to the linking or breaking of the stripe on the dislocation site, a small molecular bridge forms between the jog and straight stripe. As diffusion across the interface increases, the bridge between the jog and stripe can either grow to form a linkage or disappear to break away. The appearance of the orange-red bridge between the dislocation and the jog or stripe prior to the linking or after the breaking of the linkages is highly indicative of the gliding motion of the defects. Therefore, the appearance of the orange-red phases is highly indicative of the formation of such bridges that could enable the evolution of the defect configuration and the eventual annihilation of the defect. However, as shown in Fig. 4-18, it is notable that the appearance of the bridge does not necessarily mean that the defect will change configurations. The bridge can disappear, reverting the defect to its original configuration. As suggested by the simulative studies,[28] this is likely indicative of the presence of multiple kinetic barriers that can prevent the reconfiguration of the defect.

20200229 TEL
DSA TF3 In Situ A

Video 4-1. Ultra-high-speed imaging of a dislocation pair defect.

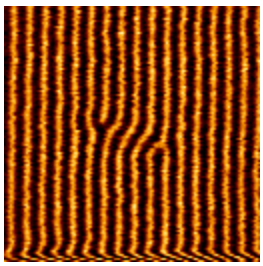


Figure 4-17 First image obtained during the ultra-high-speed imaging of a dislocation pair defect. This image was recorded at 500 × 500 nm^2, 128 × 128 pixels, and a line rate of 12 Hz.

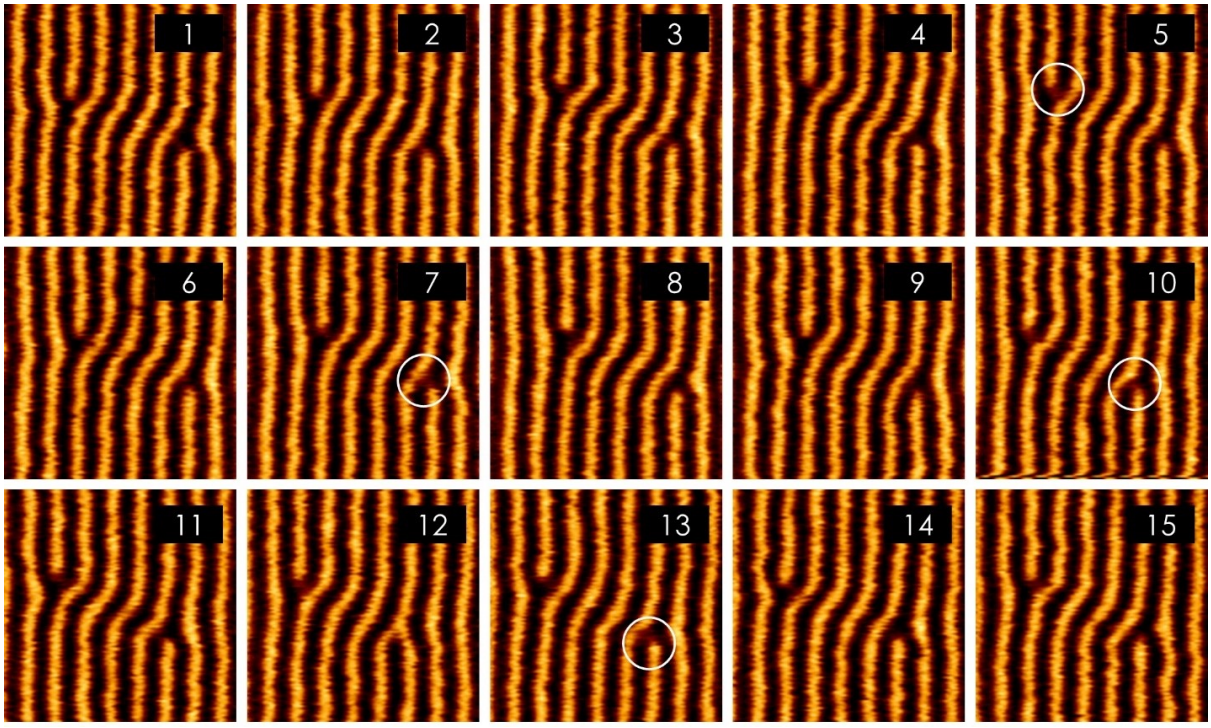


Figure 4-18. A series of images obtained during the ultra-high-speed imaging of a dislocation pair defect that shows the linking and breaking of the microdomains. These images were recorded every 2 s at 250 × 250 nm^2, 128 × 128 pixels, and a line rate of 64 Hz. The images in the series are labelled from 1 to 15 and areas that indicate the underlying gliding motion of the microdomains are highlighted in white circles.

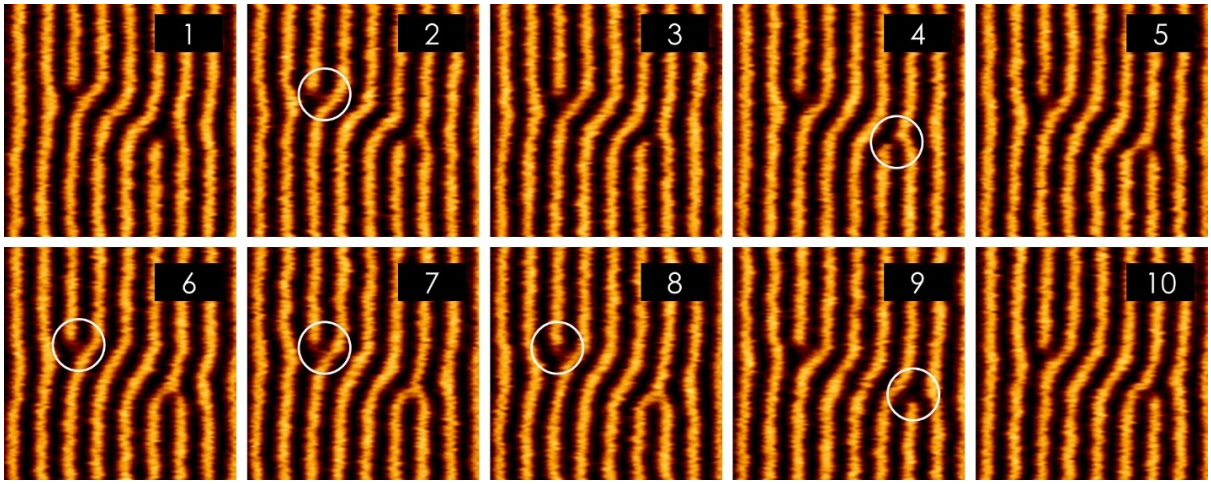


Figure 4-19. A series of images obtained during the ultra-high-speed imaging of a dislocation pair defect that shows the mechanism that results in an increase in the number of jogs separating the dislocation pair. These images were recorded every 2 s at 250 × 250 nm^2, 128 × 128 pixels, and a line rate of 64 Hz. The images in the series are labelled from 1 to 10 and areas that indicate the underlying gliding motion of the microdomains are highlighted in white circles.

Additionally, while the simulative studies showed that the dislocation can connect with the nearest jog to work towards defect annihilation, Fig. 4-19 also shows that a bridge can form between the dislocation and the adjacent longitudinally-aligned stripe. Interestingly, when a bridge is about to form between the dislocation and the adjacent longitudinally-aligned stripe is about to form, the part of the longitudinally-aligned stripe that is nearest to the dislocation bulges outwards towards the dislocation. As a bridge forms, the dislocation can link with the longitudinally-aligned stripe, transferring the core of the dislocation and once again moving away from defect annihilation. Additionally, as these events are dictated by localized stochastic movements that are largely independent of previous configurations, the initially longitudinally-aligned stripe can break away from the newly-formed dislocation core. This results in the addition of another jog stripe between the dislocation pairs, suggesting that the stochastic movement of the microdomains does not necessarily always move towards defect annihilation. Nevertheless, as shown in Fig. 4-20, if the dislocation connects with the adjacent jog, subsequent separation of the jog from the now longitudinally-

aligned stripe allows for a reduction in the number of jog dislocations, potentially moving towards defect annihilation. Furthermore, an “open-junction” defect can be observed in frame 28 in Fig. 4-20. In the previous image, a simple PS-core dislocation next to a PMMA jog can be observed. However, in frame 28, the PMMA jog stripe could be observed to separate away, leaving behind a bridge under where the jog used to be. Simultaneously, a bridge could be observed to form between the longitudinally-aligned parts of the open three-way junction. In the next frame (29), the longitudinally-aligned arms of the open three-way junction could be observed to link up, leaving the remaining arm as the core of a new dislocation. These series of images suggest that the transition state between the breaking and linking of the microdomains from one configuration to another can proceed synchronously, analogous to a nucleophilic substitution (S_N 2) reaction, if a comparison is made to mechanisms well studied in organic chemistry. However, the movement of the BCP microdomains is extremely swift. Although ultra-high-speed imaging allows for one image to be recorded every two seconds, this may still be too slow to capture every minute detail behind the translation of the microdomains. To exactly determine whether the microdomains link up and break away in a step-wise and sequential manner, synchronously, or a probabilistic mixture of both, even faster imaging capabilities may be required.

Although ultra-high-speed imaging of the dislocation pair defect continued for approximately 1 h, the dislocation defect was unfortunately never observed to completely annihilate. Instead, the number of jogs separating the dislocation pair simply fluctuated from two to five, suggesting that the defect had reach a highly metastable state. In situ imaging was then stopped to prevent thermal damage to the AFM system from long-term heating at high temperatures. Nevertheless, the ultra-high-speed imaging of the dislocation pair defect revealed the swift, real-time, and real-space evolution of the defect from one configuration to another. The development of bridges indicative of the gliding motion of the lamellar stripes could also be observed clearly. Such bridges appeared frequently but did not necessarily lead to the linking of the microdomains. Therefore, disclination defects can become highly metastable, with the edge dislocations simply switching cores from one stripe to another and

the defect does not move towards annihilation. This stochastic switching of dislocation cores likely explains why dislocations are so prevalent in DSA thin films and shows the difficulty behind the complete annihilation of all defects.

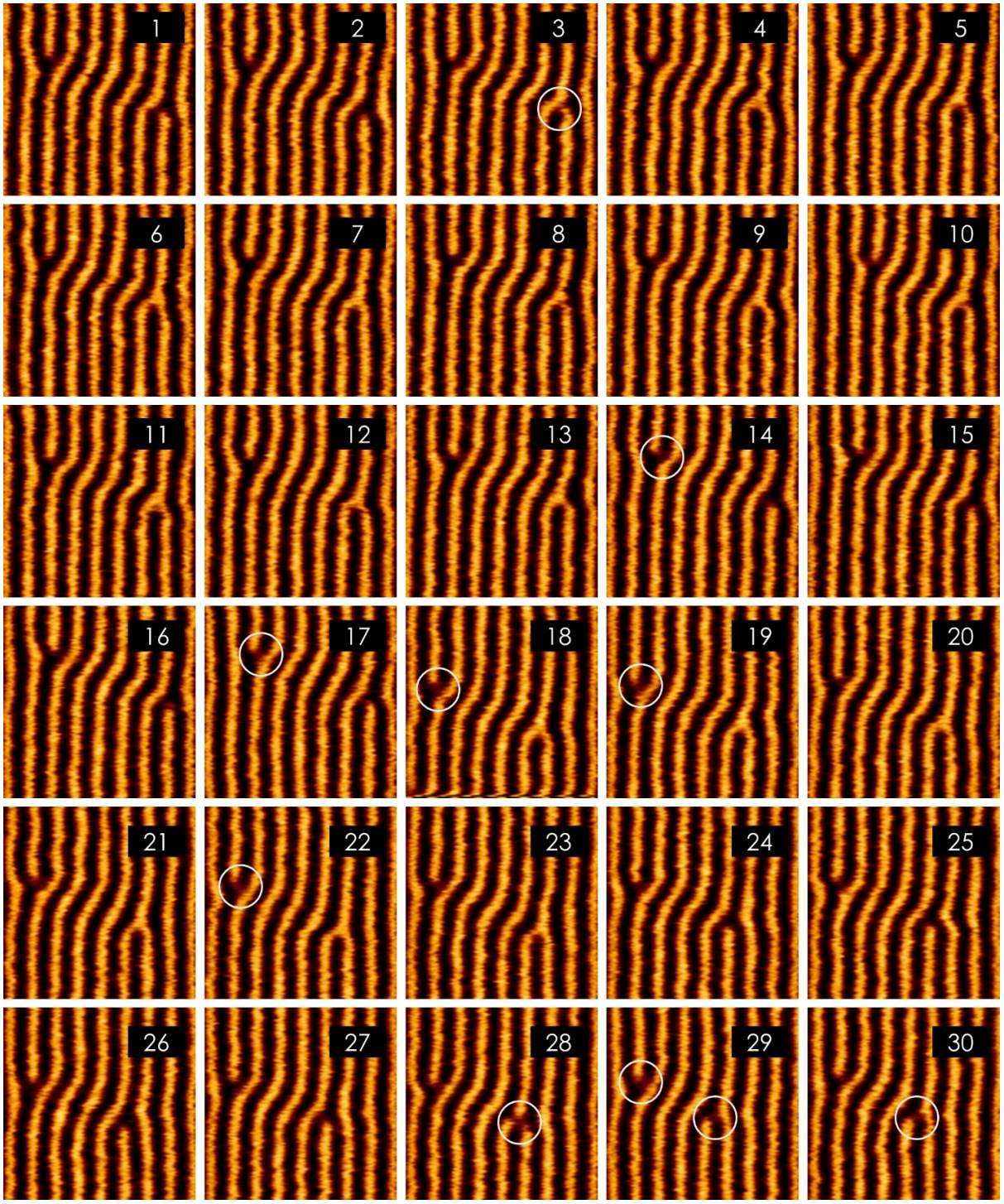


Figure 4-20. A series of images obtained during the ultra-high-speed imaging of a dislocation pair defect that shows the mechanism that results in a decrease in the number of jogs separating the dislocation pair. These images were recorded every 2 s at 250 × 250

nm^2, 128 × 128 pixels, and a line rate of 64 Hz. The images in the series are labelled from 1 to 10 and areas that indicate the underlying gliding motion of the microdomains are highlighted in white circles.

4-4 Conclusion

These defectivity studies suggest that although defects can coalesce into large complex defect areas, the mechanism for annihilation is more simplistic. The microdomains can stochastically link up and break away locally but simultaneously at any potential defect site on the thin film. The annihilation of large complex defect areas proceeds by the rearrangement of defect sites into smaller defect sub-areas that become easier to manage and can sequentially annihilate. As these small defect sub-areas annihilate sequentially, the initially large and complex defect becomes smaller and less complex, eventually becoming a small and simple defect that annihilates as well. Furthermore, it was shown that disclination defects tend to transform into dislocation defects in the course of defect annihilation, thereby explaining the increased appearance of disclination defects in DSA samples. Additionally, it was shown that defects may not always move towards annihilation. The probabilistic nature of the linking and breaking of the microdomains means that there is a chance that a defect may never heal, simply equilibrating between multiple configurations of defects. To reduce the issue of defectivity with precision, the origins and annihilation pathways of defects must be clarified and understood.

4-5 References

(1) Tong, Q.; Sibener, S. J. Visualization of Individual Defect Mobility and Annihilation within Cylinder-Forming Diblock Copolymer Thin Films on Nanopatterned Substrates. *Macromolecules* **2013**, *46* (21), 8538–8544 DOI: 10.1021/ma401629s.

(2) Hahm, J.; Lopes, W. A.; Jaeger, H. M.; Sibener, S. J. Defect Evolution in Ultrathin Films of Polystyrene-Block-Polymethylmethacrylate Diblock Copolymers Observed by Atomic Force Microscopy. *J. Chem. Phys.* **1998**, *109* (23), 10111–10114 DOI: 10.1063/1.477702.

(3) Yufa, N. A.; Li, J.; Sibener, S. J. In-Situ High-Temperature Studies of Diblock

Copolymer Structural Evolution. *Macromolecules* **2009**, *42* (7), 2667–2671 DOI: 10.1021/ma802751c.

(4) Tong, Q.; Zheng, Q.; Sibener, S. J. Alignment and Structural Evolution of Cylinder-Forming Diblock Copolymer Thin Films in Patterned Tapered-Width Nanochannels. *Macromolecules* **2014**, *47* (13), 4236–4242 DOI: 10.1021/ma500911y.

(5) Ryu, H. J.; Tong, Q.; Sibener, S. J. Time-Resolved Analysis of Domain Growth and Alignment of Cylinder-Forming Block Copolymers Confined within Nanopatterned Substrates. *J. Phys. Chem. Lett.* **2013**, *4* (17), 2890–2895 DOI: 10.1021/jz4015794.

(6) Hahm, J.; Lopes, W. A.; Jaeger, H. M.; Sibener, S. J. Defect Evolution in Ultrathin Films of Polystyrene-Block-Polymethylmethacrylate Diblock Copolymers Observed by Atomic Force Microscopy. *J. Chem. Phys.* **1998**, *109* DOI: 10.1063/1.477702.

(7) Hahm, J.; Sibener, S. J. Time-Resolved Atomic Force Microscopy Imaging Studies of Asymmetric PS-b-PMMA Ultrathin Films: Dislocation and Disclination Transformations, Defect Mobility, and Evolution of Nanoscale Morphology. *J. Chem. Phys.* **2001**, *114* (10), 4730–4740 DOI: 10.1063/1.1342239.

(8) Raybin, J.; Ren, J.; Chen, X.; Gronheid, R.; Nealey, P. F.; Sibener, S. J. Real-Time Atomic Force Microscopy Imaging of Block Copolymer Directed Self Assembly. *Nano Lett.* **2017**, *17* (12), 7717–7723 DOI: 10.1021/acs.nanolett.7b03881.

(9) Majewski, P. W.; Yager, K. G. Rapid Ordering of Block Copolymer Thin Films. *J. Phys. Condens. Matter* **2016**, *28*, 403002 DOI: 10.1088/0953-8984/28/40/403002.

(10) Kim, S. O.; Kim, B. H.; Kim, K.; Koo, C. M.; Stoykovich, M. P.; Nealey, P. F.; Solak, H. H. Defect Structure in Thin Films of a Lamellar Block Copolymer Self-Assembled on Neutral Homogeneous and Chemically Nanopatterned Surfaces. *Macromolecules* **2006**, *39* (16), 5466–5470 DOI: 10.1021/ma060087u.

(11) Doise, J.; Koh, J. H.; Kim, J. Y.; Zhu, Q.; Kinoshita, N.; Suh, H. S.; Vandenberghe, G.; Willson, C. G.; Ellison, C. J. Strategies for Increasing the Rate of Defect Annihilation in the Directed Self-Assembly of High-χ Block Copolymers. *ACS Appl. Mater. Interfaces* **2019**, *11* (51), 48419–48427 DOI: 10.1021/acsami.9b17858.

(12) Kim, J.; Wan, J.; Miyazaki, S.; Yin, J.; Cao, Y.; Her, Y. J.; Wu, H.; Shan, J.; Kurosawa, K.; Lin, G. The SMART^{TM} Process for Directed Block Co-Polymer Self-Assembly. *J. Photopolym. Sci. Technol.* **2013**, *26* (5), 573–579 DOI: 10.2494/photopolymer.26.573.

(13) Muramatsu, M.; Nishi, T.; You, G.; Ido, Y.; Kitano, T. Defect and Roughness Reduction of Chemo-Epitaxy DSA Pattern. *Proc. SPIE* **2018**, *10584*, 105840M DOI: 10.1117/12.2297185.

(14) Muramatsu, M.; Nishi, T.; You, G.; Ido, Y.; Kitano, T. Pattern Defect Reduction for Chemo-Epitaxy DSA Process. *Proc. SPIE* **2019**, *10960*, 109600W DOI: 10.1117/12.2514671.

(15) Muramatsu, M.; Nishi, T.; Ido, Y.; Kitano, T. Defect Mitigation of Chemo-Epitaxy DSA Patterns. *Proc. SPIE* **2020**, *11326*, 113260Y DOI: 10.1117/12.2551996.

(16) Chandra, A.; Nakatani, R.; Uchiyama, T.; Seino, Y.; Sato, H.; Kasahara, Y.; Azuma, T.; Hayakawa, T. Direct In Situ Observation of the Early-Stage Disorder–Order Evolution of Perpendicular Lamellae in Thermally Annealed High-χ Block Copolymer Thin Films. *Adv. Mater. Interfaces* **2019**, *6*, 1801401 DOI: 10.1002/admi.201801401.

(17) Ohta, T.; Jasnow, D.; Kawasaki, K. Universal Scaling in the Motion of Random Interfaces. *Phys. Rev. Lett.* **1982**, *49* (17), 1223–1226.

(18) Harrison, C.; Adamson, D. H.; Cheng, Z.; Sebastian, J. M.; Sethuraman, S.; Huse, D. A.; Register, R. A.; Chaikin, P. M. Mechanisms of Ordering in Striped Patterns. *Science (80-.).* **2000**, *290* (5496), 1558–1560 DOI: 10.1126/science.290.5496.1558.

(19) Dai, H. J.; Balsara, N. P.; Garetz, B. A.; Newstein, M. C. Grain Growth and Defect Annihilation in Block Copolymers. *Phys. Rev. Lett.* **1996**, *77* (17), 3677–3680 DOI: 10.1103/PhysRevLett.77.3677.

(20) Perego, M.; Ferrarese Lupi, F.; Ceresoli, M.; Giammaria, T. J.; Seguini, G.; Enrico, E.; Boarino, L.; Antonioli, D.; Gianotti, V.; Sparnacci, K.; Laus, M. Ordering Dynamics in Symmetric PS-b-PMMA Diblock Copolymer Thin Films during Rapid Thermal Processing. *J. Mater. Chem. C* **2014**, *2* (32), 6655–6664 DOI: 10.1039/c4tc00756e.

(21) Nakatani, R.; Chandra, A.; Uchiyama, T.; Nabae, Y.; Hayakawa, T. Dynamic Ordering

in High-χ Block Copolymer Lamellae Based on Cross-Sectional Orientational Alignment. *ACS Macro Lett.* **2019**, *8* (9), 1122–1127 DOI: 10.1021/acsmacrolett.9b00353.

(22) Peters, R. D.; Stasiak, P.; Matsen, M. W.; Dalnoki-Veress, K. Morphology Induced Spinodal Decomposition at the Surface of Symmetric Diblock Copolymer Films. *ACS Macro Lett.* **2013**, *2* (5), 441–445 DOI: 10.1021/mz400159s.

(23) Wu, S. Surface and Interfacial Tensions of Polymer Melts. II. Poly(Methyl Methacrylate), Poly(n-Butyl Methacrylate) and Polystyrene. *J. Phys. Chem.* **1969**, *74* (3), 632–638 DOI: 10.1021/j100698a026.

(24) Mansky, P.; Russell, T. P.; Hawker, C. J.; Mays, J.; Cook, D. C.; Satija, S. K. Interfacial Segregation in Disordered Block Copolymers: Effect of Tunable Surface Potentials. *Phys. Rev. Lett.* **1997**, *79* (2), 237–240 DOI: 10.1103/PhysRevLett.79.237.

(25) Joly, S.; Raquois, A.; Paris, F.; Hamdoun, B.; Auvray, L.; Ausserre, D.; Gallot, Y. Early Stage of Spinodal Decomposition in 2D. *Phys. Rev. Lett.* **1996**, *77* (21), 4394–4397 DOI: 10.1103/PhysRevLett.77.4394.

(26) Segal-Peretz, T.; Ren, J.; Xiong, S.; Khaira, G.; Bowen, A.; Ocola, L. E.; Divan, R.; Doxastakis, M.; Ferrier, N. J.; De Pablo, J.; Nealey, P. F. Quantitative Three-Dimensional Characterization of Block Copolymer Directed Self-Assembly on Combined Chemical and Topographical Prepatterned Templates. *ACS Nano* **2017**, *11* (2), 1307–1319 DOI: 10.1021/acsnano.6b05657.

(27) Ren, J.; Zhou, C.; Chen, X.; Dolejsi, M.; Craig, G. S. W.; Rincon Delgadillo, P. A.; Segal-Peretz, T.; Nealey, P. F. Engineering the Kinetics of Directed Self-Assembly of Block Copolymers toward Fast and Defect-Free Assembly. *ACS Appl. Mater. Interfaces* **2018**, *10* (27), 23414–23423 DOI: 10.1021/acsami.8b05247.

(28) Hur, S. M.; Thapar, V.; Ramírez-Hernández, A.; Khaira, G.; Segal-Peretz, T.; Rincon-Delgadillo, P. A.; Li, W.; Müller, M.; Nealey, P. F.; De Pablo, J. J. Molecular Pathways for Defect Annihilation in Directed Self-Assembly. *Proc. Natl. Acad. Sci. U. S. A.* **2015**, *112* (46), 14144–14149 DOI: 10.1073/pnas.1508225112.

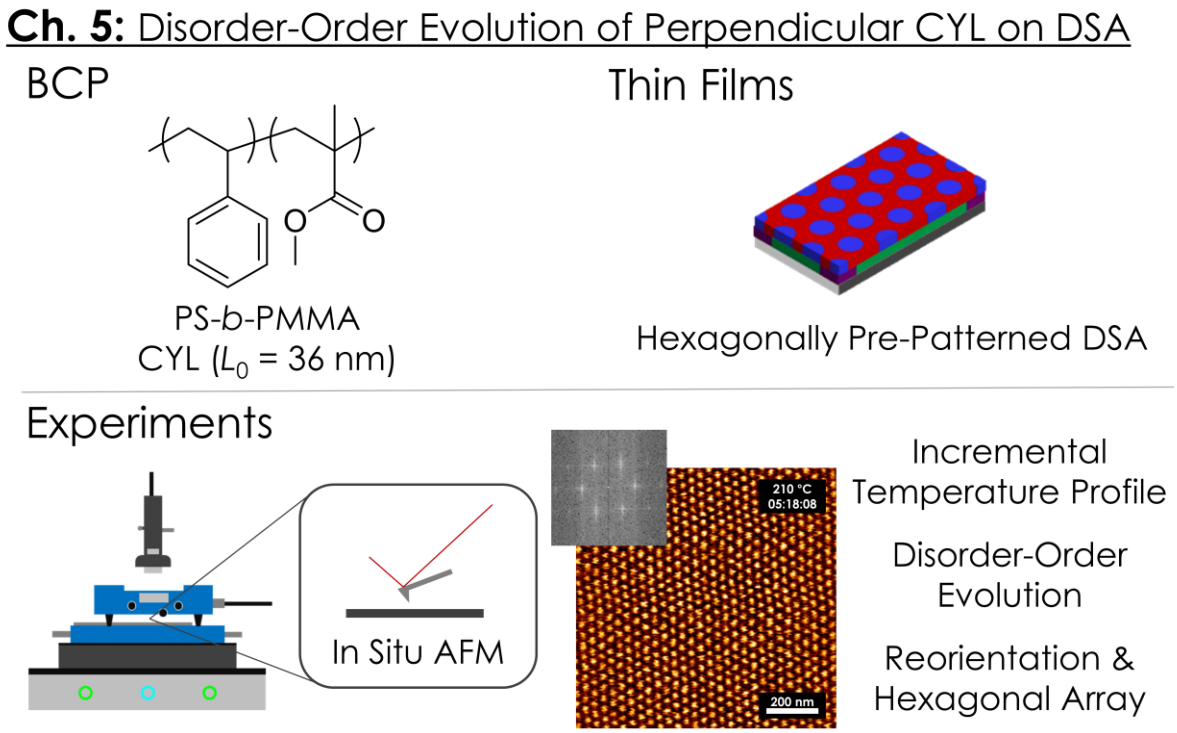
(29) Hur, S. M.; Thapar, V.; Ramírez-Hernández, A.; Nealey, P. F.; De Pablo, J. J. Defect Annihilation Pathways in Directed Assembly of Lamellar Block Copolymer Thin Films. *ACS Nano* **2018**, *12* (10), 9974–9981 DOI: 10.1021/acsnano.8b04202.

Chapter 5 Structural Evolution on Perpendicularly-Oriented PS-*b*-PMMA Hexagonally-Packed Cylinders on Chemically-Prepatterned Contact Hole Substrates

5-1 Introduction

The morphologies formed by BCPs can be controlled by changing the volume fractions of the blocks. While symmetric compositions of a diblock copolymer yield lamellar structures which can be used to produce line and space (L/S) structures for lithographic applications, asymmetric compositions can yield gyroid, cylindrical, or spherical structures. In addition to lamellae (LAM), cylindrical (CYL), and spherical (SPH) morphologies can also be used as lithographic resists. Monolayers of parallel cylinders can form similar L/S patterns to those formed by perpendicular lamellae. Additionally, monolayers of close-packed spheres can be used to develop a hexagonally-arranged pattern of dots. Such hexagonally-arranged dots could potentially be used as resists in the manufacturing of high-density bit-patterned media and magnetic storage devices. However, as parallel cylinders and close-packed spheres do not form continuous structures in the vertical direction, resists with such morphologies are limited to monolayers, thereby reducing the potential aspect ratios obtainable. On the other hand, perpendicular cylinders could form hexagonally-arranged dot structures that can extend in the vertical direction. However, defects formed by the self-assembled structures of perpendicular cylinders presents the same problems as those formed by perpendicular lamellae. Additionally, the evolution of defects in striped patterns formed by perpendicular lamellae is likely different to those formed by hexagonally-arranged dot patterns. Particularly, while lamellar defects can only move through a gliding motion which involves the interdiffusion of the microdomains, resulting in increased interfacial contact and a larger activation energy barrier for defect annihilation, cylindrical morphologies can move through a climbing motion in addition to a gliding motion. The climbing motion simply involves the parallel movement of the microdomains relative to the defect site. This is possible as a matrix domain exists in cylinders, allowing for the microdomains to move around the matrix for defect annihilation. Therefore, to work towards reducing the defectivity

of cylindrical structures for potential applications in high volume manufacturing, the growth of ordered structures and evolution of defects in cylindrical structures must be studied in detail. In this chapter, the growth of ordered structures and hexagonal arrangement of perpendicular cylinders on pre-patterned chemoepitaxial DSA substrates is studied using in situ AFM.



Schematic 5-1. Illustrative overview of the goals and content in Chapter 5.

5-2 Experimental Section

5-2-1 Instruments

A JPK Instruments NanoWizard ULTRA Speed A AFM (Bruker) equipped with a High Temperature Heating Stage (HTHS), a custom-made nitrogen (N_2) environment chamber, and an Olympus microcantilever (OCML-AC55TS) with a resonance frequency of 2.0 MHz were used to record the atomic force microscopy (AFM) images in AC mode. The setpoint was pegged to 65 – 70% of the target amplitude, while the gain was set to 400 to minimize perturbations on the sample and no side effects were observed on the thin films upon in situ AFM imaging. Images 1 × 1 μm^2 in size with a resolution of 256 × 256 pixels were obtained at a line rate of 4 Hz, yielding one image every 64 s. To maintain an inert atmosphere, N_2

was flowed into the environment chamber at 0.5 ± 0.2 L min^{-1}. The AFM images were processed by subtracting the background using JPK Data Processing software. Fast-Fourier transformation (FFT) analyses of the phase images were conducted using ImageJ and Matlab.

5-2-2 Sample Preparation

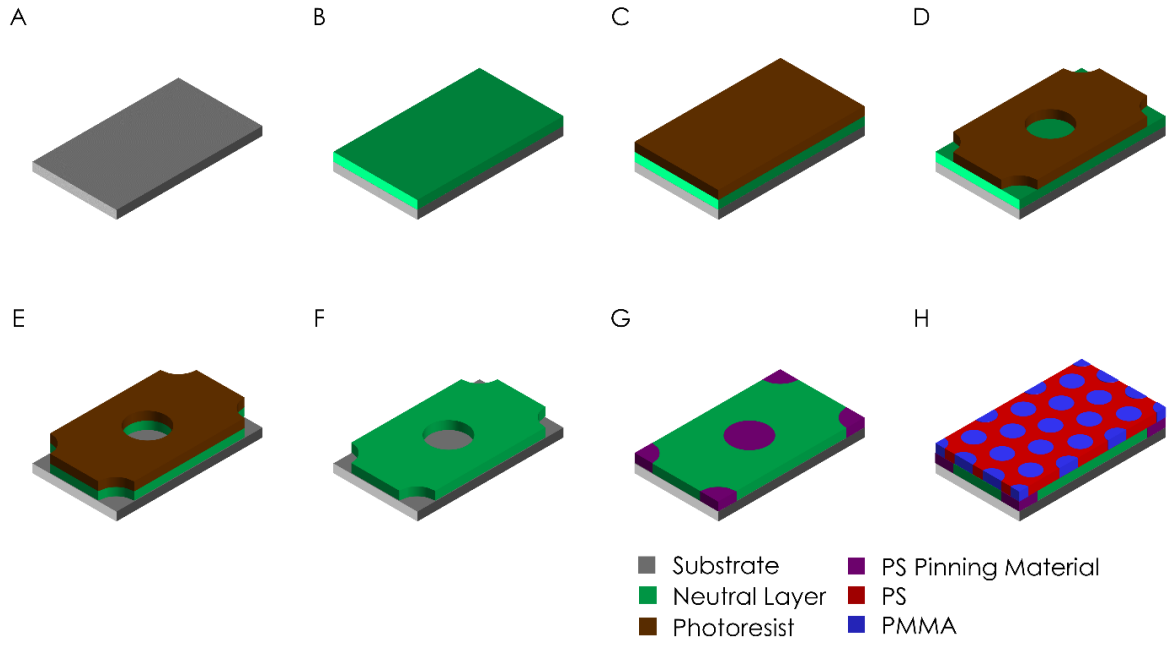
As-cast thin films containing cylinder-forming PS-*b*-PMMA on pre-patterned substrates prepared were received from Tokyo Electron Kyushu Limited and prepared as previously reported (Schematic 5-2).[1] A neutral layer was first deposited onto the substrate, followed by a resist. A 120 nm pitch hexagonal pattern at a 9X multiplication relative to a 40 nm center-to-center cylinder-forming BCP was imprinted onto the resist and a hexagonally-arranged hole pattern was developed. The hexagonal holes at 9X multiplication was subsequently transferred onto the neutral layer and the resist was stripped. A PS-preferential brush was backfilled into the hexagonal holes found on the neutral layer. A 40 nm center-to-center cylinder-forming PS-*b*-PMMA was subsequently spin-coated onto the thin film.

5-3 Results and Discussion

While the striped patterns afforded by perpendicular lamellar or parallel cylindrical patterns could potentially be used as line and space (L/S) structures for lithographic applications, the hexagonal arrangement of perpendicular cylinders could also be used in the fabrication of bit-patterned media and other high-density storage devices. Yet, little attention has been afforded to studying the self-assembly behavior of perpendicular cylinders in comparison to perpendicular lamellae or parallel cylinders. To work towards the realization of using BCPs in high volume manufacturing, the self-assembly behavior of the different morphologies of BCPs need to be studied. Herein, the first report of a real-time and real-space characterization of perpendicular lamellar structures from the disordered state to a well-ordered state is presented.

Cylinder-forming PS-*b*-PMMA with a cylinder center-to-center distance of 40 nm were deposited on pre-patterned substrates with hexagonally-arranged chemical guides as previously reported.[1] The as-cast thin films were then characterized using in situ AFM on a

heating stage equipped with a nitrogen environment chamber. With a resolution of 256 × 256 pixels, 1 × 1 μm^2 images were obtained using a line rate of 4 Hz, yielding one image every 64 s. After imaging the as-cast thin films at 25 °C for 10 min, the temperature was raised to 90 °C. The AFM was allowed to stabilize at the temperature for 5 min before imaging started. Subsequently, the temperature was raised by 2 °C increments every 5 min until a maximum annealing temperature of 210 °C. Snapshots of the in situ AFM experiment are shown in Fig. 5-1 to 5-7, and the plot of RMS roughness against temperature, calculated from the corresponding height images, is shown in Fig. 5-8.



Schematic 5-2. Schematic of the process flow for the preparation of hexagonally-arranged guide patterns for the DSA of perpendicularly-oriented cylindrical patterns of PS-*b*-PMMA. Onto a (A) substrate, (B) a neutral layer and (C) photoresist is deposited. (D) A hexagonal pre-pattern is developed on the photoresist and (E) transferred down onto the neutral layer. (F) The photoresist is removed and (G) a PS-pinning material is backfilled into the hexagonal holes in the pre-patterned neutral layer. (H) A cylinder-forming PS-*b*-PMMA is deposited and annealed to obtain a hexagonally-arranged perpendicular cylindrical pattern.

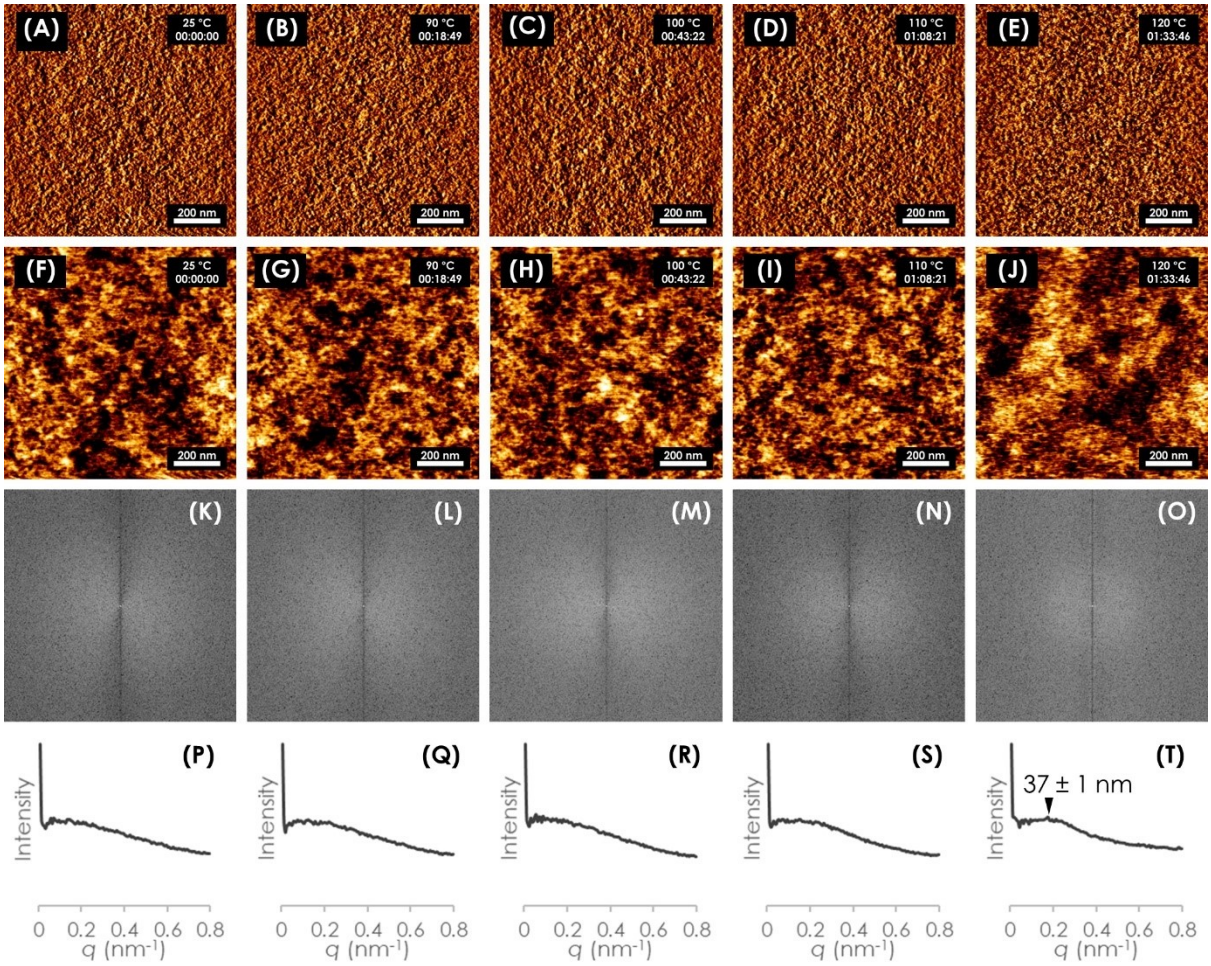


Figure 5-1. (A-E) Phase and (F-J) height images from the in situ AFM experiment on perpendicular cylinders from 25 to 120 °C. The temperature and time stamp in hours:minutes:seconds can be found in the top right of each image. (K-O) 2D-FFT images of the phase images in A-E. (P-T) 1D azimuthally-integrated profiles of the 2D-FFT images in K-O.

As previously seen in the in situ AFM experiment studying the evolution of perpendicular lamellae under incrementally increasing annealing temperatures, several stages could be found in the evolution of perpendicular cylindrical structures as well. In Fig. 5-1, snapshots of the phase and height images obtained during the in situ AFM experiment between 25 and 120 °C are shown. Additionally, a Fast-Fourier transformation (FFT) was performed on the phase images and the obtained two-dimensional (2D) profiles were subsequently azimuthally-integrated to yield one-dimensional (1D) FFT profiles. Unlike in the case of lamella-forming PS-*b*-PMMA prepared on chemically pre-patterned DSA substrates,

topographic perturbations that can be attributed to the effects of the chemical guides could not be detected in the first images obtained at 25 °C. Instead, a featureless surface, akin to BCP thin films prepared on unpatterned substrates, with random dark dots in a bright matrix is observed in the AFM images obtained at 25 °C. This is reflected in the 2D-FFT image and 1D-FFT profile where no peak could be observed. Even as the temperature increased to 90 °C, the surface remained featureless and no peaks corresponding to periodic ordering could not be detected on the FFT profiles. However, as the annealing temperature reached 120 °C, while the AFM images remain largely random and featureless, a weak, broad peak could be detected in the 1D-FFT profile. Using the equation $d = 2\pi/q^*$, where q^* is the position of the primary peak on the profile, the peak corresponds to a periodicity of roughly 37 ± 1 nm. As previously seen in the incremental annealing experiments on lamellar PS-*b*-PMMA, in this lower temperature regime, the BCP is likely simply kinetically frozen in a highly irregular, disorder-like state, as expected of as-cast BCP thin films.

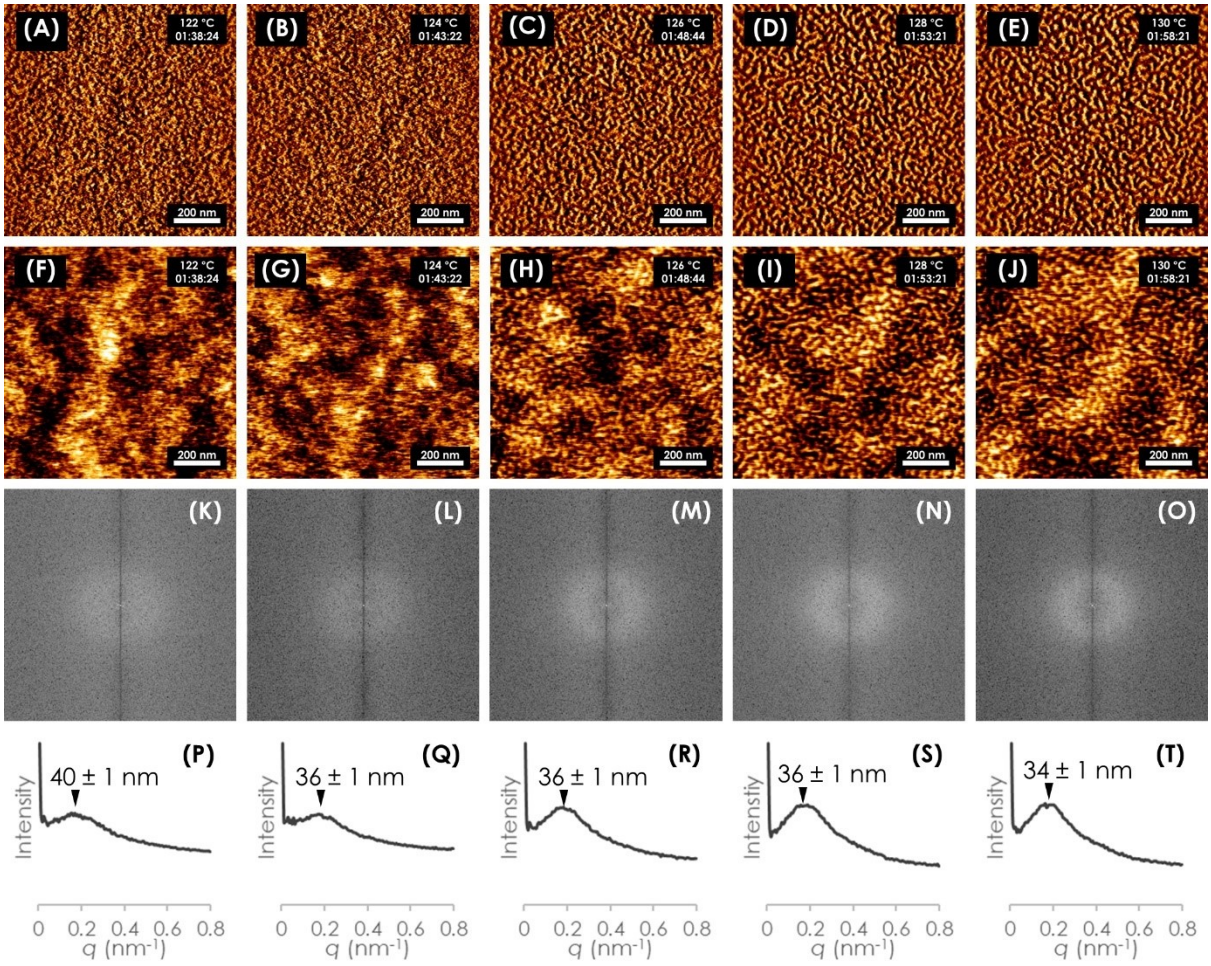


Figure 5-2. (A-E) Phase and (F-J) height images from the in situ AFM experiment on perpendicular cylinders from 122 to 130 °C. The temperature and time stamp in hours:minutes:seconds can be found in the top right of each image. (K-O) 2D-FFT images of the phase images in A-E. (P-T) 1D azimuthally-integrated profiles of the 2D-FFT images in K-O.

In the next temperature regime however, a transition from a glassy to rubbery state could be observed as short-range patterns appear on the surface. As the temperature increased from 122 to 130 °C, bright dots and short, wavy, irregular lines appear to grow in a dark matrix. While the bright dots and lines correspond to PMMA, the dark matrix can be attributed to the PS domain. Earlier studies of the early-stage evolution of ordered structures have shown that the initial structure formed at the onset of self-assembly is highly random, with the microdomains oriented randomly in three dimensions (3D).[2,3] Therefore, it is likely that the appearance of dots and lines as the BCP begins to self-assemble is indicative of the

formation of cylinders with mixed perpendicular and parallel orientation. Additionally, the growth of a ring-shaped peak that corresponds to L_0 = 36 – 40 nm could be observed in the FFT images. As the temperature rose from 122 to 130 °C, the peak grew in intensity, suggesting the sustained microphase separation of the BCP into distinct microdomains.

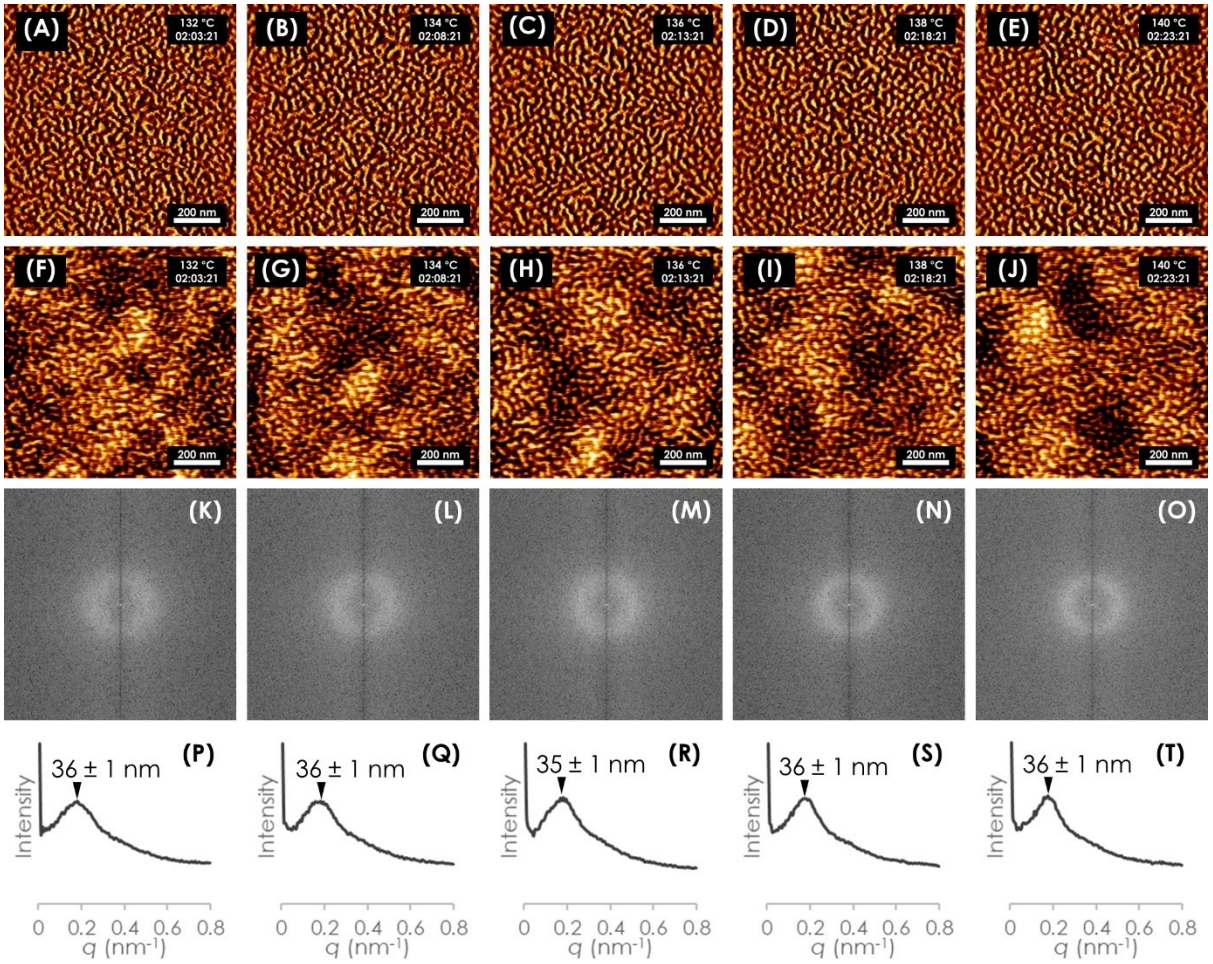


Figure 5-3. (A-E) Phase and (F-J) height images from the in situ AFM experiment on perpendicular cylinders from 132 to 140 °C. The temperature and time stamp in hours:minutes:seconds can be found in the top right of each image. (K-O) 2D-FFT images of the phase images in A-E. (P-T) 1D azimuthally-integrated profiles of the 2D-FFT images in K-O.

As the temperature increased further, the contrast between the microdomains in the phase images (Fig. 5-3) appear to intensify. Additionally, while the image recorded at 132 °C shows a mixture of highly irregular dots and lines, the irregular lines could be seen to break up into dots, suggesting that the parallel cylinders were reorienting into perpendicular

cylindrical structures. Furthermore, at 140 °C, while both dots and wavy lines remain, the shapes of the pattern appear more regular. This observation is in good agreement with the FFT analysis of the phase images, where the initially broad peak at approximately L_0 = 36 nm can be seen to sharpen with increasing temperature, indicative of increased regularity in the structures observed.

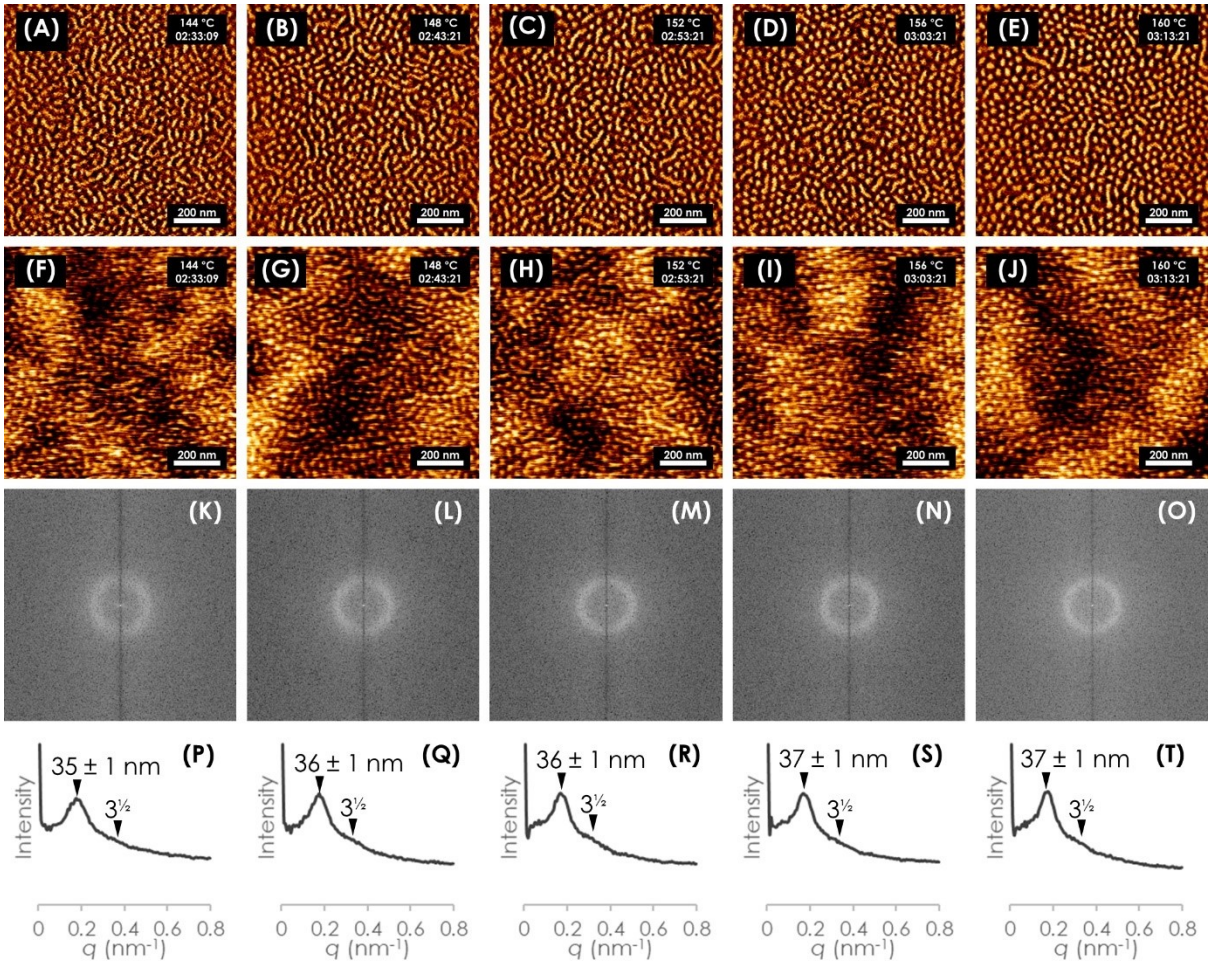


Figure 5-4. (A-E) Phase and (F-J) height images from the in situ AFM experiment on perpendicular cylinders from 144 to 160 °C. The temperature and time stamp in hours:minutes:seconds can be found in the top right of each image. (K-O) 2D-FFT images of the phase images in A-E. (P-T) 1D azimuthally-integrated profiles of the 2D-FFT images in K-O.

Further increasing the annealing temperature resulted in the continued reorientation of the cylindrical structures. Linear structures indicative of conjoined cylinders parallel to the substrate could be seen to disappear gradually as the temperature increased incrementally

to 160 °C. Additionally, while dot structures could be observed from much lower temperatures, the perpendicular cylindrical structures had little long range ordering and were packed irregularly on the film surface. However, in the temperature regime between 144 and 160 °C, increased hexagonal packing of the dots could be observed. This is indicated by the appearance of a secondary peak in the FFT profiles of the corresponding phase images. Though initially relatively weak, a gradually strengthening secondary peak at a q:q^* ratio of 1:$3^{½}$, where q^* is the position of the primary peak, could be observed. The appearance of the secondary peak at q:q^* = 1:$3^{½}$ is highly indicative of a hexagonal arrangement of periodic structures, as expected of perpendicular cylindrical structures.

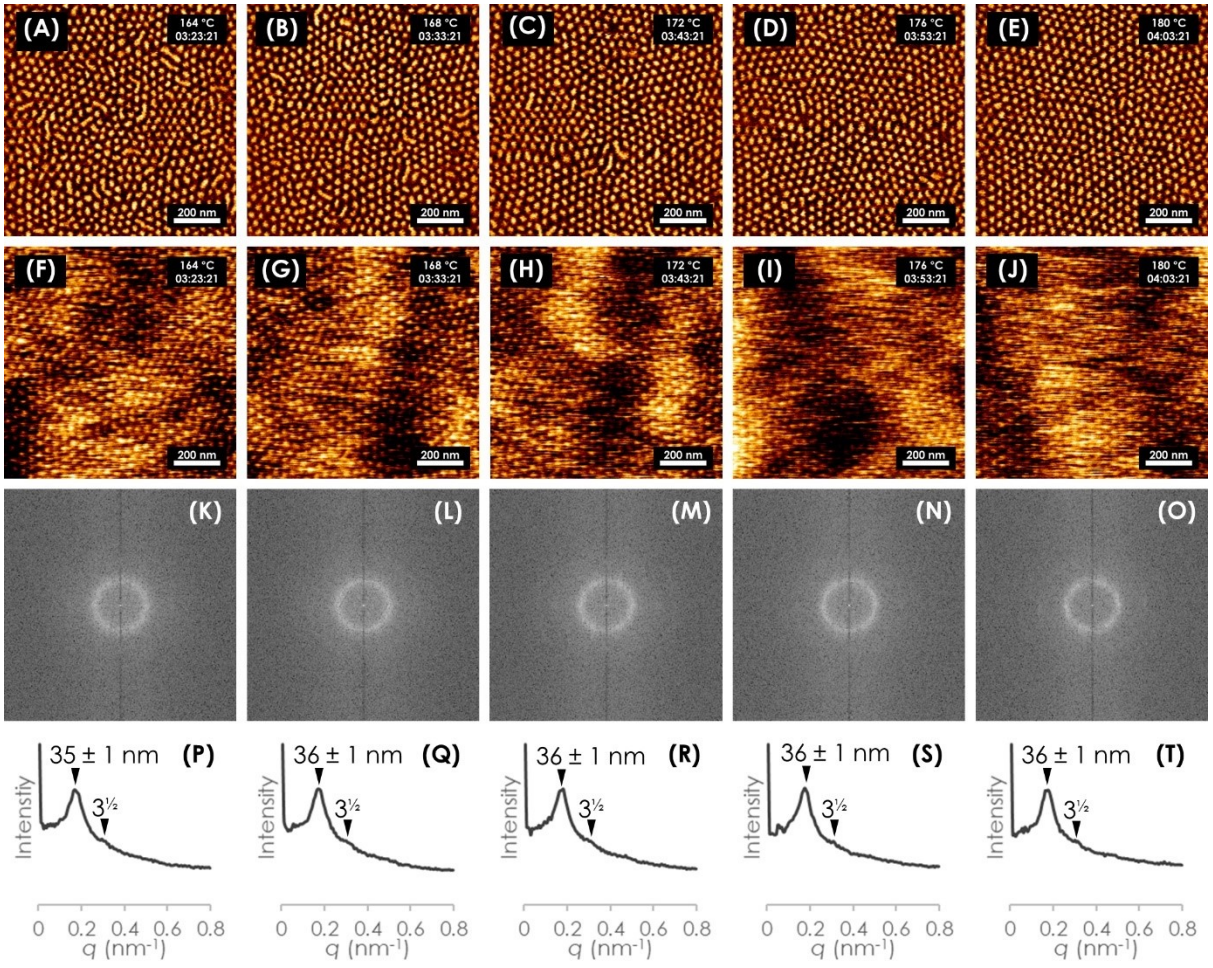


Figure 5-5. (A-E) Phase and (F-J) height images from the in situ AFM experiment on perpendicular cylinders from 164 to 180 °C. The temperature and time stamp in hours:minutes:seconds can be found in the top right of each image. (K-O) 2D-FFT images of

the phase images in A-E. (P-T) 1D azimuthally-integrated profiles of the 2D-FFT images in K-O.

In the following temperature regime of 164 to 180 °C, the linear structures corresponding to parallel cylinders could be observed to disappear. Furthermore, the grains of hexagonally-packed dots begin to grow in size and numerous defects could be observed in between the perpendicular cylindrical grains. Particularly, numerous disclinations, indicated by the appearance of a small flat, dark, PS microdomain surrounded by five bright PMMA dots arranged as if on the apexes of a pentagon could be observed. Nevertheless, as the grains of hexagonally-packed dots continue to grow in size, a sharp, intense ring could be observed in the corresponding FFT images, with L_0 of the structure stable at ~36 nm. This is in good agreement with the expected 40 nm cylinder center-to-center distance.

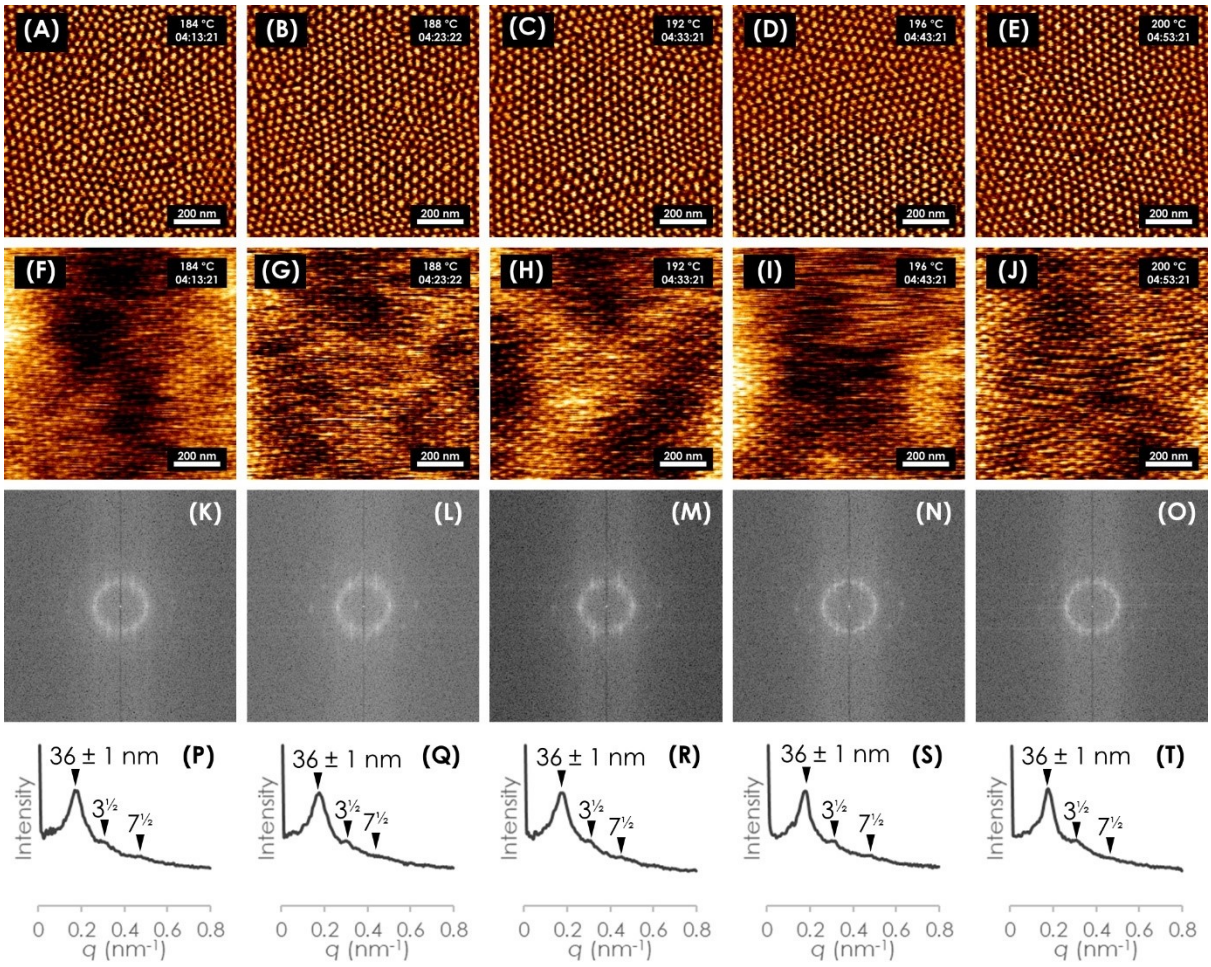


Figure 5-6. (A-E) Phase and (F-J) height images from the in situ AFM experiment on perpendicular cylinders from 184 to 200 °C. The temperature and time stamp in

hours:minutes:seconds can be found in the top right of each image. (K-O) 2D-FFT images of the phase images in A-E. (P-T) 1D azimuthally-integrated profiles of the 2D-FFT images in K-O.

Similar to the in situ AFM experiment with incrementally increasing annealing temperature of lamellae on DSA substrates, the rapid alignment of the microdomains was observed around 180 to 200 °C. In this temperature regime, increased alignment of the hexagonal grain whereby one of the longest diagonals in the hexagon is aligned longitudinally could be observed. With the growth of the hexagonal grains and increased long-range alignment, spots indicative of hexagonal arrangement appeared on the ring-shaped peak in the 2D-FFT images. Additionally, the azimuthally-integrated 1D-FFT profiles now showed higher-order peaks at q:q^* = 1:$3^{½}$:$7^{½}$, further suggesting that the microdomains exhibited increased hexagonal packing.

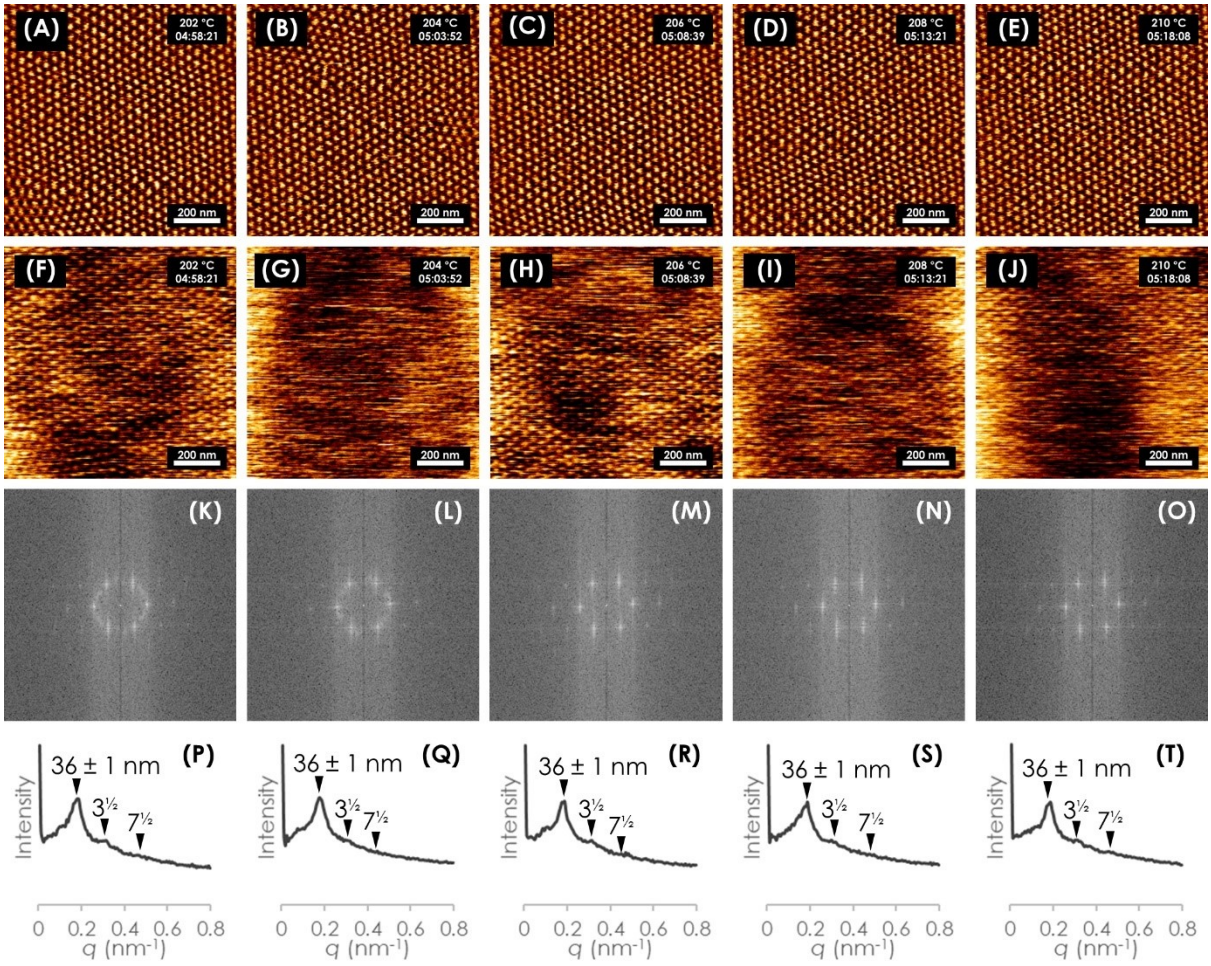


Figure 5-7. (A-E) Phase and (F-J) height images from the in situ AFM experiment on perpendicular cylinders from 202 to 210 °C. The temperature and time stamp in hours:minutes:seconds can be found in the top right of each image. (K-O) 2D-FFT images of the phase images in A-E. (P-T) 1D azimuthally-integrated profiles of the 2D-FFT images in K-O.

In the final temperature range of 202 to 210 °C, the perfect alignment of the hexagonally-arranged dots could be observed. As the temperature rose, defects between the grains disappeared and a single crystalline domain of the hexagonally-arranged dots was obtained at the end of the in situ AFM experiment at 210 °C. The FFT analyses of the images is also in good agreement with development of a well-aligned hexagonal pattern. The spots corresponding to hexagonal arrangement on the 2D-FFT images that appeared in 200 °C appear to grow stronger at 202 °C, while the ring begins to disappear. At 206 °C and higher, a ring, indicative of random alignment, could no longer be observed in the 2D-FFT

images. Instead, only sharp, intense spots corresponding to a hexagonal arrangement could be observed.

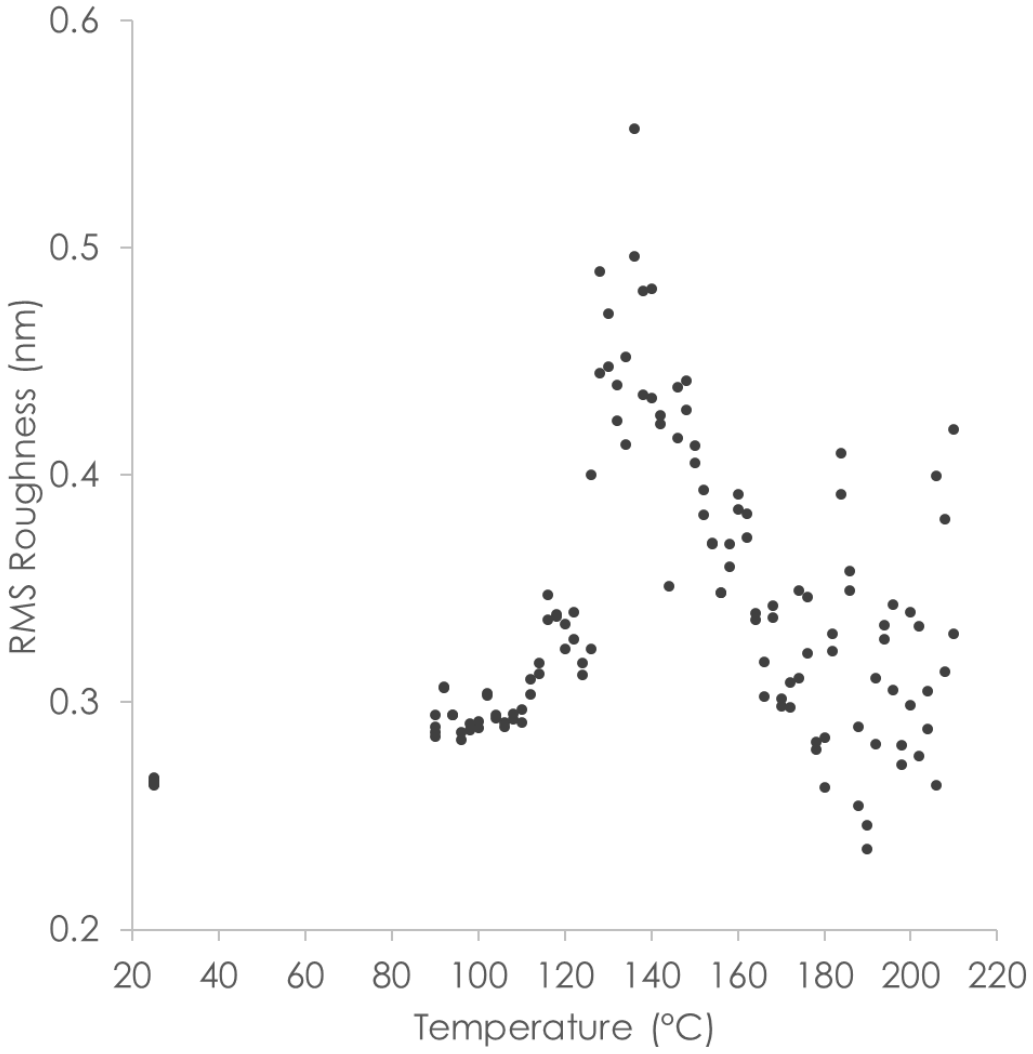


Figure 5-8. Plot of the rough-mean-squared (RMS) roughness measured for each image against the temperature.

In addition to the qualitative and FFT analyses of the phase images, a rough-mean-squared (RMS) roughness could also be measured from each height image obtained during the in situ AFM experiment. Shown in Fig. 5-8, the plot of the RMS roughness against temperature shows four distinct behaviors, similar to the plot of the RMS roughness against temperature for the in situ AFM experiment of perpendicular lamellae. At lower temperatures between 25 to 110 °C, the RMS roughness is low, as expected of spin-coated thin films, averaging at 0.29 ± 0.01 nm. However, the RMS roughness was observed to increase

sharply above 110 °C, peaking at 0.55 nm at 136 nm, before decreasing as the temperature increased to 160 °C. Above 160 °C, although thermal fluctuations could be observed, the RMS roughness returns to a relatively low average of 0.32 ± 0.04 nm. Compared to the change in RMS roughness during the in situ AFM experiment for perpendicular lamellae under incremental thermal annealing, the roughness of the cylindrical pattern appears slightly lower at both the high and low temperature regions, at roughly 0.29 or 0.32 nm for cylinders and approximately 0.35 nm for lamellae. Additionally, the sharp changes in the RMS roughness of the system occur at slightly lower temperatures for cylinders, with the RMS increasing rapidly at 110 °C and peaking at 136 °C in the cylindrical pattern, compared to 116 and 144 °C for the corresponding behaviors in the lamellar pattern. At higher temperatures though, similar behaviors could be observed. The RMS roughness could be observed to drop from their respective peaks as the temperature approached 160 °C and while significant thermal noise results in fluctuations in the RMS roughness at higher temperatures, an average RMS roughness that is roughly equal to the RMS roughness measured prior to annealing could be estimated.

5-4 Conclusion

Herein, the first report of the real-time and real-space analysis of the growth and evolution of perpendicular cylinders prepared on chemically pre-patterned DSA substrates is presented. Based on the studies of the evolution of ordered structures in BCP thin films, it was found that regardless of the morphology of the BCP, similar trends can be observed. The as-cast BCP thin films start as kinetically-frozen disorder-like states and undergo microphase separation to form short-range patterns with the nearest neighboring microdomains as the temperature rises above the glass transition temperature. In the earlier stages of self-assembly, close-range interactions dominate, resulting in the growth of randomly-aligned structures. However, with increasing temperature, the influence of the underlying DSA guides could be observed, as the grains of the BCP microdomains begin to align. Through sequential defect annihilation with increasing annealing temperature, a “defect-free” state could eventually be obtained. With such studies of the growth and

evolution of ordered structures in BCPs of varying morphologies, the realization of applying the self-assembled structures of BCPs to a variety of advanced engineering applications could potentially come to fruition.

5-5 References

(1) Muramatsu, M.; Nishi, T.; You, G.; Ido, Y.; Kitano, T. Defect and Roughness Reduction of Chemo-Epitaxy DSA Pattern. *Proc. SPIE* **2018**, *10584*, 105840M DOI: 10.1117/12.2297185.

(2) Joly, S.; Raquois, A.; Paris, F.; Hamdoun, B.; Auvray, L.; Ausserre, D.; Gallot, Y. Early Stage of Spinodal Decomposition in 2D. *Phys. Rev. Lett.* **1996**, *77* (21), 4394–4397 DOI: 10.1103/PhysRevLett.77.4394.

(3) Peters, R. D.; Stasiak, P.; Matsen, M. W.; Dalnoki-Veress, K. Morphology Induced Spinodal Decomposition at the Surface of Symmetric Diblock Copolymer Films. *ACS Macro Lett.* **2013**, *2* (5), 441–445 DOI: 10.1021/mz400159s.

Chapter 6 Synthesis of Poly(3(2,2',2",4,4',4",6-heptaethyl polyhedral oligomeric silsesquioxane)propyl methacrylate)-*block*-poly(2,2,2-trifluoroethyl methacrylate) (PMAPOSS-*b*-PTFEMA)

6-1 Introduction

The development of strongly-segregating BCPs that are capable of forming ordered patterns with sub-10 nm feature sizes is highly desirable for applications in the microelectronics industry and nanoengineering. The domain spacing achievable by BCPs is dictated by the strength of segregation, quantified by the Flory-Huggins interaction parameter χ_{eff}, and the total degree of polymerization N.[1–4] This is explained by the equation $L_0 = bN^a\chi_{eff}^{1/6}$, where a is equal to 1/2 or 2/3 in the weak or strong segregation limits, and b is the statistical segment length.[4] Additionally, since BCPs only self-assemble when $\chi_{eff}N >$ 10.5, to decrease the minimum accessible domain spacing, χ_{eff} needs to be increased while N is simultaneously decreased.[5] To that end, heteroatomic BCPs tend to possess higher χ_{eff} values as the presence of heteroatoms increases the chemical distinction and thus the strength of segregation between the blocks.

Particularly, poly(3(2,2',2",4,4',4",6-heptaethyl polyhedral oligomeric silsesquioxane)propyl methacrylate) (PMAPOSS) has shown significant potential.[6–12] Each repeating unit of PMAPOSS is functionalized with a unique, Si-containing, well-defined cage structure. This provides PMAPOSS with enhanced properties including higher thermal stabilities and increased etch resistance towards oxygen reactive ion etch (RIE) treatment.[13,14] When combined with PMMA, PMAPOSS-*b*-PMMA was shown to be able to self-assemble into highly ordered hexagonal dot patterns with sub-10 nm feature sizes and a dot density of 5.9 Tb inch^{-2}.[6]

Additionally, the F-containing polymer, poly(2,2,2-trifluoroethyl methacrylate) (PTFEMA), possesses a highly polar trifluoroethyl moiety. This fluorinated functionality also serves to increase the susceptibility of PTFEMA to various removal treatment methods such as UV irradiation.[15] When combined with PMAPOSS, PMAPOSS-*b*-PTFEMA was reported

to have a significantly high χ_{eff} value of 0.45 and was shown to be capable of forming lamellae with full-pitch feature sizes down to 11 nm.[7] Even more remarkably, PMAPOSS-*b*-PTFEMA was shown to be able to orient perpendicularly on a variety of substrates without the need for a chemically-modifying layer, and through simple ambient thermal annealing processes.[11]

In previous reports, PMAPOSS-*b*-PTFEMA was generally synthesized via the reversible addition-fragmentation chain transfer (RAFT) process, using a PMAPOSS macro-chain transfer agent (CTA).[7,9,10] While MAPOSS is easily polymerization by living anionic polymerization, the polymerization of TFEMA via living anionic polymerization typically results in side reactions that lead to the early termination of the propagating chain. Although the addition of bulky dibenzo-18-crown-6-ether (DB18C6) and sodium counter-ions was shown to mitigate the backbiting side reactions during the polymerization of TFEMA,[16] such additives could remain behind after pattern transfer and interfere with the performance of fabricated microelectronics. Therefore, to synthesize pristine PMAPOSS-*b*-PTFEMA, the RAFT process is chosen. Having said that, the order in which a PMAPOSS- and PTFEMA-containing diblock copolymer is synthesized via RAFT is not explicitly clear. While the order of monomer addition is important for living anionic polymerization, it is less so for syntheses via RDRP methods. Generally, the monomer that produces a more stable carbon radical center should be polymerized first.[17] Therefore, monomers that produce tertiary carbon radical center should be polymerized prior to monomers that produce secondary carbon radical centers. In the case of PMAPOSS and PTFEMA, the active sites are both methacryloyl functionalities. Therefore, the synthesis of PMAPOSS- and PTFEMA-containing diblock copolymers should be able to proceed via either direction. In this study, the synthesis of such PMAPOSS- and PTFEMA-containing diblock copolymers is explored using the RAFT process and a PMAPOSS or PTFEMA macro-CTA.

6-2 Experimental Section

6-2-1 Materials

2,2,2-trifluoroethyl methacrylate (TFEMA) and 2,2'-azobis(isobutyronitrile) (AIBN) were purchased from Tokyo Chemical Industry Co., Ltd. (TCI). Prior to use, AIBN was recrystallized from methanol, and TFEMA was stirred over calcium hydride (CaH_2) and distilled under reduced pressure. 3(2,2',2'',4,4',4'',6-Heptaethyl polyhedral oligomeric silsesquioxane)propyl methacrylate (MAPOSS) was purchased from Hybrid Plastics and recrystallized from methanol. 2-Cyano-2-propyl benzodithioate (CPDB), 1,1,1,3,3,3-hexafluoroisopropanol (HFIP), carbon disulfide (CS_2), 1,4-dioxane, *n*-hexane, methanol (MeOH), ethanol (EtOH), 2-propanol (IPA), chloroform ($CHCl_3$), tetrahydrofuran (THF), and toluene were purchased from Sigma Aldrich or Wako Pure Chemical Industries and used as received. Silicon (Si) wafers were immersed in piranha solution (H_2SO_4/H_2O_2 = 7:3 v/v) at 80 °C for 1 h and washed with water, acetone, and ethanol prior to use. Note, mixing piranha solution with organic solvents such as acetone can produce explosive compounds such as triacetone triperoxide (TATP) and extra care must be taken when handling.

6-2-2 Instruments

^{1}H and ^{13}C nuclear magnetic resonance (NMR) analyses were performed on a JEOL 400 MHz NMR Instrument at 400 MHz for ^{1}H NMR and 100 MHz for ^{13}C NMR using chloroform-*d* as a solvent. Fourier transform infrared (IR) spectra were obtained on a JASCO FT/IR-4100 Fourier Transform Spectrophotometer. A Shodex GPC-101 equipped with a Shodex LF804 column and THF as the eluent was used to estimate the molecular weight and dispersities of the polymer via size exclusion chromatography (SEC). Surface free energies (SFEs) of the polymers were estimated using contact angle measurements with water and diiodomethane, and the Owens-Wendt method. Small angle X-ray scattering (SAXS) analyses were conducted on a Bruker NanoSTAR (50 kV/100 mA) equipped with a 2D-PSPC detector at a camera length of 1055 nm.

6-2-3 Synthesis of PMAPOSS

Homopolymers of PMAPOSS were synthesized using the RAFT process based on a previously reported method.[7,9] As an example, the synthesis of $PMAPOSS_6$ is described as follows. CPDB (30 mg, 0.136 mmol), AIBN (7.5 mg, 0.0457 mmol), MAPOSS (3.04 g, 4.07

mmol), and toluene (7.04 g, 8.13 ml) were charged to a Schlenk tube equipped with a magnetic stir bar. After degassing via four freeze-pump-thaw (FPT) cycles, the solution was stirred at 65 °C for 8 h. Upon rapid quenching to 10 °C, the polymer was precipitated in excess methanol twice, isolated by vacuum filtration, and dried under reduced pressure at 40 °C for 24 h to yield $PMAPOSS_6$ as a pink powder (yield = 30%, 0.905 g). SEC analysis revealed M_n = 4,700 g mol^{-1} and $Đ$ = 1.11. FT-IR (KBr) v = 2964, 1733, 1462, 1415, 1255, 1114, 1014, 923 cm^{-1}. ^1H NMR ($CDCl_3$, 400 MHz): δ = 0.61-0.63 (br, 16H, CH_2CH_3, POSS-CH_2CH_2), 0.80 (br, 2H, POSS-CH_2CH_2), 0.97-0.98 (br, 24H, CH_2CH_3, back bone CH_3), 1.72 (br, 2H, back bone CH_2), 3.56 (br, 2H, OCH_2) ppm. ^{13}C NMR ($CDCl_3$, 100 MHz): δ = 3.4, 4.0, 4.5, 6.5, 8.2, 17.3, 18.3, 21.7, 44.9, 54.2, 66.8, 126.5, 128.2, 176.3, 177.1, 177.6 ppm.

6-2-4 Synthesis of PTFEMA

The synthesis of PTFEMA is similar to that of PMAPOSS and was carried out as previously reported.[10] CPDB (12.4 mg, 0.056 mmol), AIBN (1.4 mg, 0.009 mmol), TFEMA (1.209 g, 7.19 mol), and 1,4-dioxane (0.3081 g, 0.30 ml) were charged to a Schlenk tube with a magnetic stir bar. After degassing over four FPT cycles, the solution was stirred at 70 °C for 24 h and quenched by rapid cooling to 10 °C. The polymer was obtained by precipitating in hexane, isolated by vacuum filtration, and dried at 40 °C under reduced pressure to yield a pink powder. Based on SEC analysis, it was found that M_n = 24,200 g mol^{-1} and $Đ$ = 1.25. ^1H NMR ($CDCl_3$, 400 Mhz): δ = 0.79-1.23 (br,3 H, CH_3), 1.81-2.19 (br, 2H, CH_2), 4.21-4.51 (br, 2H, CH_2F_3), 7.35-7.41 (t, 2H, C*H*), 7.51-7.58 (d, 2H, C*H*) ppm.

6-2-5 Synthesis of PMAPOSS-*b*-PTFEMA in Toluene/HFIP

Similarly, PMAPOSS-*b*-PTFEMA was synthesized via RAFT based on previously reported methods.[7,9] As an example, the procedure for the synthesis of $PMAPOSS_6$-*b*-$PTFEMA_{80}$ is as follows. A $PMAPOSS_6$ macro-CTA (M_n = 4,700 g mol^{-1}, $Đ$ = 1.11, 0.42 g, 0.0894 mmol) and AIBN (7.3 mg, 0.0447 mmol) were added to a Schlenk tube equipped with a magnetic stir bar. 0.4 g of toluene-HFIP (w/w = 65/35), and TFEMA (1.50 g, 1.27 ml, 8.92 mmol) was added to the flask. After degassing with three FPT cycles, the reaction was conducted at 60 °C for 9 h. Precipitating in a 9:1 (v/v) methanol-water mixture, washing by CS_2, and drying

under reduced pressure at 40 °C for 24 h yielded $PMAPOSS_6$-*b*-$PTFEMA_{80}$ as pink powder (yield = 48%, 0.915 g). SEC analysis revealed an M_n and $Đ$ of 18,300 g mol^{-1} and 1.14, respectively. FT-IR (KBr) v = 2968, 1751, 1461, 1416, 1284, 1175, 1127, 1033, 966 cm^{-1}. ^1H NMR ($CDCl_3$, 400 MHz) δ = 0.56-0.63 (br, 16H, CH_2CH_3, POSS-CH_2CH_3), 0.70-1.35 (br, 29H, backbone CH_3, POSS-CH_2CH_3, CH_2CH_3), 1.72 (br, 2H, backbone CH_2), 1.80-2.28 (br, 4H, backbone CH_2), 3.75-3.95 (br, 2H, $OCH_2CH_2CH_2$-POSS), 4.02-4.46 (br, 2H, CH_2-CF_3) ppm. ^{13}C NMR ($CDCl_3$, 100 MHz): δ = 3.4, 4.0, 4.5, 6.5, 8.2, 16.7, 18.5, 21.7, 44.7, 45.0, 45.5, 52.2, 53.4, 53.7, 60.5, 60.9, 61.3, 61.6, 66.8, 118.7, 118.8, 121.5, 121.5, 124.2, 124.3, 126.5, 127.0, 127.1, 128.2, 174.2, 174.6, 175.2, 175.2, 175.6, 175.9, 176.3, 177.1, 177.6 ppm.

6-2-6 Synthesis of PMAPOSS-*b*-PTFEMA in 1,4-Dioxane

The synthesis of PMAPOSS-*b*-PTFEMA in 1,4-dioxane is presented. $PMAPOSS_9$ (M_n = 7000 g mol^{-1}, $Đ$ = 1.09, 0.40 g, 0.057 mmol), AIBN (4.4 mg, 0.027 mmol), TFEMA (1.48g, 8.83 mmol), and 1,4-dioxane (3.2 ml) was added to a reaction vessel equipped with a magnetic stirrer and three-way stopcock. After degassing with 15 min of Ar bubbling, the reaction was conducted at 65 °C for 8 h. The resulting BCP, $PMAPOSS_{10}$-*b*-$PTFEMA_{117}$, was obtained as a pink powder by precipitation in 9:1 (v/v) methanol-water, washed with hexane, and dried under reduced pressure for 24 h. NMR and SEC analyses revealed that the BCP exhibited M_n, $Đ$, and volume fractions of 27,300 g mol^{-1}, 1.11, and $f_{PMAPOSS}$ = 0.33, respectively. ^1H NMR ($CDCl_3$, 400 MHz) δ = 0.56-0.63 (br, 16H, CH_2CH_3, POSS-CH_2CH_3), 0.70-1.35 (br, 29H, backbone CH_3, POSS-CH_2CH_3, CH_2CH_3), 1.72 (br, 2H, backbone CH_2), 1.80-2.28 (br, 4H, backbone CH_2), 3.75-3.95 (br, 2H, $OCH_2CH_2CH_2$-POSS), 4.02-4.46 (br, 2H, CH_2-CF_3) ppm.

6-2-7 Synthesis of PTFEMA-*b*-PMAPOSS

A representative synthetic route for the synthesis of PTFEMA-*b*-PMAPOSS is presented as follows. A $PTFEMA_{72}$ macro-CTA (M_n = 12,100 g mol^{-1}, $Đ$ = 1.19, 1.66 g, 0.137 mmol), AIBN (11.3 mg, 0.069 mmol), MAPOSS (0.93 g, 1.25 mmol), and 1,4-dioxane (5.1 ml) were added to a reaction vessel equipped with a magnetic stirrer and a three-way

stopcock. The solution was degassed by 15 min of argon (Ar) bubbling and reacted at 65 °C for 8 h. The polymer was precipitated in IPA and dried under reduced pressure for 24 h to yield $PTFEMA_{72}$-*b*-$PMAPOSS_6$ as a pink powder. SEC analysis revealed M_n and $Đ$ of 16,500 g mol^{-1} and 1.09, respectively. ^1H NMR ($CDCl_3$, 400 MHz) δ = 0.56-0.63 (br, 16H, CH_2CH_3, POSS-CH_2CH_3), 0.70-1.35 (br, 29H, backbone CH_3, POSS-CH_2CH_3, CH_2CH_3), 1.72 (br, 2H, backbone CH_2), 1.80-2.28 (br, 4H, backbone CH_2), 3.75-3.95 (br, 2H, $OCH_2CH_2CH_2$-POSS), 4.02-4.46 (br, 2H, CH_2-CF_3) ppm.

6-2-8 Film Preparation

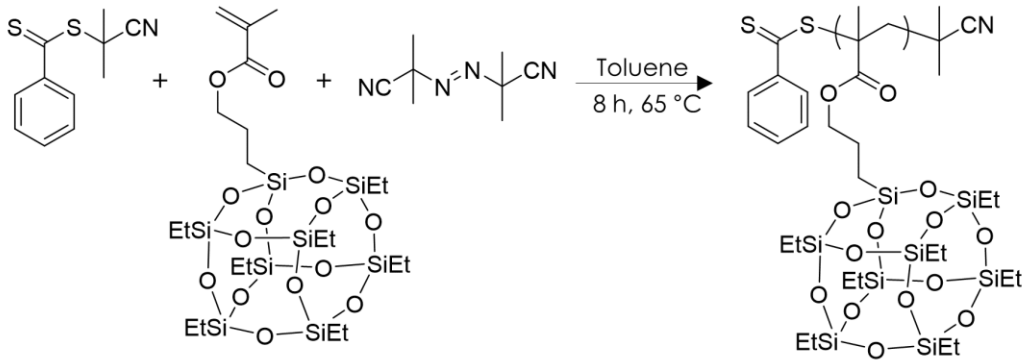
Thin films of PMAPOSS and PTFEMA were prepared on piranha-treated Si wafers by spin-coating dilute solutions of the respective polymers dissolved in $CHCl_3$ at concentrations ranging from 0.2 to 3.0 wt%, and at 7000 rpm for 30 s. Bulk samples of the BCP were prepared through the slow evaporation of a 2 wt% $CHCl_3$ solution and analyzed via SAXS after annealing at 110 °C for 24 h.

6-3 Results and Discussion

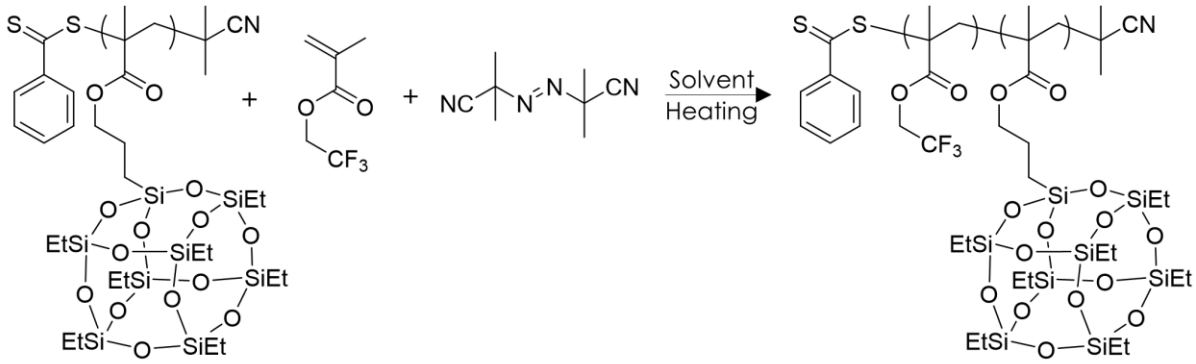
6-3-1 Synthesis and Characterization of PMAPOSS and PTFEMA

To investigate the self-assembly behavior of strongly segregating, high-χ BCPs such as PMAPOSS-*b*-PTFEMA, the homopolymers of the respective blocks were first synthesized via RAFT. As previously reported, using CPDB as a CTA and AIBN as the initiator, MAPOSS and TFEMA were successfully polymerized in toluene and 1,4-dioxane respectively. Subsequently, NMR analyses revealed chemical shifts that can be attributed to the characteristic peaks of PMAPOSS and PTFEMA. Additionally, SEC analyses revealed unimodal chromatograms and that the obtained polymers exhibited low dispersities ($Đ$ < 1.3). These results suggest that well-defined PMAPOSS and PTFEMA homopolymers had been obtained.

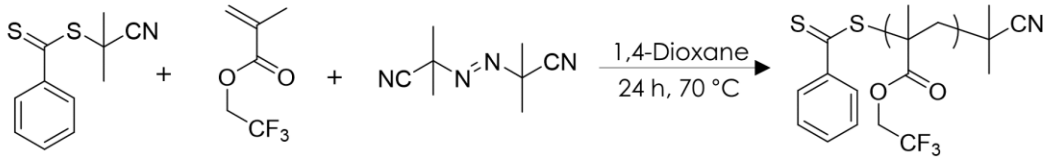
Synthesis of PMAPOSS



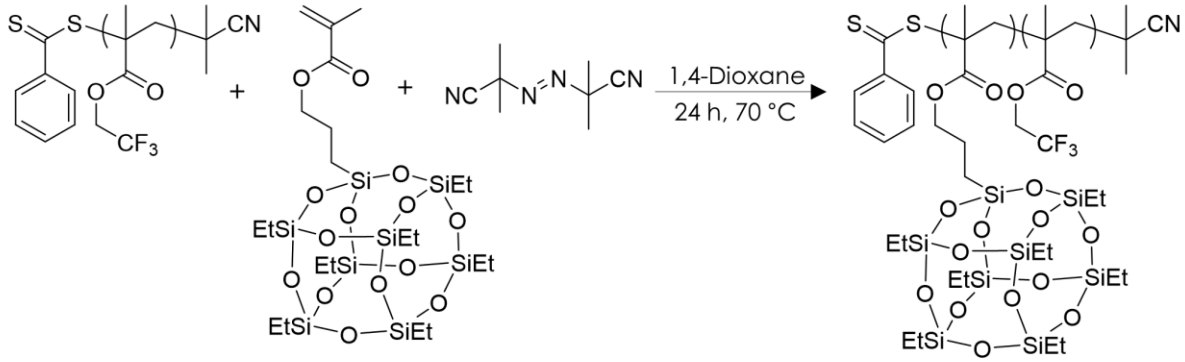
Synthesis of PMAPOSS-*b*-PTFEMA



Synthesis of PTFEMA



Synthesis of PTFEMA-*b*-PMAPOSS



Schematic 6-1. Synthetic routes for the synthesis of PMAPOSS, PMAPOSS-*b*-PTFEMA, PTFEMA, and PTFEMA-*b*-PMAPOSS.

Following the synthesis of the homopolymers, the surface free energies (SFEs) of PMAPOSS and PTFEMA were estimated by measuring the static contact angles of water and diiodomethane and applying the Owens-Wendt method. Thin films of PMAPOSS and PTFEMA were prepared by spin-coating dilute $CHCl_3$ solutions onto piranha-treated Si wafers at 7000 rpm for 30 s. The film thicknesses were then measured using an F20 Filmetrics and the plots of film thickness against concentration are shown in Fig. 6-1.

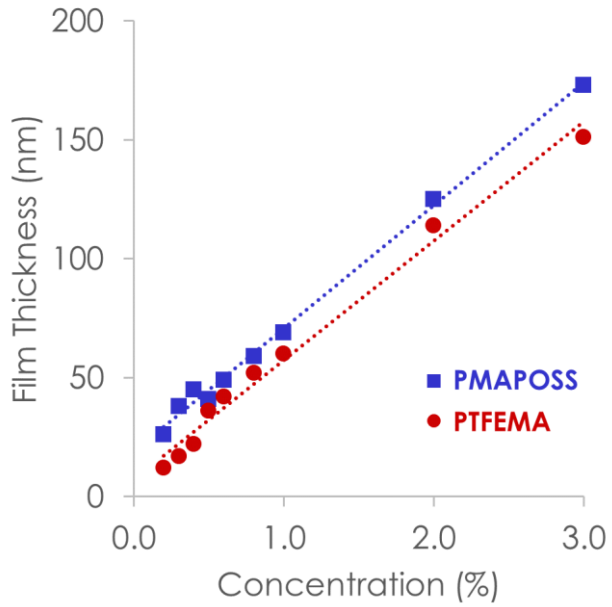


Figure 6-1. Plot of the film thickness against concentration for thin films of PMAPOSS and PTFEMA, shown in blue squares and red circles, respectively.

The plots of film thickness against concentration revealed that the film thickness obtained is directly proportional to the concentration used. Additionally, the film thickness obtained at each concentration are approximately similar for both PMAPOSS and PTFEMA, and increase at a rate of approximately 50 nm per 1.0% concentration of the polymer. When determining the contact angles of liquids on supported polymeric films, films thicker than 100 nm are generally preferred to eliminate the influence of the substrate on the top surface. Therefore, thicker PMAPOSS and PTFEMA thin films spun from 3 wt% $CHCl_3$ solutions were used when measuring the static contact angles of water and diiodomethane at 19 °C.[10] The average of five measurements of the static contact angle of water and diiodomethane on the PMAPOSS film was recorded to be 103.7 ± 0.3° and 58 ± 2°, respectively. Meanwhile, the

static contact angles on the PTFEMA film averaged to 94.3 ± 1° and 69.8 ± 0.5° for water and diiodomethane, respectively. The SFEs of the respective polymers can then be calculated using the Owens-Wendt method based on the following equations,

$(1 + \cos\theta)\gamma_l = 2(\gamma_s^d\gamma_s^p)^{1/2} + 2(\gamma_l^d\gamma_l^p)^{1/2}$	(6-1)
$\gamma_s = \gamma_s^d + \gamma_s^p$	(6-2)

where γ are the SFEs of the solid and liquid, denoted by an s or an l in the subscript, and the d and p superscripts denote the disperse and polar components, respectively.[18] This revealed SFEs of 30.3 and 0.1 mJ m^{-2} for the disperse and polar components, respectively, for PMAPOSS, and 21.0 and 3.0 mJ m^{-2} for the disperse and polar components for PTFEMA. This suggests that at 19 °C, the total SFE for PMAPOSS and PTFEMA are 30.4 and 24.0 mJ m^{-2}, respectively.

6-3-2 Planning for the Synthesis of the BCPs

In the synthesis of a BCP, generally, one block must first be synthesized, followed by another to prevent the simultaneous copolymerization of multiple monomers, resulting in a statistical copolymer rather than a BCP. For synthetic methods such as anionic polymerization, the polymerization of a monomer is generally known to go to completion after some time, depending on the monomer used, and a second monomer can be added into the same reaction vessel. While this “one-pot” reaction can be convenient, the order in which the monomers are added is important. Typically, the monomer with the strongest reactivity towards polymerization and chain extension is polymerized first, followed by monomers of lower reactivities. Although this restriction is less important for diblock copolymers, this restriction can limit the possible arrangements of multi-block polymers. On the other hand, the order of polymerization is less restrictive in RDRP. Generally, the monomer that forms a relatively stable tertiary radical should be polymerized before monomers that form secondary radicals as the tertiary radical is more stable than a secondary radical. Therefore, the polymerization could be less controlled if a monomer that forms a tertiary radical is chain extended from the end of a secondary carbon center. Additionally, unlike in anionic polymerization, BCPs are generally synthesized in multi-step

chain extension reactions as 100.0% conversion is difficult to achieve. In the case of both MAPOSS and TFEMA, the active sites are methacryloyl functionalities that form tertiary radical centers upon polymerization. Therefore, the functionally identical BCPs, PMAPOSS-*b*-PTFEMA and PTFEMA-*b*-PMAPOSS could theoretically be synthesized through a chain extension with the alternative monomer from either PMAPOSS or PTFEMA, respectively.

6-3-3 Solubilities of MAPOSS, PMAPOSS, and PTFEMA

Table 6-1. Solubilities of MAPOSS, PMAPOSS, and PTFEMA in various solvents.

Solvent	E_T^N [a]	MAPOSS	PMAPOSS	PTFEMA	PMAPOSS-*b*-PTFEMA
n-Hexane	0.009	Yes	Yes	No	Partially
CS_2	0.065	Yes	Yes	No	Partially
1,4-Dioxane	0.164	Yes	Yes	Yes	Yes
THF	0.207	Yes	Yes	Yes	Yes
$CHCl_3$	0.259	Yes	Yes	Yes	Yes
Acetone	0.355	Yes	Yes	Yes	Yes
IPA	0.546	Yes	No	Yes	No
EtOH	0.654	Yes	No	Yes	Partially
MeOH	0.762	Yes	No	Yes	Partially
HFIP	0.969	No	No	Yes	Partially
Water	1.000	No	No	No	No
TFEMA	N/A	No	No	Yes	Partially

[a]The solvents are listed in order of the normalized empirical parameter of solvent polarity, E_T^N, as listed in this reference,[19] with the exception of TFEMA.

Firstly, while TFEMA is a liquid at room temperature, the macro-CTAs of PMAPOSS and PTFEMA, and MAPOSS are solid at room temperature. Therefore, a solvent system that is capable of solvating all the components must be found. To that end, the solubilities of MAPOSS, PMAPOSS, and PTFEMA in several common and fluorine-containing solvents were investigated and the results are tabulated in Table 6-1. The solvents were listed in order of the normalized empirical parameter of solvent polarity, E_T^N.[19] Interestingly and

possibly in a troubling manner, the solubilities of PMAPOSS and PTFEMA showed opposite tendencies. Firstly, the monomer MAPOSS is generally soluble in a large variety of solvents, ranging from non-polar *n*-hexane (E_T^N = 0.009) up to relatively polar solvents such as methanol (E_T^N = 0.762). However, MAPOSS is insoluble in extremely polar solvents such as HFIP (E_T^N = 0.969) and water (E_T^N = 1.000). Upon polymerization, PMAPOSS also exhibits similar trends. While PMAPOSS is soluble in non-polar and "medium" polarity solvents such as toluene (E_T^N = 0.099), CS_2 (E_T^N = 0.065), THF (E_T^N = 0.207), $CHCl_3$ (E_T^N = 0.259), and acetone (E_T^N = 0.355), PMAPOSS is insoluble in polar solvents including alcohols (E_T^N > 0.5), HFIP, and water. In contrast, PTFEMA is insoluble in non-polar solvents with E_T^N < 0.1, but is soluble in the rest of the relatively polar solvents with E_T^N > 0.2, excepting water. The opposite tendencies for solubilities in polar and non-polar solvents for PMAPOSS and PTFEMA results in the BCP, PMAPOSS-*b*-PTFEMA, becoming only partially soluble or insoluble in most non-polar and polar solvents. Nevertheless, it was found that PMAPOSS-*b*-PTFEMA was soluble in "medium" polarity solvents, including 1,4-dioxane (E_T^N = 0.164), THF (E_T^N = 0. 207), and $CHCl_3$ (E_T^N = 0.259). Additionally, the solubility tests showed that MAPOSS and PMAPOSS were insoluble in TFEMA, while PMAPOSS-*b*-PTFEMA was only partially soluble, suggesting that as a solvent, TFEMA is relatively polar. Since TFEMA contains a trifluoroethyl moiety with a significant dipole moment, this result is not unexpected.

6-3-4 Synthesis and Characterization of PMAPOSS-*b*-PTFEMA

Although $CHCl_3$ and THF were shown to be good solvents for all components of the system, these solvents are generally avoided during radical polymerizations as the active radical can chain transfer to the solvent, possibly significantly affecting the polymerization. Therefore, a co-solvent of toluene and HFIP (w/w = 65/35) was used to dissolve the $PMAPOSS_6$ macro-CTA during the chain extension reaction with TFEMA. After degassing through three FPT cycles, the reaction was conducted at 65 °C for 8 h and the resulting BCP was precipitated in a 9:1 methanol-water (v/v) mixture. However, as the reaction conditions were less than

optimal, and perhaps in part due to the large bulky moieties of POSS, some PMAPOSS homopolymers remain unreacted. Therefore, to remove residual unreacted PMAPOSS homopolymers, the BCP was washed with CS_2 twice. Upon NMR and SEC analyses, it was found that the BCP exhibited chemical shifts that could be assigned to each characteristic moiety, and a unimodal chromatogram had been obtained. Therefore, the results indicated that $PMAPOSS_6$-*b*-$PTFEMA_{80}$ had been successfully synthesized and exhibited M_n = 18,300 g mol^{-1} and $Đ$ = 1.14. Using the densities of the homopolymers, at 1.14 and 1.45 g cm^{-3} for PMAPOSS and PTFEMA respectively, it was found that $PMAPOSS_6$-*b*-$PTFEMA_{80}$ exhibited a volume fraction of $f_{PMAPOSS}$ = 0.31.

Additionally, the solubility tests showed that MAPOSS, PMAPOSS, PTFEMA, and PMAPOSS-*b*-PTFEMA are all soluble in 1,4-dioxane, a commonly-used solvent in radical polymerizations. Therefore, the synthesis of PMAPOSS-*b*-PTFEMA in 1,4- was also investigated. A $PMAPOSS_9$ macro-CTA (M_n = 7000 g mol^{-1}, $Đ$ = 1.09), AIBN, and TFEMA were solvated in 1,4-dioxane, at a 1:2 volume ratio of monomer:solvent and reacted at 65 °C for 8 h after 15 min of degassing with Ar bubbling. Similarly, the BCP was precipitated in a 9:1 methanol-water (v/v) mixture. Although a BCP had been obtained, unreacted PMAPOSS homopolymers must also be removed (Fig. 6-2). Referring back to the solubility table, it was determined that non-polar solvents solvate PMAPOSS well, but PMAPOSS-*b*-PTFEMA could only be partially solvated, and PTFEMA was insoluble. Therefore, CS_2 could be used to selectively dissolve PMAPOSS. However, as PMAPOSS-*b*-PTFEMA is also partially soluble in CS_2, a thick slurry with extremely fine PMAPOSS-*b*-PTFEMA particles is generally obtained during the washing process. Although most of the solvent could be decanted, removing the rest of the solvent through vacuum filtration is difficult, especially since CS_2 is highly volatile. This results in more CS_2 evaporating rather than going through the filter and removing PMAPOSS. Additionally, since CS_2 is bad for health and the general environment (it smells bad and is a greenhouse gas), alternatives would be preferred. The solubility table indicated that PTFEMA is insoluble in *n*-hexane (E_T^N = 0.009), CS_2 (E_T^N = 0.065), and toluene

(E_T^N = 0.099). Excepting CS_2, alternative washing solvents that can selectively dissolve residual PMAPOSS are desirable. It was found that when excess toluene was added to PMAPOSS-*b*-PTFEMA, a turbid, light-scattering solution could be obtained, suggesting that the BCP could largely dissolve and possibly form micelle-like structures in solution. Considering the solvent polarity (E_T^N) of toluene is on the high side for non-polar solvents, at 0.099, and that PMAPOSS-*b*-PTFEMA is fully soluble in 1,4-dioxane, where E_T^N = 0.164, it is not surprising that PMAPOSS-*b*-PTFEMA can be mostly dissolved in excess toluene as well. Alternatively, *n*-hexane has a lower solvent polarity relative to CS_2 and toluene at 0.009. Therefore, it is likely that PTFEMA and PMAPOSS-*b*-PTFEMA should be least soluble in *n*-hexane, while PMAPOSS remains soluble. As an alternative to CS_2, it was found that PMAPOSS could be successfully removed by washing the precipitated crude BCP in *n*-hexane (Fig. 6-3). Subsequently, the chemical shifts found in the NMR spectrum (Fig. 6-5) could be assigned to the characteristic moieties of PMAPOSS-*b*-PTFEMA and SEC analyses also revealed a unimodal chromatogram. Additionally, it was revealed that the obtained BCP, $PMAPOSS_{10}$-*b*-$PTFEMA_{117}$, exhibited M_n = 27,300 g mol^{-1}, $Đ$ = 1.11, and $f_{PMAPOSS}$ = 0.33. Therefore, these results suggest that the synthesis of PMAPOSS-*b*-PTFEMA can be relatively flexible and adjusted. By taking advantage of differences in solubility, well-defined PMAPOSS-*b*-PTFEMA can be obtained.

6-3-5 Synthesis and Characterization of PTFEMA-*b*-PMAPOSS

As discussed earlier, the synthesis of a PMAPOSS- and PTFEMA-containing BCP could theoretically proceed by the chain extension of either PMAPOSS or PTFEMA with TFEMA or MAPOSS, respectively. As the synthesis of PMAPOSS-*b*-PTFEMA through the chain extension of PMAPOSS with TFEMA was presented above in Section 6-3-4, the synthesis of PTFEMA-*b*-PMAPOSS by a chain extension of PTFEMA is investigated next. In this case, the solvent system must be capable of solvating MAPOSS, PTFEMA, and the BCP. As shown in the solubility table, 1,4-dioxane is capable of dissolving all components of the system and it was also found that 1,4-dioxane can be used to successfully synthesize

PMAPOSS-*b*-PTFEMA. Therefore, 1,4-dioxane was also employed in the chain extension of PTFEMA. To a reaction vessel, a $PTFEMA_{72}$ macro-CTA (M_n = 12,100 g mol^{-1}, $Đ$ = 1.19), AIBN, MAPOSS, and 1,4-dioxane was added. After degassing with Ar bubbling for 15 min, the reaction was conducted at 65 °C for 8 h and the polymer was precipitated in IPA. While the synthesis of PMAPOSS-*b*-PTFEMA required a CS_2 or *n*-hexane wash to remove residual PMAPOSS homopolymers, an extra washing step is unnecessary during the synthesis of PTFEMA-*b*-PMAPOSS. The solubilities of MAPOSS, PMAPOSS, PTFEMA, and the BCP in IPA lie in an optimal spot. Although the fact that MAPOSS is a solid at room temperature usually means that removing residual unreacted monomer is difficult, MAPOSS is soluble in IPA while the BCP, PTFEMA-*b*-PMAPOSS, is not. Additionally, PTFEMA is also soluble in IPA. Therefore, any residual, unreacted MAPOSS monomers and PTFEMA homopolymers remain dissolved as the BCP precipitates out of solution in IPA. After drying, NMR analysis (Fig. 6-6) revealed chemical shifts that correspond well with the characteristic peaks, and a unimodal chromatogram was obtained during SEC analysis (Fig. 6-4). These results suggest that a well-defined $PTFEMA_{72}$-*b*-$PMAPOSS_6$ with M_n = 16,500 g mol^{-1}, $Đ$ = 1.09, and $f_{PMAPOSS}$ = 0.31 had been obtained successfully.

6-3-6 Bulk Morphologies of the Synthesized BCPs

Based on the synthetic methods described earlier, a series of PMAPOSS- and PTFEMA-containing BCPs were synthesized, with the first polymerized block mentioned earlier by convention. Bulk samples for each BCP were prepared through the slow evaporation of a 1 wt% $CHCl_3$ solution and the morphologies were analyzed by SAXS after thermal annealing at 110 °C for 24 h (Fig. 6-7 to 6-10). The results of the synthesis and characterization are summarized in Table 6-2.

Table 6-2. Characterization Results of a Series of PMAPOSS- and PTFEMA-containing BCPs.

Polymer	M_n (g mol^{-1})	$Đ$	$f_{PMAPOSS}$	f_{PTFEMA}	Morphology	L_0 (nm)
PMAPOSS$_6$-*b*-PTFEMA$_{80}$	18,300	1.14	0.31	0.69	LAM	16.2
PMAPOSS$_{10}$-*b*-PTFEMA$_{117}$	27,300	1.11	0.33	0.67	LAM	20.9
PTFEMA$_{72}$-*b*-PMAPOSS$_6$	16,500	1.09	0.31	0.69	LAM	16.2
PTFEMA$_{70}$-*b*-PMAPOSS$_6$	15,900	1.09	0.31	0.69	LAM	16.4

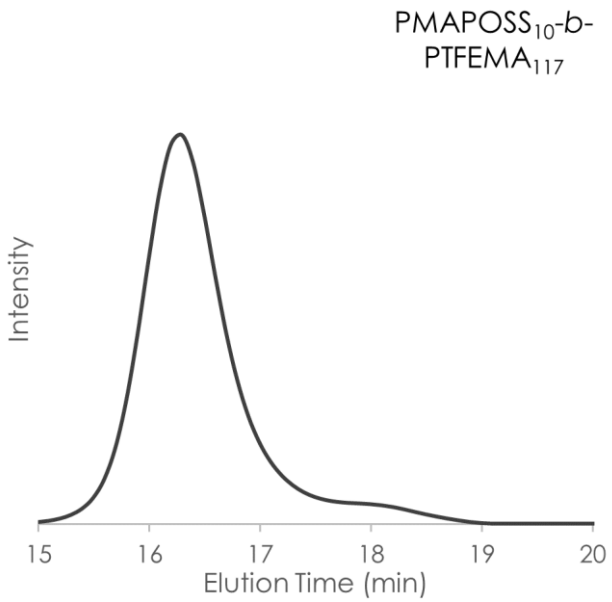


Figure 6-2. SEC chromatogram of PMAPOSS$_{10}$-*b*-PTFEMA$_{117}$ prior to washing in hexane.

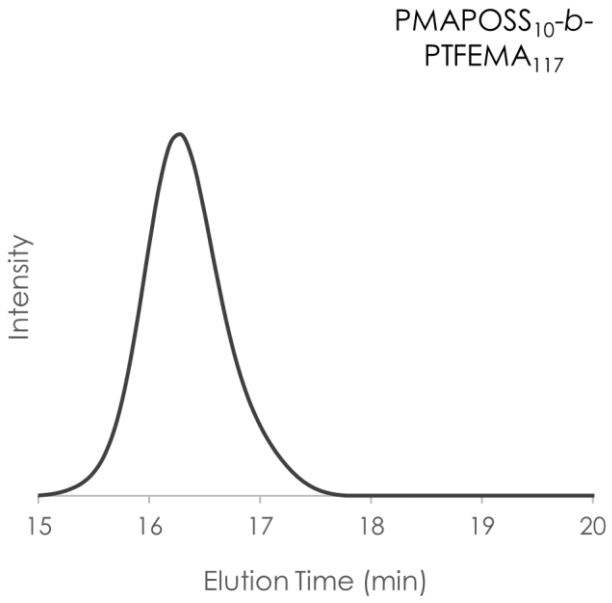


Figure 6-3. SEC chromatogram of $PMAPOSS_{10}$-*b*-$PTFEMA_{117}$ after washing in hexane.

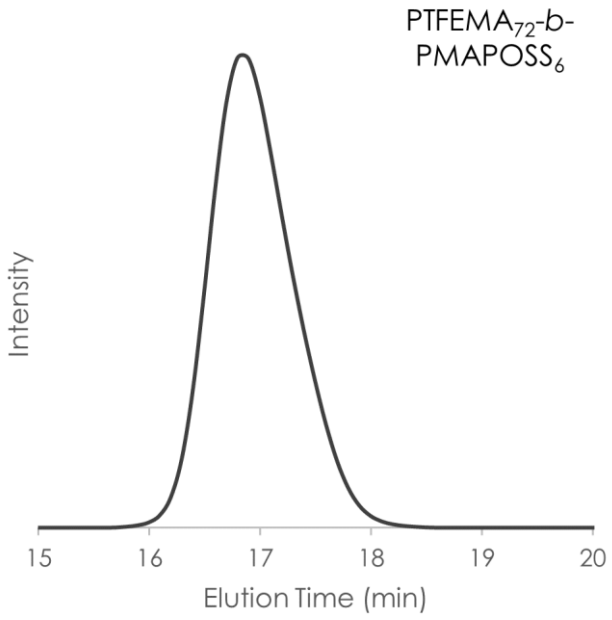


Figure 6-4. SEC chromatogram of $PTFEMA_{72}$-*b*-$PMAPOSS_6$.

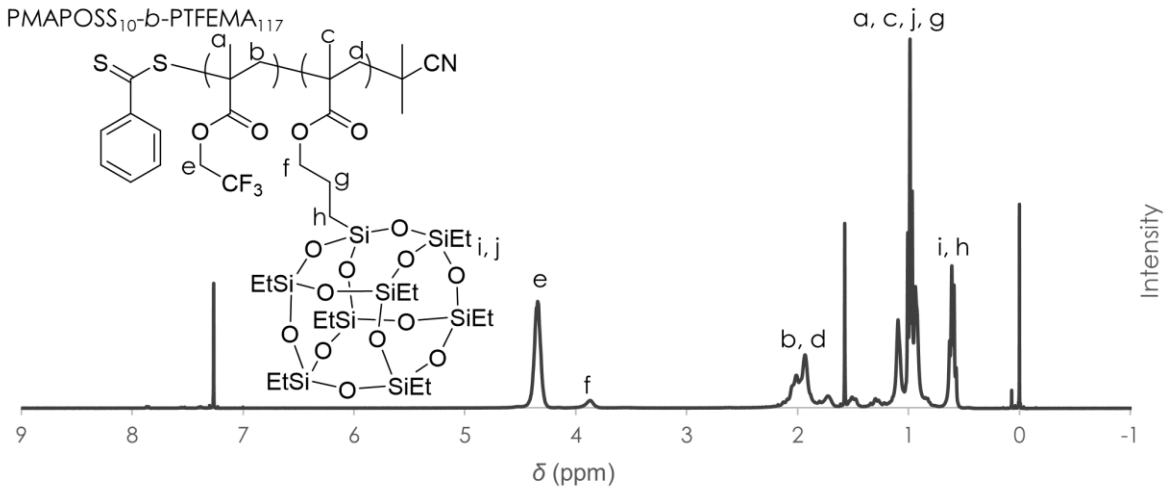


Figure 6-5. ^{1}H NMR spectrum of PMAPOSS$_{10}$-*b*-PTFEMA$_{117}$ obtained in $CDCl_3$.

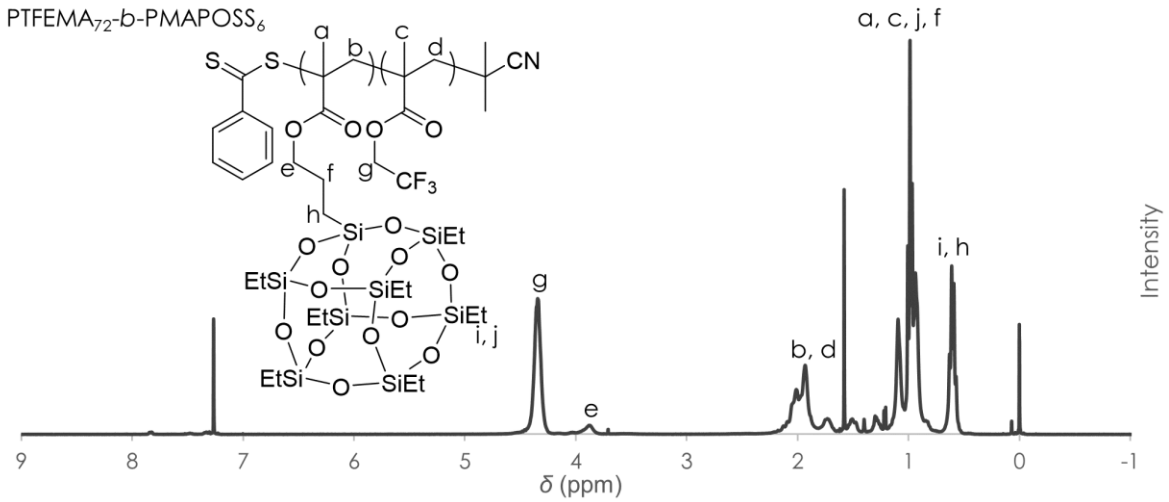


Figure 6-6. ^{1}H NMR spectrum of PTFEMA$_{72}$-*b*-PMAPOSS$_{6}$ obtained in $CDCl_3$.

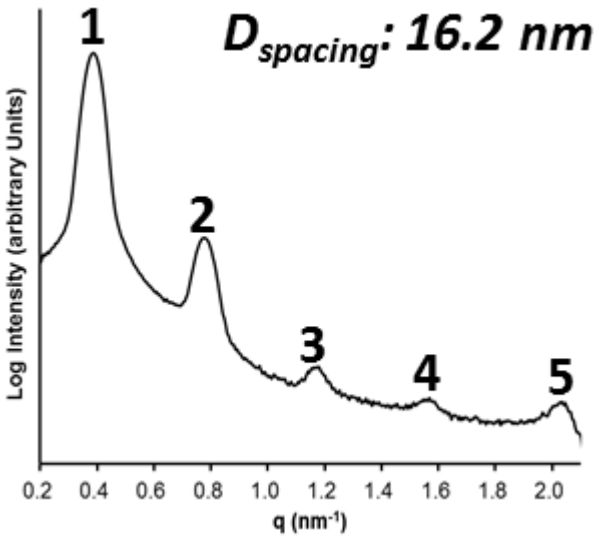


Figure 6-7. 1D SAXS profile of $PMAPOSS_6$-*b*-$PTFEMA_{80}$. Reproduced with permission from Chandra et al, *Adv. Mater. Interfaces* **2019**, *6*, 1801401. Copyright 2019 WILEY-VCH Verlag GmbH & Co., KGaA, Weinheim.

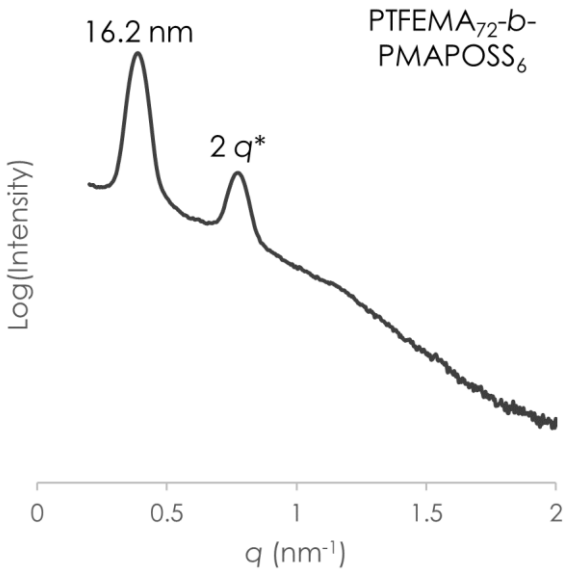


Figure 6-8. 1D SAXS profile of $PTFEMA_{72}$-*b*-$PMAPOSS_6$.

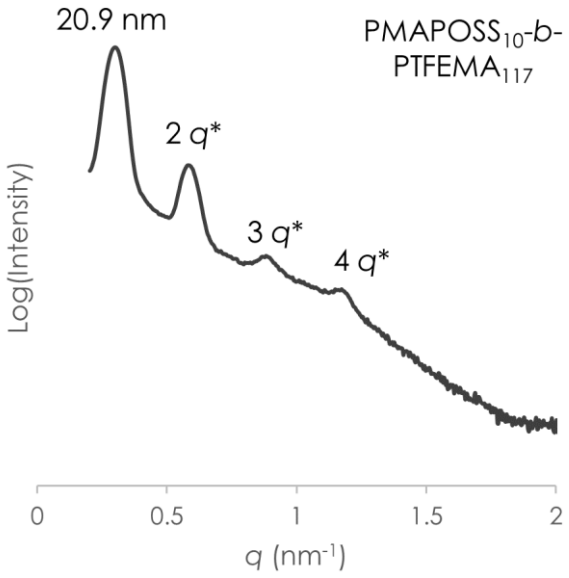


Figure 6-9. 1D SAXS profile of $PMAPOSS_{10}$-*b*-$PTFEMA_{117}$.

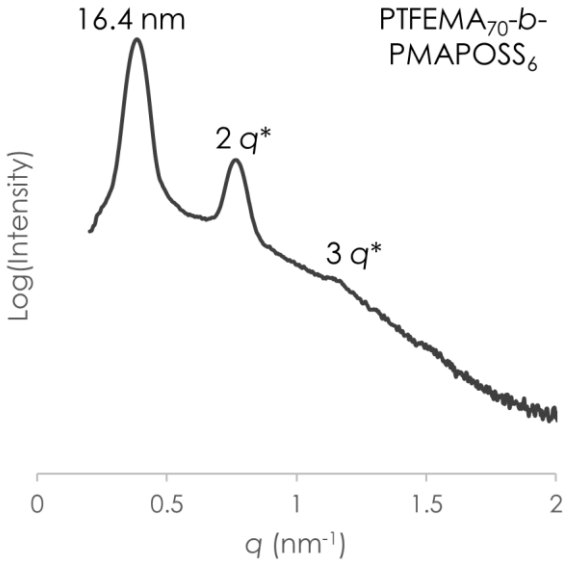


Figure 6-10. 1D SAXS profile of $PTFEMA_{70}$-*b*-$PMAPOSS_6$.

Based on the NMR and SEC analyses, it was shown that the syntheses of both PMAPOSS-*b*-PTFEMA and PTFEMA-*b*-PMAPOSS are highly repeatable and reliable, yielding BCPs of low dispersities ($Đ \leq 1.2$) regardless of which macro-CTA was used initially. Additionally, the volume fractions could be easily controlled, repeatably obtaining $f_{PMAPOSS} = 0.3$. Analyzing the bulk samples of the synthesized BCPs via SAXS revealed scattering peaks at integer ratios relative to the primary scattering peak, indicating that the BCPs form well-ordered

lamellae. Using the equation $d = 2\pi/q^*$, where q^* is the position of the primary scattering peak, L_0 for each BCP could be calculated. Aside from PMAPOSS$_{10}$-*b*-PTFEMA$_{117}$, all BCPs obtained exhibited lamellae with sub-10 nm half-pitch features. Therefore, these studies showed that functionally-identical PMAPOSS- and PTFEMA-containing BCPs could be synthesized by starting from either block to yield either PMAPOSS-*b*-PTFEMA or PTFEMA-*b*-PMAPOSS, with the block that was polymerized first mentioned first, simply by convention.

6-4 Conclusion

In this chapter, the synthesis of PMAPOSS- and PTFEMA-containing diblock copolymers was demonstrated using the RAFT process from both PMAPOSS and PTFEMA macro-CTAs. NMR, SEC, and SAXS analyses showed that the targeted syntheses of a series of sub-10 nm lamella-forming PMAPOSS-*b*-PTFEMAs and PTFEMA-*b*-PMAPOSSs had succeeded. Therefore, while the workup methods differ slightly, these results show that functionally nearly identical BCPs can be obtained by synthesizing the BCP from either direction.

6-5 References

(1) Bates, F. S.; Fredrickson, G. H. Block Copolymer Thermodynamics: Theory and Experiment. *Annu. Rev. Phys. Chem.* **1990**, *41* (1), 525–557 DOI: 10.1146/annurev.pc.41.100190.002521.

(2) Leibler, L. Theory of Microphase Separation in Block Copolymers. *Macromolecules* **1980**, *13* (6), 1602–1617 DOI: 10.1021/ma60078a047.

(3) Bates, F. S.; Fredrickson, G. H. Block Copolymers—Designer Soft Materials. *Phys. Today* **1999**, *52* (2), 32 DOI: 10.1063/1.882522.

(4) Matsen M.W., S. M. Self-Assembly of Block Copolymers. *Curr. Opin. Colloid Interface Sci.* **1996**, *1* (2011), 329–336 DOI: 10.1039/c2cs35115c.

(5) Sinturel, C.; Bates, F. S.; Hillmyer, M. A. High χ-Low N Block Polymers: How Far Can We Go? *ACS Macro Letters*. 2015, pp 1044–1050.

(6) Hirai, T.; Leolukman, M.; Jin, S.; Goseki, R.; Ishida, Y.; Kakimoto, M. A.; Hayakawa, T.; Ree, M.; Gopalan, P. Hierarchical Self-Assembled Structures from POSS-Containing

Block Copolymers Synthesized by Living Anionic Polymerization. *Macromolecules* **2009**, *42* (22), 8835–8843 DOI: 10.1021/ma9018944.

(7) Nakatani, R.; Takano, H.; Chandra, A.; Yoshimura, Y.; Wang, L.; Suzuki, Y.; Tanaka, Y.; Maeda, R.; Kihara, N.; Minegishi, S.; Miyagi, K.; Kasahara, Y.; Sato, H.; Seino, Y.; Azuma, T.; Yokoyama, H.; Ober, C. K.; Hayakawa, T. Perpendicular Orientation Control without Interfacial Treatment of RAFT-Synthesized High-χ Block Copolymer Thin Films with Sub-10 Nm Features Prepared via Thermal Annealing. *ACS Appl. Mater. Interfaces* **2017**, *9* (37), 31266–31278 DOI: 10.1021/acsami.6b16129.

(8) Kato, F.; Chandra, A.; Horiuchi, S.; Hayakawa, T. Morphological Dependence on the Addition of a Soft Middle Block Segment to Rigid POSS-Containing Triblock Copolymers for Forming Cylindrical Nanostructures. *RSC Adv.* **2016**, *6* (67), 62172–62180 DOI: 10.1039/C6RA11113K.

(9) Nakatani, R.; Takano, H.; Wang, L.; Chandra, A.; Tanaka, Y.; Maeda, R.; Kihara, N.; Minegishi, S.; Miyagi, K.; Kasahara, Y.; Sato, H.; Seino, Y.; Azuma, T.; Ober, C. K.; Hayakawa, T. Precise Synthesis of Fluorine-Containing Block Copolymers via RAFT. *J. Photopolym. Sci. Technol.* **2016**, *29* (5), 705-708.

(10) Chandra, A.; Nakatani, R.; Uchiyama, T.; Seino, Y.; Sato, H.; Kasahara, Y.; Azuma, T.; Hayakawa, T. Direct In Situ Observation of the Early-Stage Disorder–Order Evolution of Perpendicular Lamellae in Thermally Annealed High-χ Block Copolymer Thin Films. *Adv. Mater. Interfaces* **2019**, *6*, 1801401 DOI: 10.1002/admi.201801401.

(11) Takano, H.; Wang, L.; Tanaka, Y.; Maeda, R.; Kihara, N.; Seino, Y.; Sato, H.; Kawamonzen, Y.; Miyagi, K.; Minegishi, S.; Azuma, T.; Ober, C. K.; Hayakawa, T. Vertical Oriented Lamellar Formation of Fluorine- and Silicon-Containing Block Copolymers without Neutral Layers. *J. Photopolym. Sci. Technol.* **2015**, *28* (5), 649–652 DOI: 10.2494/photopolymer.28.649.

(12) Nakatani, R.; Chandra, A.; Uchiyama, T.; Nabae, Y.; Hayakawa, T. Dynamic Ordering in High-χ Block Copolymer Lamellae Based on Cross-Sectional Orientational Alignment. *ACS Macro Lett.* **2019**, *8* (9), 1122–1127 DOI: 10.1021/acsmacrolett.9b00353.

(13) Li, G.; Wang, L.; Ni, H.; Pittman, C. U. Polyhedral Oligomeric Silsesquioxane (POSS) Polymers and Copolymers: A Review. *J. Inorg. Organomet. Polym.* **2001**, *11* (3), 123–154 DOI: 10.1023/A:1015287910502.

(14) Chiacchio, M. A.; Borrello, L.; Di Pasquale, G.; Pollicino, A.; Bottino, F. A.; Rescifina, A. Synthesis of Functionalized Polyhedral Oligomeric Silsesquioxane (POSS) Macromers by Microwave Assisted 1,3-Dipolar Cycloaddition. *Tetrahedron* **2005**, *61* (33), 7986–7993 DOI: 10.1016/j.tet.2005.06.006.

(15) Maeda, R.; Hayakawa, T.; Ober, C. K. Dual Mode Patterning of Fluorine-Containing Block Copolymers through Combined Top-down and Bottom-up Lithography. *Chem. Mater.* **2012**, *24* (8), 1454–1461 DOI: 10.1021/cm300093e.

(16) Cintora, A.; Takano, H.; Khurana, M.; Chandra, A.; Hayakawa, T.; Ober, C. K. Block Copolymers Containing Stable Radical and Fluorinated Blocks with Long-Range Ordered Morphologies Prepared by Anionic Polymerization. *Polym. Chem.* **2019**, *10* (37), 5094–5102 DOI: 10.1039/c9py00416e.

(17) Goto, A.; Sato, K.; Tsujii, Y.; Fukuda, T.; Moad, G.; Rizzardo, E.; Thang, S. H. Mechanism and Kinetics of RAFT-Based Living Radical Polymerizations of Styrène and Methyl Methacrylate. *Macromolecules* **2001**, *34* (3), 402–408 DOI: 10.1021/ma0009451.

(18) Owens, D. K.; Wendt, R. C. Estimation of the Surface Free Energy of Polymers. *J. Appl. Polym. Sci.* **1969**, *13* (8), 1741–1747 DOI: 10.1002/app.1969.070130815.

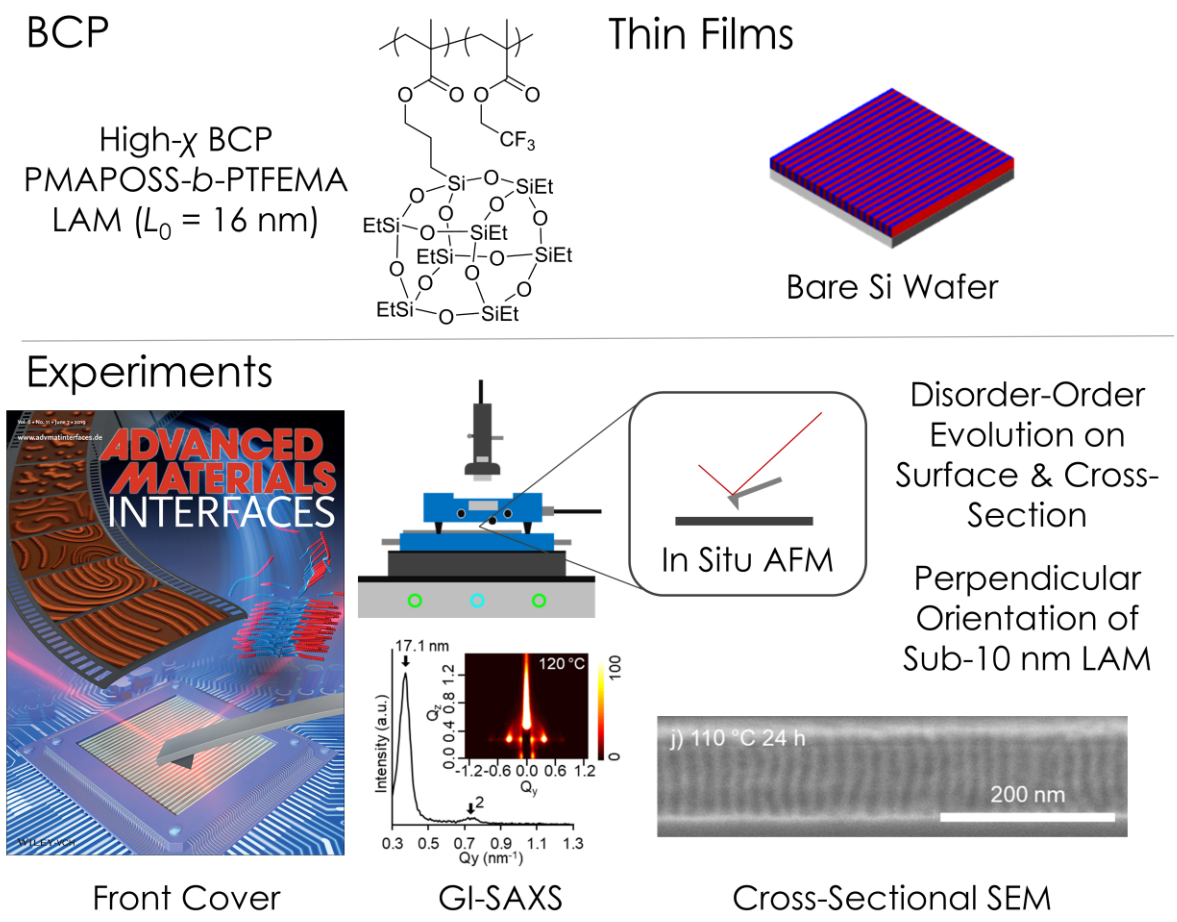
(19) Reichardt, C. Solvatochromic Dyes as Solvent Polarity Indicators. *Chem. Rev.* **1994**, *94* (8), 2319–2358 DOI: 10.1021/cr00032a005.

Chapter 7 Structural Evolution of PMAPOSS-*b*-PTFEMA Thin Films on Bare Silicon Substrates

7-1 Introduction

The realization of “defect-free” patterns with sub-10 nm features hinges on the ability to control the self-assembly behavior of high-χ BCPs on thin films. In turn, by analyzing the growth of self-assembled structures in real time and real space, the fundamentals of BCP thin film self-assembly can be revealed. Earlier studies of the growth of ordered structures on thin films have largely been restricted to low-χ BCPs or parallel morphologies.[1–10] However, as the use of high-χ BCPs and perpendicular lamellar morphologies are preferable for next-generation lithography (NGL) applications, the study of the growth of sub-10 nm perpendicular lamellar structures in strongly-segregating, high-χ BCP thin films is imperative.

In this study (Schematic 7-1), the growth of perpendicular lamellae with sub-10 nm features is studied with combinatorial in situ AFM, cross-sectional SEM, and GI-SAXS.[11] Thin films of a lamella-forming PMAPOSS-*b*-PTFEMA were prepared and thermally annealed from 50 to 120 °C at a ramping rate of 1 °C per 120 s. In situ AFM images were recorded every 30 s and compiled into a movie, whereas additional thin films were annealed based on the same thermal history and quenched at 10 °C increments for SEM and GI-SAXS analyses.



Schematic 7-1. Illustrative overview of the goals and content of Chapter 7. Adapted with permission from Chandra, A. et al, *Adv. Mater. Interfaces* **2019**, *6*, 1801401. Copyright 2019 WILEY-VCH Verlag GmbH & Co., KGaA, Weinheim.

7-2 Experimental Section

7-2-1 Materials

The PMAPOSS-*b*-PTFEMA BCPs used in this Chapter were synthesized as described in Chapter 6 and listed in Table 7-1. Si wafers were also prepared in the same manner as described in Chapter 6.

7-2-2 Instruments

Small angle X-ray scattering (SAXS) and grazing-incidence SAXS (GI-SAXS) analyses were performed on a Bruker NanoSTAR (50 kV/100 mA) equipped with a 2D-PSPC detector at a camera length of 1055 nm. Cross-sectional field-emission scanning

electron microscopy (CS-SEM) was used to image the sample cross sections on a Hitachi High Tech SU5500 FE-SEM. A Leica UMT-UCT ultramicrotome was used to prepare 70 nm thin sections of the bulk samples coated in an epoxy resin for bright-field transmission electron microscopy (TEM) imaging. TEM images were obtained on a Hitachi H7650 Zero A operating at an accelerating voltage of 80 kV. The thicknesses of thin films were measured on an F20 Filmetrics thin film analyzer. A JPK Instruments NanoWizard ULTRA Speed A AFM (Bruker) equipped with a Heating Cooling Module (HCM) and a standard Olympus microcantilever (OCML-AC55TS) with a resonant frequency of 1.9 MHz were used to record the atomic force microscopy (AFM) images in AC mode. The setpoint was set to 0.75 V, 75% of the target amplitude, to minimize perturbations on the sample and no side effects were observed on the thin films upon in situ AFM imaging. Images 1 × 1 μm^2 in size with a resolution of 512 × 512 pixels were obtained at a line rate of 17.666 Hz, yielding one image every 30 s. The AFM images were processed by subtracting the background using JPK Data Processing software.

7-2-3 Sample Preparation

Bulk samples of PMAPOSS-*b*-PTFEMA were prepared from the slow evaporation of a 1 wt% $CHCl_3$ solution. Residual solvent was removed by drying under reduced pressure for 24 h, and the samples were annealed at 110 °C for 24 h prior to SAXS analysis. The two-dimensional (2D) scattering patterns obtained via SAXS were azimuthally integrated to yield one-dimensional (1D) scattering profiles and analyzed using the equation ($q = 4\pi \sin(\theta/2)/\lambda$), where θ and λ are the scattering angle and wavelength, respectively. Based on the ratios of the positions of the peaks relative to the primary peak with the maximum scattering intensity, the morphologies of the samples were determined. Domain spacings (L_0) could then be calculated using the equation, $d = 2\pi/q^*$ where q^* is the position of the primary scattering peak. Thin films of the cylinder-forming $PMAPOSS_{12}$-*b*-$PTFEMA_{88}$ were prepared on piranha-treated bare Si wafers by spin-coating a 1 wt% $CHCl_3$ solution at 7000 rpm for 30 s. For the measurement of the SFEs, PMAPOSS and PTFEMA homopolymer thin films were prepared by spin-coating 3 wt% $CHCl_3$ solutions onto piranha-treated bare Si wafers at 7000

rpm for 30 s and dried *in vacuo* for two days. Thin films of the lamella-forming PMAPOSS$_6$-*b*-PTFEMA$_{80}$ were prepared by spin-coating 3 wt% $CHCl_3$ solutions at 7000 rpm for 30 s and dried under reduced pressure at 50 °C for 24 h.

7-3 Results and Discussion

7-3-1 Sample Preparation

To move beyond 30 nm-pitch L/S structures, the self-assembly behavior of strongly segregating, high-χ BCPs need to be studied in detail as well. For this purpose, we chose the Si- and F-containing BCP, PMAPOSS-*b*-PTFEMA, for its capability to form perpendicularly-oriented lamellae with sub-10 nm feature sizes with simple thermal annealing under ambient conditions. Using the RAFT process, PMAPOSS macro-CTAs were first prepared. The PTFEMA block was then added on through the chain extension of the PMAPOSS macro-CTAs with TFEMA. The PMAPOSS-*b*-PTFEMA BCPs were then characterized by SEC and NMR, and the results are listed in Table 1. The volume fractions of PMAPOSS and PTFEMA were calculated using densities of 1.14 g cm^{-3} and 1.45 g cm^{-3}, respectively. Subsequently, to determine the morphologies formed by the synthesized PMAPOSS-*b*-PTFEMAs, bulk films were prepared through the slow evaporation of a dilute $CHCl_3$ solution. Upon drying and annealing of the bulk samples, SAXS analysis (Fig. 7-1) of PMAPOSS$_6$-*b*-PTFEMA$_{80}$ ($f_{PMAPOSS}$ = 0.31) revealed scattering peaks at integer ratios to the primary peak. Using the equation $d = 2\pi/q^*$, where q^* is the position of the primary peak, L_0 for PMAPOSS$_6$-*b*-PTFEMA$_{80}$ can be estimated to be 16.2 nm. Additionally, TEM analysis of thin sections prepared from the ultramicrotometry of the bulk samples of PMAPOSS$_6$-*b*-PTFEMA$_{80}$ revealed long-range linear structures with approximately 16 nm periodicities (Fig. 7-2). These results suggest that PMAPOSS$_6$-*b*-PTFEMA$_{80}$ forms well-ordered lamellae with sub-10 nm (8 nm half-pitch) feature sizes. Additionally, SAXS analysis (Fig. 7-3) of the bulk sample of PMAPOSS$_{12}$-*b*-PTFEMA$_{88}$ ($f_{PMAPOSS}$ = 0.46) revealed scattering peaks at q:q^* = 1:3^{½}:4^{½}:9^{½}:13^{½}:19^{½} and an L_0 of 29.9 nm. This corresponds well with the scattering peaks of a hexagonally-packed cylindrical structure.

Table 7-1. Characterization data of the synthesized PMAPOSS-*b*-PTFEMAs.

BCP	M_n (g mol^{-1})	$Đ$	$f_{PMAPOSS}$ (vol%)	f_{PTFEMA} (vol%)	Morphology
PMAPOSS$_6$-*b*-PTFEMA$_{80}$	18,300	1.14	31	69	Lamellae
PMAPOSS$_{12}$-*b*-PTFEMA$_{88}$	29,300	1.24	46	54	Cylinders

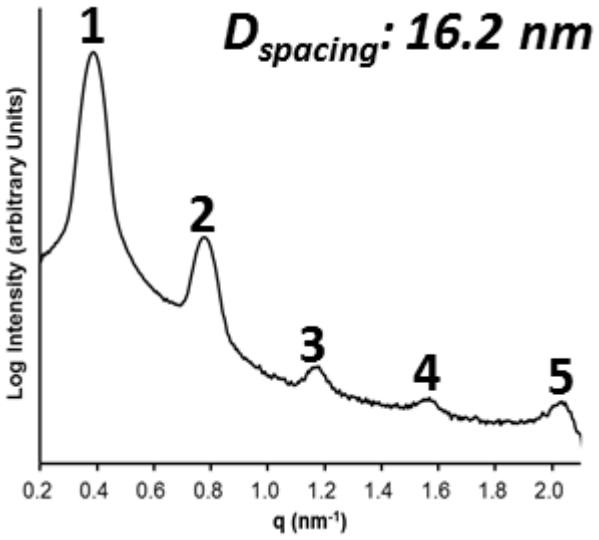


Figure 7-1. Azimuthally-integrated 1D SAXS profile of PMAPOSS$_6$-*b*-PTFEMA$_{80}$.

Reproduced with permission from Chandra et al, *Adv. Mater. Interfaces* **2019**, *6*, 1801401.

Copyright 2019 WILEY-VCH Verlag GmbH & Co., KGaA, Weinheim.

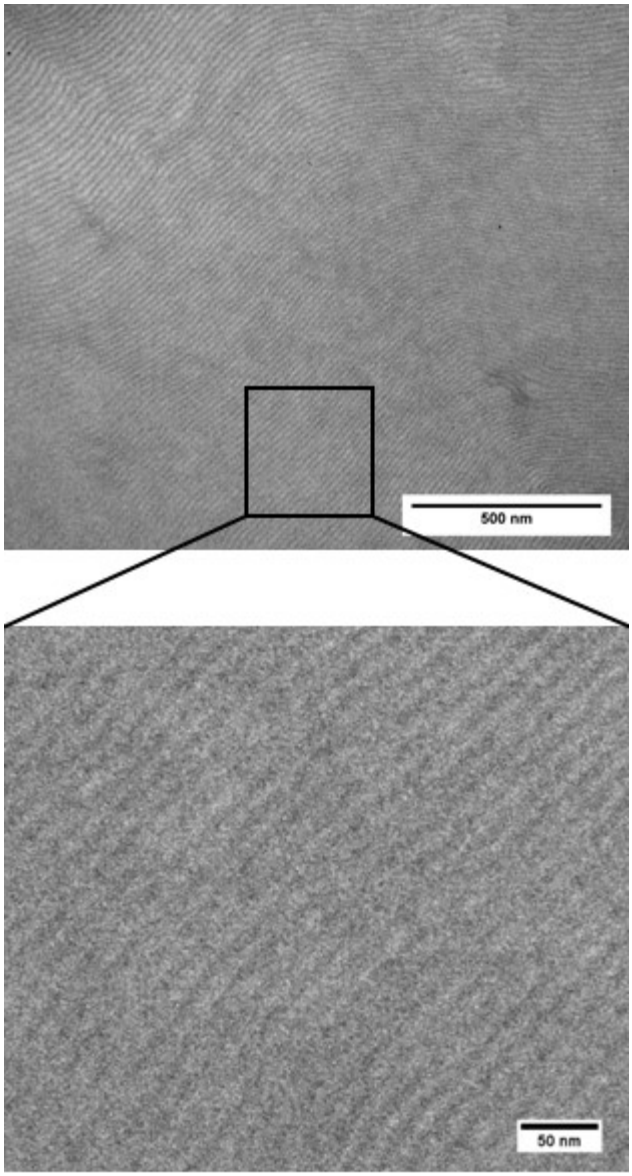


Figure 7-2. TEM images of $PMAPOSS_6$-*b*-$PTFEMA_{80.}$ Reproduced with permission from Chandra et al, *Adv. Mater. Interfaces* **2019**, *6*, 1801401. Copyright 2019 WILEY-VCH Verlag GmbH & Co., KGaA, Weinheim.

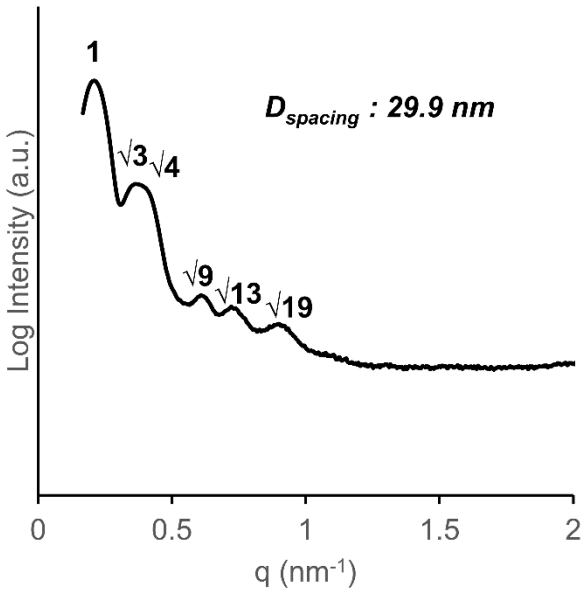


Figure 7-3. Azimuthally-integrated 1D SAXS profile of $PMAPOSS_{12}$-*b*-$PTFEMA_{88}$.

Reproduced with permission from Chandra et al, *Adv. Mater. Interfaces* **2019**, *6*, 1801401.

Copyright 2019 WILEY-VCH Verlag GmbH & Co., KGaA, Weinheim.

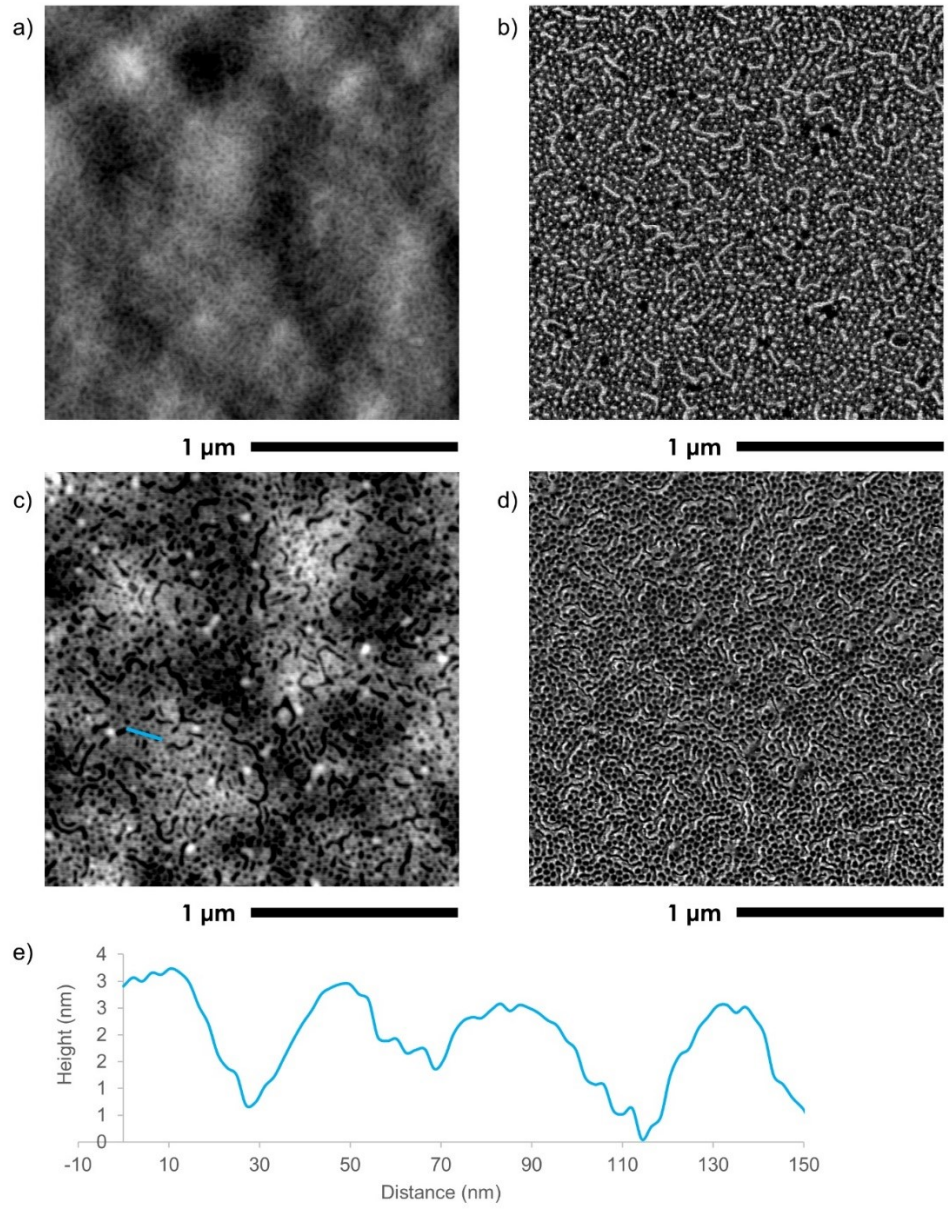


Figure 7-4. AFM (a) height and (b) phase images of a cylinder-forming PMAPOSS$_{12}$-*b*-PTFEMA$_{88}$ thin film after annealing at 110 °C for 24 h. Corresponding (c) height and (d) phase images of the same thin film after the selective removal of the PTFEMA domain via O_2-RIE. (d) Height profile of the line shown in (c). Reproduced with permission from Chandra et al, *Adv. Mater. Interfaces* **2019**, *6*, 1801401. Copyright 2019 WILEY-VCH Verlag GmbH & Co., KGaA, Weinheim.

7-3-2 Identifying the Microdomains in AFM Phase Images

When using intermittent contact or AC mode during AFM analysis, a color contrast can develop between different materials imaged on the surface. To identify the color contrast for the respective blocks in PMAPOSS-*b*-PTFEMA upon AFM imaging, thin films of the cylinder-forming $PMAPOSS_{12}$-*b*-$PTFEMA_{88}$ ($f_{PMAPOSS}$ = 0.46) were prepared. After annealing at 110 °C for 24 h, AFM analysis (Fig. 7-4) revealed the formation of a largely hexagonally-arranged dot structure of bright cores in a dark matrix, with the appearance of short linear structures akin to conjoined, parallel cylindrical cores. This suggests mixed orientation cylinders where the minor domain appears bright on AFM phase images had formed. Based on the previously reported phase diagram of PMAPOSS-*b*-PTFEMA,[12] PMAPOSS and PTFEMA are expected to be the major and minor domains respectively in $PMAPOSS_{12}$-*b*-$PTFEMA_{88}$, suggesting that PMAPOSS appears dark on the AFM phase images while PTFEMA appears bright. To test this hypothesis, PTFEMA was selectively removed using O_2-RIE under a 20 sccm O_2 flow rate, a pressure of 30 Pa, and a power of 20 W for 2 s. Following the selective removal of PTFEMA, AFM analysis revealed the formation of a matrix of hexagonally-arranged holes with randomly scattered linear trenches. This further suggests that the dark domains in the AFM phase images of PMAPOSS-*b*-PTFEMA thin films correspond to PMAPOSS, while the bright domains can be attributed to PTFEMA.

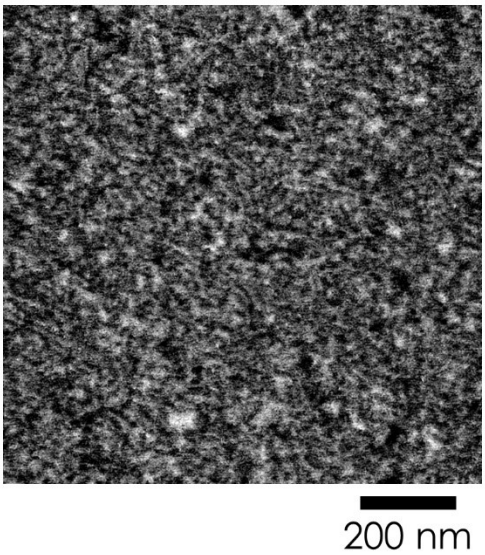


Figure 7-5. Phase image showing the featureless surface of an as-cast PMAPOSS$_6$-*b*-PTFEMA$_{80}$ thin film prior to drying. Reproduced with permission from Chandra et al, *Adv. Mater. Interfaces* **2019**, *6*, 1801401. Copyright 2019 WILEY-VCH Verlag GmbH & Co., KGaA, Weinheim.

7-3-3 Thermal Annealing for Combinatorial Studies

Following the identification of the domains in the phase images of PMAPOSS-*b*-PTFEMA, the growth and evolution of ordered structures in thin films of the lamella-forming PMAPOSS$_6$-*b*-PTFEMA$_{80}$ can be studied in detail. Firstly, PMAPOSS$_6$-*b*-PTFEMA$_{80}$ thin films were prepared on piranha-treated bare Si wafers by spin-coating a 3 wt% $CHCl_3$ solution at 7000 rpm for 30 s. Using an F20 Filmetrics, the thin films were shown to exhibit a thickness of approximately 140 nm and an AFM phase image of the as-cast thin film is shown in Fig. 7-5. Before further analysis, the thin films were dried *in vacuo* at 50 °C for 24 h to remove residual solvent. As the drying temperature was below the glass transition temperatures of both blocks ($T_{g,\,PMAPOSS}$ = 82 °C, $T_{g,\,PTFEMA}$ = 75 °C),[13,14] no change was observed in the thin film after drying.

To study the evolution of ordered structures in thin films of the high-χ, lamella-forming PMAPOSS$_6$-*b*-PTFEMA$_{80}$, the thin films were analyzed using high-speed in situ AFM on a JPK NanoWizard ULTRA Speed A AFM equipped with a heating stage (HCM). After

imaging at room temperature, the temperature was raised to 50 °C, the temperature at which the thin films were dried previously with no changes observed. Subsequently, the annealing temperature was increased by 1 °C increments every 120 s, up to a maximum temperature of 120 °C. Meanwhile, real-space and real-time in situ AFM images were recorded at an imaging area of 1 × 1 μm^2, a resolution of 512 × 512 pixels, and a line rate of 17.666 Hz, yielding one image every 30 s. The images were subsequently compiled into a time-lapsed movie with snapshots shown in Fig. 7-6. Additionally, $PMAPOSS_6$-*b*-$PTFEMA_{80}$ thin films were prepared using the same spin-coating and incrementally increasing thermal annealing conditions were prepared. These thin films were quenched at 10 °C increments between 50 and 120 °C and analyzed using GI-SAXS and CS-SEM after lightly etching the PTFEMA domain with O_2-RIE to increase contrast.

7-3-4 Growth of Perpendicular Lamellae from "Disorder"

Using combinatorial studies of in situ AFM, GI-SAXS, and CS-SEM, the evolution of perpendicular lamellae in high-χ BCP thin films from the as-cast state was revealed. Furthermore, three stages could be identified in the thermal annealing and self-assembly process of PMAPOSS-*b*-PTFEMA. At temperatures lower than the T_g's of the BCP ($T_{g,\ PMAPOSS}$ = 82 °C, $T_{g,\ PTFEMA}$ = 75 °C),[13,14] the first stage can be found between 25 and 70 °C. Meanwhile, the second stage was found near the T_g's of the BCP, at 70 to 100 °C, and the final stage was observed at higher temperatures, between 100 and 120 °C.

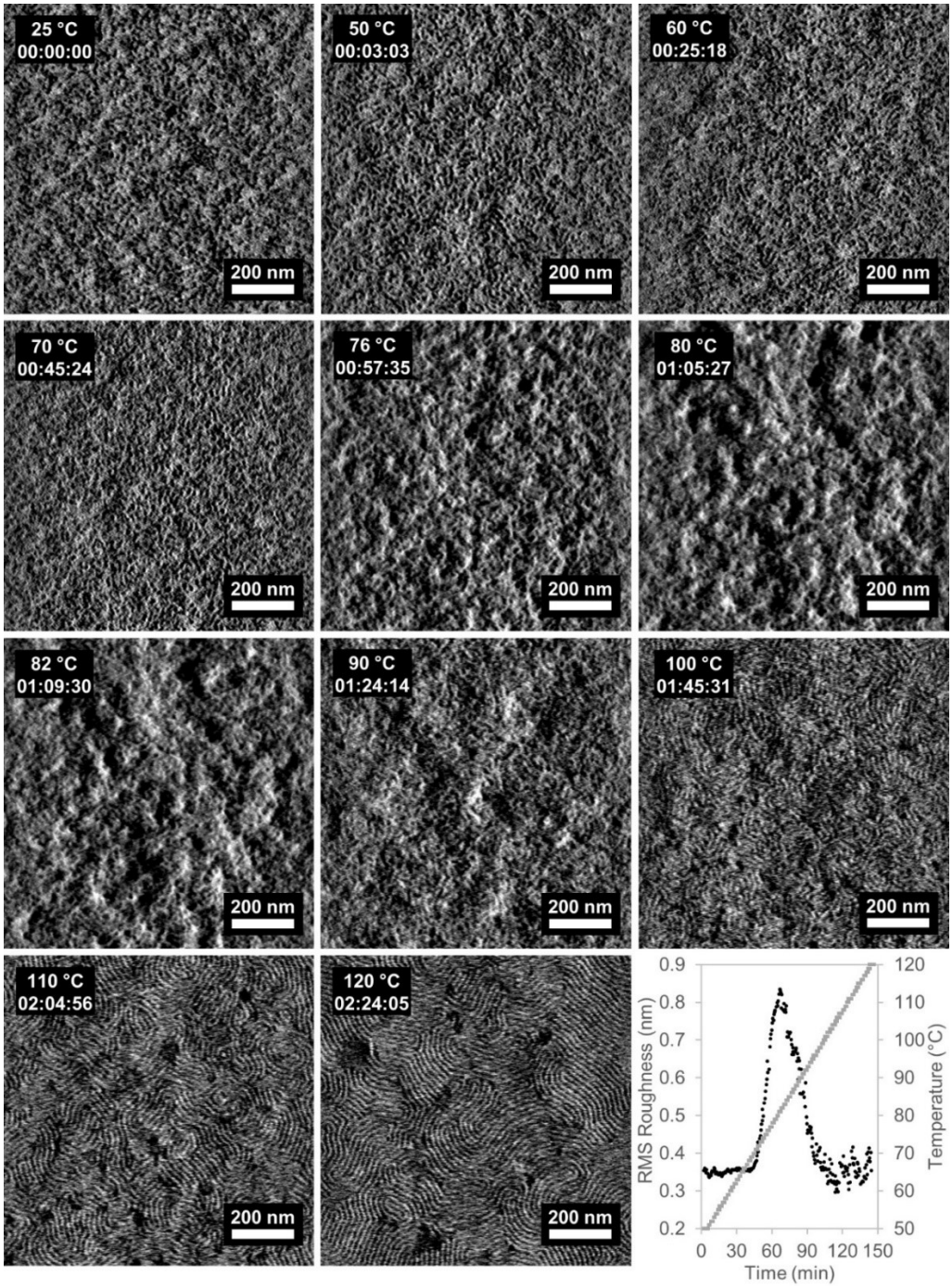


Figure 7-6. Snapshot AFM phase images during the in situ annealing of PMAPOSS-*b*-PTFEMA. The temperature and time in hours:minutes:seconds can be found on the top left of each image, and the calculated RMS roughness against time is found on the bottom right. Reproduced with permission from Chandra et al, *Adv. Mater. Interfaces* **2019**, *6*, 1801401. Copyright 2019 WILEY-VCH Verlag GmbH & Co., KGaA, Weinheim.

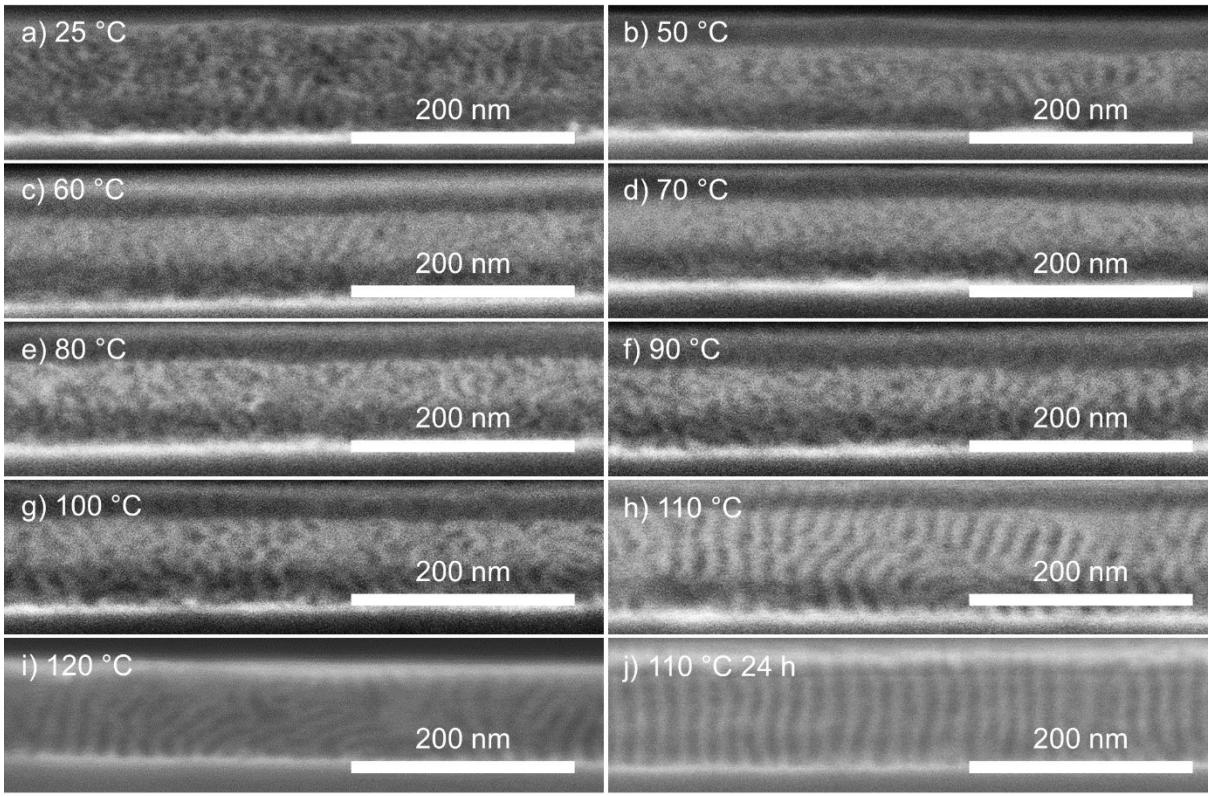


Figure 7-7. SEM images of the cross-sections of PMAPOSS-*b*-PTFEMA thin films annealed (a-i) incrementally up to the temperature shown in the top left or (j) at 110 °C for 24 h. Reproduced with permission from Chandra et al, *Adv. Mater. Interfaces* **2019**, *6*, 1801401. Copyright 2019 WILEY-VCH Verlag GmbH & Co., KGaA, Weinheim.

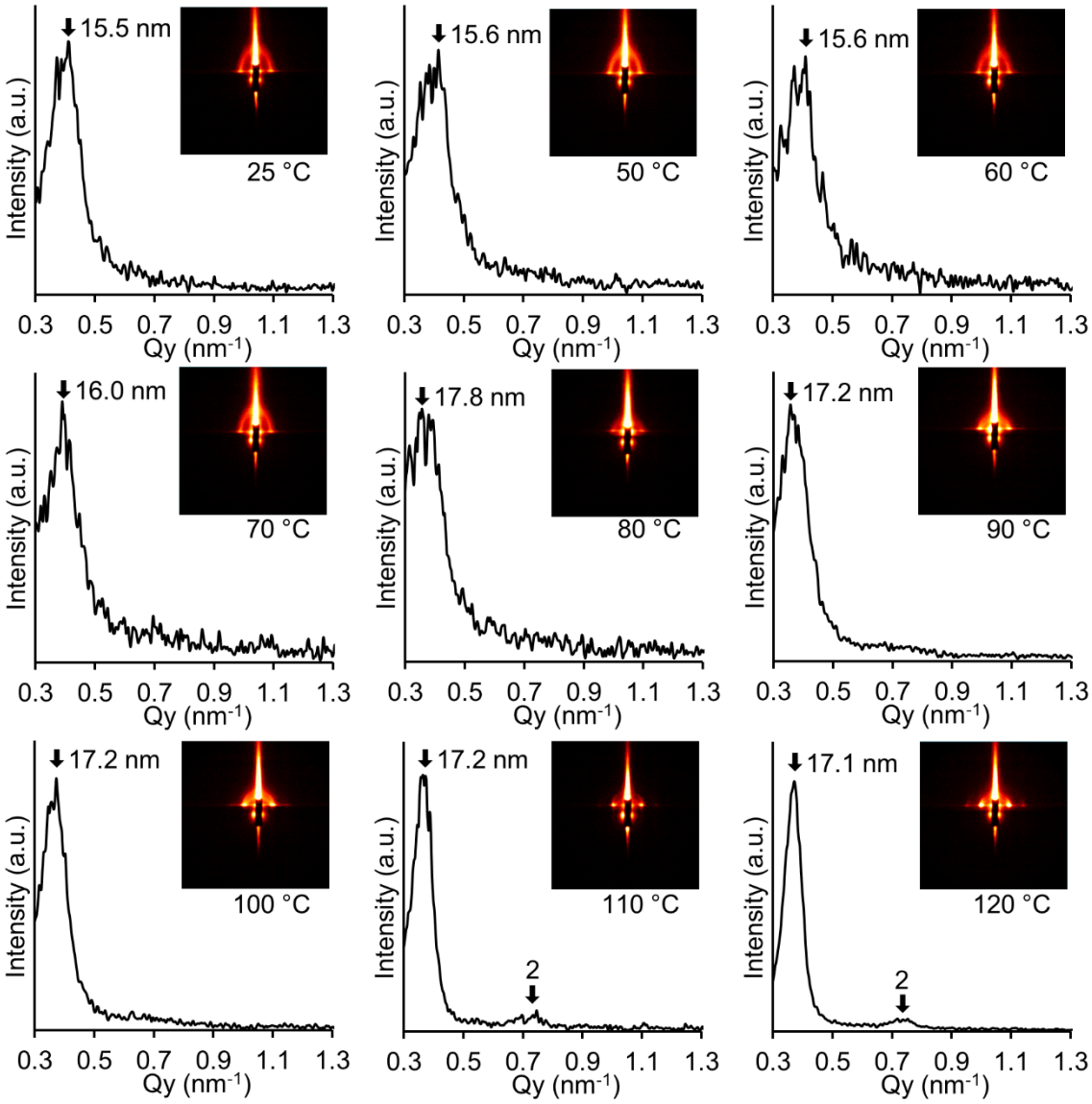


Figure 7-8. In-plane one-dimensional (1D) GI-SAXS profiles on PMAPOSS-*b*-PTFEMA thin films annealed incrementally up to the temperature shown in each frame. The original two-dimensional (2D) GI-SAXS scattering pattern is inset on the top right of each profile. Reproduced with permission from Chandra et al, *Adv. Mater. Interfaces* **2019**, *6*, 1801401. Copyright 2019 WILEY-VCH Verlag GmbH & Co., KGaA, Weinheim.

Firstly, the AFM phase image obtained at 25 °C showed a generally featureless surface with dark dots randomly scattered about in a bright matrix, as observed in the as-cast thin films prior to drying at 50 °C for 24 h. Although increasing the temperature causes the imaged area to shift about due to thermal fluctuations, the featureless surface remains largely unchanged even as the temperature increased to 70 °C. Calculating the root-mean-

squared (RMS) roughness from the corresponding height images in this temperature regime revealed a low average value of approximately 0.352 ± 0.006 nm, as expected of a smooth thin film surface prepared via spin-coating. Based on SEM analyses of the cross-sections of the thin films annealed up to 70 °C (Fig. 7-7), similar poorly-ordered, random structures were observed. Furthermore, GI-SAXS analyses revealed a half-ring in the two-dimensional (2D) scattering profiles of the thin films annealed up to 70 °C. Additionally, a single primary scattering peak could be observed in the in-plane one-dimensional (1D) GI-SAXS profiles. Using the equation $d = 2\pi/q^*$, where q^* is the position of the primary peak, a periodicity of approximately 15.7 ± 0.2 nm can be calculated from the GI-SAXS profiles (Fig. 7-8). These results suggest that the structure formed by the BCP upon spin-coating is a highly-random, poorly-ordered state that is locally microphase separated. This is in good agreement with earlier simulation studies.[15] Additionally, since the T_g's of the BCP are higher at around 75 to 82 °C, the microdomains are likely simply kinetically frozen in the disorder-like initial state formed upon spin-coating. Furthermore, the L_0 of the thin film at approximately 15.7 nm, is slightly lower compared to that of the equilibrated L_0 measured in the bulk film, previously recorded to be 16.2 nm. This suggests that while locally microphase-separated, the chains of the BCP were deposited in an unrelaxed, kinetically frozen state upon solvent evaporation during spin-coating. Therefore, as the BCP is restricted to the glassy state below the T_g, the BCP remains in a random state with significant mixing and interfacial contact between the domains.

As the temperature approaches the T_g's of the BCP, microphase separation and self-assembly can be expected to begin. Conventionally, the formation of self-assembled structures is known to originate from a nucleation and growth or spinodal decomposition mechanism. In the case of asymmetric diblock copolymers, the free energy barrier for nucleation scales with $N^{0.5}|f - 0.5|^5$, where N is the total degree of polymerization and f is the volume fraction of one domain. Expressed in units of k_BT, where k_B is the Boltzmann's constant and T is the absolute temperature, the free energy barrier to nucleation, ΔF, can be used to determine the stability of the initial state. At $\Delta F > 1$, the initial disordered state is

considered metastable, with self-assembly proceeding via a slow first-order phase transition in a nucleation and growth mechanism. For $\Delta F < 1$, the metastability of the initial state is less well-defined, and as ΔF approaches 0, self-assembly transitions from a slow nucleation and growth mechanism to a swift spinodal decomposition. However, if there is no nucleation barrier, the disordered state is unstable and self-assembly proceeds via a swift spinodal decomposition process that occurs simultaneously throughout the sample. For the $PMAPOSS_6$-*b*-$PTFEMA_{80}$ used in this study, $N = 86$ and $f_{PMAPOSS} = 0.31$. Therefore, ΔF can be estimated to be approximately 0.003 $k_B T$. With this near zero-value of ΔF, PMAPOSS-*b*-PTFEMA can be expected to begin self-assembly via a spinodal decomposition-like mechanism.

Therefore, as the annealing temperature approached the T_g's of BCP, the growth of self-assembled structures could be detected between 70 and 100 °C. Particularly, the RMS roughness of the thin film was observed to rapidly increase from 70 °C, suggesting a spinodal decomposition-like process was beginning. The RMS roughness then peaked at 0.83 nm at 82 °C, before rapidly decaying as the temperature increased further. Additionally, compositional fluctuations could be observed in the phase images above 70 °C, with the appearance of short linear and small flat structures around 76 °C, approximately half-way between 70 and 82 °C. The simultaneous appearance of ordered structures throughout the thin film is as expected for a spinodal decomposition-like process. The appearance of both linear structures and flat, dark areas in the phase image suggests the presence of both perpendicular and parallel lamellae, with the flat, dark areas being attributed to local segregation of PMAPOSS onto the free interface. These results are in good agreement with previous studies that showed that short-range local interactions dominate at the early stages of self-assembly, resulting in random combinations of the nearest neighboring microdomains, and the development of a structure with mixed orientations.[16–18]

At temperatures above 82 °C, where the RMS roughness of the thin film peaked, the grains of the perpendicular lamellae could be observed to grow as defects gradually disappeared between the grains. However, at the same time, the initially small, dark, flat

areas attributed to parallel lamellae also coalesced and grew into relatively large junction defect sites situated between various perpendicular lamellar grains. Furthermore, GI-SAXS analyses revealed that the L_0 of the microdomains had increased from approximately 15.7 nm in the lower temperature regime to 17.8, 17.2, and 17.2 nm at 80, 90, and 100 °C. This can likely be attributed to the BCP chains relaxing and locally rearranging to adopt comparatively favorable configurations during the self-assembly process. Additionally, randomly-oriented lines with holes and short tubular structures could be observed in the cross sections of the thin films. This randomly-oriented PMAPOSS matrix is similar to that observed in the lower temperature regime, suggesting that self-assembly begins at the film surface and slowly propagates into the internal structure. Previous studies have also suggested that lamellae first develop at the interfaces and gradually propagate towards the internal structure of the thin films.

Finally, a temperature regime characterized by the growth of the lamellar grains through sequential defect annihilation was found between 100 and 120 °C. As the lamellar grains linked together and broke away from neighboring grains, larger grains with long-range ordering developed. However, the flat dark domains that appeared earlier also coalesced to form larger junction defects of parallel, surface-segregated PMAPOSS. Additionally, the calculated RMS roughness in this temperature regime averaged to 0.35 ± 0.03 nm. This indicates that a similar roughness compared to the as-cast thin film had been obtained. Furthermore, 17 nm full-pitch lamellae with mixed perpendicular, tilted, and parallel orientations could be detected in the cross sections of the thin film via SEM imaging. Compared to an optimized annealing condition of 110 °C for 24 h, the mixed orientational lamellae suggests that the parallel junction defects are highly metastable and relatively long annealing is required to reorient the microdomains. Furthermore, in this temperature regime, GI-SAXS analyses revealed L_0 was approximately 17.1 ± 0.1 nm, lining up well with the L_0 measured in the AFM and CS-SEM experiments.

While increases in the RMS roughness at the onset of self-assembly has yet to be fully explained, it can likely be attributed to the translation and growth of the BCP

microdomains during the spinodal decomposition-like process. Lamellae are by definition bilayers of distinct phases. To minimize the free energy of the system, well-aligned, defect-free bilayers of lamellae are ideal as interfacial contact between the different phases can be minimized while maximizing entropic stretching of the BCP chains. However, to work towards defect-free lamellae, the BCP must undergo a gliding motion that involves the interdiffusion of one domain into another. While the final defect-free state possesses the lowest free energy, the diffusion of one microdomain into another for defect annihilation results in a large enthalpic penalty. However, at the initial stages of self-assembly, the BCP nanostructure starts in a highly random, mixed, and defective state. Therefore, as the temperature is raised above the T_g's of the BCP, the microdomains work towards reducing interfacial contact between the distinct phases. Since the cross-sectional studies suggested that self-assembly starts at the free interface while the internal structure remains kinetically trapped, the free interface enables the BCP chains to flow on top of neighboring domains. The lack of confinement in the free interfaces gives the microdomains an extra degree of freedom to move into for defect annihilation. However, as the temperature increases further and the internal structure of the BCP thin film is no longer kinetically trapped, the BCP chains are also capable of moving and diffusing with the internal structure of the thin film. This results in an initial increase in the RMS roughness of the thin film upon the onset of self-assembly. However, as self-assembly propagates within the internal thin film, the BCP chains no longer need to extend up into the free interface to move towards defect annihilation, thereby reducing the RMS roughness of the thin film, making it return to an value that is roughly similar to the original RMS roughness prior to annealing.

7-4 Conclusion

Using a high-speed AFM and the strongly segregating BCP, PMAPOSS-*b*-PTFEMA, the real time and real space tracking of the evolution of sub-10 nm perpendicular lamellae was realized. Such studies had been largely inaccessible in the past as a high-speed AFM that is stable at a wide range of elevated temperatures had not been developed. Additionally, most high-χ BCPs typically require the use of solvent vapor annealing or a top-

coat to control the interfacial affinities of the BCP and induce perpendicular orientation. This restricted self-assembly studies of high-χ BCPs to ex situ studies and the development of ordered structures could not be observed in real time. However, without being limited to simply analyzing the film surface, combinatorial GI-SAXS and cross-sectional SEM analyses revealed additional information regarding the self-assembly behavior within the depths of the thin film. It was shown that self-assembly and perpendicular orientation begins on the film surface for the structures formed by PMAPOSS-*b*-PTFEMA and that self-assembly can start earlier on the film surface, resulting in the growth of the lamellae proceeding via gliding motions that extend onto the surface, increasing the surface roughness at the start of the self-assembly process. However, as the surface and inner depths of the thin film begin self-assembling at higher temperatures, the gliding motion of the lamellar layers can be contained within the thin film and the surface roughness returns to the original values. With these studies, we were able to directly document and elucidate the characteristic stages of self-assembly in a high-χ, perpendicular lamella-forming BCP, paving the way for developing defect-free structures of such high-χ BCPs and the realization of sub-10 nm lines and spaces for lithographic applications using BCPs.

7-5 References

(1) Mayes, A. M.; Russell, T. P.; Bassereau, P.; Baker, S. M.; Smith, G. S. Evolution of Order in Thin Block Copolymer Films. *Macromolecules* **1994**, *27*, 749–755.

(2) Peters, R. D.; Stasiak, P.; Matsen, M. W.; Dalnoki-Veress, K. Morphology Induced Spinodal Decomposition at the Surface of Symmetric Diblock Copolymer Films. *ACS Macro Lett.* **2013**, *2* (5), 441–445 DOI: 10.1021/mz400159s.

(3) Collin, B.; Chatenay, D.; Coulon, G.; Ausserre, D.; Gallot, Y. Ordering of Copolymer Thin Films As Revealed by Atomic Force Microscopy. *Macromolecules* **1992**, *25* (5), 1621–1622 DOI: 10.1021/ma00031a042.

(4) Horvat, A.; Sevink, G. J. A.; Zvelindovsky, A. V.; Krekhov, A.; Tsarkova, L. Specific Features of Defect Structure and Dynamics in the Cylinder Phase of Block Copolymers. *ACS Nano* **2008**, *2* (6), 1143–1152 DOI: 10.1021/nn800181m.

(5) Knoll, a; Lyakhova, K. S.; Horvat, a; Krausch, G.; Sevink, G. J. a; Zvelindovsky, a V; Magerle, R. Direct Imaging and Mesoscale Modelling of Phase Transitions in a Nanostructured Fluid. *Nat. Mater.* **2004**, *3* (12), 886–891 DOI: 10.1038/nmat1258.

(6) Morkved, T. L. L.; Lopes, W. a. A.; Hahm, J.; Sibener, S. J. J.; Jaeger, H. M. M. Silicon Nitride Membrane Substrates for the Investigation of Local Structure in Polymer Thin Films. *Polymer (Guildf).* **1998**, *39* (16), 3871–3875 DOI: 10.1016/S0032-3861(97)10218-X.

(7) Harrison, C.; Adamson, D. H.; Cheng, Z.; Sebastian, J. M.; Sethuraman, S.; Huse, D. A.; Register, R. A.; Chaikin, P. M. Mechanisms of Ordering in Striped Patterns. *Science (80-.).* **2000**, *290* (5496), 1558–1560 DOI: 10.1126/science.290.5496.1558.

(8) Tsarkova, L.; Horvat, A.; Krausch, G.; Zvelindovsky, A. V.; Sevink, G. J. A.; Magerle, R. Defect Evolution in Block Copolymer Thin Films via Temporal Phase Transitions. *Langmuir* **2006**, *22* (19), 8089–8095 DOI: 10.1021/la0613530.

(9) Hahm, J.; Lopes, W. A.; Jaeger, H. M.; Sibener, S. J. Defect Evolution in Ultrathin Films of Polystyrene-Block-Polymethylmethacrylate Diblock Copolymers Observed by Atomic Force Microscopy. *J. Chem. Phys.* **1998**, *109* (23), 10111–10114 DOI: 10.1063/1.477702.

(10) Raybin, J.; Ren, J.; Chen, X.; Gronheid, R.; Nealey, P. F.; Sibener, S. J. Real-Time Atomic Force Microscopy Imaging of Block Copolymer Directed Self Assembly. *Nano Lett.* **2017**, *17* (12), 7717–7723 DOI: 10.1021/acs.nanolett.7b03881.

(11) Chandra, A.; Nakatani, R.; Uchiyama, T.; Seino, Y.; Sato, H.; Kasahara, Y.; Azuma, T.; Hayakawa, T. Direct In Situ Observation of the Early-Stage Disorder–Order Evolution of Perpendicular Lamellae in Thermally Annealed High-χ Block Copolymer Thin Films. *Adv. Mater. Interfaces* **2019**, *6*, 1801401 DOI: 10.1002/admi.201801401.

(12) Nakatani, R.; Takano, H.; Chandra, A.; Yoshimura, Y.; Wang, L.; Suzuki, Y.; Tanaka, Y.; Maeda, R.; Kihara, N.; Minegishi, S.; Miyagi, K.; Kasahara, Y.; Sato, H.; Seino, Y.; Azuma, T.; Yokoyama, H.; Ober, C. K.; Hayakawa, T. Perpendicular Orientation Control without Interfacial Treatment of RAFT-Synthesized High-χ Block Copolymer

Thin Films with Sub-10 Nm Features Prepared via Thermal Annealing. *ACS Appl. Mater. Interfaces* **2017**, *9* (37), 31266–31278 DOI: 10.1021/acsami.6b16129.

(13) Ishida, Y. Study on the Synthesis and Self-Assembly of Polymers with Cage Silsesquioxane Side Chain, Tokyo Institute of Technology, 2011.

(14) Maeda, R.; Hayakawa, T.; Ober, C. K. Dual Mode Patterning of Fluorine-Containing Block Copolymers through Combined Top-down and Bottom-up Lithography. *Chem. Mater.* **2012**, *24* (8), 1454–1461 DOI: 10.1021/cm300093e.

(15) Forrey, C.; Yager, K. G.; Broadaway, S. P. Molecular Dynamics Study of the Role of the Free Surface on Block Copolymer Thin Film Morphology and Alignment. *ACS Nano* **2011**, *5* (4), 2895–2907 DOI: 10.1021/nn103502p.

(16) Joly, S.; Raquois, A.; Paris, F.; Hamdoun, B.; Auvray, L.; Ausserre, D.; Gallot, Y. Early Stage of Spinodal Decomposition in 2D. *Phys. Rev. Lett.* **1996**, *77* (21), 4394–4397 DOI: 10.1103/PhysRevLett.77.4394.

(17) Peters, R. D.; Stasiak, P.; Matsen, M. W.; Dalnoki-Veress, K. Morphology Induced Spinodal Decomposition at the Surface of Symmetric Diblock Copolymer Films. *ACS Macro Lett.* **2013**, *2* (5), 441–445 DOI: 10.1021/mz400159s.

(18) Ren, J.; Zhou, C.; Chen, X.; Dolejsi, M.; Craig, G. S. W.; Rincon Delgadillo, P. A.; Segal-Peretz, T.; Nealey, P. F. Engineering the Kinetics of Directed Self-Assembly of Block Copolymers toward Fast and Defect-Free Assembly. *ACS Appl. Mater. Interfaces* **2018**, *10* (27), 23414–23423 DOI: 10.1021/acsami.8b05247.

This page was intentionally left blank.

Chapter 8 Conclusion and Future Prospects

8-1 Closing Remarks

At first glance, the self-assembly behavior of BCPs appears to be a complicated process that is completely random and seemingly impossible to control. However, by breaking up the complicated self-assembly process into individual parts and finding solutions to each issue, progress towards using self-assembled materials in practical, everyday applications can be made. In this thesis, the most compelling challenges towards applying the self-assembled structures of BCPs to next-generation lithographic applications were addressed. Particularly, the fundamental nature of how defects form, evolve, and disappear has been an elusive issue that remained difficult to study. For applications involving bottom-up self-assembly processes, the ability to control the formation or removal of defects in the pattern is imperative. Therefore, the mechanisms behind the formation, evolution, and annihilation of ordered structures and defects were investigated using a combination of metrologies, mainly revolving around high-speed in situ AFM, allowing for the real-time and real-space tracking of individual structures on BCP thin films.

As outlined in Chapter 1, the General Introduction, the several nanometer-scale ordered structures formed by BCPs could be applied to nanofabrication technologies. However, issues such as the need to reduce the stochastic growth of random, defective structures and controlling the chemistries that give birth to BCP candidates capable of forming the required ordered patterns on thin films at sub-10 nm length scales while remaining free of metal residues and possessing sufficiently high etch contrasts between the blocks, were highlighted.

In Chapter 2, an early attempt was made to *direct the self-assembly* process of lamella-forming PS-*b*-PMMA thin films prepared on COOL process DSA substrates. Using high-speed AFM imaging coupled with the in situ annealing of the thin films, the growth and evolution of surface structures was observed in real-time and real-space from the disordered state to a microphase-separated, ordered state. However, it was found that the chemistries

and interfacial affinities of the DSA guide stripes and the neutral layers worked to facilitate the growth of orientational defects instead of allowing for the perpendicular orientation and long-range alignment of lamellar stripes of PS-*b*-PMMA.

To address the issue of substrate chemistries, PS-*b*-PMMA thin films prepared using the SMART^{TM} flow DSA process were studied in Chapters 3 and 4. With neutral layers that erase preferential interactions between the substrate and the lamellar PS-*b*-PMMA microdomains, weakly PS-preferential guide stripes deposited between the neutral layers facilitate the perpendicular orientation and long-range alignment of the striped patterns. Using an incrementally increasing temperature profile and in situ AFM, the early-stage glass transition, origins of self-assembled structures, and eventual evolution into well-aligned striped patterns was studied in Chapter 3. Subsequently, using isothermal annealing conditions, the types of defects that appeared during the self-assembly of PS-*b*-PMMA on SMART^{TM} process DSA thin films were identified and the respective mechanisms for the formation and annihilation of the identified defects were detailed in Chapter 4.

Without being limited to simple linear structures, a perpendicular cylinder-forming PS-*b*-PMMA thin film prepared on DSA substrates with a hexagonal pre-pattern was studied in Chapter 5. While the line and space structures formed by perpendicular lamellae can be used in the nanofabrication of devices such as field effect transistors, the hexagonal pattern formed by an array of hexagonally-arranged perpendicular cylinders can also be used in the nanofabrication of devices such as bit-patterned media. Additionally, as linear structures and hexagonal dotted structures are fundamentally different, the evolution, growth, reorientation, and hexagonal arrangement of the two-dimensional dotted grains were studied using high-speed in situ AFM as well.

Aside from the growth of defect structures, the minimization of the feature sizes formed by BCPs must also be reduced. The previous chapters mainly focused on the self-assembly behavior of PS-*b*-PMMA, a BCP that is incredibly useful as the similar surface affinities of the blocks facilitate the perpendicular orientation of the microdomains. However,

the low chemical dissimilarities limit the minimum domain spacing achievable by PS-*b*-PMMA. To that end, novel strongly-segregating, high-χ BCPs must be used. Therefore, the synthesis and self-assembly behavior of a hybrid, organic-inorganic BCP, PMAPOSS-*b*-PTFEMA, was investigated in Chapters 6 and 7. The addition of heteroatoms such as silicon and fluorine can serve to greatly increase not just the chemical dissimilarities, but also the etch contrast between the blocks. Additionally, as both blocks exhibited similar surface affinities, analogous to the blocks of PS-*b*-PMMA, PMAPOSS-*b*-PTFEMA is capable of forming perpendicular lamellae on silicon wafers using simple ambient thermal annealing processes. Upon optimizing the synthetic route of PMAPOSS-*b*-PTFEMA via the metal-free RAFT process in Chapter 6, the growth and evolution of sub-10 nm perpendicular lamellar structures was investigated in detail using a combination of in situ AFM, GI-SAXS, and cross-sectional SEM in Chapter 7. Using such combinatorial studies, changes on the surface and depths of the thin film could be studied, building a better picture of the self-assembly behavior and perpendicular orientation of such high-χ BCPs.

Based on these studies, it was found that regardless of the chemical structure, the morphology, or the length scale of the BCPs used, a number of common self-assembly behaviors could be determined. Mainly, there were three stages in the evolution of self-assembled structures, a kinetically-frozen state below the T_g's of the BCP, a glass transition and microphase separation into short-range, random structures near the T_g's of the BCP, and a reorientation and long-range coarsening stage at temperatures much higher than the T_g's of the BCP. These stages are characterized by changes in the RMS roughness of the film surface, starting off at a low value characteristic to smooth, spin-coated thin films at the first stage, followed by a sharp increase in the surface roughness as the glass transition occurs, and finally a return to a low surface roughness similar to the as-cast values in the final stages of domain coarsening at high temperature. Such changes reflect the complicated processes and interplay between the interfaces that drive the self-assembly behavior of BCPs confined onto thin films. Furthermore, detailed tracking of the changes in individual

defects on SMART^{TM} process DSA substrates have revealed the detailed annihilation pathways of characteristic defects formed by lamellar BCP patterns. Using ultra-high-speed in situ AFM, the stochastic gliding motion of the BCP microdomains could even be documented in real-time and real-space.

With a stronger foundation that can explain the detailed mechanisms behind the self-assembly of BCPs, the means to remove, or even deliberately add structures to a BCP pattern could be realized. While DSA has lost some appeal for high volume manufacturing at the 30-40 nm pitch technology node when compared to EUVL, DSA remains competitive as a low-cost, low energy requirement, multi-patterning technology for the nanofabrication of sub-10 nm feature sizes. Therefore, by optimizing the self-assembly behavior and DSA processes for high-χ BCPs, the industrial implementation of DSA could potentially be achieved in the future. Furthermore, living organisms are built from and rely upon natural self-assembly, self-organization, and self-replication processes. By understanding how soft materials form nano-assemblies, the key to controlling self-assembly could be attained, forging new pathways for the nanofabrication of not just simple electronic devices, but perhaps even artificial organelles and other biological systems.

Appendix: Supporting Information

A-1 Matlab Codes for Orientational Order Parameter

```
clear
close all

%Variable
Width=2000; %Width of the image (nm)

%Multiple image import
RGB=dir('filepath');
for column=1:length(RGB)
    fileName=strcat('filepath',RGB(column).name);
    [pathstr,name,ext]=fileparts(fileName);

    RGB2=imread(fileName);
    disp(fileName);

Gray=rgb2gray(RGB2);
I=im2uint8(Gray);
[xsize,ysize]=size(I);
figure1=figure('visible','off');
imshow(RGB2);
figure2=figure('visible','off');
imshow(I);

%Spatial Calibration factor
SpaCalf=Width/xsize; %Put width of the image. 1000 means 1um.
```

```
%Fourier transform
A=fft2(I);
ImgFFTabs=abs(fftshift(A));
ImgFFTphase=angle(fftshift(A));
ImgFFT=abs(A).*exp(1i*angle(A));

%for visualization
ImgFFTx=log(ImgFFTabs+1);
max_out=max(ImgFFTx(:));
min_out=min(ImgFFTx(:));
ImgFFTx=(ImgFFTx-min_out)/(max_out-min_out);
figure3=figure('visible','off');
imshow(ImgFFTx);

%Get the dimensions of the image. numberOfColorBands should be = 1.
[rows0,columns0,numberofcolorbands]=size(ImgFFTx);
maxDistance=(floor(xsize)-floor(xsize/2));

%Start Radial Profile
profileSums=zeros(1,maxDistance);
profileCounts=zeros(1,maxDistance);
for column0=1:columns0
   for row0=1:rows0
      thisDistance=round(sqrt((row0-rows0/2)^2+(column0-columns0/2)^2));
      if thisDistance>=maxDistance
         continue;
      elseif thisDistance<=0
```

```
            continue;
        else

profileSums(thisDistance)=profileSums(thisDistance)+double(ImgFFTabs(row0,column0));
        profileCounts(thisDistance)=profileCounts(thisDistance)+1;
        end
    end
end

%Divide the sums by the counts at each distance to get the average profile.
avgRadPrf=profileSums./profileCounts;
LavgRadPrf=log10(avgRadPrf);
RadDis=1:length(avgRadPrf);
q=2*pi./(SpaCalf*((RadDis./columns0).^-1));
Sdata=smoothdata(LavgRadPrf,'gaussian',6);
[pks,locs,w,p]=findpeaks(Sdata,RadDis,'WidthReference','halfprom','SortStr','descend');
llocs=2*pi./(SpaCalf*((pks./columns0).^-1));
Peak=[llocs;pks;w;p];
[xs,ys]=size(Peak);
index=find(Peak(1,:)<Peak(1,1));
Peak(:,index)=[];
nSdata=smoothdata(LavgRadPrf,'gaussian',6);
[npks,nlocs,nw,np]=findpeaks(nSdata,RadDis,'WidthReference','halfprom','SortStr','descend'
);
nnlocs=2*pi./(SpaCalf*((nlocs./columns0).^-1));
nPeak=[nnlocs;npks;nw;np];
[nxs,nys]=size(nPeak);
nindex=find(nPeak(1,:)<nPeak(1,1));
```

```
nPeak(:,nindex)=[];
L0=2*pi./nPeak(1,1);

figure4=figure('visible','off');
hold on
plot(q,LavgRadPrf,'bo','MarkerSize',1,'LineWidth',1.1);
plot(q,nSdata,'-','Color','r','LineWidth',1);
plot(nPeak(1,:),nPeak(2,:)+.1,'rv','MarkerFaceColor','r');
plot([nPeak(1,1)*1.05 nPeak(1,1)*1.2],[min(LavgRadPrf) max(LavgRadPrf)],'-.','Color','k');
plot([nPeak(1,1)*0.95 nPeak(1,1)*0.8],[min(LavgRadPrf) max(LavgRadPrf)],'-.','Color','k');
text(nPeak(1,:),nPeak(2,:)+.2,num2str((1:numel(nPeak(2,:)))'));
xlim([min(q) max(q)]);
ylim([min(LavgRadPrf) max(LavgRadPrf)]);
set(gca,'ytick',[])
pbaspect([1 1 1]);
title('Average Radial Profile');
legend(sprintf('Experimental data (L_{0}=%.1f (nm))',L0),'Smoothed data');
xlabel('q [nm^{-1}]');
ylabel('Average Intensity Level');

%Image Filtering
%Initialize parameters for the circle such as location and radius.
circleCenterX=rows0/2;
circleCenterY=columns0/2;
circleRadius=nlocs(1,1)*1.2;
circleRadius2=nlocs(1,1)*0.8;

%Initialize an image to a logical image of the circle.(High-pass filter)
```

```
circleImage=false(rows0,columns0);
[x1,y1]=meshgrid(1:columns0,1:rows0);
circleImage((x1-circleCenterX).^2+(y1-circleCenterY).^2<=circleRadius^2)=true;

%Initialize an image to a logical image of the circle.(Low-pass filter)
circleImage2=true(rows0,columns0);
[x2,y2]=meshgrid(1:columns0,1:rows0);
circleImage2((x2-circleCenterX).^2+(y2-circleCenterY).^2<=circleRadius2^2)=false;

%Display it in the plot.
ImgFilter=ImgFFTx.*(circleImage.*circleImage2);
ImgFilteri=ImgFFTphase.*(circleImage.*circleImage2);
ImgIFilterabs=exp(ImgFilter*(max_out-min_out)+min_out);
ImgIFilter=ImgIFilterabs.*exp(1i*ImgFilteri);
ImgIFFT=ifft2(ifftshift(ImgIFilter));
X=max(max(abs(ImgIFFT)));
ImgIFFTnorm=ImgIFFT+max(max(abs(ImgIFFT)));
ImgIFFTF=sqrt(ImgIFFTnorm.*conj(ImgIFFTnorm));
ImgOut=ImgIFFTF/max(max(ImgIFFTF));
figure5=figure('visible','off');
imshow(ImgFilter);

%Gauss averaging
L0=2*pi./nPeak(1,1);
Sigma=sqrt((L0/SpaCalf-1)/2);
Imgblur=imgaussfilt(ImgOut,Sigma);
figure6=figure('visible','off');
imshow(Imgblur);
```

```
%Fourier transform2
A2=fft2(Imgblur);
ImgFFTabs2=abs(fftshift(A2));
ImgFFTphase2=angle(fftshift(A2));
ImgFFT2=abs(A2).*exp(1i*angle(A2));

%for visualization2
ImgFFTx2=log(ImgFFTabs2+1);
max_out2=max(ImgFFTx2(:));
min_out2=min(ImgFFTx2(:));
ImgFFTx2=(ImgFFTx2-min_out2)/(max_out2-min_out2);

%Get the dimensions of the image. numberOfColorBands should be = 1.
[rows02,columns02,numberofcolorbands2]=size(ImgFFTx2);
maxDistance2=(floor(rows02)-floor(rows02/2));

%Start Radial Profile
profileSums2=zeros(1,maxDistance2);
profileCounts2=zeros(1,maxDistance2);
for column02=1:columns02
   for row02=1:rows0
      thisDistance2=round(sqrt((row02-rows0/2)^2+(column02-columns02/2)^2));
      if thisDistance2>=maxDistance2
         continue;
      elseif thisDistance2<=0
         continue;
      else
```

```
profileSums2(thisDistance2)=profileSums2(thisDistance2)+double(ImgFFTabs2(row02,colu
mn02));
        profileCounts2(thisDistance2)=profileCounts2(thisDistance2)+1;
        end
    end
end

%Divide the sums by the counts at each distance to get the average profile.
avgRadPrf2=profileSums2./profileCounts2;
LavgRadPrf2=log10(avgRadPrf2);
RadDis2=1:length(avgRadPrf2);
q2=2*pi./(SpaCalf*((RadDis2./columns02).^-1));
Sdata2=smoothdata(LavgRadPrf2,'gaussian',6);
[pks2,locs2,w2,p2]=findpeaks(Sdata2,RadDis2,'WidthReference','halfprom','SortStr','descen
d');
llocs2=2*pi./(SpaCalf*((pks2./columns02).^-1));
Peak2=[llocs2;pks2;w2;p2];
[xs2,ys2]=size(Peak2);
index2=find(Peak2(1,:)<Peak2(1,1));
Peak2(:,index2)=[];
nSdata2=smoothdata(LavgRadPrf2,'gaussian',6);
[npks2,nlocs2,nw2,np2]=findpeaks(nSdata2,RadDis2,'WidthReference','halfprom','SortStr','d
escend');
nnlocs2=2*pi./(SpaCalf*((nlocs2./columns02).^-1));
nPeak2=[nnlocs2;npks2;nw2;np2];
[nxs2,nys2]=size(nPeak2);
nindex2=find(nPeak2(1,:)<nPeak2(1,1));
```

```
nPeak2(:,nindex2)=[];
L02=2*pi./nPeak2(1,1);

figure7=figure('visible','off');
hold on
plot(q2,LavgRadPrf2,'bo','MarkerSize',1,'LineWidth',1.1);
plot(q2,nSdata2,'-','Color','r','LineWidth',1);
plot(nPeak2(1,:),nPeak2(2,:)+.1,'rv','MarkerFaceColor','r');
plot([nPeak2(1,1)*1.05 nPeak2(1,1)*1.05],[min(LavgRadPrf2)
max(LavgRadPrf2)],'-.','Color','k');
plot([nPeak2(1,1)*0.95 nPeak2(1,1)*0.95],[min(LavgRadPrf2)
max(LavgRadPrf2)],'-.','Color','k');
text(nPeak2(1,:),nPeak2(2,:)+.2,num2str((1:numel(nPeak2(2,:)))'));
xlim([min(q2) max(q2)]);
ylim([min(LavgRadPrf2) max(LavgRadPrf2)]);
set(gca,'ytick',[])
pbaspect([1 1 1]);
title('Average Radial Profile');
legend(sprintf('Experimental data (L_{0}=%.1f (nm))',L02),'Smoothed data');
xlabel('q [nm^{-1}]');
ylabel('Average Intensity Level');

%Thresholding
Avg=sum(Imgblur(:))/numel(Imgblur);

%Binarization
ImgThr=imbinarize(Imgblur,Avg);
ImgThin=bwmorph(ImgThr,'thin',Inf);
```

```
ImgIvFFT=ifft2(fft2(ImgThin));
Imgblur2=imgaussfilt(ImgIvFFT,Sigma);
figure8=figure('visible','off');
imshow(ImgThr);
figure9=figure('visible','off');
imshow(ImgThin);
figure10=figure('visible','off');
imshow(Imgblur2);

%Calculate Image Imtensity Difference
[rows1,columns1]=size(Imgblur2);
for column1=1:columns1-1
   for row1=1:rows1-1
      ImgDx(row1,column1)=Imgblur2(row1+1,column1)-Imgblur2(row1,column1);
      ImgDy(row1,column1)=Imgblur2(row1,column1+1)-Imgblur2(row1,column1);
   end
end

%Calculate Orientation angle
ImgArc=atan(ImgDy./ImgDx);
ImgArcF=ImgArc.*180/pi;
figure11=figure('visible','off');
imagesc(ImgArcF,[-90 90]);colormap(hsv);
pbaspect([1 1 1]);
axis off
c=colorbar('Ticks',[-90,-45,0,45,90]);
c.Label.String='Orientation angle (^{o})';
```

```
%Order Parameter
OP=cos((rmmissing(ImgArcF)-90)*2*pi/180);
OrderParameter=sum(OP(:))/numel(OP);
disp(OrderParameter);

%Calculate orientation angle
ImgArc=atan(ImgDy./ImgDx);
ImgArcF=ImgArc.*180/pi;

figure11=figure('visible','on');
imagesc(ImgArcF,[-90 90]);
colormap(hsv);
pbaspect([1 1 1]);
axis off
c=colorbar('Ticks',[-90,-45,0,45,90]);
c.Label.String='Orientation angle ({°})';

%Calculate correlation length
[rows2,columns2]=size(ImgArc);
maxDis=floor(xsize/5);
profSums=zeros(1,maxDis);
profCounts=zeros(1,maxDis);

rl=randperm(rows2,floor(rows2/Ran));
rm=randperm(columns2,floor(columns2/Ran));
rn=randperm(rows2,floor(rows2/Ran));
ro=randperm(columns2,floor(columns2/Ran));
for l=1:length(rl)
```

```
    sl=rl(l);
    for m=1:length(rm)
        sm=rm(m);
        for n=1:length(rn)
            sn=rn(n);
            for o=1:length(ro)
                so=ro(o);
                Distance=round(sqrt((sl-sn)^2+(sm-so)^2));
                if Distance>maxDis
                    continue;
                elseif Distance<=0
                    continue;
                end
                profSums(Distance)=profSums(Distance)+cos(2*(ImgArc(sn,so)-ImgArc(sl,sm)));
                profCounts(Distance)=profCounts(Distance)+1;
            end
        end
    end
end

%Divide sums by counts at each distance to get average profile
avgPrf=profSums./profCounts;

%Curve fitting by least squares method
E=100;
xdata=1:length(avgPrf);
ydata=avgPrf*E;
fun=@(x,xdata) x(1)*exp(-xdata.x(2));
```

```
x0=[0.5*E,50];
x=lsqcurvefit(fun,x0,xdata,ydata);

%plot
S=get(0,'ScreenSize');

figure12=figure('Position',S,'visible','on');

hold on
plot(xdata*SpaCalf,(ydata/E)/(x(1)/E),'bo','MarkerSize',2,'LineWidth',1.1);
plot(xdata*SpaCalf,exp(-xdata*SpaCalf/(x(2)*SpaCalf)),'r-','LineWidth',1.1);
pbaspect([1 1 1]);
title('Correlation length','FontSize',12);
legend({sprintf('experimental data (L+{0}=%.1f (nm))',L0),sprintf('fitting function: exp(-r/%.1f
(nm))',x(2)*SpaCalf)},'FontSize',12,'northeast');
xlabel('r: Distance [nm]','FontSize',12);
ylabel('Autocorrelation Intensity','FontSize',12);
set(gca,'FontSize',14);
set(0,'DefaultAxesLineWidth',2);

%export as excel files
q1=rot90(q,3);
SFile1=rot90(LavgRadPrf,3);
SFile2=rot90(LavgRadPrf2,3);
EFile1=horzcat(q1,SFile1);
EFile2=horzcat(q1,SFile2);
savefile1=[pathstr '/' 'CM' '/' name '-bef.xlsx'];
savefile2=[pathstr '/' 'CM' '/' name '-aft.xlsx'];
```

```
savefile3=[pathstr '/' 'CM' '/' name '-OP.xlsx'];
xlswrite(savefile1,EFile1);
xlswrite(savefile2,EFile2);
xlswrite(savefile3,OrderParameter);



%save file
figures=[figure1,figure2,figure3,figure4,figure5,figure6,figure7,figure8,figure9,figure10,figure1
1,figure12];
for f=1:numel(figures)
    fig=figures(1,f);
    fname=strcat(name,'-%d');
    filename=sprintf(fname,f);
    savefile=[pathstr '/' 'CM' '/' filename '.tif'];
    print(fig,'-dtiff','-r600',savefile)
end


end
```

A-2 Matlab Codes for Correlation Length

```
clear
close all

%Variables
Width=1000; %Width of the image (nm)
Ran=6; %Frequeny of random number generation (The bigger the number is, the smaller
amount of calculation becomes.)
```

```
%Multiple image import
RGB=dir('filepath');
for column=1:length(RGB)
    fileName=strcat('filepath',RGB(column).name);
    [pathstr,name,ext]=fileparts(fileName);

    RGB2=imread(fileName);
    disp(fileName);

Gray=rgb2gray(RGB2);
I=im2uint8(Gray);
[xsize,ysize]=size(I);
figure1=figure('visible','off');
imshow(RGB2);
figure2=figure('visible','off');

%Spatial Calibration factor
SpaCalf=Width/xsize;

%Fourier filtering
A=fft2(I);
ImgFFTabs=abs(fftshift(A));
ImgFFTphase=angle(fftshift(A));
ImgFFT=abs(A).*exp(1i*angle(A));

%for visualization
ImgFFTx=log(ImgFFTabs+1);
max_out=max(ImgFFTx(:));
```

```
min_out=min(ImgFFTx(:));
ImgFFTx=(ImgFFTx-min_out)/(max_out-min_out);
figure3=figure('visible','off');
imshow(ImgFFTx);

%Get the dimensions of the image. numberOfColorBands should be = 1.
[rows0,columns0,numberofcolorbands]=size(ImgFFTx);
maxDistance=(floor(xsize)-floor(xsize/2));

%Start Radial Profile
profileSums=rmmissing(zeros(1,maxDistance));
profileCounts=rmmissing(zeros(1,maxDistance));
for column0=1:columns0
   for row0=1:rows0
      thisDistance=round(sqrt((row0-rows0/2)^2+(column0-columns0/2)^2));
      if thisDistance>=maxDistance
         continue;
      elseif thisDistance<=0
         continue;
      end

profileSums(thisDistance)=profileSums(thisDistance)+double(ImgFFTabs(row0,column0));
      profileCounts(thisDistance)=profileCounts(thisDistance)+1;
   end
end

%Divide the sums by the counts at each distance to get the average profile.
avgRadPrf=profileSums./profileCounts;
```

```
LavgRadPrf=log10(avgRadPrf);
RadDis=1:length(avgRadPrf);
q=2*pi./(SpaCalf*((RadDis./columns0).^-1));
Sdata=smoothdata(LavgRadPrf,'gaussian',6);
[pks,locs,w,p]=findpeaks(Sdata,RadDis,'WidthReference','halfprom','SortStr','descend');
llocs=2*pi./(SpaCalf*((pks./columns0).^-1));
Peak=[llocs;pks;w;p];
[xs,ys]=size(Peak);
index=find(Peak(1,:)<Peak(1,1));
Peak(:,index)=[];
nSdata=smoothdata(LavgRadPrf,'gaussian',6);
[npks,nlocs,nw,np]=findpeaks(nSdata,RadDis,'WidthReference','halfprom','SortStr','descend'
);
nnlocs=2*pi./(SpaCalf*((nlocs./columns0).^-1));
nPeak=[nnlocs;npks;nw;np];
[nxs,nys]=size(nPeak);
nindex=find(nPeak(1,:)<nPeak(1,1));
nPeak(:,nindex)=[];
L0=2*pi./nPeak(1,1);

figure4=figure('visible','off');
hold on
plot(q,LavgRadPrf,'bo','MarkerSize',1,'LineWidth',1.1);
plot(q,nSdata,'-','Color','r','LineWidth',1);
plot(nPeak(1,:),nPeak(2,:)+.1,'rv','MarkerFaceColor','r');
plot([nPeak(1,1)*1.2 nPeak(1,1)*1.2],[min(LavgRadPrf) max(LavgRadPrf)],'-.','Color','k');
plot([nPeak(1,1)*0.8 nPeak(1,1)*0.8],[min(LavgRadPrf) max(LavgRadPrf)],'-.','Color','k');
text(nPeak(1,:),nPeak(2,:)+.2,num2str((1:numel(nPeak(2,:)))'));
```

```
xlim([min(q) max(q)]);
ylim([min(LavgRadPrf) max(LavgRadPrf)]);
set(gca,'ytick',[])
pbaspect([1 1 1]);
title('Average Radial Profile');
legend(sprintf('Experimental data (L_{0}=%.1f (nm))',L0),'Smoothed data');
xlabel('q [nm^{-1}]');
ylabel('Average Intensity Level');

%Image Filtering
%Initialize parameters for the circle such as location and radius.
circleCenterX=rows0/2;
circleCenterY=columns0/2;
circleRadius=nlocs(1,1)*1.1;
circleRadius2=nlocs(1,1)*0.9;

%Initialize an image to a logical image of the circle.(High-pass filter)
circleImage=false(rows0,columns0);
[x1,y1]=meshgrid(1:columns0,1:rows0);
circleImage((x1-circleCenterX).^2+(y1-circleCenterY).^2<=circleRadius^2)=true;

%Initialize an image to a logical image of the circle.(Low-pass filter)
circleImage2=true(rows0,columns0);
[x2,y2]=meshgrid(1:columns0,1:rows0);
circleImage2((x2-circleCenterX).^2+(y2-circleCenterY).^2<=circleRadius2^2)=false;

%Display it in the plot.
ImgFilter=ImgFFTx.*(circleImage.*circleImage2);
```

```
ImgFilteri=ImgFFTphase.*(circleImage.*circleImage2);
ImgIFilterabs=exp(ImgFilter*(max_out-min_out)+min_out);
ImgIFilter=ImgIFilterabs.*exp(1i*ImgFilteri);
ImgIFFT=ifft2(ifftshift(ImgIFilter));
X=max(max(abs(ImgIFFT)));
ImgIFFTnorm=ImgIFFT+max(max(abs(ImgIFFT)));
ImgIFFTF=sqrt(ImgIFFTnorm.*conj(ImgIFFTnorm));
ImgOut=ImgIFFTF/max(max(ImgIFFTF));
figure5=figure('visible','off');
imshow(ImgFilter);

%Gauss averaging
L0=2*pi./nPeak(1,1);
Sigma=sqrt((L0/SpaCalf-1)/2);
Imgblur=imgaussfilt(ImgOut,Sigma);
figure6=figure('visible','off');
imshow(Imgblur);

%Thresholding
Avg=sum(Imgblur(:))/numel(Imgblur);

%Binarization
ImgThr=imbinarize(Imgblur,Avg);
ImgThin=bwmorph(ImgThr,'thin',Inf);
ImgIvFFT=ifft2(fft2(ImgThin));
Imgblur2=imgaussfilt(ImgIvFFT,Sigma);
figure8=figure('visible','off');
imshow(ImgThr);
```

```
figure9=figure('visible','off');
imshow(ImgThin);
figure10=figure('visible','off');
imshow(Imgblur2);

%Calculate Image Intensity Difference
[rows1,columns1]=size(Imgblur2);
for column1=1:columns1-1
   for row1=1:rows1-1
      ImgDx(row1,column1)=Imgblur2(row1+1,column1)-Imgblur2(row1,column1);
      ImgDy(row1,column1)=Imgblur2(row1,column1+1)-Imgblur2(row1,column1);
   end
end

%Calculate Orientation angle
ImgArc=atan(ImgDy./ImgDx+1e-100);
ImgArcF=ImgArc.*180/pi;

%Start Calculation Correlation Length
[rows2,columns2]=size(ImgArc);
maxDis=floor(xsize/5);
profSums=zeros(1,maxDis);
profCounts=zeros(1,maxDis);

rl=randperm(rows2,floor(rows2/Ran));
rm=randperm(columns2,floor(columns2/Ran));
rn=randperm(rows2,floor(rows2/Ran));
ro=randperm(columns2,floor(columns2/Ran));
```

```
for l=1:length(rl)
    sl=rl(l);
    for m=1:length(rm)
        sm=rm(m);
        for n=1:length(rn)
            sn=rn(n);
            for o=1:length(ro)
                so=ro(o);
                Distance=round(sqrt((sl-sn)^2+(sm-so)^2));
                if Distance>maxDis
                    continue;
                elseif Distance<=0
                    continue;
                end
                profSums(Distance)=profSums(Distance)+cos(2*(ImgArc(sn,so)-ImgArc(sl,sm)));
                profCounts(Distance)=profCounts(Distance)+1;
            end
        end
    end
end

%Divide the sums by the counts at each distance to get the average profile.
avgPrf=profSums./profCounts;

%curve fitting by least square method
E=100;%save file

xdata=1:length(avgPrf);
```

```
ydata=avgPrf*E;
fun=@(x,xdata) x(1)*exp(-xdata/x(2));
x0=[0.5*E,50];
x=rmmissing(lsqcurvefit(fun,x0,xdata,ydata));

%plot
S=get(0,'ScreenSize');
figure11=figure('Position',S,'visible','off');
hold on
plot(xdata*SpaCalf,(ydata/E)/(x(1)/E),'bo','MarkerSize',2,'LineWidth',1.1);
plot(xdata*SpaCalf,exp(-xdata*SpaCalf/(x(2)*SpaCalf)),'r-','LineWidth',1.1);
pbaspect([1 1 1]);
title('Correlation length','FontSize',12);
legend({sprintf('experimental data (L_{0}=%.1f (nm))',L0),sprintf('fitting function: exp(-r/%.1f
(nm))',x(2)*SpaCalf)},'FontSize',12,'northeast');
xlabel('r: Distance [nm]','FontSize',12);
ylabel('Autocorrelation Intensity','FontSize',12);
set(gca,'FontSize',14);
set(0,'DefaultAxesLineWidth',2);

figures=[figure1,figure2,figure3,figure4,figure5,figure6,figure8,figure9,figure10,figure11];
for f=1:numel(figures)
    fig=figures(1,f);
    fname=strcat(name,'-%d');
    filename=sprintf(fname,f);
    savefile=[pathstr '/' 'CL' '/' filename,'.tif'];
    print(fig,'-dtiff','-r600',savefile)
end
```

```
end
```

A-3 List of In Situ AFM Videos

Thin Film	In Situ AFM Conditions	Content	File Name
SMART Flow L/S DSA TF1	90 – 230 °C at 2 °C/5 min	Overall In Situ Video (Phase)	20200211 TEL DSA TF1 In Situ AFM Movie AC2.avi
SMART Flow L/S DSA TF1	90 – 230 °C at 2 °C/5 min	Overall In Situ Video (Combined)	20200211 TEL DSA TF1 In Situ AFM Movie Combined AC6.avi
SMART Flow L/S DSA TF3	210 °C, 5 h (128 s/image)	Overall In Situ Video (Phase)	20200229 TEL DSA TF3 In Situ AFM Movie Main 210C AC2.avi
SMART Flow L/S DSA TF3	210 °C, 5 h (128 s/image)	Focus on Final Dislocation Defect	20200229 TEL DSA TF3 In Situ AFM Movie Final Defect Focus in Main 210C AC2.avi
SMART Flow L/S DSA TF4	200 °C, 1 h 40 min	Overall In Situ Video (Phase)	20200308 TEL DSA TF4 In Situ AFM Movie 200C AC2.avi
SMART Flow L/S DSA TF2	190 °C, 6 h	Overall In Situ Video (Phase)	20200227 TEL DSA TF2 190C In Situ AFM Movie Phase AC2.avi
SMART Flow L/S DSA TF5	170 °C, 12 h	Overall In Situ Video (Phase)	20200311 TEL DSA TF5 In Situ AFM Movie 170C AC2.avi
SMART Flow L/S DSA TF6	160 °C, 6 h	Overall In Situ Video (Phase)	20200315 TEL DSA TF6 In Situ AFM Movie 160C AC2.avi
SMART Flow L/S DSA TF5	170 °C, 12 h	Focus on Multiple Bridge Defect	20200311 TEL DSA TF5 In Situ AFM Movie 170C Defect One Focus AC2 Speed200.avi
SMART Flow L/S DSA TF5	170 °C, 12 h	Focus on Parallel Defect Evolution/Annihilation	EvolAnnihil Parallel Defect 170C AC6.avi
SMART Flow L/S DSA TF4	200 °C, 1 h 40 min	Focus on Disclination Pair Defect	DisclinationPair Defect Captioned AC2.avi
SMART Flow L/S DSA TF2	190 °C, 6 h	Focus on +½ Apposing Disclinations	ApposingDisclination Defect Captioned AC2.avi
SMART Flow L/S DSA TF2	190 °C, 6 h	Focus on Dislocation Pair Defect	20200227 TEL DSA TF2 190C In Situ AFM Movie Defect Four DislocPair AC2.avi
SMART Flow L/S DSA TF2	190 °C, 6 h	Focus on Complex Defect Area One (Short)	20200227 TEL DSA TF2 190C In Situ AFM Movie Defect One AC2.avi
SMART Flow L/S DSA TF2	190 °C, 6 h	Focus on Complex Defect Area One (Long)	20200227 TEL DSA TF2 190C In Situ AFM Movie Defect Two AC2.avi
SMART Flow L/S DSA TF3	210 °C, 5 h (2 – 10 s/image)	Super High Speed Focus on Dislocation Pair	UltraHighSpeed Dislocation 1200X AC2.avi
Contact Hole DSA (x,y = 1,0)	90 – 220 °C at 2 °C/5 min	Overall In Situ Video (Phase)	20200302 TEL Contact DSA xy10 In Situ AFM Movie AC2.avi
Contact Hole DSA (x,y = 1,0)	90 – 220 °C at 2 °C/5 min	Overall In Situ Video (Combined)	20200302 TEL Contact DSA xy10 In Situ AFM Movie Combined AC3 500x.avi
PMAPOSS-*b*-PTFEMA	30 – 120 °C at 1 °C/2 min	In Situ Video (Phase)	Time Lapsed AFM Video.avi

List of Publications and Presentations

Publications Related to this Dissertation

1. A. Chandra, Y. Nabae, T. Hayakawa Towards Optimizing the Directed Self-Assembly of Block Copolymers. (Under Preparation)
2. A. Chandra, R. Nakatani, Y. Nabae, T. Hayakawa Defect Annihilation Pathways in the Directed Self-Assembly of Perpendicular Lamellae as Documented in Real-Time and Real-Space via High-Speed In Situ Atomic Force Microscopy. (Under Preparation)
3. A. Chandra, R. Nakatani, Y. Nabae, T. Hayakawa Real-Time and Real-Space Evolution of Perpendicular Lamellae and Cylinders on Chemoepitaxial Directed Self-Assembly Substrates. (Under Preparation)
4. A. Chandra*, R. Nakatani*, T. Uchiyama, Y. Seino, H. Sato, Y. Kasahara, T. Azuma, T. Hayakawa Direct In Situ Observation of the Early-Stage Disorder-Order Evolution of Perpendicular Lamellae in Thermally Annealed High-χ Block Copolymer Thin Films. *Adv. Mater. Interfaces* **2019**, *6*, 1801401. (Front Cover)
5. R. Nakatani*, A. Chandra*, T. Uchiyama, Y. Nabae, T. Hayakawa Dynamic Ordering in High-χ Block Copolymer Lamellae Based on Cross-Sectional Orientational Alignment. *ACS Macro Lett.* **2019**, *8* (9), 1122-1127. (Supplementary Cover)
6. R. Nakatani, H. Takano, A. Chandra, Y. Yoshimura, L. Wang, Y. Suzuki, Y. Tanaka, R. Maeda, N. Kihara, S. Minegishi, K. Miyagi, Y. Kasahara, H. Sato, Y. Seino, T. Azuma, H. Yokoyama, C. K. Ober, T. Hayakawa Perpendicular Orientation Control without Interfacial Treatment of RAFT Synthesized High-χ Block Copolymer Thin Films with sub-10 nm Features Prepared via Thermal Annealing *ACS Appl. Mater. Interfaces* **2017**, *9* (37), 31266-31278. (Forum Article)
7. R. Nakatani, H. Takano, L. Wang, A. Chandra, Y. Tanaka, R. Maeda, N. Kihara, S. Minegishi, K. Miyagi, Y. Kasahara, H. Sato, Y. Seino, T. Azuma, C. K. Ober, T. Hayakawa Precise Synthesis of Fluorine-Containing Block Copolymers via RAFT. *J. Photopolym. Sci. Technol.* **2016**, *29* (5), 705-708.

Other Publications

8. R. Rattanakawin, K. Yoshimoto, A. Chandra, T. Hayakawa, M. Tosaka, S. Yamago, M. Ohshima Highly Ordered Nanocellular Polymeric Foams Generated by UV-Induced Chemical Foaming. *ACS Macro Lett.* (Under Review)
9. L. Dong, A. Chandra, K. Wylie, R. Nakatani, Y. Nabae, T. Hayakawa The Role of Liquid Crystalline Side Chains for Long-range Ordering in the Block Copolymer Thin Films. *J. Photopolym. Sci. Technol.* **2020**, *33* (5), 529-536.
10. K. Wylie, L. Dong, A. Chandra, Y. Nabae, T. Hayakawa Modifying the Interaction Parameters of a Linear ABC Triblock Terpolymer by Functionalizing the Short Reactive Middle Block to Induce Morphological Change. *Macromolecules* **2020**, *53* (4), 1293-1301.
11. A. Cintora, H. Takano, M. Khurana, A. Chandra, T. Hayakawa, C. K. Ober Block Copolymers Containing Stable Radical and Fluorinated Blocks with Long-Range Ordered Morphologies Prepared by Anionic Polymerization. *Polym. Chem.* **2019**, *10*, 5094-5102.
12. K. Azuma, T. Komamura, A. Chandra, F. Kato, Y. Nabae, T. Hayakawa Inducing Periodic Nanostructures and Porosity in Polythiophene Films via Block Copolymer Templating. *J. Polym. Sci., Part A: Polym. Chem.* **2019**, *57*, 1105-1112.
13. Y. Yoshimura, A. Chandra, Y. Nabae, T. Hayakawa Chemically Tailored High-χ Block Copolymers for Perpendicular Lamellae via Thermal Annealing. *Soft Matter* **2019**, *15*, 3497-3506. (Front Cover)
14. T. Azuma, Y. Seino, H. Sato, Y. Kasahara, K. Kodera, K. Miyagi, M. Shiraishi, R. Matsuki, T. Kosaka, T. Himi, S. Nagahara, A. Chandra, R. Nakatani, T. Hayakawa, K. Yoshimoto, T. Omosu, M. Takenaka Defect Dynamics in Directed Self-Assembly of Block Copolymers. *Proc. SPIE* **2018**, *10586*, 105860S.
15. L. Gao, A. Chandra, Y. Nabae, T. Hayakawa Inducing Defects in Ordered Mesoporous Carbons via the Block Copolymer-Templated High-Temperature Carbonization of Nitrogen-Containing Polymeric Precursors. *Polym. J.* **2018**, *50*, 389-396. (Front Cover)

16. F. Kato*, A. Chandra*, H. Asano, H. Shimomoto, E. Ihara, M. Tokita, T. Hayakawa Self-Assembly of Hierarchical Structures using Cyclotriphosphazene-Containing Poly(substituted methylene) Block Copolymers. *ACS Macro Lett.* **2018**, *7* (1), 37-41.
17. F. Kato, S. Sugimoto, A. Chandra, T. Hayakawa Morphology Control and Inducing a Curvature on the Domain Interface by Increasing the Steric Bulk of Polymethacrylate in POSS-containing Diblock Copolymers. *J. Polym. Sci., Part A: Polym. Chem.* **2017**, *55* (13), 2234-2242.
18. F. Kato, A. Chandra, S. Horiuchi, T. Hayakawa Morphological Dependence on the Addition of a Soft Middle Block Segment to Rigid POSS-Containing Triblock Copolymers for Forming Cylindrical Nanostructures. *RSC Adv.* **2016**, *6*, 62172-62180.
19. L. Gao, K. Azuma, Y. Kushima, K. Okuhara, A. Chandra, T. Hayakawa Well-Ordered Nanostructure Formation of Wholly Aromatic Poly(amic acid)s in Spin-casted Thin Films. *J. Photopolym. Sci. Technol.* **2016**, *29* (2), 247-250.

    *These authors contributed equally.

List of Presentations

1. Ordering and Defectivity in Sub-10 nm Perpendicular Lamellar Block Copolymer Thin Films

   A. Chandra, R. Nakatani, T. Uchiyama, Y. Nabae, T. Hayakawa

   APS March Meeting 2020 (Oral) *Denver, CO, U.S.A.* (Mar 2, 2020; Canceled due to COVID-19)
2. Comparing the Surface Affinities of Perpendicular Lamella-Forming Polymers

   A. Chandra, R. Nakatani, T. Uchiyama, Y. Nabae, T. Hayakawa

   3rd Workshop on Plastic Electronics and Related Science and Technology (Poster) *Tokyo, Japan* (Nov 18, 2019)
3. Growth of Perpendicular Lamellae in High-χ Block Copolymer Thin Films

   A. Chandra, R. Nakatani, T. Uchiyama, Y. Nabae, T. Hayakawa

International Student Workshop on Aromatic Functional Polymers (Oral) *Tokyo, Japan* (Nov 14, 2019)

4. Development of Ordered Structures and Defects in Sub-10 nm Perpendicular Lamellar Thin Films

   A. Chandra, R. Nakatani, T. Uchiyama, Y. Nabae, T. Hayakawa

   5th International Symposium on DSA (Oral) *Milan, Italy* (Oct 17, 2019)

5. Evolution of Perpendicular Lamellae in High-χ Block Copolymers via In Situ Atomic Force Microscopy

   A. Chandra, R. Nakatani, T. Uchiyama, Y. Nabae, Y. Seino, H. Sato, Y. Kasahara, T. Azuma, T. Hayakawa

   4th International Symposium on DSA (Oral) *Sapporo, Japan* (Nov 12, 2018)

6. In Situ AFM Studies of Perpendicular Lamellae Evolution

   A. Chandra, R. Nakatani, T. Uchiyama, Y. Nabae, T. Hayakawa

   Japan-Korea Joint Symposium (JKJS) on Polymer Science 2018 (Poster) *Sapporo, Japan* (Jul 24, 2018)

7. Evolution of Ordered Patterns and Defects in Strongly-Segregating Block Copolymer Thin Film Surfaces and Cross-Sections

   A. Chandra, T. Hayakawa

   Research Group on Precisely Designed Network Polymer (Poster) *Tokyo, Japan* (Mar 19, 2018; Poster Award)

8. Time-Lapsed AFM Observations of the Evolution of Perpendicular Lamellae in Thermally-Annealed BCP Thin Films

   A. Chandra, R. Nakatani, Y. Seino, H. Sato, Y. Kasahara, P. Jiravanichsakul, T. Azuma, T. Hayakawa

   The Society of Polymer Science, Japan (SPSJ) 66th Symposium on Macromolecules (Oral) *Matsuyama, Japan* (Sep 20, 2017)

9. Bulk and Thin Film Morphological Studies of Fluorine-Containing Block Copolymers Synthesized via RAFT

A. Chandra, R. Nakatani, T. Hayakawa

IUPAC-PSK40 International Conference on Advanced Polymeric Materials (Poster) *Jeju, Korea* (Oct 6, 2016)

Acknowledgements

The work in this thesis was carried out at the Hayakawa Group, Tokyo Institute of Technology, School of Materials and Chemical Technology, Department of Materials Science and Engineering in Tokyo, Japan between September 2017 and July 2020, and was only realized with the help and support of numerous people.

Firstly, I would like to extend my deepest gratitude to my advisor, Prof. Teruaki Hayakawa, and Prof. Yuta Nabae. The completion of this thesis and the foundations that have been built for my future career could not have been realized without their guidance, insight, and advice. Under their tutelage, I have gained significant experience in not just academic research on polymer synthesis and thin film physics, I learned what it takes to be a responsible researcher. I was also given the opportunities to write proposals and obtain my own research grants and scholarships. Thank you, I am deeply grateful for the help and support.

In no particular order, I would also like to thank Prof. Hidetoshi Matsumoto, Prof. Toshiaki Ougizawa, Prof. Takeshi Serizawa, and Prof. Masatoshi Tokita for being part of my doctoral thesis committee. Thank you for taking the time and consideration for helping me review and improve on my work.

Additionally, I am extremely grateful to Prof. Kenji Yoshimoto and Prof. Mikihito Takenaka of Kyoto University, and Dr. Tsukasa Azuma and his team at the Evolving Nano-Process Infrastructure Development Center (EIDEC). Working with Prof. Yoshimoto, Prof. Takenaka, and Dr. Azuma under the EIDEC project has been extremely fruitful, yielding great advances in our understanding of the fundamental physics and behaviors behind the directed self-assembly (DSA) process of block copolymers.

Furthermore, I am thankful for having worked with Prof. Hiroshi Jinnai and Prof. Takeshi Higuchi of Tohoku University. Learning more about TEM definitely helped in finessing my approach towards studying BCP self-assembly.

I would also like to thank Prof. Atsushi Goto, of the Dept. of Chemistry at Nanyang Technological University, Singapore for taking me in as an exchange student from December 2018 to February 2019. Working with him on the development of random copolymer brushes using surface-initiated and iodine-mediated reversible deactivation radical polymerization has significantly advanced my understanding on radical polymerization and surface chemistry. Additionally, the study abroad experience gave me the opportunity to investigate the career paths available in Singapore, allowing me to expand my horizons and potential future plans. I also extend my thanks to the members of the Goto group for their hospitality and help with experiments.

I would like to thank Prof. Michele Perego of CNRS for the highly insightful discussions at conferences and especially for the invitation to join their lab in Italy to work together on a collaborative project investigating the extremely early stage evolution of self-assembly structures prepared using rapid thermal annealing. However, it was highly unfortunate that the COVID-19 outbreak put a stop to this international collaboration. Nevertheless, I do hope that there are further opportunities for our labs to collaborate in the future.

I am grateful to Dr. Makoto Muramatsu, Dr. Seiji Nagahara, and their team at Tokyo Electron Kyushu and Tokyo Electron for providing us with DSA samples, and for the numerous visionary talks at conferences throughout the years. With their help and support, I have managed to significantly improve my own understanding of the self-assembly process of BCPs and I hope to have been able to return their contributions as well.

I thank Prof. Yuji Wada of the Dept. of Applied Chemistry at the Tokyo Institute of Technology for his support with the scanning electron microscopy experiments. I am also grateful to Ryohei Kikuchi and Jun Koki of the Ookayama Materials Analysis Division, Tokyo Institute of Technology for their support and for showing me the ropes around ultramicrotomy and TEM.

I am also deeply grateful to Prof. Padma Gopalan, of the Dept. of Materials Science and Engineering at the University of Wisconsin–Madison (UW-Madison). Having mentored me as an undergraduate student at the UW-Madison, I began my foray into research on polymers in her group. Since then, we have continued to meet and have insightful discussions at conferences and during her visits to our group. I was also able to meet my current advisor, Prof. Hayakawa, when I was in her group in 2014. Therefore, I am where I am today precisely because I had joined her group so many years ago. Thank you for the support and advice over the years.

I would also like to show my gratitude to Dr. Urs Frey and Dr. Florent Seichepine who mentored me during my internship at RIKEN QBiC in 2014. Particularly, it was Florent who first taught me how to use an AFM, a JPK Instruments NanoWizard 2 no less, an SEM, and introduced me to working in a clean room and how to prepare a simple circuit using a traditional resist and photolithographic machine. These past experiences have prepared me well till now and I hope to continue to build upon my experiences as I embark on my career in the microelectronics industry.

In addition, I would like to thank the many professors I met at numerous conferences around the world. In no particular order, I am grateful to Prof. Christopher K. Ober (Cornell University, U.S.A.), Prof. Chris Ellison (University of Minnesota, U.S.A.), Prof. Paul Nealey (University of Chicago, U.S.A.), Prof. Du Yeol Ryu (Yonsei University, Korea), Prof. Chrisophe Sinturel (CNRS/Université d'Orléans, France), and Prof. Sang Ouk Kim (KAIST, Korea) for the wonderful discussions we had at numerous occasions over the years.

I am also grateful to the Ministry of Education, Culture, Sports, Science and Technology – Japan (MEXT) for providing me with financial support during my doctoral studies. I also thank the staff at the International Student Exchange Division and the Student Support Center, Tokyo Institute of Technology for their help with matters pertaining to my

scholarship. Additionally, I thank the TEPCO Memorial Foundation for their research grant to partially support my research endeavors.

I would also like to thank the former and current members of the Hayakawa Group for the discussions, friendship, and support throughout the years. In particular, I would like to especially thank Ryuichi Nakatani for providing most of the Matlab codes used for the quantitative analysis of the AFM images, and also Takumi Uchiyama for sharing some of his polymers with me. I am deeply grateful for the support from my parents, my family, my dear partner Chun Mei, and also my close friends; special mention to Clarence for listening to my near-daily complaints and sighs. Without their care and encouragement, I would not have been able to pursue my studies and research interests. Thank you for everything.

Alvin Chandra